Vibrational spectroscopy of adsorbed hydrogenous species studied by inelastic incoherent neutron scattering

Ian James Braid

Ian James Braid

ABSTRACT

VIBRATIONAL SPECTROSCOPY OF ADSORBED HYDROGENOUS SPECIES STUDIED BY INELASTIC INCOHERENT NEUTRON SCATTERING

Inelastic incoherent neutron scattering (INS) spectra of hydrogen strongly chemisorbed at coverages of greater than one monolayer on Pd black (Drijfhout, Amsterdam) were obtained (77K) without interference from adsorbed or type-C adsorbed hydrogen. The spectra were assigned by comparison with the vibrational spectra of transition-metal hydridocarbonyl compounds and indicated the occupation by H of two-fold bridging and terminal sites, the relative population of the terminal sites increasing at higher hydrogen coverage.

INS spectra (*ca* 20 to 850 cm^{-1}; 10, 16 and 77K) of *c*-C_3H_6 adsorbed in $Co_4Na_4Al_{12}Si_{12}O_{48}$, and of *c*-$C_3H_6$ and *c*-C_3D_6 in $Mn_{3.5}Na_5Al_{12}Si_{12}O_{48}$ zeolite were consistent with C_{3v} symmetry of the M(II)-cyclopropane sorption complexes (M=Co or Mn).

INS spectra (320 to 2230 cm^{-1}; 77K) of Kadox 25 ZnO and H_2 adsorbed on ZnO were obtained. The ν_s and ν_δ modes of type I Zn-H surface species were observed at 829 and 1708 cm^{-1}. Recent assignments in the literature of the ν_δ mode of type I O-H species and the ν_{as} mode of type II $Zn^{H}Zn$ species to weak IR bands at 850 and 1475 cm^{-1} respectively were not corroborated by the INS results. The INS spectrum of ZnO contained an intense feature at 1346 cm^{-1} which was unchanged on H_2 adsorption, and assigned to bulk impurities. Raman and IR data of ZnO were also discussed.

INS spectra (*ca* 20 to 850 cm^{-1}; 10 and 77K) of C_2H_2 and C_2D_2 adsorbed in partially Ni^{++} ion-exchanged zeolite-Y indicated that the admolecules were non-linear (C_{2v} symmetry) and laterally bonded to the surface.

Bands centred at 774, 684, 546 and 75 cm^{-1} in the INS spectra (*ca* 20 to 850 cm^{-1}; 10 and 77K) of H_2O adsorbed in $Ca_6Al_{12}Si_{12}O_{48}$ zeolite at coverages of one H_2O molecule per Ca^{++} ion or less were assigned to the wagging, twisting and rocking modes and to the doubly degenerate hindered translations parallel to the surface, respectively of H_2O adsorbed at Ca^{++} sites.

INS spectra (10K) of H_2 adsorbed by $Zn_{4.5}Na_{3.0}Al_{12.5}Si_{11.5}O_{48}$ zeolite showed bands at 72 and 155 cm^{-1}, assigned to the tunnelling transitions $E_1 \rightarrow E_2$ and $E_1 \rightarrow B$ respectively between the sublevels of the ground torsional state of a rigid H_2 rotor, confined to a plane parallel to the adsorbed surface, in a six-fold potential well of barrier height 29±3 kJ mol^{-1}.

VIBRATIONAL SPECTROSCOPY OF ADSORBED HYDROGENOUS SPECIES STUDIED BY INELASTIC INCOHERENT NEUTRON SCATTERING

by

IAN JAMES BRAID

A candidate for the Degree of Doctor of Philosophy

Department of Chemistry
University of Durham.

October 1983

To my parents and C.D.

ACKNOWLEDGEMENTS

I am indebted to my supervisors, Dr. J. Howard and the late Professor T.C. Waddington for their help, encouragement and enthusiasm towards the work in this thesis, and my sincere gratitude is due to them. I would also like to thank Dr. J. Tomkinson (Neutron Beam Division, Rutherford Laboratory) for helpful discussions.

Gratitude is also expressed to Mr. D.H.C. Harris and staff at the Atomic Energy Research Establishment, Harwell, and to A. Murani at the Institut Laue-Langevin, Grenoble, for their patience and guidance in operation of the neutron spectrometers. The provision of an S.E.R.C./CASE studentship by the Science and Engineering Research Council and the United Kingdom Atomic Energy Authority is acknowledged.

Finally, I would like to thank Mrs. M. Wilson for her secretarial skill in typing the manuscript.

I. J. BRAID
Durham, 1983.

DECLARATION

The work described in this thesis has not been submitted for any other degree and is the original work of the author except where acknowledged by reference.

Work in this thesis has formed the whole, or part, of the following publications:

(1) Inelastic neutron scattering study of hydrogen adsorbed on impure palladium black.
Braid, I.J., Howard, J. and Tomkinson, J.
Chem.Soc., Faraday Trans.2, 79, 253-262, 1983.

(2) Spectroscopic studies of hydrogen adsorbed on zinc oxide (Kadox 25).
Howard, J., Braid, I.J. and Tomkinson, J.
J.Chem.Soc., Faraday Trans.1, in press (1983).

CONTENTS

CHAPTER ONE

INTRODUCTION

1.1 Introduction

In this thesis we present the vibrational spectra of small hydrogenous molecules, such as acetylene, cyclopropane or hydrogen, adsorbed at a variety of surfaces, including variously ion-exchanged zeolites, palladium black and zinc oxide. An overview of the adsorbent properties is given in Section 1.4.

Incoherent inelastic neutron scattering (INS) was used as our primary technique for obtaining the vibrational spectra of the adsorbed species, the principle advantages of INS over the more familiar spectroscopies such as infrared (IR) or Raman being the high sensitivity of INS to vibrational modes involving hydrogen atom displacements and the facility with which low frequency transitions, say below 500 cm^{-1}, can be observed.

On molecular adsorption, a non-linear molecule may lose up to six degrees of translational and rotational freedom giving rise to a maximum of six hindered translational and torsional modes of the admolecule with respect to the surface. In the case of a linear molecule, a maximum of five degrees of freedom and five hindered translations and torsions are involved. In the main, these hindered modes occur at low frequencies, say below 500 cm^{-1}, and thus INS is well-suited for the study of such modes, particularly if displacements of hydrogen atoms are involved.

The significance of vibrational data on adsorbed species is outlined in Section 1.2.

1.2 Vibrational spectroscopy and heterogeneous catalysis

Very many industrial chemical processes rely on heterogeneous catalysis at the gas/solid interface. Such reactions proceed by adsorption of at least one reactant and knowledge of the nature of the adsorbed species, of details of the bonding to the catalyst and of the structure of the surface itself, is of importance.

Vibrational spectroscopy allows direct observation of the modes of the adsorbate-adsorbent bond(s) and thus provides information on the nature and strength of such bonds.

The identification of the internal modes of vibration of an admolecule allows inferences to be drawn on the structure of the adsorbed species. Observation of bands due to the internal modes of the admolecule which are greatly different in frequency, intensity and shape to those of the free reactant is strong evidence of chemisorption and the formation of new chemical species at the surface. On the other hand, if the spectrum of the admolecule differs from that of the free molecule only in small intensity and frequency shifts of the bands, then this is suggestive of physiosorption, but does not of itself rule out chemisorption.[1]

The conclusions drawn from a vibrational spectroscopic experiment on the structure of the adsorbent and on possible changes of the surface during adsorption are often more limited than those appertaining to the adsorbate. This is partly because of the interplay of three features of the adsorbent, *viz*: the bulk properties of the solid; the overall properties of the surface and their perturbation by the adsorbate; and the properties of the surface local, on an atomic scale, to the admolecule.

For metals and semiconductors, these interactions are particularly important in regard to the electronic properties and possible surface reconstructions on adsorption.[1,2] Such phenomena are better studied by electrical, *eg* work function change,[1] and diffraction, *eg* LEED,[3] methods rather than by vibrational spectroscopy.

Thus vibrational spectroscopy can be used to determine the structure of intermediates involved in catalysis at the gas/solid interface. Although we have not carried out such experiments, the changes in intensity of a vibrational band during the course of a reaction can provide kinetic and mechanistic information, provided that the band can be associated with a particular species.[1] However, two caveats must be borne in mind when extending the results of experiments in surface science to catalysts as used in industry. Firstly, adsorption is usually studied in the laboratory using very much milder conditions and chemical components of far greater purity than are employed in industrial processes. Secondly, the dominant species on a surface is not necessarily the intermediate *via* which a given catalytic reaction proceeds.

A knowledge of the energy levels of an admolecule allows calculation of the molecular partition function, Z, and hence of various thermodynamic properties, *eg* the standard molar enthalpy relative to the absolute zero energy.[4] However, these calculations can only be made for favourable cases. For example, in order to evaluate the vibrational contribution to Z, not only must the normal mode frequencies be known but in addition all of the anharmonicity constants or as many of the overtone frequencies of each normal mode up to a level that their contribution to Z becomes negligible.[5]

1.3 A survey of vibrational spectroscopies for adsorbed species

This survey is written with particular regard to the adsorbents studied in this thesis, *viz* zeolites, a semiconducting metal oxide (ZnO) and Pd black.

1.3.1 Infrared spectroscopy

Infrared (IR) transmission is the most common method of detecting the vibrational modes of adsorbed species.[6-9] High surface area samples are needed so that the resultant IR spectrum contains a considerable contribution from the surface species as distinct from the bulk of the sample. Species adsorbed on a variety of surfaces may be studied, *eg* insulating and semiconducting oxides, zeolites, supported and bulk metal powders.[6-9] The principle disadvantage of IR spectroscopy is that absorptions from the substrate often arise, masking bands from the admolecules. In the case of self-supporting zeolite samples, wide regions of complete absorption commonly occur below 1200 cm^{-1}.[10] Furthermore, conventional light sources are of low intensity in the low wavenumber region, say below 300 cm^{-1}, and thus it is difficult using transmission IR to observe a large portion of the *ca* 0 to 500 cm^{-1} region in which bands to modes of adsorbate-adsorbent bonds often arise. The bands observed in many IR studies of adsorbed species are frequently restricted to the strongly IR active internal modes of the admolecule.[6-9]

In addition to the usual electromagnetic selection rules, a surface selection rule[11] operates in the IR spectra of molecules adsorbed at highly polarisable surfaces such as metals. Only those modes with a component of the dipole-moment-

change perpendicular to the surface are IR active.[11]

Transmission Fourier transform IR spectroscopy (FTIR) has been used to study adsorption by strongly IR absorbing or scattering solids such as CaO and MgO.[9,12] The FTIR technique has the advantage over dispersive methods of shorter observation times and therefore can be used to minimise possible changes in the sample during data acquisition. Time resolved spectra of surface species are more readily obtained by FTIR than by dispersive IR methods which may be limited to a narrow frequency range unless the time constant of the observed reaction is large compared to the time needed for data collection.[9] The formation of $NO^{\delta-}$ and $NO^{\delta+}$ species during NO adsorption on silica supported Rh has been followed using time resolved FTIR.[9]

The sensitivity of IR spectroscopy can be improved by recording reflectance spectra. Using diffuse reflectance Fourier transform IR spectroscopy it is possible to obtain vibrational spectra of species adsorbed by strongly absorbing materials from *ca* 800 cm^{-1} extending to the near IR region.[12] For example, the method has been used[12] to study the adsorption of C_2H_4 by a Mn(II)A zeolite in the range 4000 to 7500 cm^{-1}. The spectrum showed bands assigned to overtone and combination modes of C_2H_4 molecules held by a weak, π-bonding interaction at specific sites. Diffuse reflectance spectroscopy can be extended to the ultraviolet region, up to *ca* 40,000 cm^{-1}, and has been used to study the electronic properties of transition metal ions in zeolites.[13]

Multiple internal reflection IR spectroscopy is sufficiently sensitive to study the adsorption of monolayer

films.[14] However, a transparent reflection element is required which restricts the range of suitable adsorbents, *eg* adsorption by bulk metals is difficult to study with this technique.[14]

High sensitivity is achieved by IR ellipsometric spectroscopy which has been used to obtain vibrational spectra of less than 0.01 monolayer coverages of CO on Ni(100) single crystal planes.[15] This technique is a modification of IR specular reflectance spectroscopy in which the polarisation of the light is modulated prior to incidence on the sample. IR ellipsometric spectroscopy is principally sensitive to the adsorbate-adsorbent interface and is largely insensitive to any ambient gas phase.[15]

1.3.2 Raman Scattering

Species adsorbed on oxides, on bulk metals and, with some restrictions, on zeolites can be studied using Raman scattering over a wide frequency range, 50 to 4000 cm^{-1}.[16,17] Raman spectroscopic studies of zeolites are very often hampered by the weakness of the resultant scattering and, especially when transition metal ions are present, by intense fluorescence backgrounds.[16,17] Most published Raman studies of species adsorbed by zeolites are restricted to alkali and alkaline earth metal ion-exchanged substrates.[16,17] For such zeolites, the fluoresence can be reduced by calcination at, say 723K.[17] The problem of the fluoresence backgrounds could be overcome in general by using picosecond pulsed lasers and gated detectors.

The sensitivity of laser Raman spectroscopy is just sufficient to study adsorption by metal single crystals, *eg* weak

Raman bands have been reported for CO on Ni(111), Ni(110) and Ni(100) crystal planes.[18] Raman studies of species adsorbed from the gas phase on metal blacks and supported metal powders have also been reported[16] but the observed Raman bands are generally weak because of considerable light absorption by the darkly coloured substrates.

Precautions must be taken in Raman studies of weakly adsorbed species that the intense laser beam does not cause desorption.

1.3.3 Electron energy loss spectroscopy

Electron energy loss spectroscopy (EELS) can be used to observe the vibrational modes of species adsorbed on metal surfaces.[3,19,20] EELS is of similar sensitivity to transmission IR spectroscopy and can be used to study adsorption at single crystal metal surfaces. The accessible energy range is *ca* 300 to 4000 cm^{-1} and can be extended to the visible region.[19] Amongst the disadvantages of EELS are the modest resolution (*ca* 40 to 80 cm^{-1}) and the fact that the overpressure of the adsorbate gas must be less than *ca* 5 x 10^{-5} torr, precluding high pressure chemisorption studies.[19] A molecular transition is EELS active for scattering in the specular direction if it is allowed by both the dipole-moment-change and surface selection rules, whereas all normal modes are active for out-of-specular scattering.[19,20]

1.3.4 Inelastic incoherent neutron scattering

Electromagnetic and the surface selection[11] rules do not apply to inelastic incoherent neutron scattering (INS).

All normal modes of vibration are INS active provided they involve displacement of nuclei with non-zero incoherent neutron scattering cross-sections, σ_{inc}. The value of σ_{inc} for ^{1}H is an order of magnitude greater than that of any other nucleus which gives rise to an effective INS selection rule: those modes involving significant displacements of ^{1}H nuclei will dominate the INS spectra of hydrogenous materials.[22]

Being uncharged, neutrons have a high penetrability into matter and are not preferentially scattered by surfaces. A neutron may have travelled almost the full depth of a sample before being scattered. For study by INS, an adsorbate must scatter much more strongly than its adsorbent and an ideal system is a non-hydrogenous catalyst of high surface area supporting a hydrogenous adsorbate. The flux of monochromated neutrons from present-day sources is too low to study adsorption at single crystal surfaces. The adsorbents used in this thesis are all weak incoherent neutron scatterers and the lowest surface area material used was ZnO ($7.8\ m^2g^{-1}$). Because of the greater quantity of adsorbent compared to the adsorbate used in our INS experiments, the scattering from the adsorbent is not negligible but it can be subtracted from spectrum of the adsorbent plus adsorbate since the scattering intensity from the adsorbed species is found to be comparable to, and sometimes greater than, that of the background material alone.

The low effective (*ie* flux limited) sensitivity of INS enables spectra to be obtained of adsorbates at solid surfaces in equilibrium with their own vapour, unlike EELS.

In contrast with IR spectroscopy, vibrational modes of adsorbate-adsorbent bonds are readily observed using INS.

Because of the different selection rules, INS, IR and Raman data are complementary.[21,22]

The principle disadvantages of INS are the long counting times, up to 36 hours, needed for adequate statistics and, on occasion, the moderate resolution. However, it is our experience that the intrinsic INS band widths of adsorbate-adsorbent vibrations are often greater than the width of the spectrometer resolution function. The best resolution ($\Delta E/E$) of our INS data is *ca* 2%, obtained using the IN4 instrument (Chapter Four).

Further general comments on neutron scattering are given in Section 1.5.

1.4 Adsorbents studied - generalities and industrial applications

1.4.1 Zeolites

Some general comments regarding zeolites are given here but detailed discussion of their structure and properties is reserved until Chapter Three.

Zeolites are crystalline, hydrated aluminosilicates which, as synthesised or as found in nature, contain cations of the group IA and group IIA metals.[23] These cations are readily replaced by ion-exchange with other monovalent or polyvalent cations, *eg* transition metals or rare-earths.

Zeolites may be classified (Chapter Three) according to the structure of the aluminosilicate framework which extends in three dimensions, forming interconnected channels and voids in which are located the water molecules and metal cations. Intrazeolite water is, in general, easily removed and those

zeolites which retain their structure on dehydration are termed molecular sieves.[23] The cavities of a dehydrated zeolite are available for the adsorption of host molecules and the maximum size of the host molecule which can be accommodated is determined by the dimensions of the cavities and the locations and radii of the cations. Within a zeolite, the adsorbate may bond to a metal cation and/or to the aluminosilicate framework *eg* by hydrogen bonding to the oxygen ions. Because of the large electric field within the voids and because competing ligands (*eg* H_2O or O_2) can be removed by prior evacuation, the intrazeolitic metal ions may be found in unusual oxidation states or bonded to otherwise weakly coordinating ligands. For example, stable complexes of *c*-C_3H_6 and *c*-N_3H_3 are formed with Mn(II) and Co(II) ions in zeolite cages.[24,25]

Zeolites have catalytic and selective sorption properties which depend on the framework structure and the Si/Al ratio and can be readily further modified by ion-exchange. The possible sorption sites and the geometry of the sorption complexes can be determined by X-ray diffraction.[26]

The major industrial use of zeolites is as cracking catalysts in the refining of crude oil (Table 1.1). This accounts for over 95% of zeolite usage in the free world, and in the U.S.A., one third of all processed crude oil is treated in this way, amounting to 5×10^6 barrels a day in 1979.[27]

The second most important industrial usage of zeolites is as a component in the dual functional catalysts employed in hydrocracking (Table 1.1). In this process, low grade, high boiling point oil distillates are upgraded by cracking followed by hydrogenation of unsaturates in the product

to yield heating and fuel oils, petrochemical feedstocks, *etc.* Hydrocracking accounted for 1.5 x 10^6 barrels of oil per day in the U.S.A. in 1979.[27]

TABLE 1.1 Principle Industrial Usage of Zeolite Catalysts, adapted from ref. 27.

Application	Annual usage tons	Principle zeolite catalysts[a]	Reference
Catalytic cracking	220,000	RX, RY, RHY RMgY	27
Hydrocracking	1,200	Co,Mo,W or Pt-Pd on mordenite	27
Petrochemicals, *eg.* benzene alkylation, xylene isomerisation	200	RY, ZSM-5	27
NO_X reduction by NH_3	<100	H-mordenite	27
H_2 production from H_2/hydrocarbon mixtures	-	-	29
O_2 production from air	-	zeolite 5A	29

Note a. R = rare earth.

Breck[28] has recently discussed the less common commercial applications of zeolites. The potential industrial applications of zeolites are as yet far from fully exploited.[28] Probable future advances are in the continued development of processes based on the shape-selective ZSM-5 zeolites[30], and of zeolite catalysts for the cracking of low grade crude oils or for the control of pollutants to meet environmental legislation.[27,28]

1.4.2 Palladium

Table 1.2 lists the estimated annual utilisation of Pd in the U.S.A. and includes figures for Pt for comparison.

In the chemical industries, Pd supported on charcoals and alumina is employed as a selective catalyst for hydrogenation and dehydrogenation of intermediates in the manufacture of plastics, synthetic fibres, rubbers, dyestuffs, pesticides, pharmaceuticals and for the purification of gas streams.[31] The extensive use in the U.S.A. of Pd and other group VIIIB metals in the oxidation to CO_2 and H_2O of CO and hydrocarbons in the exhaust from the internal combustion engine (Table 1.2) is expected to decline in future with the development of cheaper catalysts and modification of engine design, *etc.*[31]

TABLE 1.2 Estimated annual consumption of Pd and Pt in the U.S.A., 1979-1983, from ref. 31.

Application	Annual usage, kg x 10^2	
	Pt	Pd
Exhaust control catalysts for vehicles	235	53
Catalysts for chemical processing	40	75
Catalysts for petroleum processing	31	2.7
Catalysts for NH_3 oxidation	17	0.3
Others (non-catalytic)	11	16

1.4.3 Zinc Oxide

Zinc oxide is used industrially as an adsorbent for the removal of H_2S and other sulphur containing gases from petroleum and natural gas.[32-34] In terms of the nature of surface intermediates and reaction mechanisms, zinc oxide is one of the best characterised oxide catalysts.[35] However, the precise nature of some surface species formed by hydrogen adsorption on zinc oxide is still not clear[35] and thus we undertook an INS study of hydrogen adsorption on zinc oxide in an attempt to further characterise these species (Chapter Seven).

1.5 Neutron Scattering

As well as measurement of the vibrational spectrum, neutron scattering may be used to give a wide range of information on the structure and dynamics of condensed matter, depending on the nature of the sample and how the neutron scattering experiment is carried out. There are several properties of the neutron which make neutron scattering a useful technique in the study of condensed matter:[36-41]

(a) Firstly, the kinetic energies of thermal neutrons are of the same order of magnitude as the spacing of many energy levels in molecules. The energy of a transition may be accurately measured by choosing the incident neutron energy such that the transfer of energy between the neutron and the excitation involves a large percentage change in the neutron energy. Energy transfers from 1×10^{-4} to 3×10^{3} cm^{-1} can be investigated at the Institut Laue-Langevin (I.L.L.),Grenoble,[42] facilitating the study of molecular vibrations, rotations and reorientations, nuclear spin and tunnelling transitions.

(b) Secondly, the wavelength of a thermal neutron is of similar magnitude to the interatomic distances in condensed matter and interference effects will arise in the scattered neutron waves, dependent on the atomic structure.[36] The available neutron wavelength range at the I.L.L. is 0.5 to *ca* 100Å [42] and as well as crystal diffraction studies, investigations of the overall structure of, say, polymers or colloid particles are possible.[36]

(c) Thirdly, the neutron, being uncharged, has a high penetrability into matter. Except for magnetic atoms, neutrons are principally scattered by nuclear forces. The nuclear

interaction varies in an irregular fashion across the periodic table and differs for each nuclide of a given element.[37] This contrasts with the rapid increase of the X-ray scattering amplitude with atomic number. Neutron diffraction is therefore better suited than X-ray diffraction to accurately locating the positions of hydrogen (as ^{2}H) and other light atoms in crystals which also contain heavier atoms.

(d) Fourthly, the neutron has a magnetic dipole moment and thus interacts with unpaired electrons in a sample. Elastic magnetic scattering yields data on the spatial arrangement of magnetic atoms and the distribution of unpaired electrons.[38] The energies of magnetic transitions are obtained from inelastic magnetic scattering.[38] In this thesis we are concerned entirely with nuclear scattering and magnetic interactions will not be considered further.

A given sample will scatter neutrons both elastically and inelastically. Both the elastic and the inelastic components may generally be further divided into coherent and incoherent parts, giving four possible types of scattering. The information obtained from each type of scattering is as follows. Elastic coherent scattering is the familiar Bragg diffraction.[39] Inelastic coherent scattering gives data on the phonon modes of crystals and their dispersion relations.[40] Elastic incoherent scattering gives information on the geometry and dynamics of reorientational and diffusive motions of molecules.[41] Inelastic incoherent scattering, hereafter abbreviated to INS, is sensitive to the dynamics of individual atoms of a sample.[22] The vibrational density of states of the sample may be determined from INS data, weighted by the amplitude of

of vibration, by the incoherent scattering cross section and by the Debye-Waller factor of the scattering nucleus (Chapter Two). It is with INS that this thesis is concerned.

REFERENCES

1. Ponec, V., Knor, Z. and Cerny S., Adsorption on Solids, Butterworths, London, 1974.

2. Rhodin, T.N. and Ertl, G.(Eds.), The Nature of the Surface Chemical Bond, North Holland, Amsterdam, 1979.

3. Ertl, G. and Kuppers, J., Low Energy Electrons and Surface Chemistry, Verlag Chemie, Weinheim, 1974.

4. Frankiss, S.G. and Green, J.H.S. in Chemical Thermodynamics (Chem.Soc.London), 1, 268, 1973.

5. Burdett, J.K. in Spectroscopy, vol.2 (Ed.Straughan, B.P. and Walker, S.), Chapman and Hall, London, 1976.

6. Little, L.H., Infrared Spectra of Adsorbed Species, Academic Press, New York, 1966.

7. Hair, M.L., Infrared Spectroscopy in Surface Chemistry, Dekker, New York, 1967.

8. Kiselev, A.V. and Lygin, V.I., Infrared Spectra of Surface Compounds, Wiley, New York, 1975.

9. Hair, M.L. and Bell, A.T. (Eds.), Vibrational Spectroscopies for Adsorbed Species, ACS Symposium Series, No. 137, Washington D.C., 1980.

10. Kadir, Z.A., Ph.D. Thesis, University of Durham, 1983.

11. Pearce, H.A. and Sheppard, N., Surf.Sci., 59, 205, 1976.

12. Klier, K. in ref. 9.

13. Kellerman, R. and Klier, K. in Surface and Defect Properties of Solids (Chem.Soc.London), 4, 1, 1975.

14. Allara, D.L. in ref. 9.

15. Fedyk, J.D. and Dignam, M.J. in ref. 9.

16. Morrow, B.A. in ref. 9.

17. Angell, C.L., J.Phys.Chem., 77, 222, 1973.

18. Stencel, J.M. and Bradley, E.B., J. Raman Spectrosc., 8, 203, 1979.

19. Dubois, L.H. and Somorjai, G.A. in ref. 9.

20. Thiel, P.A. and Weinberg, W.H. in ref. 9.

21. Hall, P.G. and Wright, C.J. in Chemical Physics of Solids and their Surfaces (Chem.Soc.London), 7, 89, 1978.

22. Howard, J. and Waddington, T.C. in Advances in Infrared and Raman Spectroscopy (Ed.Clark,R.J.H. and Hester, R.E.), Vol.7, Heyden, London, 1980.

23. Breck, D.W., Zeolite Molecular Sieves: Structure, Chemistry and Uses, Wiley Interscience, New York, 1974.

24. Cruz, W.V., Levng, P.C.W. and Seff, K., J.Am.Chem.Soc., 100, 6997, 1978.

25. Kim, Y. and Seff, K., J.Am.Chem.Soc., 99, 7057, 1977.

26. Seff, K. Acc.Chem.Res., 9, 121, 1976.

27. Vaughan, D.E.W. in Properties and Applications of Zeolites (Ed. Townsend, R.P.), Chem.Soc., London, 1980.

28. Breck, D.W. in ref. 27.

29. Armond, J.W. in ref. 27.

30. Kokotailo, G.T. and Meier, W.M. in ref. 27.

31. Chaston, J.C., Pt Metals Review, 26, 3, 1982.

32. Farha, F.F. Jnr., and Gardner, L.L., U.S. Patent U.S. 4,313,820 (1980).

33. Ikonnikov, V.G., Obysov, A.V., Titel'man, L.I., Dantsig, M.L., Sobolevskii, V.S., Shirokov, Yu.G., Furmer, Yu.V., Semenova, T.A., Khrutskii, O.P., and Povelko, V.Z., U.S.S.R. Patent SU 874,134 (1981).

34. Toa Nenryo, K.K.K., Jpn. Kokai Tokkyo Koho, JP 81,164,124 (1981).

35. John, C.S. in Catalysis (Chem.Soc.London), 3, 169, 1980.

36. Thomas, R.K. in Molecular Spectroscopy (Chem.Soc.London), 6, 232, 1979.

37. Bacon, G.E., Neutron Diffraction, Clarendon Press, Oxford,1975.

38. Squires, G.L., Introduction to the Theory of Thermal Neutron Scattering, Cambridge University Press, Cambridge, 1978.

39. Speakman, J.C. in Molecular Structure by Diffraction Methods (Ed. Truter, M.R.), Chem.Soc.London, vols.1-6, 1973-1978.

40. Pawley, G.S. in Chemical Applications of Thermal Neutron Scattering, (Ed.Willis, B.T.M.), Oxford University Press, Oxford, 1973.

41. Springer, T. in Quasielastic Neutron Scattering for the Investigation of Diffusive Motions in Solids and Liquids, Springer-Verlag, Berlin, 1972.

42. Neutron Beam Facilities at the I.L.L. High Flux Reactor, 1, Institut Laue-Langevin Report, Grenoble, 1981.

CHAPTER TWO

NEUTRON SCATTERING THEORY

2.1 Introduction

There are three mechanisms *via* which a neutron may be scattered by a molecule or by an isolated atom.[1-3] Firstly, scattering may arise from the interaction of the nuclear forces between the neutron and the nuclei of the target. Secondly, magnetic scattering may occur through interaction of the magnetic dipole moment of the neutron with the magnetic dipole moment of any unpaired electrons in the target. Thirdly, the magnetic dipole moment of the neutron may interact with the Coulomb field of the nuclei and electrons of the target. The nuclear and the purely magnetic interactions are of similar strength and the Coulomb interaction is negligible in comparison. In this chapter we are concerned with the nuclear scattering only.

Some basic properties of the neutron are listed in Table 2.1.

TABLE 2.1 Basic properties of the neutron, from ref.[3]

mass	=	1.675×10^{-27} kg
charge	=	0
spin	=	½
magnetic dipole moment	=	-1.913 nuclear magnetons
	=	-9.663×10^{-27} JT^{-1}

A thermal neutron with velocity $\underline{v}$ and mass m has a de Broglie wavelength λ given by

$$\lambda = \frac{h}{mv} \tag{2.1}$$

where h is Planck's constant. The neutron wavevector $\underline{k}$ is defined[3] to have magnitude

$$k = \frac{2\pi}{\lambda} \tag{2.2}$$

its direction being that of $\underline{v}$. The momentum of the neutron is thus $\hbar\underline{k}$. In addition, the neutron energy E is given by

$$E = \frac{1}{2} mv^2 = \frac{h^2}{2m\lambda^2} = \frac{\hbar^2 k^2}{2m} \qquad (2.3)$$

Inserting values for the physical constants, equations 2.3 become[3]

$$E = 42.18 \times 10^6 v^2 = \frac{660.2}{\lambda^2} = 16.72\ k^2$$

where E is in cm^{-1}, v in ms^{-1}, λ in $\mathring{A}$ and k in $\mathring{A}^{-1}$.

In any neutron scattering experiment, the neutrons involved may undergo changes in their momenta and/or their energy.[4] Let the incident neutrons have energy E_o and wavevector $\underline{k}_o$, and the scattered neutrons have energy E_f and wavefector $\underline{k}_f$. The scattering vector $\underline{Q}$ is defined by (Fig.2.1)

$$\underline{Q} = \underline{k}_o - \underline{k}_f$$

and hence $$|\underline{Q}| = (k_o^2 + k_f^2 - 2k_o k_f \cos 2\theta)^{\frac{1}{2}} \qquad (2.4)$$

where 2θ is the scattering angle (Figure 2.1). The momentum transfer during the scattering event is $\hbar\underline{Q}$.

Figure 2.1 Vector diagram for scattering of a neutron of incident wavevector $\underline{k}_o$ and final wavevector $\underline{k}_f$

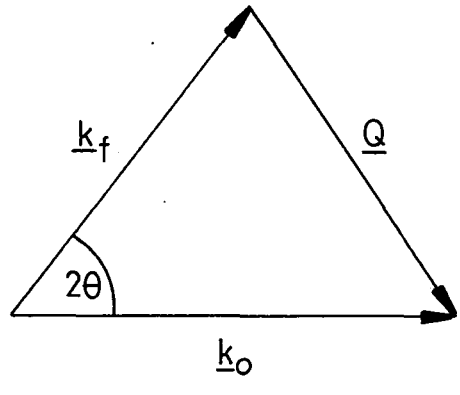

The energy transfer, ΔE, on scattering is

$$\Delta E = E_o - E_f = \frac{\hbar}{2m}(k_o^2 - k_f^2) = \hbar\omega = h\nu \qquad (2.5)$$

where ν is the frequency and ω the angular frequency associated with the quantum of energy transferred.

2.2 Neutron scattering cross-sections

Consider a monochromatic beam of neutrons of energy E_o incident on a target (Figure 2.2). The target is for the moment regarded as a general collection of atoms and may be in the form of a crystal, amorphous solid, liquid or gas.[3] In a typical neutron scattering experiment, the number of neutrons scattered in a given direction (θ,ϕ) is measured as a function of their final energy, E (Figure 2.2). The measured quantity is called the partial differential cross-section and is defined by[3]:

$$\frac{d^2}{d\Omega dE} = \frac{\text{(number of neutrons with final energy between E and E+dE scattered into the solid angle d}\Omega\text{ in the direction }(\theta,\phi)\text{ per second)}}{\Phi d\Omega dE} \qquad (2.6)$$

where Φ is the incident neutron flux. The partial differential cross-section has dimensions of [area]. The total scattering cross-section is defined thus[3]:

$$\sigma = \text{(number of neutrons scattered in all directions per second)}/\Phi \qquad (2.7)$$

The partial differential cross-section and the total scattering cross-section are related by:

$$\sigma = \int_{\substack{\text{all}\\ \text{directions}}} \int_o^\infty \frac{d^2\sigma}{d\Omega dE}\, dE d\Omega. \qquad (2.8)$$

Fig. 2.2 The geometry of a neutron scattering event, taken from ref. 1.

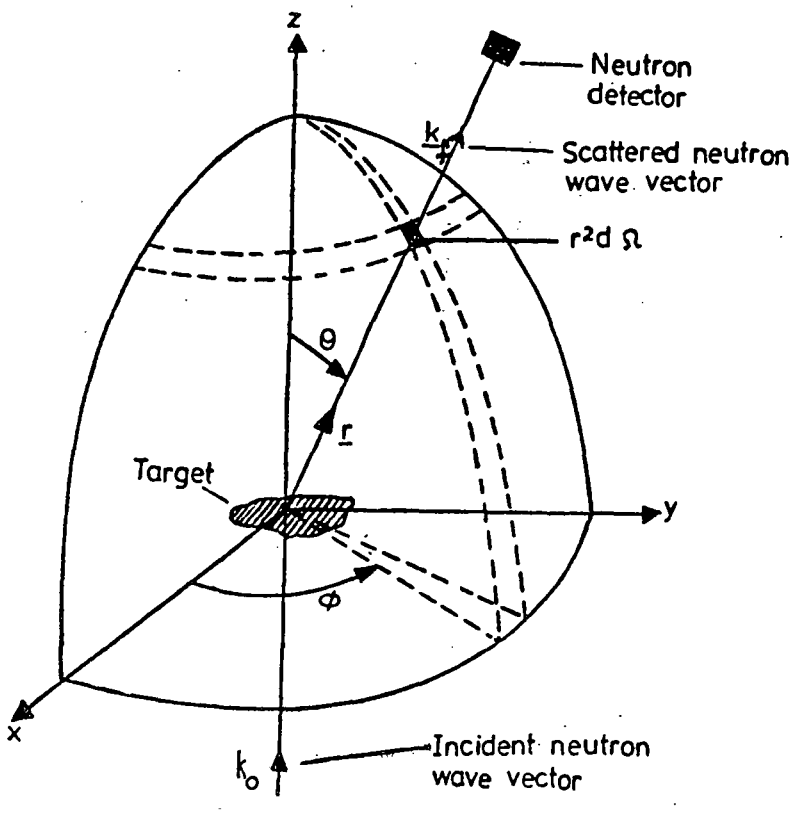

2.3 Neutron scattering by a single fixed nucleus

There is no exact expression known for the neutron-nucleus interaction. Experimentally, the interaction is known to be of short range, some 10^{-14} to 10^{-15} m.[1] Because this range is very much shorter than the neutron wavelength of *ca* 10^{-10}m, the scattering is isotropic from a single, fixed nucleus, *ie* from a nucleus which is considered to suffer no recoil on scattering.[1] The theory of nuclear scattering of neutrons is based on first order perturbation theory. Fermi[5] has shown that within first order perturbation theory, the only form of the neutron-nucleus potential which predicts isotropic scattering from a single, fixed nucleus is the so-called Fermi pseudopotential, $V(\underline{r})$:

$$V(\underline{r}) = \frac{2\pi\hbar^2}{m} b\, \delta(\underline{r} - \underline{R}) \qquad (2.9)$$

where m is the neutron mass, b is the scattering length of the fixed target nucleus (see below), $\underline{r}$ and $\underline{R}$ are the position vectors of the neutron and nucleus respectively, and δ is the Dirac delta-function.[1] It is to be noted that first order perturbation theory is not strictly applicable to the nuclear scattering of thermal neutrons because the scattering interaction, although of short range, is strong.[1] In addition, the Fermi pseudopotential does not correspond closely to the true potential. The justification for using the pseudopotential and first order perturbation theory is that they give the required result of isotropic scattering from a single, fixed nucleus.[3]

Since it refers to a fixed nucleus, the scattering length b in equation 2.9 is known as the bound scattering length. The scattering from a nucleus of mass M which is free to recoil is also described by equation 2.9 if b is replaced by the so-

called free scattering length, b_f, such that[3]

$$b_f = b \frac{M}{m+M} \quad . \tag{2.10}$$

The value of b (equation 2.9) and hence of b_f is a property of the target nucleus and is obtained experimentally. In general, b and b_f are complex quantities, the imaginary parts representing neutron absorption. For the nuclei considered in this thesis, neutron absorption occurs to only limited extents and further discussion of scattering lengths will be confined to the real parts, which describe neutron scattering. The real part may be either positive, indicating no phase change in the neutron-wave on scattering, or negative if the phase changes by π.[1,3]

2.4 Neutron scattering from a collection of nuclei

The Fermi pseudopotential (equation 2.9) is used as an approximate description of the scattering potential between a neutron and an individual nucleus present in a general collection of other scattering nuclei. Thus the scattering potential remains a function of the scattering length of the target nucleus and independent of the direction (θ,ϕ) of scatter (Figure 2.2). For the moment we regard the scattering nucleus as fixed in space.

In general, the value of the bound scattering length b differs for each isotope of the scattering nucleus and also depends on the spin state of the combined neutron-nucleus system. Consider an isotope with non-zero nuclear spin I. The spin of the neutron-nucleus system is then I + ½ or I - ½. The scattering lengths for the two spin states are different and denoted by

b^+ and b^- respectively. The number of spin states associated with spin $I + \frac{1}{2}$ is[3]

$$2(I + \tfrac{1}{2}) + 1 = 2I + 2 \qquad (2.11)$$

and the number of states associated with spin $I-\frac{1}{2}$ is

$$2(I - \tfrac{1}{2}) + 1 = 2I \qquad (2.12)$$

The total number of spin states is $4I + 2$. If the neutrons are unpolarised and the nuclear spins of the target are randomly oriented, then the scattering length b^+ occurs[3] with probability $(2I+2)/(4I+2)$ and b^- occurs with probability $2I/(4I+2)$. The average scattering length, $\bar{b}$, from a collection of fixed nuclei of a single isotope is then[3]

$$\bar{b} = \frac{1}{2I+1} \left\{ (I + 1)b^+ + Ib^- \right\} \qquad (2.13)$$

If the scattering system comprises an element containing several isotopes, then the relative abundance C_z of each isotope z must be taken into account. Therefore, the average scattering length, $\bar{b}$, of a collection of fixed nuclei of several different isotopes, is[3]

$$\bar{b} = \sum_z \frac{C_z}{2I_z+1} \left\{ (I_z+1)b_z^+ + I_z\, b_z^- \right\} \qquad (2.14)$$

where I_z, b_z^+ and b_z^- are the nuclear spin and the scattering lengths of the isotope z. The parameter b is known as the coherent scattering length of the element or nuclide.[3] The mean square scattering length, $\overline{b^2}$, of the collection of fixed nuclei is given by:[3]

$$\overline{b^2} = \sum_z \frac{C_z}{2I_z+1} \left\{ (I_z+1)(b_z^+)^2 + I_z(b_z^-)^2 \right\} \qquad (2.15)$$

If the nuclei are free to recoil on scattering their effective scattering lengths are reduced and the average scattering length becomes

$$\bar{b}_{\substack{\text{free}\\ \text{recoil}}} = \sum_z \frac{C_z}{(1+M_z/m)(2I_z+1)} \left\{ (I_z+1)b_z^+ + I_z b^- \right\} \qquad (2.16)$$

and also

$$\overline{(b^2)}_{\substack{\text{free}\\ \text{recoil}}} = \sum_z \frac{C_z}{(1+M_z/m)^2(2I_z+1)} \left\{ (I_z+1)(b_2^+)^2 + I_z(b_z^-)^2 \right\} \qquad (2.17)$$

where m is the neutron mass and M_z the mass of isotope z.

The total cross-section for scattering from an assembly of fixed nuclei is given by[1,3]

$$\sigma = 4\pi\overline{b^2} \qquad (2.18)$$

and for an assembly of nuclei which are free to recoil, by

$$\sigma_{\substack{\text{free}\\ \text{recoil}}} = 4\pi\overline{(b^2)}_{\substack{\text{free}\\ \text{recoil}}} \qquad (2.19)$$

In any molecule in the solid state, the nuclei are neither fixed nor totally free to recoil[6] and the total scattering cross-section lies between the limits given by equations 2.18 and 2.19. We discuss this below, after first considering the types of scattering which can contribute to the total scattering cross-section.

In a typical sample used in a neutron scattering experiment, the scattering lengths will vary in a random way from nucleus to nucleus, owing to the random orientation of nuclear spins or the presence of isotopes, or both.[3] The nuclear scattering

from the sample may be considered in two parts, *viz* coherent and incoherent scattering. The coherent scattering is the same scattering which would arise if the scattering length of each nucleus was made equal to the mean value, $\bar{b}$, the positions and motions of the nuclei being left unchanged.[3] In the real sample, the random distribution of the scattering lengths from $\bar{b}$ gives rise to incoherent scattering.[3] The observed scattering is the sum of the coherent and incoherent parts and therefore:

$$\frac{d^2\sigma}{d\Omega dE} = \left(\frac{d^2\sigma}{d\Omega dE}\right)_{coh} + \left(\frac{d^2\sigma}{d\Omega dE}\right)_{inc} \qquad (2.20)$$

where the subscripts coh and inc denote coherent and incoherent scattering respectively. The coherent scattering cross-section may be written[3] as:

$$\sigma_{coh} = 4\pi(\bar{b})^2 \qquad (2.21)$$

and, since the total scattering cross-section is

$$\sigma = 4\pi\overline{b^2} \quad , \qquad (2.18)$$

the incoherent scattering cross-section is given by:

$$\sigma_{inc} = 4\pi(\overline{b^2} - (\bar{b})^2) \quad . \qquad (2.22)$$

Both incoherent and coherent scattering may be further divided into elastic and inelastic scattering. The type of information obtained from each of the four subdivisions of nuclear scattering was outlined in Chapter One.

In the case of nuclear scattering from a single isotope of zero nuclear spin, the scattering is entirely coherent since $\overline{b^2} = (\bar{b})^2$.

If the appropriate scattering lengths are used, equations 2.21 and 2.22 apply to nuclei which may be rigidly fixed, free to recoil or in an intermediate situation.

We now evaluate the bound-nucleus scattering cross-sections due to ^1H nuclei present in a target molecule. Koester[7] has reported that for ^1H, $b^+ = 1.085 \times 10^{-14}$m and $b^- = -4.750 \times 10^{-14}$ m. For ^1H, I = ½ and so equation 2.13 gives

$$\bar{b} = \frac{3}{4}b^+ + \frac{b^-}{4}$$

and $\bar{b} = -0.374 \times 10^{-14}$m.

Equation 2.15 yields (putting $C_z = 1$)

$$\overline{b^2} = \frac{3}{4}(b^+)^2 + \frac{1}{4}(b^-)^2$$

$$\overline{b^2} = 6.52 \times 10^{-28}\ m^2$$

Thus in the bound-nucleus limit, equation 2.21 gives

$$\sigma_{coh} = 4\pi(\bar{b})^2$$

$$\sigma_{coh} = 1.76 \times 10^{-28}\ m^2,$$

and equation 2.22 gives $\sigma_{inc} = 4\pi(\overline{b^2} - (\bar{b})^2)$

$$\sigma_{inc} = 80.2 \times 10^{-28}\ m^2.$$

For scattering by nuclei of mass M which are free to recoil, equation 2.10 gives

$$\left(\sigma_{coh}\right)_{\substack{free\\recoil}} = 4\pi(\bar{b})^2 \left(\frac{M}{m+M}\right)^2 \qquad (2.23)$$

and $$\left(\sigma_{inc}\right)_{\substack{free\\recoil}} = 4\pi(\overline{b^2} - (\bar{b})^2)\left(\frac{M}{m+M}\right)^2 \qquad (2.24)$$

where m is the neutron mass. Thus for ^1H nuclei, the values of the coherent and incoherent scattering cross-sections are both a factor of four smaller at the free-recoil limit than at the bound-nuclei limit. But regardless of the extent of recoil, the scattering from an assembly of ^1H nuclei is predominantly incoherent.

In Table 2.2 we list the bound-nuclei values of σ_{coh} and σ_{inc} for the elements and their isotopes relevant to this thesis. From equation 2.24, the difference between the bound-nucleus and free-recoil limits of the incoherent scattering cross-section of a nucleus of mass M decreases with increasing M and is greatest for ^1H. However, even at the free-recoil limit, the incoherent scattering cross-section of an ^1H nucleus is greater by at least a factor of four than that of any other nucleus listed in Table 2.2. It is shown below (Section 2.8) that the contribution to the observed value of $\left(\frac{d\sigma^2}{d\Omega dE}\right)_{inc}$ from those vibrational modes of a sample which displace nuclei type L, depends, *inter alia*, on the mean square displacement and the value of σ_{inc} of the nuclei type L. Other factors (*ie* the vibrational force constants) being equal, the mean square displacement is largest for those nuclei of lowest mass. It is therefore a good approximation (*ie* subject to concentration) that in most hydrogenous systems, the total incoherent cross-section will be dominated by that of the ^1H nuclei.[6]

All of the neutron cross-sections calculated for the molecules studied in this thesis appertain to the bound-nuclei limit (Table 2.2). The effect on the neutron scattering intensity of the vibrational modes of our samples is accounted for by the function $S_{inc}(\underline{Q},\omega)$ (Section 2.5).

TABLE 2.2 Neutron scattering cross-sections of various elements and their isotopes at the bound-atom limit

Atomic number	Element or isotope (natural abundance, %)	σ_{coh} barns[a]	σ_{inc} barns[a]
1	H (99.98)[b]	1.8	80.2
	D (0.02)	5.6	2.0
6	C	6.5	0.0
	^{13}C (1.1)	5.5	1.0
8	O	4.23	0.0
	^{17}O (0.04)	4.20	
	^{18}O (0.02)	4.52	
11	Na	1.65	1.7
13	Al	1.50	0.0
14	Si	2.16	0.0
20	Ca	2.73	0.5
	^{40}Ca (97.0)	3.0	0.1
	^{44}Ca (2.1	0.4	
23	V	0.03	5.1
25	Mn	1.9	0.4
27	Co	0.79	5.2
28	Ni	13.3	4.7
	^{58}Ni (67.9)	26.1	
	^{60}Ni (26.2)	1.00	
	^{61}Ni (1.2)	7.3	
	^{62}Ni (3.7)	9.5	
	^{64}Ni (1.1)	0.02	
30	Zn	4.1	0.1
	^{64}Zn (48.9)	3.9	
	^{66}Zn (27.8)	5.0	
	^{68}Zn (18.6)	5.6	
46	Pd	4.5	0.3
78	Pt	11.3	0.7

Notes:

a. 1 barn = 1 x 10^{-28} m

b. The cross-sections for ^{1}H are taken from Koester,[7] the remaining cross-sections from Willis.[8]

2.5 Incoherent inelastic neutron scattering and molecular vibrations

We need to express the experimentally observed partial differential cross-sections in terms of the structure and dynamics of the target system. These properties are described by the scattering functions $S_{inc}(\underline{Q},\omega)$ and $S_{coh}(\underline{Q},\omega)$ such that[1,6]:

$$\left(\frac{d^2\sigma}{d\Omega dE}\right)_{inc} = \frac{k_f}{k_o}\frac{\sigma_{inc}}{8\pi^2\hbar} S_{inc}(\underline{Q},\omega) \qquad (2.25)$$

$$\text{and } \left(\frac{d^2\sigma}{d\Omega dE}\right)_{coh} = \frac{k_f}{k_o}\frac{\sigma_{coh}}{8\pi^2\hbar} S_{coh}(\underline{Q},\omega) \qquad (2.26)$$

Although mathematically they are functions, $S_{inc}(\underline{Q},\omega)$ and $S_{coh}(\underline{Q},\omega)$ are often referred to as scattering <u>laws</u>.

In this thesis we are concerned with incoherent scattering and in particular with the interaction of thermal neutrons with the normal modes of vibration of the target molecule. In deriving an expression for $S_{inc}(\underline{Q},\omega)$ it is assumed that there is negligible interaction between the rotational (r) and vibrational (v) motions of the scattering molecule, and that both the r and v motions are uncoupled from the translational (t) motions.[6] The incoherent scattering function is then a convolution (*) of the scattering functions for the t, r and v motions:[6]

$$S_{inc}(\underline{Q},\omega) = S_t(\underline{Q},\omega) * S_r(\underline{Q},\omega) * S_v(\underline{Q},\omega) \qquad (2.27)$$

The bands which arise in the inelastic incoherent neutron scattering spectra presented in this thesis are due to $S_v(\underline{Q},\omega)$, these bands being broadened by S_t and S_r. The broadening is more important for liquids and gases than for solids.[6]

Zemach and Glauber[9] have discussed the scattering function for molecular vibrations. It was shown that for an oriented assembly of harmonic oscillators in the form of a single crystal:[9]

$$\left(\frac{d^2\sigma}{d\Omega dE}\right)_{inc} = \frac{k_f}{k_o} \frac{1}{8\pi^2\hbar} \sum_L \sigma_{inc}^L \prod_a \left\{ \exp\left[-(\underline{Q}\cdot\underline{C}_L^a)^2 \frac{\hbar}{2\omega_a M_L} \right.\right.$$

$$\left. \times \coth\left(\frac{\hbar\omega_a}{2K_BT}\right)\right] \exp\left(\frac{-n_a\hbar\omega_a}{2K_BT}\right)$$

$$\times I_{n_a}\left[\frac{(\underline{Q}\cdot\underline{C}_L^a)^2\hbar}{2\omega_a M_L \sinh(\hbar\omega_a/2K_BT)}\right]$$

$$\left. \times \delta\left(\hbar\omega - \hbar\sum_a n_a\omega_a\right)\right\} \qquad (2.28)$$

where:

n_a is the number of quanta of energy $h\omega_a$ transferred during the scattering process ($n_a>0$ for neutron energy gain and $n_a<0$ for neutron energy loss);

a is an index for the normal modes of vibration;

ω_a is the angular frequency of the normal mode;

$\hbar\omega$ is the energy change of the neutron;

M_L is the mass of the L^{th} nucleus,

I_{n_a} the modified Bessel function;

K_B is Boltzmann's constant and

$\underline{C}^a_L$ is the normalised polarisation vector defining the direction of displacement of the L^{th} nucleus in the normal mode a.

The mean amplitude of vibration, $\langle\underline{u}_L^a\rangle$, of the L^{th} nucleus in the normal mode a is given by[6,10]

$$\langle\underline{u}_L^a\rangle = \left(\frac{\hbar}{2M_L\omega_a}\coth\frac{\hbar\omega_a}{2K_BT}\right)^{\frac{1}{2}} \left|\underline{C}^a_L\right| . \qquad (2.29)$$

From equation 2.28, the partial differential cross-section is a series of delta functions which arise whenever the energy transfer of the neutron equals that of a normal mode, or that of overtones or combinations of normal modes, of the sample.[6]

In equation 2.28, I_{n_a} is the modified Bessel function of the first kind. Experimentally, the argument of the Bessel function is found to be small (<0.01) in many cases and as a result the function may be approximated by the first term in its power series expansion:[6]

$$I_{n_a}(X) = \left(\frac{X}{2}\right)^{|n_a|} \Big/ |n_a|! \qquad (2.30)$$

Exceptions to the small argument case are discussed in Section 2.10.1. In equation 2.28 the product of the series Π_a is the contribution of the L^{th} nucleus to the incoherent scattering law of the molecule, *ie* equation 2.28 may be written as:

$$\left(\frac{d^2\sigma}{d\Omega dE}\right)_{inc} = \frac{k_f}{k_o} \frac{1}{8\pi^2\hbar} \sum_L \sigma^L_{inc} S^L_{inc}(\underline{Q},\omega) \qquad (2.31)$$

From equations 2.28, 2.30 and 2.31:

$$S^L_{inc}(\underline{Q},\omega) = \prod_a \exp\left[-(\underline{Q}\cdot\underline{C}^a_L)^2 \frac{\hbar}{2M_L\omega_a} \coth\left(\frac{\beta}{2}\right)\right]$$

$$\times \exp(-n_a\beta/2)$$

$$\times \frac{1}{|n_a|!}\left[\frac{\hbar(\underline{Q}\cdot\underline{C}^a_L)^2}{4M_L\omega_a \sinh(\beta/2)}\right]^{|n_a|}$$

$$\times \delta(\hbar\omega - \hbar\sum_a |n_a|\omega_a) , \qquad (2.32)$$

where $\beta = \hbar\omega_a/(K_B T)$. Equation 2.32 gives the scattering function for the nuclei type L of a molecule arising from the transfer of n_a quanta energy $h\omega_a$ to the normal mode a.

2.6 Elastic incoherent neutron scattering

For elastic scattering, $n_a = 0$ for all n_a and equation 2.32 becomes

$$S_{inc}(\underline{Q},\omega) = \exp\left\{\frac{\hbar}{2M_L} \sum_a \frac{-(\underline{Q}\cdot C_L^a)^2}{\omega_a} \coth\left(\frac{\beta}{2}\right)\right\} \qquad (2.33)$$

which may be written

$$S_{inc}(\underline{Q},\omega) = \exp\ (-2W_L) \qquad (2.34)$$

where $\exp(-2W_L)$ is the Debye-Waller factor of the L^{th} nucleus, which involves a contribution from all the normal modes of the sample. From equation 2.29

$$W_L = \frac{1}{2} \sum_a (\underline{Q}\cdot \underline{u}_L^a)^2 \ . \qquad (2.35)$$

2.7 Inelastic incoherent scattering from a fundamental normal mode of vibration

Since the inelastic incoherent neutron scattering from hydrogenous samples arises principally from the ^1H nuclei, hereafter we will drop the summation over L in those equations which are derived from equations 2.28, 2.31 and 2.32 and discard the superscript L from the $S_{inc}^L(\underline{Q},\omega)$ terms.

Putting n_a=+1 (neutron energy gain) in equation 2.32 for one normal mode and n_a=0 for the remainder, gives:[6]

$$S^{+1}_{inc}(\underline{Q},\omega) = \sum_a \exp(-2W_L) \frac{\hbar(\underline{Q}\cdot\underline{C}^a_L)^2}{2M_L\omega_a} r_a \delta(\hbar\omega - \hbar\omega_a), \qquad (2.36)$$

where r_a is the Base occupation factor defined thus

$$r_a = [\exp(\beta)-1]^{-1} \qquad (2.37)$$

An expression for $S_{inc}(\underline{Q},\omega)$ for neutron energy loss (n_a=-1) can be obtained in a similar way. Equation 2.38 is a combined expression, applying to both neutron energy loss and neutron energy gain, for the scattering function arising from a single, fundamental normal mode[6]:

$$S_{inc}(\underline{Q},\omega) = \sum_a \exp(-2W_L) \frac{\hbar(\underline{Q}\cdot\underline{C}^a_L)^2}{2M_L\omega_a} (r_a+\tfrac{1}{2}\mp\tfrac{1}{2}) \delta(\hbar\omega-\hbar\omega_a) \qquad (2.38)$$

where if n_a=+1, the -½ term is used and if n_a=-1, the +½ term is used.

Neutron scattering experiments may be carried out by detecting neutrons which have either gained or lost energy; all of our INS data were obtained in the neutron energy loss mode. From the principle of detailed balance, the relationship between the scattering function for neutron energy loss and neutron energy gain, is

$$S^{+}_{inc}(\underline{Q},\omega) = \exp(\beta)\ S^{-}_{inc}(\underline{Q},\omega) \qquad (2.39)$$

where the superscripts + and - denote neutron energy gain and loss, respectively. It is convenient to define a scattering function $\tilde{S}_{inc}(\underline{Q},\omega)$ which is even in energy transfer, such that[1]:

$$\tilde{S}^{+}_{inc}(\underline{Q},\omega) = \tilde{S}^{-}_{inc}(\underline{Q},\omega) = \exp(\tfrac{-\beta}{2})\ S^{+}_{inc}(\underline{Q},\omega) \qquad (2.40)$$

Egelstaff[11] has defined the function $S(\alpha,\beta)$ such that

$$S(\alpha,\beta) = K_B T\ \tilde{S}_{inc}(\underline{Q},\omega) \qquad (2.41)$$

where $\alpha = \hbar^2 Q^2/(2M_L K_B T)$ (2.42)

and $\beta = \hbar\omega/(K_B T)$. (2.43)

The equations for $S_{inc}(Q,\omega)$ given thus far, apply to single crystals. All the samples used in our INS studies were polycrystalline powders. By averaging over all possible sample orientations, equations 2.33 to 2.38 may be rewritten[6] for polycrystalline samples, making the substitutions

$$W_L = W_L(\omega_a) \tag{2.44}$$

and $$(Q\cdot C_L^a)^2 = Q^2 |C_L^a|^2 \quad . \tag{2.45}$$

Equation 2.44 expresses the fact that, for a polycrystalline sample, the Debye-Waller factor is mode dependent. Thus, for a polycrystalline sample, equations 2.38 and 2.40 give

$$\tilde{S}_{inc}(Q,\omega) = \frac{\hbar Q^2}{4M_L\omega_a \sinh(\beta/2)} \exp(-2W_L(\omega_a))g(\omega) \tag{2.46}$$

where $$g(\omega) = \sum_a \left| C_L^a \right|^2 \delta(\hbar\omega - \hbar\omega_a) \tag{2.47}$$

and $g(\omega)$ is the amplitude-weighted frequency distribution. From equation 2.46

$$g(\omega) = 4M_L\omega\sinh(\beta/2) \frac{\tilde{S}_{inc}(Q,\omega)}{Q^2} \exp(+2W_L(\omega)) \tag{2.48}$$

Egelstaff[11] has defined the function $P(\alpha,\beta)$ which is directly proportional to the amplitude-weighted frequency distribution, such that

$$P(\alpha,\beta) = \frac{K_B T}{\hbar} g(\omega) \tag{2.49}$$

and therefore

$$P(\alpha,\beta) = 2\beta\sinh(\beta/2) \exp(+2W_L(\omega_a)) \frac{S(\alpha,\beta)}{\alpha} \tag{2.50}$$

The function $P(\alpha,\beta)$ is calculated from data collected at non-zero momentum transfer and is therefore not ideal for comparison

with optical data. A function more suited to this comparison is $\rho(\beta)$, defined by:

$$\rho(\beta) = 2\beta\sinh(\beta/2)\exp(+2W_L(\omega_a)) \lim_{\alpha\to 0}\left(\frac{\tilde{S}_{inc}(Q,\omega)}{Q^2}\right) \quad (2.51)$$

Thus $\rho(\beta)$ may be evaluated by extrapolating to zero α the data collected for the same energy transfer at several different values of α.[6]

The function $P(\alpha,\beta)$ is used extensively for the presentation of data recorded by neutron time-of-flight (t.o.f.) spectrometers. Typically, the t.o.f. spectra are presented as the sum of data collected over several different angles of detection, *ie* a plot of $\sum_{i=1}^{t} P(\alpha,\beta)$ against $\tilde{\nu}$ is produced, where there are t scattering angles.[6] The summation over t, which is possible if the observed modes show little dispersion, improves the statistics of the data but reduces the momentum-transfer resolution.

2.8 Computation of the functions $S(Q,\omega)$ and $P(\alpha,\beta)$ from INS data

Under neutron energy loss conditions, equation 2.38 gives for a series of fundamental, harmonic modes of vibration:

$$S_{inc}(Q,\omega) = \sum_a \exp(-2W_L(\omega_a))Q^2\left|\underline{C}_L^a\right|^2 \frac{\hbar}{2\mu_L\omega_a}(r_a+1)(\hbar\omega-\hbar\omega_a) \quad (2.52)$$

where $r_a+1 = \exp(\beta/2)/(2\sinh(\beta/2))$ (2.53)

From the work of Hamilton[12] for molecular modes of vibration, the M_L term in equation 2.38 has been replaced in equation 2.52 by μ_L, where μ_L is the reduced mass of the scattering unit with respect to the remainder of the molecule. The scattering unit is to be understood as comprising those atoms of the molecule which undergo significant displacements during the normal mode a.

According to Hamilton,[12] for a vibrational mode of translational character:

$$\mu_L = M \tag{2.54}$$

and for a librational mode:

$$\mu_L = I_R/r^2 \tag{2.55}$$

where M is the mass of the scattering unit, r is the perpendicular distance between the scattering nucleus L and the axis of rotation and I_R is the moment of inertia of the scattering unit about the axis of libration. In interpreting the INS spectra of adsorbed species presented in this thesis, the admolecules are considered to be scattering units which vibrate as a whole with respect to adsorbents of infinitely heavy mass. For hydrogen atomically adsorbed by our ZnO and Pd black samples (Chapters Five and Seven), the reduced mass, μ_L, of the adatom is set equal to unity.

If $\underline{u}_L(t)$ is the displacement at some instant t of the atom L due to the normal modes of vibration of the sample then

$$\underline{u}_L(t) = \sum_a \underline{C}_L^a \, q_a(t)/\mu_L \tag{2.56}$$

where q_a is the normal coordinate for mode a. For a harmonic oscillator[10]:

$$\langle q_a^2 \rangle = \frac{\hbar}{2\omega_a} \coth\left(\frac{\hbar\omega_a}{2K_B T}\right) \tag{2.57}$$

where $\langle q_a^2 \rangle$ is the mean square value of q_a.

Thus in the harmonic approximation, the $Q^2|\underline{C}_L^a|^2$ term of equation 2.52 becomes

$$\sum_a \ldots Q^2 |\underline{C}_L^a|^2 \ldots = \sum_a \ldots Q^2 |\underline{C}_L^a|^2 \langle q_a^2 \rangle \frac{2\omega_a}{\hbar \coth(\beta/2)} \ldots \quad (2.58)$$

$$= \sum_a \ldots Q^2 \langle (U_L^a)^2 \rangle \frac{2\omega_a \mu_L}{\hbar \coth(\beta/2)} \ldots \quad (2.59)$$

where $\langle (u_L^a)^2 \rangle$ is the mean square amplitude of vibration of the nucleus L in the normal mode a.

Using equation 2.59, equation 2.52 gives for a fundamental, harmonic mode of vibration:

$$S_{inc}(\underline{Q}, \omega) = \sum_a \exp(-2W_L(\omega_a)) Q^2 \langle (u_L^a)^2 \rangle \frac{\delta(\hbar\omega - \hbar\omega_a)}{(1+\exp(-\beta))} \quad (2.60)$$

The normalised vibrational density of states, $Z(\omega)$, of the sample is defined to be the fraction of the normal modes whose frequencies lie in the range ω to $\omega + d\omega$, such that[3]

$$\int_0^{\omega_{max}} Z(\omega) d\omega = 1 \quad (2.61)$$

where ω_{max} is the maximum frequency of the normal modes of vibration. A crystal of N atoms has 3N normal modes and so

$$3N.Z(\omega) = \sum_a \delta(\hbar\omega - \hbar\omega_a) \quad (2.62)$$

The function $Z(\omega)$ may be regarded as a series of delta-like functions, each of which corresponds to a particular normal mode and whose height represents the degeneracy of the mode, *eg*

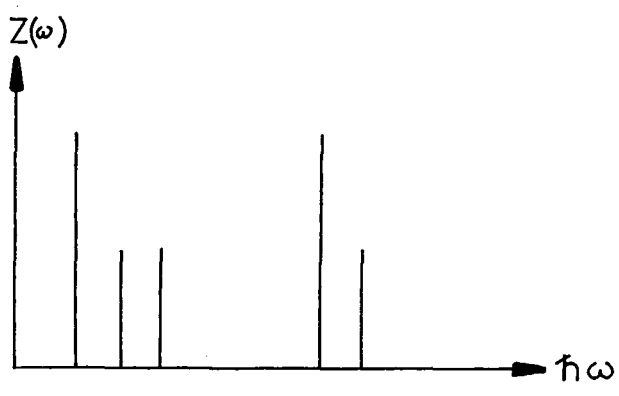

The principle use of incoherent inelastic neutron scattering is to obtain the $Z(\omega)$ of a given sample, since by substitution of equation 2.62 into 2.60 one obtains for a fundamental, harmonic mode of vibration:

$$S_{inc}(\underline{Q}, \omega_a) = \exp(-2W_L(\omega_a))Q^2\langle(u_L^a)^2\rangle \times \frac{3N\ Z(\omega_a)}{(1+\exp(-\beta))} \quad , \tag{2.63}$$

which may be rewritten as

$$S_{inc}(\underline{Q}, \omega_a) = \exp\frac{(-2W_L(\omega_a))Q^2 Z(\omega_a)(r_a+1)3N}{2\mu_L\omega_a} \cdot \tag{2.64}$$

using equations 2.56 and 2.57.

Combining equations 2.25 and 2.63, one may write

$$\left(\frac{d^2\sigma}{d\Omega dE}\right)_{inc} = \frac{k_f}{k_i}\ \frac{3N}{8\pi^2\hbar}\ \sum_L\ \sigma_{inc}^L\ \sum_a \left\{\frac{Z(\omega_a)}{(1+\exp(-\beta))} \times Q^2\langle(u_L^a)^2\rangle\exp(-2W_L(\omega_a))\right\} \tag{2.65}$$

which provides the basis for our earlier statement (Section 2.4) that the partial differential incoherent neutron scattering cross-section depends, in part, on the product of terms such as $\bar{\sigma}_{inc}^L \cdot \langle(u_L^a)^2\rangle$.

The function $S_{inc}(\underline{Q},\omega)$ is frequently used to present INS spectra recorded on beryllium fitter detector (b.f.d.) spectrometers since, under certain conditions, the data as recorded are directly proportional to $S_{inc}(\underline{Q},\omega)$ (Chapter Four). With the possible exception of the $\exp(-2W_L(\omega_a))$ term, the evaluation of which is discussed in Section 2.9, all of the terms in equations 2.63 and 2.64 are either known or constants for a particular sample.

Thus it is possible to test an assignment scheme of a b.f.d. spectrum by predicting relative INS band intensities using either equation 2.63 or equation 2.64 and comparing the predicted and observed values. All of our b.f.d. spectra were recorded at 77K, the minimum energy transfer being $56cm^{-1}$. Values of the $(1+\exp(-\beta))^{-1}$ and (r_a+1) terms in equations 2.63 and 2.64 appropriate to our b.f.d. spectra are listed in Table 2.3, which shows that these terms may be set equal to unity to a good approximation for transitions above $200cm^{-1}$. This approximation becomes more accurate as the value of β $(=\hbar\omega/(K_BT))$ increases.

TABLE 2.3 The values of the functions $(1+\exp(-\beta))^{-1}$ and (r_a+1) at 77K for various energy transfers

Energy transfer $\hbar\omega$, cm^{-1}	Value of $(1+\exp(-\beta))^{-1}$ at 77K (to 3 sig. fig.)	Value of $r_a+1 = \frac{\exp(\beta/2)}{2\sinh(\beta/2)}$ at 77K to 3 sig. fig.)
56	0.740	1.55
70	0.787	1.38
100	0.866	1.21
200	0.977	1.02
300	0.996	1.01

An equation which allows INS band intensities to be predicted in terms of $P(\alpha,\beta)$ may be obtained in the following way. From equation 2.50 one obtains for a fundamental mode:

$$P(\alpha,\beta) = \frac{2\mu_L\omega_a K_B T}{\hbar Q^2(r_a+1)} \; S_{inc}(Q,\omega)\exp(+2W_L(\omega_a)) \qquad (2.66)$$

The computer programs used for reduction of t.o.f. data calculate $P(\alpha,\beta)$ from equation 2.66 using a value of $S_{inc}(Q,\omega)$ obtained

directly from the observed scattering intensity *via* relationships based on equation 2.25 (see Chapter Four). All the remaining terms in equation 2.66 are easily computed except for μ_L and $\exp(+2W_L(\omega_a))$. These latter two terms are set equal to unity by the programs since they are mode dependent quantities and cannot be evaluated for an INS band until after its assignment. Thus if $P^{comp}(\alpha,\beta)$ denotes the value computed by the data reduction programs and $P(\alpha,\beta)$ the true value of the function, then:

$$P(\alpha,\beta) = P^{comp}(\alpha,\beta) \cdot \mu_L . \exp(+2W_L(\omega_a)) \quad . \tag{2.67}$$

From the definition[11] of $P(\alpha,\beta)$:

$$P(\alpha,\beta) = \frac{K_B T}{\hbar} \cdot 3N. \; Z(\omega_a) \tag{2.68}$$

and so

$$P^{comp}(\alpha,\beta) = \frac{K_B T}{\hbar} \cdot \frac{3N.Z(\omega_a)}{\mu_L} .\exp(-2W_L(\omega_a)) \tag{2.69}$$

If more than one type of scattering nucleus L gives rise to significant scattering, then equation 2.70 below may be used for a given assignment scheme to predict the relative band intensities, R^{comp}, which would be observed in the t.o.f. spectra produced by the data reduction programs:

$$P^{comp} \propto \sum_L \sigma^L_{inc} \; \frac{Z(\omega_a)}{\mu_L} \exp(-2W_L(\omega_a)) \quad . \tag{2.70}$$

In subsequent chapters, all references to $P(\alpha,\beta)$ signify the function $P^{comp}(\alpha,\beta)$, the superscript comp having been dropped.

2.9 Evaluation of the Debye-Waller factor in neutron scattering

The Debye-Waller factor (D.W. factor) represents the reduction in scattered neutron intensity due to the thermal motion of the target nuclei. It is the $\exp(-2W_L(\omega_a))$ term in equation 2.46 and, by definition, for a single crystal:

$$2W_L(\omega_a) = (\underline{Q}\cdot\underline{u}_L^a)^2 \qquad (2.71)$$

for the nucleus L in mode a. The D.W. factor of a single crystal depends on the relative orientation of the crystal and the scattering vector and in general differs for each mode of vibration. For a single crystal comprising an assembly of harmonic oscillators in a cubic lattice, equation 2.71 becomes

$$2W_L = Q^2 \langle \tilde{u}_L^2 \rangle \qquad (2.72)$$

where $$\langle \tilde{u}_L^2 \rangle = \frac{1}{3} \sum_a \langle (u_L^a)^2 \rangle \qquad (2.73)$$

ie $\langle \tilde{u}_L^2 \rangle$ is the mean square displacement of the L^{th} nucleus in any direction. The quantity $\langle \tilde{u}_L^2 \rangle$ is isotropic and contains a contribution from all the vibrational modes which displace the L^{th} nucleus. Because of this isotropy, the D.W. factor is mode independent for this example.

Evaluation of the D.W. factor for a polycrystalline sample requires an averaging of $(\underline{Q}\cdot\underline{u}_L^a)^2$ in equation 2.71 over all possible orientations of the sample for each mode a and each nucleus L. A formalism for carrying out the orientational averaging has been published by Thomas and Ghosh[13]. According to these authors, the D.W. factor for a fundamental mode of a harmonic oscillator of a powder sample is given by:

$$\exp(-2W_L(\omega_a)) = \exp(-Q^2 V_L^a) \tag{2.74}$$

where

$$V_L^a = \frac{1}{5}\left\{ \mathrm{Tr}\underline{\underline{A}}_L + 2\left(\frac{\underline{\underline{A}}_L : \underline{\underline{B}}_L^a}{\mathrm{Tr}\underline{\underline{B}}_L^a}\right)\right\} \tag{2.75}$$

and $$\underline{\underline{A}}_L = \sum_a \underline{\underline{B}}_L^a \,, \tag{2.76}$$

where $\underline{\underline{A}}_L$ and $\underline{\underline{B}}_L^a$ are second order tensors and : represents the outerproduct of the two tensors followed by double contraction.[14] The tensors may be represented by 3 x 3 matrices, whose trace is indicated by Tr $\underline{\underline{A}}_L$ and Tr $\underline{\underline{B}}_L^a$. In deriving equations 2.74 to 2.76, it was assumed that no coupling occurred between internal modes and the intermolecular modes of vibration and that $2W_L(\omega_a) << 1$. The tensor $\underline{\underline{B}}_L^a$ represents the mean square displacement of the scattering nucleus in the mode a and its components may be calculated from[10] equation 2.77:

$$\langle (u_L^a)^2 \rangle = \frac{\hbar}{2\omega_a \mu_L} \coth(\beta/2) \tag{2.77}$$

The tensor $\underline{\underline{A}}_L$ represents the total mean square displacement of nucleus L and is the result of the summation of the displacements of the nucleus due to all modes of vibration.[14] Because of this summation, $\underline{\underline{A}}_L$ is independent of ω_a. Equations 2.75 and 2.76 show that V_L^a contains a contribution from all modes of vibration of the L^{th} nucleus but that the mode a makes the greatest contribution. Thus in general, V_L^a is anisotropic and hence both V_L^a and the D.W. factor are mode dependent. Thomas and Ghosh[13] have discussed the energy dependence of the D.W. factor for special cases of isotropy of the tensors $\underline{\underline{A}}_L$ and $\underline{\underline{B}}_L^a$ (Table 2.4).

TABLE 2.4 The mode dependence of the Debye-Waller factor in various approxmations

Model or approximation	Form of tensors		Form of $W_L(\omega_a)$	Form of $W_L(\omega_a)$ in the linear approximation[a]
	$\underline{\underline{A}}_L$	$\underline{\underline{B}}^a_L$		
Anisotropic	Anisotropic	Anisotropic	Mode dependent	$\frac{1}{10} Q^2 \left\{ Tr\underline{\underline{A}}_L + 2(\underline{\underline{A}}_L : \underline{\underline{B}}^a_L / Tr\underline{\underline{B}}^a_L) \right\}$
Partially isotropic	Anisotropic	Isotropic	Mode independent	$\frac{1}{6}Q^2\ Tr\underline{\underline{A}}_L$, valid only in linear approximation
Isotropic	Isotropic	Isotropic or anisotropic	Mode independent	$\frac{1}{6}Q^2\ Tr\underline{\underline{A}}_L$ rigorously valid

Notes:

This table has been taken from Thomas and Ghosh.[13]

a. The linear approximation is: $2W_L(\omega_a) << 1$.

Using the symbols of Thomas and Ghosh,[13] equation 2.72 for a single crystal would become

$$2W_L = Q^2 < \tilde{u}_L^2 > \equiv Q^2 \mathrm{Tr}\, \underline{\underline{A}}_L .$$

Griffin and Jobic[15] have recently published a theory of the D.W. factor for the internal modes of a single molecular crystal. The theory assumes that the internal vibrations have equal D.W. factors. Two conditions must be met for the theory to apply.[15] Firstly, the internal modes should be of much higher frequency than the intermolecular modes such that no coupling occurs between the two types of vibration. Secondly, it is required that $h\omega_a' >> K_B T$ where ω_a' is the angular frequency of the lowest frequency internal mode. Under these conditions it was shown[15] that the intermolecular modes made no contribution to the D.W. factor of the internal modes. This was rationalised[15] by proposing that in observing high frequency modes, one was probing such short times (*ca* $10s^{-15}$) that the lower frequency internal modes did not have time to be effective ($\omega \lesssim 10^{-13}$s).

The effect of the intermolecular modes on the observed INS spectrum of the internal modes was to broaden each band arising from an internal mode. Thus the observed band width of an internal mode is the result of three factors:

1. the intrinsic band width of the mode;
2. a recoil broadening from the intermolecular modes and
3. the resolution function of the spectrometer.

Dorner and Griffen[16] have extended the theory of Griffen and Jobic[15] to include the spectrometer resolution. If the energy resolution, $\Delta\omega$, of the spectrometer is such that $\Delta\omega < \omega_D$, where

ω_D is the maximum angular frequency of the intermolecular modes, then it was shown[16] that the intermolecular modes give rise to shoulders on the band observed at ω_I due to the internal mode of frequency ω_I. For poorer spectrometer resolution, *ie* $\Delta\omega \gtrsim \omega_D$, then one returns to the original case of Jobic and Griffen[15] since the shoulders are unresolved from the resonance at ω_I which appears to be broadened by the intermolecular modes.[16]

Howard, Boland and Tomkinson[17] (HBT) have combined the theories of Griffen and Jobic[15] and of Thomas and Ghosh[13] to obtain expressions for the D.W. factors of the internal modes a polycrystalline sample. The HBT theory considers that the D.W. factors are mode-independent and is thus more general than the Griffen and Jobic[15] discussion. If the two conditions required by the Griffen and Jobic theory[15] apply, then, according to HBT,[17] equations 2.74 to 2.76 give the D.W. factor of an internal mode provided that all the summations required by these three equations are restricted to the internal modes. Thus the D.W. factor of the internal modes of a polycrystalline sample contains contributions from only the internal modes of vibration.

For our samples of hydrogen atomically adsorbed by ZnO (Chapter Seven), the HBT theory can be used to evaluate the D.W. factors for the vibrational modes of the H adatoms with respect to the surface since these vibrations are unlikely to be strongly coupled with the lattice modes of the adsorbent, all of which occur at lower frequencies.

There is no published formalism for the D.W. factor of internal modes which arise at frequencies similar to the inter-

molecular modes. In the case of an adsorbed molecule, the vibrations fall into three categories:

1. the internal modes of the admolecule;
2. the lattice modes of the adsorbent, and
3. the hindered translations (t) and hindered torsions(τ) of the admolecule with respect to the adsorbent. This thesis is largely concerned with the t and τ modes of adsorbed molecules. The t and τ modes are generally found to occur either in the same frequency region of the lattice modes or at only slightly higher frequencies. Therefore coupling between the lattice modes and the t and τ modes cannot be ruled out and the equations 2.74 to 2.76 do not apply to the D.W. factors of the t and τ modes. However, because of the lack of an adequate, published theory for such coupling, we have assumed in subsequent chapters that any interaction between the t and τ modes and the adsorbent lattice modes does not affect the observed frequencies or band intensities.

An experimental value of the D.W. factor for <u>any</u> fundamental mode observed in the INS spectrum of a polycrystalline sample may be obtained in the following way. Within the harmonic approximation, the D.W. factor for a polycrystalline sample is written thus:

$$2W_L(\omega_a) = Q^2 < U_L^2(\omega_a) > \qquad (2.78)$$

where $U_L^2(\omega_a)$ is an experimental value of the contribution to the D.W. factor from the amplitude of vibration of nucleus L in mode a. In general, $<U_L^2(\omega_a)>$ has a different value for each mode. In t.o.f. neutron spectroscopy one obtains a series of spectra covering the same energy range but recorded at

different scattering angles, *ie* at different values of $\underline{Q}$. Substitution of equation 2.78 into 2.69 gives

$$P^{comp}(\alpha,\beta) \propto \frac{T.Z(\omega)}{\mu_L} \exp(-Q^2<U_L^2(\omega_a)>) \qquad (2.79)$$

and therefore

$$\ln\left[P^{comp}(\alpha,\beta)\right] = \ln\left[\frac{c'T.Z(\omega)}{\mu_L}\right] - Q^2<U_L^2(\omega_a)> \qquad (2.80)$$

where c' is the constant of proportionality of equation 2.79. A value of $-<U_L^2(\omega_a)>$ is obtained for a fundamental mode from the slope of a plot of $\ln[P^{comp}(\alpha,\beta)]$ against Q^2 for the appropriate INS band.

Similar arguments apply if the t.o.f. spectra are presented in terms of $S(\underline{Q},\omega)$, equations 2.64 and 2.78 giving

$$\ln\left[\frac{S(Q.\omega)}{Q^2}\right] = \ln\left[\frac{c''Z(\omega).(r_a+1)}{\mu_L.\omega.(1+\exp(-\beta))}\right] - Q^2\,U_L^2(\omega_a) \; . \qquad (2.81)$$

where c'' is a constant.

The momentum-transfer dependence of the band intensity, measured in terms of $P(\alpha,\beta)$, of a fundamental mode in a neutron energy loss spectrum is given by the $\exp(-Q^2<U_L^2(\omega_a)>)$ term in equation 2.79. At a given energy transfer, Q^2 increases on raising the scattering angle. Within a neutron energy loss spectrum recorded at a particular scattering angle, Q^2 decreases as the energy transfer is raised. If the neutron energy loss spectrum is measured in terms of $S(\underline{Q},\omega)$, the band intensity of a fundamental mode depends on the function $Q^2\exp(-Q^2<U_L^2(\omega_a)>)$, according to equations 2.64 and 2.78.

This function increases for low values of Q^2, attains a maximum and then decreases as Q^2 is further increased. The variation of band intensity of a fundamental mode in a $S(\underline{Q},\omega)$ spectrum depends on the value of $\langle U_L^2(\omega_a)\rangle$ for the particular mode as well as on Q^2.

The physical significance of $\langle U_L^2(\omega_a)\rangle$ is as follows. According to the HBT theory,[17] the value of $\langle U_L^2(\omega_a)\rangle$ for a high frequency internal mode of a sample contains contributions from only the internal modes, provided that the lattice modes occur at frequencies much lower than the internal modes.

Although the theory of the D.W. factor for the t and τ modes of an adsorbed molecule is poorly developed, the experimental values of $\langle U_L^2(\omega_a)\rangle$ for such modes must be regarded as containing a contribution from each of the following: the internal modes of the admolecule; the t and τ modes themselves and the lattice modes of the adsorbent.

2.10 The intensity of overtone and combination bands

2.10.1 Mode-independent Debye-Waller factors

From equation 2.32, the intensity of an overtone in which n_a quanta are transferred to one normal mode depends upon terms such as:[6]

$$\exp\left\{\frac{-n_a\hbar\omega_a}{2K_BT}\right\}\frac{1}{|n_a|}\left\{\frac{\hbar(\underline{Q}\cdot\underline{C}_L^a)^2}{4m_L\omega_a\sinh(\beta/2)}\right\}^{|n_a|} \qquad (2.82)$$

provided that the Debye-Waller factor is mode-independent. In equation 2.82, the factor which is raised to the power $|n_a|$

is usually small (<0.01) and so the fundamental of a given mode generally has a greater INS intensity than its overtones. Scattering from multiphonon modes involves the transfer of quanta to different normal modes and the band intensity is low, being controlled by the product of several terms similar to equation 2.82, in the mode-independent Debye-Waller case.

If Q is large and β small, the small argument expansion (equation 2.30) of the Bessel function and hence expression 2.82 are invalid. Marshall and Lovesey[1] have shown that under these conditions, the overtone contribution for complex molecules manifests itself as an increase in the background and not as discrete bands.

2.10.2 Mode-dependent Debye-Waller factors

It has been shown[18] that for temperatures and frequencies at which $(1+\exp(-\beta))^{-1} \simeq 1$ (Table 2.3), equation 2.63 for a fundamental harmonic mode may be rewritten as:

$$S_{inc}(Q,\omega) \propto Q_1^2 \frac{\mathrm{Tr}\underline{\underline{B}}(\omega)}{3} \exp(-Q_1^2 V_L^a), \qquad (2.82)$$

where Q_1 is the magnitude of the scattering vector for the fundamental mode. The equivalent expression for the first overtone of a harmonic mode which has a fundamental frequency ω, is given by[18]:

$$S_{inc}(Q,\omega) \propto Q_2^4 \left[\frac{\mathrm{Tr}\underline{\underline{B}}^2 + 2(\underline{\underline{B}}:\underline{\underline{B}})}{30}\right] \exp(-Q_2^2 X_L^a) \qquad (2.83)$$

where $\underline{\underline{B}}$ is used as an abbreviation for $\underline{\underline{B}}(\omega)$, and Q_2 is the magnitude of the scattering vector for the first overtone, and

$$X_L^a = \frac{1}{7}\left\{(\mathrm{Tr}\underline{\underline{B}})^2 \mathrm{Tr}\underline{\underline{A}} + 4(\underline{\underline{B}}:\underline{\underline{A}})\mathrm{Tr}\underline{\underline{B}} + 2(\underline{\underline{B}}:\underline{\underline{B}})\mathrm{Tr}\underline{\underline{A}} + 8(\underline{\underline{B}}:(\underline{\underline{B}}\cdot\underline{\underline{A}}))\right\} \Big/ \left\{\mathrm{Tr}\underline{\underline{B}}^2 + 2(\underline{\underline{B}}:\underline{\underline{B}})\right\} \qquad (2.84)$$

In equations 2.83 and 2.84, tensor $\underline{\underline{B}}$ is evaluated using the frequency, ω, of the fundamental transition.

From equations 2.32, 2.35 and 2.66, putting $n_a=-2$ in equation 2.32, the intensity of the first overtone of a harmonic mode in a $P^{comp}(\alpha,\beta)$ spectrum calculated by the data reduction programs at the I.L.L. is given by

$$P^{comp}(\alpha,\beta) \propto \frac{Q_2^2}{2\mu_L\omega_a} Z(\omega_a)(r_a+1)\exp(-Q_2^2 X_L^a) \qquad (2.85)$$

where ω_a is the frequency of the fundamental mode.

For a sample in which the internal modes of vibration do not couple with the intermolecular modes, the D.W. factors in equations 2.82, 2.83 and 2.85 may be evaluated using equations 2.75 and 2.76, restricting the summation in equation 2.76 to the internal modes. Similarly for the modes of an adsorbate with respect to a surface, the D.W. factors may be calculated using equations 2.75 and 2.76, neglecting the adsorbent lattice modes from the summation in equation 2.76, provided that the lattice modes do not couple with, *ie* occur at much lower frequencies than, the adsorbate modes. In the case of the t and τ modes of an admolecule which arise at frequencies similar to those of the adsorbent phonons, the D.W. factors may be evaluated by equating the V_L^a and X_L^a terms of equations 2.82 and 2.85 with the experimental values of $\langle U_L^2(\omega_a)\rangle$ obtained from the Q-dependence of the INS band intensities of the fundamental and first overtone modes, respectively.

2.11 Nuclear scattering from H_2 and D_2 molecules

According to Springer,[19] a selection rule for neutron scattering from a molecule of total nuclear spin I' is that only transitions for which $\Delta I'=0$ or ± 1 are allowed.

H_2 exists in two spin states, orthohydrogen in which the proton spins are parallel ($I'=1$) and parahydrogen in which the spins are antiparallel ($I'=0$). In normal hydrogen, the relative population of the ortho-H_2 and para-H_2 states is 2.98:1 at room temperature.[20] The cross-sections of these two spin modifications depend on the value of $\Delta I'$ during the scattering event.

Squires[3] has discussed the nuclear scattering of a beam of unpolarised neutrons by molecules whose nuclear spins I' are randomly oriented with respect to the beam.

2.11.1 Coherent scattering from H_2

After Squires,[3] we have for H_2 that $\sigma_{coh} = 4\pi(\bar{b})^2$ if $\Delta I' = 0$ (*ie* no spin-flipping) and $\sigma_{coh} = 0$ if $\Delta I' = 1$ (*ie* if spin-flipping occurs), where $\bar{b}$ is the mean scattering length of the individual ^1H nuclei. Thus coherent scattering from H_2 arises solely from non-spin-flipping transitions. Ortho-H_2 and para-H_2 contribute equally to the coherent scattering which is independent of I'.

2.11.2 Incoherent scattering from H_2

Again after Squires,[3] for H_2 one finds that

$\sigma_{inc} = \frac{4\pi}{3} B^2 I'(I'+1)$ if $\Delta I'=0$ (*ie* no spin-flipping) and
$\sigma_{inc} = \frac{8\pi}{3} B^2 I'(I'+1)$ if $\Delta I'=1$ (*ie* if spin-flipping occurs),
where $B = \frac{b^+-b^-}{2I'+1}$ and b^+ and b^- are properties of the individual ^1H nuclei (Section 2.4). Thus σ_{inc} is zero for para-H_2 and the incoherent scattering from H_2 arises from the ortho modification alone. The value of σ_{inc} for spin-flipping of ortho-H_2 is twice that for non-spin-flipping.

2.11.3 Neutron scattering from D_2

The deuteron is a boson, having a nuclear spin I=1. Thus D_2 exists in singlet, triplet and quintet nuclear spin states which are equally populated at all accessible temperatures.[21] Neutron scattering cross-sections, obtained from the formulae given by Squires,[3] are listed in Table 2.5 for the nuclear spin states of D_2.

TABLE 2.5 Fixed-nuclei neutron scattering cross-sections for D_2

Nuclear spin state of D_2 molecule	σ_{coh}		σ_{inc}	
	no spin-flipping	spin-flipping	no spin-flipping	spin-flipping
Singlet	$4\pi(b^+)^2$	0	0	0
Triplet	$\frac{4\pi}{9}(2b^+ + b^-)^2$	0	$\frac{16\pi}{27}(b^+ - b^-)^2$	$\frac{8\pi}{27}(b^+ - b^-)^2$
Quintet	$\frac{4\pi}{25}(3b^+ + 2b^-)^2$	0	$\frac{16\pi}{25}(b^+ - b^-)^2$	$\frac{8\pi}{25}(b^+ - b^-)^2$

Note: $b^+(9.2 \times 10^{-15}\ m^{22})$ and $b^-(0.16 \times 10^{-15}\ m^{22})$ are fixed-nuclei scattering lengths for deuteron-nucleus systems of combined spin $I' + \frac{1}{2}$ and $I' - \frac{1}{2}$ respectively, where I' is the nuclear spin of the D_2 molecule.

REFERENCES

1. Marshall, W. and Lovesey, S.W., Theory of Thermal Neutron Scattering, Clarendon Press, Oxford, 1971.

2. Egelstaff, P.A. (Ed.), Thermal Neutron Scattering, Academic Press, London, 1965.

3. Squires, G.L., Introduction to the Theory of Thermal Neutron Scattering, Cambridge University Press, Cambridge, 1978.

4. Hall, P.G. and Wright, C.J. in Chemical Physics of Solids and their Surfaces, vol.7, Chemical Society Specialist Periodical Report, London, 1978.

5. Fermi, E., Ric Sci, 7, 13, 1936.

6. Howard, J. and Waddington, T.C. in Advances in Infrared and Raman Spectroscopy, vol.7, (Clark, R.J.H. and Hester, R.E., Eds.), Heyden, London, 1980.

7. Koester, L., Springer Tracts in Modern Physics, vol.80, Springer-Verlag, Berlin, 1977.

8. Willis, B.T.M. (Ed.), Chemical Applications of Thermal Neutron Scattering, Oxford University Press, Oxford, 1973.

9. Zemach, A.C. and Glauber, R.J., Phys.Rev., 101,118, 1956.

10. Cyvin, S.J., Molecular Vibrations and Mean Square Amplitudes, Elsevier, Amsterdam, 1968.

11. Egelstaff, P.A., Inelastic Scattering of Neutrons in Solids and Liquids, Proc.Symp., Vienna, 1960.

12. Hamilton, W.C., Nat.Bureau of Standards Special Publication Number 301, p.193, 1969.

13. Thomas, M.W. and Ghosh, R.E., Mol.Phys., 29, 1489, 1975.

14. Howard, J., Ludman, C.J., Waddington, T.C. and Tomkinson, J., Chem.Phys., 46, 361, 1980.

15. Griffin, A. and Jobic, H., J.Chem.Phys., 75, 5940, 1981.

16. Dorner, B. and Griffin, A. J.Chem.Phys., 78, 890, 1983.

17. Howard, J., Boland, B.C. and Tomkinson, J., Chem.Phys., 77, 145, 1983.

18. Waddington, T.C., Howard, J., Brierley, K. and Tomkinson, J., Chem.Phys., 64, 193, 1982.

19. Springer, T. in Dynamics of Solids and Liquids by Neutron Scattering (Ed. Lovesey, S.W. and Springer, T.), Springer-Verlag, Berlin,1977, p.290.

20. Egelstaff, P.A., Haywood, B.C. and Webb, F.J., Proc.Phys.Soc., 90, 681, 1967.

21. Pauling, L. and Wilson, E.B., Introduction to Quantum Mechanics, McGraw-Hill, New York, 1935.

22. Egelstaff, P.A. and Poole, M.J., Experimental Neutron Thermalisation, Pergamon, Oxford, 1969.

CHAPTER THREE

ZEOLITE STRUCTURES

3.1 Introduction

Zeolites are a class of porous, crystalline aluminosilicates of general formula $M_{x/n}[(AlO_2)_x(SiO_2)_y]\cdot wH_2O$, where M is a cation of valency n, w is the number of water molecules and [ ] denotes the framework composition.[1] Typically, the ratio y/x is the range 1 to 5, depending on the zeolite structure. The cations M are present in sufficient number to balance the single negative charge of each Al(III) atom. Extending in three dimensions, the aluminosilicate framework comprises AlO_4^- and SiO_4 tetrahedra which are linked by sharing oxygen ions. There are no unshared oxygens in the structure and the TO_4 tetrahedra (T=Al or Si) are known[2] as primary building units. A zeolite aluminosilicate framework may be envisaged as being constructed from subunits which are specific arrays of TO_4 tetrahedra.[1] These subunits, or secondary building units[2] are linked to form three dimensional polyhedra which are in turn joined up to form the overall framework structure. The linking of the secondary building units and of the polyhedra is *via* the shared oxygen ions of the component TO_4 tetrahedra.

The secondary building units as devised by Meier[2] are illustrated in Fig.3.1and some of the polyhedra found in zeolite structures are given in Fig.3.2.

Zeolites are classified into seven structural groups depending on the constituent secondary building units of their aluminosilicate framework.[2] In this thesis we are concerned with zeolite type-A, which belongs to that group of zeolites having the double four-ring (Fig.3.1) as the common structural unit, and with zeolite type-Y, which is a member of that group of zeolites having the double six-ring (Fig.3.1) as the common secondary building unit.[2] Both zeolites type-A and type-Y

Fig 3.1 The secondary building units in zeolite structures[1,2].

Only the positions of the tetrahedral silicon and aluminium atoms are shown[1]. The oxygen atoms lie near the centres of the connecting solid lines,which are not intended to represent bonds[1].

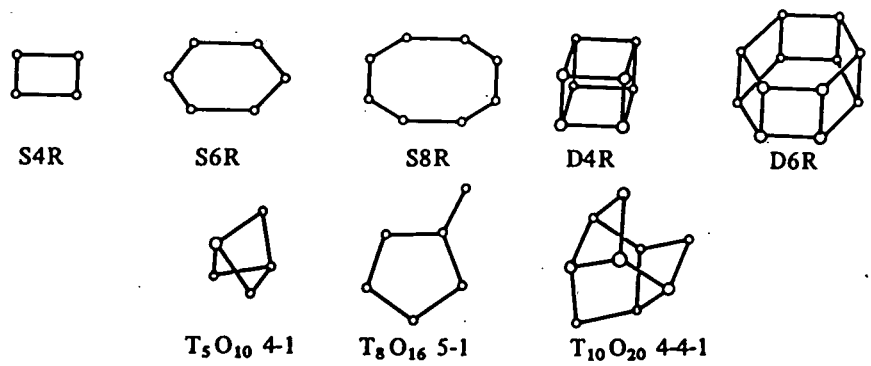

Fig 3.2 Some polyhedra in zeolite frameworks, taken from ref. 1.

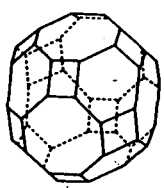

truncated cubo-octahedron

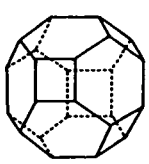

truncated octahedron or sodalite unit

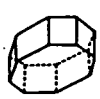

8-double ring

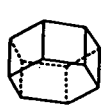

6-double ring or hexagonal prism

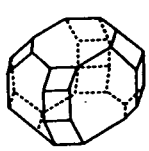

18-hedron

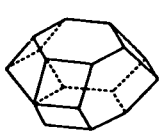

11-hedron

contain the polyhedral sodalite unit in their aluminosilicate frameworks (Fig.3.2) and these sodalite units are arranged differently with respect to each other in the two types of zeolite.

The sodalite unit is a truncated octahedron, or 14-hedron, whose vertices are defined by 24 T ions (Fig.3.2). There are 36 oxygen ions; these lie approximately halfway between the vertices but displaced from the edges of the 14-hedron (Fig.3.2). The sodalite unit has 8 hexagonal and 6 square faces. The distance between diagonally opposite points of the 14-hedron which are not impinged upon by the O ions is the free diameter of the polyhedron, equal to 6.6Å.[1]

3.2 Type-A zeolites

Type-A zeolites are a class of synthetic zeolites, the fully sodium ion exchanged form of which has a pseudo unit-cell (see below) composition of $Na_{12}Al_{12}Si_{12}O_{48}\cdot 27H_2O$ when completely hydrated.[1] The water of hydration is easily removed in its entirety by evacuation at 723K. We will refer to fully sodium ion exchanged zeolite-A by the abbreviation $Na_{12}A$, which is to be taken to indicate the fully dehydrated form unless otherwise specified.

In A-type zeolites, the sodalite units are linked together octahedrally by bridging O ions between their square faces (Fig.3.3). This linking extends in three dimensions throughout the (ideal) crystal and generates larger cavities of free diameter 11.4Å.[1] These later cavities are 26-hedra, or truncated cubo-octahedra, defined by 48 T ions at the vertices and comprising six octahedral faces, eight hexagonal faces and twelve

Fig 3.3 The aluminosilicate framework of type-A zeolites, after refs. 1,2.

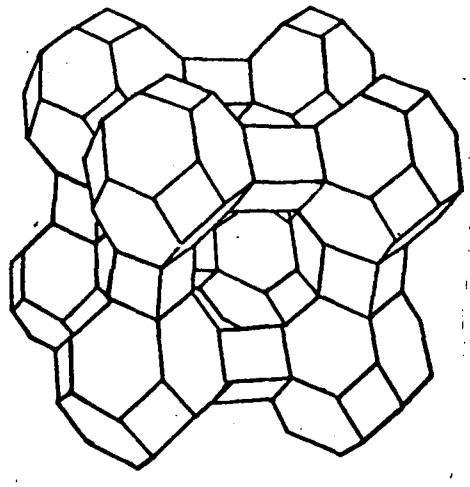

Fig 3.4 The ordering of Al^{3+} and Si^{4+} ions in type-A zeolites, after ref. 10.

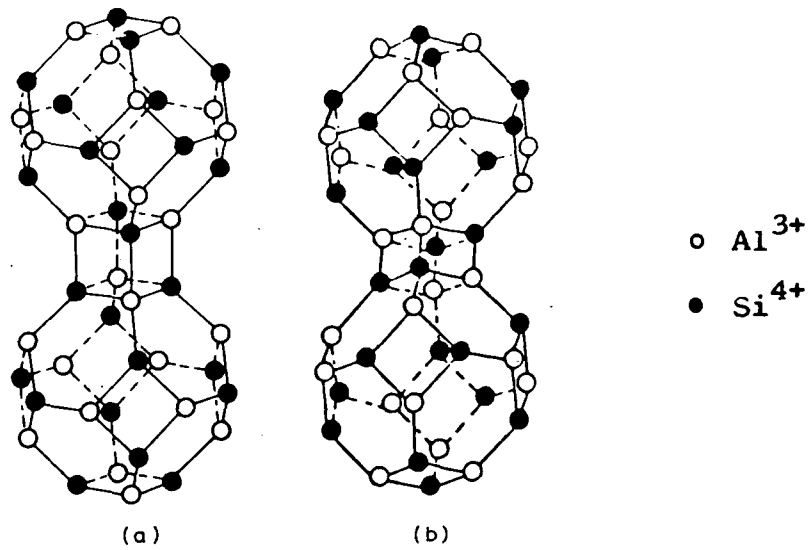

In (a) the Al^{3+} and Si^{4+} ions alternate rigorously, in accord with the Loewenstein rule[5]. In (b) the 3:1 ordering scheme of $Al^{3+}$and Si^{4+} ions proposed by Thomas et al[10] is illustrated.

square faces (Fig.3.2). Within a given zeolite structure, the largest cavities are labelled α-cages, the second largest as β-cages, etc. Thus in A-type zeolites the 26-hedra are the α-cages and the sodalite units are the β-cages. The 26-hedron is also referred to, somewhat loosely, as a supercage although strictly this term is reserved for the larger α-cages of faujasite-type zeolites (Section 3.3).

Entry into the α-cage of an A-type zeolite can be made from any of the six adjacent 14-hedra, through 16-membered $Al_4Si_4O_8$ rings.[3] These rings are termed 8-oxygen rings (or windows) because their mean free diameter of 4.2Å is defined by the ionic radius of the oxygen ions.[3] Passage between an α-cage and a β-cage is possible *via* a 12-membered $Al_3Si_3O_6$ ring (6-oxygen ring) of mean free diameter 2.2Å. Thus there are two interconnecting pore systems in type-A zeolites, one of diameter 11.4Å with 4.2Å constructions, the other of alternate 11.4Å and 6.6Å cavities separated by 2.2Å constructions.[3]

Early powder X-ray diffraction studies[4] of $Na_{12}A$ indicated a cubic structure. If the Si and Al ions were not differentiated, the pseudo unit-cell of the $Na_{12}Al_{12}Si_{12}O_{48}$ resulted with unit cell parameter a = *ca* 12.3Å and space group $Pm\bar{3}m$.[4] However, in A-type zeolites the Si:Al ratio is 1:1 which, according to Loewenstein's electrostatic valence rule,[5] necessitates a rigorous alternation of SiO_4 and AlO_4^- tetrahedra. This ordering of tetrahedra requires that the true unit cell constant is *ca* 24.6Å and lowers the symmetry of the space group to the cubic $Fm\bar{3}c$.[6-9] The true unit cell contains 8 pseudo unit cells and 192 TO_4 tetrahedra.

Recent work of Thomas and co-workers[10,11] using powder neutron diffraction, magic angle spinning ^{29}Si n.m.r. and electron

microscopy has shown that the Loewenstein rule is in fact violated in $Na_{12}A$ zeolite. The n.m.r. data indicated that each Si(IV) ion was linked, tetrahedrally, *via* shared oxygen ions to three Al(III) ions and one Si(IV) ion, and *vice versa*. This 3:1 ordering scheme of AlO_4^- and SiO_4 tetrahedra is illustrated in Fig.3.4, along with the previously accepted 4:0 ordering scheme (*ie* each Si(IV) ion linked via bridging O ions to 4 Al(III) ions and *vice versa*). Thomas *et al*[10,11] showed that weak reflections reported in published LEED[12-14] and X-ray diffraction studies[6,9] of $Na_{12}A$ samples were consistent with the repeat unit of the structure being comprised of two linked β-cages (Fig.3.4). This provides crystallographic evidence that the true unit cell of $Na_{12}A$ contains eight pseudo unit cells. The powder neutron diffraction data of Thomas *et al*[10,11] for $Na_{12}A$ indicated a rhombohedral space group $R\bar{3}$, the β-cages being slightly distorted from cubic symmetry. Within the same 3:1 ordering scheme, the cubic space group Pn3n (a = *ca* 24.6Å) could also be desired for $Na_{12}A$.[11]

It is conceivable that the short range Si/Al ordering in a zeolite would depend upon its method of preparation. Thomas *et al*[15] have shown this to be the case for the aluminosilicates sodalite and cancrinite but all the synthetic methods of producing $Na_{12}A$ zeolite so far studied[15] have resulted in the same 3:1 ordering scheme.

Hereafter, we will discuss A-type zeolites in terms of the pseudo unit cell, *eg* $Na_{12}Si_{12}Al_{12}O_{48}\cdot wH_2O$, rather than in terms of the true unit cell.

There are three crystallographically distinct types of

oxygen ion in the framework of A-type zeolites: O(1) ions are the bridging ions between sodalite units; O(2) and O(3) ions at distinguishable sites found in both the 6-oxygen and 8-oxygen rings.[16] The Si-O-Al bond angles reported for hydrated and dehydrated $Na_{12}A$ zeolites are listed in Table 3.1.

Table 3.1 Some reported bond angles in $Na_{12}A$ zeolite

zeolite	bond	angle	ref.
hydrated $Na_{12}A$	Si-O(1)-Al	145.5°	6
	Si-O(2)-Al	159.5°	6
	Si-O(3)-Al	144.1°	6
dehydrated $Na_{12}A$	Si-O(1)-Al	145.1°	17
	Si-O(2)-Al	165.6°	17
	Si-O(3)-Al	145.5°	17

The Na^+ cations in $Na_{12}A$ may be ion-exchanged for other monovalent or polyvalent cations. In dehydrated zeolites, the exchangeable cations are generally held at specific sites with respect to the framework and may be located by single crystal X-ray diffraction. Using the nomenclature of Barrer,[16] the available cation sites in type-A zeolites are listed in Table 3.2. The number of cations present in the zeolite may be less than the total number of sites available and the cations are then distributed to minimise the free energy of the system. In a fully hydrated zeolite, the cations are themselves hydrated and have only a weak interaction with the framework. The fully hydrated cations are mobile.

The cation locations in hydrated $Na_{12}A$ zeolite have been determined from X-ray single crystal[6] and powder diffraction[4,18-20]

Table 3.2 Cation locations in type-A zeolite after ref.[16]

Description of site	Designation	Number of sites available per pseudo unit cell
In the centre of an 8-oxygen ring	S1	3
Adjacent to an 8-oxygen ring but displaced into the α-cage	S1*	
In the centre of a 6-oxygen ring	S2	8
Adjacent to a 6-oxygen ring but displaced into the α-cage	S2*	
Adjacent to a 6-oxygen ring but displaced into the β-cage	S2′	
Against a 4-oxygen ring	S3	12
In the centre of a β-cage	SU	1
In the centre of an α-cage	S4	1

studies. In the single crystal results,[6] eight Na^+ ions per pseudo unit cell were found at S2* sites on the 3-fold axes of the 6-oxygen rings and were tetrahedrally coordinated to three oxygen ions of the 6-ring and one water molecule. The remaining four Na^+ ions could not be located with certainty.[6] However, it is likely that three Na^+ ions were positioned at S1* sites and that one Na^+ ion, probably fully hydrated, was sited at S4.[6]

Single crystal X-ray diffraction studies[17,21,22] of dehydrated $Na_{12}A$ zeolite show that eight Na^+ ions were again located at S2* sites on the 3-fold axes but that each of these ions had moved closer to its adjacent 6-oxygen ring on dehydration. A further three Na^+ ions were each positioned in the plane of an eight-oxygen ring (S1 sites), there being one Na^+ ion per ring. These cations were displaced from the centres of the rings towards three O(2) ions.[17,22] The twelfth Na^+ ion was found to be statistically distributed over the twelve equivalent S3 sites, positioned on a 2-fold axis normal to a 4-oxygen ring.[17,22] On the basis of increasing distance from the aluminosilicate oxygen ions, the strength of the bonding to the framework of the cations at the various sites in dehydrated $Na_{12}A$ decreases in the order S2*>S1>S3.

On dehydration of $Na_{12}A$ zeolite, the pseudo unit cell parameter a is decreased by approximately 0.02Å;[1] for the dehydrated zeolite it has been reported[22] that a = 12.292(2)Å at 298.7K (Pm3m space group).

The cation positions in the partially ion exchanged zeolites that were used in our INS studies are discussed in the relevant chapters below.

3.3 Type-Y zeolites

Type-Y, and also type-X, zeolites are synthetic examples of the so-called faujasite group of zeolites, the members of which share a common framework structure.[1,16] Faujasite is a naturally occurring zeolite with this structure. The distinction between X and Y zeolites is based on the Si:Al ratio; those zeolites for which $1.0 \lesssim Si:Al < 1.5$ being classified as type-X and those zeolites for which $1.5 \lesssim Si:Al \lesssim 3.0$ being labelled type-Y.[1] The only faujasite-type zeolite investigated in this thesis had an Si:Al ratio of 1.3 (Chapter Eight) although it was classified by the manufacturers (Strem Chemicals) as a type-Y zeolite. Despite the low Si:Al ratio of this material, we will refer to it as a Y-type zeolite in accord with the manufacturers' description.

The aluminosilicate framework of the faujasite-type zeolites may be regarded as built up from sodalite units, linked by bridging O ions across their hexagonal faces.[1] The resulting structure is very open (Fig.3.5), the sodalite units being held in a tetrahedral configuration with respect to each other and enclosing large, nearly spherical voids (*ca* 12Å diameter) known as 26-hedra of type II[1] or supercages. Each supercage is surrounded tetrahedrally by four other supercages from which it is separated by 12-oxygen rings of 8 to 9Å diameter.[1]

There are four crystallographically distinct types of framework oxygen ion in faujasite-type zeolites (Fig.3.6) and typical T1--O-T2 bond angles are listed in Table 3.3. Adopting the classification system of Barrer,[16] the available cation positions in type-Y zeolites are listed in Table 3.4 and some are illustrated in Fig.3.6.

Fig. 3.5 The aluminosilicate framework of type-Y zeolites, after ref. 1.

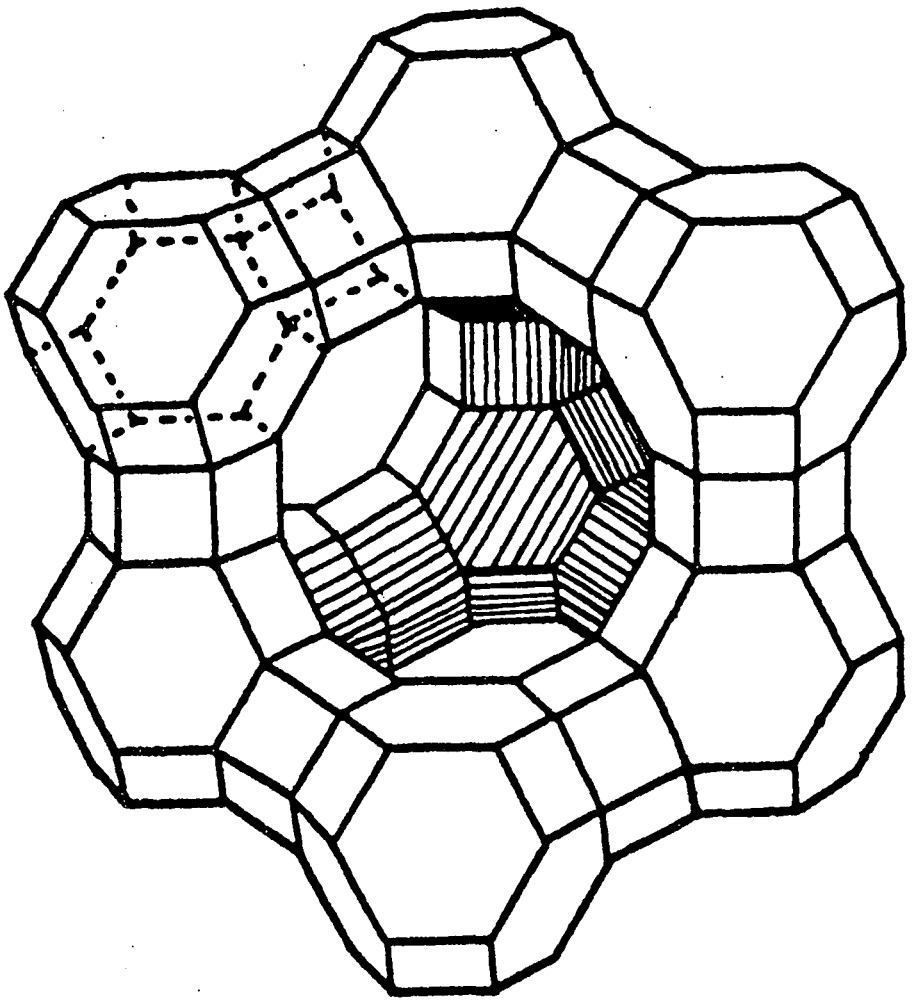

Fig. 3.6 The idealised cation and oxygen anion positions in faujasite-type zeolites, taken from ref. 34.

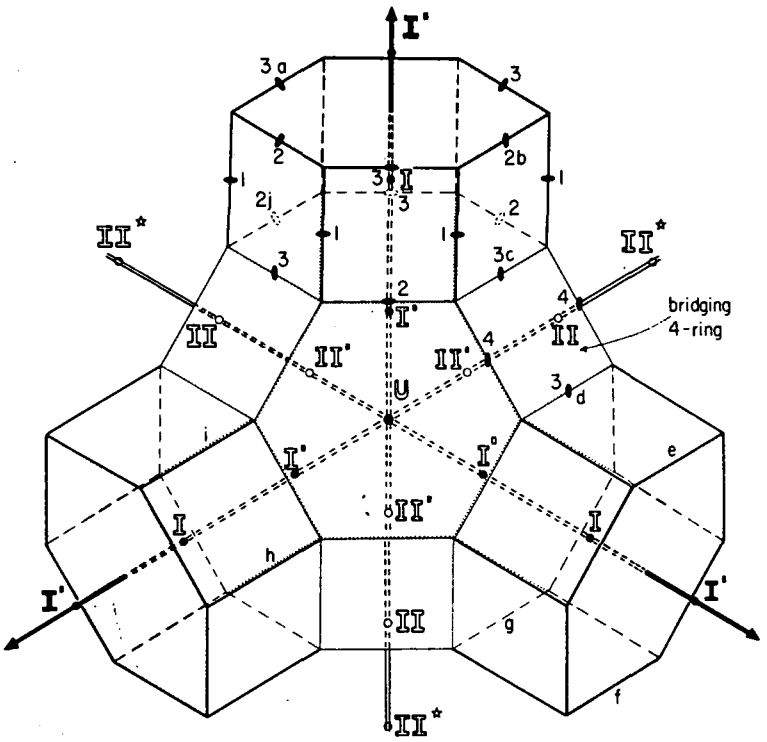

The intersections of the polyhedral edges show the positions of T *atoms. Oxygen atoms are shown at the mid-points of the edges, but should be displaced to correspond to a tetrahedral environment for each* T *atom. Some of the positions for the 4 types of oxygens are shown. The center of the truncated octahedron is marked by U. Four axes of inverse 3-fold symmetry pass through this point: 3 are visible, and 1 is hidden because it lies perpendicular to the plane of the diagram. Four hexagonal prisms share a hexagonal face with the truncated octahedron; 1 is hidden at the back side. The cation sites are: I at the center of an hexagonal prism, I' displaced from a shared hexagonal face into the sodalite cage, II' displaced from an unshared hexagonal face into the sodalite cage, II slightly displaced into the supercage, and II* displaced considerably into the supercage.*

Table 3.3 Some reported bond angles in faujasite-type zeolites

BOND	BOND ANGLE		
	Hydrated NaX $Na_{88}Al_{88}Si_{104}O_{384}\cdot 220H_2O$ ref. 23	Natural faujasite (hydrated) ref.24	Dehydrated NaY $Na_{57}Si_{135}Al_{57}O_{384}$ ref.25
T1-O(1)-T2	132.4°	140.6°	150°
T1-O(2)-T2	141.5°	140.3°	156°
T1-O(3)-T2	136.3°	145.1°	141°
T1-O(4)-T2	146.8°	140.6°	138°

Table 3.4 Cation locations in type-Y zeolites after ref.[16]

Description of site	Designation	Number of sites available per unit cell
In the centre of a hexagonal prism linking adjacent sodalite cages	I	16
In a sodalite cage, adjacent to a hexagonal prism	I′	32
In the centre of a sodalite cage	U	8
In a 6-oxygen ring linking a sodalite cage and a supercage	II	32
Near a 6-oxygen ring of site II, but displaced into the supercage	II*	
Near a 6-oxygen ring of site II, but displaced into the sodalite cavity	II′	
In the supercage, adjacent to a square face of the sodalite cavity	III	48
In the centre of a supercage	IV	8
In the 12-oxygen window of a supercage	V	16

No X-ray diffraction study of hydrated zeolite-Y has appeared in the literature but X-ray powder diffraction studies of natural faujasite[24] and of hydrated NaX zeolite ($Na_{80}Al_{80}Si_{112}O_{384}\cdot xH_2O$)[20] have been published, along with a single crystal X-ray diffraction study of hydrated NaX ($Na_{88}Al_{88}Si_{104}O_{384}\cdot 220H_2O$).[23] In the single crystal study of hydrated NaX,[23] 9 Na^+ ions per unit cell were located at sites I, 8 Na^+ ions at sites I´ and 24 Na^+ ions at sites II. The remaining Na^+ ions were unlocated and assumed to be hydrated and mobile.[23] The unit cell parameter was 25.028(5)Å within the cubic space group Fd3m.[23]

An X-ray powder diffraction study of dehydrated zeolite Y ($Na_{57}Al_{57}Si_{135}O_{384}$) has located 30.0±0.5 Na^+ ions per unit cell at sites II, 19.5±0.5 Na^+ ions at sites I´ and 7.5±0.5 Na^+ ions at sites I.[25] The unit cell parameter was 24.71(2)Å at room temperature within the space group Fd3m.[25]

The cation positions in the partially ion exchanged type-Y zeolites which were used in our INS studies are discussed in Chapter Eight.

3.4 The modes of vibration of zeolites

IR spectroscopy,[26,27,28] and to a lesser extent Raman spectroscopy,[28] has been extensively used to study the framework vibrations of a wide variety of zeolites.

Flanigen *et al*[28] have investigated the framework vibrations of many zeolites in the range 1300 cm^{-1} to 200 cm^{-1}. Each zeolite exhibited its own characteristic IR spectrum but there were similarities between the spectra of zeolites with related structures.[28] Two classes of IR band arose in the 1300 to 200 cm^{-1}

region[28]: (1) those due to the internal modes of the TO_4 tetrahedra and which were insensitive to variations in the framework structure; and (2), those arising from vibrations of the external linkages between tetrahedra which depended upon the framework structure and were related to the presence of some types of secondary building units and building block polyhedra. Both classes of IR bands were found to occur within characteristic frequency regions[28] (Table 3.5). IR spectra of zeolites A, X and Y obtained by Flanigen *et al*[28] in the region of the framework vibrations are shown in Fig. 3.7.

A shift to lower frequencies of zeolite framework modes with decreasing Si:Al ratio has been observed by many authors[26-29]. The ν_{as}(T-O) and ν_{sym}(T-O) internal stretching modes of TO_4 tetrahedra and the bands associated with the double six-ring and the double 12-ring of NaX and NaY zeolites have been reported by Flanigen *et al*[28] to show a linear decrease in frequency with increasing Al content (Fig.3.8).

All of the data thus far presented from the results of Flanigen *et al*[28] appertain to hydrated zeolites containing alkali metal or $(CH_3)_4N^+$ charge balancing cations. Dehydration of zeolites containing alkali metal and no other types of cation causes only minor distortion of the aluminosilicate framework and gives rise to minimal changes in the IR spectra from 1300 to 200 cm^{-1}.[1,28] In both hydrated and dehydrated zeolites, multivalent cations cause greater distortion of the framework than do monovalent cations. Thus IR bands arising from zeolite skeletal modes are sensitive to the charge, and radius, of multivalent intra-zeolitic cations. This is illustrated in Fig. 3.9 by the IR spectra of dehydrated NaX and CaX published to Zhadanov *et al*.[27]

Table 3.5 The characteristic frequency regions (cm^{-1}) of zeolite skeletal vibrations, after Flanigen *et al*[28]

Internal modes of TO_4 tetrahedra	wavenumber region
T-O antisymmetric stretch	1250 - 950 (vs)
T-O symmetric stretch	720 - 650
T-O bending mode	500 - 420 (s)

Modes of linkages between TO_4 tetrahedra	wavenumber region
modes of double-rings	650 - 500
pore opening modes	420 - 300
T-O symmetric stretch	820 - 750
T-O asymmetric stretch	1130 - 1050 (sh)

s = strong, vs = very strong, sh = shoulder

Fig. 3.7 The IR spectra of A,X and Y zeolites, illustrating some skeletal vibrations, taken from ref. 28.

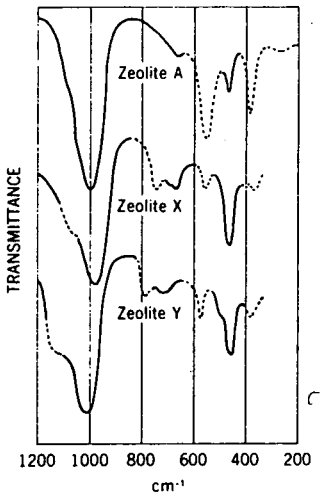

Dotted lines indicate those vibrations whose frequencies are insensitive to changes in the zeolite structure while dotted lines indicate structure-sensitive modes. The Si/Al ratio in the X zeolite was 1·2 and in Y, 2·5.

Fig 3.8 The variation in frequency of several IR bands with the fraction of Al in the framework for X and Y zeolites, taken from ref. 28.

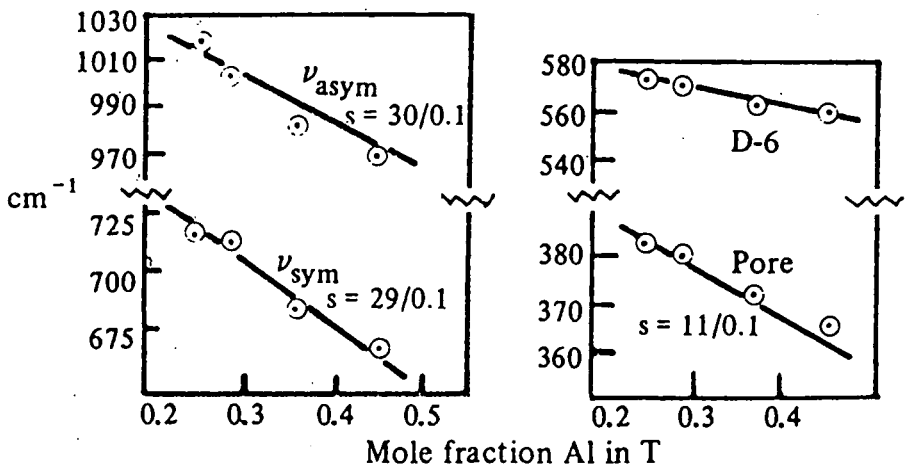

Fig. 3.9 The IR spectra published by Zhadanov et al[27] of (a) NaX and (b) CaX zeolites after vacuum dehydration at 673K for 4 hours.

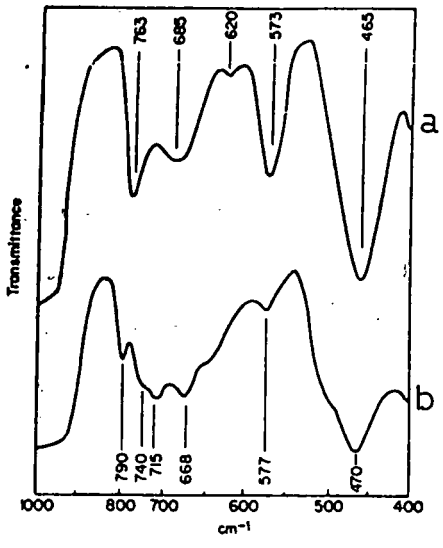

Fig 3.10 Regions of the IR spectra of CaY zeolite published by Flanigen et al[28] after dehydration, dehydroxylation and rehydration.

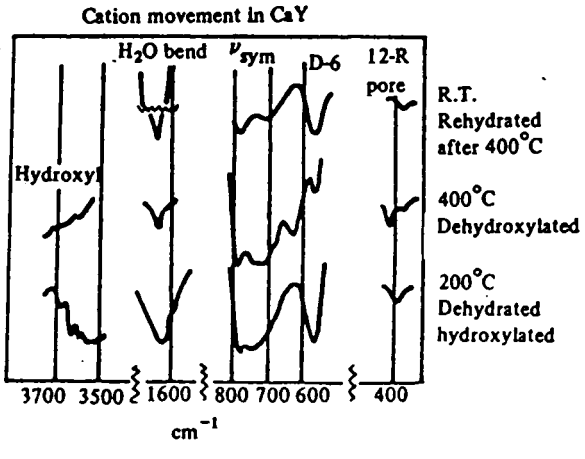

In contrast to zeolites containing group IA cations, dehydration of zeolites exchanged with multivalent cations generally results in considerable movement of the cations and correspondingly large framework distortions which can be observed using IR spectroscopy.[1,28] For example, Flanigen *et al*[28] have observed changes in the IR spectrum of CaY zeolite on dehydration in the band due to ν_{sym}(T-O) which arises in the region *ca* 710 to 750 cm^{-1}, in the double six-ring band near 570 cm^{-1} and in the pore-opening band at 390 cm^{-1} (Fig. 3.10). These changes were reversed on rehydration and were interpreted as arising from movement during dehydration of Ca^{++} ions from positions within the β-cage to site I of the double six-ring units.[28]

The far-IR spectra of dehydrated, metal-cation-containing zeolites show bands below 300 cm^{-1} which have been assigned[30-32] to the stretching modes with respect to the aluminosilicate framework of the metal cations (Table 3.6).

Table 3.6 Frequencies (cm^{-1}) assigned to vibrational modes of cations in dehydrated type-X and type-Y zeolites, from ref.[30]

Assignment	NaX	KX	CaX	NaY	KY	CaY
site I	160		287	167	107	256
6-ring sites (I′,II,II′)	190	156	273	180	133	227
site III	67	58				

Evidence that these bands (Table 3.6) are due to the metal cations is provided by their non-observation in the far-IR spectra of hydrogen ion forms of the zeolites, *eg* HY or HX, and by the following relationship. For group IA, and also for group IIA, cations the frequencies of these bands vary with $m^{-1/2}$, where m is the cation mass, provided that the cation site and charge,

the zeolite Si:Al ratio and the presence, if any, of adsorbed molecules are unaltered.[30-32]

The modes of those cations which are not sterically constrained by the zeolite framework show a shift to lower frequencies on hydration[30] due to weakening of the cation-framework interaction, *eg* in KX zeolite the vibration of K^+ cations at 6-ring sites shifts from 156 to 122 cm^{-1}.

The low frequencies of the modes associated with site III cations (Table 3.6) are consistent with the result[1,16] that occupation by cations of the sites III in faujasite-type zeolites is generally energetically disfavoured over occupation of the 6-ring and hexagonal prism sites.

We reiterate that framework vibrations of dehydrated zeolites give rise to very weak bands in INS spectra. The incoherent neutron scattering cross section, σ_{inc}, of O, Al and Si are zero and for dehydrated zeolites containing no adsorbents, the only skeletal modes which can be observed by INS are those which displace cations with non-zero values of σ_{inc}, *eg* Na^+ (σ_{inc} = 1.7 barns[33]). Modes involving displacement of cations with appreciable values of σ_{inc}, *eg* Co^{2+} for which σ_{inc} = 5.2 barns[33], are readily observed in the INS spectra of dehydrated zeolites (Chapter Six).

REFERENCES

1. Breck, D.W., Zeolite Molecular Sieves: Structure, Chemistry and Use, Wiley-Interscience, New York, 1974.

2. Meier, W.M., Molecular Sieves, Society of Chemical Industry, London, 1968.

3. Seff, K., Acc.Chem.Res., 9, 121, 1976.

4. Breck, D.W., Eversole, W.G., Milton, R.M., Reed, T.B. and Thomas, T.L., J.Am.Chem.Soc., 78, 5963, 1956.

5. Loewenstein, W., Am.Mineral, 39, 92, 1954.

6. Gramlich, V. and Meier, W.M., Z.Kristallogr., 133, 134, 1971.

7. Thoni, W., Z.Kristallogr., 142, 142, 1975.

8. Pluth, J.J. and Smith, J.V., J.Phys.Chem., 83, 741, 1979.

9. Pluth, J.J. and Smith, J.V., J.Am.Chem.Soc., 102, 4704, 1980.

10. Thomas, J.M., Bursill, L.A., Lodge, E.A., Cheetham, A.K., and Fyfe, C.A., J.Chem.Soc., Chem Commun., 276 (1981).

11. Bursill, L.A., Lodge, E.A., Thomas, J.M., and Cheetham, A.K., J.Phys.Chem., 85, 2409, 1981.

12. Bursill, L.A., Lodge, E.A. and Thomas, J.M., Nature, 286, 113, 1980.

13. Thomas, J.M., Millward, G.R. and Bursill, L.A., Phil.Trans. R.Soc., A300, 43, 1981.

14. Lodge, E.A., Bursill, L.A. and Thomas, J.M., J,Chem.Soc., Chem.Commun., 875 (1980).

15. Thomas, J.M., Klinowski, J., Fyfe, C.A., Hartman, J.S. and Bursill, L.A., J.Chem.Soc., Chem.Commun., 678 (1981).

16. Barrer, R.M., Zeolites and Clay Minerals as Sorbents and Molecular Sieves, Academic Press, London, 1978.

17. Yanagida, R.Y., Amaro, A.A. and Seff, K., J.Phys.Chem., 77, 805, 1973.

18. Reed, T.B. and Breck, D.W.,J.Am.Chem.Soc., 78, 5972, 1956.

19. Howell, P.A., Acta Cryst., 13, 737, 1960.

20. Broussard, L. and Shoemaker, D.P., J.Am.Chem.Soc., 82, 1041, 1960.

21. Smith, J.V. and Dowell, L.G., Z.Kristallogr., 126, 135, 1968.

22. Subramian, V. and Seff, K., J.Phys.Chem., 77, 805, 1973.

23. Olson, D.H., J.Phys.Chem., 74, 2758, 1970.

24. Baur, W.H., Am.Mineral., 49, 697, 1964.

25. Eulenberger, G.R., Shoemaker, D.P. and Keil, J.G., J.Phys.Chem., 71, 1812, 1967.

26. Milkey, R.G., Am.Mineral, 45, 990, 1960.

27. Zhadanov, S.P., Kiselev, A.V., Lygin, R.J., and Titova, I.I., Russ.J.Phys.Chem., 38, 1299, 1964.

28. Flanigen, E.M., Khatami, H. and Szmanski, H.A., Adv.Chem.Ser. 101, 201, 1971.

29. Stubican, V. and Roy, R., Am.Mineral, 46, 32, 1961.

30. Butler, W.M., Angell, C.L., McAllister, W. and Risen, W.M., J.Phys.Chem., 81, 2061, 1977.

31. Brodskii, I.A., Zhadanov, S.P. and Stanevich, A.E., Op.Specktrosk, 30, 58, 1971.

32. Brodskii, I.A. and Zhadanov, S.P. in Proc.5th Int.Conf. Zeolites (Naples 1980), Ed.L.V.C. Rees, Heyden, London, 1980.

33. B.T.M. Willis (Ed.), Chemical Applications of Thermal Neutron Scattering, Oxford University Press, London, 1973.

34. Smith, J.V. in Molecular Sieve Zeolites I (Ed.Gould,R.F.), Adv.Chem.Ser., 101, 171, 1971.

CHAPTER FOUR

EXPERIMENTAL

4.1 INS sample cells

The INS sample cells (Fig.4.1) were thin walled Al cans which had Al/Co friction welds, stainless steel/glass seals which could withstand liquid helium temperatures, and glass break-seals. In Section 4.2.4 the purpose of the break seals is described. The beam windows were made of Al, which has the advantages of being easily machined, of having a zero incoherent neutron scattering cross-section, and a very low thermal neutron absorption cross-section.[1] Both cylindrical and flat types of INS cell were used (Fig. 4.1), the former allowing greater amounts of weakly scattering samples to be used.

Fig. 4.1 Typical flat and cylindrical INS sample cells

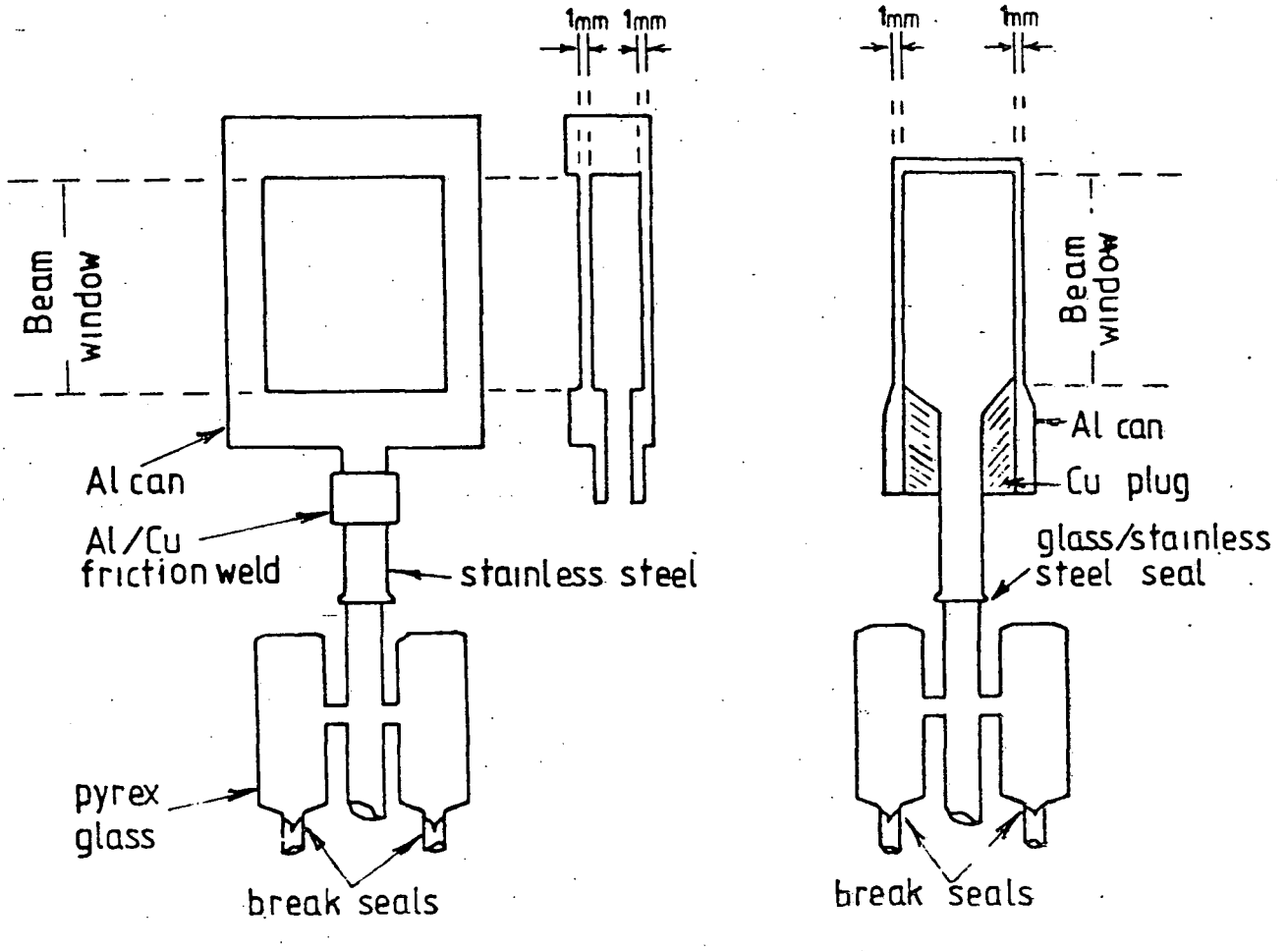

NOT TO SCALE

4.2 Sample preparation

Details of the ion-exchange of the various zeolites are given in the relevant chapters below.

Elemental analysis of the zeolites was carried out by the Departmental service at the University of Durham, using a Perkin-Elmer 403 atomic absorption spectrometer. For A-type zeolites, known quantities of the sample were dissolved in dilute nitric acid and measured against the appropriate aqueous standards. In the case of Y-type zeolites, the sample was first digested in hydrofluoric acid and perchloric acid before dissolving in dilute nitric acid and measurement against the relevant aqueous standards. Analysis was made for Al, Si and the exchangeable cations for all our samples.

4.2.1 Zeolite dehydration

Except for NiNaY (Section 4.2.2), all the zeolites were dehydrated using a technique developed by J. Howard.[2] The zeolite, typically 20 to 70g, was placed in a silica bulb which had a graded silica/pyrex seal allowing it to be glass-blown to a vacuum line at point A (Fig. 4.2). The vacuum pump would be either an oil diffusion pump or a turbomolecular pump depending on availability. After evacuation to 1×10^{-5} torr, the sample was heated with a cylindrical, electric furnance to 623K at such a rate that the pressure remained below 1×10^{-4} torr. This would take 36 to 48 hours, depending on the quantity and nature of the zeolite. On reaching 623K, the sample was then heated to 723K over 2 hours. The furnance was then removed and the sample vessel sealed by torch near point A (Fig.4.2), pumping being continued. When cool, the powder was tapped into

Fig. 4.2 Apparatus used for vacuum drying of zeolites.

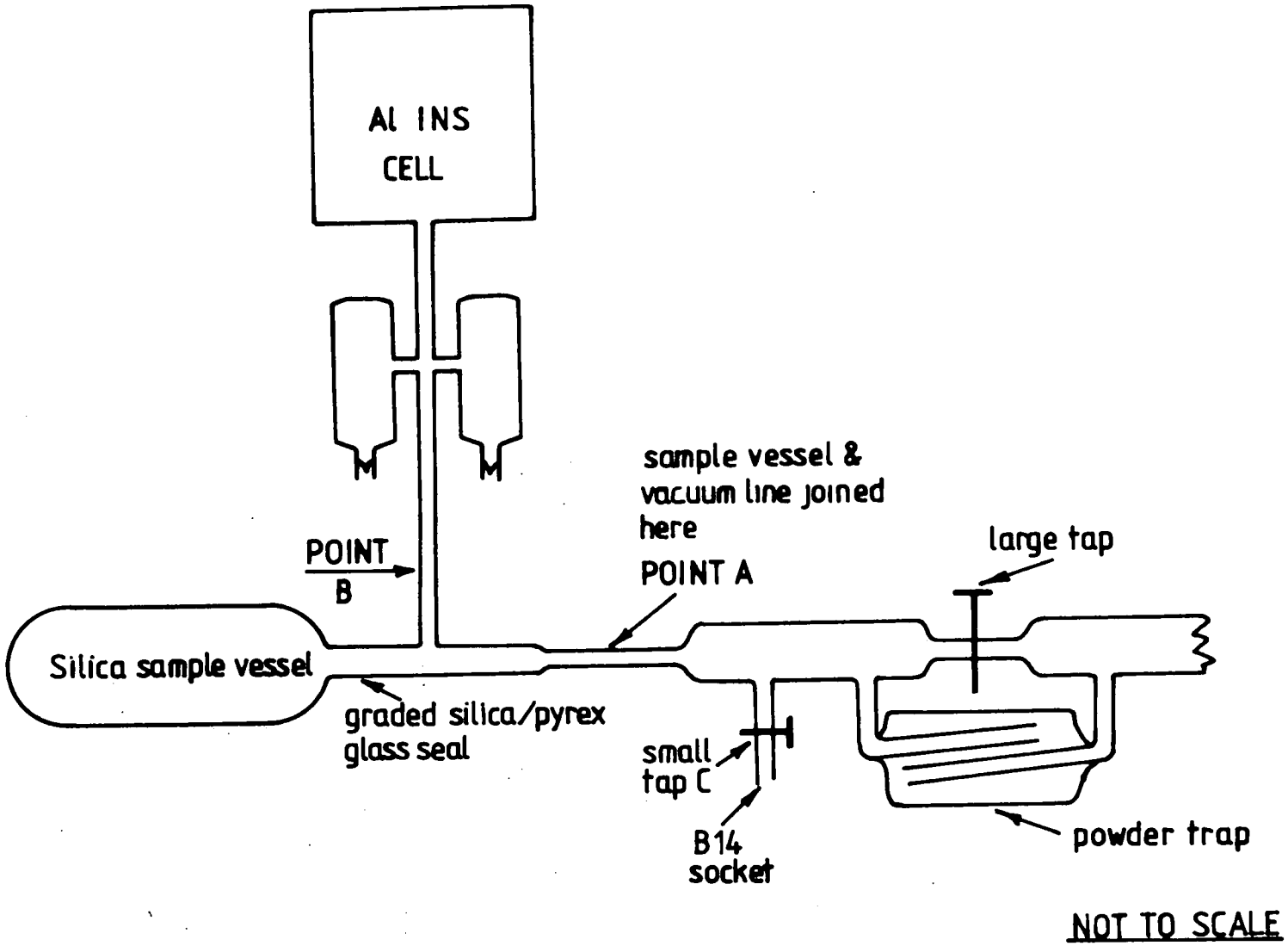

the INS cell which was sealed at point B (Fig. 4.2). The INS spectrum of the dehydrated sample was obtained and used as a background for the spectra of the zeolite plus adsorbate.

4.2.2 Pre-treatment of NiNaY and ZnO samples

These samples were heated in dried O_2 before evacuation. The apparatus of Fig.4.2 was used, the O_2 supply being connected *via* tap C. Further details are given in Chapters Seven (ZnO) and Eight (NiNaY).

4.2.3 Pre-treatment of Pd black samples

Fig. 4.3 shows the greaseless vacuum system used for the pre-treatment of Pd black. Surface oxygen was removed from the Pd surface by H_2 titration, resulting in the formation of H_2O which was easily desorbed. The composition of the gas phase during the titration was monitored with a quadrupole mass spectrometer. Further details are given in Chapter Five.

4.2.4 Adsorption of gases

The following technique was used for the adsorption of gases by dehydrated zeolites and of H_2 by the pre-treated ZnO and Pd samples (Chapters Seven and Five).

A greaseless vacuum system was used (Fig. 4.4), the gas bulb A and the INS cell F being glass-blown to the system. The break seals B of the gas bulb and INS cell (Fig. 4.4) allowed these vessels to be glass-blown to the vacuum line without contamination of their contents. By dropping, under the control of a magnet, a steel ball-bearing onto the break seal, the contents of each vessel could then be exposed to the vacuum

Fig. 4.3 Vacuum system used for pretreatment of Pd black samples.

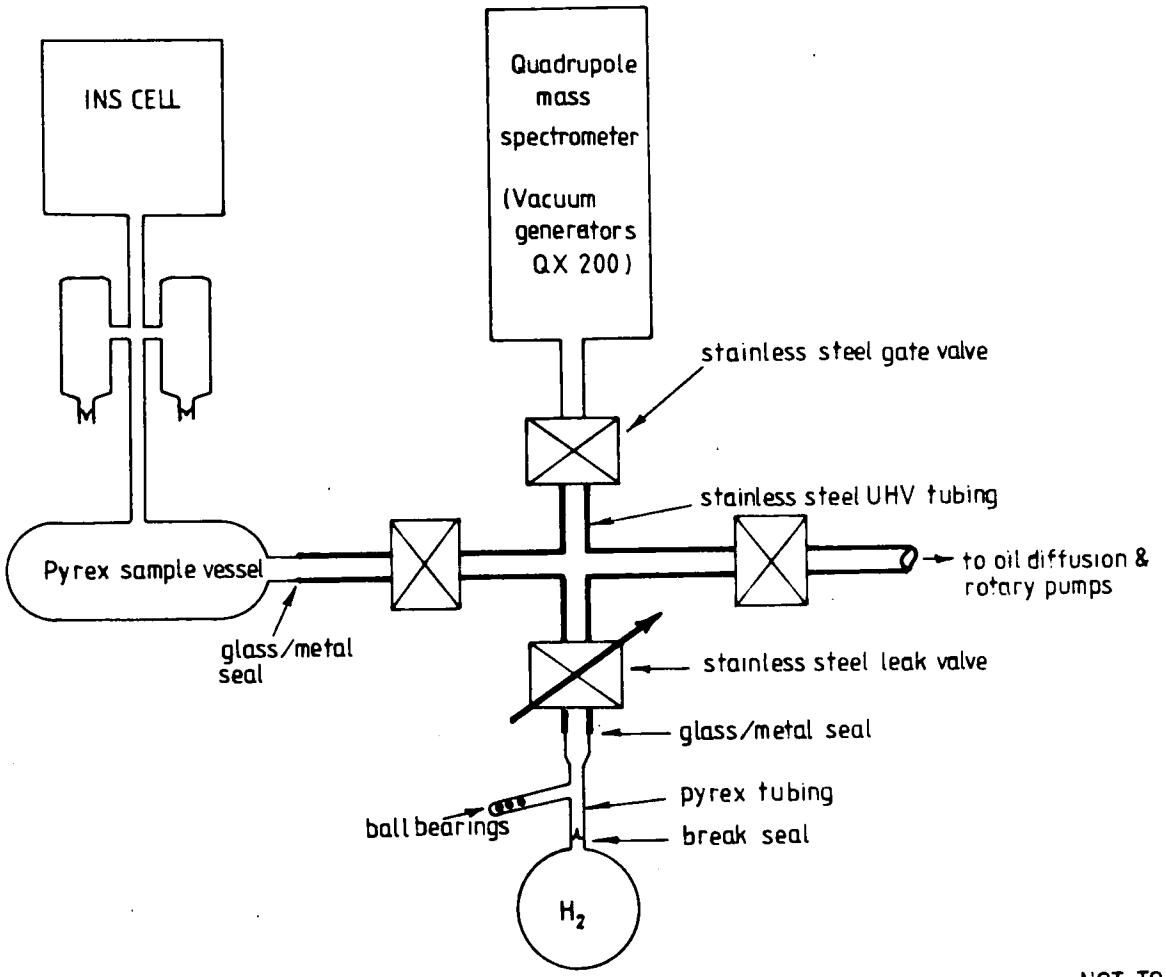

Fig. 4.4 Apparatus used for adsorption of gases.

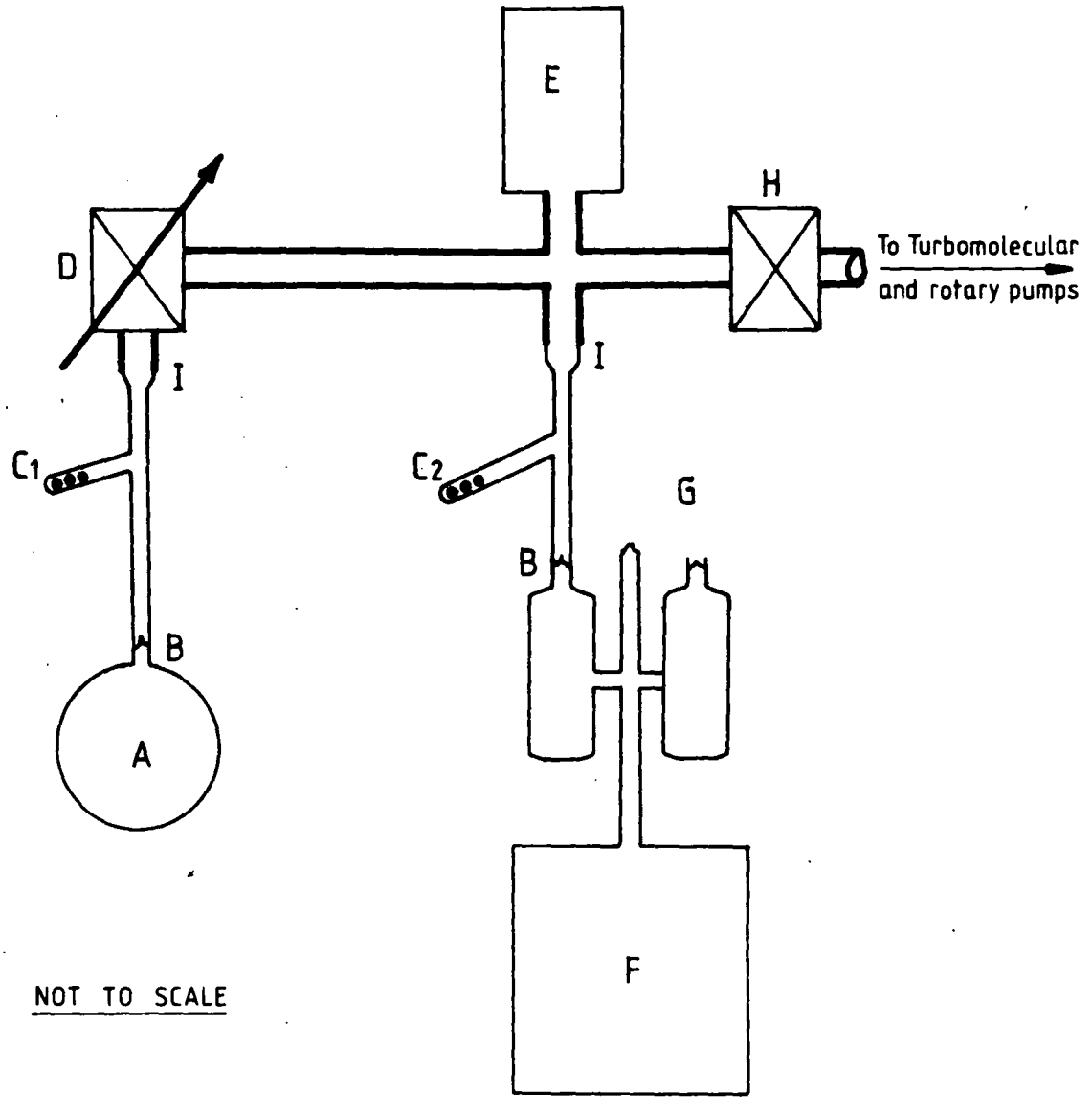

A Bulb containing adsorbate gas
B Break-seal
C_1, C_2 Side-arms containing steel ball-bearings
D Leak valve
E Pressure Gauge (e.g. Leybold-Heraeus 1VS strain gauge type)
F INS cell
G Point at which sample can was sealed by torch after adsorption of gas
H Bellows valve
I Stainless steel / glass seal

Heavy lines denote stainless steel vacuum tubing
Lighter lines denote pyrex tubing

system. We refer to that part of the vacuum system (Fig.4.4) between the valves D and H as the sample handling part of the system. The bulb A, side-arm G and connecting tubing up to valve D is called the gas handling part of the system (Fig.4.4). The bulb A was of known volume and had been previously filled to a known pressure with the adsorbate gas at a known temperature.

The adsorption procedure was as follows.

1. The system was evacuated to 1 x 10^{-5} torr or less and valves D and H (Fig.4.4) were then closed.
2. The break seal of bulb A was opened by dropping a steel ball-bearing on it with the aid of a magnet.
3. By alternately opening and closing valves D and H, the pressure in the gas handling part of the system was adjusted such that it contained the required amount of gas to be adsorbed. The pressure was noted at each stage during this operation. This enabled the volumes of the gas handling and sample handling parts of the system to be calculated, assuming the adsorbate was an ideal gas, since the quantity of gas initially contained in bulb A was known.
4. With valves D and H closed, the break seal to the INS cell was opened.
5. Valve D was then gradually opened to admit the adsorbate to the sample. After *ca* 10 minutes, the lower half of the INS cell was immersed in liquid nitrogen. The cell was further immersed as the adsorption proceeded.
6. After valve D had been fully opened and the pressure had come to equilibrium, the INS cell, while still immersed in liquid nitrogen, was sealed by torch at point G (Fig. 4.4). The liquid nitrogen was allowed to evaporate, the INS sample slowly regaining room temperature.

Using the ideal gas equation, the quantity of gas adsorbed was calculated from the pressure in the line measured immediately before sealing the INS cell and from the volume of the system. Allowance was made for the volume of the INS cell, estimated from the internal dimensions of the Al can and the glass neck.

4.2.5 The adsorption of water by Ca_6-A zeolite

Demineralised water was poured *via* a side-arm into a glass phial fitted with a break seal. The side-arm was attached to a vacuum line and dissolved air removed from the H_2O by successive freeze-pump-thaw cycles. The phial was sealed by torch at a point along the side-arm and the quantity of water in the vessel determined by weighing.

The adsorption apparatus (Fig. 4.5) was assembled and connected to a grease-free vacuum system by glass blowing. After evacuation to 1×10^{-5} torr or less, the glass tube was sealed by torch at point B (Fig. 4.5). The break-seals D and E were opened and the INS cell immersed in liquid nitrogen. The glassware was heated to 323K using electric heating tape and heating was continued for 30 minutes after all visible traces of liquid had disappeared. The INS cell was then sealed by torch at point C (Fig. 4.5).

4.3 Neutron scattering spectrometers

4.3.1 The IN4 time-of-flight spectrometer

IN4 (Fig. 4.6) is a time-of-flight (t.o.f.) spectrometer on a thermal beam tube at the I.L.L., Grenoble which may

Fig. 4.5 Apparatus used for the adsorption of H_2O by Ca_6-A zeolite.

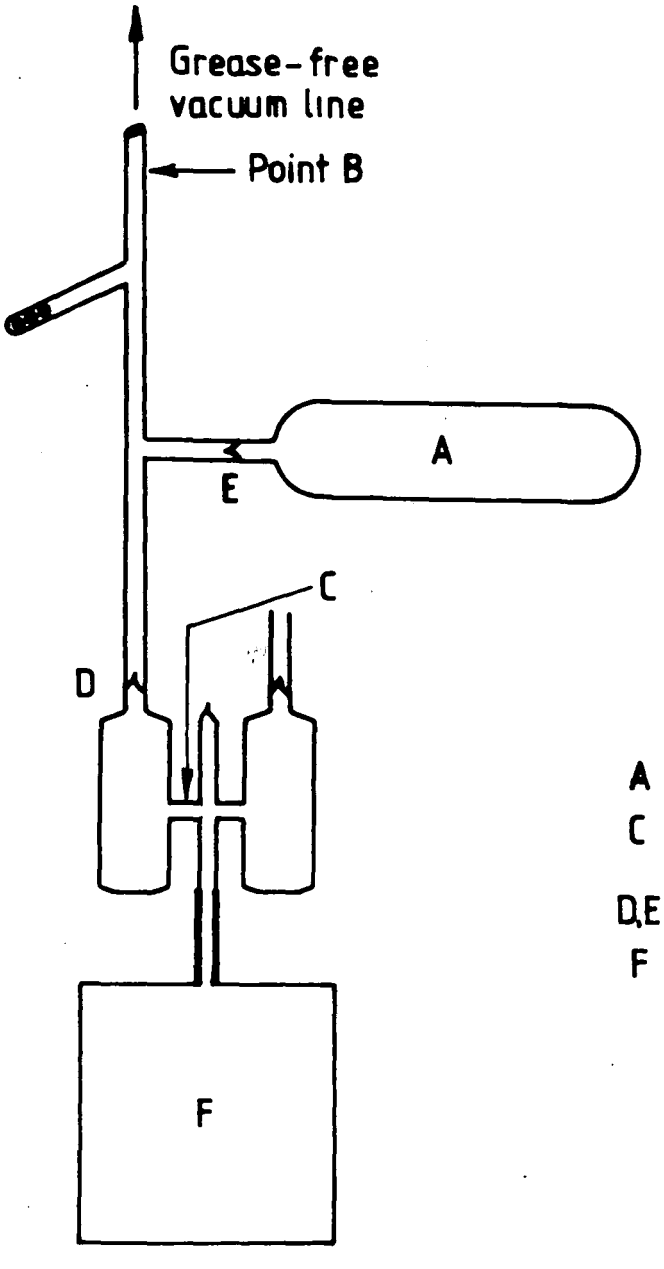

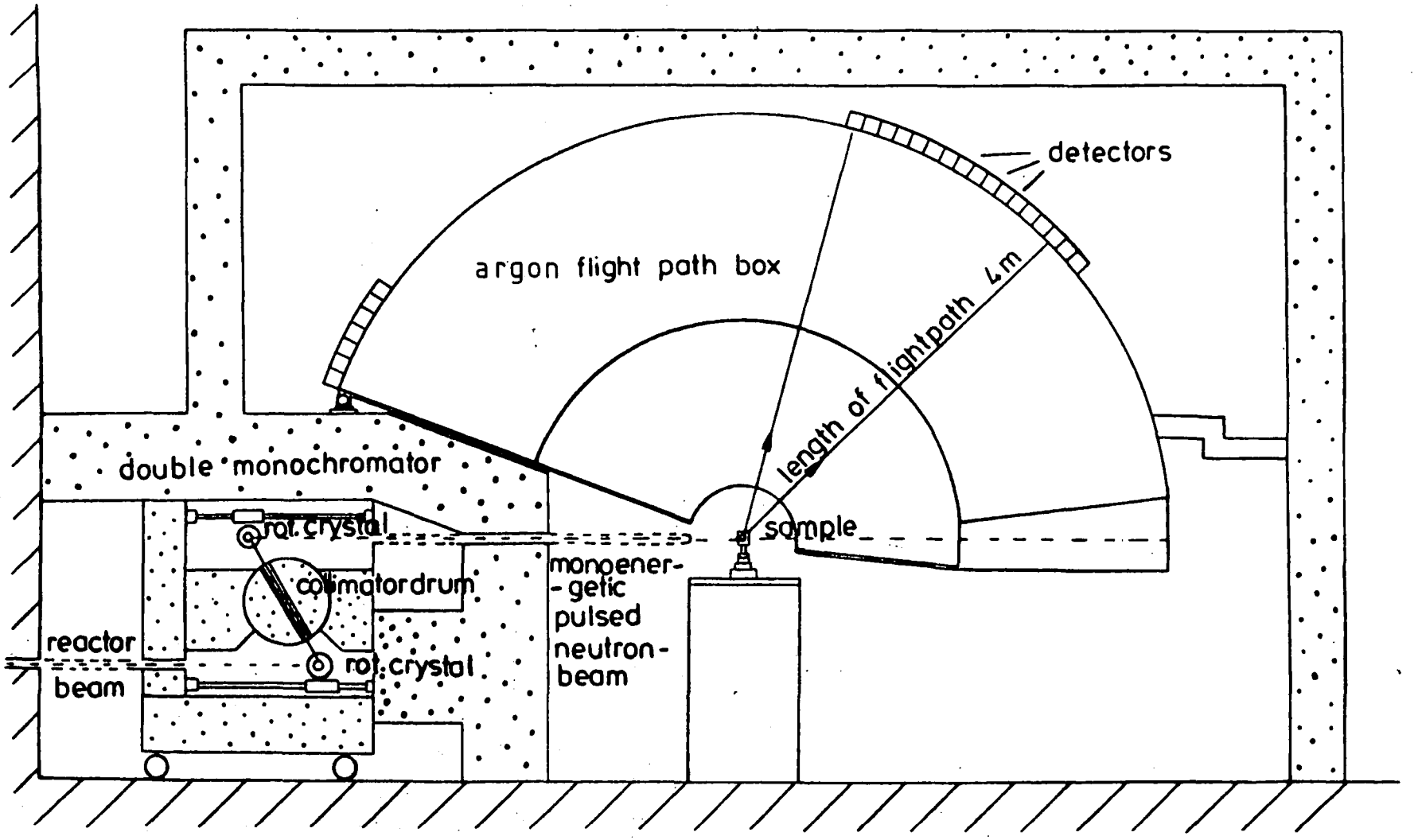

Fig. 4·6 The IN4 Time-of-Flight Spectrometer, ILL Grenoble[3]

be used for a wide range of energy (0 to *ca* 400 cm^{-1}) and momentum transfers. Various options in the spectrometer set-up are available but only those which we used are described here.

The monochromator consisted of two rotating crystals of pyrolytic graphite which were mounted on parallel rails and separated by a rotatable collimator (Fig. 4.6). The relative phasing of the crystals' rotation and their distance apart were adjusted such that only those neutrons of the required energy were reflected from the crystals. The reflecting planes were C(0004) which enabled a monoenergetic beam to be produced in the range 113 to 407 cm^{-1}. Rotation of the crystals resulted in a pulsed monochromatic beam.

The double monochromator reduced order contamination and the small spread of energies in the monochromated beam at the cost of a reduced neutron flux and also resulted in a very low background from epithermal neutrons.

A fusion chamber monitor placed immediately before the sample measured the neutron flux incident on the sample. For a monochromated energy of 240 cm^{-1}, the incident flux is *ca* 1.7×10^4 neutrons cm^{-2} s^{-1}. [3,4] The energy resolution $\Delta E/E$ depends, in part, on the incident neutron energy and the transition energy and is typically *ca* 2% in our IN4 spectra.

The sample containers were mounted horizontally in a chamber under an He gas pressure of *ca* 10^{-2} torr and maintained at low temperatures (10 to 16K) by a variable temperature He cryostat (not illustrated). The sample cans, if of the flat cell type (Section 4.1) were oriented at 45° to the beam. The incident beam was masked such that it was 30mm in the vertical

plane and sufficiently wide in the horizontal plane to illuminate the entire (interior) length of the sample can. Counting times for zeolite samples, whether dehydrated or containing an adsorbate, were *ca* 36 hours.

The scattering from a 2mm thick vanadium plate was also recorded. The scattering from vanadium is predominantly incoherent and, apart from a small effect due to the Debye-Waller factor, is isotropic to a good approximation. The isotropy of the scattering allowed the relative efficiencies of the detectors to be determined. In addition, absolute scattering cross-sections could be obtained if the total numbers of scattering atoms in the vanadium sheet and the sample were known. We used the vanadium data only for calibration of the detector efficiencies.

The flight path box (Fig. 4.6) consisted of an aluminium housing filled with Ar gas. Around the outside of this box were 67 positions for the detector boxes, covering a range of scattering angles from -9^{o} to 140^{o}. Each of the 48 available detector boxes contained six ^{3}He detectors and associated electronics, and spanned an angular width of 2.25^{o}. The detector boxes were positioned over the periphery of the aluminium housing according to the requirements of the experiment; in general those angles corresponding to back scattering, rather than forward scattering, were preferred.

The spectrometer was operated in neutron energy loss mode which, for IN4, gives better resolution than neutron energy gain. The samples were held at low temperatures so that those neutrons which were inelastically scattered caused excitations from the vibrational and rotational ground states of the molecule. Low

temperatures also minimise the reduction in scattered neutron intensity from the Debye-Waller factor (Chapter Two).

Energy analysis of the scattered neutrons was achieved by measuring the time taken to travel from the sample to the detectors. Those neutrons which lost least energy to the sample arrived at the detectors first. For each neutron pulse, the time of arrival of the neutrons was recorded in channels of width 8μs with 508 channels per pulse. The data acquisition system was controlled by a dedicated PDP11 computer which added data from successive pulses to obtain a plot of scattered neutron counts against channel number t. Conversion of the recorded data into the functions (SQ,ω) and $P(\alpha,\beta)$ was carried out using computer programs available at the I.L.L.[5] The calculations were based on the following considerations.

1. In order to improve the statistics of the data, the counts recorded from several different runs and by adjacent detectors could be summed for each t.o.f. channel. Let C_s be the counts per channel thus obtained for the sample and C_b the counts per channel for the background. For each detector of group of summed detectors, the quantity y_t, the corrected number of counts in channel t, was computed from:

$$y_t = \left(\frac{a_s c_s}{v} - \frac{a_b c_b}{v} \right) \frac{N_v \sigma_v}{N_s \sigma_s} \quad \frac{1}{\Delta\tau} \quad \frac{1}{a_3} \quad \frac{\varepsilon_o}{\varepsilon_t}$$

where

a_s = number of pre-sample monitor counts for vanadium run / number of pre-sample monitor counts for sample run ;

a_b = number of pre-sample monitor counts for vanadium run / number of pre-sample monitor counts for background run ;

V = total counts in the vanadium eleastic peak for the given detector group;

N_V, N_S = number of scattering nuclei cm^{-2} in the neutron beam direction in the vanadium and sample respectively;

σ_S; σ_V = bound atom cross sections for vanadium and sample respectively.

a_3 is a factor which is computed by the programs, and corrects for multiple elastic scattering and adsorption in the vanadium sample. It depends on the incident neutron energy, the width of the vanadium sample which is assumed to be in the form of a flat sheet, the angle of the sheet to the incident beam and the scattering angle;

ε_o and ε_t are empirically determined detector efficiencies for elastically scattered neutrons and those which are inelastically scattered and recorded in channel t;

$$\Delta\tau = \frac{\text{channel width}}{\text{sample-detector distance}} \simeq \frac{8}{4}\ \mu s.m^{-1}$$

2. The infinite energy channel, t_∞, is that t.o.f. channel which is switched open when neutrons have just arrived at the sample. Any neutron detected in this channel would have a zero time-of-flight. Those neutrons detected in some channel t have a reciprocal velocity τ, given by

$$\tau = (t-t_\infty).\ \Delta\tau$$

The reciprocal velocity scale is therefore linear with respect to channel number and starts at zero at the infinite energy channel.

3. For each channel, the following parameters are computed[5,6]

(a) Alpha

By definition: $\alpha = \hbar^2 Q^2/(2MK_BT)$

where $\underline{Q}$ is the scattering vector, M is the mass of the scattering nucleus, K_B is Boltzmann's constant and T the absolute temperature. Since $Q^2 = k_o^2 + k^2 - 2k_o k\cos\theta$, where k_o and k are the neutron wave vectors before and after scattering through an angle θ, then

$$\alpha = \frac{\hbar^2}{2AK_BT}\ 1.5079 \times 10^{49} \left(\frac{1}{\tau_o^2} + \frac{1}{\tau^2} - \frac{2\cos\theta}{\tau_o \tau} \right)$$

where A is the atomic weight of the scattering unit in AMU and τ_o is the reciprocal velocity of elastically scattered neutrons.

(b) Beta

By definition, $\beta = \frac{\hbar\omega}{K_BT}$

and $\hbar\omega = \frac{\hbar^2}{2m} \cdot \left(k_o^2 - k^2\right) = \Delta E$

so that $\beta = \frac{2.54 \times 10^{22}\ \hbar^2}{2mK_BT} \cdot \left(\frac{1}{\tau_o^2} - \frac{1}{\tau^2}\right)$

where m is the neutron mass, ΔE is the energy lost by the scattered neutrons and ω the radial frequency associated with ΔE.

(c) The scattering vector, $\underline{Q}$, is given in A^{o-1} by

$$\left|\underline{Q}\right| = 1589 \left(\frac{1}{\tau_o^2} + \frac{1}{\tau^2} - \frac{2\cos\theta}{\tau_o \tau} \right)^{\frac{1}{2}}$$

(d) The scattering functions are calculated from:

$$S(\alpha,\beta) = \frac{K_B T \times 10^{16}\ \tau^4\ \exp(\beta/2)\ y_t}{m\tau_o} \quad ;$$

$S(Q,\omega) = \exp(-\beta/2)\ S(\alpha,\beta)/(K_B T)$ for neutron energy loss; and

$P(\alpha,\beta) = 2\beta \sinh(\beta/2)\ S(\alpha,\beta)/\alpha.$

4.3.2 The DIDO beryllium filter detector spectrometer

Fig. 4.7 shows the DIDO beryllium filter detector (b.f.d.) spectrometer. The sample table (H) is fixed to the large shielding drum (I) which rotates about a vertical axis through the point P in Fig. 4.7.

A thermal neutron beam emerging from the DIDO 10H hole is monochromated by Bragg reflection from a single Al crystal. The Al(111) crystal planes were used for scans from 97 to 419 cm^{-1} and the Al(311) planes for scans from 339 to 887 cm^{-1}.

The neutron energy incident on the sample is increased stepwise by incremental rotations of the monochromator crystal. The rotation of the crystal and of the large shielding drum required to maintain the sample at the correct take-off angle are achieved automatically by computer control. Counting at each monochromated energy was continued until a pre-determined number of counts had been recorded by monitor J placed before the sample (Fig.4.7).

The maximum flux of monochromated neutrons was 1.3×10^6 neutrons $cm^{-2}s^{-1}$ which occurred at 440 cm^{-1} using the Al(111) plane.[7] The beam size at the sample was 7 x 3cm. The sample cans were held vertically in a liquid N_2 cryostat (77K) and those of the

Fig. 4.7 The DIDO b.f.d. spectrometer[7].

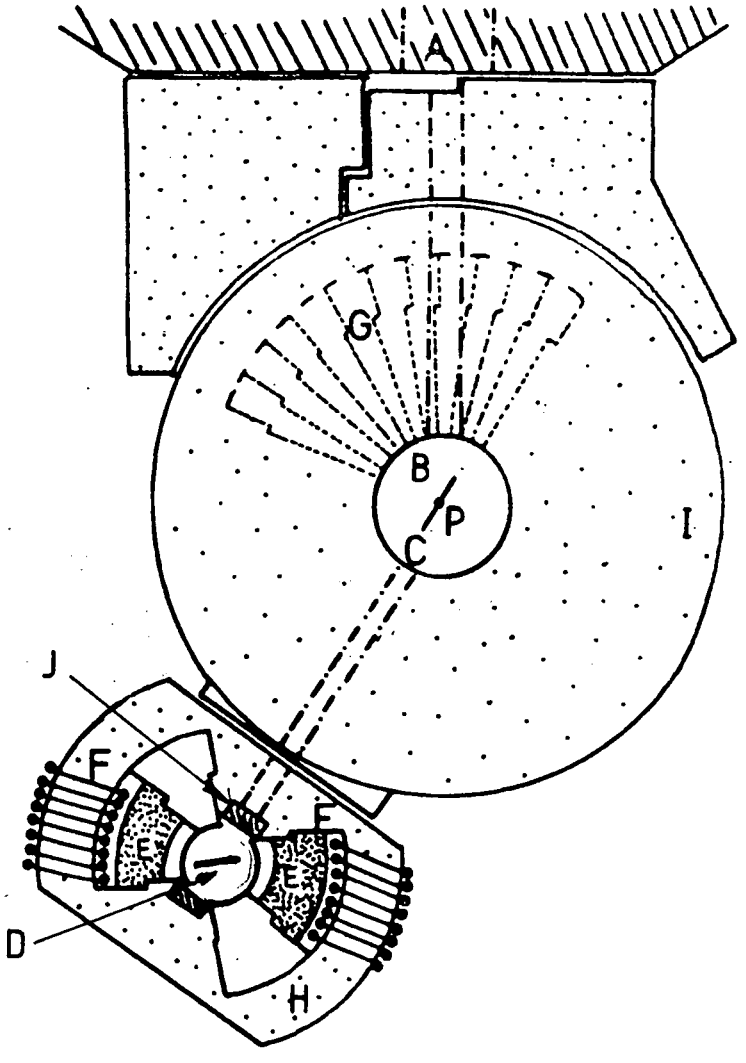

A	In pile collimators	G	Shielding segments
B	Monochromator	H	Sample table
C	Beam shutter	I	Large shielding drum
D	Sample position	J	Monitor (^{235}U fission chamber)
E	Be filter blocks (cooled)	P	Vertical axis of rotation of drum I and monochromator crystal B
F	BF_3 detector arrays		

flat, rectangular variety (Section 4.1) were oriented at $45^{o}\pm5^{o}$ to the incident beam (Fig. 4.7).

Only those neutrons which, having been scattered by the sample, have energies of *ca* $42cm^{-1}$, or less, can pass through the Be filter to be counted by two banks of eight $^{10}BF_3$ detectors (Section 4.3.6). Neutrons with energies greater than $42cm^{-1}$ are Bragg scattered by the Be blocks and do not reach the detectors. Let E_O be the energy of the neutrons incident on the sample and E_S be the energy of an INS active transition in the sample. Neutron energy loss spectra are obtained by incrementing E_O and detecting those neutrons for which

$$E_O - E_S \lesssim 42cm^{-1}.$$

The Be blocks are cooled to 77K by liquid N_2 which increases the transmission of neutrons with energies below $42cm^{-1}$.

4.3.3 The beryllium filter detector spectrometer, INIB

This spectrometer is designed to cover higher energies (*ie* 327 to *ca* 2500 cm^{-1}) than the DIDO b.f.d. and uses neutrons from the hot source at the I.L.L. The hot source is a graphite block at 2000K which increases, compared to a thermal source, the flux of neutrons with energies greater than *ca* 650 cm^{-1}.

The neutron beam is monochromated by combined rotation and translation of a single Cu crystal (Fig. 4.8). The Cu(200) reflecting planes were used for monochromation in the range 320 to 960 cm^{-1} and the Cu(220) planes for the range 807 to 2230 cm^{-1}. Motion of the Cu crystal and the rotation of the shielding drum (Fig. 4.8) about the sample position was under computer control.

Fig. 4.8 The IN1B spectrometer[8].

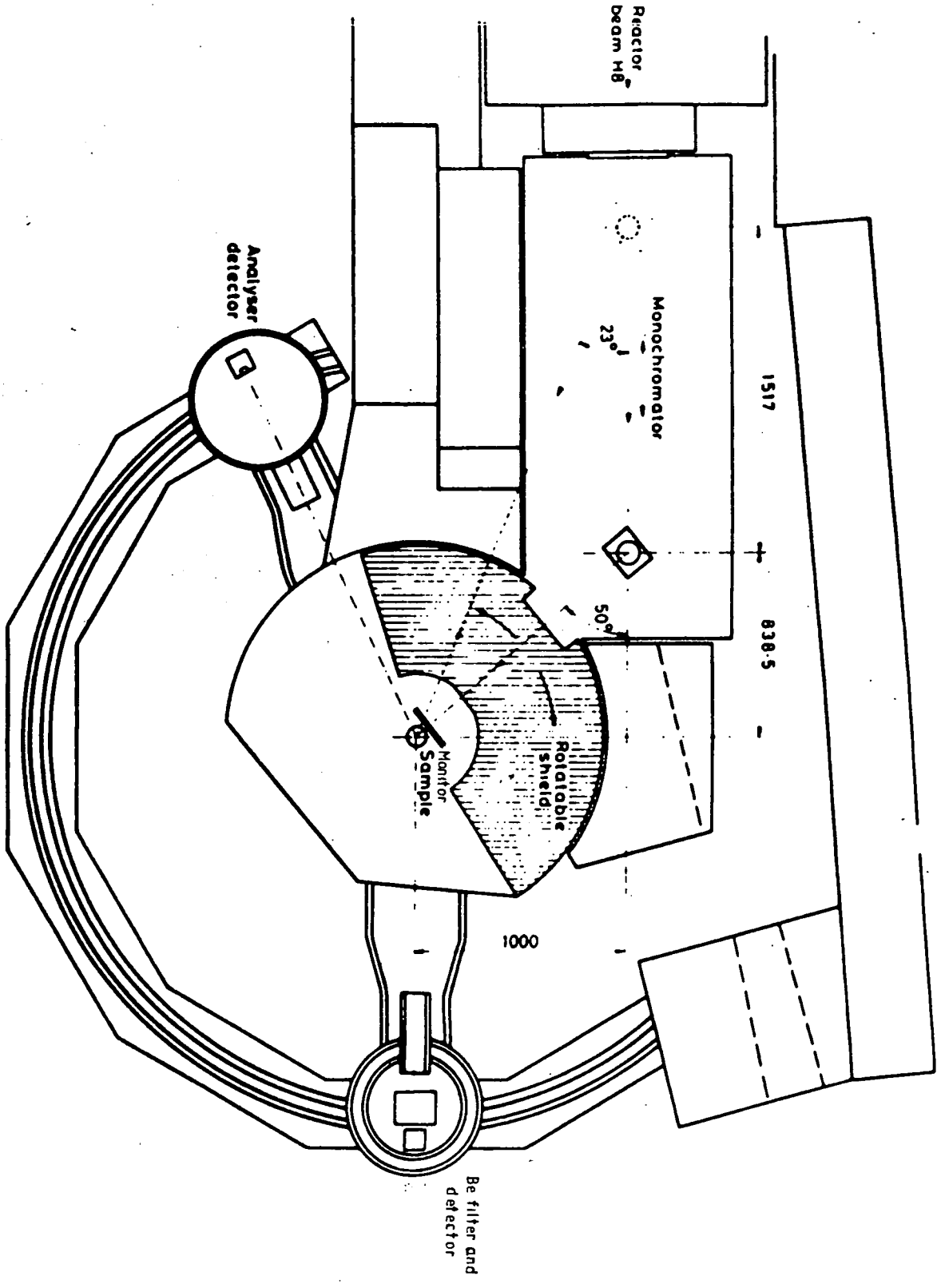

The beam size at the sample is 5.3 x 6.4cm and the flux at $807cm^{-1}$ [Cu(220)] 3 x 10^7 neutrons.cm^{-2}.s^{-1} and at $1614cm^{-1}$ [Cu(220)] 1.3 x 10^7 neutrons.cm^{-2}.5^1. [8,9] The sample cans were held vertically in a liquid nitrogen cryostat (77K). Only cylindrical cans were used with this spectrometer.

The Be filter (77K) and the bank of six ^{3}He detectors are mounted on a rail. The detectors were positioned for a scattering angle of 40^o.

The principles of operation of the INIB spectrometer are similar to those of the DIDO b.f.d. Both instruments were used to obtain neutron energy loss spectra, each point in a given spectrum being normalised to a constant number of monitor counts.

4.3.4 Treatment of data obtained by b.f.d. spectrometers

The monitors placed before the samples in the DIDO b.f.d. and INIB spectrometers are of the ^{235}U-fission chamber type, for which it is known[10,11] that:

$$\text{monitor efficiency} \propto E_o^{-\frac{1}{2}}$$

where E_o is the incident neutron energy. Now for a powder sample, we have:[11]

$$\frac{d^2\sigma}{d\Omega dE} = \frac{k_f}{k_o} \cdot \frac{\sigma_{inc}}{4\pi} \cdot S_{inc}(Q,\omega) \qquad (4.1)$$

where σ_{inc} is the incoherent neutron cross-section of the scattering nucleus, k_o and k_f are the moduli of the neutron wave-vectors before and after scattering and $d^2\sigma/(d\Omega dE)$ is the partial differential scattering cross-section. Since the b.f.d.

spectra were recorded for a constant number of monitor counts at each incident energy:[11]

$$\text{detected counts} \quad \alpha \quad \frac{d^2\sigma}{d\Omega dE} \cdot E_o^{-\frac{1}{2}} = \frac{d^2\sigma}{d\Omega dE} \cdot k_o \tag{4.2}$$

Thus from equations 4.1 and 4.2,

$$\text{detected counts} = \frac{k_f \sigma_{inc}}{4\pi} \quad S_{inc}(\underline{Q},\omega) \tag{4.3}$$

In a b.f.d. experiment, k_f is approximately constant and if we make the customary approximation (Chapter Two) that σ_{inc} is constant across the spectrum, then the measured b.f.d. spectrum is directly proportional to $S_{inc}(\underline{Q},\omega)$.

In Chapter Two, it was shown that the band intensity in a neutron energy loss spectrum was given for a fundamental, harmonic mode of vibration:

$$S_{inc}(\underline{Q},\omega) \quad \alpha \quad \frac{Q^2(r_a+1)}{M_L \cdot \tilde{\nu}_a} \quad g(\tilde{\nu}_a) \exp(-2W_L(\tilde{\nu}_a)) \tag{4.4}$$

where $\tilde{\nu}_a$ is the wavenumber of the normal mode a, M_L is the mass of the scattering nucleus L, $\exp(-2W_L(\tilde{\nu}_a))$ is the mode-dependent Debye-Waller factor, $g(\tilde{\nu}_a)$ is the amplitude weighted density of vibrational states and

$$r_a + 1 = \frac{\exp(\beta/2)}{2\sinh(\beta/2)}$$

where $\beta = hc\tilde{\nu}_a/(2K_BT)$ and c is the velocity of light (cm/s). In general:

$$Q^2 = k_o^2 + k^2 - 2k_o k\cos \tag{4.5}$$

where θ is the scattering angle. For a b.f.d. spectrometer, $k_o^2 >> k^2$ and if $\theta = 90^o$, then

$$Q^2 \approx k_o^2 \tag{4.6}$$

Now $hc\tilde{\nu}_a = \hbar^2 k_o^2/(2m)$ (4.7)

where m is the neutron mass, Thus, from equations 4.6 and 4.7:

$$Q^2 = \frac{8\pi^2 cm}{h} \cdot \tilde{\nu}_a \quad (4.8)$$

For samples in which the scattering from a particular nuclide L (*eg* ^1H) dominates, equations 4.3, 4.4 and 4.8 give for a b.f.d. spectrum which has been normalised to constant monitor counts:

$$\text{detected counts} \propto g(\tilde{\nu}_a)\exp(-2W_L(\tilde{\nu}_a))(r_a+1). \quad (4.9)$$

All our b.f.d. spectra were recorded at 77K. In Chapter Two, it was shown (Table 2.) that to a good approximation at this temperature, the (r_a+1) term of equation 4.9 could be set equal to unity for transition frequencies greater than $200cm^{-1}$. For transitions below 200 cm^{-1}, the (r_a+1) term is to be specifically evaluated for accurate calculation of relative INS band intensities *via* equation 4.9.

Equation 4.9 was derived for scattering angles close to 90^o. In the case of the INIB spectrometer, scattering angles of 40^o were used and the proportionality of equation 4.9 does not hold. However, $g(\tilde{\nu}_a)$ may be obtained for INIB spectra *via* equation 4.5.

The relationship (equation 4.3) that the detected number of counts is directly proportional to $S(Q,\omega)$ of the sample assumes that the only neutrons which reach the detectors are those which have been scattered by the sample. This assumption is not strictly valid. The DIDO b.f.d. spectrometer has a large, time variable background caused by the reactor, adjacent instruments, etc. This is also experienced using INIB, but to

a lesser extent. Time normalisation of b.f.d. spectra is used to minimise the effects of the variable background. Consider a sample comprising an adsorbent plus adsorbate. Let the number of counts detected per second with this sample in the beam be A, then we write:

$$A = C_s + C_b + \frac{\int_o^{t_1} C_v(t)\,dt}{t_1} \qquad (4.10)$$

where t_1 is the time taken for the monitor to detect a pre-selected number, N, of neutrons;

C_s = counts per second from the sample (adsorbent + adsorbate);

C_b = counts per second from the sample container, cryostat walls, etc.;

$C_v(t)$ = the time dependent background (counts/second) from external sources.

Now consider a sample comprising an adsorbent with a clean surface, *eg* a dehydrated zeolite, and let B be the number of counts per second recorded with this sample in the beam. We have:

$$B = C_r + C_b + \frac{\int_o^{t_2} C'_v(t)\,dt}{t_2} \qquad (4.11)$$

where t_2 is the time for the monitor to detect N neutrons;

C_r = counts per second from the adsorbent;

$C'_v(t)$ = the time dependent background (counts/second).

From equations 4.10 and 4.11,

$$A-B = C_s - C_r + \frac{\int_o^{t_1} C_v(t)\,dt}{t_1} - \frac{\int_o^{t_2} C'_v(t)\,dt}{t_2} \; . \qquad (4.12)$$

For the b.f.d. spectrometers, $t_1 \neq t_2$ and $C_v \neq C'_v$, in general. If we assume that at an average time $\frac{1}{2}(t_1+t_2)$, the time dependent backgrounds are similar, equation 4.12 becomes:

$$(A-B)(t_1+t_2)/2 = (C_s-C_r)(t_1+t_2)/2 \qquad (4.13)$$

The b.f.d. spectra of adsorbed species are presented in this work as time normalised counts, *ie* $(A-B)(t_1+t_2)/2$, against incident neutron energy. Clearly, such spectra are subject to large errors if the two time dependent backgrounds (equation 4.12) are greatly different at the average time $(t_1+t_2)/2$. However, experience has shown that this is rarely the case and a time normalised spectrum is, in general, found to be a smoothed version of an uncorrected one.[12]

The b.f.d. spectra of dehydrated zeolites and other cleaned adsorbents are presented in this work as Bt_2 against incident neutron energy. From equations 4.3 and 4.11, such a spectrum depends on $S(Q,\omega)$ of the sample but also contains a contribution from the sample container etc. and the time variable background. This latter contribution is greater in the DIDO b.f.d. data than in the INIB results.

4.3.5 The relationship between transition frequencies and band maxima in b.f.d. spectra

The peak of a band in a b.f.d. spectrum does not correspond to the true transition frequency of the sample, but is greater by an amount Δ. A method of calculating Δ, which is an energy dependent quantity, has been given by Taylor and Howard.[13]

According to Taylor and Howard,[13] the response of a b.f.d. spectrometer depends on the transmission window of Be (Figure 4.9(a)) and the detector efficiency, which for $^{10}BF_3$ and ^3He counters is dominated by an $(\text{energy})^{-\frac{1}{2}}$ factor (Figure 4.9(b)). Convolution of these two factors gives the instrumental response

Fig 4·9
The a) transmission of Be and b) counter efficiency of a b.f.d. spectrometer.[13]

a)

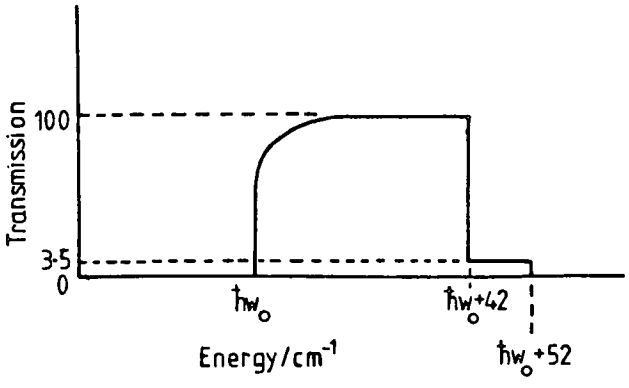

$\hbar\omega_o$ is the energy of an INS active transition

b)

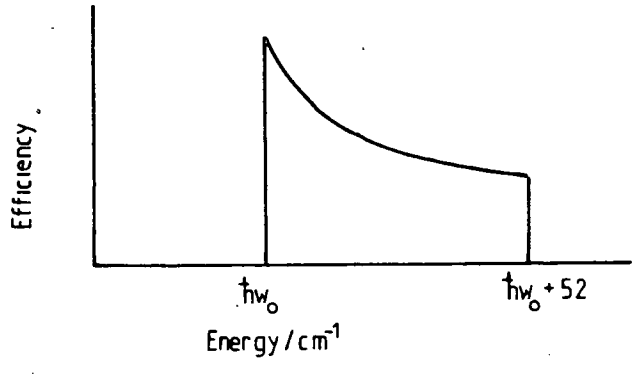

Fig 4·10 Taken from ref. 13

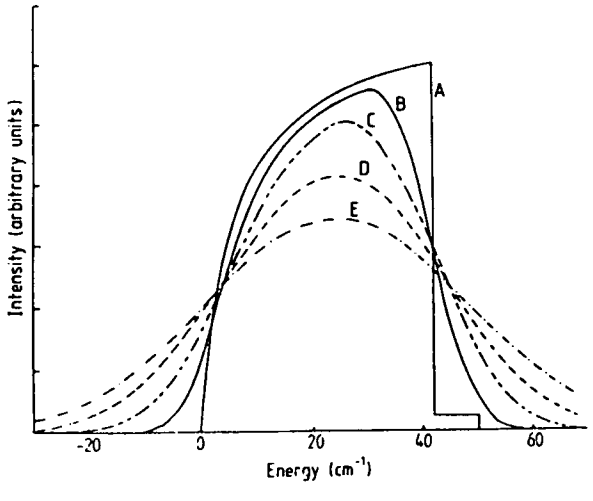

Calculated response functions of a BFD spectrometer (assuming a Gaussian energy distribution for the monochromatic beam) for four values of σ ($\sigma = 5$, 10, 15, 20 cm^{-1}; curves B, C, D, E respectively). Curve A is the response function for a delta function input.

from a transition in the sample of energy $\hbar\omega_o$ (Figure 4.10, curve A). Thus far, the incident neutron beam has been considered to be strictly monoenergetic. In practice, the incident beam contains a distribution of energies, arising from the mosaic spread of the monochromator crystal and the finite width of the collimator slits.[13] Following Taylor and Howard,[13] the distribution of incident neutron energy is assumed to be Gaussian:

$$f(E_o) = (2\pi\sigma^2)^{-\frac{1}{2}} \exp(-E_o^2/2\sigma^2) \qquad (4.14)$$

where E_o is the energy of the neutron incident on the sample and σ^2 is the variance. Convolution of $f(E_o)$ with the detector efficiency and Be transmission function gives[13] curves B to E in Figure 4.10. As σ increases, the displacement of the peak maximum from the true transition energy at $\hbar\omega_o$ falls from $42cm^{-1}$ and has been shown[13] to asymptotically approach a value of $24.5cm^{-1}$. The value of σ depends on E_o which in turn is related to the scattering angle θ of the white neutron beam on the monochromating crystal. For first order Bragg reflection from the monochromator:

$$E_o = \hbar^2\pi^2/(2md^2\sin^2\theta) \qquad (4.15)$$

where d is the crystal plane spacing and m the neutron mass. The major source of error in the monochromation of neutrons for both INIB and the DIDO b.f.d. is the angular spread, $\delta\theta$, in the white beam incident on the monochromator crystal[13]. From equation 4.15, one obtains

$$E_o = 2E_o.\cot\theta.\delta\theta$$

and $\cot\theta$ is obtained *via* equation 4.9, from:

$$\theta = \arcsin\left(\frac{\hbar^2\pi^2}{2md^2E_o}\right)^{\frac{1}{2}} \qquad (4.16)$$

Taylor and Howard[13] have identified δE_o with the full width at half maximum of the Gaussian function of equation 4.14:

$$\delta E_o = 2\sqrt{2}\sigma$$

and therefore

$$\sigma = (2)^{-\frac{1}{2}} . E_o . \cot\theta . \delta\theta$$

Thus σ and thence Δ can be calculated as a function of E_o for given values of the monochromator plane spacing, d (equation 4.16), and $\delta\theta$. Correction factors, Δ, published for the DIDO b.f.d. spectrometer ($\delta\theta = 1.2^o$) are shown Figures 4.11(a).[13] We have obtained the correction factors Δ for INIB (Figure 4.11)b)) using an assumed value of $\delta\theta = 0.5^o$, the true error in the collimation being unknown.

The abscissae of the b.f.d. spectra presented in this work represent the incident neutron energy, E_o. The true transition frequencies of the bands are indicated on the spectra. We estimate the precision to which band maxima and hence transition frequencies can be determined using both the INIB and DIDO b.f.d. spectrometers is $\pm 15 cm^{-1}$.

4.3.6 Neutron detectors

A neutron is detected by registering the voltage pulse from the ion-avalanche generated in the counter from the reactions[14]

$$^{10}_{5}B + ^{1}_{0}n = ^{7}_{3}Li + ^{4}_{2}He + 2.8MeV \quad (^{10}BF_3 \text{ detectors}) \text{ or}$$

$$^{3}_{2}He + ^{1}_{0}n = ^{1}_{1}H + ^{3}_{1}H + 0.76MeV \quad (^{3}He \text{ detectors}).$$

Fig. 4.11 Plots of Δ against frequency of observed band maximum for b.f.d. spectrometers.

a. DIDO b.f.d. spectrometer (diagrams taken from ref. 13).

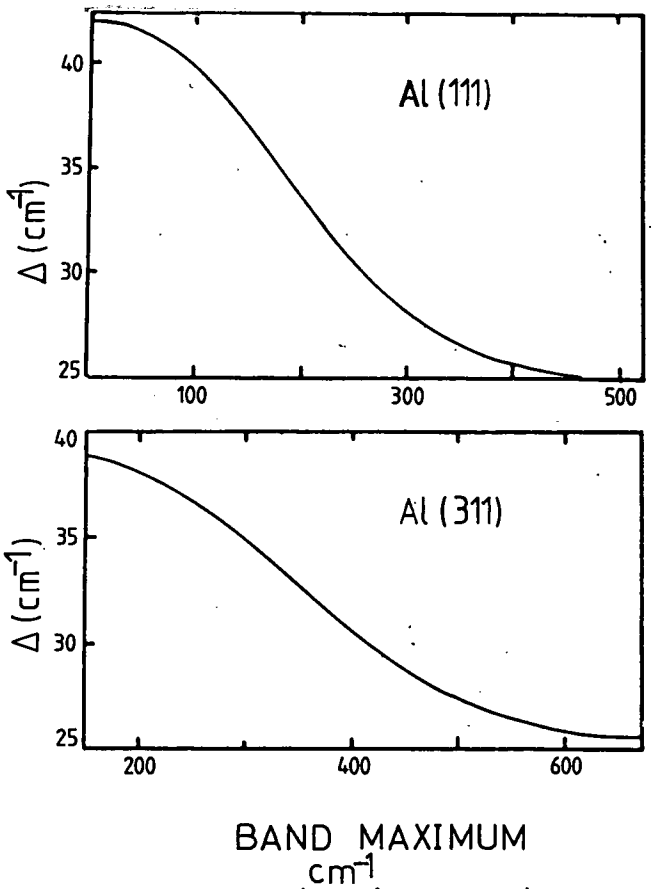

b. IN1B spectrometer (this work).

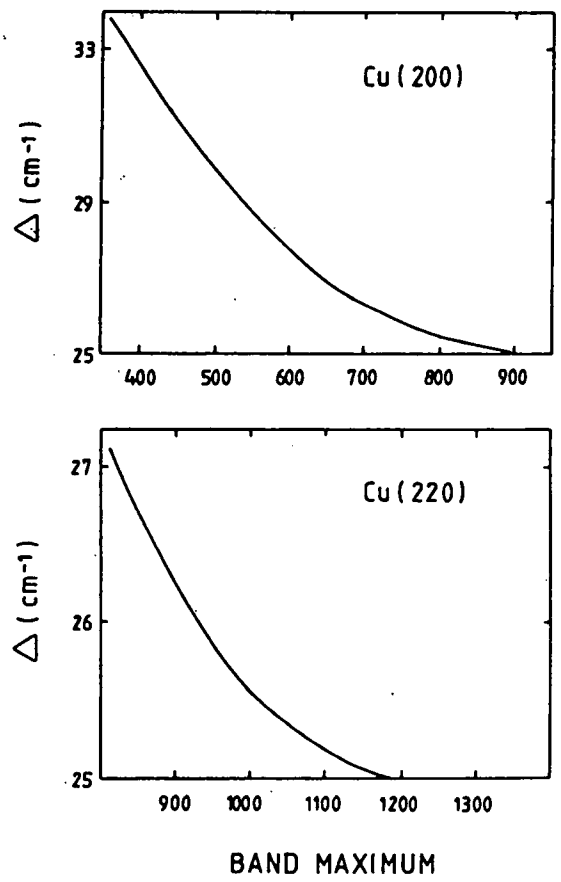

4.4 Optical spectrometers

The optical spectrometers used were:

Near infrared: Perkin Elmer 580B grating spectrometer

Raman : Cary 82 using the 514.5nm line of a Spectra-Physics argon laser.

The vacuum cell[15] used to obtain the IR spectra of a self-supporting disc of ZnO (Chapter Seven) was made of stainless steel and used 5mm wide KSR5 windows.

We estimate the precision of the Raman spectrometer to be $\pm 3 cm^{-1}$ and that of the IR spectrometer to be $\pm 2 cm^{-1}$.

REFERENCES

1. Hughes, D.J. and Harvey, J.A., Neutron Cross Sections, BNL325, Brookhaven National Laboratory, New York, 1955.

2. Howard, J., Ph.D. Thesis, University of Durham, 1976.

3. Neutron Beam Facilities at the I.L.L. High Flux Reactor, 1; Institut Laue-Langevin Report, Grenoble, 1981.

4. Suck, J.-B., Absolute Intensities and Resolution of the Elastic Line Measured at some Incident Neutron Energies at the Double Monochromator Rotating Crystal T-O-F Spectrometer IN4, Unpublished Institut Laue-Langevin Internal Report 77SU17T, Grenoble, 1977.

5. Ghosh, R.E., FORTRAN programs PRIME and CROSSX.

6. Baston, A.H., The Collection and Processing of Data from Three Time-of-Flight Neutron Spectrometers, AERE Harwell Report M2570, 1972.

6. Baston, A.H. and Harris, D.H.C., AERE Harwell Report R9278, 1978.

8. Neutron Beam Facilities at the I.L.L. High Flux Reactor, Institut Laue-Langevin Report, Grenoble, 1977.

9. Graham, D., Ph.D. Thesis, University of Durham, 1980.

10. Egelstaff, P.A.(Ed.), Thermal Neutron Scattering, Academic Press, London, 1965.

11. Howard, J. and Waddington, T.C., J.Phys.Chem., 85, 2467, 1981.

12. Robson, K., Ph.D. Thesis, University of Durham, 1980.

13. Taylor, A.D. and Howard, J., J.Phys.E:Sci.Instrum., 15, 1359, 1982.

14. Bacon, G.E., Neutron Diffraction, 3rd Edition, Clarendon Press, Oxford, 1975.

15. Kadir, Z.A., Ph.D. Thesis, University of Durham, 1983.

CHAPTER FIVE

AN INELASTIC NEUTRON SCATTERING STUDY OF HYDROGEN ADSORBED ON IMPURE PALLADIUM BLACK

5.1 Introduction

5.1.1 Hydrogen adsorption by Group VIII metals

The surface species resulting from the chemisorption of hydrogen on Group VIII metals depend, *inter alia*, upon the metal itself, the crystallographic orientation of the surface, the coverage of H, the temperature and the nature of any supporting material.

Ni, Pd and Pt behave similarly towards hydrogen in the following respects:

1. The isosteric heats of adsorption, extrapolated to zero coverage, of hydrogen on various Ni, Pd and Pt surfaces are of a similar magnitude and listed in Table 5.1.
2. H_2/D_2 exchange experiments and the second order desorption kinetics observed in temperature programmed adsorption studies[1] show that hydrogen is dissociatively chemisorbed on Ni, Pd and Pt. The adsorbed phase is mobile on Ni/SiO_2 [2] above 195K and on Pd[3] and Pt[4] films at 77K and above.
3. The coverage of hydrogen on the three metals, defined as θ = the number of adsorbed H atoms/the number of metal surface atoms, reaches saturation at values greater than unity and approaches the value of 2, depending on the nature of the surface and the experimental conditions. For example, for 6% Pt supported on SiO_2 at 300K, $\theta_{max} = 1.8$[5] and for Pd(100) at 170K, $\theta_{max} = 1.35$.[6]

The differences in the behaviour of the metals towards H_2 will now be discussed and in Tables 5.2 to 5.4, we list LEED results and structural inferences from vibrational data for

TABLE 5.1 Isosteric heats of adsorption of hydrogen on Group VIII metal surfaces

Sample	Isosteric heat of H_2 adsorption kJ/mol	Method	Note	reference
Pd Film	92 ± 4	surface potential measurements		41
Pd (110)	102	$\Delta\psi$ versus θ measurements	constant up to θ = *ca* 0.5	23
Pd (100)	103	" " " "	constant up to θ = *ca* 0.9	6
Pd (111)	87	" " " "	constant up to θ = *ca* 0.5	23
Drifjhout Pd black	65 ± 10	volumetric studies	θ = 1.34	20
Pd on active C	90 ± 5	" "		20
Pd on active C, type-C chemisorption	36.4	" "		19
Heat of formation of α-PdH	24	" "		18
Pt black) weak chemi-	42	temperature programmed desorption		5
Pt/SiO_2) sorption				5
Pt/Al_2O_3) strong chemi-	96	" " "		5
Ni (111)	97	$\Delta\psi$ versus θ measurements		1
Ni (110)	82 to 90	" " " "		1

θ = surface coverage of H atoms, in monolayers

$\Delta\psi$ = work function change on hydrogen adsorption.

TABLE 5.2 Structural data for hydrogen chemisorbed on nickel

Surface	symmetry of adsorption site	Method	Temperature, K	Coverage, θ, monolayers	Reference
Raney Ni	C_{3v}	INS	?	0.4, 1.0	data obtained by[7] re-assigned by[8]
Raney Ni	C_{3v}	INS	≥ 150	0.3 to 1.0	9
Ni (111)	C_{3v}	LEED			10
Ni (111)	C_{3v}	EELS	170	-	11
Ni (111)	C_{3v}	pseudopotential calculations	-	1.0	12
Ni (100)	(disordered)	LEED			13
Ni (100)	C_{4v}	EELS	200	0.9	14
Ni (110)	C_{2v}, or C_{4v} if surface reconstructs on adsorption	He diffraction	100	1.0[a]	15

Note: (a) Interpretation[15] of results based on Demuth, J.E., J.Coll. Interface Sci., 58, 184, 1977.

TABLE 5.3 LEED results for hydrogen chemisorbed on palladium single crystal planes

	Pd(100)	Pd(110)	Pd(111)	Pd(S) - [9(111)x(111)]
LEED pattern	ordered c(2x2)	(1x2)	(1x1) No extra spots but I/V curve changed	-
Symmetry of proposed surface site	C_{4v}	see footnote (a)	C_{3v}	see footnote(b)
θ, monolayers	0.3 - 0.6	< 1.0	< 1.0	< 1.0
$\Delta\psi$(max),eV	+ 0.20	+ 0.36	+ 0.18	+ 0.23
temperature,K	*ca* 60-250	308-398	308-398	-
reference	6	23	23	23

θ = surface coverage of Hatoms

$\Delta\psi$ (max) = maximum work function change on hydrogen adsorption

Notes

(a) Since the absolute surface coverage was unknown, no model was proposed for the (110) surface site. It was likely that there was more than one H atom per unit surface mesh.

(b) The variation of isosteric enthalpy of adsorption with coverage θ indicated preferential adsorption at steps at low θ.

TABLE 5.4 LEED results for hydrogen chemisorbed on platinum single crystal planes

	Pt(100)	Pt(111)	Pt(S) - [6(111)x(100)]	Pt(S) - [9(111)x(111)]
LEED pattern	(2x2)	(1x1)	see footnote(a)	(2 x 2)
symmetry of proposed surface site	-	C_{3v}	-	-
θ, monolayers	-	*ca* 1.0	-	-
temperature,K	873-1273[b]	110-150	873-1273[b]	873-1273[b]
reference	49	50	49	49

Notes

(a) Disordered adsorption occurred on the terraces but ordered adsorption at the steps.

(b) Christmann and Ertl have since shown that H_2 is adsorbed rapidly on any clean surface of Pt even at ambient temperatures [50,51].

hydrogen chemisorbed on Ni, Pd and Pt. For all three metals, the principal adsorption sites include those of highest possible symmetry on a given crystal plane, *e.g.* C_{3v} on the (111) planes, C_{4v} on the (100). In the case of Ni these are the only occupied sites - only one type of surface species forms on a given crystal plane and there is no strong evidence for on-top sites.[7-15]

Pd behaves as Ni, but only for coverages of less than one monolayer. At higher coverages, the present INS data indicate that sites of lower symmetry, and more than one type of site, are occupied and that the higher symmetry sites are vacated. This is discussed below (Sections 5.3, 5.4.4).

The major surface species at high coverages of H on Pt are the high symmetry sites but at low coverages the adsorption occurs preferentially at on-top sites.[5] Unlike Ni and Pd, both these types of site may be filled simultaneously. Again unlike Ni and Pd, the formation of the high symmetry species on Pt is activated, albeit slightly. The activation energy for adsorption of H at the 3-fold sites of Pt(111) has been measured variously as 21±8 kJ mol^{-1} [5] and 40 kJ mol^{-1}.[16]

An explanation of the different behaviour of each metal is provided by UPS studies of H chemisorbed on the (111) planes of Ni, Pd and Pt which revealed differences in the electronic details of bonding.[17]

It was shown that for Pd and Pt, in common with most other transition metals, the bonding to the H adatom was primarily through the d-band electrons, whereas for Ni the d-band interaction was very weak and the bonding was through the s-band. This difference between the metals was rationalised by considering:

1. the greater polarisability of the 4d and 5d atomic orbitals (a.o.'s) compared to 3d;
2. the greater difference in polarisability between 4s a.o.'s and 3d a.o.'s than exists between 5s and 4d or 6s and 5d a.o.'s. The trends in polarisability of the a.o.'s are reflected in the corresponding band widths in the bulk metal;
3. energy band calculations show that Ni has a greater number of s-electrons per atom in the valence band (Ni: 0.55-0.62; Pd: 0.31; Pt: *ca* 0.42).[17]

5.1.2 The sorption of hydrogen by palladium

Unlike Ni and Pt, absorption of H_2 into the bulk of Pd occurs readily and extensively, stoichiometries up to $PdH_{0.7}$ are achieved by direct reaction under moderate conditions.[18] There are two phases in the absorbed hydrogen/palladium system;[18] a phase diagram is shown in Fig.5.1. The hydrogen atoms occupy octahedral interstices in both phases.[18]

Turning now to surface phenomena, we note that there are two types of chemisorption of H_2 on Pd:[19]

1. a strong, dissociative chemisorption with an isosteric enthalpy of adsorptipn, q_{iso}, which is slightly plane dependent, *e.g.* 102 kJ $mole^{-1}$ for Pd (110), see Table 5.1;
2. a weak, "type-C", chemisorption for which q_{iso} is 36.4 kJ $mole^{-1}$ at a total coverage of $\theta = 1.34$.[19] This weak chemisorption occurs only after one strongly chemisorbed monolayer has been formed. The type-C hydrogen is said to be in dynamic equilibrium with, and a precursor of, interstitial hydrogen.[19] It is desorbed with kinetics of first order in surface coverage and so is probably atomic hydrogen.[19] According to Lynch and Flanagan[19] it may be

Figure 5.1 A phase diagram of the pure palladium/adsorbed hydrogen system, after ref. 18.

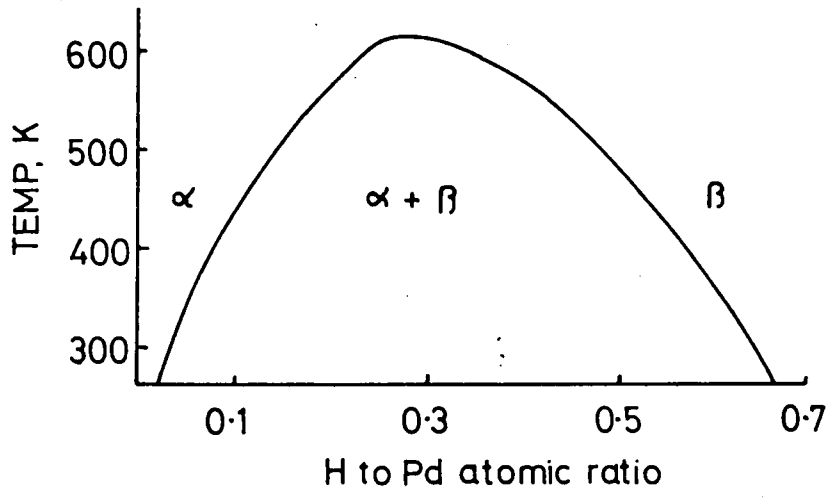

phase	structure	lattice constant, Å
metal	fcc	3.891
α (solution phase)	fcc	3.894, amount H≤3 atom %
β (hydride phase)	fcc	4.018 for $PdH_{0.6}$

held at a surface bridging site or, according to Konvalinka and Scholten[20], just below the surface in octahedral holes.

5.1.3 The sorption of hydrogen by palladium black supplied by Drijfhout, Amsterdam

A sample of Pd black supplied by Drijfhout, Amsterdam, has been reported as adsorbing H_2 to a maximum of one monolayer.[20] Only the strongly chemisorbed H is present on the surface, type-C H and absorbed H being absent. ESCA analysis of the surface of this Pd sample has shown the presence of Zn (5 to 10 atom %) and Pb (3 atom %) contaminants.[20] This material's unusual adsorption properties, which include the lowering of the enthalpy of adsorption q_{iso} to *ca* 65 kJ $mole^{-1}$ (Table 5.1), are probably due to the electropositive surface impurities. These impurities will have two effects:

1. they will raise the d-electron density at the surface;
2. the energy of an H atom dissolved in the bulk of a metal can be described as the sum of a Coulombic term and an elastic term.[21] The elastic term arises from the coherent expansion of the lattice necessary to accommodate the interstitial atoms. This term must be of a significant value in the case of Pd for the following reasons.

   On the first exposure of a Pd sample to H_2, X-ray line broadening[22] has shown a slight surface reconstitution in favour of the (111) plane and LEED[23] a small expansion of the lattice of 2% between the surface and inner (111) planes. It is also known that the first time a Pd sample is exposed to H_2 it will absorb a different quantity of H_2 than it will on all subsequent occasions.[18] It is proposed here that

the effect of the surface impurities is to render the elastic term unfavourable to the formation of interstitial or type-C H on the Drijfhout sample.

The Drijfhout Pd black is therefore suited for the study of strongly chemisorbed hydrogen without interference from type-C or adsorbed hydrogen. The nature of the adsorbed hydrogen may be obtained from the number and the intensities of the bands in its INS spectrum. In view of this and the success of INS in obtaining the vibrational spectra of H chemisorbed on pure metal blacks,[24-26] we have obtained the INS spectra of hydrogen adsorbed by Drijfhout Pd black.

Although we have achieved hydrogen uptakes in excess of one monolayer on Drijfhout Pd black, our INS spectra indicate that type-C and interstitial hydrogen were not formed (Section 5.3).

5.1.4 The rationale of the assignment scheme used for the INS spectra of hydrogen adsorbed by Drijfhout palladium black

Our assignment of the INS spectra of the Drijfhout Pd/H_2 system (Section 5.3) is based upon a comparison with the vibrational spectra of transition metal hydridocarbonyl compounds.

The validity of using transition metal cluster compounds, as models for metal surface-adsorbate systems has received much discussion in the literature.[27-30] In general, even the largest cluster compounds (34 metal atoms) do not resemble bulk metals in the electronic details of their bonding. However, the local environment of a given ligand and its nearest metal atoms in a cluster complex can provide reasonable estimates of the likely stoichiometry, orientation, bond order, length, and

angle of a similar species adsorbed at a metal surface.[28] We shall use the vibrational spectra of transition metal hydridocarbonyl complexes to predict the likely vibrational frequencies of hydrogen adsorbed at various sites (Section 5.3). The spectra of the hydridocarbonyls were obtained by INS techniques,[8] and the frequencies of those normal modes involving significant motion of the hydride ligand are summarised in Fig. 5.2.

Our evidence (Section 5.3) indicates that the only occupied multiply bonded surface sites on Drijfhout Pd black, at $\theta > 1$, have C_{2v} symmetry. The normal modes of vibration of $(\mu_2\text{-H})M_2$ hydridocarbonyls, used as models for these sites, are drawn in Fig. 5.3, (M denotes a transition metal atom). Only modes 1, 2 and 3 are relevant to this work. The "M-M stretch" of the hydridocarbonyls corresponds, in the case of metal surfaces, to (1) lattice modes of the bulk metal; (2) surface phonons of the metal perturbed by the adsorbed H atom and (3) unperturbed surface phonons of the metal.

A weakness of the hydridocarbonyl/surface comparison is the lack of data for the $(\mu_4\text{-H})M_4$ species, which have yet to be synthesised. Although hydrogen absorbed in transition metal hydrides has been used as a model for H chemisorbed at 4-fold sites,[31] the bonding in such hydrides cannot be the same as that found at metal surfaces. For interstitial hydrogen at tetrahedral sites it is known that $\nu_{sym} \propto r^{-a}$ where $\underline{a}$ is a constant, and r is the M-H bond length.[32] Such a relationship has not been reported to apply to chemisorption and is not applied to the present data.

Fig. 5.2 Range of characteristic features in the vibrational spectra of transition metal hydridocarbonyls and rare earth hydrides (0 to 2300 cm^{-1}). Data collated from refs. 8 and 32.

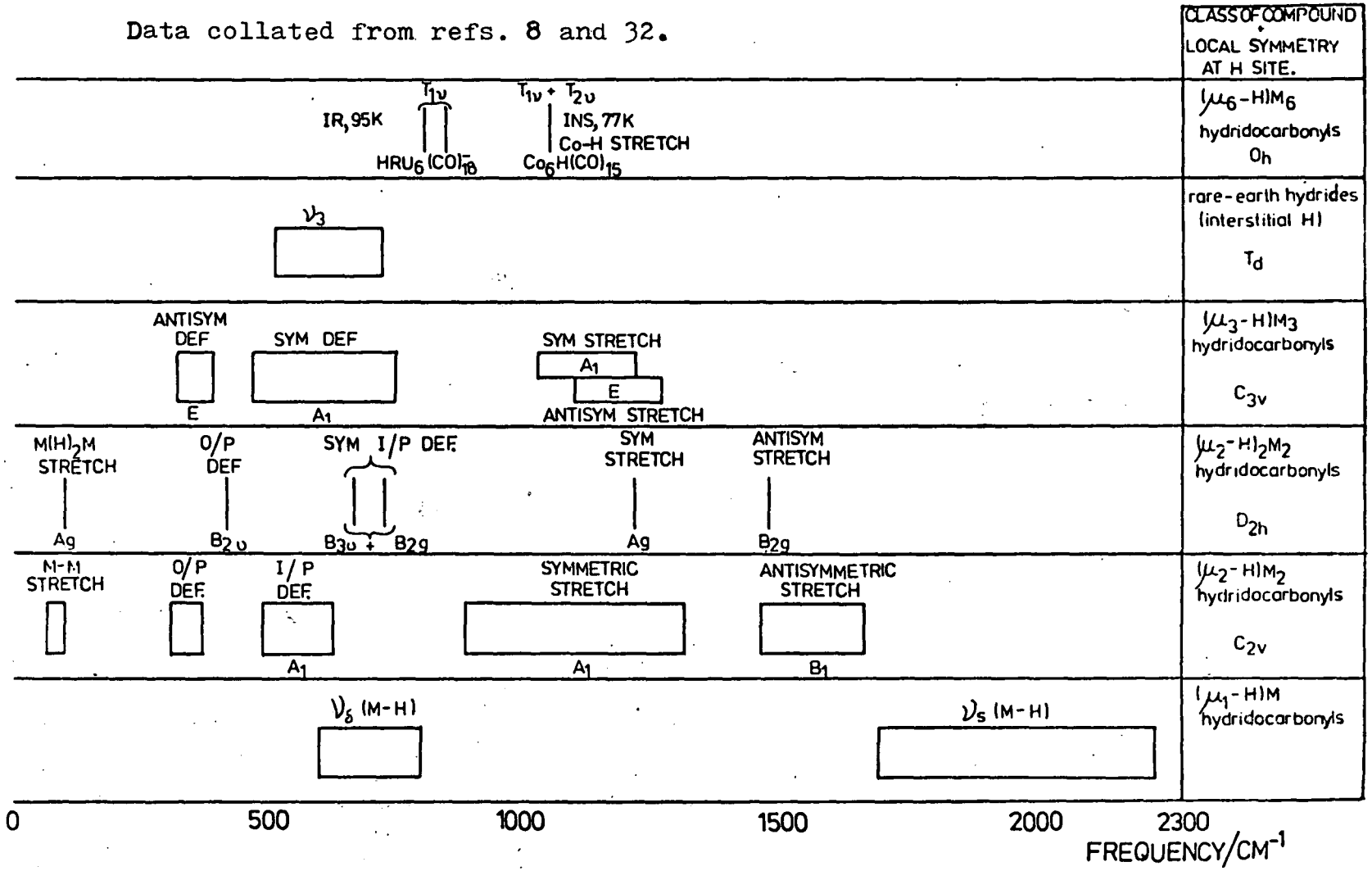

Fig. 5.3 The normal modes of vibration of $(\mu_2\text{-H})M_2$ hydridocarbonyl compounds. M denotes a transition metal atom.

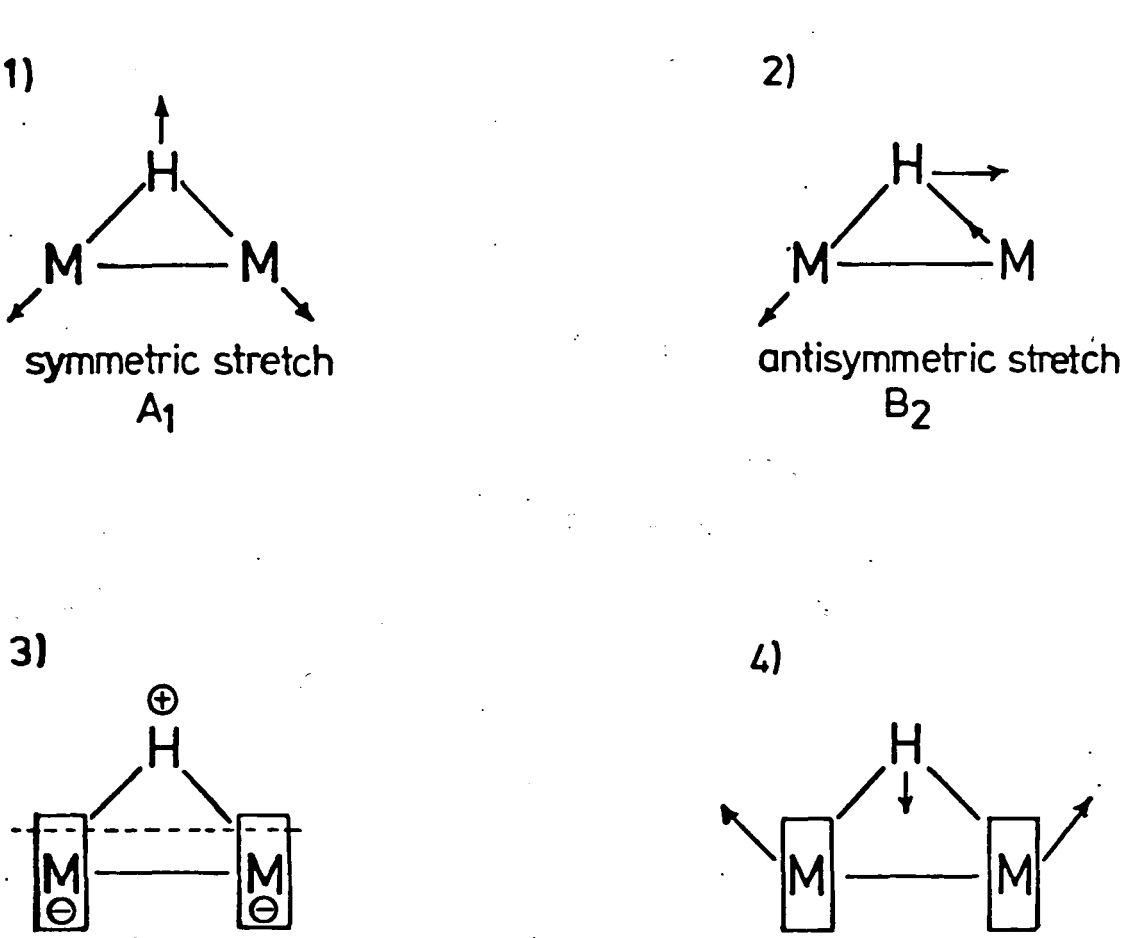

The box drawn around the M atoms signifies deformation of the M-CO skeleton. Only modes 1,2 and 3 have analogs for H adsorbed at a site of C_{2v} symmetry on a metal surface.

The effect of the carbonyl ligands in hydridocarbonyl complexes on the dynamics of the hydride ligand is not well understood. However, Kelly[31] has produced tentative evidence that the frequencies of the H atom in these complexes are not greatly perturbed from those expected for H bound at surface sites of appropriate geometry. Indeed co-adsorption of 0.25 monolayers of CO with a hydrogen monolayer on Raney Ni at 77K showed that "a substantial fraction of adsorbed hydrogen was neither displaced nor vibrationally perturbed by CO".[31]

5.2 Experimental

5.2.1 Sample preparation

The samples consisted of *ca.* 56g of Pd black (97.9%) obtained from H. Drijfhout, Amsterdam. The hydrogen was 99.995% pure and supplied by Masonlite, Chatham, Kent. Cleaning of the Pd was achieved by heating in an H_2 atmosphere to 473K followed by evacuation with a diffusion pump to less than 3×10^{-6} torr at that temperature. Small aliquots of H_2 (5×10^{-6} torr) were exposed to the Pd sample, which was kept open to the pumps, until the addition of H_2 caused no increase in the partial pressure of H_2O. It was then concluded that the Pd was free of surface oxygen. The amount of H_2O was monitored with a quadrupole mass spectrometer (Vacuum Generators QX200) which also showed that the sample handling part of the vacuum system was entirely free of pump oil. The major components of the residual gas during the preparation were CO, H_2O and H_2.

5.2.2 INS experiments

The INS spectra of Drijfhout Pd+H_2 were obtained on two b.f.d. spectrometers, INIB and the DIDO b.f.d. The latter was used to examine the low frequency range 97 to 334 cm^{-1} not covered by INIB. All the spectra were recorded at 77K.

(a) The adsorption of hydrogen by the Drijfhout palladium black samples used for the INIB spectra

Two successive adsorptions of hydrogen were carried out at 293K on the same sample of Drijfhout Pd black, referred to as sample 1(56.0g). The first adsorption (91 $cm^3 H_2$NTP) was achieved by maintaining a pressure of hydrogen above the sample of *ca* 10 torr (9.6 torr maximum) until the required uptake of hydrogen had occurred. The second adsorption (122 cm^3 total H_2 NTP) was performed by exposing the sample to a known volume containing hydrogen at 95 torr (293K).

The B.E.T. surface area of the Pd black prior to the cleaning treatment has been reported[20] as $6m^2/g$ and the number of Pd atoms at the surface of Pd blacks[33] as $1.2 \times 10^{19} m^{-2}$. Assuming no sintering occurred, the surface coverages (θ) for the INIB experiment (sample 1) are 1.2 and 1.7 monolayers. We discuss the fact that θ is greater than unity in Section 5.3.4 below.

(b) The adsorption of hydrogen by the Drijfhout palladium black samples used for the DIDO b.f.d. spectra

The INS spectra of two coverages of hydrogen on each of two samples of Drijfhout Pd black, referred to as samples 3 and 4, were obtained using the DIDO b.f.d. spectrometer. Both Pd samples were prepared as above (Section 5.2.1) and dosed with hydrogen in the following way. The required uptake of hydrogen

was achieved by repeatedly exposing the Pd, held at 77K, to a known volume of hydrogen (*ca* 10 torr measured at 293K), the H_2 reservoir being isolated from the sample and refilled before adding each successive dose. The amounts of hydrogen sorbed by sample 2 (56.4g Pd) were 56cm^3 NTP and 191 cm^3 total (NTP), and by sample 3 (55.5g Pd) were 131 cm^3 NTP and 238 cm^3 total (NTP). The final overpressure of H_2 in each adsorption at 77K was $\leq$ 0.75 torr. Thus at 77K the surface coverages for sample 2 are 0.8 and 2.8 monolayers; and for sample 3, 1.8 and 3.2 monolayers. No thermal transpiration corrections[34] have been made to these figures which are therefore slight underestimates of the true H_2 uptake. The higher coverages exceed the maximum value of θ = 1.0 reported to be possible for hydrogen adsorption on Drijfhout Pd black by Konvalinka and Scholten.[20] This discrepancy is discussed in Section 5.3.4 where we argue that the hydrogen is either strongly chemisorbed or physisorbed on samples 2 and 3, at 77K, absorption and weak chemisorption not having occurred.

During the transfer of the samples to the b.f.d. spectrometer after the adsorptions, the samples will have returned to room temperature for about one hour.

5.3 Results

5.3.1 Introduction

The INS spectra of the Drijfhout Pd/H_2 system obtained on INIB are shown in Figs. 5.4 and 5.5 and the transition frequencies summarised in Table 5.5. We will assign the INS spectra of the adsorbed species by comparing these data with the vibrational spectra of transition metal hydridocarbonyls and from the observed changes in intensity of the INS bands with surface coverage.

Fig. 5.4 Beryllium filter detector (IN1B) spectrum of Drijfhout Pd black plus adsorbed hydrogen, 1.2 monolayers coverage, 77K. The symbols + and o indicate data collected on the Cu(200) and Cu(220) monocnromator planes respectively.

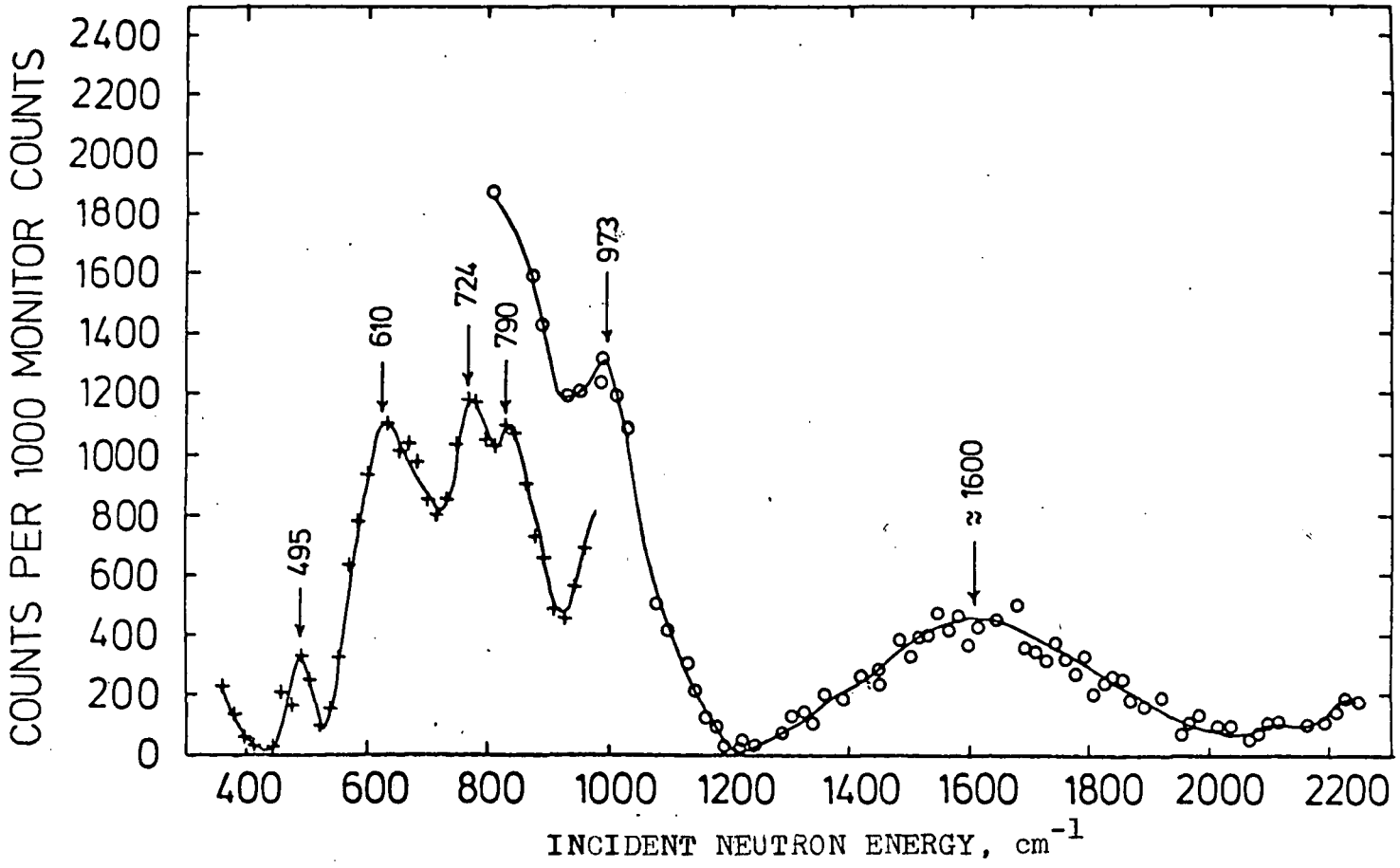

Fig. 5.5 Beryllium filter detector (IN1B) spectrum of Drijfhout Pd black plus adsorbed hydrogen, 1.7 monolayers coverage, 77K. The symbols + and o indicate data collected on the Cu(200) and Cu(220) monochromator planes respectively.

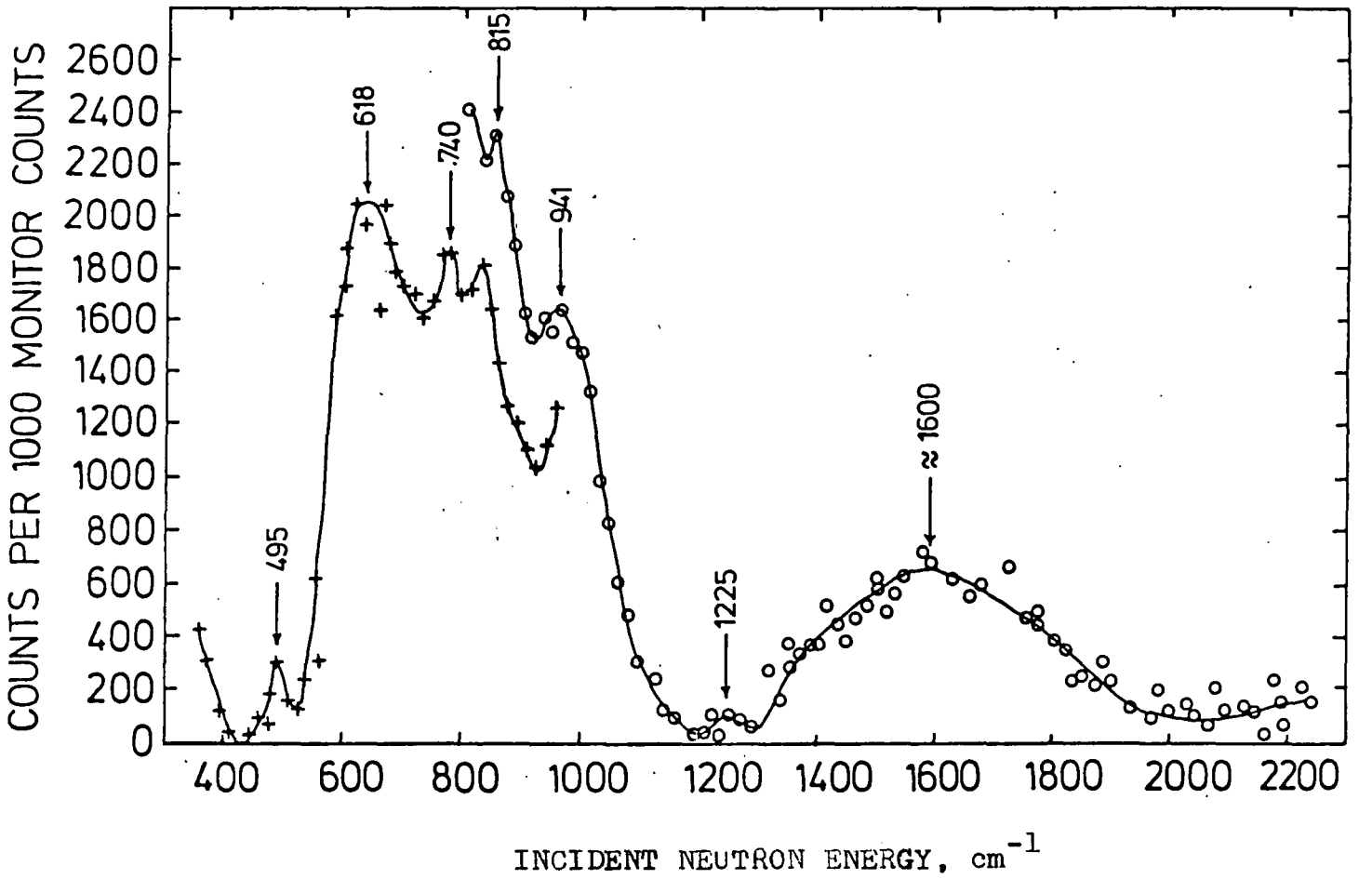

TABLE 5.5 Summary of the assignments of the INIB spectra (77K) of hydrogen adsorbed on Drijfhout Pd black (cm^{-1})

Unassigned		Pd (100)		Pd (111)		Assignment
1.2 monolayers	1.7 monolayers	1.2 monolayers	1.7 monolayers	1.2 monolayers	1.7 monolayers	
fig.5.4	fig.5.5	fig.5.4	fig.5.5	fig.5.4	fig.5.5	
495	495					?
				610	618	bending modes of $(\mu_1\text{-H})Pd$
		724	740			ν_{sym} $(\mu_2\text{-H})Pd_2$
				790	815	ν_{sym} $(\mu_2\text{-H})Pd_2$
		973	941			bending modes of $(\mu_1\text{-H})Pd$
					1225w	overtone (2x618)
		*ca.*1600s,b	*ca.*1600s,b	*ca.*1600s,b	*ca.*1600s,b	ν_{a5} $(\mu_2\text{-H})Pd_2$
		*ca.*2200 to 2300	*ca.*2200 to 2300	*ca.*2200 to 2300	*ca.*2200 to 2300	stretching mode of $(\mu_1\text{-H})Pd$

b = broad; s = strong; w = weak.

Since neither pure Zn nor pure Pb adsorb hydrogen[1] we are very unlikely to observe bands due to Zn-H or Pb-H species. Our data will therefore be interpreted solely in terms of surface palladium-hydrogen species. In addition, since the incoherent cross section of both ^{12}C and ^{16}O are zero, there will be no bands due to incoherent scattering from carbonaceous groups such as Pd-CO. Nor will such species give rise to coherent scattering, which can occur in incoherent INS spectra such as Figs.5.4-5.11 under certain conditions, according to Bredov.[51] The concentration of surface contaminants is unknown but most likely to be too low to give strong bands from coherent scattering. Also, the formation of ordered surface layers of impurities of sufficient area to cause detectable coherent scattering is unlikely on our samples.

The possibility that we have observed transitions due to adsorbed H_2O in the spectra of adsorbed hydrogen (Figs.5.4,5.5) is discounted for reasons given below (Section 5.3.2(a)).

5.3.2 INIB spectra of hydrogen adsorbed by Drijfhout Pd black

(a) The 1600 cm^{-1} band

The INIB spectra (Figs. 5.4, 5.5) show an intense broad band centred at *ca* 1600 cm^{-1} which indicates that the major surface species are of the Pd$\diagup^{H}\diagdown$Pd bridge type, since the INS spectra of $(\mu_2\text{-H})M_2$ hydridocarbonyls show a strong band in the 1470-1670 cm^{-1} region, assigned to the asymmetric stretch of the M$\diagup^{H}\diagdown$M moiety (Fig. 5.2).

There is little structure in the 1050-1250 cm^{-1} region, where from $(\mu_3\text{-H})M_3$ hydridocarbonyl data the ν_a and ν_s modes of H at a 3-fold surface site would be expected.

The evidence, therefore, is for the predominance of H at 2-fold surface sites. Only three normal modes are expected from such species (Fig. 5.3) and so the complexity of the spectra suggest that at least two distinct 2-fold sites are available. In accord with this, the large observed full-width at half maximum (FWHM) of the 1600 cm^{-1} band suggests that this band may arise from more than one unresolved transition. The instrumental resolution ($\Delta E/E$) at 1600 cm^{-1} is of the order of 15% (*i.e.* 240 cm^{-1}) whereas the FWHM of the 1600 cm^{-1} band for the second coverage of H on sample 1 (Fig.5.5) is 470 cm^{-1}. Removing the instrumental contribution to the observed band width, one obtains a FWHM of $(470^2-240^2)^{\frac{1}{2}}$ cm^{-1}, *i.e.* about 400 cm^{-1}. In the case of an adsorbed atomic species, the non-instrumental contributions to the band width are:

(1) the collisional broadening from the momentum transfer $\hbar Q$ during the scattering event. At 1600 cm^{-1}, Q = 8.7 $\mathring{A}^{-1}$ on INIB:

(2) the potential energy well in which the H atom resides moving with the metal lattice vibrations.

We feel that (1) will be the dominant contribution to the band width. However, experience of the beryllium filter spectra of a wide range of materials[35] indicates that a band width of 400 cm^{-1} is too large to have arisen from a single normal vibration of a unique species. As a first approximation, we consider that the 1600 cm^{-1} band comprises the unresolved transitions of two similar species of similar surface concentration undergoing the same normal vibration. Two Gaussians were fitted to the 1600 cm^{-1} band with the constraint that the peak heights and FWHM were, approximately, equal. For sample 1 the peak maxima arose at -

lower coverage		higher coverage	
band maxima, cm^{-1}	FWHM, cm^{-1}	band maxima, cm^{-1}	FWHM, cm^{-1}
1522	370	1492	260
1627	350	1658	240

We consider, therefore, that the 1600 cm^{-1} band arises from the unresolved ν_a vibrations of Pd$\diagup^{H}\diagdown$Pd species at two distinct surface sites. For reasons explained below (Section 5.3.2(b)), these sites are most probably on the (111) and (100) crystal planes.

Horiuti and Toya[36] have predicted that the band width of s-type chemisorbed H (embedded between the electronic surface of the metal and the outermost layer of metal atoms) is of the order of 100 cm^{-1}, while that of r-type H (at conventional on-top sites above the electronic surface) is $\sim$20 cm^{-1}. Although the s-type H is said to have only one quantised vibration relative to the surface (*i.e.* normal to it) and so is not an accurate description of the observed $(\mu_2 - H)Pd_2$ species, the band widths of the present INS spectra (Figs. 5.4, 5.5) provide some support for the theoretical calculations.

The ν_δ mode of water occurs at 1595 cm^{-1}.[37] Thus a possible contribution to the 1600 cm^{-1} band is from surface H_2O formed either from reaction of H_2 with unremoved surface oxygen or co-adsorbed with the hydrogen. Both origins are experimentally unlikely, indeed a Pd+H sample exposed to the atmosphere, which would bear considerably more surface H_2O than the unexposed samples, gave only a weak and unstructured INS spectrum (Fig. 5.6). The presence of surface H_2O on the present samples is therefore ruled out.

Fig. 5.6 Beryllium filter detector (IN1B) spectrum of Drijfhout Pd black plus H_2O at 77K.

A background spectrum of Pd black has been subtracted. The symbols x and + indicate data collected using the Cu(200) and Cu(220) monochromator planes respectively.

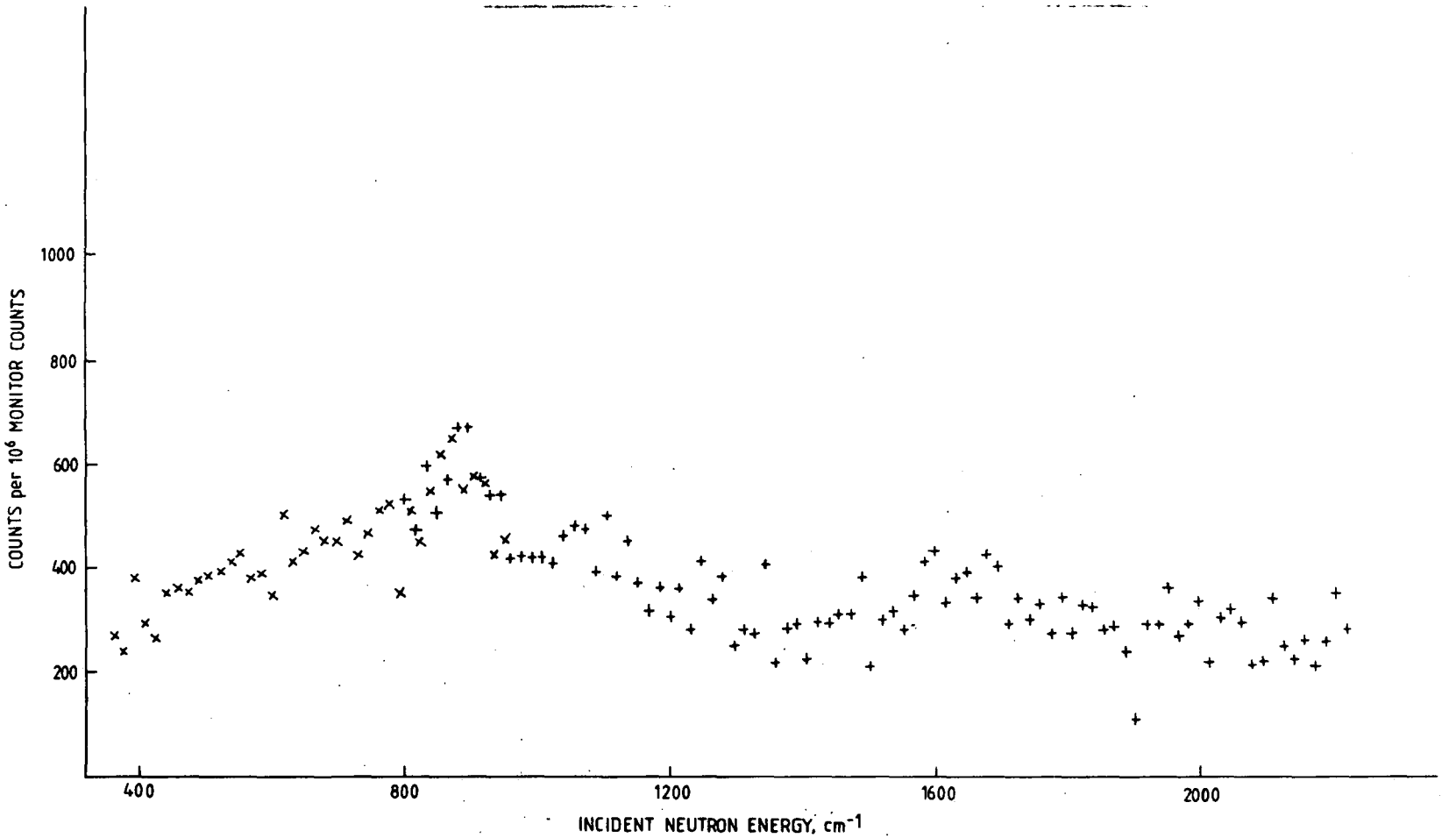

(b) The 618 cm^{-1} and 941 cm^{-1} bands

On normalising the spectra obtained at high and low coverage on sample 1 to the area under the 1600 cm^{-1} band, the approximate change in intensity, relative to the 1600 cm^{-1} band, of each band with surface coverage, was determined. The band at 1600 cm^{-1} was chosen for the normalisation because its large intensity and separation from other bands allowed for accurate determination of its area. Choosing any other band which appeared in both spectra would have given the same information but the estimation of band area would have been more difficult and less accurate. The normalised spectra are shown in Fig.5.7. Changes in the intensities of the other bands are discussed below.

The band at 618 cm^{-1} shows a greater increase in intensity on increasing coverage θ than any other band (Fig. 5.7) and so cannot be due to the previously assigned 2-fold bridging sites. By comparison with the hydridocarbonyl data (Fig. 5.2), it is assigned to the degenerate bending modes of a terminal Pd-H species. The very weak band at 1225 cm^{-1}, only observed at the higher surface coverage (Fig. 5.7), may then be assigned to the first overtone of the 618 cm^{-1} band (2 x 618 cm^{-1} = 1236 cm^{-1}).

The band at 941 cm^{-1} shows an apparent change in wavenumber with increasing coverage but this is difficult to quantify since it sits on a strongly sloping baseline (Fig. 5.7). Because this band does not increase in intensity as much as the 1600 cm^{-1} band, it is tentatively assigned to the bending modes of H terminally bound at a site which reached saturation coverage below the pressure used in the higher coverage experiment.

Fig. 5.7 Beryllium filter detector (IN1B) spectra of Drijfhout Pd black plus adsorbed hydrogen at 77K: broken line line 1.2 monolayers coverage; solid line 1.7 monolayers coverage.

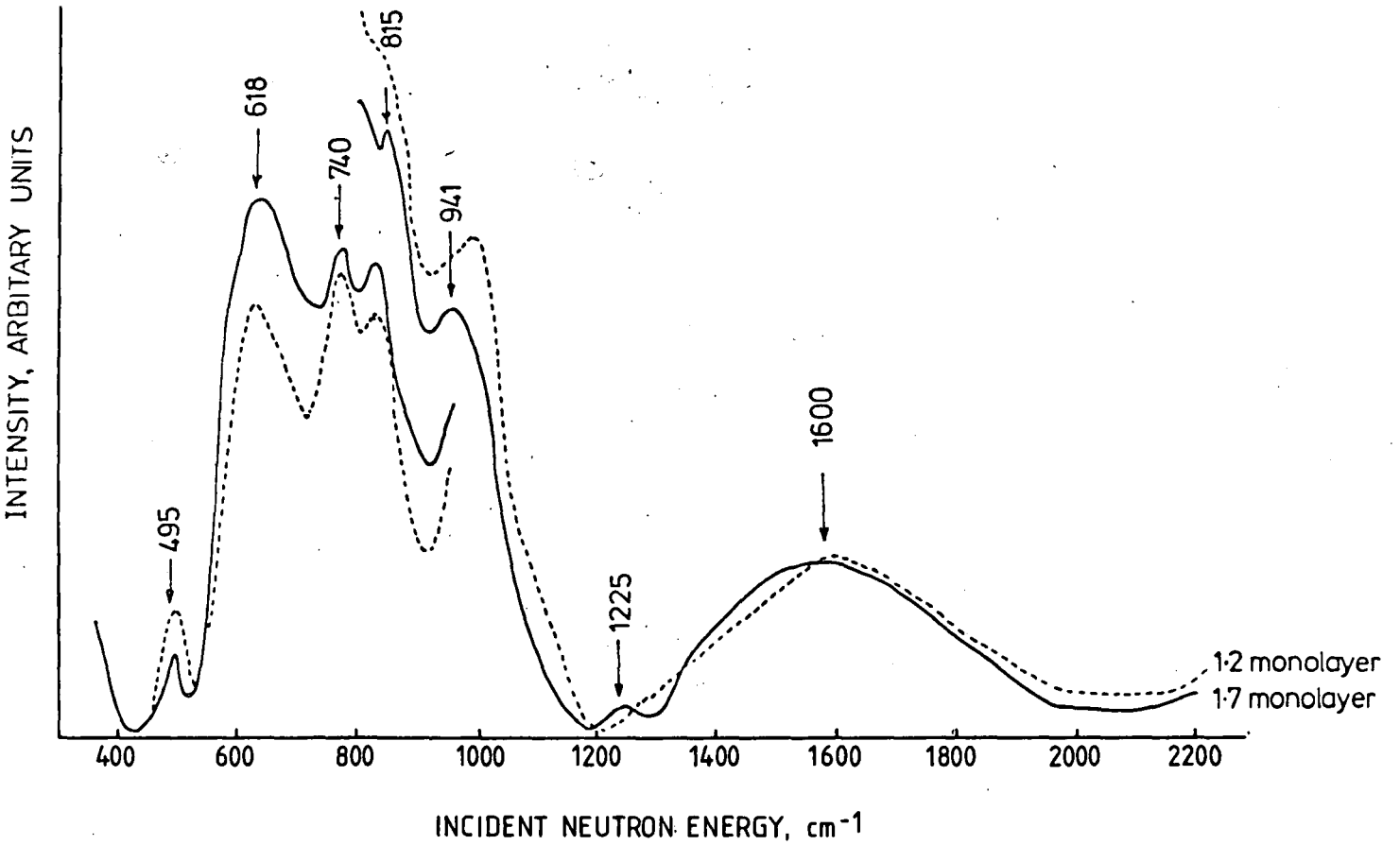

The crystal planes exposed at the surface of Pt and Pd blacks are those which are most densely packed.[38] The surfaces of Pd crystallites supported on active carbon comprise the following crystal planes:[38]

Pd (111) 70%

Pd (100) 25%

Pd (110) 5%

We assume that the present Pd black has a similar distribution of surface planes, and to decide whether the adsorption sites on one particular plane will be filled in preference to the sites on another, we note the following:

1. The numerical values of the heat of desorption and (isosteric) heat of adsorption for a given surface-H species are very close.[21] The activation energies of H adsorption on single crystal surfaces and on bulk samples of Pd are zero or extremely low.[6,13,19,23]

2. Hydrogen/deuterium exchange experiments[3] on Pd film indicate mobile dissociative adsorption at 77K. It is likely that the H adsorbed on the Drijfhout Pd black was mobile under the experimental conditions used, and thus:

3. The relative population of H on each crystal plane will depend on the available area of the plane and on the free energy change on adsorption.

4. We now estimate how the free energy of adsorption, ΔG, varies between the crystal planes exposed at the Drijfhout Pd black surface. The appropriate enthalpy term, ΔH, is given by the isosteric heat of adsorption, q_{iso}, which includes the heat of adsorption of the H_2 molecule and the heat associated with the necessary rehybridisation of the orbitals of the metal surface atoms: $\Delta H = -q_{iso}$. The values of q_{iso} extrapolated to zero coverage are listed in Table 5.1; on low index crystal planes

of Pd they are constant to one half monolayer coverage and we must assume that the differences between these planes is maintained at coverages of greater than one monolayer. It must also be assumed that the surface contaminants on the Drijfhout Pd black affect these heats equally on each crystal plane.

The differential entropy of adsorption, $\Delta\bar{S}$, at a constant pressure p is given by[34]

$$\Delta\bar{S} = \frac{-q_{iso}}{T} - R\ln{}^{p}/_{p^o}$$

where T = temperature, R = gas constant, p^o = standard pressure chosen for the gas phase.

Ertl *et al*[6] have reported that the maximum value of $\Delta\bar{S}$ for Pd(100)/H_2 is -295 $Jk^{-1}(\text{mole } H_2)^{-1}$ at a coverage of one monolayer and for $p^o = 10^{-8}$ torr. So at, say, 77K and 50 torr, we have

$$T\Delta S = -77\ (295 + 8.314\ \ln\ (5 \times 10^{9}))\ J.mol^{-1}$$

$$T\Delta S = -37.0 \qquad kJ.mol^{-1}$$

The absolute value of q_{iso} for the Pd(100)/H_2 system is reported[6] to fall rapidly as the coverage is increased above 0.9 monolayers, the smallest value measured being -77.4 kJ $mole^{-1}$ at $\theta = 1.25$. So at 77K and for $\theta>1$, we have

$$\Delta H < T\Delta S < 0$$

$$\Delta G < 0$$

The difference between the q_{iso} ($\theta=0$) for adsorption on various crystal planes of Pd is less than the likely $T\Delta S$ terms. If the trend in $T\Delta S$ with θ for each crystal plane follows the trend in q, then the surface sites will be occupied in order of decreasing adsorption enthalpy.

Given the above assumptions, we conclude that at $\theta>1$ on the Drijfhout Pd black, the (100) sites will fill preferentially to the (111) sites although they are less numerous.

In view of the thermodynamic predictions above and the change in their intensities with hydrogen dosage, the bands at 618 and 941 cm^{-1} are assigned to vibrations parallel to the surface of on-top, Pd-H species on the (111) and (100) planes respectively. On these planes the modes are doubly degenerate; the perpendicular vibrations are expected in the region 2000-2250cm^{-1} Both spectra (Figs. 5.4, 5.5) of sample 1 do show a small increase in scattered neutron intensity in the region of 2200 cm^{-1} but the spectra were not recorded at higher frequencies and the level of background scattering is not well defined. This intensity does however suggest the existence of perpendicular modes of terminally bound hydrogen in this region.

(c) The remaining bands

The 740 cm^{-1} band intensity is essentially unchanged on increasing coverage, the small difference being due to the large change in the neighbouring 618 cm^{-1} band. The band at 790 cm^{-1} shows a small increase in intensity. By comparison with the hydridocarbonyl data, both these bands are assigned to the symmetric stretch of two different $(\mu_2\text{-H})Pd_2$ species. Again, since the sites on the (100) planes are expected to approach saturation first, the 740 cm^{-1} band is assigned to adsorption on the (100) plane and the 790 cm^{-1} on the (111) plane.

The intensity of the band at 495 cm^{-1} remains almost constant with coverage and is difficult to correlate with adsorption at on-top, 2-fold or 3-fold sites. Neither can this band arise from absorbed or type-C hydrogen. The vibrations of α and β Pd hydrides have been reported at 552 and 460 cm^{-1} respectively, using INS.[26] Under the conditions used in the H_2 adsorptions on sample 1 (Section 5.2.2(a)), only the α-hydride phase, and not the β, is

formed in pure Pd blacks.[39] If the α-hydride was present then we would expect a band to arise at *ca* 550 cm^{-1} with a markedly increased intensity at the high coverage. Such behaviour was not observed (Fig.5.7). Type-C hydrogen is reported as being in dynamic equilibrium with the interstitial hydrides,[19] and therefore must also be absent from these samples. We are consequently unable to suggest an assignment for the transition at 495 cm^{-1}.

5.3.3 The DIDO b.f.d. spectra of hydrogen adsorbed on Drijfhout palladium black

The spectra of the Drijfhout Pd black after sample preparation (samples 2 and 3) but before H_2 adsorption are shown in Figs. 5.8a, 5.9a and summarised in Table 5.6. Both spectra show bands at 128, 158, 193, 244 and 306 cm^{-1} which we assign to lattice modes. The density of states of pure Pd has been calculated[40] to contain two broad bands centred between 110-140 cm^{-1} and 187-202 cm^{-1}, and INS from a pure Pd+H system[26] has observed two lattice modes at 129±5 and 194±7 cm^{-1}. The band at 306 cm^{-1} in our spectra (Figs. 5.8a, 5.9b) has not previously been reported and may be related to the Zn and Pb contaminants.

Two coverages of hydrogen were obtained on samples 2 and 3, the spectra are presented in Figs. 5.8b,c; 5.9b,c and listed in Table 5.6. These data suffer from a very poor signal to noise ratio and no additional bands appear in the spectra of either sample on increasing the hydrogen coverage. We will therefore discuss the results with reference to the spectrum of the second coverage of hydrogen on sample 3 (Fig. 5.9c, saturation coverage, see Section 5.2.2(b)) which shows the best statistics. Above 400 cm^{-1} (Fig. 5.9c), a band was seen at 477 cm^{-1} and broad

Figs. 5.8 Beryllium filter detector (DIDO b.f.d.) spectra (77K) of Drijfhout Pd black, sample 2.

Fig. 5.8a Spectrum of pd black sample 2 after pretreatment (no background subtracted).

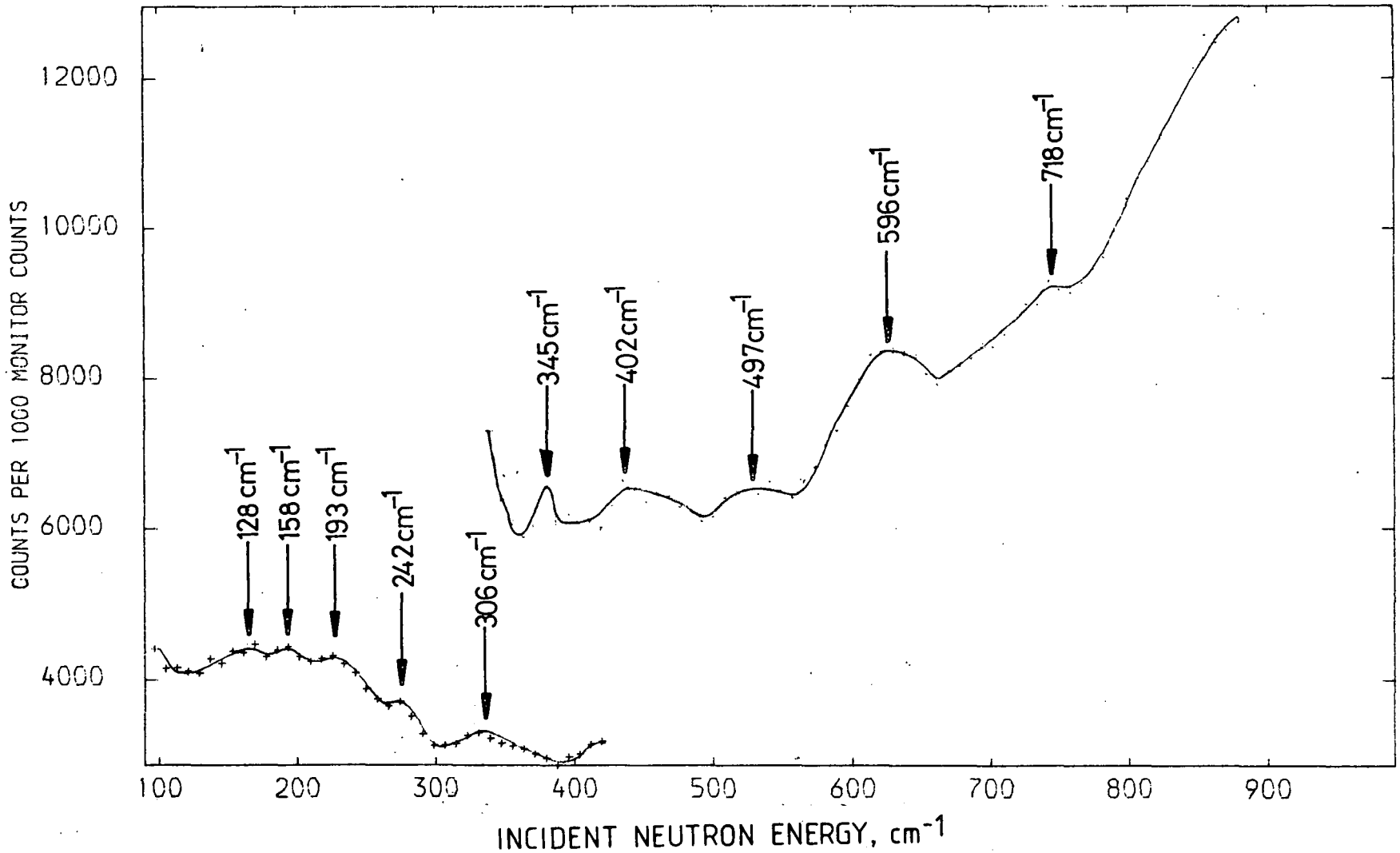

Fig. 5.8b Spectrum (77K) of Pd black sample 2 plus adsorbed hydrogen, 0.8 monolayers coverage. A background spectrum of Pd black has been subtracted.

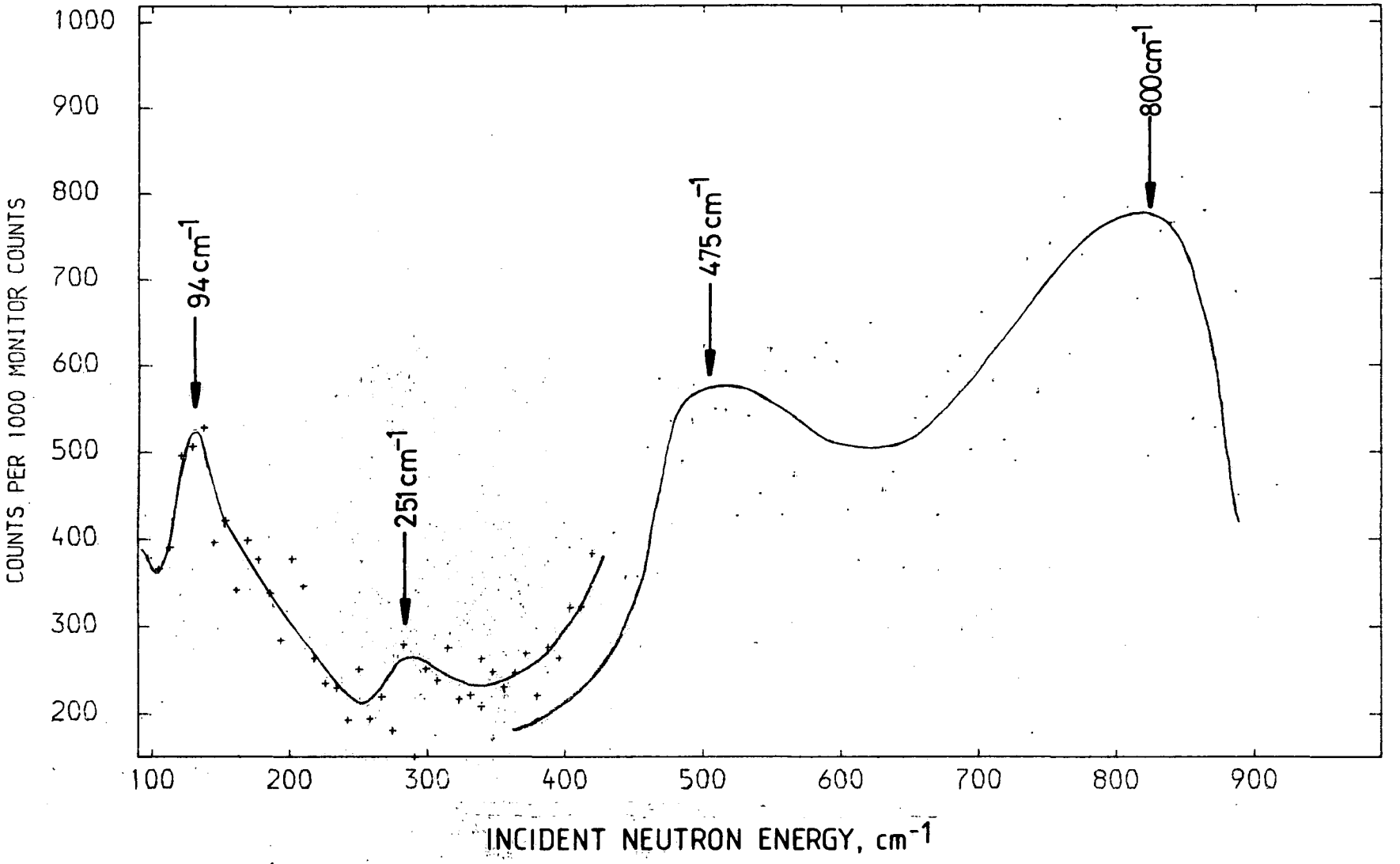

Fig. 5.8c Spectrum (77K) of Pd black sample 2 plus adsorbed hydrogen. The sample can contained sufficient hydrogen to saturate the surface. A background spectrum of Pd black has been subtracted.

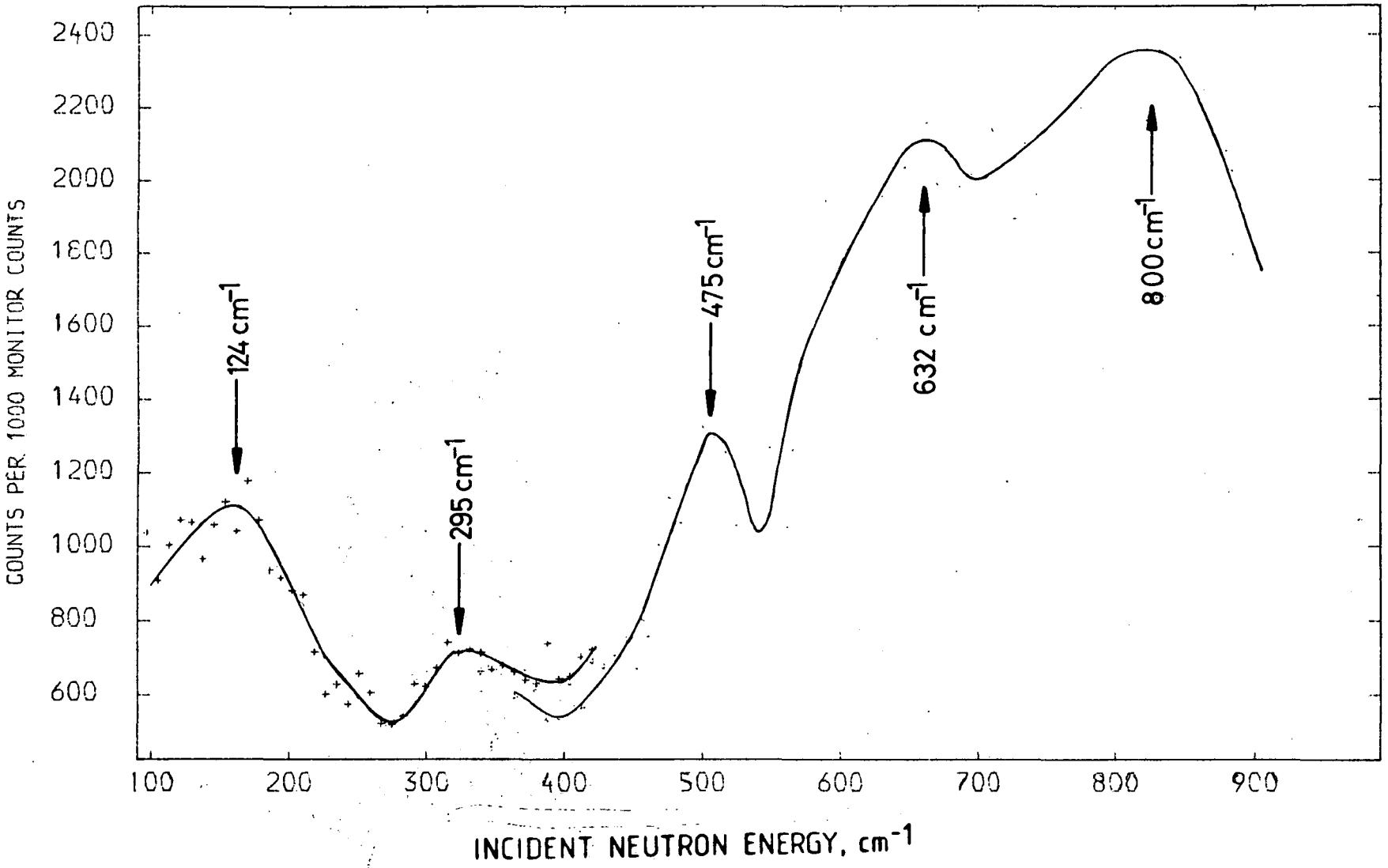

Figs. 5.9 Beryllium filter detector (DIDO b.f.d.) spectra (77K) of Drijfhout Pd black, sample 3.

Fig. 5.9a Spectrum of Pd black sample 3 after pretreatment (no background subtracted).

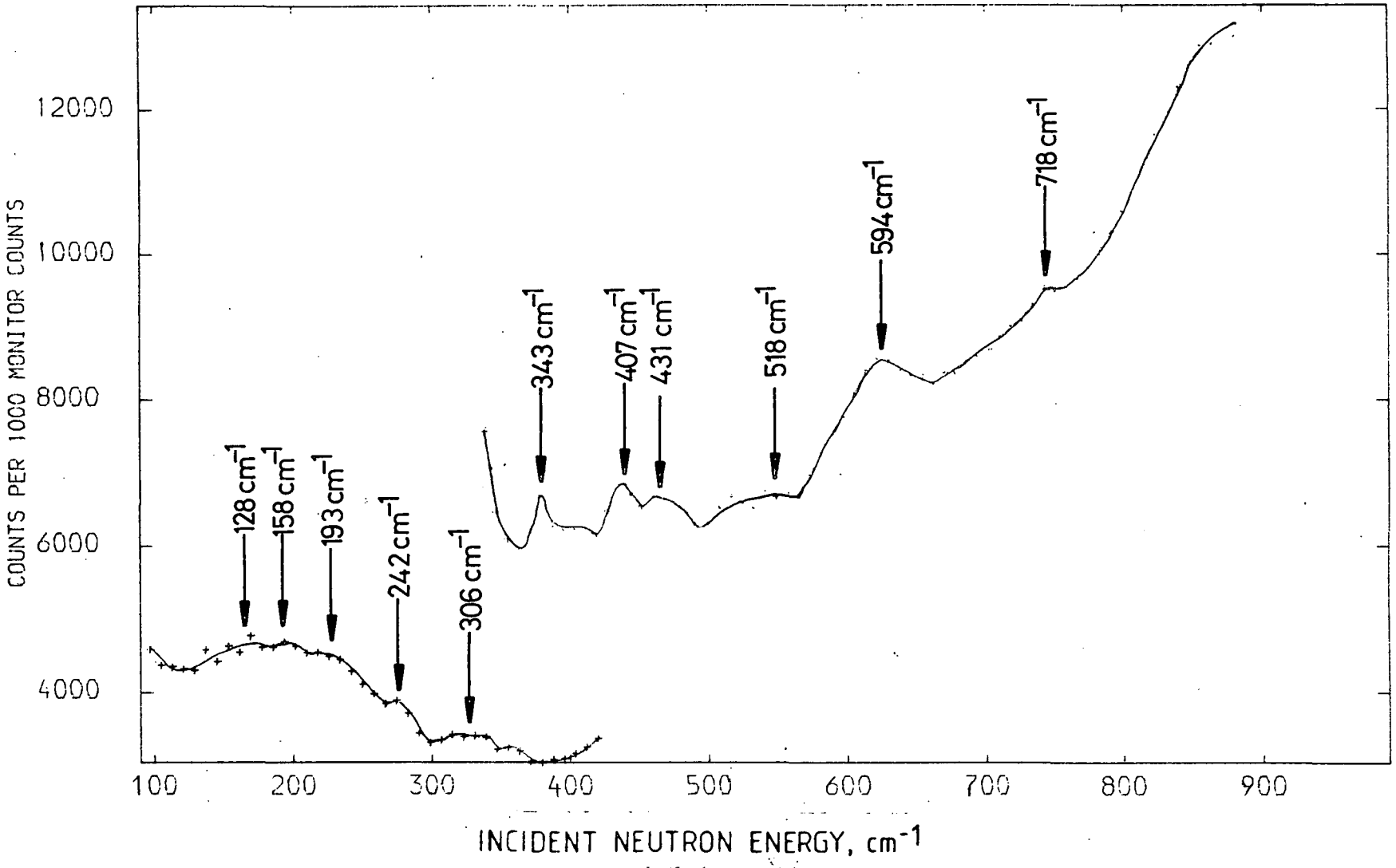

Fig. 5.9b Spectrum (77K) of Pd black sample 3 plus adsorbed hydrogen, 1.8 monolayers coverage. A background spectrum of Pd black has been subtracted.

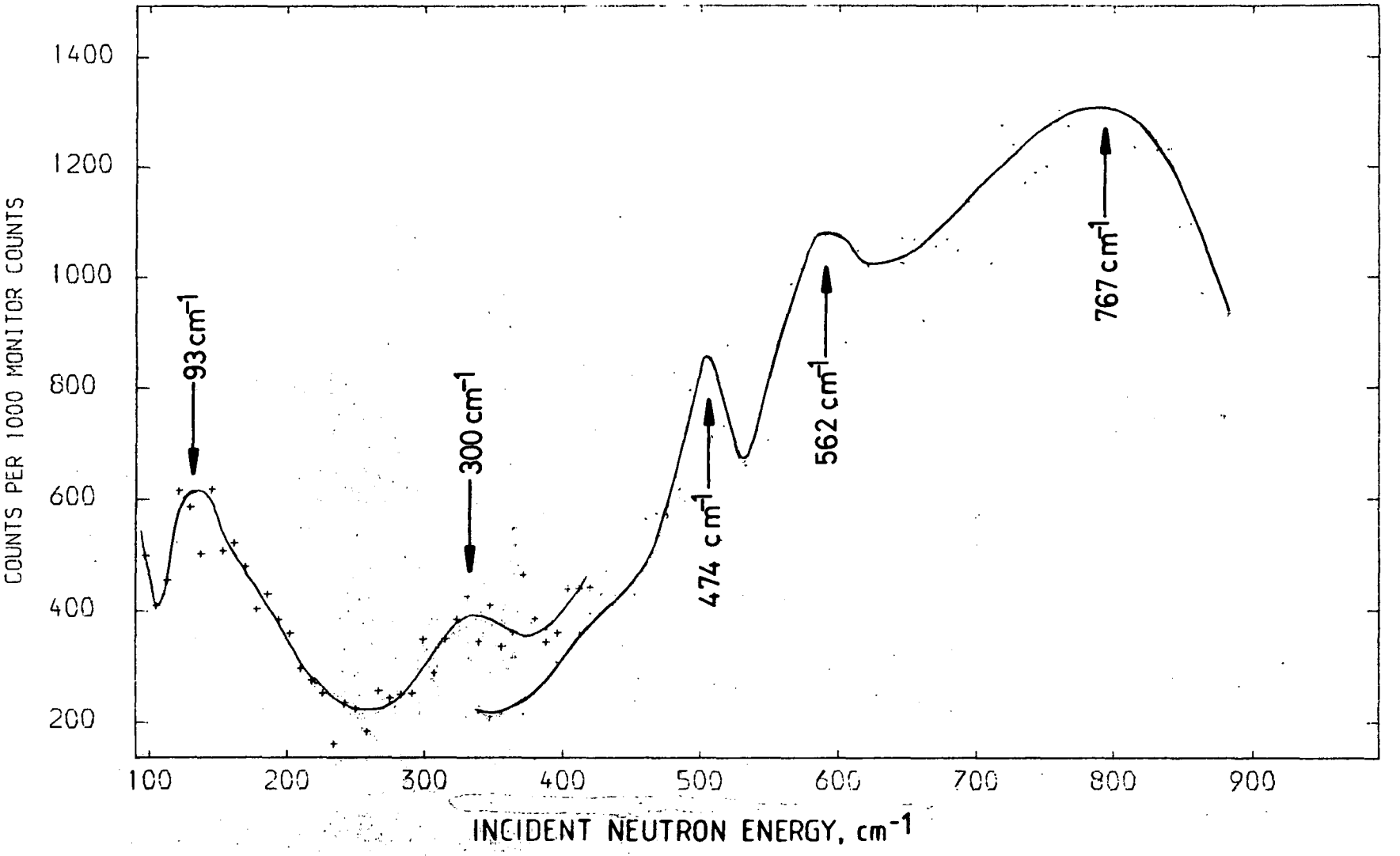

Fig. 5.9c Spectrum (77K) of Pd black sample 3 plus adsorbed hydrogen. The sample can contained sufficient hydrogen to saturate the surface. A background spectrum of Pd black has been subtracted.

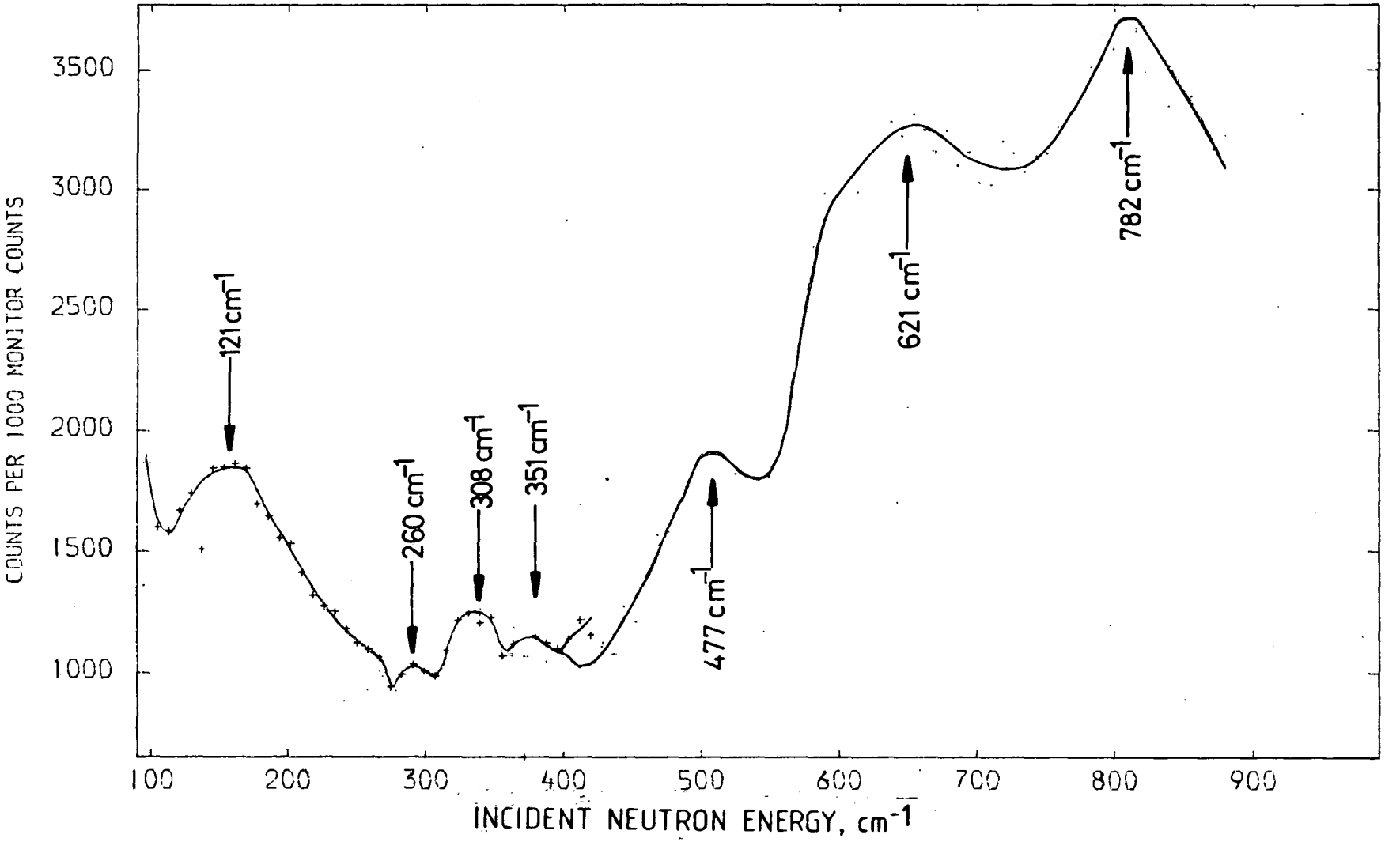

TABLE 5.6 Summary of the assignments of the DIDO b.f.d. spectra (77K) of hydrogen adsorbed on Drifjhout Pd black (cm^{-1})

sample 2			sample 3			sample
Pd background	0.8	saturation[a]	Pd background	1.8	saturation[a]	coverage of hydrogen, monolayers
fig.5.8a	fig.5.8b	fig.5.8c	fig.5.9a	fig.5.9b	fig.5.9c	assignment
	*ca.*94s,b			*ca.*93s,b		
128 m		*ca.*124s,b	128 m		121s,b	)
158 m			158 m			)
193 m			193 m			)
242 m	*ca.*251 m	*ca.*295 m	242 m		260vw	) lattice modes
306 m			306 w	*ca.*300?	308 m	)
(345)			(343)			instrument artifact[b]
					351vw	
402 m			407 m			
			431 m			
	475 s	475 s		474 s	477 s	
497 m			518 m			
596 s			594 s			
		632 s		*ca.*562 s	621 vs	bending mode $(\mu_1\text{-H})Pd$
718w			718w			
	*ca.*800vs	*ca.*800vs		767vs	767vs	unresolved ν_{sym} modes of $(\mu_2\text{-H})Pd_2$ on various crystal planes

b = broad; m = medium; s = strong; v = very; w = weak.

(a) The sample can contained sufficient hydrogen to saturate the surface with adsorbed hydrogen (see Section 5.2.2.2)

(b) This feature arises from a double Bragg reflection from the Al monochromator (see Chapter 3).

features centred at 620 and *ca* 780 cm^{-1}, corresponding to bands at 495, 618 and 740 and 815 cm^{-1} observed using INIB (Fig. 5.5), the latter two bands being unresolved by the DIDO b.f.d. spectrometer.

The 495 cm^{-1} band was not assigned in the INIB spectra. Again, because the corresponding *ca* 477 cm^{-1} band in the DIDO b.f.d. spectra (Figs. 5.8, 5.9) shows no large gain in relative intensity on increasing the coverage θ, we reject the possibility that it is due to an interstitial hydride or type-C hydrogen. In accord with this, the absorption of H_2 by (pure) Pd is an activated process and occurs to a negligible extent at 77K.[18] Nor does the 477 cm^{-1} band correlate with bands expected from surface hydrogen (Section 5.3.2) and it remains unassigned.

Below 400 cm^{-1}, a band is observed in the spectrum of sample 3, second coverage of hydrogen (Fig. 5.9c), at 295 cm^{-1} and a broad band at 124 cm^{-1} which are both assigned to unresolved lattice modes of the Drijfhout Pd.

In summary, the DIDO BFD spectra confirm the frequencies of modes observed using INIB in the common range of the spectrometers and show bands in the density of states of the Drijfhout Pd in the range 128 to 306 cm^{-1}.

The most important feature of the DIDO BFD spectra is the absence of bands ascribable to adsorbed hydrogen in the region 260 to 477 cm^{-1}, the lowest frequency band observed using INIB. No bands, therefore, are observed due to the bending modes of H at two-fold sites. This may be because these vibrations are unresolved from lattice modes, or because they have low relative intensities.

5.3.4 Comments on the sorption of hydrogen in excess of one monolayer by Drijfhout palladium black

We have obtained surface coverages of hydrogen in excess of one monolayer on Drijfhout Pd black (Sections 5.2.2(a)(b)), despite the observation of Konvalinka and Scholten[20] that the uptake stops after the formation of one strongly held monolayer. The maximum pressure used by these authors[20] was 2.25 torr H_2 at 233 K and the additional uptake by our samples must be due to the greater pressures and in the case of the DIDO b.f.d. experiments, the lower temperature (77K) used in our adsorption experiments (Section 5.2).

That INS is a very sensitive method of detecting absorbed hydrogen is shown by the reported[26] b.f.d. spectrum of 10^{-2} torr H_2 sorbed at 358K by pure Pd black. This sample contained a very low concentration of interstitial hydrogen, corresponding to PdH_n, $n<10^{-3}$, and yet the spectrum (Fig. 5.10a), clearly shows bands due to the α-PdH and β-PdH hydrides.[26] The absence of bands assignable to interstitial hydrogen in our INS spectra of Drijfhout Pd+H (Sections 5.3.2(c), 5.3.3) is therefore strong evidence that H_2 absorption did not occur. Type-C hydrogen, which is reported[19] to be formed in dynamic equilibrium with absorbed hydrogen, must also have been absent from our samples.

Thus all the hydrogen sorbed by sample 1 (INIB experiments) is likely to have been strongly chemisorbed, with the possible exception of the species causing the unassigned 495 cm^{-1} band.

The saturation coverage of H chemisorbed on a variety of Group VIII metal surfaces lies in the range $1.0<\theta\leq2.0$ (Section 5.1.1). Thus the surfaces of samples 2 and 3 in the higher coverage experiments (θ=2.8 and 3.2 respectively) on the DIDO

Fig. 5.10a Beryllium filter detector spectrum of Pd black with hydrogen adsorbed at 10^{-2} torr, taken from ref. 26.

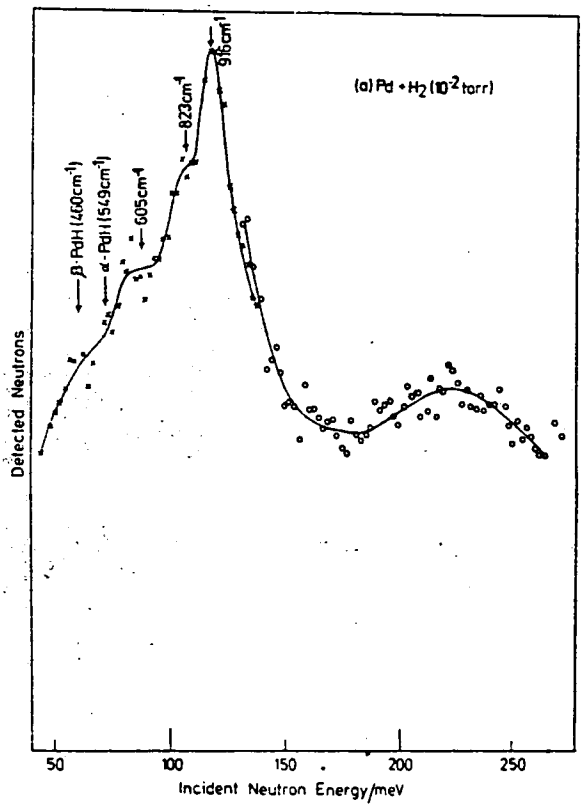

Fig. 5.10b T.o.f. spectrum of Pd black with hydrogen adsorbed at 10 torr, taken from ref. 26.

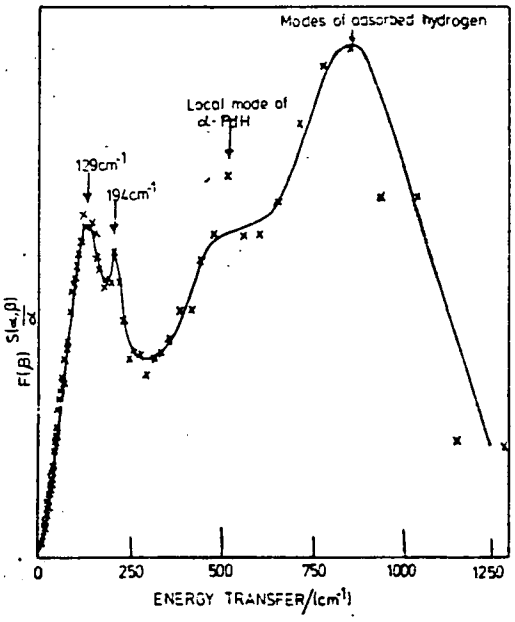

TABLE 5.7 Proposed reassignments of the INS spectrum (77K) of hydrogen adsorbed on pure palladium black (cm^{-1})

frequency, cm^{-1} ($P_{H2} > 10^{-2}$ torr	assignment (ref. 26)	alternative assignment (this work)
129	lattice mode	)
194	lattice mode	)
460	β - PdH	) concurred
549	α - PdH	)
605	H_2O	ν_δ of $(\mu_2\text{-H})Pd_2$, crystal plane unassigned.
823	$(\mu_2\text{-H})Pd_2$ vibration perpendicular to surface	ν_s of $(\mu_2\text{-H})Pd_2$ on Pd (100)
916	$(\mu_2\text{-H})Pd_2$ vibration parallel to surface	ν_s of $(\mu_2\text{-H})Pd_2$ on Pd (111)
≃1700	H-O-H deformation and/or combination 823 + 916	ν_{as} of $(\mu_2\text{-H})Pd_2$ on Pd (111) and Pd (100)

The data are taken from ref.26. See also fig. 5.10

b.f.d. are saturated with strongly chemisorbed hydrogen. The extra hydrogen uptake must have been physisorbed at 77K for the following reasons. On opening the sample cans at room temperature after obtaining the spectra of the second coverages of hydrogen, the cans were found to contain a significant overpressure of H_2, *i.e.* greater than 12 torr, the maximum pressure measurable with the Baratron gauge used. However, the final overpressure of H_2 during the adsorptions at 77K was $\lesssim$0.75 torr. Thus the H_2 sorbed in excess of the strong chemisorption was weakly held by the Pd, indicative of physisorption. Surface potential measurements[41] have shown the presence of physisorbed hydrogen on Pd films at 77K for $\theta \gtrsim 0.85$ (1×10^{-3} torr H_2). The physisorbed H_2 was easily removed by evacuation at 77K to 1×10^{-4} torr.[41]

5.4 Previously published data on the Pd/H system

5.4.1 The INS spectrum of hydrogen adsorbed on uncontaminated Pd black

The INS spectrum of H_2 adsorbed on pure Pd black has been reported[26] and is shown in Fig. 5.10 and Table 5.7. A broad peak at *ca* 1700 cm^{-1} was assigned by the authors[26] to the deformation mode (ν_δ) of co-adsorbed water by comparison with Pt/H INS data.[25] No bands were observed above 2000 cm^{-1} and therefore terminal H was stated to be absent. These assignments were made before the recent INS studies on hydridocarbonyls had been conducted. Using the hydridocarbonyl data, we propose a reassignment of the INS data on the pure Pd-H system.

We submit that the only surface species present were H adsorbed at 2-fold bridging sites. Any 3-fold surface sites must be unoccupied because of the absence of bands in the range

ca 1030 to 1270 cm^{-1}. The broad band at *ca* 1700 cm^{-1} (Fig. 5.10) is assigned to modes of surface Pd$\overset{H}{\diagup\diagdown}$Pd species; as with the data discussed above (Section 5.3.2(a)) its width is indicative of the occupation of sites on more than one crystal plane.

As with Drifjhout Pd black, we assume that the majority of crystal planes exposed at the surface of this pure sample are the (111) planes, with most of the remainder being (100) planes. The most intense band, at 916 cm^{-1} (Fig. 5.10), and the 823 cm^{-1} band are then assigned to the symmetric stretch of H at 2-fold sites on the (111) and (100) crystal planes respectively.

The 605 cm^{-1} band is now tentatively assigned to the ν_δ mode of a surface Pd$\overset{H}{\diagup\diagdown}$Pd species on one of these two crystal planes, although it occurs at a much higher frequency than the analaogous out-of-plane deformation of $(\mu_2\text{-H})Pd_2$ hydridocarbonyls (Fig. 5.2). The ν_δ mode of hydrogen adsorbed on the other crystal plane at a 2-fold site must either occur below 400 cm^{-1} or be submerged in the poorly resolved low frequency part of the spectrum (Fig.5.10).

5.4.2 An infra red study of hydrogen adsorbed by palladium

An IR-reflection study[42] (4000-360 cm^{-1}) of hydrogen adsorbed at pressures of 30 to 730 torr (393K) on an annealed palladium hydride film ($PdH_{0.6}$) showed two bands, at 760 cm^{-1} and 880 cm^{-1}. The 880 cm^{-1} band was the more intense and assigned to modes of H at sites of C_{3v} symmetry on (111) surface crystal planes and the 760 cm^{-1} band to H at sites of C_{4v} symmetry at (100) surface planes. The hydride has significant metal properties[18,26] and the surface selection rule is operative-dipole moment changes parallel to the surface will not give bands

in the IR spectra. Thus the 760 and 880 cm^{-1} bands were said[42] to involve H atom displacements perpendicular to the surface. The two IR bands were very poorly resolved and the transition frequencies were determined by fitting two curves to the observed spectrum, an inaccurate method since the true band widths were not known.[26]

Our INS spectra of the Drijfhout Pd/H system (Section 5.3) indicate that at high coverages(θ>1) hydrogen occupies only 2-fold and on-top sites on Pd. In view of the INS results, we suggest a reassignment of the IR data.[42] The surface coverage of H was not stated in the IR experiment[42] but is likely to have exceeded one monolayer at the pressures used. Thus H is most probably held at 2-fold and/or on-top sites on the palladium hydride film. By comparison with the hydridocarbonyl data (Fig. 5.2), the 880 cm^{-1} IR band is reassigned to the ν_s mode of H at a 2-fold site, which we will refer to as site I. There are two possibilities for the 760 cm^{-1} band:

1. The ν_s mode of H at a 2-fold site, distinct from site I above;
2. the ν_δ mode of H at an on-top site.

Possibility (2) is unlikely - this mode involves only small H atom displacements perpendicular to the surface and will give a very weak IR band. We therefore prefer assignment (1) for the 760 cm^{-1} band. No other bands were reported in the IR spectrum.[42] The ν_a and ν_δ modes of H at 2-fold sites are predicted by the surface selection rule to be very weakly IR active.

5.4.3 Published thermodynamic, kinetic and electrical measurements for hydrogen adsorbed on Pd

Flash desorption studies[43] of polycrystalline wires between 100 and 1000K showed 4 different states of sorbed H.

One state, α, occurred only after cooling the filament to 100K and desorbed at 250K with an activation energy of 54-58 kJ $mole^{-1}$. This state has been ascribed to both the β-hydride phase[43] and to molecularly adsorbed H_2.[21] The 3 other states: β_1, β_2, β_3, desorbed at temperatures above 350K with activation energies[43] of 92, 105 and 146 kJ $mole^{-1}$. The β_3 state was only weakly present. The close agreement between the activation energies of desorption and the enthalpies of adsorption (Table 5.1) indicates that the activation energy for dissociative chemisorption is very low.[21]

Surface potential measurements[41] of hydrogen adsorbed and absorbed at 78K on an annealed Pd film showed the existence of 3 surface species. At very low coverages, $\theta \lesssim 1 \times 10^{-2}$, the H_2 is dissociatively adsorbed to form an electronegative species. At higher coverages, up to $\theta \simeq 0.7$, the major surface state is an electropositive form of dissociated hydrogen. Another electropositive, but weakly held, molecular form of H_2 is adsorbed at coverages approaching 1 monolayer (θ = *ca* 0.85).

These results, however, need qualifying. Firstly, the method gives a surface potential which is an average for all the variously bonded states of H adsorbed on the crystal planes exposed at the surface of the film. Secondly, the experimental conditions were such that the electropositive species were adsorbed on a Pd hydride film rather than Pd metal. Work function measurements[6,23] of adsorption on single crystal planes of Pd (Table 5.3) under conditions where there was no absorption showed that the H adatoms were the negative part of a weak dipole. The latter results were an average over all the surface species on the chosen crystal plane.

Combining the results of these two techniques shows that even at 77K the adsorption of H_2 is dissociative and molecular adsorption occurs only at high coverage. This is in accord with isotherm measurements and H_2/D_2 exchange experiments,[3,18,44] and is the same behaviour as shown by Ni/H systems.[1,2]

5.4.4 Published structural data for hydrogen chemisorbed on single crystal planes of Pd

LEED, TDS and work function-change, $\Delta\psi$, measurements have been used by Ertl *et al*[6,23] to study the adsorption of H on single crystal planes of Pd under conditions where absorption into the bulk was negligible.

On Pd (100), a c(2x2) LEED pattern was seen at low temperatures (<260K) for coverages of less than one monolayer. This arose from adsorption at 4-fold surface sites. The variation in intensity of the adsorbate diffraction spots with surface coverage at 105K showed a maximum at $\theta = 0.5$.

Increasing the temperature at constant θ caused the pattern to disappear indicating disorder of the adlayer above a critical temperature. The experimental phase diagram (Temperature versus θ) thus produced was interpreted as arising from the operation of repulsive, through bond forces (nn) between nearest H neighbours on identical 4-fold sites and attractive forces (nnn) between next nearest neighbours. Below $\theta = 0.5$, the surface was not randomly covered but the adsorbate formed islands of the c(2x2) structure held together by the balance of the nn and nnn forces.

The work function change, $\Delta\psi$, for hydrogen chemisorption on Pd (100) was proportional to surface coverage up

to $\theta \simeq 0.9$ whereafter $\Delta\psi$ increased more rapidly with θ, but still approximately linearly. The H particles have a small partial negative charge and a dipole moment of 2.1×10^{-2} Debye which is constant with coverage for $\theta < 0.9$. At higher coverage, the average dipole moment increased, reaching 3.1×10^{-2} Debye at saturation ($\theta = 1.35$).

The isosteric heat of adsorption, q_{iso}, derived from the empirical relation between θ and $\Delta\psi$ and also from the Clausius-Clayperon equation, was constant at 103 kJ $mole^{-1}$ with θ until $\theta > 0.9$, whereafter it fell rapidly, reaching 77KJ $mole^{-1}$ at $\theta = 1.25$.

TDS spectra up to 550K[6] showed a single peak at T_{max} = 360K which developed a low temperature shoulder at greater than 1 monolayer coverage.

In summary, Ertl *et al*[6] proposed that identical, 4-fold, sites were uniquely occupied on Pd (100) at $\theta < 1$; since these sites must be fully saturated at $\theta = 1$, the abrupt changes in $\Delta\psi$, q_{iso} and the shoulder in the TDS spectra arose from adsorption at sites of different geometry, e.g. terminal and/or bridging. Their results could not distinguish between the new types of site or whether the 4-fold sites remained unoccupied at $\theta > 1$.

The results of chemisorption on other planes of Pd are summarised in Table 5.3 in which the proposed surface sites obtain for coverages of less than a monolayer.

Combining the conclusions of the LEED and the present INS work, at less than 1 monolayer coverage hydrogen is chemisorbed on low index planes of Pd at only the sites of highest possible symmetry, whereas at increasing coverages ($\theta > 1$) 2-fold bridging, and later terminal, sites are occupied, the high symmetry sites

having been vacated. Consistent with this view are the results of the pseudopotential calculations of Louie[45] for an ordered monolayer of H chemisorbed on the Pd (111) surface. The adsorption was predicted to occur at 3-fold hollow sites in preference to on-top sites.

5.5 A reassignment of the previously published INS spectra of hydrogen adsorbed by Pt black

The INS spectra of hydrogen adsorbed by platinum black reported by Howard *et al*[25] are shown in Fig. 5.11 and summarised, along with three different assignment schemes, in Table 5.8. The assignment scheme due to Howard *et al*[25] is not accepted for the following reasons:

1. The authors[25] admitted the possibility of the presence of some surface water on their Pt samples. A broad INS band at 1751 cm^{-1} (Fig. 5.11a; $3x10^{-2}$ torr H_2) which showed a shift to lower frequencies on increasing the hydrogen overpressure (Table 5.8) was accordingly assigned to the ν_δ mode of surface water. However, the INS spectrum of Pt+H_2O (Fig. 5.11b, 1.5 torr H_2O) showed only a weak band at *ca* 1695 cm^{-1}, the intensity of which was much lower than that of the 1751 cm^{-1} band in the Pt/H spectra (Fig. 5.11a). If, therefore, the 1751 cm^{-1} band (Fig. 5.11a) was due to adsorbed water, then the intensity of this band indicates that the quantity of surface water would have been large, comparable to the amount of adsorbed hydrogen. The most likely origins of surface water are co-adsorption with the hydrogen or reaction of hydrogen with unremoved surface oxygen, but both sources are unlikely to yield such large amounts of H_2O. Therefore it is proposed here that the 1751 cm^{-1} band in the Pt/H spectra (Fig. 5.11a) arose from modes of adsorbed hydrogen.

Fig. 5.11a,b Pt black plus hydrogen adsorbed at 3 x 10^{-2} torr (a) with Pt background subtracted, (b) with Pt plus adsorbed water spectrum subtracted. Taken from ref.25.

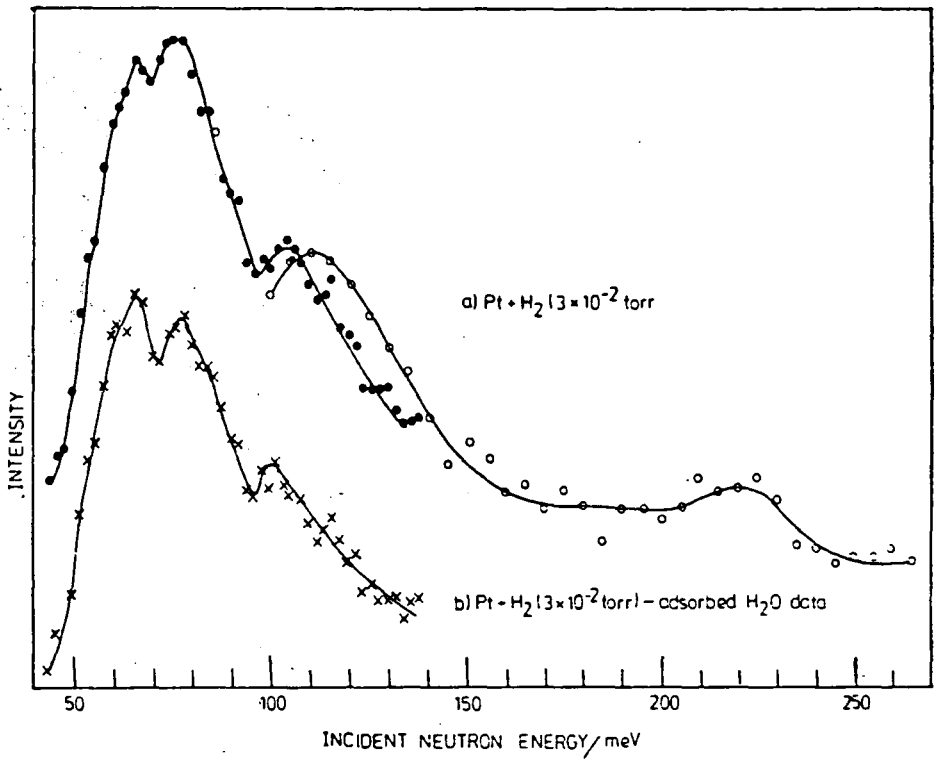

Platinum black plus hydrogen adsorbed at 3 X 10^{-2} torr (a) with the background subtracted (b) with the adsorbed water spectrum subtracted.

Fig. 5.11c,d Pt black plus hydrogen adsorbed at (c) 1 torr, (d) 634 torr. Taken from ref. 25.

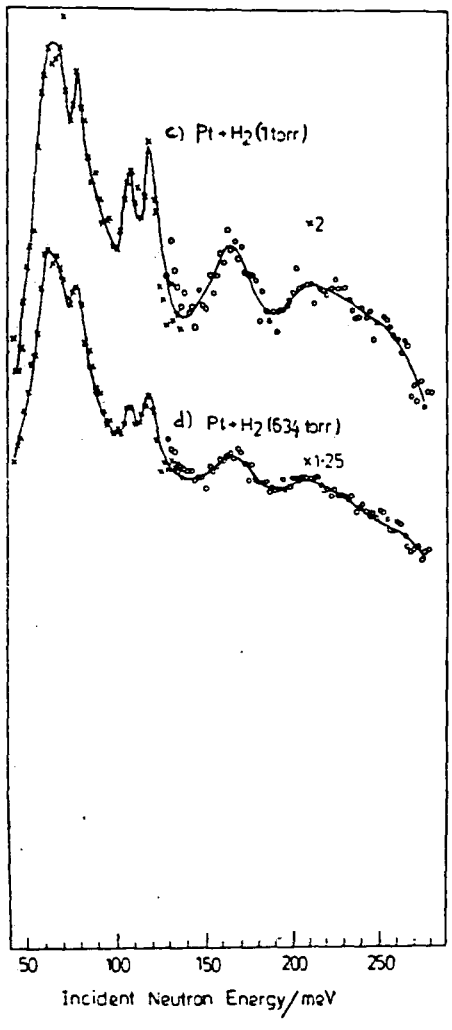

TABLE 5.8 Summary of the INS spectra recorded at 77K for hydrogen adsorbed at room temperature on platinum black. Spectral data taken from ref. 25.

$Pt + H_2$ $3x10^{-2}$ torr Fig.5.11a	$Pt + H_2$ 1 torr Fig.5.11c	$Pt + H_2$ 634 torr Fig.5.11d	original assignment (ref.25)	first alternative assignment (ref. 8)	second alternative assignment (this work)
500	512	496	)	ν_δ $(\mu_2\text{-H})Pt_2$, species X	ν_δ $(\mu_1\text{-H})$Pt on Pt (111)
590	616	616	) all 3 modes of $(\mu_2\text{-H})Pt_2$	i/p def. $(\mu_2\text{-H})Pt_2$, species X	ν_δ $(\mu_1\text{-H})$Pt on Pt (100)
815	856	848	)	ν_s $(\mu_2\text{-H})Pt_2$, species X	ν_s $(\mu_2\text{-H})Pt_2$, crystal plane unassigned
	936	936	ν_δ $(\mu_1\text{-H})$Pt	ν_δ $(\mu_1\text{-H})$Pt	ν_s $(\mu_3\text{-H})Pt_3$ on Pt (111)
	1296	1296	?	ν_s $(\mu_2\text{-H})Pt_2$, species Y	ν_{as} $(\mu_3\text{-H})Pt_3$ on Pt (111)
1751	1696	1656	ν_δ surface H_2O	ν_a $(\mu_2\text{-H})Pt_2$, species X & Y	ν_{as} $(\mu_2\text{-H})Pt_2$, crystal plane unassigned
	2000 to 2250	2000 to 2250	ν_s $(\mu_1\text{-H})$Pt	ν_s $(\mu_1\text{-H})$Pt	ν_s $(\mu_1\text{-H})$Pt on Pt (111) and Pt (100)

i/p def. = in-plane deformation mode.

In column 5, X and Y denote the species formed by hydrogen adsorption at two different 2-fold surface sites.

2. The bands at 500, 590 and 815 cm^{-1} in the Pt/H spectra (Fig. 5.11a, $3x10^{-2}$ torr H_2) were assigned by Howard *et al*[25] to the three modes of H at a 2-fold bridging site but the hydridocarbonyl data (Fig. 5.2) shows these frequencies are too low to include the antisymmetric stretching mode.

3. The band at 1296 cm^{-1} (Figs. 5.11c,d; 1 and 634 torr H_2), which occurred only at higher coverages, remained unexplained.

A different assignment scheme,[8] based on the hydridocarbonyl data, assigned the 1296 cm^{-1} band to the symmetric stretch of a $(\mu_2\text{-H})Pt_2$ species which was formed at high coverage only. The frequency shift of the 1751 cm^{-1} band to 1656 cm^{-1} on increasing coverage was ascribed to the overlapping of the bands due to the ν_a modes of this 2-fold species with that of a different $(\mu_2\text{-H})Pt_2$ state which was present at all coverages.

This scheme, unfortunately, cannot be entirely correct. The band at 616 cm^{-1} cannot be due to the same species as the 856 cm^{-1} band because of the change in relative intensity with coverage (c.f. spectra for 1 and 634 torr H_2). Also the *ca* 616 cm^{-1} band was assigned to a mode of adsorbed hydrogen corresponding to the in-plane deformation of $(\mu_2\text{-H})M_2$ hydridocarbonyls but this mode has no analogue for surface hydrogen (Fig. 5.3).

We now give a reassignment (see Table 5.8) of the INS Pt/H spectra shown in Fig. 5.11, based on the hydridocarbonyl data.

The band at 500 cm^{-1} (Fig. 5.11a) is intense in the low coverage spectrum ($3x10^{-2}$ torr) and becomes the strongest band at the higher coverages. It must therefore be due to a different H species than the other bands.

The 590 cm^{-1} band is the most intense at low θ and, along with the 500 cm^{-1} band, dominates the spectrum at high θ (634 torr).

We assign both bands to terminally bound H, the 590 cm^{-1} to sites on the (10$\bar{0}$) surface planes and the 500 cm^{-1} to sites, which are expected to be more numberous, on the (111) planes. These modes are the (degenerate) vibrations of H parallel to the surface; the perpendicular modes, expected in the region 2000 to 2250 cm^{-1}, were only seen for H_2 doses of 1 torr and above, probably because of the large momentum transfer at these high frequencies reducing the INS band intensities.

The bands at 815 and 1751 cm^{-1} ($3x10^{-2}$ torr H_2) appear at all coverages. They cannot be caused by the same surface species as the 500 or 590 cm^{-1} bands because they become relatively weaker at high θ. By comparison with the hydridocarbonyl data (Fig. 5.2) they are assigned to the modes of H at a 2-fold site, the 1751 cm^{-1} band to the antisymmetric stretch and the 815 cm^{-1} to the symmetric stretch. These bands shift to 848 and 1656 cm^{-1} at high θ (634 torr H_2) possibly because of lateral interactions between adsorbed H particles on the more crowded surface. There are no bands assignable to the ν_δ mode of the Pt$\diagup^{H}\diagdown$Pt surface species. The band intensity from this mode may be intrinsically weak or it may arise below the low frequency limit (337 cm^{-1}) of the Pt/H spectra (Fig. 5.11). The analogous out-of-plane deformation mode of $(\mu_2\text{-H})M_2$ hydridocarbonyls lies in the range 310 to 370 cm^{-1} (Fig. 5.2).

The 936 and 1296 cm^{-1} bands in the Pt/H spectra (1 torr H_2) exhibit their maximum intensities at 1 torr and do not appear at lower coverage. This suggests multiple-bonding sites; noting the intensity of the 1296 cm^{-1} band it is assigned to the antisymmetric stretch (an E mode) of H at a 3-fold site and the 936 cm^{-1} band to the symmetric stretch (A_1).

5.6 Estimation of bond angles and bond lengths for H species on Drijfhout Pd black

Two methods of estimating bond angles from vibrational frequencies have recently been published, one by Katovic and McCartey,[46] the other by N. Sheppard *et al.*[47] Both methods are derived from equations given by Herzberg[37] for the force constants of XY_2 (C_{2v}) molecules. Using the central force field model, Katovic assumed that $\nu_\sigma << \nu_s$ and Sheppard *et al* made the equivalent approximation in their valence force field model that the force constant of the bending mode was much less than that of the bond stretching mode. By modifying Katovic's equation[46] to include ν_δ we obtain:

$$\frac{\nu_a^2}{\nu_s^2 + \nu_\delta^2} = \frac{M_m^{-1} + M_H^{-1}(1 - \cos\alpha)}{M_m^{-1} + M_H^{-1}(1 + \cos\alpha)}$$

where $\alpha = \hat{MHM}$ bond angle, M_m=mass of metal atom, M_H = mass of hydrogen atom. Sheppard's equation[47] becomes

$$\frac{\nu_a^2}{\nu_s^2 + \nu_\delta^2} = \tan^2\left(\frac{\alpha}{2}\right)$$

We shall use the Katovic equation in preference to the Sheppard equation since the derivation of the latter takes M_m to be infinite. The method still assumes that

$$a_{33} << a_{11}\,(1 + M_m M_H^{-1}\,(1 + \cos\alpha))$$

and also makes the probably less reasonable assumption of central forces (a_{11} = force constant for Pd-H stretch, a_{33} = force constant for Pd-Pd stretch).

We have calculated (Table 5.9) the bond angles, α, of the surface Pd$\overset{H}{\diagup\diagdown}$Pd species of the Drifjhout Pd sample using the Katovic formula and assuming $\nu_\delta << \nu_s$, since the ν_δ frequencies are unknown.

TABLE 5.9 Bond angles, α, and bond lengths, r, for H adsorbed at 2-fold sites on Drijfhout Pd black

Crystal plane	coverage	$\alpha^{o}, \pm 1^{o}$	$r\text{Å}, \pm 0.01\text{Å}$
Pd (111)	1.2	129	1.53
Pd (111)	1.7	127	1.54
Pd (100)	1.2	130	1.52
Pd (100)	1.7	129	1.52

The errors in α and r are those which arise from an uncertainty of $\pm$ 15 cm^{-1} in the vibrational frequencies.

Both the (100) and (111) planes of Pd are close packed, thus the Pd-H bond lengths (Table 5.9) are given by $r.\text{cosec}^{\alpha}/_{2}$, where r = 1.375Å is the atomic radius of Pd. However, the sum of the Bragg-Slater radii[48] of Pd and H is 1.65Å, greater than the predicted bond lengths. This shows that the assumptions $\nu_\delta << \nu_s$ and of the central force field model are very poor. Indeed, even for a simple molecule such as H_2O in the gas phase, the central force field model leads to inaccurate predictions.[37]

5.7 Conclusions

The INS spectra of H adsorbed on Pt and two different Pd samples, assigned by comparison with the vibrational spectra of transition metal hydridocarbonyl compounds, show the occup-

ation of 2-fold bridging sites on each metal surface.

On Pt, terminal and 3-fold sites are also filled while on pure Pd, adsorption occurs only at the 2-fold sites. Adsorption at a unique type of site on Pd and a multiplicity of sites on Pt confirms the results of other surface techniques, published in the literature.

As the coverage approached $\theta=2$ on Drifjhout Pd black, on-top sites became filled along with the 2-fold sites. In several respects the Drifjhout Pd black is more similar to Pt black than to pure Pd black, as witness the complexity of its INS spectrum of adsorbed hydrogen, indicating the existence of several surface states, and in the lower isosteric heat of adsorption. This can be explained by the raising of the d-electron density at the Drijfhout Pd surface by the Zn and Pb contaminants, intermediate between the value for Pd (the lesser) and Pt (the greater).

Previously published data, principally LEED results, indicate that sites of high symmetry, e.g. C_{3v} on (111) planes, are occupied at coverages of less than 1 monolayer on Pt and Pd. The INS data show that at higher coverages, such sites are vacated in favour of 2-fold bridging sites and, except for 'pure' Pd, on-top sites.

CHAPTER FIVE - REFERENCES

1. Wedler, G., Chemisorption: an Experimental Approach (Translated by Klemperer, D.F.), Butterworths, London, 1976.

2. Schuit, G.C.A. and Van Reijen, L.L., Advan.Catal., 10, 242, 1958.

3. Suhrmann, R., Schumicki, G. and Wedler, G., Z.Phys.Chem. (Frankfurt), 10, 184, 1957.

4. Gentsch, H., Z.Phys.Chem. (Frankfurt), 35, 69, 1961.

5. Candy, J.P., Fouilloux, P., and Renouprez, A.J., J.Chem.Soc., Faraday Trans.1, 76, 616, 1980.

6. Behm, R.J., Christmann, K. and Ertl, G., Surf.Sci., 99, 320, 1980.

7. Renouprez, A.J., Fouilloux, P., Goudourier, G., Tocchetti, D. and Stockmeyer, R., J.Chem.Soc., Faraday Trans.1, 73, 1, 1977.

8. Graham, D., Ph.D. Thesis, University of Durham, 1980.

9. Cavanagh, R.R., Kelly, R.D. and Rush, J.J., J.Chem.Phys., 77, 1540, 1982.

10. Christmann, K., Bull.Soc.Chim.Belg., 88, 519, 1979.

11. Ho, W., Di Nardo, N.J. and Plummer, E.W., J.Vac.Sci.Technol., 17, 134, 1980.

12. Upton, T.H. and Goddard, W.A., Phys.Rev.Lett., 42, 472, 1979.

13. Christmann, K., Ertl, G. and Schober, O., Surf.Sci., 40, 61, 1973.

14. Andersson, S., Chem.Phys.Lett., 55, 185, 1978.

15. Reider, K.H. and Engel, T., Phys.Rev.Lett., 43, 373, 1979.

16. Christmann, K., Ertl, G. and Pignet, T., Surf.Sci., 54, 365, 1976.

17. Demuth, J.E., Surf.Sci., 65, 369, 1977.

18. Lewis, F.A., The Palladium/Hydrogen System, Academic Press, New York, 1967.

19. Lynch, J.F. and Flanagan, T.B., J.Phys.Chem., 77, 2628, 1973.

20. Konvalinka, J.A. and Scholten, J.J.F., J.Catal., 48, 374, 1977.

21. Wicke, E., Brodowsky, H. and Züchner, H., in Hydrogen in Metals, Vol.2 (Alefeld, G. and Völkl, J., Eds.), Springer-Verlag, Berlin, 1978.

22. Janko, A., Palczewska, W., and I. Szymerska, J.Catal., 61, 264, 1980.

23. Conrad, H., Ertl, G. and Lata, E.E. SurfSci., 41, 435, 1974.

24. Asada, H., Toya, T., Motahashi, M., Sakamoto, M. and Hamaguchi, Y., J.Chem.Phys., 63, 4078, 1975.

25. Howard, J., Waddington, T.C. and Wright, C.J. in Neutron Inelastic Scattering 1977, Vol.2, p.499, International Atomic Energy Agency, Vienna, 1978.

26. Howard, J., Waddington, T.C. and Wright, C.J., Chem.Phys.Lett., 56, 258, 1978.

27. Messmer, R.P. in The Nature of the Surface Chemical Bond (Rhodin, T.N. and Ertl, G., Eds.), North Holland, Amsterdam, 1979.

28. Muetterties, E.L., Rhodin, T.N., Band, E., Brucker, C.F. and Pretzer, W.R., Chem.Rev., 79, 91, 1979.

29. Muetterties, E.L., Israel J.Chem., 20, 84, 1980.

30. Evans, J., Chem.Soc.Rev., 10, 159, 1981.

31. Kelly, R.D., Rush, J.J., Madey, T.E., Chem.Phys.Lett., 66, 159, 1979.

32. Ross, D.K., Martin, P.F., Oates, W.A., and Khoda-Bakhsh, Z.Phys.Chem. (Frankfurt), 114, 221, 1979.

33. Sermon, P.A., J.Catal., 24, 460, 1972.

34. Ponec, V., Knor, Z. and Černý, S., Adsorption on Solids, Butterworths, London, 1974.

35. Howard, J. and Waddington, T.C. in Advances in Infrared and Raman Spectroscopy, Vol.7, (Clark, R.J.H. and Hester, R.E., Eds.), Heyden, London, 1980.

36. Horiuti, J. and Toya, T., in Solid State Surface Science, Vol.1 (Green, M.,Ed.), Dekker, New York, 1969.

37. Herzberg, G., Molecular Spectra and Molecular Structure, II, Infrared and Raman Spectra of Polyatomic Molecules, Van Nostrand Reinhold, New York, 1945.

38. Sundquist, B.E., Acta.Metall., 12, 67, 1964.

39. Clewley, J.D., Curran, T., Flanagan, T.B. and Oates, W.A., J.Chem.Soc., Faraday Trans.1, 69, 449, 1973.

40. Brockhouse, B.N. and Miller, A.P., Can.J.Phys., 49, 704, 1971.

41. Dus, R., Surf.Sci., 42, 324, 1973.

42. Ratajczykowa, I., Surf.Sci., 48, 549, 1975.

43. Aldag, A.W. and Schmidt, L.D., J.Catal., 22, 260, 1971.

44. Wicke, E. and Nernst, G.H., Ber.Bunsenges, Phys.Chem., 68 224, 1964.

45. Louie, S.G., Phys.Rev.Lett., 42, 476, 1979.

46. Katovic, V. and McCartey, Inorg.Chem., 17, 1268, 1978.

47. Jayasooriya, U.A., Chesters, M.A., Howard, M.W., Kettle, S.F.A., Powell, D.B. and Sheppard, N., Surf.Sci., 93, 526, 1980.

48. Slater, J.C., J.Chem.Phys., 41, 3199, 1964.

49. Lang, B., Joyner, R.W. and Somorjai, G.A., Surf.Sci., 30, 454, 1972.

50. Christmann, K. and Ertl, G., Surf.Sci., 60, 365, 1976.

51. Burch, R. in Chemical Physics of Solids and their Surfaces, Vol.8, Specialist Periodical Report, The Royal Society of Chemistry, London, 1980.

52. Bredov, M.M., Kotov, B.A., Okuneva, N.M., Oskotskii, V.S. and Shakh-Budagov, A.L., Soviet Phys.-Solid State, 9, 214, 1967.

CHAPTER SIX

AN I.N.S. STUDY OF CYCLOPROPANE ADSORBED BY Co (II) and Mn (II) PARTIALLY ION-EXCHANGED A-TYPE ZEOLITES

6.1 Introduction

We present the vibrational spectra (*ca.* 1 to 850 cm^{-1}) obtained by INS of cyclopropane adsorption complexes in Co (II) and Mn (II) partially exchanged A-type zeolites.

These complexes are unusual in that they are stable organometallic complexes of cyclopropane. This contrasts with the stability of extra-zeolite transition-metal complexes of cyclopropane; attempts to synthesise these latter materials result in fracture of the cyclopropane ring, generally forming π-allyl ligands. The present work is an example of the use of zeolites, coupled with vacuum techniques, to study the complexes of a very weak Lewis base, C_3H_6, without interference from competing ligands from a solvent or the atmosphere.[20]

The following considerations provide the rationale for this work:

1. The X-ray crystal structure of these two zeolite adsorption complexes of C_3H_6 have been published by Seff *et al.*[20] However, on the basis of our INS spectra of these samples, we argue below that the two structures published by Seff should be somewhat modified (see Section 6.3).
2. The isomerisation of cyclopropane to propane is used as a test of the Brönsted acidity of zeolite catalysts.
3. Cyclopropane has attracted considerable theoretical interest. When described by the Walsh model[1,2] it has both Mobius and Hückel orbital systems.[3]

The IR and Raman spectra of gaseous, liquid and crystalline phases of cyclopropane have been extensively discussed in the literature.[4-15] The data are listed in Table 6.1. The high frequency limit of our INS data is 850 cm^{-1}; the ν_{14} mode of gas phase C_3H_6 occurs below this limit, at 739 cm^{-1} (Table 6.1). Two other internal modes of C_3H_6, ν_7 at 854 cm^{-1} and ν_{11} at 867 cm^{-1} (gas phase frequencies, Table 6.1) will also give some intensity in our INS spectra of adsorbed cyclopropane.

In the gas phase, cyclopropane has D_{3h} symmetry. Under this point group those modes transforming as A_2' (ν_4) or A_1'' (ν_5) are formally Raman and infrared inactive. On complexation within a zeolite, the cyclopropane adsorption complex generally adopts either C_{3v} or C_{2v} symmetry (see below). Under C_{3v}, the modes ν_4 and ν_5 remain optically inactive but they become active under C_{2v} (Table 6.2). Assignment of the frequencies of these modes is therefore important since their observation would help decide the geometry of the adsorption complex. The assignment of these modes for uncomplexed C_3H_6 was first achieved by Duncan and McKean[6] using two independent approaches which led to the same result. These were:

(1) examination of the contours of overtone and combination bands in the vapour phase under high resolution and,

(2) the i.r. spectra of crystalline films at 78K - modes of all symmetry species are active in the crystalline phase. The vibrational spectrum of the solid state is consistent with a C_{2v} factor group, a C_s site and two molecules per orthorhombic unit cell.[12]

Normal coordinate analyses of cyclopropane carried out after reliable assignments of all the fundamental modes had been made, have been published by Levin and Pearce,[14] Duncan

TABLE 6.1 The frequencies of the fundamental modes of vibration of cyclopropane-h_6 as reported in the literature

Symmetry species (D_{3h})	Activity (D_{3h})	Mode number (after ref.14)	Gas phase ν/cm^{-1}	Liquid Raman 203K ν/cm^{-1}	Crystal 80K ν/cm^{-1}	
			ref.14	ref.10	ref.12	reference
						comments
A_1'	R	ν_1	3038.0	3010	3011.7, 3007.6	u.c.s.
		ν_2	1479.0	1453	1458.0, 1446.8	u.c.s.
		ν_3	1188.0	1189	1185.0, 1183.2	u.c.s.
A_2'	inact	ν_4	1070.0	n.o.	-	
A_1''	inact	ν_5	1126.0	n.o.	1129.8, 1123.2	u.c.s.
A_2''	i.r.	ν_6	3101.7	n.o.	-	
		ν_7	854.0	n.o.	856.4, 849.4	u.c.s.
E'	R+i.r.	ν_8	3024.4	3028	3028, 3022	-
		ν_9	1437.7	1435	{1435.4, 1433.9} {1432.5, 1421.6}	s.g.s.& u.c.s.
		ν_{10}	1028.4	1025	{1029.8, 1026.0} {1023.1, 1020.4}	s.g.s.& u.c.s.
		ν_{11}	868.5	867	{869.0, 867.2 864.2, 862.5 860.8}	s.g.s. & u.c.s.
E''	R	ν_{12}	3082.0	3077	{3071.5, 3070 3062.5}	s.g.s.& u.c.s.
		ν_{13}	1188.0	1179	{1202.2, 1197.6 1189.4}	s.g.s.& u.c.s.
		ν_{14}	739.0	742	747.7, 741.7	s.g.s.

inact = inactive; i.r. infrared active; R = Raman active, all under D_{3h} selection rules.

n.o. = not observed; s.g.s. = site group splitting;

u.c.s. = unit cell splitting

TABLE 6.2

(a) Correlation of the D_{3h}, C_{3v} and C_{2v} point groups from ref.16

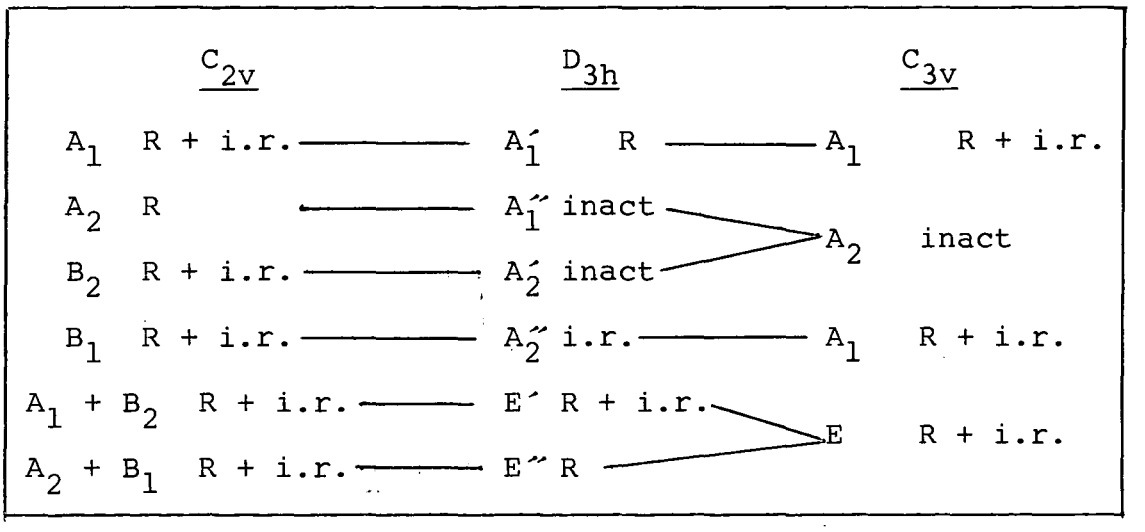

R = Raman active

i.r. = infrared active

inact = inactive

(b) Symmetries of the normal modes of cyclopropane under various point groups

(1) gas phase: $\Gamma^{D_{3h}}_{vib} = 3A_1 + A_2' + 4E' + A_1'' + 2A_2'' + 3E''$

(a) face bonded adsorption complex: $\Gamma^{C_{3v}}_{vib} = 5A_1 + 2A_2 + 7E$

(e) edge bonded adsorption complex $\Gamma^{C_{2v}}_{vib} = 7A_1 + 4A_2 + 5B_1 + 5B_2$

and Burns,[7] and Kirokawa *et al.*[15] In the following discussion we will use the numbering scheme of Levin and Pearce to label the normal modes of vibration.

6.2 Experimental

Throughout this chapter, we will use M(II) to represent Co(II) or Mn(II). The number of adsorbed gas molecules per supercage will be denoted by the symbol θ.

Zeolites of approximate composition $Mn_{3.5}Na_5Al_{12}Si_{12}O_{48}$ and $Co_{4.0}Na_{4.0}Al_{12}Si_{12}O_{48}$ were produced by exchange of Linde 4A zeolite (supplied by B.D.H.) at room temperature in 0.1M solutions of $MnSO_4$ (B.D.H. AnalaR) and $Co(NO_3)_2$ (B.D.H. AnalaR) respectively. The volume of the solution was chosen such that it contained a 10% excess over the stoichiometric amount of M(II) ions calculated necessary to produce the required degree of ion-exchange. The exchange was stopped after one week and the zeolite washed with H_2O, dried (*ca.* 340K) and analysed for M(II) and Na(I) content. A second exchange in a 0.1M solution of $MnSO_4$ or $Co(NO_3)_2$ at room temperature for one week was carried out. Again the volume of exchange solution was such it contained a 10% excess over the amount of M(II) ions that would have been necessary under stoichiometric conditions for the additional degree of ion-exchange. The zeolite was then washed, dried and re-analysed. The precise compositions of the partially exchanged zeolites are given in Tables 6.3 and 6.4 and we will hereafter refer to them by CoNaA or MnNaA as appropriate.

The C_3H_6 (99.8%) was supplied by Matheson Ltd., U.S.A., and the C_3D_6 (98%D) by Merck, Sharp and Dohme, Canada. The

TABLE 6.3 Summary of experimental details for the INS spectra of the CoNaA/ cyclopropane adsorption complexes

spectrometer	IN4	IN4	DIDO bfd	DIDO bfd
zeolite composition	$Co_{4.0}Na_{4.0}Al_{11}Si_{13}O_{48}$		$Co_{4.1}Na_{3.8}Al_{13}Si_{12}O_{48}$	
gas	C_3H_6	C_3H_6	C_3H_6	C_3H_6
temperature of INS run/K	16	16	77	77
coverage/molecules per supercage (θ)	0.9	1.8	0.7	3.0
maximum pressure during adsorption/torr	23	23	340	450
residual overpressure of cyclopropane in sample can/torr	<0.1	1.5	2.1	0.2
% scattering from adsorbed gas	10	20	11	50
$\frac{\sigma_{inc}\ \text{adsorbed cyclopropane}}{\sigma_{inc}\ \text{zeolite}}$	16	30	11	52

TABLE 6.4 Summary of experimental details for the INS spectra of the MnNaA/ cyclopropane adsorption complexes

spectrometer	IN4	IN4	IN4	DIDO bfd	DIDO bfd
zeolite composition	$Mn_{3.6}Na_{4.8}Al_{12}Si_{12}O_{48}$	$Mn_{3.4}Na_{5.2}$	$Al_{12}Si_{12}O_{48}$	$Mn_{3.4}Na_{5.2}$	$Al_{12}Si_{12}O_{48}$
gas	C_3H_6	C_3D_6	C_3D_6	C_3H_6	C_3H_6
temperature of INS run/K	10	10	10	77	77
coverage/molecules per supercage (θ)	1.2	1.5	2.3	0.9	1.8
maximum pressure during adsorption (torr)	15	53	62	300	340
residual overpressure of cyclopropane in sample can/torr	0.2	<0.1	<0.1	4.6	1.1
% scattering from adsorbed gas	11	1.3	2.0	10	20
$\frac{\sigma_{inc}\ \text{adsorbed cyclopropane}}{\sigma_{inc}\ \text{zeolite}}$	59	1.8	2.8	42	84

adsorption and sample preparation techniques were as given in Chapter Four. The experimental details are summarised in Tables 6.3 and 6.4.

The t.o.f. spectra presented in this chapter were obtained on the IN4 spectrometer at the I.L.L., Grenoble. All of these data have been treated in the following way. The number of scattered neutron counts was corrected for detector efficiency and incident neutron flux using standard I.L.L. programs. From this may be produced a plot of corrected counts against neutron time-of-flight, t. The resultant plot is a curve sitting on a non-zero, flat baseline. On conversion of such a plot to $P(\alpha,\beta)$ against energy transfer, the flat baseline becomes a curve whose gradient increases rapidly at high energy transfers. This arises from the dependence of $P(\alpha,\beta)$ on t^4 (Chapter Two); the t.o.f. spectra refer to neutron energy loss processes and large energy transfers therefore imply high values of t. In order to obtain accurate values of the intensities of the bands in the $P(\alpha,\beta)$ plots, a computer program to subtract the flat baseline from the corrected number of neutron counts and then to recalculate $P(\alpha,\beta)$ has been written. The baseline of the $P(\alpha,\beta)$ graphs shown in this chapter is the line $P(\alpha,\beta) = C$, where C is a number close to zero compared with the maximum value of $P(\alpha,\beta)$ in each spectrum. The statistics of our results are such that the data points of some spectra show a spread about this line at high energy transfers. The effect of this baseline subtraction may be seen by comparing Figs. 6.1 (a) and (b).

Since there are more data points at high energy transfers than at low, the data points of the $P(\alpha,\beta)$ plots were grouped

Fig. 6.1a T.o.f. spectrum (16K) of dehydrated CoNaA zeolite, scattering angle 83.1^0.
Neither a flat base-line nor a background have been subtracted fom these data.

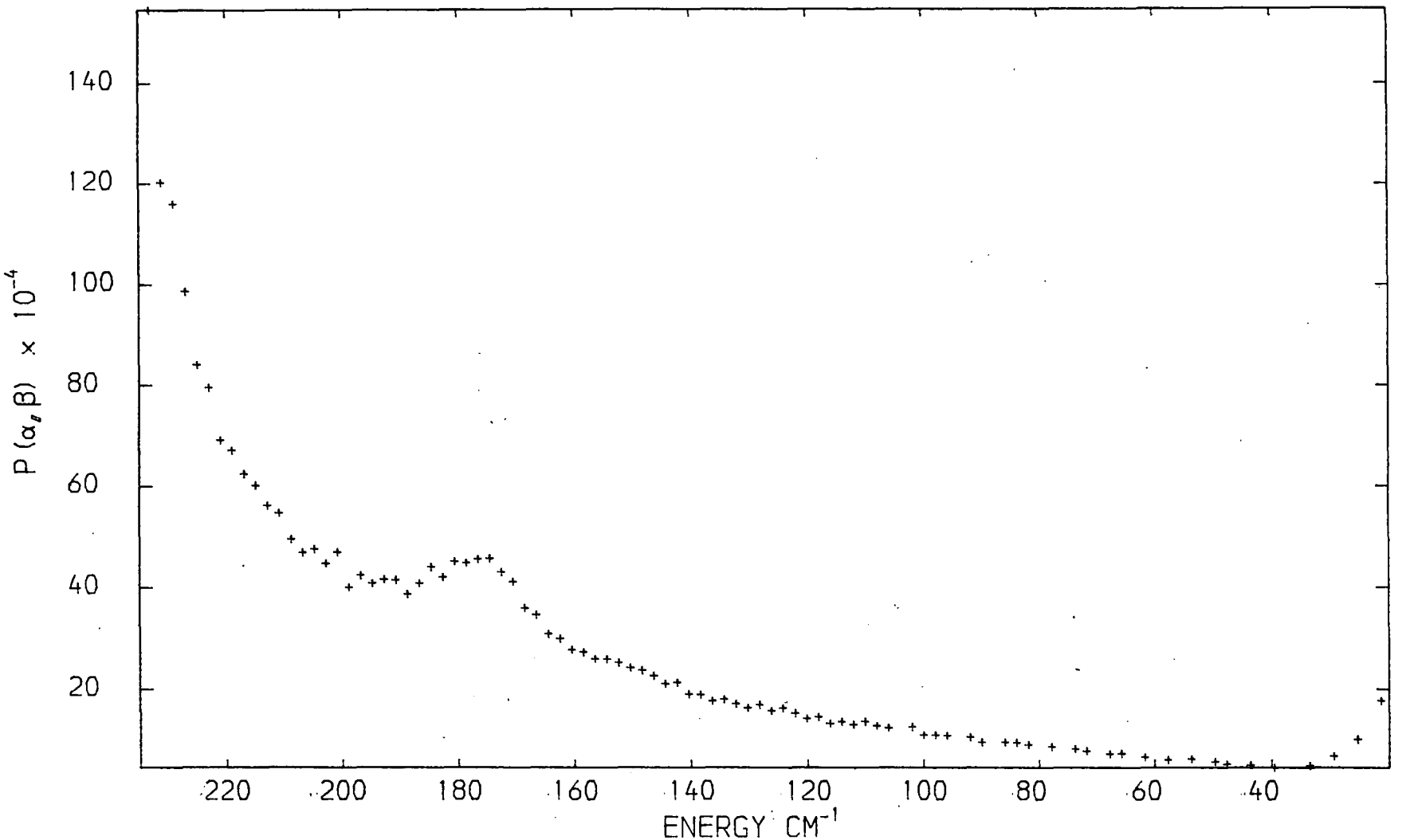

Fig 6.1b T.o.f. spectrum (16K) of dehydrated CoNaA zeolite after the subtraction of a flat baseline, scattering angle 83.1°.

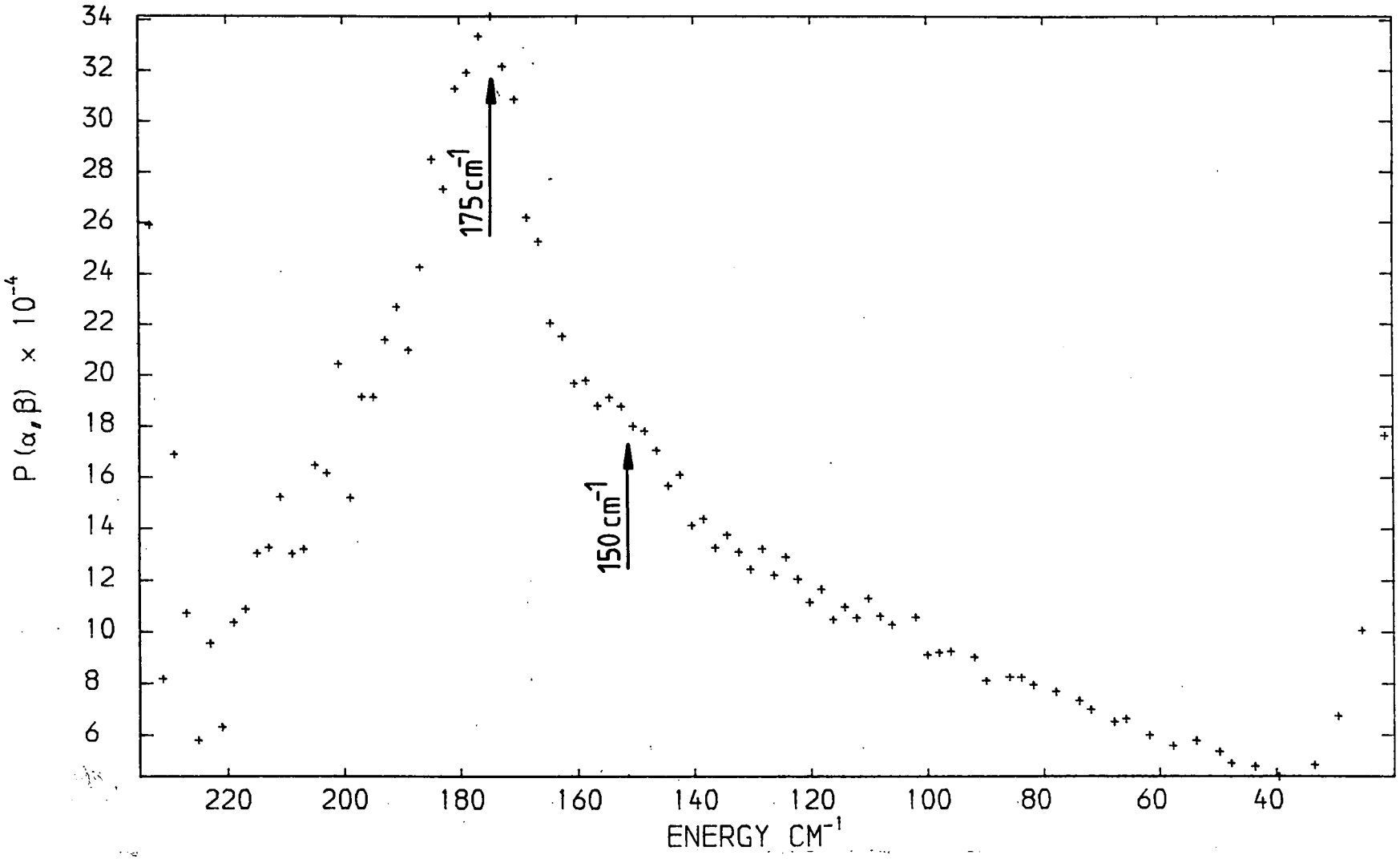

into equal energy (4 cm^{-1}) bins. The grouping of the data points was applied after the subtraction of the baseline and recalculation of $P(\alpha,\beta)$. Finally, a program was written to fit Gaussian curves to the $P(\alpha,\beta)$ spectra. This program was modified from one written at Newcastle Polytechnic which in turn used curve fitting routines developed by Pitha and Jones.[17] In the t.o.f. spectra presented in this chapter, the dashed lines represent the fitted Gaussian curves and the continuous line the sum of the Gaussians. The experimental points are shown by crosses. Because of the statistical spread in the data points of the t.o.f. spectra there is no unique fit to the data.

The b.f.d. spectra shown in this chapter were obtained on the DIDO b.f.d. spectrometer at A.E.R.E., Harwell.

6.3 The crystal structure of the cyclopropane adsorption complexes

Seff *et al*[18-20] have obtained the crystal structures of dehydrated Co_4Na_4-A, $Mn_{4.5}Na_3$-A and the cyclopropane adsorption complexes Co_4Na_4-A·$4C_3H_6$, $Mn_{4.5}Na_3$-A·$4C_3H_6$ by single crystal X-ray diffraction. The salient interatomic distances and angles are listed in Table 6.5. The CoNaA and MnNaA zeolites show small but significant differences between their common bond angles and lengths.[18-20] In both zeolites, each cation occupies a 6-oxygen ring position, lying on the three-fold axis of the ring (see Fig. 6.2). Those rings containing M(II) ions are tetrahedrally arranged about the α-cage while the Na^+ ions define a second tetrahedron, interleaved with the first (Fig. 6.2).

TABLE 6.5 Bond lengths and angles in Co_4Na_4-A and Mn_4Na_4-A zeolites and their sorption complexes. From refs. 18-20

zeolite	deviations from (III) plane at O(3), Å		M(II)-O(3) distance Å	M(II)-C distance Å	O(3)-M-O(3) angle, degrees	O(3)-M-C angle degrees
	M(II)	Na^+				
Co_4Na_4-A dehydrated	0.34	-0.56	2.077(18)	-	117.5(1)	-
Co_4Na_4-A·$4C_3H_6$	0.61	-0.09	2.174(7)	2.813(66)	112.5(4)	99(1)
Mn_4Na_4-A dehydrated	-0.11	0.46	2.11(1)	-	119.6(1)	-
Mn_4Na_4-A·$4C_3H_6$	0.45	-0.61	2.122(8)	3.088(65)	115.7(6)	96(1)

In columns 2 and 3, a positive deviation denotes that the cation lies within the α-cage, at an S2* site.

A negative deviation denotes an S2′ site, within the β-cage.

Fig. 6.2a A stereoview of the $Co_4Na_4A.4C_3H_6$ pseudo-unit cell, taken from ref. 20. Ellipsoids of 20% probability are used.

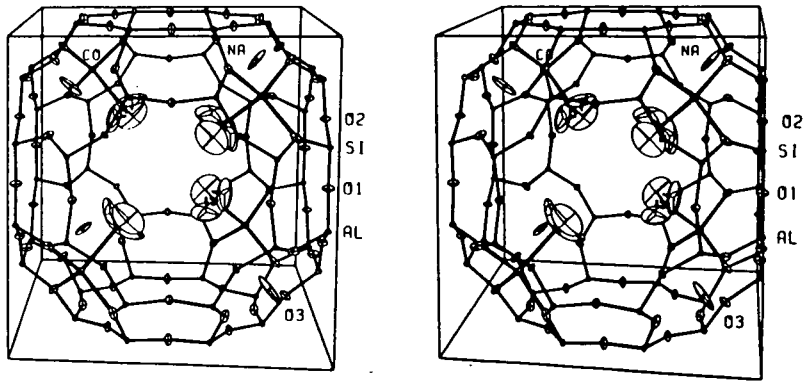

Fig. 6.2b A stereoview of the $Mn_4Na_4A.4C_3H_6$ pseudo-unit cell, taken from ref. 20. Ellipsoids of 20% probability are used.

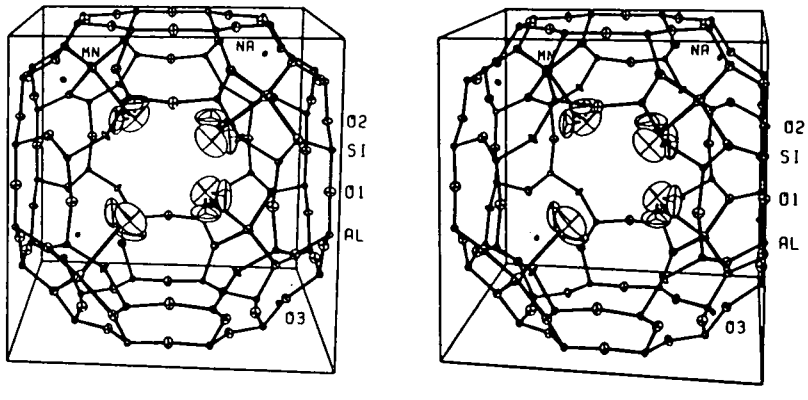

Fig. 6.3 Coordination environment of Co(II) ions in $Co_4Na_4A.4C_3H_6$ and Mn(II) ions in $Mn_4Na_4A.4C_3H_6$, after ref. 20. Ellipsoids of 10% probability are used.

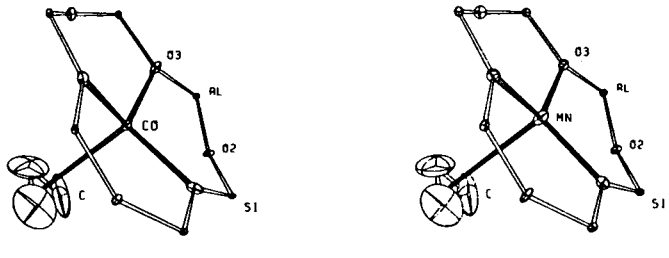

In dehydrated Co_4Na_4-A, the Co(II) ions occupy S2* sites while the Na^+ ions are located at S2' sites. This positioning of M(II) and Na^+ ions on opposite sides of the ring is reversed in $Mn_{4.5}Na_3$-A, the Mn(II) ions occupying S2' sites (Table 6.5). In these dehydrated zeolites, both the Mn(II) and Co(II) ions have nearly trigonal planar coordination with the O(3) atoms of the 6-oxygen rings.

On coordination to cyclopropane, both the Mn(II) and Co(II) ions advance into the α-cage but remain associated with the trigonally arranged O(3) atoms. The coordination geometry of the M(II) ions becomes approximately tetrahedral. Each cyclopropane molecule is bonded to one M(II) ion such that the three-fold axes of the 6-oxygen ring and the carbon ring coincide. According to Seff[20] the cyclopropane is face bonded to the M(II) cation, the M(II)-C_3H_6 complex adopting C_{3v} symmetry (see Fig. 6.3). We note, however, that the thermal ellipsoids for the C atoms are very large (the authors[20] have used ellipsoids of 10% probability in Fig. 6.3 rather than the more usual 50%).

In the complexes of both zeolites, the Na^+ ions are found in the sodalite cavity (Table 6.5) and so cannot coordinate to the cyclopropane.[20]

There are two unusual features of the structures of the cyclopropane sorption complexes published by Seff.[20]

1. The Mn-C and Co-C distances are long, 3.09 and 2.81Å respectively. Such distances are probably too long for any π-bonding between the metal ion and the ligand. In a Ni(II) complex of triphenylcyclopropene, where such π-bonding does operate between the Ni(II) cation and the face bonded C_3 ring, the distance between the

cation and the plane of the C_3 ring is very much shorter, 1.76Å.[20] However, we have assigned a band in the INS spectra of cyclopropane adsorbed by CoNaA and MnNaA to a hindered rotation about the C_3 symmetry axes of the M(II)-C_3H_6 complexes (Section 6.5). The barrier to the rotation, calculated from the frequency of this band, indicates that π-bonding between the cation and C_3H_6 ligand does occur and thereby suggests shorter M(II)-C_3H_6 bond lengths (see Section 6.7.1).

Furthermore, the published[20] Mn-C and Co-C distances both require extremely close intermolecular contacts between the H atoms of C_3H_6 molecules adsorbed within the same supercage. These contacts are so close (see below) as to imply severe deformation of the coadsorbed molecules, for which the X-ray[20] and our INS data (Section 6.5) provide no evidence. We have calculated the distance between the H atoms of two coadsorbed C_3H_6 ligands, assuming that the geometry of the adsorbed C_3H_6 molecule is identical to that in the gas phase. We have also taken the distance from the plane defined by the O(3) atoms bonded to the M(II) cation to the centre of the supercage to be 0.5 x 12.146Å in both zeolites. (From the X-ray results,[20] the pseudo-unit-cell constants for MnNaA·4C_3H_6 and CoNaA·4C_3H_6 are 12.146(4)Å and 12.147(2)Å respectively).

The intermolecular H---H distance is shortest when the two C_3H_6 rings adopt an eclipsed configuration; for CoNaA we calculate this distance to be 1.40Å and for MnNaA, 1.18Å. If the C_3H_6 molecules are staggered by 60°, the H---H separation is maximised; for CoNaA this H---H distance becomes 2.16Å and for MnNaA, 2.00Å. These distances are shorter than twice the van der Waals radius, r_{vw}, of hydrogen (1.2[21] to 1.45[22] Å), which is further evidence that the M(II)-C distances reported

by Seff[20] are too long. Let us consider that the M(II)-C length may be shortened until the intermolecular H---H distance exceeds $2r_{vw}$ but without changing any other aspects of the geometry of the two coadsorbed C_3H_6 ligands. Then taking r_{vw}=1.2Å and assuming the C_3H_6 molecules can adopt an eclipsed configuration, we obtain a maximum possible value for the M(II)-C distance, which for CoNaA is 2.2Å and 2.4Å for MnNaA.

In evaluating the maximum M(II)-C bond length we have held constant the distance between the M(II) cation and the plane of the O(3) atoms to which the cation is bonded. The X-ray values[20] of 0.61Å (M=Co) and 0.45Å (M=Mn) were used for this distance. At these maximum values of the M(II)-C bond length, the distance between the planes of the C atoms of the adsorbed C_3H_6 molecules is the same in both the MnNaA and CoNaA zeolite systems. This is important in the calculation of the non-bonded interaction between coadsorbed C_3H_6 molecules, discussed in Section 6.6.2.

It is conceivable that the $\hat{HCH}$ bond angle of adsorbed C_3H_6 may be different from the gas-phase value. Any variation in this bond angle would depend on the M(II)-C bond length and possibly involve rehybridisation at the carbon atoms. Thus we cannot estimate the possible deformation of the bond angles of adsorbed C_3H_6 since there are too many undefined parameters.

In summary, geometrical considerations support the conclusion following from the observation of a τ_z mode in our INS spectra of adsorbed cyclopropane (Section 6.5, 6.6.2) that the published[20] M(II)-C distances are too long.

2. The second unusual feature is the apparent shortening of the intramolecular C-C distance in C_3H_6 from the gas phase value of 1.51Å to 1.1Å on complexation. This, however, was considered by Seff *et al*[20] to be an artifact of the large, anisotropic thermal parameters for carbon. Accordingly, the authors held that their data did not show that the C-C bonds had been shortened on adsorption.

Smaller thermal parameters for the C atoms of the cyclopropane ring could not be given because of problems with the observed X-ray data and its analysis, which we now summarise.

(1) The number of statistical significant reflections used in the structure refinement was low, 373 from a total number of 854 for the Co_4Na_4-A complex and 331 from a total of 852 for the Mn_4Na_4-A complex. The final R values for the published structures of Co_4Na_4-A·$4C_3H_6$ and Mn_4Na_4-A·C_3H_6 were 0.062 and 0.077 respectively.

(2) No X-ray absorption corrections were applied to the data.

(3) The positions of the C atoms could not be accurately determined - ellipsoids of 10% probability (instead of the more usual 50% probability) were used for carbon in the published diagrams of the crystal structure (e.g. Fig.6.2). The standard deviations listed for the C thermal parameters are large; for the Mn_4Na_4·A-$4C_3H_6$ complex they range from 20% to 254%, and for Co_4Na_4·$4C_3H_6$ from 19% to 45%. Indeed, the initial data refinement suggested that there were 24 carbon atoms in each CoNaA supercage (23 for MnNaA), corresponding to eight C_3H_6 molecules. Since this is unreasonable on steric grounds, the subsequent refinements were based on the assumption that each supercage was occupied by four C_3H_6 molecules.

(4) According to Seff,[20] the Na-O(3) and M(II)-O(3) distances reported for the M(II)NaA-C_3H_6 systems may be respectively too short and too long. The reported values refer to averaged positions of the atoms in two types of 6-oxygen rings, *i.e.* those rings associated with Na^+ ions and those with M(II) ions.[20] The resulting errors were not quantified, but they apparently do not affect the positions of the M(II) ions, nor, therefore, the intermolecular contacts we have calculated for coadsorbed C_3H_6 molecules.

To summarise, the published X-ray single crystal diffraction data[20] of Mn_4Na_4-A·$4C_3H_6$ and Co_4Na_4-A·C_3H_6 do not, in our opinion, incontrovertibly define some of the detailed aspects of the geometry of the cyclopropane adsorption complexes. Although our INS data, discussed below, are consistent with Seff's proposal[20] of face bonding of the C_3H_6 molecule to the M(II) cation, the INS results suggest shorter M(II)-C_3H_6 distances than those deduced from the X-ray work (Sections 6.5, 6.6). The discrepancy between the INS and X-ray results is in large part due to the modest statistical quality of the X-ray data and the resulting difficulties with the structure refinement. Despite such problems, however, the value of crystallographic data on adsorbed species cannot be overestimated. Although in this respect zeolites present a number of difficulties, the pioneering work of the group led by Professor Seff has yielded results of considerable interest and relevance. It does appear, however, that in some cases the interpretation of the X-ray data is not unambiguous and this has led to some inaccuracies in the published results.

6.4 Published studies of adsorbed cyclopropane

6.4.1 Spectroscopic

(a) Tam *et al*[23] have reported Raman spectra of cyclopropane adsorbed on alkali metal exchanged zeolites X (see Table 6.6) The splitting of an E′ mode (ν_{11}, a C-C sketal stretch[14] of C_3H_6 on adsorption on LiX and NaX was cited as evidence for a lowering of the adsorbate symmetry from D_{3h} (gas phase) to C_{2v}. This was indicative of an edge-on, in-plane interaction with the cation, rather than of a face bonded adsorption complex (symmetry C_{3v}).

No splitting of the ν_{11} mode was observed in the case of C_3H_6 on KX and CsX zeolites. However, the edge bonding model was still preferred on the basis of the cation dependence of the frequency of the ν_3 mode. This is an in-plane breathing mode of the C_3 ring and thus will be more sensitive to in-plane cation interactions than to interactions perpendicular to the ring. But since the reason for proposing an edge bonded complex in Li13X and Na13X was the splitting of the ν_{11} mode, and the shifts of the ν_3 frequency are small, we hold that the Raman data do not incontrovertibly distinguish between the C_{3v} and C_{2v} adsorption complexes in KX and CsX zeolites.

Moreover, we note that for a complex of C_{2v} symmetry the ν_4 (CH_2 wag, B_2 under C_{2v}) and ν_5 (CH_2 twist, A_2) modes become Raman active (see Table 6.2). They remain Raman inactive for a C_{3v} complex. In the gas phase they have symmetry A_2' (ν_4) and A_1'' (ν_5) and have been located at 1070 and 1126 cm^{-1}.[6] No extra Raman bands were reported on the adsorption of cyclopropane between 867 (LiX) and 1184 cm^{-1} (CsX), assigned to ν_{11} and ν_3 respectively. Although the ν_{11} mode (E′ under D_{3h}) is Raman active for a C_{3v} complex it remains degenerate.

TABLE 6.6 Selected bands observed in the Raman spectra ($\Delta\nu$, cm^{-1}) of cyclopropane adsorbed on CsX, KX, NaX and LiX zeolites. Data taken from ref. 23.

Assignment D_{3h} point group	liquid	CCl_4 solution	CsX	KX	NaX	LiX	assignment C_{2v} point group
$\nu_{11}E'$ ring deformation	867	867s	860s	852s	866s 852sg	867s 848sh	A_1 B_2
ν_3A_1' ring breathing	1189	1187vs	1184vs	1184vs	1185vs	1187vs	A_1

s = strong, sh = shoulder, vs = very strong

Thus the Raman spectrum of an edge bonded complex (C_{2v}) should show a splitting of the ν_{11} mode (at *ca.* 869 cm^{-1}) and two additional bands due to ν_4 (at *ca.* 1070 cm^{-1}) and ν_5 (at *ca.* 1126 cm^{-1}). A face bonded complex (C_{3v}) gives rise to no new Raman bands and no splitting of the ν_{11} mode. Therefore the results for cyclopropane adsorbed on CsX and KX are consistent with a sorption complex of symmetry C_{3v} but not C_{2v} as proposed by Tam *et al.*[23] For LiX and NaX the data are not fully consistent with either adsorption geometry. Adsorption at two different cation sites might explain the apparent splitting of the ν_{11} mode but in this case one would expect to observe splitting of other modes, and this was not observed.

The strength of the adsorption interaction, measured by the shift of the ν_3 frequency and the splitting of ν_{11}, increased with the polarising power of the cation. This suggested[23] that the bonding was principally due to a cation-induced dipole interaction. We argue later (Section 6.7) that the availability of d-electron density on the cation leads to π-bonding with the cyclopropane ring and a face bonded (C_{3v}) adsorption complex in preference to an edge bonded complex.

(b) Infrared studies

The IR spectra of C_3H_6 adsorbed by $Co_{5.5}Na_{1.0}Al_{12}Si_{12}O_{48}$ and $Mn_{5.5}Na_{1.0}Al_{12}Si_{12}O_{48}$ type-A zeolites have been reported [24] and are shown in Figures 6.4 and 6.5.

On adsorption of C_3H_6 in CoNaA, two additional IR bands were seen,[24] at 1430 and 1456 cm^{-1} (Fig. 6.4). The 1430 cm^{-1} band was assigned[24] to the ν_9 scissors mode which is IR active

Fig. 6.4 Infrared spectra of: a. CoNaA zeolite at 293K <u>in vacuo</u> after vacuum dehydration at 593K; b. dehydrated CoNaA + C_3H_6 at 293K; c. C_3H_6 gas. Taken from ref.24.

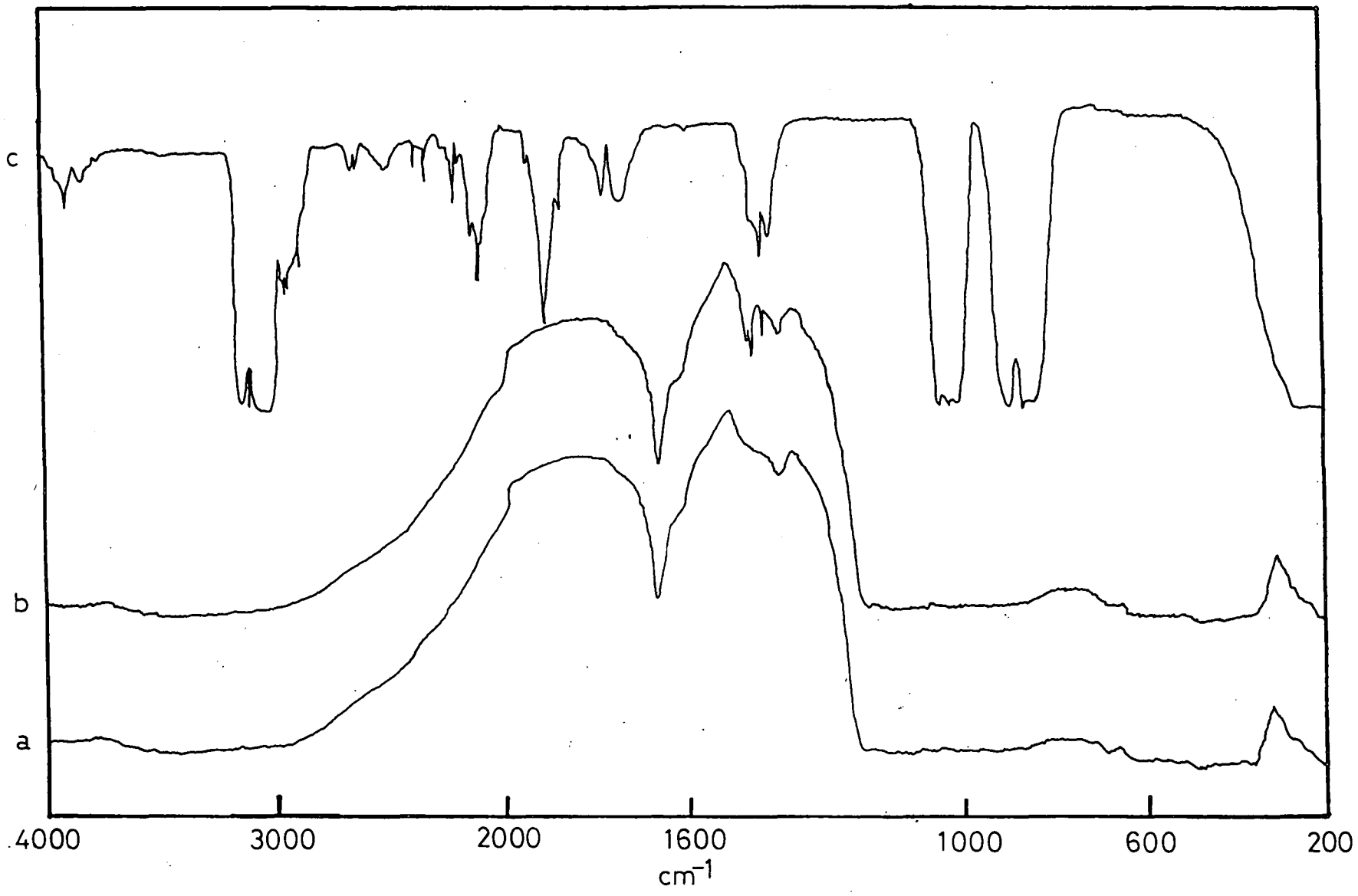

Fig. 6.5 Infrared spectra of: a. MnNaA zeolite in vacuo at 293K after vacuum dehydration at 593K; b. dehydrated MnNaA zeolite at 293K; c. C_3H_6 gas. Taken from ref. 24.

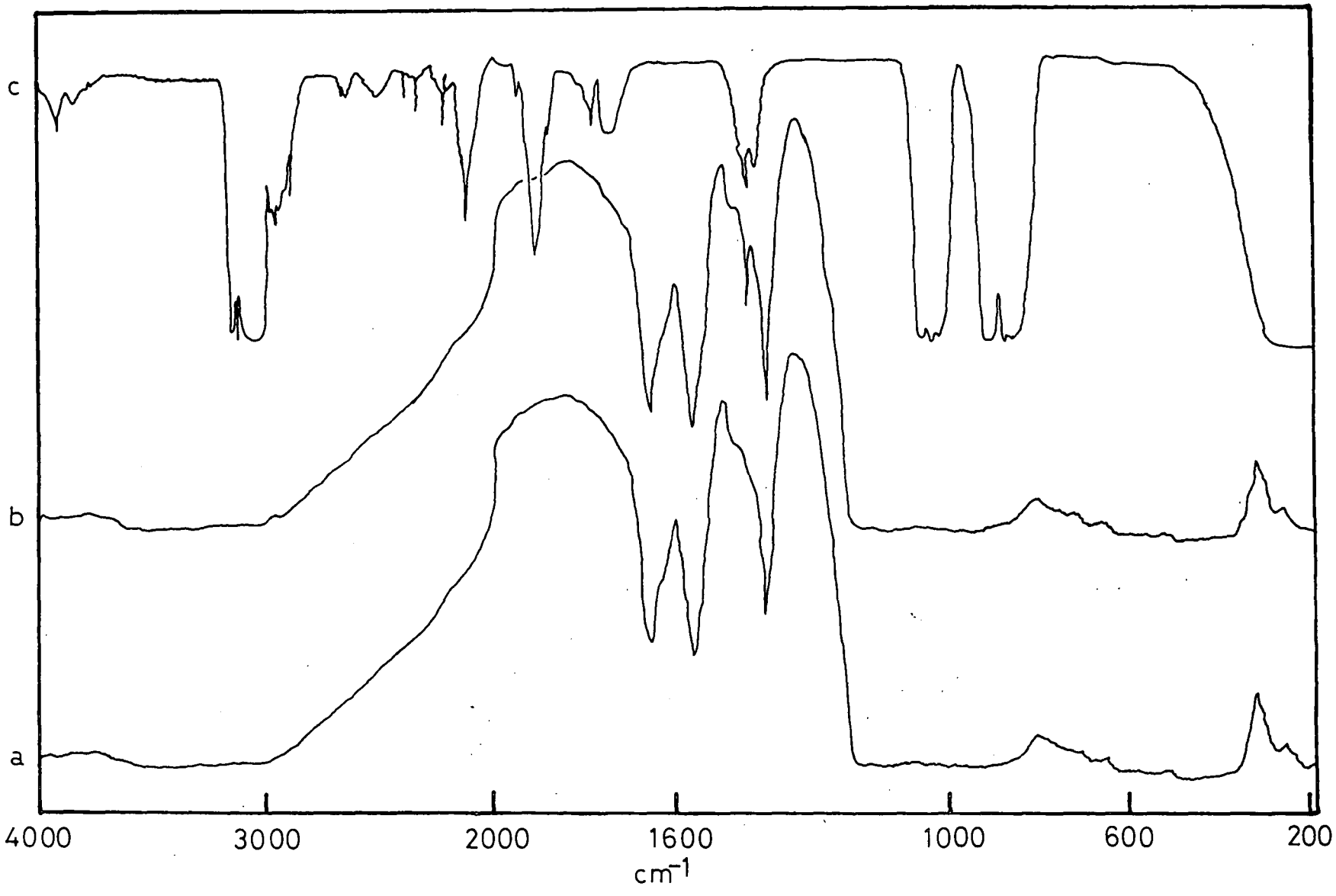

for the D_{3h}, C_{3v} and C_{2v} point groups, transforming as E', E and $A_1 + B_2$ respectively (Table 6.2). The shift from the gas phase frequency of 1438 cm^{-1} indicated that the transitions of adsorbed, rather than gas phase, C_3H_6 were observed. The 1456 cm^{-1} band in the CoNaA + C_3H_6 IR spectrum (Figure 6.4) was assigned to the first overtone of ν_{14}. The ν_{14} fundamental occurs at 739 cm^{-1} in the gas phase.[14] We propose here an alternative assignment of the 1456 cm^{-1} band. Under the point group D_{3h}, the overtone $2\nu_{14}$ transforms as $A_1' + E'$. Fermi resonance of the A_1' component of $2\nu_{14}$ (2 x 739 = 1478 cm^{-1}) with ν_2 (1479 cm^{-1}, A_1') has been observed[9] in the Raman spectrum of gas phase C_3H_6, giving rise to two strong Q-branches at 1455 and 1507 cm^{-1}, superimposed on the S-branch of the ν_9 band. The $2\nu_{14}$ mode is IR active through the E' component (Table 6.2) and has been assigned by Baker and Lord[57] to a very weak feature at 1480 cm^{-1} in the IR spectrum of gas phase C_3H_6. Therefore, two possible assignments of the 1456 cm^{-1} band in the IR spectrum[24] of CoNaA + C_3H_6 (Figure 6.4) are to either $2\nu_{14}$ or to the lower frequency component of the $2\nu_{14}/\nu_2$ Fermi diad. Because the observed band was intense (Figure 6.4), we prefer the second assignment. The higher frequency transition of the Fermi doublet, expected at *ca* 1507 cm^{-1}, was not observed[24] in the CoNaA + C_3H_6 IR spectrum; it was possibly unresolved from the low frequency edge of the strong, broad zeolite absorbance centred at 1610 cm^{-1} (Figure 6.4).

The observation[24] of the two IR bands at 1430 and 1456 cm^{-1} due to C_3H_6 adsorbed by CoNaA is consistent with both C_{3v} and C_{2v} symmetry of the sorption complex.

The MnNaA + C_3H_6 IR spectrum (Figure 6.5) showed[24] only one band, at 1435 cm^{-1}, ascribable to adsorbed C_3H_6. It was

assigned[24] to the ν_9 scissors mode. The "$2\nu_{14}$" band was not observed and was said[24] to be masked by the structured spectrum of the MnNaA zeolite. Again the IR data for the MnNaA + C_3H_6 system are consistent with an adsorption geometry of either C_{3v} or C_{2v}.

In conclusion, we note that IR spectroscopy can only distinguish between C_3H_6 adsorption complexes of C_{3v} or C_{2v} symmetry by the observation of an A_2' (D_{3h}) mode (Table 6.2). Only the CH_2 wag, ν_4, has this symmetry; it has been assigned at 1070 cm^{-1} in the gas phase.[14] Unfortunately, this region of the IR spectrum is masked by strong zeolite absorbances for both CoNaA and MnNaA and no changes at *ca* 1070 cm^{-1} were observed[24] on the adsorption of C_3H_6.

(c) An I.R. study of C_3H_6 adsorbed in $NiNa_{10}A$ zeolite

An early I.R. study[25] of C_3H_6 adsorbed in $NiNa_{10}$-A zeolite (at 293K, 760 torr) showed that the C_3H_6 was reversibly, but exclusively, held by Ni^{++} ions, which were all located in six-oxygen rings. The Ni^{++} ions adopted a tetrahedral coordination with three oxygens of the six-ring and the adsorbate molecule, as found by Seff[20] for Co_4Na_4-A/C_3H_6 and $Mn_{4.5}Na_3$-A/C_3H_6 complexes. The coordination geometry of the C_3H_6 ring could not be established from these high frequency data.[25]

6.4.2 N.m.r. studies of adsorbed cyclopropane

Turkevitch *et al*[26] have studied cyclopropane adsorption in Na13Y zeolite by ^{13}C and ^{1}H n.m.r. The equivalence of the protons implied a completely symmetric adsorbed state and the narrow line width indicated surface mobility of the cyclopropane molecules. Since the observed chemical shift was independent of coverage and temperature, it was not due to a dynamic equilibrium between strongly adsorbed, localised species and mobile physisorbed molecules. Thus in Na13Y cyclopropane is physisorbed and forms a mobile phase whereas the Raman data for Na13X[23] indicates a stronger, localised adsorption at Na^+ sites. The difference between the two zeolites may be related to the stronger electric fields within the 13X cavities.

An ^{1}H and ^{13}C n.m.r. study at 301 to 303K by Naccache *et al*[27] of cyclopropane adsorbed on HY zeolite, PtY zeolite and Pt/SiO_2 has shown that the adsorbed C_3H_6 was held parallel to the adsorbent surface and retained the gas phase symmetry of D_{3h}. To explain the different signs of the chemical

shift on adsorption of the ^{1}H and ^{13}C, it was postulated that each C-C bond lengthened while the molecule's π-electron system remained fixed.[27] However, the basis of this ring expansion model has been questioned.[26] The n.m.r. results of Naccache *et al*[27] are also in disagreement with those of a published IR/mass spectroscopy study.[28] The latter technique indicated isomerisation of C_3H_6 on adsorption on HY zeolite at room temperature (Section 6.4.3).

6.4.3 Isomerisation studies

At temperatures above 473K, cyclopropane is isomerised to propene in zeolites Na13X, Na13Y and H13Y.[29,30] The reaction is catalysed by Brönsted acid sites, is first order in *c*-C_3H_6 and proceeds via a non-classical protonated cyclopropane ion[30]:

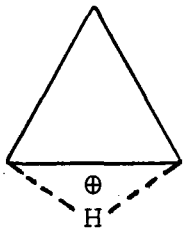

The activation energy in Na13X is 125kJ mol^{-1} which compares with 270kJ mol^{-1} for the homogeneous gas phase reaction.[29]

At room temperature, an IR/mass spectroscopy study[28] showed that the major product of *c*-C_3H_6 adsorption in HY zeolite was 2-methylpropane, possibly formed via a non classical methylated cyclopropane cation. The Raman and n.m.r. studies[28] discussed above have shown that the cyclopropane molecule remains intact when adsorbed on Na13X and Na13Y, respectively, at room temperature.

6.5 Results

6.5.1 Introduction

The lowest frequency internal vibration of cyclopropane-h_6 in the gas phase occurs at 739 cm^{-1} (ν_{14}, principally a CH_2 twisting mode) and at 526 cm^{-1} in cyclopropane-d_6. From published INS results,[31] we expect the maximum shifts of the low frequency internal modes of a small organic molecule on complexation with the M(II) ions to be at most a few tens of wavenumbers.

The present INS data for adsorbed cyclopropane are totally dissimilar from the optical spectra of solid cyclopropane.[10,12] There are no bands observed in the vibrational spectrum of solid C_3H_6 between those due to ν_{14} (which shows[12] a site splitting of 3 cm^{-1} in the Raman at 77K, see Table 6.1), and the lattice modes which occur at 132, 118, 109, 100 and 92 cm^{-1} in the Raman, along with possible, weak IR bands at 60 and 52 cm^{-1}.[10,12] We have no evidence for a non-uniform distribution of adsorbed cyclopropane in our samples, nor do our INS spectra (Figs.6.9, 6.11-6.18 below) show any correspondence with the spectrum of solid C_3H_6. We therefore discount the possibility that we have observed any modes of solid cyclopropane.

The INS bands observed below *ca.* 742 cm^{-1} will have arisen from either hindered translations and hindered rotations of the adsorbed molecule with respect to the zeolite framework, or from amplified zeolite modes. We will refer to the hindered translations and rotations as the external modes of the adsorbate.

There is a concentration of electron density in the C_3H_6 molecule at the centre of the carbon ring and at a point midway along each C-C bond, displaced outside the ring, 0.32Å from the C-C axis[1,32] (Section 6.7). On the basis of this electron distribution, the two most likely geometries of the M(II)-C_3H_6 complex are thus:

1. face bonding of the C_3H_6 ring to the M(II) ion, giving a complex of C_{3v} symmetry, as predicted by the X-ray diffraction results of Seff[20] (Figs. 6.2, 6.3);
2. edge bonding of the C_3H_6 ring to the M(II) ion, giving a complex of C_{2v} symmetry.

In view of the difficulties associated with the X-ray diffraction experiment,[20] (see Section 6.3), we now consider how the INS spectra of the two possible adsorption geometries would differ.

The external modes of a C_{3v} complex are drawn in Fig.6.6 and will give rise to 4 INS bands, the torsions and translations parallel to the surface both being doubly degenerate. In contrast an edge bonded complex of C_{2v} symmetry would give 6 INS bands due to the external modes, which are shown in Fig.6.7.

As shown in Chapter Two, the relative intensity I^P of the fundamentals of the hindered rotations and torsions in the INS spectrum of a powder sample is given in the harmonic approximation by:

$$I^P \propto \sum_i \sigma_{inc}^i \frac{Z(\tilde{\nu})}{\mu_i} \exp[-2W] \qquad (6.1)$$

where:
the sum over i is, in principle, carried out for each isotope i (see below);

Fig 6.6 External modes of a face-bonded intrazeolitic cyclopropane complex of C_{3v} symmetry.

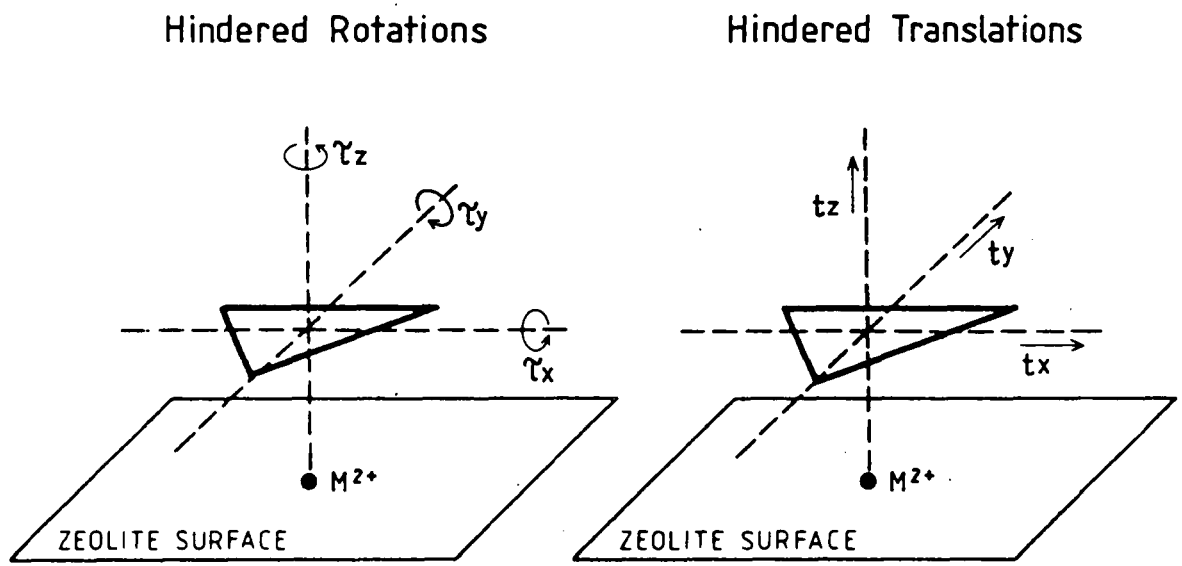

τz = C_3 torsion
$\tau x, \tau y$ = tilt

tz = symmetric stretch
tx, ty = rock

Fig. 6.7 The external modes of an edge-bonded intrazeolitic cyclopropane complex of C_{2v} symmetry.

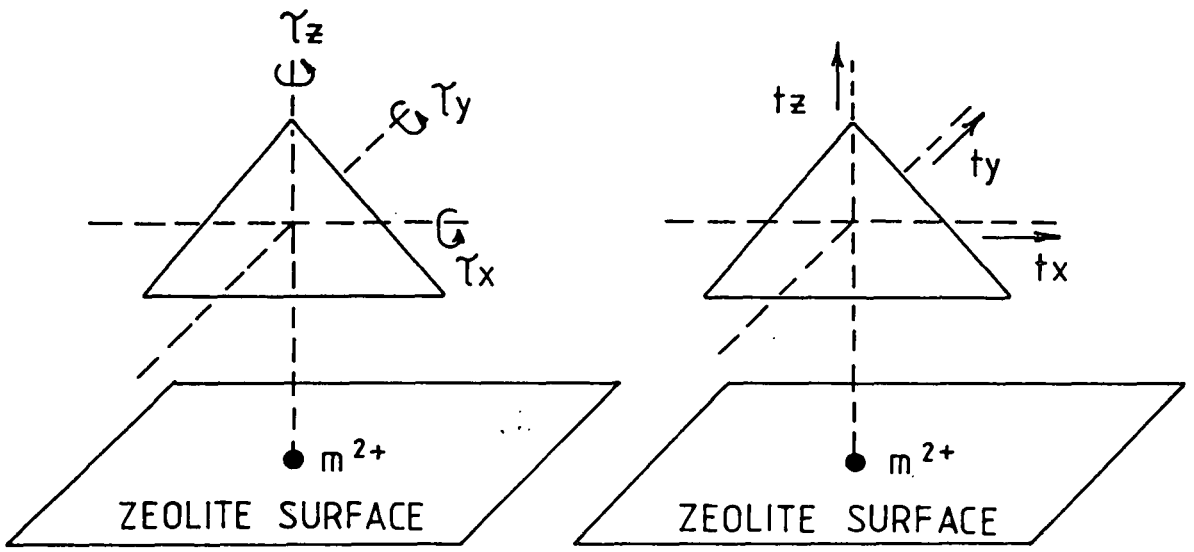

$\tau z = C_2$ torsion

$\tau x =$ flap

$\tau y =$ antisymmetric stretch

tz = symmetric stretch

tx = rock

ty = wag

σ_{inc}^{i} is the incoherent inelastic neutron scattering cross section of the nucleus of type i;

$Z(\tilde{\nu})$ is the vibrational density of states;

$\tilde{\nu}$ is the frequency of the mode in cm^{-1};

exp[-2W] is the Debye Waller factor, discussed below and

μ_i is the effective mass of the oscillator, given by

translational modes: $\mu_i = n_i/M$ (6.2)

torsional modes: $\mu_i = \sum_j r_j^2/I_R$ (6.3)

where M is the mass of the scattering entity;

n_i is the number of nuclei of isotope i displaced in the mode;

I_R is the moment of inertia of the scattering entity about the relevant rotation axis;

and r_j is the radius of gyration of the j^{th} nucleus of isotope i, the sum over j (equation 6.3) being over all j nuclei displaced during the mode.

Since σ_{inc} of ^{12}C is zero, the sums over i in equations 6.1 to 6.3 are carried out for only the ^{1}H atoms of the C_3H_6 adsorbate and for D of C_3D_6.

In equation 6.1 the superscript P in the I^P term is used to emphasise that the intensity is measured in terms of $P(\alpha,\beta)$.

If we make the approximations that the Debye Waller factor (DWF), exp [-2W] in equation 6.1, is isotropic and energy independent, we may write:[33]

$$-2W = Q^2\langle U_i^2\rangle$$

where $\hbar Q$ is the momentum transfer during the scattering event and $\langle U_i^2 \rangle$ is the total mean square displacement of the i^{th} nucleus. The value of $\langle U_i^2 \rangle$ is isotropic and equal to the sum of the mean square amplitudes of vibration over all modes involving the nucleus i. Both the internal and external modes of the molecule may contribute to the sum.[33]

More generally, the DWF is mode dependent and has a different value for each INS band. The $\langle U_i^2 \rangle$ becomes a function of frequency $\tilde{\nu}$. Although the mean square amplitudes of all modes of vibration of the nucleus i are summed to find the value of $\langle U_i^2(\tilde{\nu}) \rangle$, those modes occurring at a given frequency $\tilde{\nu}$ are effectively weighted more strongly in the summation.[33] Thus $\langle U_i^2(\tilde{\nu}) \rangle$ is, in general, anisotropic in the case of a mode dependent DWF.

The energy dependence of the DWF can be tested by plotting the observed intensity, I^P_{OBS}, of a given band as $\ln I^P_{OBS}$ against Q^2 for the spectra obtained at different scattering angles. A straight line of gradient $-\langle U_i^2(\tilde{\nu}) \rangle$ will be obtained for a given band provided the intensity arises solely from a fundamental mode (or degenerate fundamentals) and there is no contribution from overtones or combinations. If the DWF is mode independent the measured values of $\langle U_i^2(\tilde{\nu}) \rangle$ will be constant. They will differ if the DWF is mode dependent. We present and discuss the plots for each sample in Sections 6.5.4 and 6.5.9 below. In Section 6.5.11 we discuss the magnitude of the values of $\langle U_i^2(\tilde{\nu}) \rangle$ estimated from our INS spectra for the H atoms of adsorbed C_3H_6.

Only the $Z(\tilde{\nu})/\mu$ term in equation 6.1 depends upon our choice of the assumed geometry of the adsorption complex. In

Table 6.7 we list the values of this term for the external modes of cyclopropane-M(II) complexes of C_{2v} and C_{3v} symmetry - these values are relative and the smallest numerical value of $Z(\tilde{\nu})/\mu$ for each adsorption geometry has been set equal to unity. By comparing the observed intensities with those calculated using equation 6.1 for the bands in an INS spectrum we can check for the self-consistency of the assignment of those bands.

Also included in Table 6.7 are the deuteration shifts ($\tilde{\nu}_D/\tilde{\nu}_H$) of these modes, calculated within the harmonic approximation. The deuteration shifts are quoted to three significant figures to illustrate the small differences between the predicted values. This is one significant figure more than is warranted by the probable 2% error in the values of the band centres by the IN4 spectrometer.

That the cyclopropane ring remains intact and does not isomerise to propene or form 2-methylpropane on adsorption is shown by the non-observation of methyl torsion modes. These torsions would give rise to very intense INS bands in the region 100-400 cm^{-1}. [31] The IR spectra, obtained by other workers[24], of C_3H_6 adsorbed at room temperature on CoNaA and MnNaA have shown no evidence for the formation of propene or open chain alkanes.

6.5.2 The t.o.f. spectrum of dehydrated CoNaA

The t.o.f. spectrum of dehydrated $Co_{4.0}Na_{4.0}Al_{11}Si_{13}O_{48}$ is shown in Fig.6.1(b) above. Fig.6.1(b) contains a band at 175 cm^{-1} and a weak feature at *ca.* 150 cm^{-1}. As the scattering angle is increased both band intensities, measured on an absolute scale, decrease and the estimation of the transition frequencies becomes less accurate due to

TABLE 6.7 The relative values of $Z(\tilde{\nu})/\mu$ in equation 6.1 for the modes of cyclopropane complexes of Co(II) and Mn(II) in partially exchanged zeolite A

symmetry of $M(II)-C_3H_6$ complex	mode	description	$Z(\tilde{\nu})/\mu$ for D atom of C_3H_6	$Z(\tilde{\nu})/\mu$ for D atom of C_3D_6	deuteration shift $\tilde{\nu}_D/\tilde{\nu}_H$
C_{3v}	τ_z	C_3 torsion	2.2	1.9	0.873
	τ_x and τ_y	tilt	4.4	3.9	0.871
	t_z	symmetric stretch	1.0	1.0	0.935
	t_x and t_y	rock	2.0	2.0	0.935
C_{2v}	τ_z	C_2 torsion	2.2	1.9	0.871
	τ_x	flap	2.2	1.9	0.871
	τ_y	antisymmetric stretch	2.2	1.9	0.873
	t_z	symmetric stretch	1.0	1.0	0.935
	t_x	rock	1.0	1.0	0.935
	t_y	wag	1.0	1.0	0.935

$Z(\tilde{\nu})$ = vibrational density of states at frequency $\tilde{\nu}$ cm^{-1}

μ = effective oscillator mass

the increasing statistical spread of the data points. Both bands show a variation in frequency of $\pm 4 cm^{-1}$ over the Q range studied (3.8 to 5.4 $\AA^{-1}$ for the *ca.* 175 cm^{-1} band, 3.8 to 5.7$\AA^{-1}$ for the *ca.* 150 cm^{-1} band).

In dehydrated CoNaA and MnNaA, the only nuclei with non-zero incoherent neutron scattering cross sections, σ_{inc}, are Co, Mn and Na(σ_{inc} = 5.2, 0.4 and 1.7 respectively).[34] For a given zeolite, the relative INS intensity of a mode involving motion of a nucleus N is approximately proportional to

$$\sigma_{inc} \times \frac{\text{no. of nuclei of type N per zeolite pseudo-unit cell}}{\text{atomic mass of nuclide N}}$$

provided that the force constants of the modes thus compared are equal. For Co_4Na_4A, this expression is 0.35 for Co and 0.30 for Na, while for $Mn_{3.6}Na_{4.8}A$ it is 0.03 for Mn and 0.36 for Na. Although the t.o.f. spectra of dehydrated CoNaA show two bands (Fig.6.1(b)), no bands were observed in the corresponding spectra of dehydrated MnNaA (Fig.6.14, Section 6.5.7 below). It is likely that the difference between these spectra arises from the difference in σ_{inc} between the Co(II) and Mn(II) ions. Thus we assign the bands at 175 and 150 cm^{-1} in the t.o.f. spectrum of CoNaA (Fig. 6.1(b)) to rattling modes of the Co(II) cation. Since the σ_{inc} for the Na(I) ions are similar for the two zeolites, we would expect any band due to displacement of the Na(I) ions to appear in either both or neither of the spectra of dehydrated MnNaA and CoNaA. Thus we rule out the possibility that the 175 and 150 cm^{-1} bands in the t.o.f. spectrum of dehydrated CoNaA are due to modes involving the Na(I) ions.

6.5.3 The b.f.d. spectrum of dehydrated CoNaA

The spectrum, Fig. 6.8, shows considerable structure in the 400 to 750 cm^{-1} region. These features are artifacts arising from problems associated with positioning of the beam stop which, it was later discovered, remained partially in the beam during the recording of the spectrum. The features are removed on subtraction of this background spectrum (Fig. 6.8) from the spectra of the adsorption complexes. A band at 244 cm^{-1} in the b.f.d. spectrum of CoNaA (Fig. 6.8) has also been observed in the spectra of a wide range of samples, both zeolitic and non-zeolitic, obtained on the DIDO b.f.d. spectrometer. Thus the feature at 244 cm^{-1} is most probably an instrumental artifact. It is removed from the b.f.d. spectra of CoNaA plus adsorbed C_3H_6 (Section 6.5.6.) by the process of time normalisation, discussed in Chapter Three.

The b.f.d. spectrum of dehydrated CoNaA shows a relatively intense band at 151 cm^{-1} and a weaker band at 303 cm^{-1} (Fig. 6.8). The 151 cm^{-1} band is assigned to unresolved intensity from the two lattice modes which were observed at 150 and 175 cm^{-1} in the t.o.f. spectrum (Fig. 6.1 (b)), and the 303 cm^{-1} band to the first overtone of the 151 cm^{-1} component.

The major differences in the experimental variables behind the b.f.d. and t.o.f. spectra of dehydrated CoNaA (Figs. 6.1(b), 6.8) are as follows.

1. The resolution of the b.f.d. spectrometer is poorer than that of the IN4 t.o.f. spectrometer. If the INS bands of CoNaA are intrinsically broad then the features which were resolved at 175(s) and 150(w) cm^{-1} by the t.o.f. spectrometer may become merged in the b.f.d. spectra.

Fig. 6.8 Beryllium filter detector (DIDO b.f.d.) spectrum (77K) of dehydrated CoNaA zeolite, with no background subtracted.

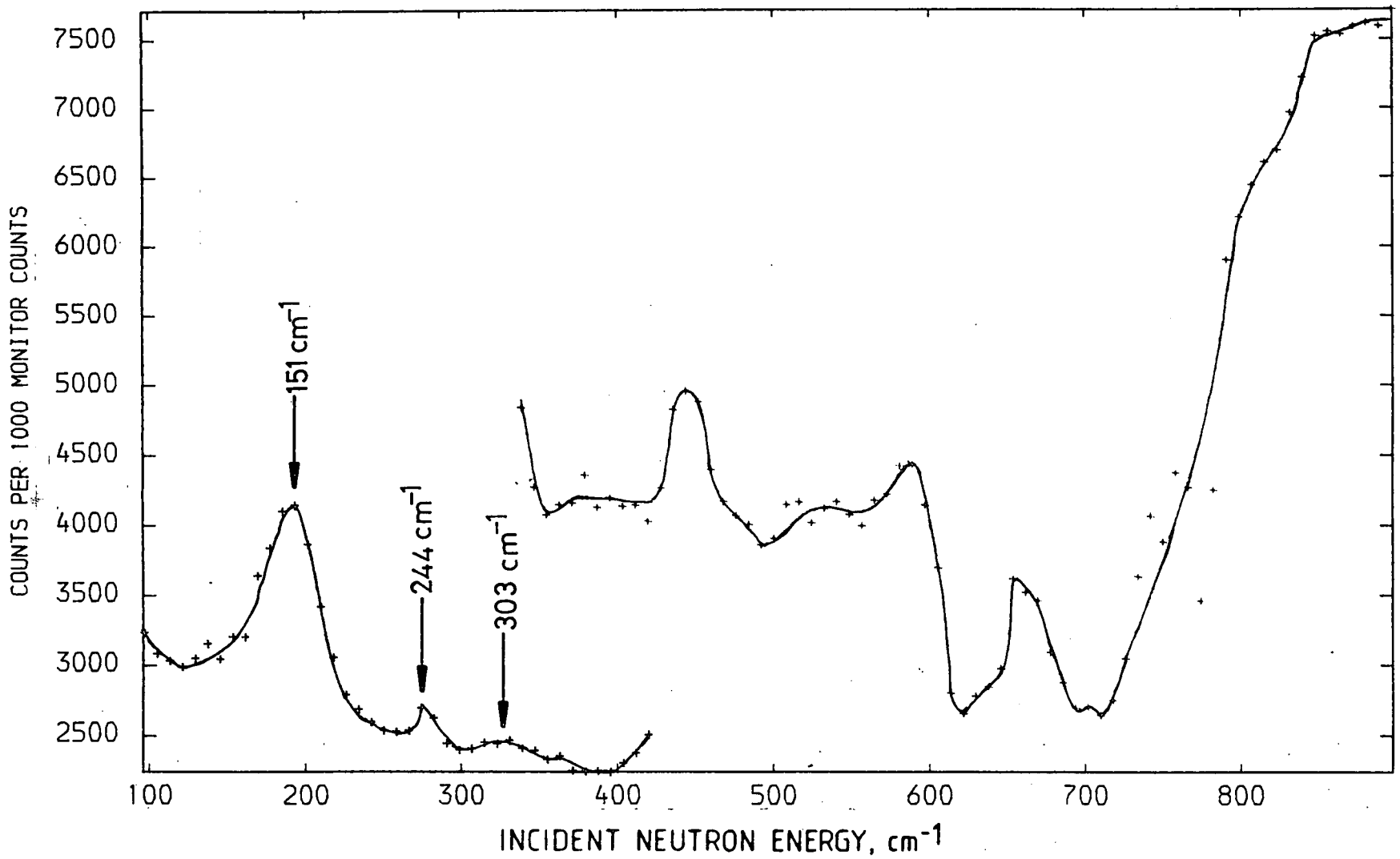

2. The t.o.f. spectra are represented as $P(\alpha,\beta)$ versus energy transfer whereas the b.f.d. spectra represent $S(Q,\omega)$ versus energy. On converting the function $S(Q,\omega)$ to $P(\alpha,\beta)$, those bands arising at high energy transfers will apparently gain in intensity with respect to those at lower energy transfers. However, this does not explain the frequency difference between the most intense band below 200 cm^{-1} in the b.f.d. (151 cm^{-1}) and t.o.f. spectra (175 cm^{-1}) of dehydrated CoNaA.

Of lesser importance than points (1) and (2) above are the following differences between the b.f.d. and t.o.f. experiments:

3. the momentum transfer $\hbar Q$, equivalent at 151 cm^{-1} to $Q = 2.8\text{Å}^{-1}$ for the b.f.d. and 3.8 to 5.7Å^{-1} for the t.o.f. spectra;
4. the temperature, 77K (b.f.d.) and 16K (t.o.f.);
5. the sample composition, $Co_{4.1}Na_{3.8}Al_{12}Si_{12}O_{48}$ (b.f.d.) and $Co_{4.0}Na_{4.0}Al_{11}Si_{13}O_{48}$ (t.o.f.).

None of these differences can fully explain the discrepancies between the t.o.f. and b.f.d. spectra of dehydrated CoNaA in the region 100 to 200 cm^{-1} (Figs. 6.1(b), 6.8). Both sets of spectra were obtained under conditions of neutron energy loss. The temperature difference cannot account for the absence of the higher frequency band (175 cm^{-1}) in the b.f.d. spectrum, which was obtained at higher sample temperatures than the t.o.f. data. Also, the two lattice modes showed little, if any, dispersion in the t.o.f. spectra (e.g. Fig. 6.1(b)) and the small difference in sample composition is unlikely to have had such a pronounced effect.

The spectrum of a polycrystalline Al block obtained by other workers[35] on the DIDO b.f.d. spectrometer shows, in the region 100 to 350 cm^{-1}, two bands, at 177 cm^{-1}(s) and 294 cm^{-1}(m). Thus we can eliminate any possibility that the 151 cm^{-1} band in the b.f.d. spectrum of dehydrated CoNaA (Fig. 6.8) is due to the Al sample can. Because the t.o.f. spectrum of dehydrated MnNaA contains no structure over the range *ca.* 0 to 220 cm^{-1} (Section 6.5.7), the band at 175 cm^{-1} in the t.o.f. spectrum of CoNaA (Section 6.5.2) must be due to the zeolite itself and not the Al sample can.

Finally, we note that poor correlation between low frequency b.f.d. and t.o.f. INS spectra of zeolitic species has been observed by other workers.[36,37]

6.5.4 The t.o.f. spectra of CoNaA+C_3H_6, 0.9 molecules/supercage

The t.o.f. spectra obtained at 16K for a coverage, θ, of 0.9 molecules per pseudo unit cell are shown for 3 different scattering angles, γ, in Figs. 6.9 (a-c). The transition frequencies, $\tilde{\nu}$, and band intensities, I^P_{OBS}, obtained by fitting Gaussians to the 4 observed maxima are listed in Table 6.8. A small apparent variation in the frequency of each band with scattering angle reflects the precision of the curve fitting rather than dispersion. The largest frequency variation is 7.8%, shown by the band arising at 47 cm^{-1} for $\gamma = 92.3^o$ and 51 cm^{-1} for $\gamma = 126^o$ (Table 6.8, Figs. 6.9). This band is the most difficult to fit accurately, being the least well resolved. The energy resolution ($\Delta E/E_o$), of the IN4 spectrometer is approximately 2%.

Figs 6.9 T.o.f. spectra (16K) of CoNaA zeolite plus adsorbed C_3H_6, coverage 0·9 molecules per pseudo-unit cell. The background spectra of the dehydrated zeolite have been subtracted.

Fig 6.9a Scattering angle 68·3°.

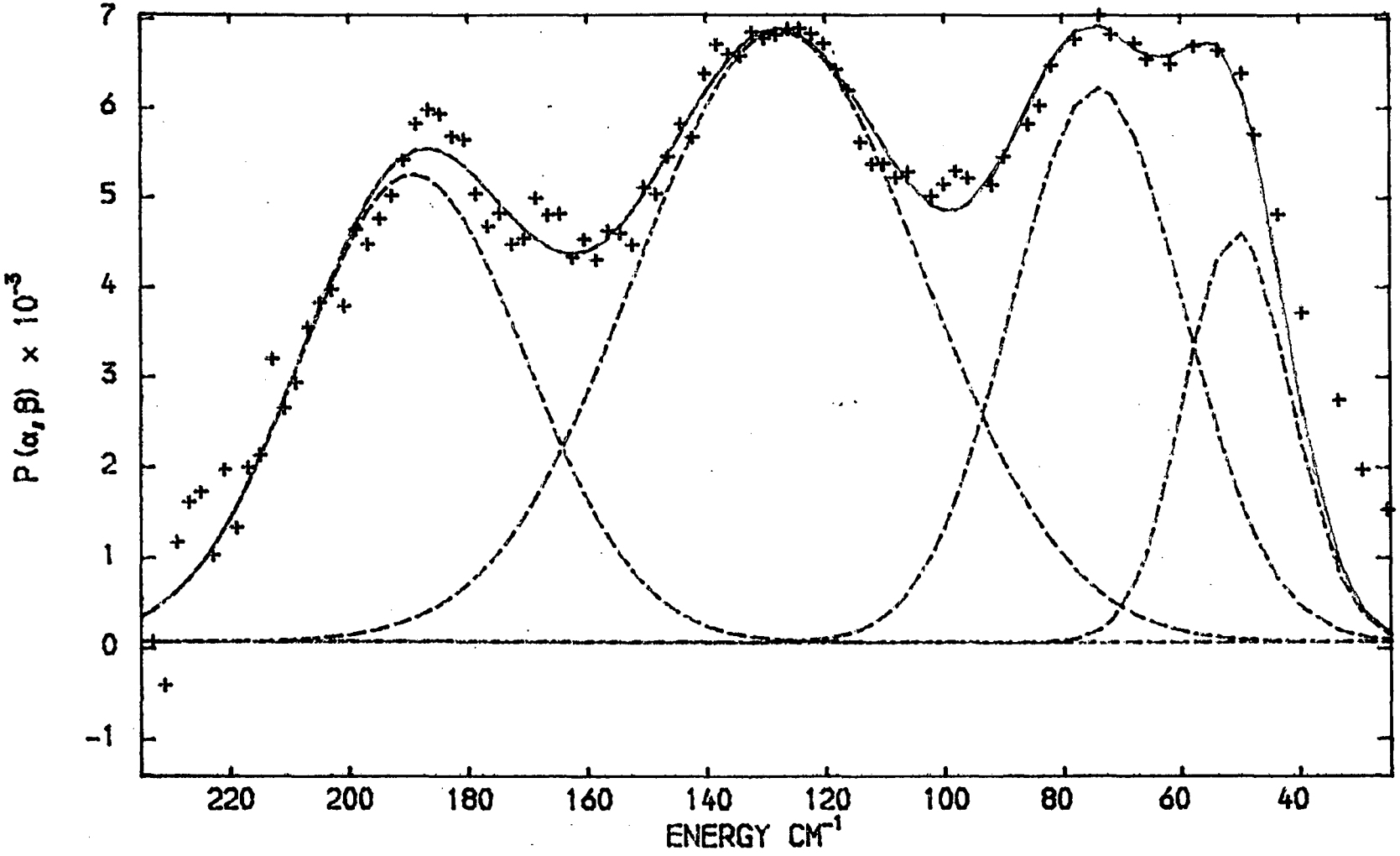

Fig 6.9b CoNaA zeolite plus C_3H_6, coverage 0·9 molecules per pseudo-unit cell, background subtracted.
Scattering angle 92.3°, temperature 16K.

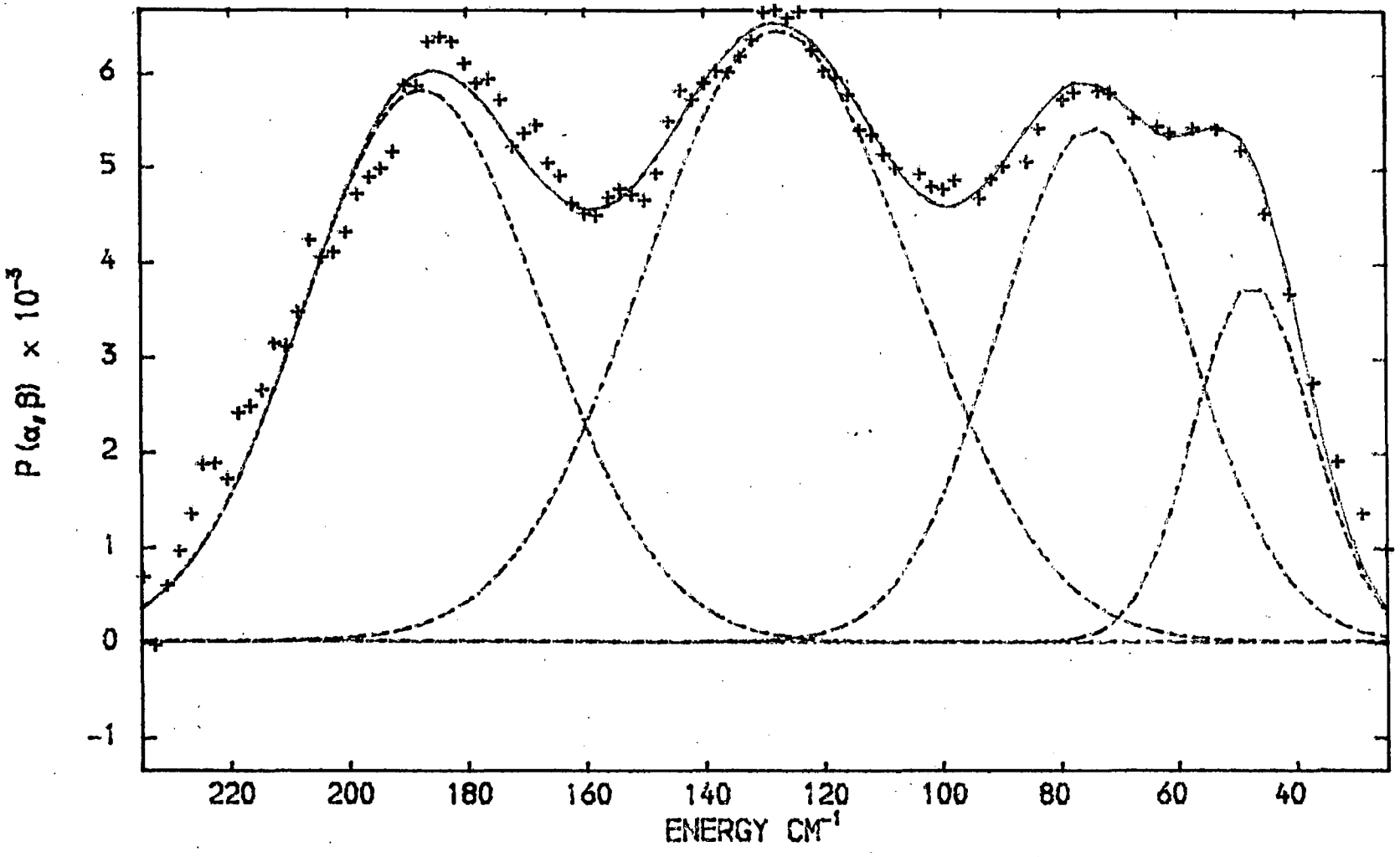

Fig 6.9c CoNaA zeolite plus C_3H_6, coverage 0·9 molecules per pseudo-unit cell, background subtracted.
Scattering angle 126·0°, temperature 16K.

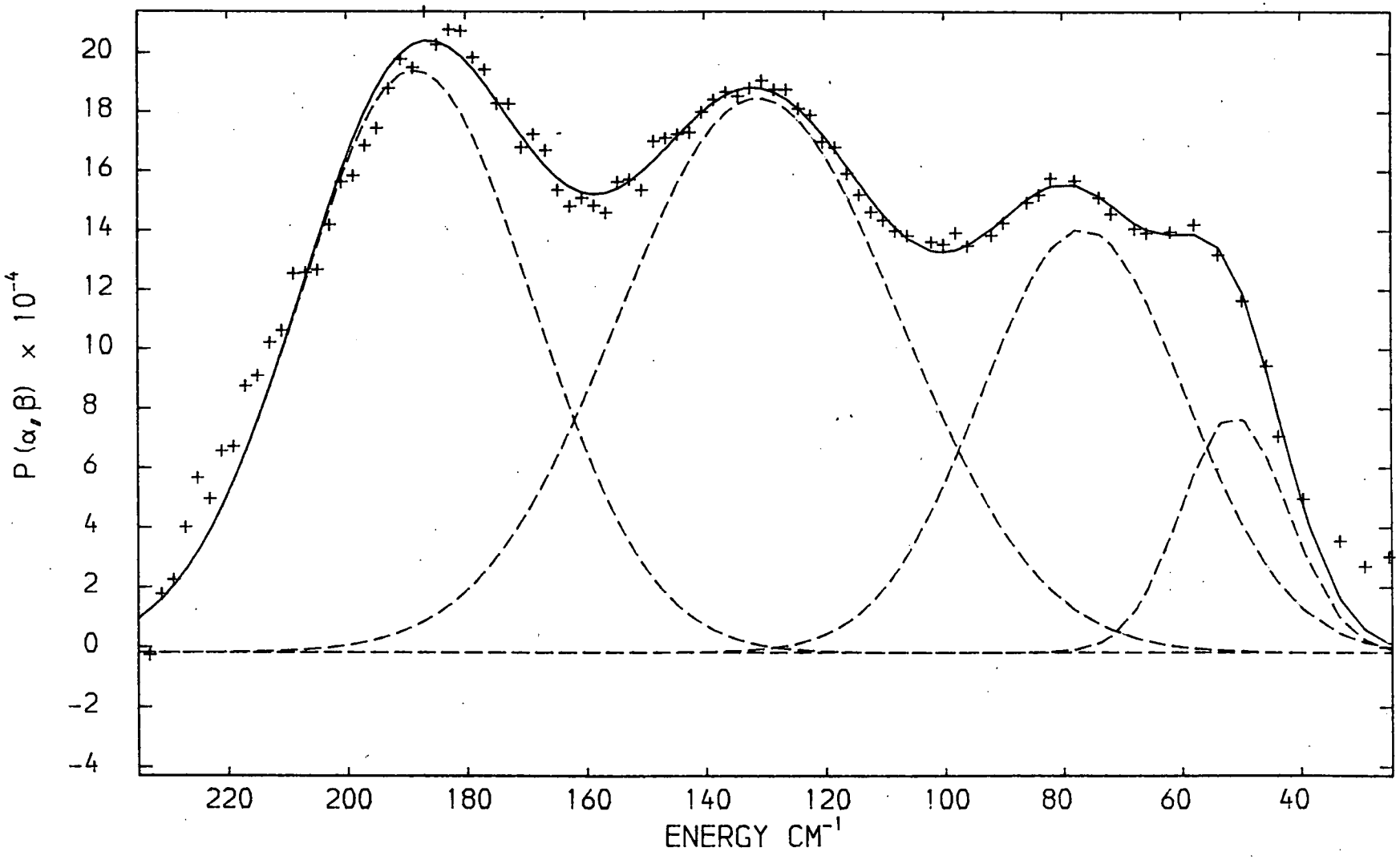

TABLE 6.8 Assignment of the t.o.f. spectra of cyclopropane adsorbed in CoNaA zeolite (16K), assuming C_{3v} symmetry for the adsorption complex

Sample	CoNaA + C_3H_6 (θ = 0.9)											
scattering angle, ^{o} figure	68.3 6.9a				92.3 6.9b				126.0 6.9c			
assignment	ν, cm^{-1}	Q^2, $Å^{-2}$	I^P_{OBS}	I^P_{CALC}	ν, cm^{-1}	Q^2, $Å^{-2}$	I^P_{OBS}	I^P_{CALC}	ν, cm^{-1}	Q^2, $Å^{-2}$	I^P_{OBS}	I^P_{CALC}
t_x and t_y	189	14.0	2.4	2.0	188	20.5	3.1	2.9	188	30.0	5.4	4.5
τ_x and τ_y	128	15.5	4.0	4.3	128	24.7	3.9	5.1	131	36.8	6.1	6.6
τ_z	74	17.2	2.2	2.6	75	28.0	2.3	3.2	77	42.4	3.5	4.1
t_z	50	18.0	1.0	1.0	47	29.8	1.0	1.0	51	45.0	1.0	1.0

Notes

ν = band frequency, $\hbar Q$ = momentum transfer during the scattering event, I^P_{OBS} = ratio of observed band intensities, I^P_{CALC} = ratio of calculated intensities.

The highest frequency band in these t.o.f. spectra (Figs.6.9) occurs at 189 cm^{-1} (γ = 68.3°) and the b.f.d. spectra (Figs. 6.12, 6.13; Section 6.5.6 below) show no bands ascribable to cyclopropane between 185 cm^{-1} and the region of perturbed gas phase modes. The four bands observed in the t.o.f. spectra (Figs. 6.9) are therefore due to the six fundamental modes of adsorbed cyclopropane. The observation of four distinct bands as opposed to six indicates C_{3v} rather than C_{2v} symmetry of the Co-C_3H_6 complex and the relative INS intensities expected for a C_{3v} complex can be predicted using equations 6.1 to 6.3. In order to carry out these calculations, we first need to estimate the total mean square displacement, $\langle U^2(\tilde{\nu})\rangle$, of the H atoms of the C_3H_6 adsorbate. As explained in Section 6.5.1, the plot of $\ln I^P$ against Q^2 for each INS band of adsorbed C_3H_6 is expected to be a straight line of gradient $-\langle U^2(\tilde{\nu})\rangle$ given that the band arises from a fundamental (harmonic) mode. In Fig.6.10 we show the $\ln I^P \nu . Q^2$ plot for each band in the spectrum of CoNaA+C_3H_6, θ = 0.9. The points (Fig. 6.10) were fitted by linear regression to straight lines and the correlation coefficients of the fitting are listed in Fig. 6.10. The fitted lines are not good fits to the calculated points which appear to lie on curves (Fig.6.10). There is a systematic deviation from linearity which arises from the fact that the observed intensities, obtained from the fitting of Gaussian curves, in a given spectrum are correlated. The gradients of the least squares lines are also listed on Fig.6.10. The value of $\langle U_i^2(\tilde{\nu})\rangle$ thus obtained for each mode is physically plausible and will be used to calculate the relative intensities of the INS bands of the intrazeolitic M(II)-C_3H_6 complex for a

Fig. 6.10 A plot of ln I^P against Q^2 for the INS spectra of $CoNa+C_3H_6$, coverage 0.9 molecules per supercage, 16K (see fig 6.7).

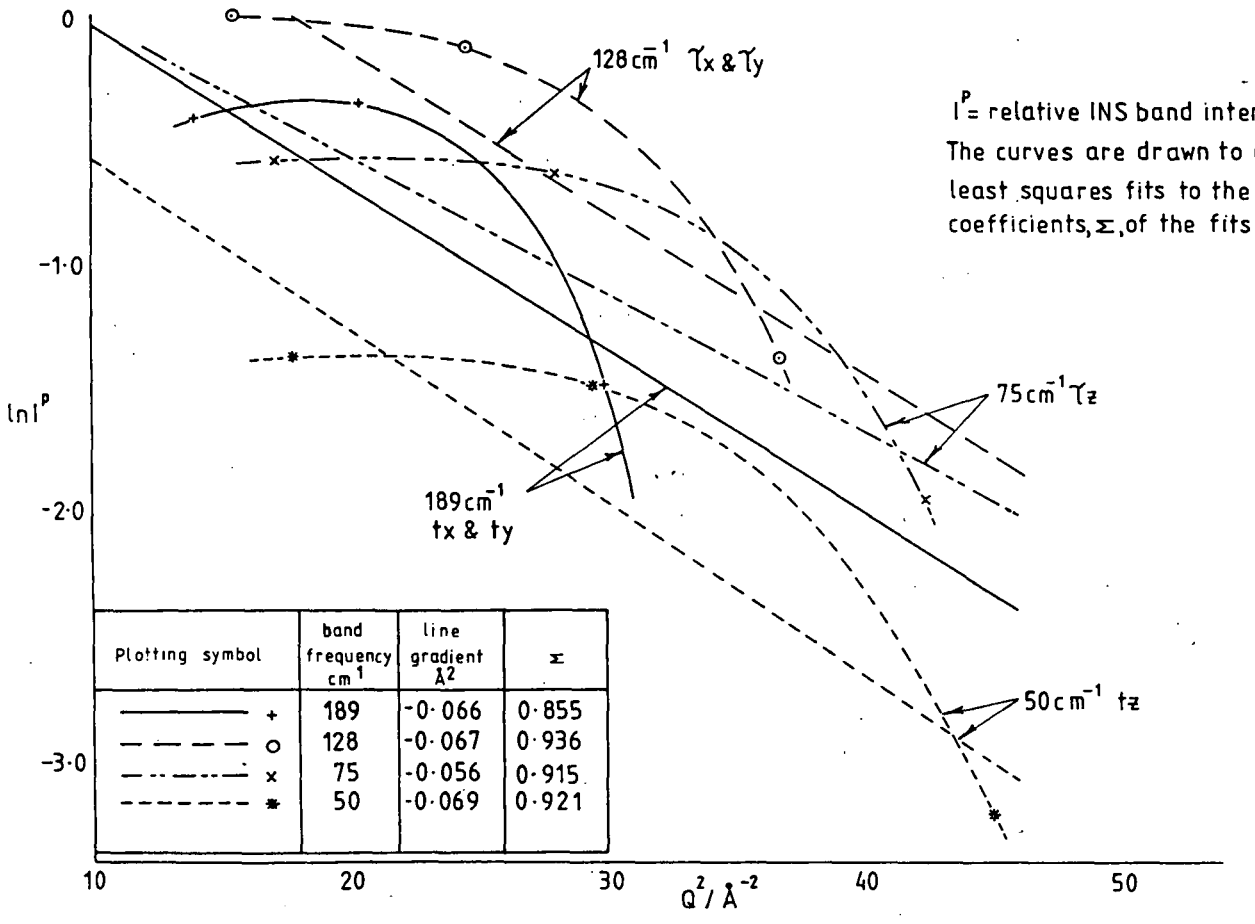

I^P = relative INS band intensity, $\hbar Q$ = momentum transfer during scattering event. The curves are drawn to guide the eye through the data points. The lines are least squares fits to the points calculated for each band. The correlation coefficients, Σ, of the fits are listed in the key.

particular adsorption geometry. Our justification for using these values of $\langle U_i^2(\tilde{\nu})\rangle$ (Fig.6.10) is the good correspondence between the observed and predicted INS band intensities (see below). The magnitude of the $\langle U_i^2(\tilde{\nu})\rangle$ is discussed in Section 6.5.11 below.

In Table 6.8 we list the relative intensities, I^P_{CALC}, calculated using equations 6.1 to 6.3 for a C_{3v} adsorption complex of C_3H_6 with CoNaA zeolite. Because the equations give relative intensity values we have arbitrarily set the observed, I^P_{OBS}, and calculated relative intensities equal to unity for the lowest frequency band in the spectrum recorded at each scattering angle, γ. Our assignment scheme is therefore tested by a comparison of I^P_{OBS} and I^P_{CALC} for the other three bands at each γ. There is good agreement for the spectra recorded at scattering angles of 68.3^o and 126.0^o; although at $\gamma = 92.3^o$ the degenerate τ_x and τ_y modes are less intense than predicted, an effect which we are unable to explain.

That the agreement between the observed and predicted band intensities (Table 6.8) is no worse for a given band at high values of Q^2, *i.e.* high scattering angles, than at lower values indicates the presence of at most a small contribution to the observed intensities from overtone modes.

The predicted and observed intensities of the 189 cm^{-1} and 74 cm^{-1} bands are about equal (Table 6.8). Their assignment to the degenerate (t_x and t_y) translations and the τ_z torsion respectively is corroborated by the following facts.

1. In the INS spectra of benzene adsorbed by Nal3X and fully exchanged AgX zeolites the τ_z mode occurred at a lower

frequency than the degenerate (t_x and t_y) modes.[38] (The benzene was face-bonded to the Na^+ or Ag^+ cation).

2. For higher coverages of C_3H_6 within CoNaA, our INS data (Section 6.5.5 below) indicate the splitting of the τ_z torsion into unresolved in-phase and out-of-phase components at frequencies below *ca.* 110 cm^{-1} while the *ca.* 187 cm^{-1} band remains largely unaffected.

6.5.5 The t.o.f. spectrum of CoNaA+C_3H_6, coverage θ = 1.8 molecules per supercage

The spectrum (Fig.6.11) shows two broad bands centred at 181 and 123 cm^{-1}. Below *ca.* 110 cm^{-1}, the spectrum is unresolved and a single, very broad shoulder is observed. The shoulder is irregular in shape and appears to contain contributions from several unresolved bands at frequencies below 110 cm^{-1}, *e.g.* at *c.a.* 105, 90 cm^{-1}.

Compared with the lower coverage spectra (Fig.6.9), the high coverage spectra (Fig.6.11) shows an increase in intensity in the *c.a.* 80 to 120 cm^{-1} region. In the lower coverage case (θ = 0.9), two bands were observed below 110 cm^{-1}, at 74 cm^{-1} (τ_z) and at *c.a.* 50 cm^{-1} (t_z) (Fig. 6.9). The loss of resolution in this frequency region of the θ = 1.8 spectrum (Fig. 6.11) is most likely caused by splitting of the τ_z torsion to in-phase and out-of-phase components through non-bonding interactions between cyclopropane molecules adsorbed within the same α-cage. A similar effect has also been observed for acetylene[39], ethylene[40] and benzene[38] adsorbed in AgX zeolites, although in these cases the bands due to the in-phase and out-of-phase components of the τ_z torsion of coadsorbed molecules were resolved. The intermolecular interactions between C_3H_6 molecules are discussed further in Section 6.6.2.

Fig 6.11 T.o.f. spectrum (16K) of CoNaA zeolite plus adsorbed C_3H_6, coverage 1·8 molecules per pseudo-unit cell. A background spectrum of the dehydrated zeolite has been subtracted. Scattering angle 83.1°.

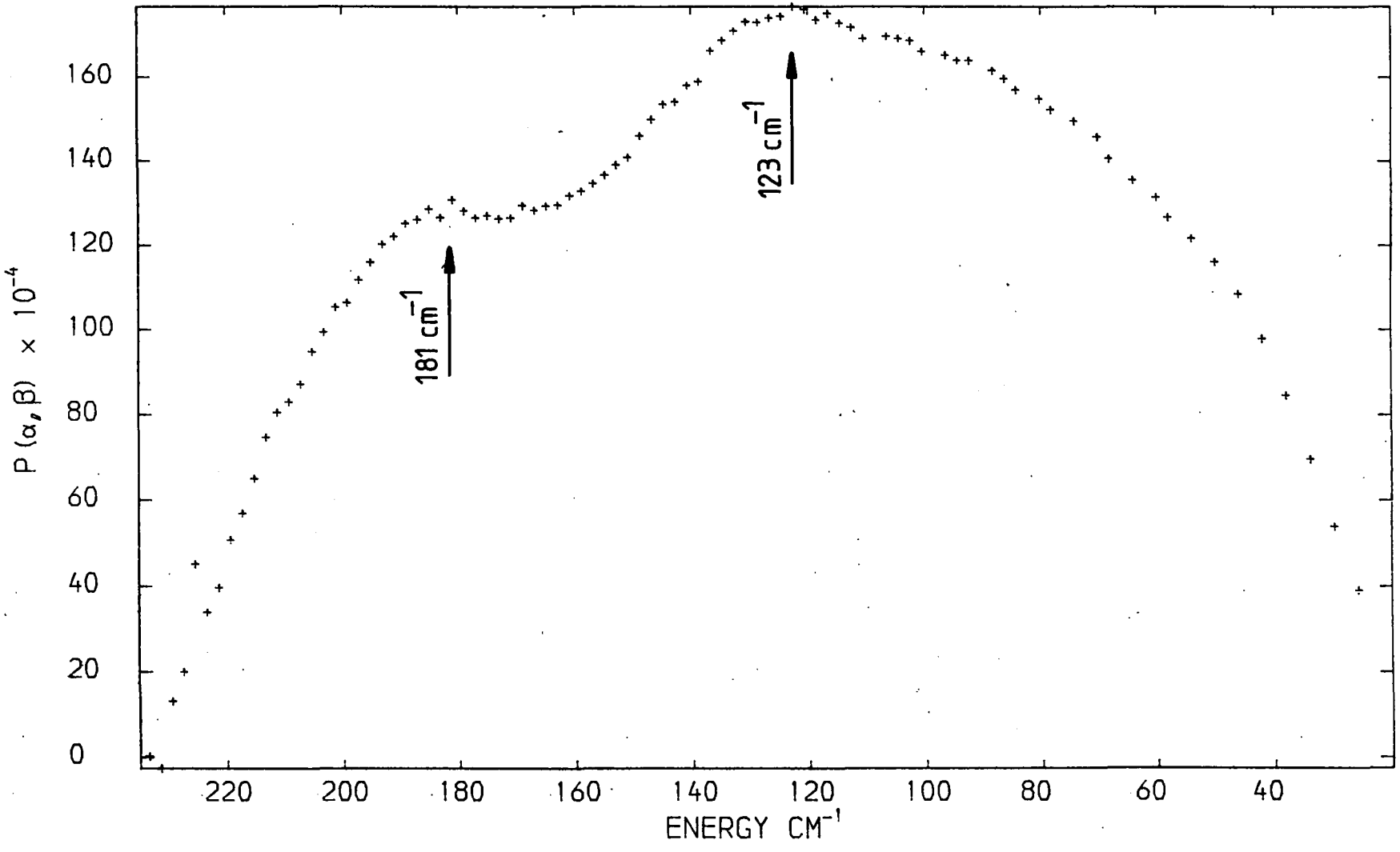

The bands at 181 and 123 cm^{-1} in the spectrum of CoNaA+C_3H_6, θ = 1.8 (Fig.6.11), are assigned to the degenerate (t_x and t_y) and the (τ_x and τ_y) modes, respectively. These modes were observed at 189 and 128 cm^{-1} respectively in the lower coverage spectrum (Section 6.5.4).

6.5.6 The b.f.d. spectra of CoNaA + C_3H_6

The b.f.d. spectra obtained at 77K for coverages of 0.7 and 3.0 molecules per supercage are shown in Figs. 6.12 and 6.13 respectively. The major reason for obtaining these data was to look for any additional modes due to adsorbed C_3H_6 at frequencies higher than those observed using the IN4 t.o.f. spectrometer (Sections 6.5.4, 6.5.5) but below the frequencies of the internal vibrations.

In both spectra (Figs. 6.12, 6.13) a shoulder occurs at 185 cm^{-1} (very weak in the low coverage spectrum). The degenerate t_x and t_y modes were observed at this frequency in the t.o.f. data (Fig. 6.9) and therefore we have observed modes due to adsorbed cyclopropane in the b.f.d. spectra (Figs.6.12,13). Below 185 cm^{-1}, there is poor correspondence between the b.f.d. and t.o.f. spectra of CoNaA + C_3H_6. This may arise, in part, from the inferior resolution of the b.f.d. spectrometer. The discrepancy between the low frequency (<185 cm^{-1}) part of the b.f.d. spectra (Figs. 6.12, 6.13) and the t.o.f. results (Fig.6.9) has been previously observed in other INS studies.[36,37]

The bands at or above 749 cm^{-1} in the b.f.d. results (Figs. 6.12, 6.13) arise from perturbed internal modes of the adsorbed C_3H_6. In the low coverage results, a band centred at 805 cm^{-1} contains unresolved intensity from the ν_7 (854 cm^{-1})

Fig. 6.12 Beryllium filter detector (DIDO b.f.d.) spectrum (77K) of CoNaA zeolite plus C_3H_6, coverage 0.7 molecules per supercage. A background spectrum of the dehydrated zeolite has been subtracted.

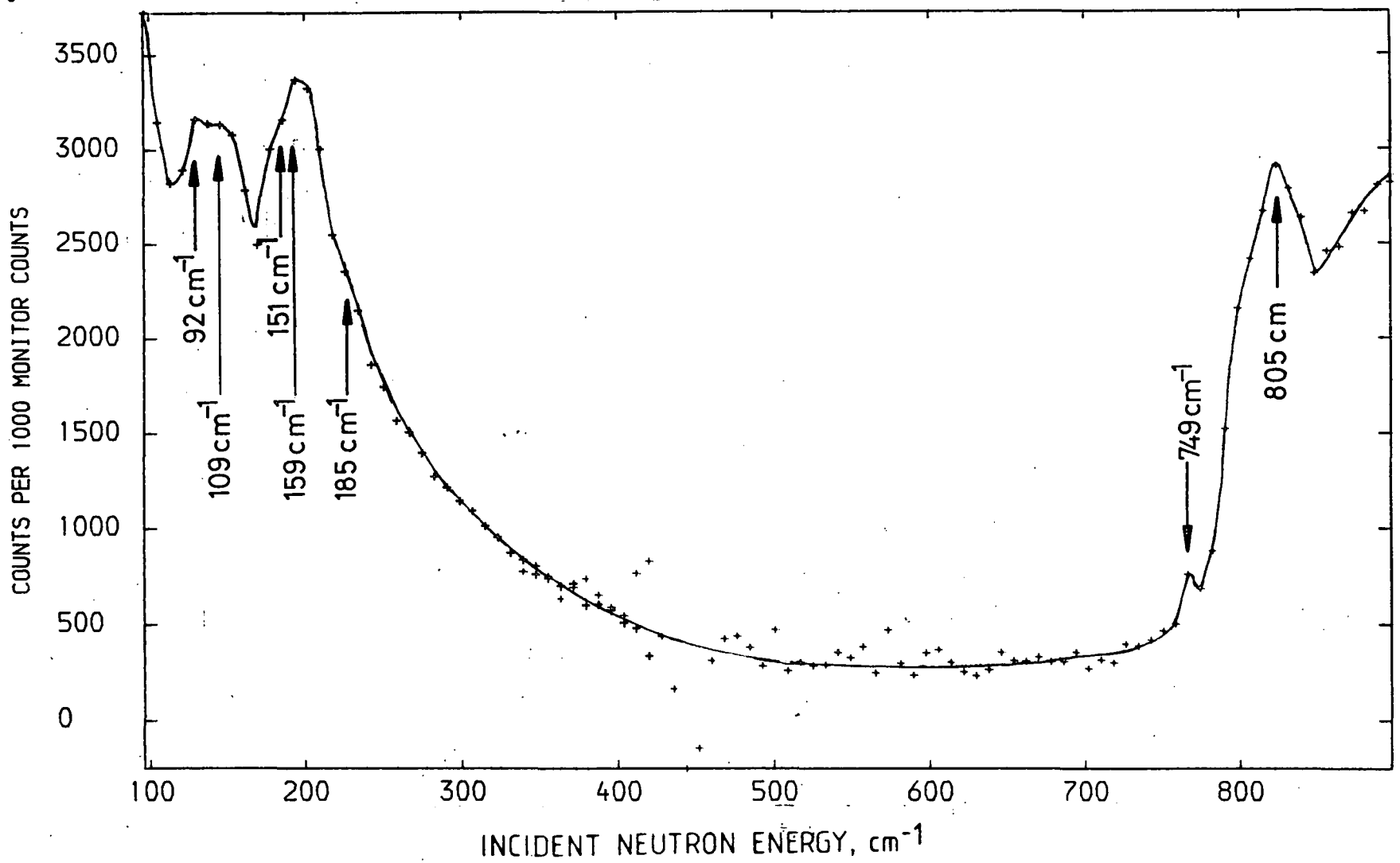

Fig. 6.13 Beryllium filter detector (DIDO b.f.d.) spectrum (77K) of CoNaA zeolite plus C_3H_6, coverage 3.0 molecules per supercage. A background spectrum of the dehydrated zeolite has been subtracted.

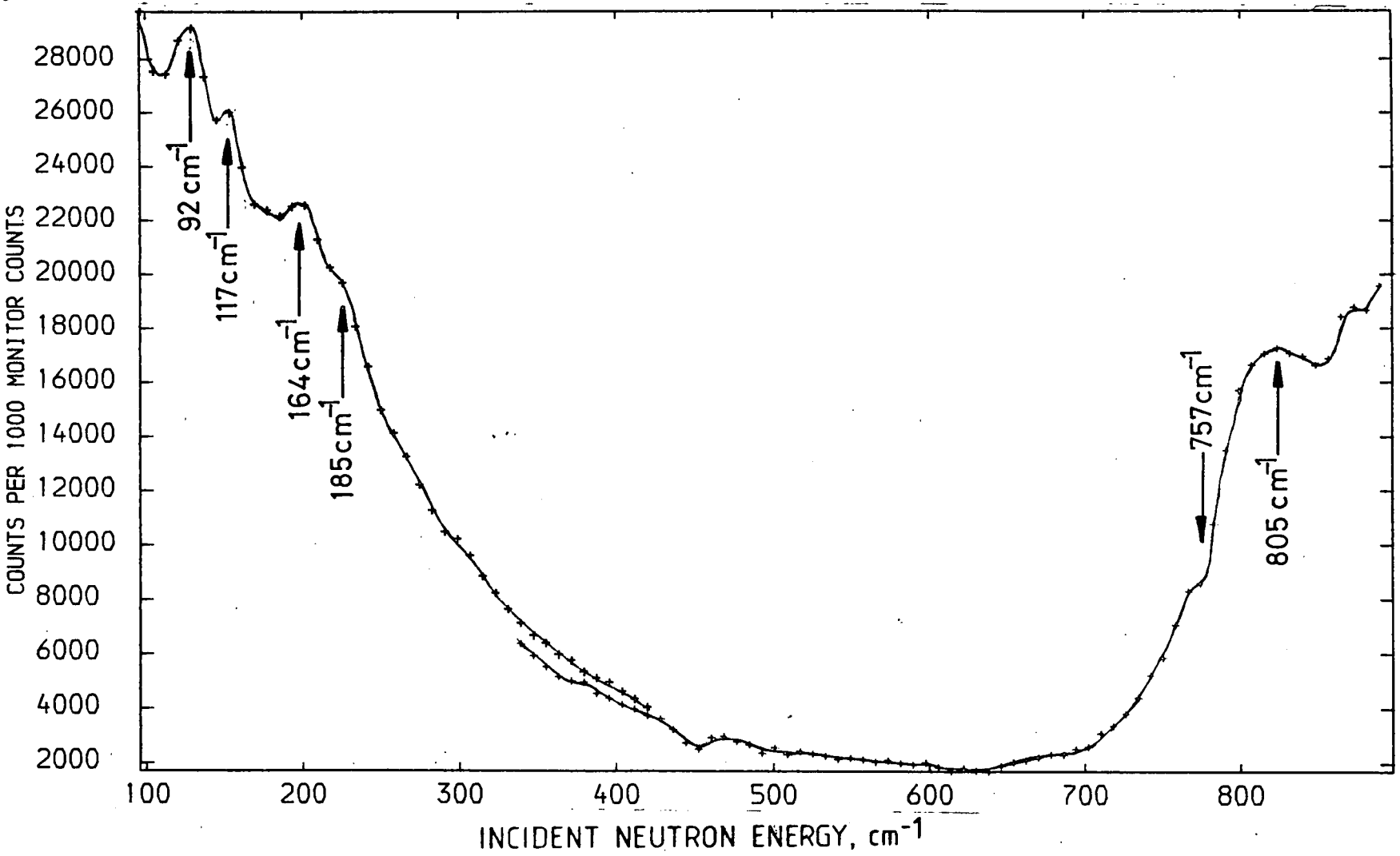

and ν_{11} (869 cm^{-1}) internal modes, the frequencies in brackets being those reported for C_3H_6 in the gas phase (Table 6.1). The weaker band at 749 cm^{-1} is assigned to the ν_{14} (739 cm^{-1}) mode of adsorbed C_3H_6. In the higher coverage case (Fig.6.13) the bands due to the perturbed internal modes arise at 757 and 805 (broad) cm^{-1}. The apparent shift of 8 cm^{-1} of the 757 cm^{-1} band with increasing coverage is within the error of *ca* ± 16 cm^{-1} (corresponding to two data points of Figs. 6.12, 6.13) associated with the measurement of the band centres.

The most important feature of the two b.f.d. spectra of CoNaA + C_3H_6 (Figs. 6.12, 6.13) is the absence of bands between 185 and 749 cm^{-1}. Thus our tenet (Section 6.4) that there are only four INS bands due to the external modes of C_3H_6 adsorbed on CoNaA is justified. This number of INS bands is consistent with a Co-C_3H_6 complex of C_{3v} symmetry but inconsistent with what would be expected for a C_{2v} complex.

6.5.7 The t.o.f. spectrum of dehydrated MnNaA

The t.o.f. spectrum of dehydrated $Mn_{3.4}Na_{5.2}A$ is devoid of any resolved features (Figs. 6.14(a),(b)). These figures illustrate the effect of subtracting a flat baseline from the corrected number of scattered neutron counts before the calculations of $P(\alpha,\beta)$ - the spectrum after this subtraction (Fig. 6.14(b)) shows unresolved intensity over the region 40 to 200 cm^{-1} which is not readily apparent in the uncorrected data (Fig. 6.14(a)).

The t.o.f. spectrum (10K) of dehydrated $Mn^{3.6}Na^{4.8}A$ was also obtained. It is very similar to that of $Mn_{3.4}Na_{5.2}A$ (Fig. 6.14) and therefore not shown.

Fig. 6.14a T.o.f. spectrum (10K) of dehydrated MnNaA zeolite, scattering angle 64.5^0. Neither a flat baseline nor a background have been subtracted from these data.

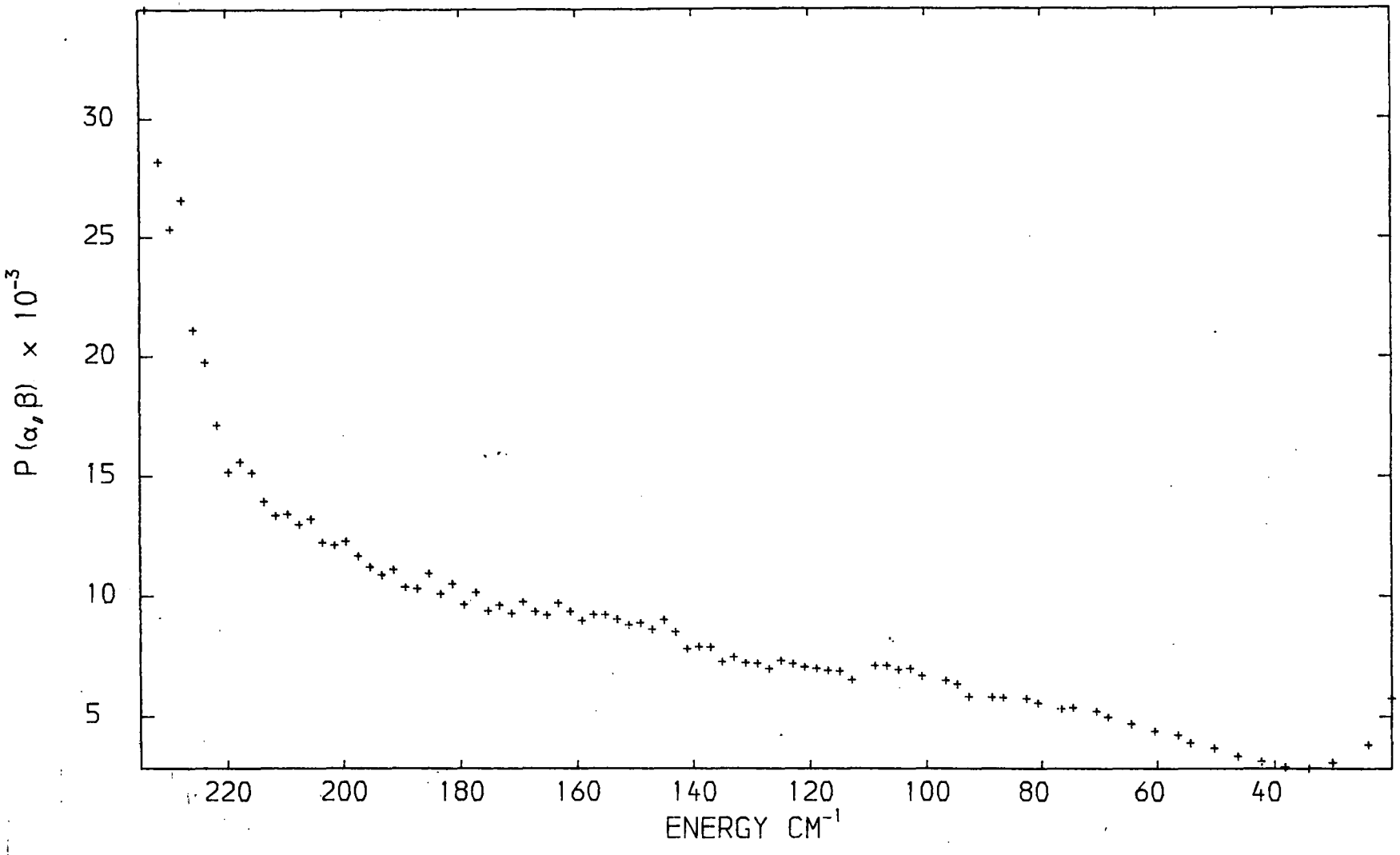

Fig. 6.14b T.o.f. spectrum (10K) of dehydrated MnNaA zeolite, scattering angle 64.5^0, after subtraction of a flat baseline.

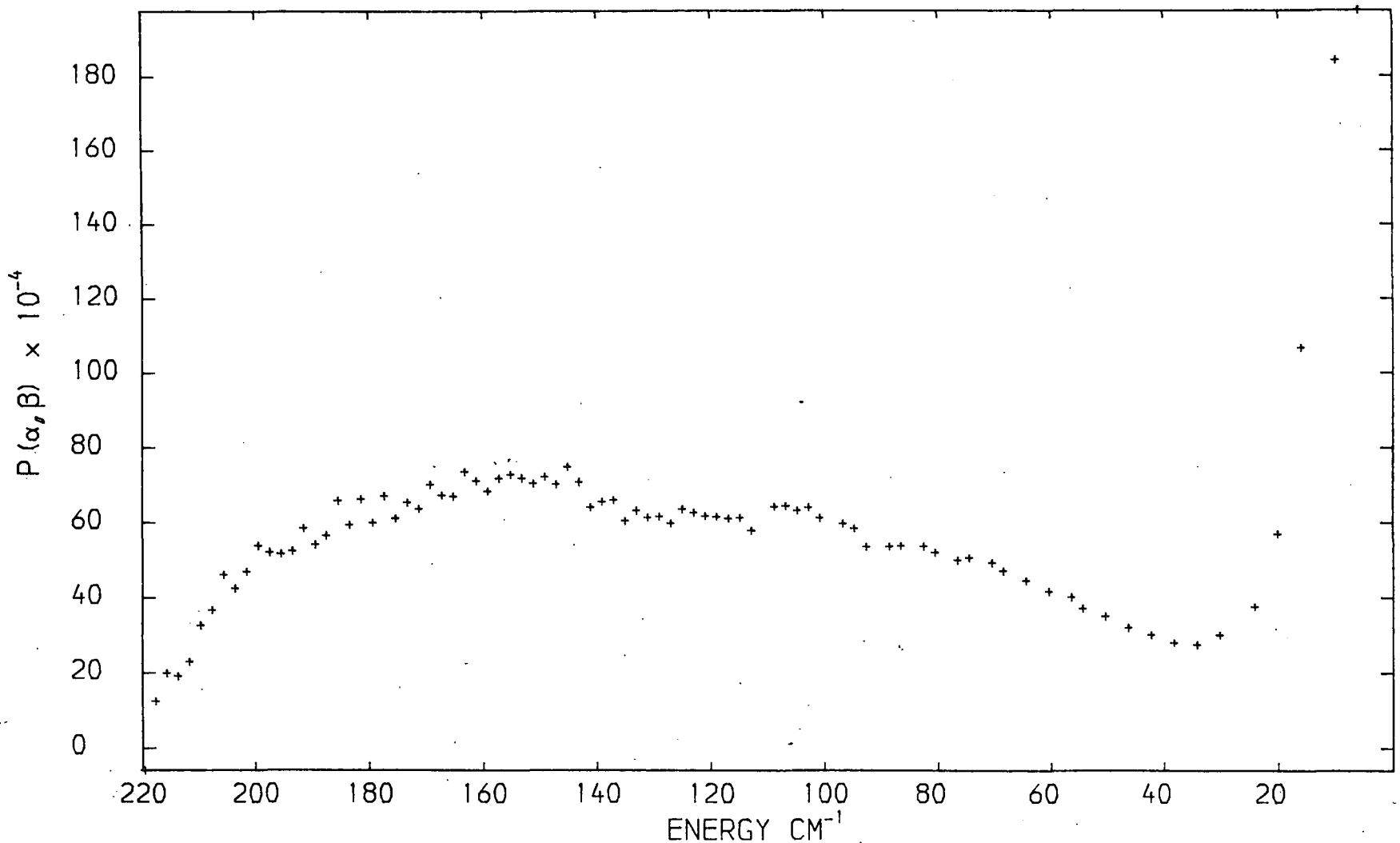

The lack of bands in the dehydrated MnNaA spectrum (Fig.6.14) contrasts with the spectrum of dehydrated CoNaA (Fig.6.1(b)) which shows bands due to zeolite lattice modes involving displacement of Co nuclei. The reason for the difference in the spectra of the two M(II)NaA zeolites was discussed in Section 6.5.2.

6.5.8 The b.f.d. spectrum of dehydrated MnNaA

The b.f.d spectrum obtained at 77K of dehydrated $Mn_{3.4}Na_{5.2}A$ is shown in Fig. 6.15. The features observed in the region 400 to 750 cm^{-1} and the weak band at 244 cm^{-1} are instrumental artifacts. Similar features were observed in the b.f.d. spectrum of dehydrated CoNaA (Fig. 6.8) and their origin is discussed in Section 6.5.3. There is a very weak band at 159 cm^{-1} in the b.f.d spectrum of MnNaA (Fig. 6.15) which was not observed in the t.o.f. spectra (Fig.6.14) recorded at 10K. A similar discrepancy was observed between the t.o.f. and b.f.d. spectra of dehydrated CoNaA (Figs. 6.1(b), 6.8) and possible reasons are discussed in Section 6.5.3. In view of the weakness of the 159 cm^{-1} band in the MnNaA b.f.d. spectrum (Fig. 6.15), it is likely to give only very weak intensity, if any, in the t.o.f. spectra (10K) of MnNaA plus adsorbed cyclopropane (the latter data are discussed in Section 6.5.9).

6.5.9 The t.o.f. spectra of MnNaA + cyclopropane

In this section we shall refer to cyclopropane-h_6 by "$C_3{}^1H_6$" and use "C_3H_6" to denote both cyclopropane-h_6 and cyclopropane-d_6.

The t.o.f. spectra obtained at 10K from MnNaA+$C_3{}^1H_6$ (coverage θ = 1.2 molecules per supercage) and of MnNaA + C_3D_6

Fig. 6.15 Beryllium filter detector (DIDO b.f.d.) spectrum of dehydrated MnNaA zeolite at 77K, with no background subtracted.

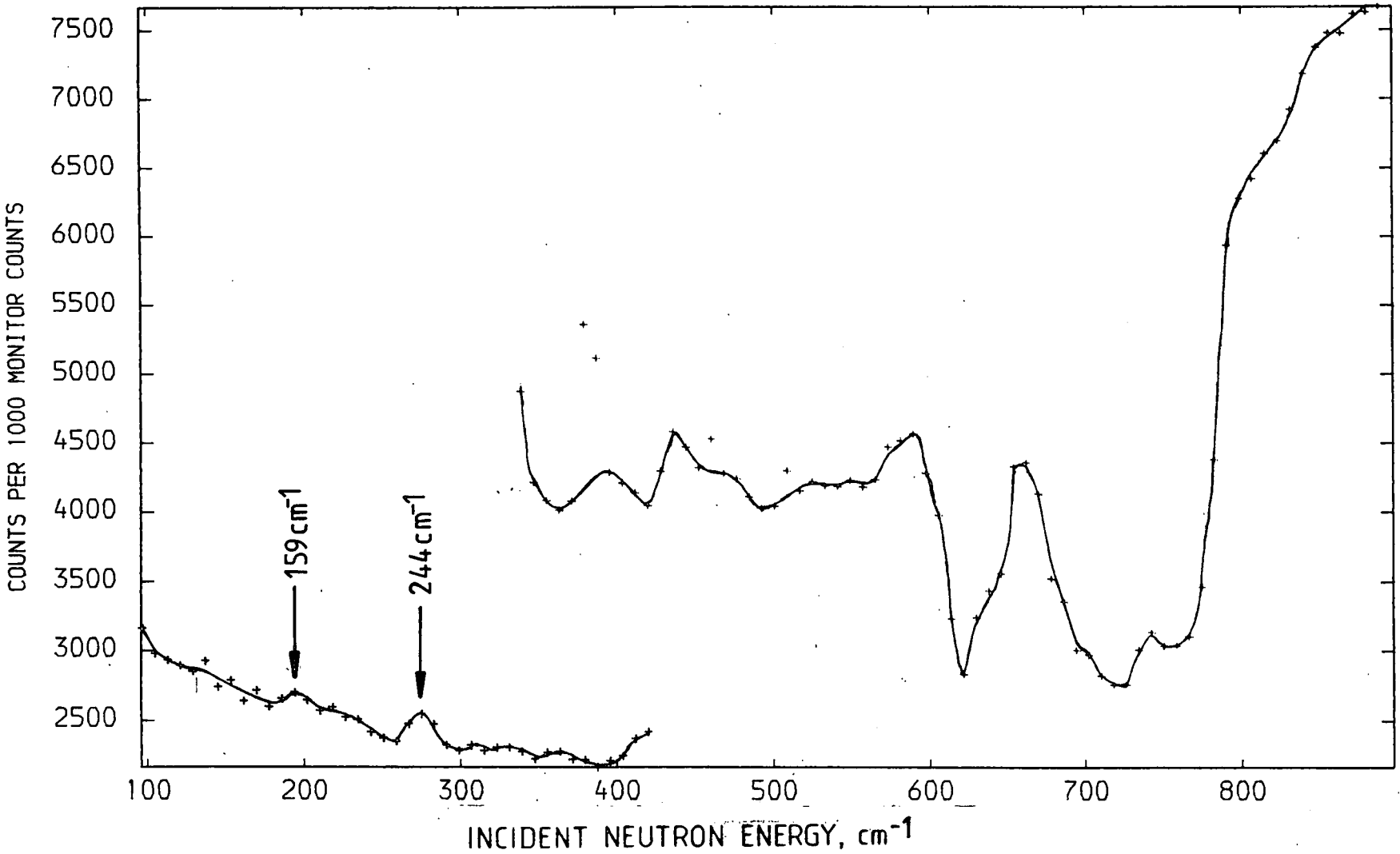

(two coverages, θ = 1.5 and 2.3) are shown in Figs. 6.16 to 6.18. The spectrum of each sample is presented for three scattering angles. Tables 6.9 and 6.10 list the transition frequencies and band intensities obtained from the Gaussian curve fitting. The spectrum of MnNaA + $C_3{}^1H_6$ at 63.6° (Fig. 6.16(a)) shows three prominent bands at 149, 111 and 33 cm^{-1}. In addition, there is some structure in the region 50 to 100 cm^{-1} which is reproduced at all scattering angles (Figs. 6.16(a) to (c)), suggesting the presence of additional, unresolved features. The intensities and width of this region are too great to have arisen from a single band and we have here fitted (Figs.6.16(a) to (c)) two Gaussian curves. Although this gives an acceptable fit to the data points, there is no unique fit (Section 6.2) and we cannot entirely preclude the possibility that there are more than two bands in the 50 to 100 cm^{-1} region. Thus a total of five bands were fitted to the MnNaA + $C_3{}^1H_6$ t.o.f. spectra (Fig. 6.16). For the same reasons, five bands have been fitted to the spectra of adsorbed C_3D_6 (Figs. 6.17, 6.18).

6.5.9(a) The assignment of the MnNaA + cyclopropane t.o.f. spectra

The b.f.d. spectra of MnNaA + $C_3{}^1H_6$ (Section 6.5.10 below) show that all the external modes of adsorbed $C_3{}^1H_6$ occur at or below 142 cm^{-1}, within the energy transfer range of the t.o.f. spectrometer. Nor are there any strong bands in the spectra of dehydrated MnNaA from *ca.* 1 to 177 cm^{-1} (Figs.6.14,6.15). Thus the five curves fitted to the t.o.f. spectra (Figs. 6.16 to 6.18) represent, to a first approximation, all the bands due to the external modes of the adsorbed C_3H_6. If the Mn-C_3H_6 complex adopted C_{2v} symmetry, one would expect six bands in the t.o.f. spectra, or four bands in the case of C_{3v} symmetry.

Figs 6.16 T.o.f. spectra (10K) of MnNaA zeolite plus adsorbed C_3H_6, coverage 1·2 molecules per pseudo-unit cell. The background spectra of the dehydrated zeolite have been subtracted.

Fig 6.16a Scattering angle 63.6°.

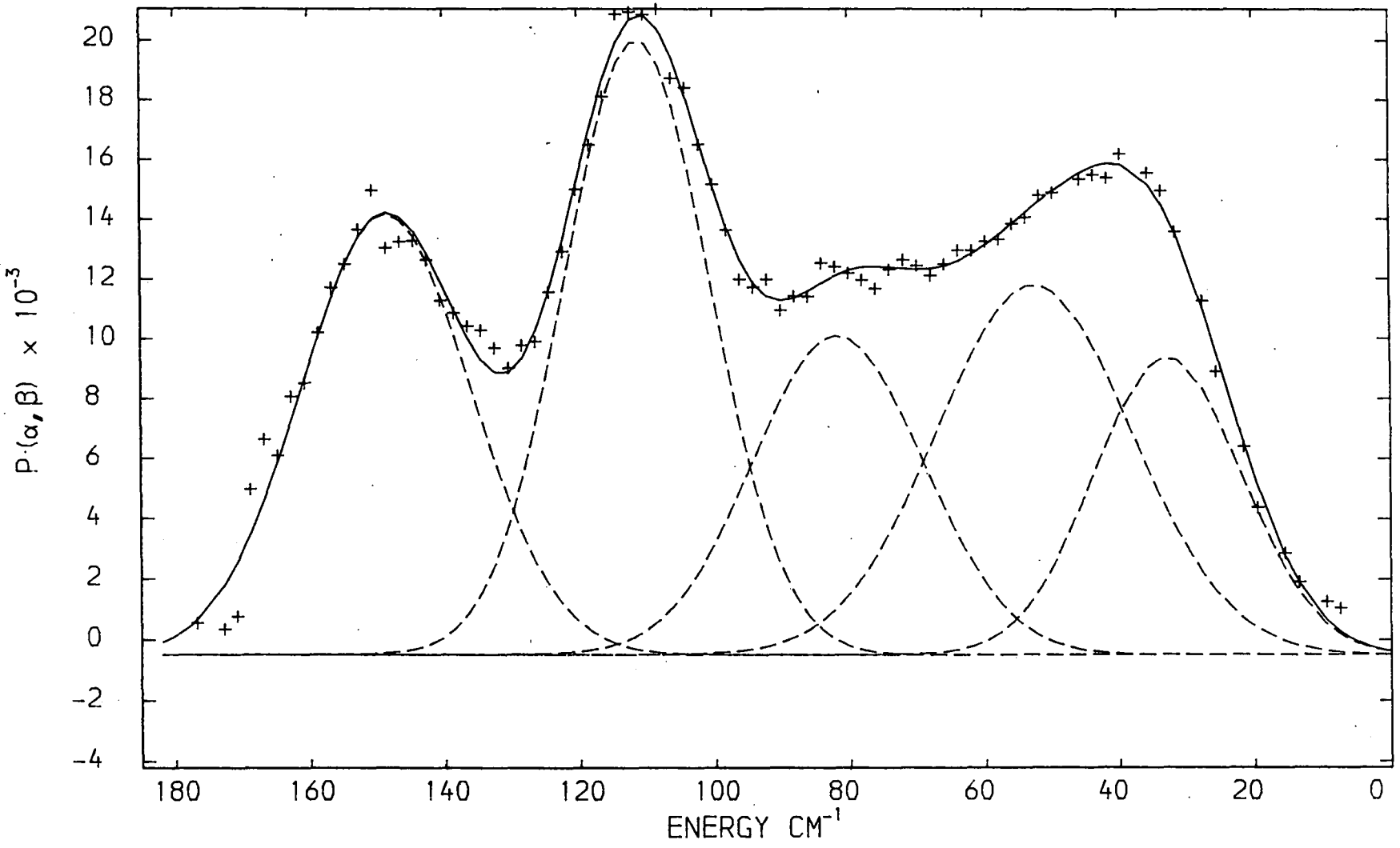

Fig. 6.16b MnNaA zeolite plus C_3H_6, coverage 1·2 molecules per pseudo-unit cell, background subtracted.
Scattering angle 88·9°, temperature 10K.

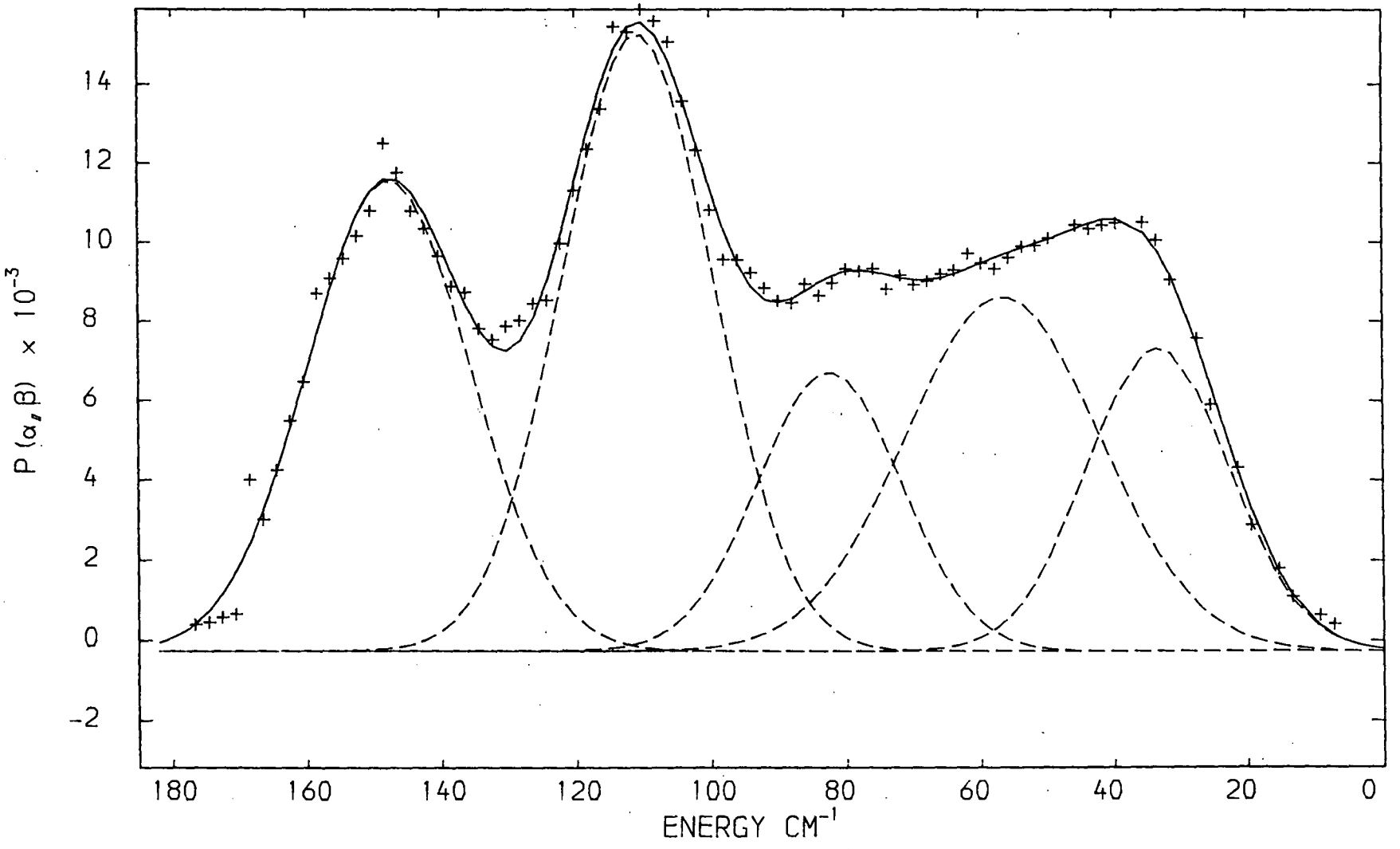

Fig 6.16c MnNnA zeolite plus C_3H_6, coverage 1.2 molecules per pseudo-unit cell, background subtracted.
Scattering angle 136.1°, temperature 10K.

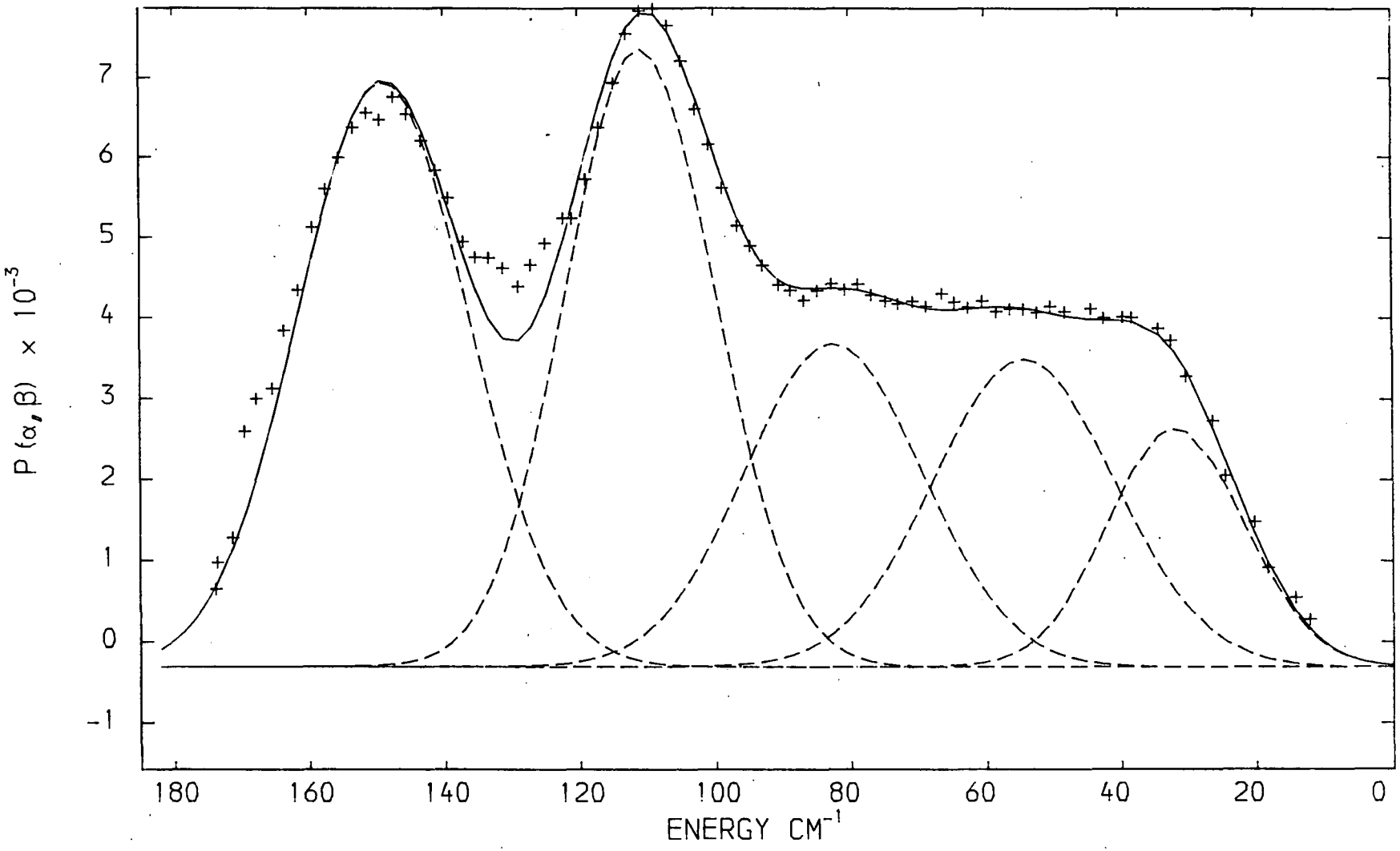

Figs 6.17 T.o.f. spectra (10K) of MnNaA zeolite plus adsorbed C_3D_6, coverage 1·5 molecules per pseudo-unit cell. The background spectra of the dehydrated zeolite have been subtracted.

Fig 6.17a Scattering angle 64·5°.

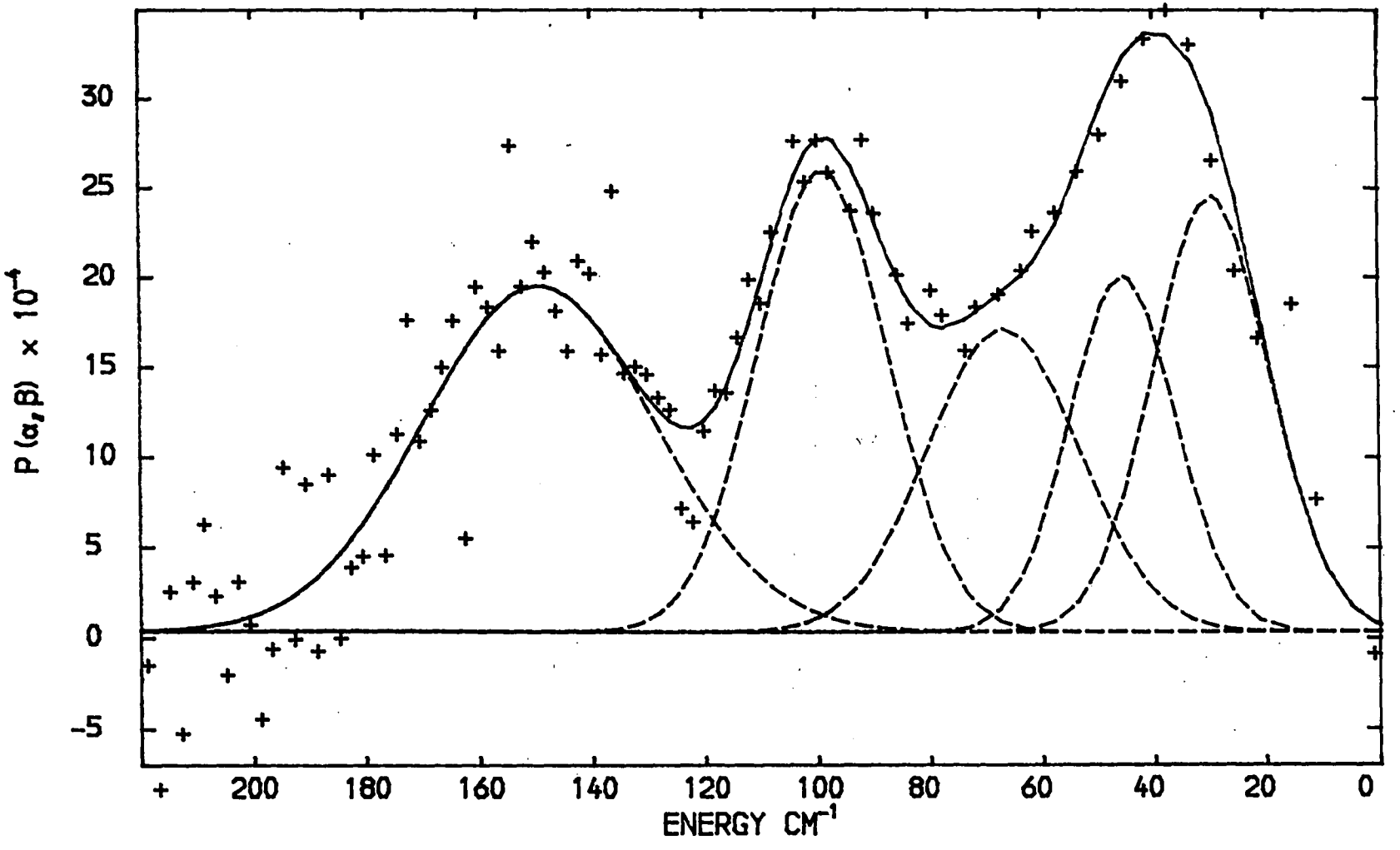

Fig 6.17b MnNaA zeolite plus C_3D_6, 1·5 molecules per pseudo-unit cell, background subtracted. Scattering angle 92·3°, temperature 10K.

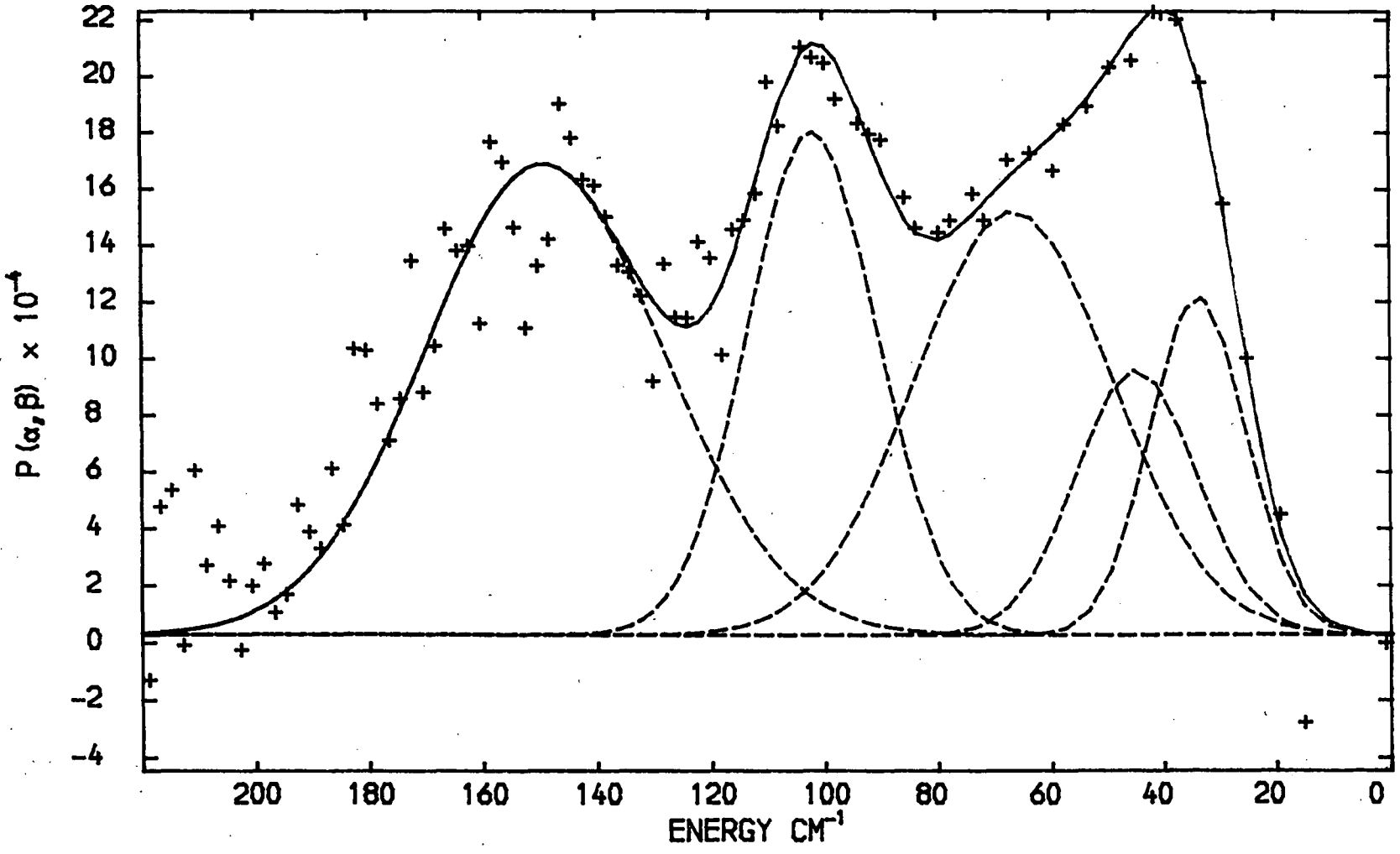

Fig 6.17c MnNaA zeolite plus C_3D_6, 1·5 molecules per pseudo-unit cell, background subtracted. Scattering angle 137·3°, temperature 10K.

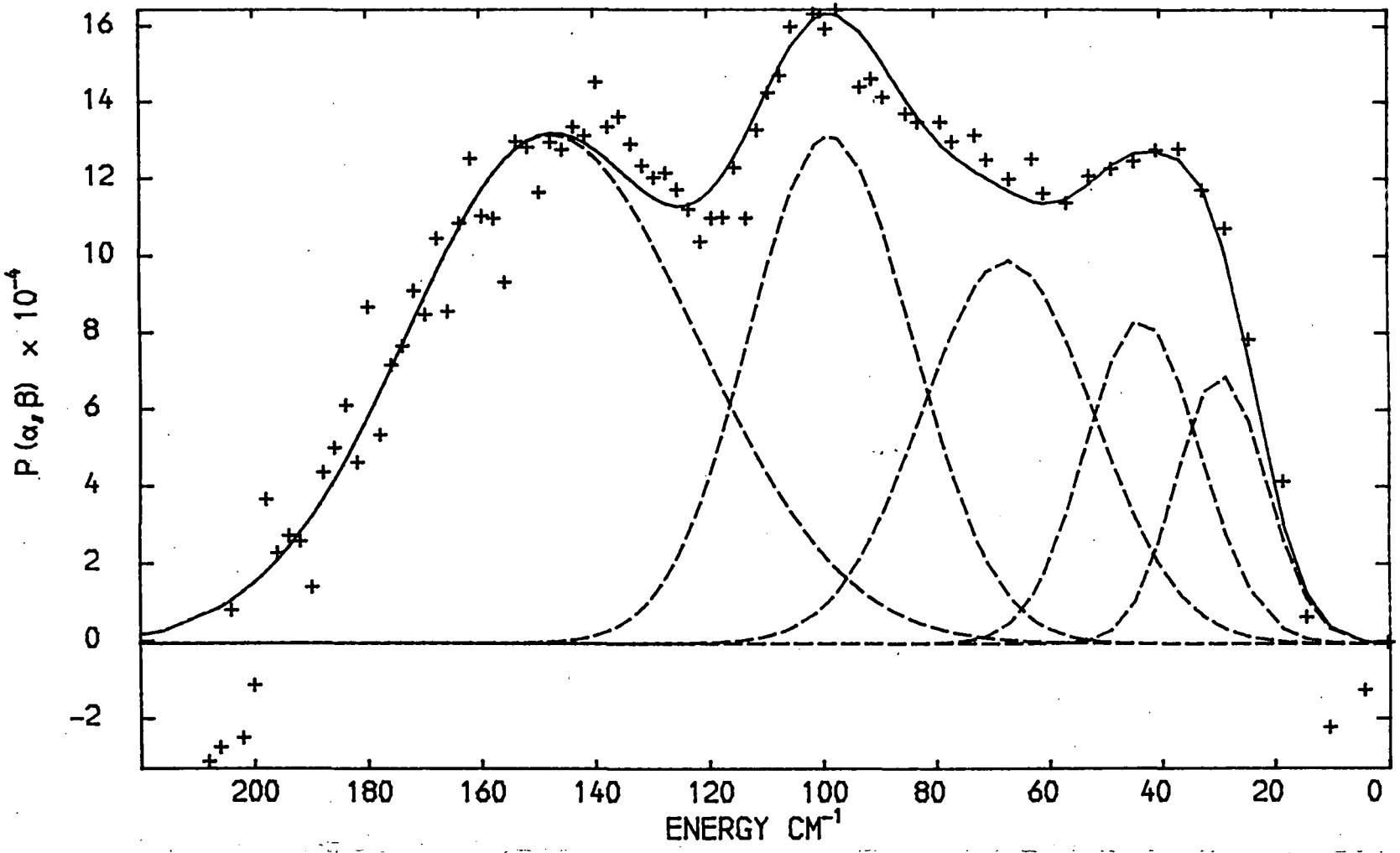

Figs 6.18 T.o.f. spectra (10K) of MnNaA zeolite plus adsorbed C_3D_6, coverage 2·3 molecules per pseudo-unit cell. The background spectra of the dehydrated zeolite have been subtracted.

Fig 6.18a Scattering angle 64·5°.

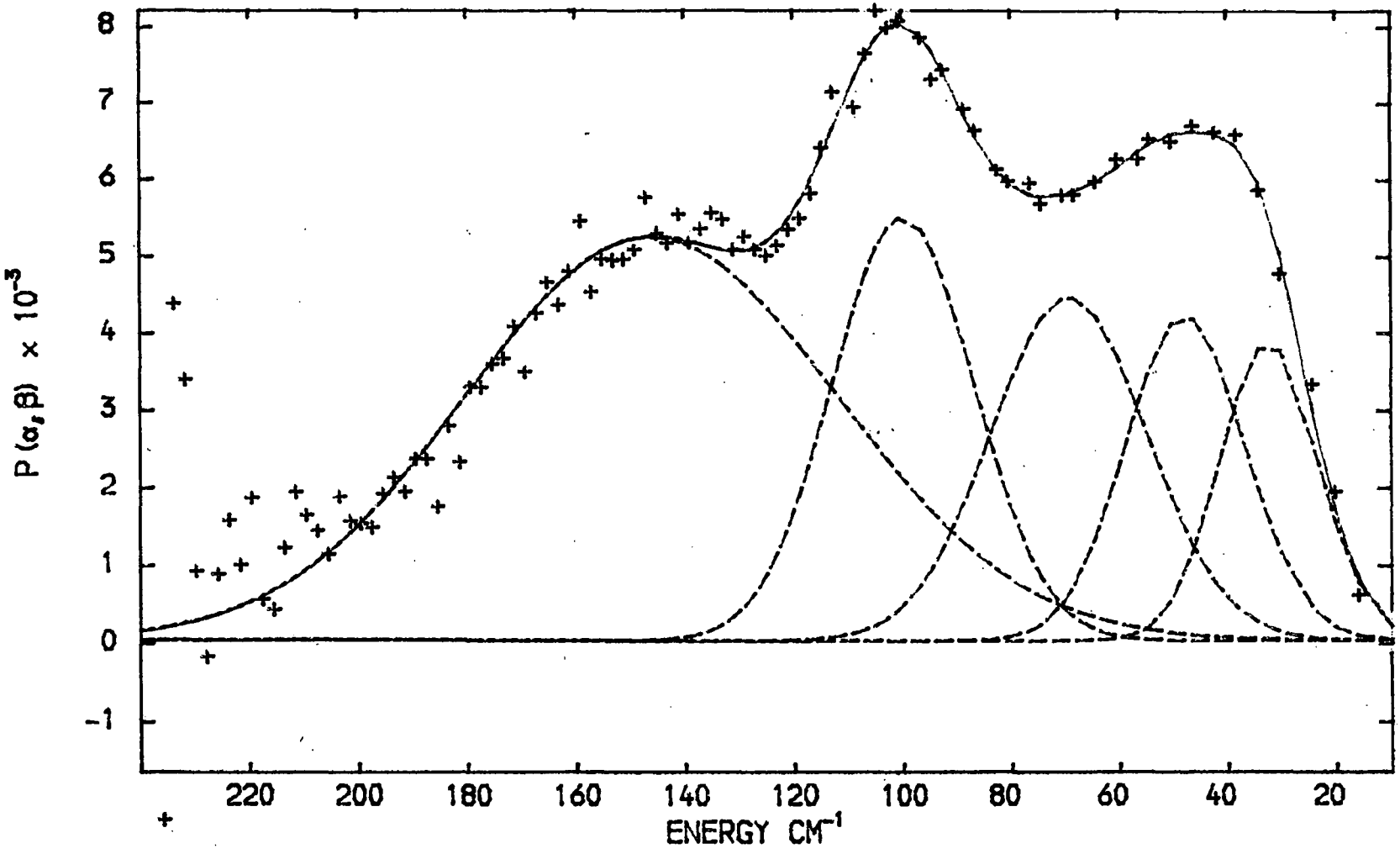

Fig 6.18b MnNaA zeolite plus C_3D_6, coverage 2·3 molecules per pseudo-unit cell, background subtracted.
Scattering angle 92·3°, temperature 10K.

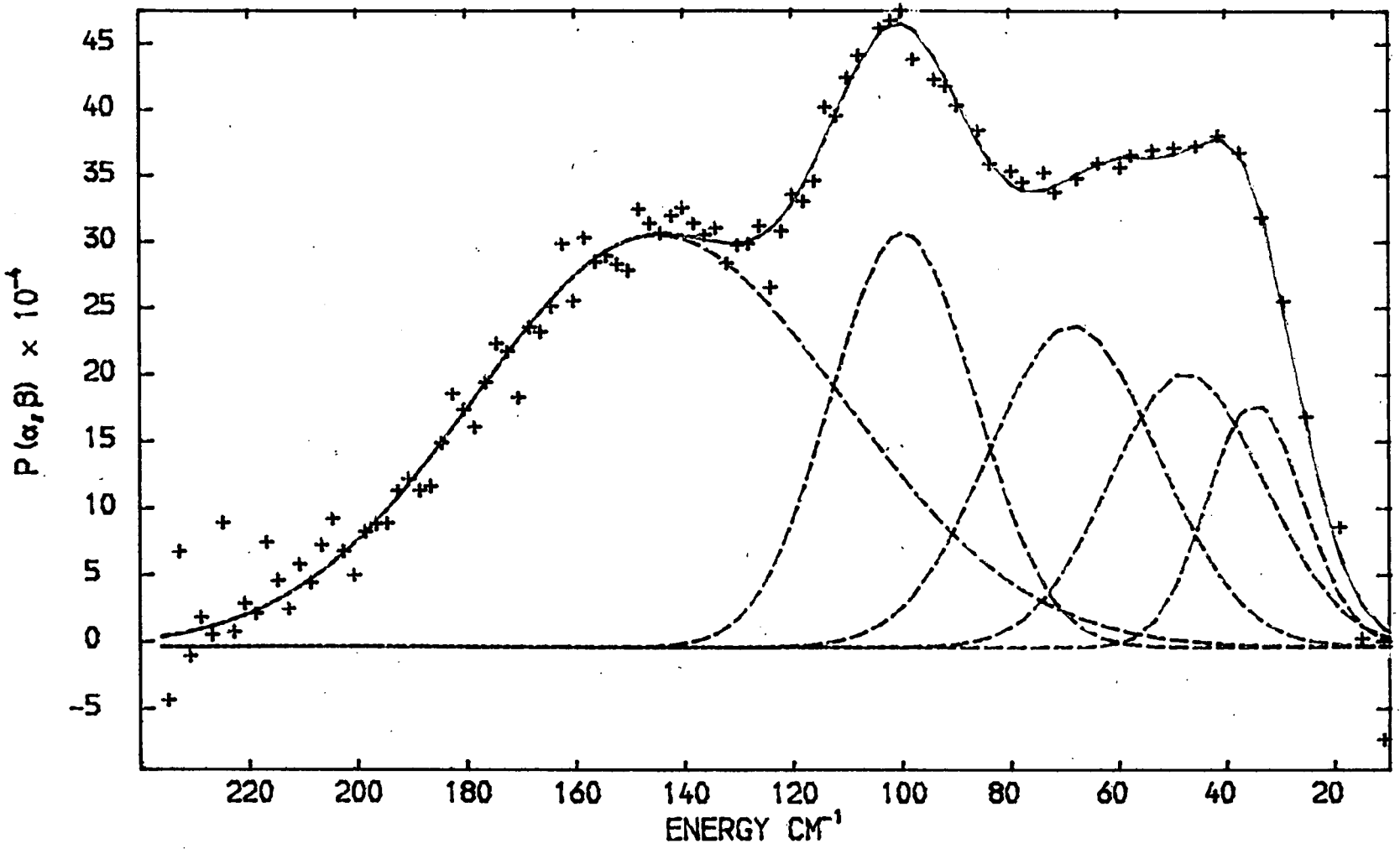

Fig 6.18c MnNaA zeolite plus C_3D_6, coverage 2·3 molecules per pseudo-unit cell, background subtracted.
Scattering angle 137·3°, temperature 10K.

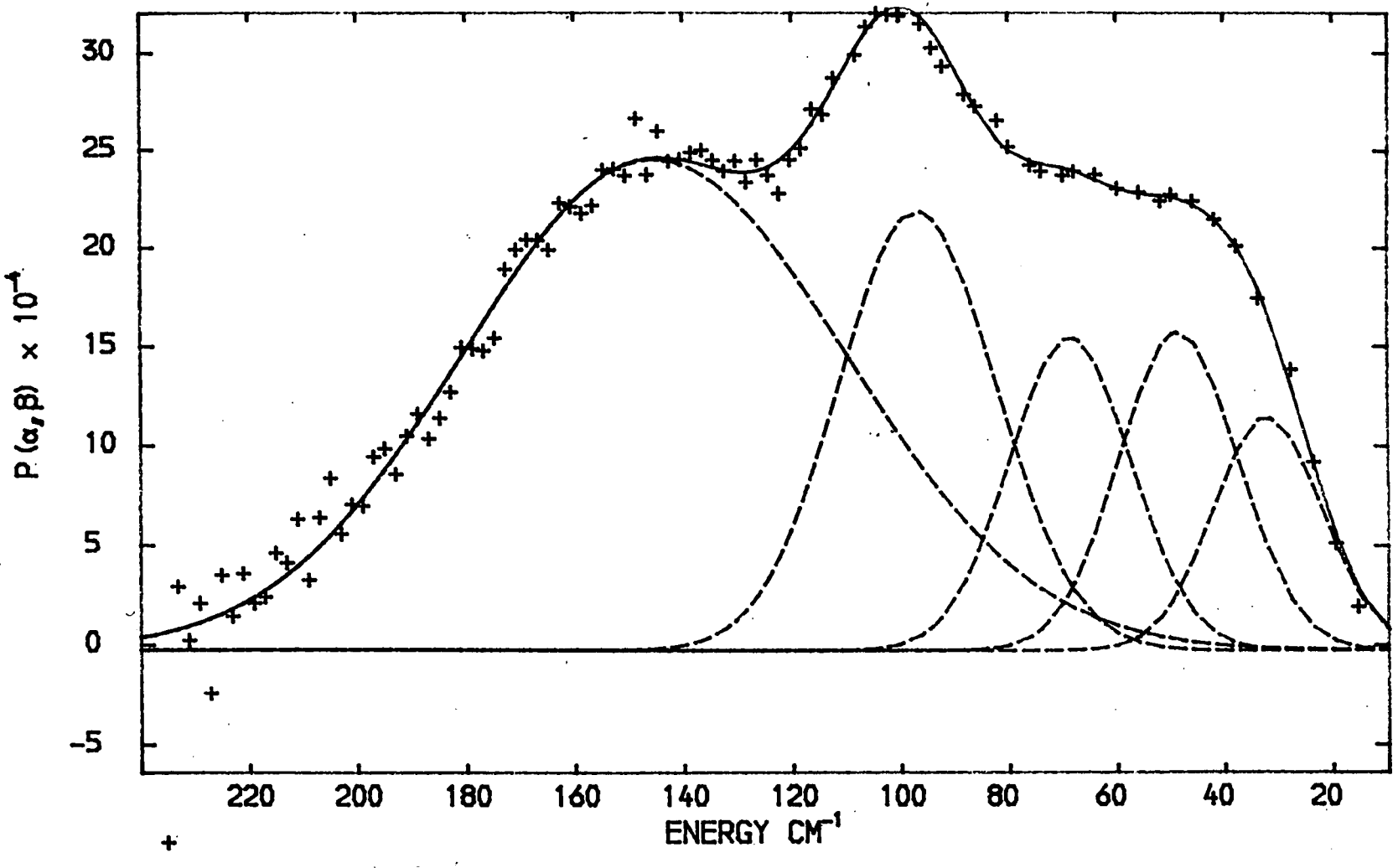

TABLE 6.9 Assignment of the t.o.f. spectra of cyclopropane-h_6, adsorbed in MnNaA zeolite (10K), assuming C_{3v} symmetry for the adsorption complex

sample	MnNaA+C_3H_6, θ=1.2											
scattering angle, °	63.6°				88.9°				136.1°			
figure	6.16a				6.16b				6.16c			
assignment	ν, cm^{-1}	Q^2, $Å^{-2}$	I^P_{OBS}	I^P_{CALC}	ν, cm^{-1}	Q^2, $Å^{-2}$	I^P_{OBS}	I^P_{calc}	ν, cm^{-1}	Q^2, $Å^{-2}$	I^P_{OBS}	I^P_{CALC}
t_x and t_y	149	10.0	1.7	1.7	148	15.6	1.8	2.1	149	25.2	3.1	3.0
τ_x and τ_y	111	10.6	2.0	4.8	111	17.8	2.1	4.1	111	30.2	2.9	5.1
τ_z (	82[a]	11.3	1.2	2.1[a]	82	19.4	0.9	2.4[a]	83	33.6	1.8	2.7[a]
+ (												
(	53[a]	12.1	1.6	2.0[a]	57	20.4	1.6	2.0[a]	54	36.8	1.7	2.0[a]
? (												
t_z	33	12.7	1.0	1.0	33	22.3	1.0	1.0	32	39.2	1.0	1.0

Notes

ν band frequency, $\hbar Q$ = momentum transfer during the scattering event, I^P_{OBS} = ratio of observed band intensities, I^P_{CALC} = ratio of calculated band intensities

a. The spectrum was unresolved in this region and was approximately fitted to two Gaussian curves, one of which was assigned to τ_z, the other remaining unassigned. It could not be determined which fitted curve was best assigned to τ_z. The value of I^P_{CALC} for each of these two bands refer to that calculated for a τ_z mode arising at the given frequency.

TABLE 6.10 Assignment of the t.o.f. spectra of cyclopropane-d_6 adsorbed in MnNaA zeolite (10K), assuming C_{3v} symmetry for the adsorption complex

sample	MnNaA+C_3D_6 (θ= 1.5)											
scattering angle, figure	64.5° 6.17a				92.3° 6.17b				137.3° 6.17c			
assignment	ν, cm^{-1}	Q^2, $Å^{-2}$	I^P_{OBS}	I^P_{CALC}	ν, cm^{-1}	Q^2, $Å^{-2}$	I^P_{OBS}	I^P_{CALC}	ν, cm^{-1}	Q^2, $Å^{-2}$	I^P_{OBS}	I^P_{CALC}
t_x and t_y	149	13.6	1.6	2.6	149	23.4	3.4	4.5	147	37.9	6.1	9.7
τ_x and τ_y	99	14.8	1.2	4.7	102	26.3	2.0	7.2	99	43.8	3.4	13.3
τ_z (												
+ (	67[a]	15.8	0.9	2.5[a]	67	28.6	2.6	3.9[a]	67	47.3	2.7	7.0[a]
? (	46[a]	16.4	0.8	2.4[a]	45	29.9	1.0	3.3[a]	44	49.9	1.5	5.0[a]
t_z	30	16.9	1.0	1.0	34	30.1	1.0	1.0	29	51.5	1.0	1.0

sample	MnNaA+C_3D_6 (θ= 2.3)											
scattering angle, figure	64.5° 6.18a				92.3° 6.18b				137.3° 6.18c			
assignment	ν, cm^{-1}	Q^2, $Å^{-2}$	I^P_{OBS}	I^P_{CALC}	ν, cm^{-1}	Q^2, $Å^{-2}$	I^P_{OBS}	I^P_{CALC}	ν, cm^{-1}	Q^2, $Å^{-2}$	I^P_{OBS}	I^P_{CALC}
t_x and t_y	146	13.6	5.1	1.5	145	23.6	6.4	1.9	145	38.2	7.4	2.3
τ_x and τ_y	100	14.8	2.1	3.2	100	26.5	2.5	3.6	97	44.0	2.7	4.3
τ_z (												
+ (	69[a]	15.7	1.9	1.8[a]	68	28.4	2.3	1.3[a]	69	47.2	1.5	1.1[a]
? (	48[a]	16.3	1.3	1.8[a]	47	29.7	1.8	1.9[a]	49	49.4	1.5	1.9[a]
t_z	32	16.8	1.0	1.0	35	30.5	1.0	1.0	32	51.2	1.0	1.0

Note a: Please see footnote (a) of table 6.9

Because of the overall similarity between the t.o.f. spectra of $C_3{}^1H_6$ adsorbed on MnNaA and CoNaA zeolites (Figs.6.16, 6.9), we consider that the Mn-C_3H_6 complex is of C_{3v} symmetry. The question of the fifth, additional INS band is discussed below.

We will use equation 6.1 to predict the relative intensities, I^P, of the INS bands of the C_{3v} adsorption complex, assuming that the bands arise from the fundamental modes of harmonic oscillators. The plots of $\ln I^P_{OBS}$ against Q^2 used to obtain the Debye-Waller factors for H and D of the $C_3{}^1H_6$ and C_3D_6 adsorbates are shown in Figs. 6.19 to 6.21. The numerical values of the $\langle U_i^2(\tilde{\nu})\rangle$ obtained (Figs. 6.19 to 6.21) are discussed in Section 6.5.11.

The relative INS band intensities calculated using these values for C_3H_6 adsorbed in MnNaA zeolite are listed in Tables 6.9 and 6.10. In these tables, the bands fitted at 82 and *ca.* 53 cm^{-1} ($C_3{}^1H_6$, Table 6.9) and at *ca.* 69 and 48 cm^{-1} (C_3D_6, Table 6.10) are taken to represent unresolved intensity from the τ_z mode of adsorbed C_3H_6 and some other, unassigned mode. The calculated intensity listed for each of these bands refers to the relative band intensity which would be given by a pure τ_z mode arising at that frequency.

(i) MnNaA + $C_3{}^1H_6$, θ = 1.2

For this sample, there is excellent agreement between the observed and predicted relative intensity of the 149 cm^{-1} band (Table 6.9). The fitting of five bands to the spectrum has reduced the I^P_{OBS} of the 111 cm^{-1} band in favour of the intensity of the 82 and 53 cm^{-1} bands. This comment also applies to the three middle frequency bands of the C_3D_6 data (Table 6.10).

Fig. 6.19 A plot of ln I^P against Q^2 for the the INS spectra of MnNaA+C_3H_6, coverage 1.2 molecules per supercage, 10K (see fig. 6.16).

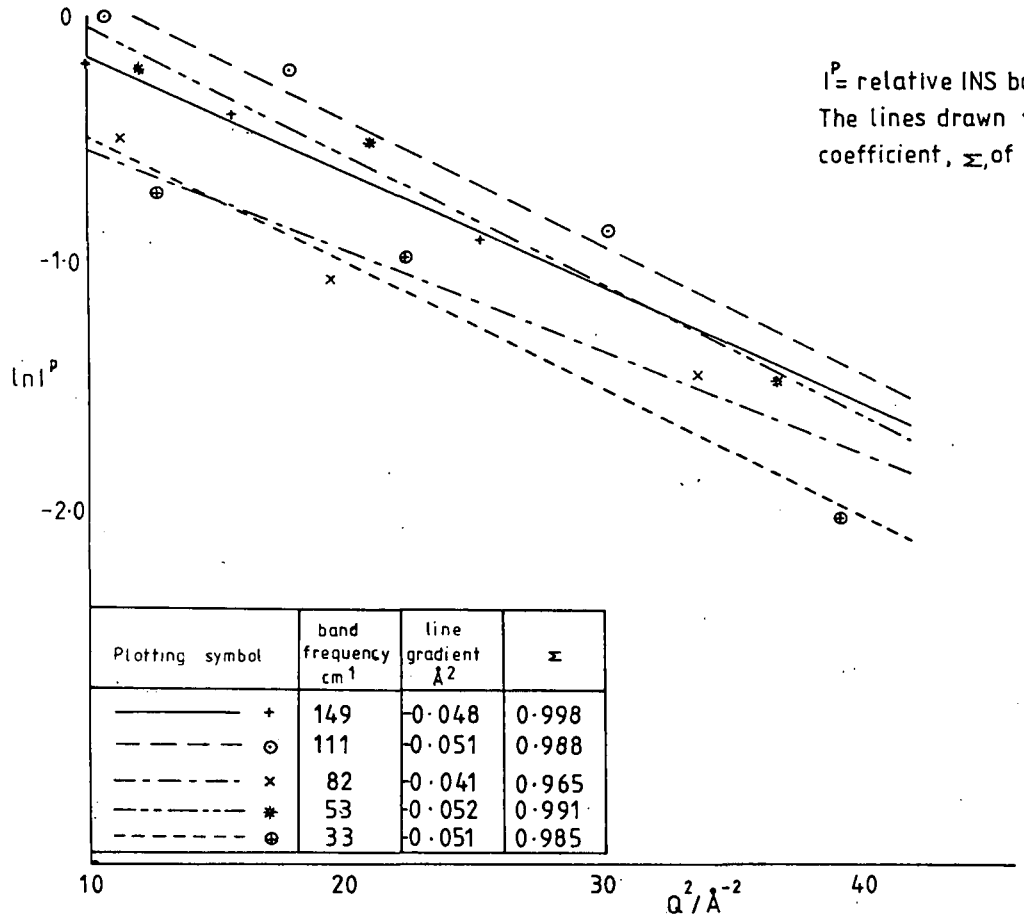

Plotting symbol	band frequency cm⁻¹	line gradient Å²	Σ
——— +	149	-0·048	0·998
— — — ⊙	111	-0·051	0·988
— - — - ×	82	-0·041	0·965
— - - — *	53	-0·052	0·991
- - - - ⊕	33	-0·051	0·985

I^P = relative INS band intensity $\hbar Q$ = momentum transfer during scattering event. The lines drawn through the points are least squares fits. The correlation coefficient, Σ, of the fits are listed in the key.

Fig. 6.20 A plot of ln I^P against Q^2 for the INS spectra of MnNaA+C_3D_6, coverage 1.5 molecules per supercage, 10K (see fig. 6.17).

I^P = relative INS band intensity $\hbar Q$ = momentum transfer during scattering event. The lines drawn through the points are least squares fits. The correlation coefficient, Σ, of the fits are listed in the key.

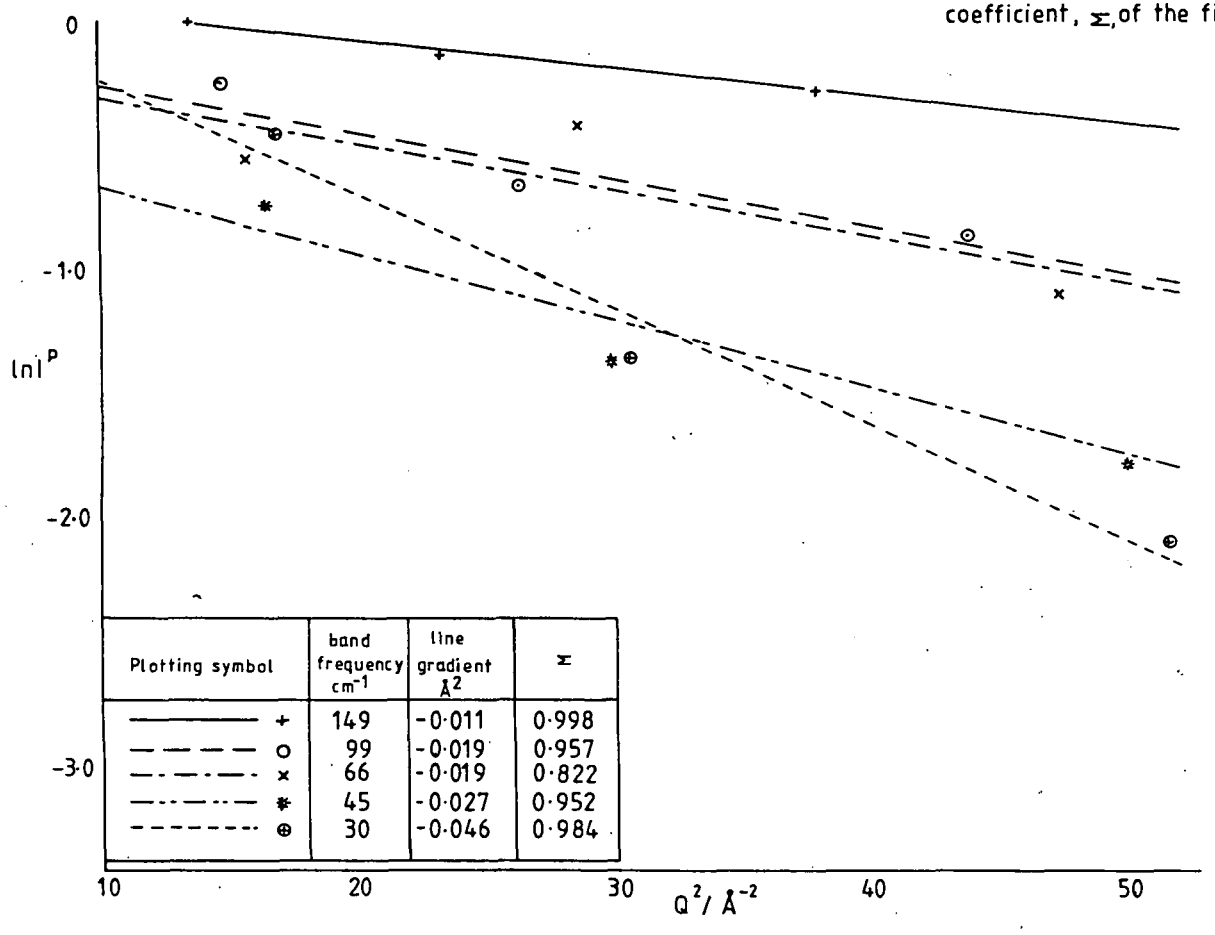

Plotting symbol	band frequency cm^{-1}	line gradient $Å^2$	Σ
——— +	149	-0·011	0·998
— — — — o	99	-0·019	0·957
—·—·—· ×	66	-0·019	0·822
—··—··— *	45	-0·027	0·952
- - - - - - - ⊕	30	-0·046	0·984

Fig. 6.21 A plot of ln I^P against Q^2 for the INS spectra of MnNaA+C_3D_6, coverage 2.3 molecules per supercage, 10K (see fig. 6.18).

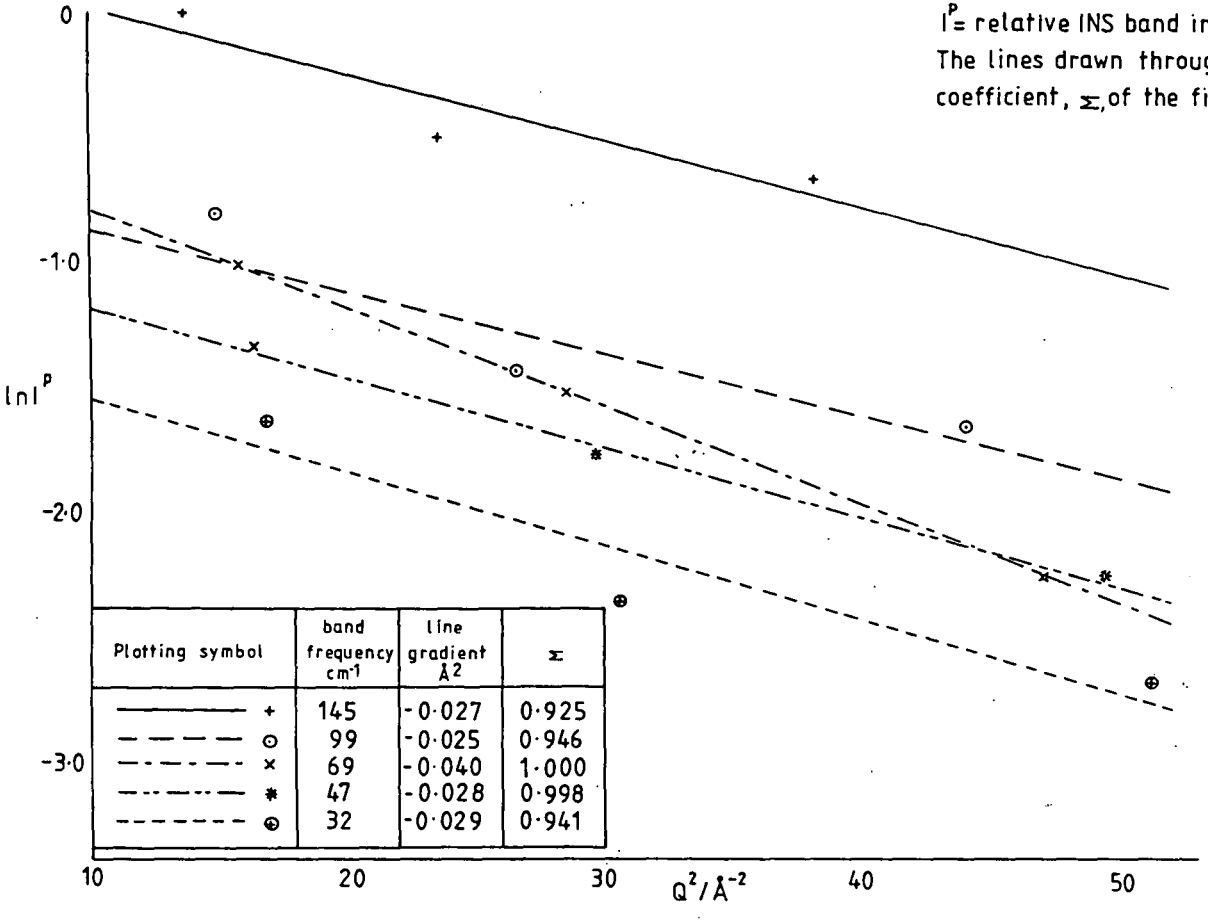

I^P = relative INS band intensity $\hbar Q$ = momentum transfer during scattering event. The lines drawn through the points are least squares fits. The correlation coefficient, Σ, of the fits are listed in the key.

(ii) MnNaA + C_3D_6, θ = 2.3

The trends with frequency and Q^2 of the observed band intensities, I^P_{OBS}, of the *ca.* 100, 69 and 48 cm^{-1} bands are reproduced by the calculated values, I^P_{CALC} (Table 6.10). The *ca.* 146 cm^{-1} band is observed to be very much more intense than calculated for the degenerate t_x and t_y fundamentals. This band is also of much greater intensity than those at lower frequencies. We can calculate the contribution to the observed intensity of the 146 cm^{-1} band from the first overtone of the τ_z mode, which for these purposes we assume to have a fundamental frequency of 69 cm^{-1} (2 x 69 = 138 cm^{-1}). If $I(t_x+t_y)$ is the calculated intensity of the 146 cm^{-1} band and $I(2\tau_z)$ is that of the first overtone of the τ_z mode at 138 cm^{-1}, then from Chapter Two:

$$\frac{I(t_x+t_y)}{I(2\tau_z)} = \frac{Z(\tilde{\nu}_1)\exp(-Q_1^2\langle u_1^2\rangle)/\mu_1}{Q_2^2 Z(\tilde{\nu}_2)(r_a+1)\exp(-Q_2^2\langle U_2^2\rangle)/(2\mu_2\omega_2)}$$

where the subscript 1 denotes quantities appertaining to the $t_x + t_y$ band and subscript 2 to $2\tau_z$;

$Z(\tilde{\nu}_1)$ is the vibrational density of states at frequency $\tilde{\nu}_1$ cm^{-1};

μ_1 and μ_2 denote the reduced masses of the oscillator, equal to 0.1250 and 0.2378 amu respectively;

$\tilde{\nu}_1$ is the frequency of the $t_x + t_y$ band (146 cm^{-1});

$\tilde{\nu}_2$ is the frequency of the τ_z fundamental (69 cm^{-1}) and

ω_2 its angular frequency;

$\hbar Q_1$ is the momentum transfer at 146 cm^{-1} (Table 6.10);

$\hbar Q_2$ is the momentum transfer for the $2\tau_z$ overtone at 138 cm^{-1},

Q_2^2 is equal to 13.8, 24.0 and 39.0 $Å^{-2}$ for scattering angles of 64.5, 92.3 and 137.3° respectively;

$$\text{and } r_a + 1 = \frac{\exp(\hbar c\tilde{\nu}/(2K_B T))}{2\sinh(\hbar c\tilde{\nu}/(2K_B T))}$$

where c in $cm.s^{-1}$ is the velocity of light, T the absolute temperature and K_B is Boltzmann's constant. Anticipating Section 6.5.11(c) below, we make the approximation that the D atoms of adsorbed C_3D_6 behave as isotropic oscillators and take $\langle U^2 \rangle = 65 \times 10^{-3}$ Å^2 for both the $2\tau_z$ overtone and the t_x and t_y fundamentals. For scattering angles of 64.5, 92.3 and 137.3° (Table 6.10), we calculate the intensity ratio $I(t_x+t_y)/(2\tau_z)$ in the MnNaA + C_3D_6(θ=2.3) spectra to be equal to 10.7, 6.2 and 3.9, respectively. Thus the contribution to the intensity of the 146 cm^{-1} band in the MnNaA + C_3D_6(θ=2.3) spectra (Table 6.10) from $2\tau_z$ is calculated to increase markedly as the scattering angle is raised. However, the discrepancy, of a factor of *ca* 3.4, between the values of I^P_{OBS} and I^P_{CALC} for the 146 cm^{-1} band of this sample remains approximately constant with scattering angle (Table 6.10, lower half). Therefore, the high observed intensity of the 146 cm^{-1} band in the MnNaA + C_3D_6 (θ=2.3) spectrum (Table 6.10) does not arise from a large contribution from $2\tau_z$. We are unable to completely explain the intensity of the 146 cm^{-1} band.

(iii) MnNaA + C_3D_6, θ = 1.5

The agreement between the observed and calculated band intensities (Table 6.10) is poor. This can be ascribed to the poor statistics of the t.o.f. spectra (Figs. 6.17) - the fitted band intensities I^P_{OBS} are subject to possible large errors. This also affects the values of I^P_{CALC} since the estimated values of $\langle U^2 \rangle$ (equation 6.1) are not as reliable as for the other zeolite/C_3H_6 samples. It is because of errors

in $\langle U^2 \rangle$ that the I^P_{CALC} for bands at approximately equal frequencies in the low and high coverage MnNaA + C_3D_6 data are dissimilar in several cases (Table 6.10).

At the highest setting angle, 137.3°, the observed intensities of the low frequency bands are considerably reduced by the high values of Q^2 - *c.f.* Figs.6.17 and 6.17(c). Thus the largest errors in the curve fitting arise for three bands, and the discrepancies between the I^P_{OBS} and I^P_{CALC} is greatest for the 137.3° spectrum.

(b) The deuteration shifts of the intrazeolite Mn-C_3H_6 complex

The observed deuteration shifts of the bands in the t.o.f. spectra of the Mn-C_3H_6 complex are given in Table 6.11 along with those calculated for a complex of C_{3v} symmetry. Since there is no systematic variation of the frequency of the INS bands with scattering angle, the observed shifts were calculated by taking the average value of the quantities

$$\frac{\nu_D,\text{min}}{\nu_H,\text{max}} \quad \text{and} \quad \frac{\nu_D,\text{max}}{\nu_H,\text{min}}$$

where "min" refers to the lowest frequency of the band in the spectra at all three scattering angles of a given mode of a given sample (Tables 6.9, 6.10), and "max" refers to the highest frequency. The tabulated errors in the deuteration shifts are simply the difference between this average value and $\nu_D,\text{min}/\nu_H,\text{max}$ (Table 6.11). Since the deuteration shifts calculated for the torsions of both a C_{3v} and a C_{2v} complex are of the same magnitude, and smaller than the shifts of the translational modes (Table 6.7), these shifts cannot be used on their own to determine the adsorption geometry. However, the shifts for MnNaA+C_3H_6 are consistent with our assignment under the C_{3v} point group of the observed bands (Table 6.11).

TABLE 6.11 The deuteration shifts of the bands in the t.o.f. spectra of cyclopropane adsorbed in MnNaA zeolite (10K)

The spectra are shown in Figs.6.16 to 6.18 and summarised in Tables 6.9 and 6.10.

observed deuteration shift		calculated deuteration shift $\left(\nu_D/\nu_H\right)$	mode
$\frac{\nu_D, \theta = 1.5}{\nu_H, \theta = 1.2}$	$\frac{\nu_D, \theta = 2.3}{\nu_H, \theta = 1.2}$		
1.00 ±0.01	1.00 ±0.01	0.94	t_x and t_y
0.91 ±0.01	0.89 ±0.01	0.87	t_x and t_y
0.812 ±0.005	0.83 ±0.01	0.87[a]	τ_z and ?
0.82 ±0.05	0.87 ±0.05		
0.95 ±0.07	1.00 ±0.09	0.94	t_z

θ = surface coverage of $C_3{}^1H_6$ or C_3D_6 in molecules per supercage

The deuteration shifts are those calculated for a C_{3v} adsorption complex.

Note a. The listed deuteration shift refers to the τ_z component only of an unresolved feature in this region of the spectra.

(c) The 50 to 100 cm^{-1} region of the MnNaA + $C_3{}^1H_6$ t.o.f.spectra

The unresolved intensity in the 50 to 100 cm^{-1} region of the MnNaA + $C_3{}^1H_6$ spectra (Fig.6.16, Table 6.9) has been ascribed to the τ_z mode of adsorbed $C_3{}^1H_6$ and some other transition of about equal intensity (Section 6.5.9 (a) (i)). Although two bands, at *ca.* 82 and 53 cm^{-1}, have been fitted to this region, there exists no unique fit to the data and we have not assigned the τ_z mode to either band. We do state that the τ_z torsion of Mn-$C_3{}^1H_6$ occurs in the range 82 to 53 cm^{-1}. The transition which is unresolved from τ_z remains unassigned. It is unlikely to be an overtone of the t_z mode, the fundamental of which

occurred at 33 cm^{-1} in the spectrum of MnNaA+$C_3{}^1H_6$ (Fig.6.16, Table 6.9). We have rejected this explanation since the overtone was not observed in the CoNaA + $C_3{}^1H_6$ t.o.f. spectra (Fig.6.8). A second explanation of the unassigned transition is that the 82 and 53 cm^{-1} bands arise from splitting of the τ_z mode through interaction of cyclopropane molecules adsorbed within the same supercage, as was observed in the high coverage t.o.f. spectrum of CoNaA + $C_3{}^1H_6$ (θ = 1.8, Fig. 6.11). However, this explanation must also be rejected, on intensity grounds. For example, the coverage of θ = 1.2 used for the spectrum of MnNaA + $C_3{}^1H_6$ (Figs.6.16) is too low for these so-called[42] correlation field effects to have given rise to the strong but unresolved intensity in the region *ca.* 50 to 80 cm^{-1}.

Similar considerations apply to the *ca.* 80 to 45 cm^{-1} region of the MnNaA + C_3D_6 t.o.f. results, to which two bands at about 67 and 46 cm^{-1} were fitted (Figs. 6.17, 6.18, Table 6.10).

(d) Summary of the assignment of the MnNaA+C_3H_6 t.o.f. spectra.

By analogy with the CoNaA+C_3H_6 data (Section 6.4.4), the t.o.f. spectra of cyclopropane adsorbed on MnNaA zeolite (Figs. 6.16 to 6.18) have been assigned taking the symmetry of the adsorption complex to be C_{3v}. Given the lack of resolution in the 50 to 100 cm^{-1} region of the MnNaA+$C_3{}^1H_6$ spectra, the resulting assignment scheme is not inconsistent with the observed results.

6.5.10 The b.f.d. spectrum of MnNaA + C_3H_6

The b.f.d. spectrum obtained at 77K for a coverage of θ = 1.8 molecules per supercage is shown in Fig. 6.22. A

Fig. 6.22 Beryllium filter detector (DIDO b.f.d.) spectrum (77K) of MnNaA zeolite plus C_3H_6, coverage 1.8 molecules per supercage. A background spectrum of the dehydrated zeolite has been subtracted.

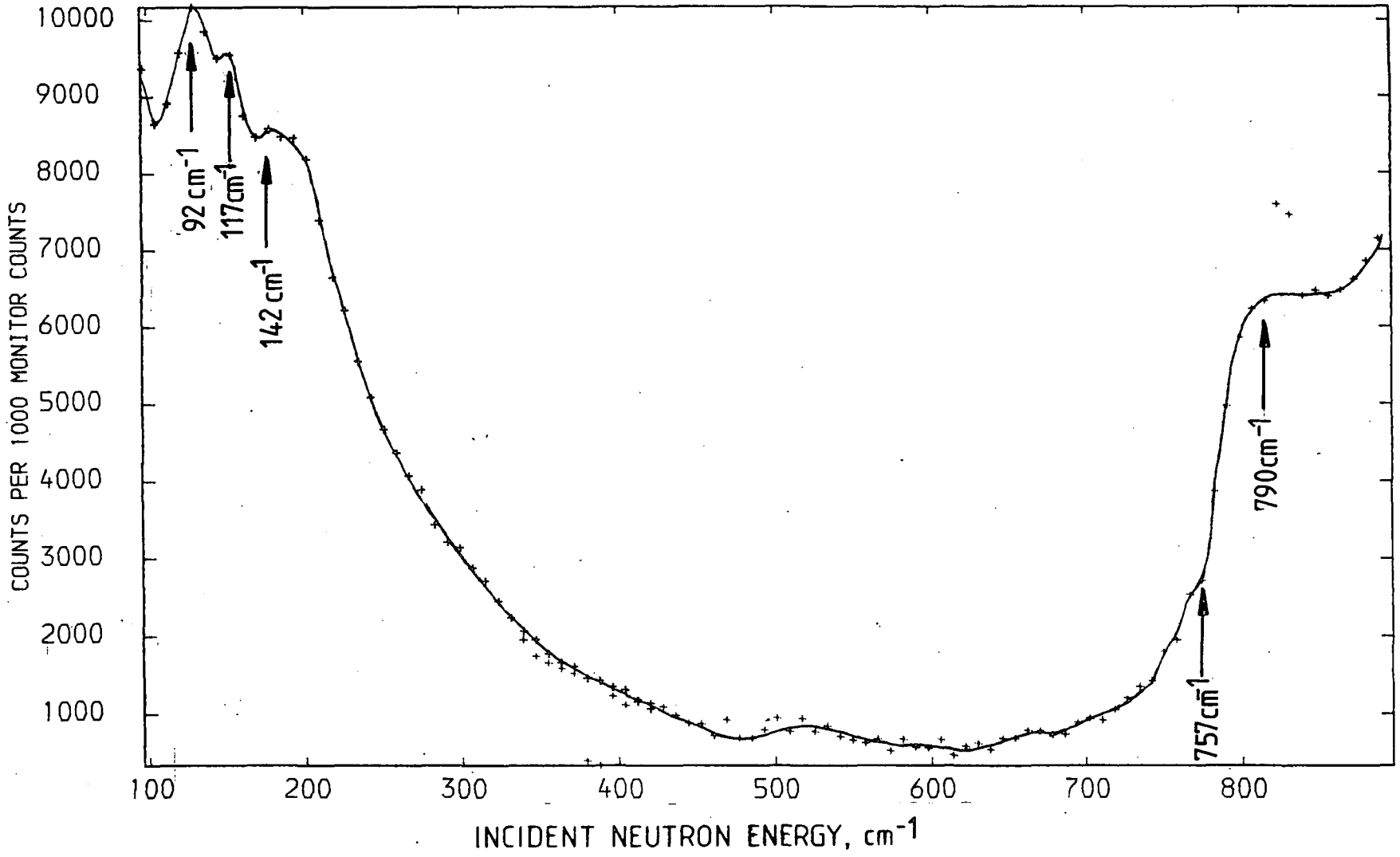

strong band at 142 cm^{-1} is assigned to the degenerate t_x and t_y modes of adsorbed C_3H_6 which occurred at 149 cm^{-1} in the t.o.f. results (Fig. 6.16). A broad feature with peaks at 92 and 117 cm^{-1} in Fig. 6.22 must contain a significant contribution from the degenerate τ_x and τ_y modes of adsorbed C_3H_6 which were observed at 111 cm^{-1} in the t.o.f. spectra (Fig.6.16). There is a poor correspondence between the b.f.d. (Fig. 6.22) and t.o.f. (Fig.6.16) spectra of MnNaA + C_3H_6 at and below *ca.* 142 cm^{-1}. Similar discrepancies were observed between the b.f.d. and t.o.f. spectra of CoNaA + C_3H_6 and possible reasons were discussed in Section 6.5.6. The same arguments will apply to the MnNaA + C_3H_6 data.

A broad band at 790 cm^{-1} in Fig. 6.22 is assigned to unresolved intensity from the perturbed internal modes ν_7 and ν_{11} of adsorbed C_3H_6 and a weak shoulder at 757 cm^{-1} to the ν_{14} mode. (The frequencies of these modes in the gas phase are: ν_7, 854 cm^{-1}; ν_{11}, 869 cm^{-1}; ν_{14} 739 cm^{-1} (Table 6.1)). This region of the b.f.d. spectrum is very similar to that observed for CoNaA + C_3H_6 (Section 6.5.6).

A b.f.d. spectrum of MnNaA + C_3H_6 was obtained at 77K for a lower coverage of θ = 0.9. This spectrum also showed the bands at 92, 117 and 142 cm^{-1}. No other bands were observed, the statistics above 750 cm^{-1} being poor. We have not shown this spectrum since it is so similar to the high coverage case.

The most important aspect of the b.f.d. spectra of MnNaA + C_3H_6 (Fig. 6.22) is the absence of bands between 142 and 790 cm^{-1}. Thus all the external modes of adsorbed C_3H_6 lie within the frequency range of the t.o.f. spectra (Fig.6.16).

6.5.11 The mean square displacements of the atoms of cyclopropane adsorbed in MnNaA and CoNaA

Firstly, we discuss the errors in the values of the $\langle U_i^2(\tilde{\nu})\rangle$ estimated from our INS spectra for the H (or D) atoms of adsorbed cyclopropane. The errors are difficult to quantify since they depend on the accuracy of the fitting of Gaussians to the observed spectra.

(a) Adsorbed cyclopropane-h_6

For $C_3{}^1H_6$ adsorbed at low coverage in CoNaA, and in MnNaA, there is a variation of *ca.* 23% between the $\langle U_i^2(\tilde{\nu})\rangle$ for the modes of each sample (Figs. 6.10, 6.19). This variation is unlikely to be greater than the errors in the determination of $\langle U_i^2(\tilde{\nu})\rangle$ based on the Gaussian curve fitting to the experimental data. Taking $\langle U_i^2(\tilde{\nu})\rangle$ to be independent of frequency within the accuracy of our measurements, we obtain from the $\ln I^P$ *v.* Q^2 plot for the INS spectra of CoNaA + C_3H_6 at 16K (Fig. 6.10) an unweighted average value of $\langle U_i^2\rangle$ for the H atoms of 0.065Å^2. Similarly, the average value of $\langle U_i^2\rangle$ for the H atoms of MnNaA + C_3H_6 at 10K is 0.050Å^2, (the τ_z mode, which was not definitely assigned, is not included in this average). These averaged values of $\langle U_H^2\rangle$ represent experimental values of the total mean square displacement of an isotropic oscillator (Section 6.5.1). The value of $\langle U_H^2\rangle$ for adsorbed cyclopropane will contain contributions from the internal and external modes of the C_3H_6 and from those zeolite lattice modes which displace the H atoms. We reiterate that by the term external modes we mean the hindered rotations and translations of the molecule. The contribution from the zeolite lattice mode arises because the following conditions apply[43]:

(1) there is no large difference in frequency between the external modes and the lattice modes;

(2) the Debye frequencies, ω_D, of the M(II)NaA+C_3H_6 samples are not known, but the t.o.f. spectra (Figs. 6.16 to 6.18) were obtained at temperatures for which it is very likely that $K_BT \lesssim \hbar\omega_D$, where K_B is Boltzmann's constant and T the absolute temperature.

(b) Adsorbed cyclopropane-d_6

The wide variation in the estimates of $\langle U_i^2(\tilde{\nu})\rangle$ (Fig.6.20) for the low coverage of C_3D_6 on MnNaA results from the modest statistics of the data in the t.o.f. spectrum (Fig.6.17), a consequence of the small incoherent inelastic neutron scattering cross section of the D nucleus. The same considerations apply to the differences in the $\langle U_i^2(\tilde{\nu})\rangle$ for the modes of adsorbed C_3D_6 at a given coverage (Figs. 6.20, 6.21) as to those of adsorbed $C_3{}^1H_6$ (Section 6.5.11(a)). Applying the isotropic approximation to the D atoms MnNaA + C_3D_6 we obtain an average value of $\langle U_D^2\rangle$ of 0.025Å^2 at low coverage and 0.028Å^2 at high coverage (the τ_z mode is excluded from these averages, see Section 6.4.11 (a)). The change in the value of $\langle U_D^2\rangle$ on increasing coverage is probably within the errors associated with those values. For both coverages of C_3D_6, the values of the $\langle U_i^2(\tilde{\nu})\rangle$ for the D nuclei are less than those of the protons of adsorbed $C_3{}^1H_6$, as expected for the more massive deuteron (*c.f.* Figs. 6.19 to 6.21).

(c) A comparison of the total square displacements of adsorbed cyclopropane obtained by X-ray and INS techniques

It is our purpose in this section to compare the total mean square displacements $\langle U_i^2\rangle$ of the atoms of adsorbed C_3H_6 as

estimated from the X-ray diffraction results of Seff[20] with those from our INS spectra. As with our INS results, the values of $\langle U_i^2 \rangle$ obtained from diffraction results contain contributions from all modes of vibration displacing the atom of type i. Because the values of $\langle U_i^2 \rangle$ obtained *via* the two routes refer to different sample conditions and different atoms (see below), we can only check whether or not they are mutually consistent.

(i) MnNaA + C_3H_6

Using standard methods,[44] we have evaluated the mean square displacement matrix B_C of the C atoms of adsorbed C_3H_6 from the anisotropic temperature coefficients published by Seff.[20] We find

$$\underline{\underline{B}}_C = \begin{pmatrix} 0.095 \pm 0.045 & 0 & 0 \\ 0 & 0.410 \pm 0.087 & 0 \\ 0 & 0 & 0.410 \pm 0.087 \end{pmatrix} \text{Å}^2$$

The overall B-factor, B_C^{iso}, represents an effective value of the mean square displacement of an atom in the isotropic approximation[44]:

$$B_C^{iso} = \frac{1}{3} \text{Trace } \underline{\underline{B}}_C \quad .$$

From the X-ray data,[20] $B_C^{iso} = 0.305 \pm 0.073 \text{Å}^2$ for the C atoms of MnNaA + C_3H_6 at 299K. From our INS data (Section 6.4.11(a)) we obtain an isotropic average value for the H atoms of MnNaA + C_3H_6 at 10K of 0.050Å^2. This is inconsistent with the value of B_C^{iso} above, which is greater by a factor of six. The difference between the two estimates of the mean square atomic displacements arises from the following factors.

(1) The INS values refer to the H atoms, the X-ray values to the C atoms, of the C_3H_6 adsorbate. However, we would expect $\langle U^2 \rangle$ to be greater for H than the more massive C, under the same conditions.

(2) Temperature difference exists between the X-ray (299K) and INS experiments (10K). However, the factor of six between the two estimates of $\langle U^2 \rangle$ is probably too great to have been entirely caused by this.

(3) The most likely cause of the discrepancy between the INS and diffraction estimates of $\langle U^2 \rangle$ is the modest statistics of the diffraction data (Section 6.3). The large value of B_C^{iso} (above) is a reflection of poorly located atoms in the X-ray experiment.

(ii) CoNaA + C_3H_6

From the X-ray data of Seff,[20] we calculate that at 299K

$$\underline{\underline{B}}_C = \begin{pmatrix} 0.096 \pm 0.039 & 0 & 0 \\ 0 & 0.435 \pm 0.083 & 0 \\ 0 & 0 & 0.435 \pm 0.083 \end{pmatrix} \text{Å}^2$$

and

$$B_C^{iso} = 0.322 \pm 0.065 \text{ Å}^2$$

for the C atoms of C_3H_6 adsorbed in CoNaA. The unweighted average isotropic value of $\langle U^2 \rangle$ for the H atoms of CoNaA+C_3H_6 at 16K is, from our INS spectra (Section 6.5.11(a)), equal to 0.065Å^2, a factor of five less than B_C^{iso}. Our comments above on the discrepancy for MnNaA + C_3H_6 also apply here.

(d) The contribution of the external modes of adsorbed $C_3{}^1H_6$ to the total mean square displacement of the H atoms

If $\langle U_H^2 \rangle$ represents the total mean square displacement of the H atoms due to all the modes of vibration of adsorbed $C_3{}^1H_6$, in the isotropic approximation, and $\langle u_H^2(\tilde{\nu}) \rangle$ the mean square amplitude of the H atom in a mode of frequency $\tilde{\nu}$, we may write:

$$\langle U_H^2 \rangle = \sum_I \langle u_H^2(\tilde{\nu}_I) \rangle + \sum_E \langle u_H^2(\tilde{\nu}_E) \rangle + \sum_L \langle u_H^2(\tilde{\nu}_L) \rangle \qquad (6.4)$$

where the subscript I is an index for the internal modes of $C_3{}^1H_6$, E for the external modes of adsorbed $C_3{}^1H_6$ and L for the zeolite lattice modes. For a simple harmonic oscillator undergoing a fundamental mode, the value of $\langle u^2(\tilde{\nu}) \rangle$ is given by[45]:

$$\langle u^2(\tilde{\nu}) \rangle = \frac{16.759}{\mu\tilde{\nu}} \coth\left[\frac{hc}{2k_BT}\right] \qquad (6.5)$$

The symbols were defined in Section 6.5.1. Values of $\langle u^2(\tilde{\nu}_E) \rangle$ calculated from equation 6.5 are listed in Table 6.12.

Consider a proton of the methylene group of adsorbed C_3H_6 whose C atom lies on the y-axis of Fig. 6.6. The external modes of the molecule, *viz.* the hindered rotational and translational modes, contribute to the displacement of the proton in the following way. The instantaneous proton displacement in the x-direction arises from the t_x, τ_z and τ_y modes; in the y-direction from the t_y mode only and in the z-direction from the t_z and τ_x modes. Thus, from Table 6.12, the mean square displacement of the proton due to the external modes of adsorbed C_3H_6 in CoNaA at 16K are 0.035Å^2 in the x-direction, 0.002Å^2 in the y-direction and 0.034Å^2 in the z-direction. Such a

TABLE 6.12 The mean square amplitudes of vibration of the H atoms in the external modes of adsorbed C_3H_6

sample	mode	frequency $\tilde{\nu}_E$, cm^{-1}	$\langle U_H^2(\tilde{\nu}_E)\rangle$ $Å^2$	$\langle U_H^2\rangle$ $Å^2$
$CoNaA+C_3H_6$	t_x and t_y	189	0.002	0.065
	τ_x and τ_y	128	0.010	
	τ_z	75	0.023	
θ = 0.9, 16K	t_z	50	0.024	
$MnNaA+C_3H_6$	t_x and t_y	149	0.003	0.050
	τ_x and τ_y	111	0.009	
	τ_z	either 82 or 53	either 0.014 or 0.030	
θ = 1.2, 10K	t_z	33	0.035	

Notes:

$\langle u_H^2(\tilde{\nu}_E)\rangle$ is the mean square amplitude of vibration of an H atom in an external mode of adsorbed C_3H_6 of frequency $\tilde{\nu}_E$, calculated from equation 6.5 (Section 6.5.11(d))

$\langle U_H^2\rangle$ is the total mean square displacement of an H atom due to all the modes of vibration of adsorbed C_3H_6, in the isotropic approximation. These values were estimated from the variation of INS band intensity with Q^2 (Section 6.5.11(a))

The two values of the mean square amplitude of vibration quoted for the τ_z mode of $MnNa+C_3H_6$ depend on the assignment of the τ_z mode, see Section 6.5.9(c).

---

displacement might be represented by an ellipsoid where semi-axes a, b and c in the x, y and z-directions respectively were such that $a \simeq c \gtrsim b$. On grounds of symmetry, the ellipsoids representing the mean square displacement due to the external modes of the protons of the other two methylene groups of C_3H_6 are related that of the proton already discussed by a rotation

of $\pi/3$ or $2\pi/3$ about the molecular C_3 axis.

The value of $\frac{1}{3}\sum_E \langle u_H^2(\tilde{\nu}_E)\rangle$ is an approximation to the contribution of the external modes to the total mean square displacement $\langle U_H^2\rangle$ of the proton, which we have shown to be almost isotropic (Section 6.5.11(a)). For CoNaA+C_3H_6 at 16K we calculate $\frac{1}{3}\sum_E \langle u_H^2(\tilde{\nu}_E)\rangle$ to be 0.024Å^2 while $\langle U_H^2\rangle$ = 0.065Å^2 (Table 6.12). The difference between the two quantities will be mainly due to zeolite lattice modes, which are expected to make a significant contribution to the total proton displacement under the experimental conditions used for our t.o.f. spectra (Section 6.5.11(a)).

Repeating the calculations of $\langle U_H^2(\tilde{\nu}_E)\rangle$ for MnNaA+C_3H_6 at 10K, we obtain a value of 0.044Å^2 for the mean square proton displacement in the z-direction and 0.003Å^2 in the y-direction. For the x-direction we calculate a value of 0.042Å^2 if the τ_z mode occurs at 53 cm^{-1}, or 0.026Å^2 if τ_z arises at 82 cm^{-1} (Table 6.12). The value of $\frac{1}{3}\sum\langle u_H^2(\tilde{\nu}_E)\rangle$ is 0.030Å^2 for τ_z = 53 cm^{-1} (or 0.024Å^2 if τ_z = 82 cm^{-1}) which is less than the total mean square proton displacement, $\langle U_H^2\rangle$, of 0.050Å^2. As with the case of CoNaA+C_3H_6, this discrepancy is expected and is caused by the large contribution of zeolite lattice modes to $\langle U_H^2\rangle$.

6.6 Barriers to rotation of cyclopropane adsorbed in M(II)NaA zeolites

6.6.1 Introduction

Our assignment of bands in the INS spectra of adsorbed cyclopropane to τ_z modes (Section 6.5) necessarily implies the existence of a barrier to rotation about the C_3 axis of the adsorption complex. In general, the potential energy, V′, opposing internal rotation in molecules can be written as a periodic function of the angle of rotation, α. For a function which is symmetric about $\alpha = 0^{\circ}$:

$$V'(\alpha) = \frac{V_N}{2}(1 - \cos N\alpha) + \frac{V_{2N}}{2}(1 - \cos 2N\alpha) + \ldots \qquad (6.6)$$

where N is the barrier multiplicity and V_N the barrier height. Equation 6.6 will be used to describe the potential barrier associated with the τ_z torsion of a C_3H_6 molecule adsorbed within an M(II)NaA zeolite. As a first approximation in the case of adsorbed C_3H_6 we take N=3 and set $V_3=V_6$. The V_6 term has been included to account for the 3-fold symmetry of the O(3) atoms to which the M(II) cation is bonded (Fig. 6.3). The torsional barrier height V_3 is not affected by the V_6 term since a $\cos 6\alpha$ function is unity at both the minimum and maximum points on the $\cos 3\alpha$ curve. However, a V_6 term does affect the shape of the potential function $V'(\alpha)$ depending on the relative phases of the V_3 and V_6 terms.[46] By including in equation 6.6 a V_6 term of the same sign as V_3, the potential energy well defined by $V'(\alpha)$ is broadened,[46] except at the base and top of the well where the shape of $V(\alpha)$ is unchanged. For a high potential barrier, the internal rotation described by equation 6.6 is restricted to a torsional oscillation, of frequency $\tilde{\omega}$, about the potential minimum:

$$\omega = \frac{1}{2\pi} (f/I)^{\frac{1}{2}} \qquad (6.7)$$

where f = force constant of the harmonic oscillations

I = moment of inertia of the oscillator about the rotation axis.

From the properties of simple harmonic oscillators:

$$V(\alpha) = \frac{1}{2} f\alpha^2 \qquad (6.8)$$

but

$$f = \frac{-d^2V}{d\alpha^2} \qquad (6.9)$$

So we have for the torsion:

$$\omega = \frac{1}{\pi} \left[\frac{45}{8} \frac{V_3}{I} \right]^{\frac{1}{2}} \qquad (6.10)$$

The values of V_3 thus calculated from the frequencies of the τ_z mode are listed in Table 6.13. Application of equation (6.6) to the MnNaA data assumes negligible interaction between cyclopropane molecules adsorbed within the same supercage, which we discuss below. The τ_z mode was unresolved in all the t.o.f. spectra of cyclopropane adsorbed by the MnNaA zeolites but curve fitting gave two estimates (only one of which can be even approximately correct) in each spectrum for the transition frequency (Section 6.5.9(c)). The frequencies have been taken from the spectra recorded at the lowest scattering angle (Tables 6.8 to 6.10). At higher scattering angles the intensity in these spectra (Figs. 6.9, 6.16 to 6.18) is reduced by the increased values of Q^2 and the curve fitting becomes less accurate. Thus two possible values are listed in Table 6.13 for the torsional barrier in each MnNaA/cyclopropane sample. Given the errors involved in the curve fitting, the listed potential barriers (Table 6.13) must be regarded as approximate, but we

TABLE 6.13 Barriers to rotation, V_3, about the C_3 axis of cyclopropane adsorption complexes in CoNaA and MnNaA zeolites

zeolite	gas	coverage molecules per supercage	torsional frequency τ_z, cm^{-1}	potential barrier V_3, $kJmol^{-1}$
CoNaA	C_3H_6	0.9	74	3.5
EITHER[a]				
MnNaA	C_3H_6	1.2	82	4.2
MnNaA	C_3D_6	1.5	67	3.7
MnNaA	C_3D_6	2.3	69	3.9
OR[a]				
MnNaA	C_3H_6	1.2	53	1.8
MnNaA	C_3D_6	1.5	46	1.8
MnNaA	C_3D_6	2.3	48	1.9

Note

a. Two possible values are given for V_3 and the frequency of the τ_z mode for the MnNaA data for reasons explained in Section 6.6.1

---

can infer that V_3 for cyclopropane adsorbed in MnNaA zeolite is *ca.* 2 to 4 $kJ\,mol^{-1}$; equal, within experimental error, to the barrier of 3.5 $kJ\,mol^{-1}$ in CoNaA. These values of V_3 are about an order of magnitude smaller than the barriers calculated for the transition metal coordination complexes of ethylene and acetylene.[31] They are, however, comparable with values of 1.1 kJ mol^{-1} reported for ethylene adsorbed at low coverage on fully exchanged AgX zeolite,[40] and 3.8 and 2.2 $kJ\,mol^{-1}$ for ethylene adsorbed at two different sites on

$Ag_{12}A$ zeolite.[37] The significance of the torsional barrier V_3 is discussed in Section 6.7.1.

6.6.2 The interaction between cyclopropane molecules adsorbed within the same supercage

When two cyclopropane molecules are adsorbed within the same supercage, the non-bonding interaction between the adsorbed molecules may split the τ_z mode into two components. It can be shown (Section 6.6.2(b)) that these components correspond to in-phase (i.p.) and out-of-phase (o.p.) rotation of the two molecules. As an example, a splitting of 34 cm^{-1} has been observed for ethylene adsorbed in fully exchanged AgX zeolite.[40]

(a) An estimation of the non-bonding potential between two coadsorbed cyclopropane molecules

Consider two C_3H_6 molecules adsorbed within the same supercage of an M(II)NaA zeolite and let α_1 and α_2 be the angular displacements of the two molecules about their C_3 axes during the τ_z torsion. The non-bonding potential between the C_3H_6 molecules is a function of α_1 and α_2 and will be denoted by $V''(\alpha_1,\alpha_2)$. This non-bonding potential differs for i.p. and o.p. rotations of the molecules and will be denoted by $V''_{ip}(\alpha_1,\alpha_2)$ and $V''_{op}(\alpha_1,\alpha_2)$ respectively, when the distinction is necessary. Using equation 6.11 below, derived by Williams[47] for the non-bonding interactions between molecules in hydrocarbon crystals, we can evaluate the potential V'':

$$V''(\alpha_1,\alpha_2) = \sum_{ij}\sum (A_{ij}d_{ij}^{-6} + B_{ij}\exp(-C_{ij}d_{ij})) \qquad (6.11)$$

$$\text{for } d_{ij} \leq d_{ij}^{max} ,$$

where i is an index for all the atoms of one C_3H_6 molecule

and j for all the atoms of the second C_3H_6 molecule, and d_{ij} is the distance between atoms i and j of different C_3H_6 ligands. The values of parameters A_{ij}, B_{ij} and C_{ij} differ for H---H, C---C and C---H interactions and values published by Williams[47] are listed in Table 6.14 Interactions between atoms separated by a distance greater than d_{ij}^{max} (Table 6.14) are not included in the total value of V''.

TABLE 6.14 Parameters given by Williams for the non-bonding interactions between hydrocarbons. (See Section 6.6.2(a) and ref. 47).

Interaction	A, kJ mol^{-1}	B, kJ mol^{-1}	C, Å^{-1}	d_{ij}^{max}, Å
H---H	-27.3	2654	-3.74	5.0
C---H	-125	8766	-3.67	5.5
C---C	-568	83630	-3.60	6.0

It is the barrier height, E'', defined by the potential function $V''(\alpha_1, \alpha_2)$ which determines the magnitude of the splitting of the two components of the τ_z mode(Section 6.6.2(b)).

The interatomic distance d_{ij} (equation 6.11) is a function of α_1 and α_2. We have written a computer program to calculate d_{ij} and hence V'' and E'' as the two C_3H_6 molecules rotate about their C_3 axes, for both i.p. and o.p. rotations. In order to calculate d_{ij} we must first define the geometry of the two C_3H_6 rotors, shown diagrammatically in Fig. 6.23. Obtained from the X-ray results of Seff,[20] the following details of the geometry are relevant here.

(1) The axes of rotation of the C_3H_6 molecules, *i.e.* the C_3 axes, are inclined at the tetrahedral angle with respect to each other (c.f. Fig. 6.2);

Figs. 6.23 Diagrams to show the geometry of two coadsorbed C_3H_6 molecules in a zeolite type-A supercage.

Fig. 6.23a Elevation view (not to scale).

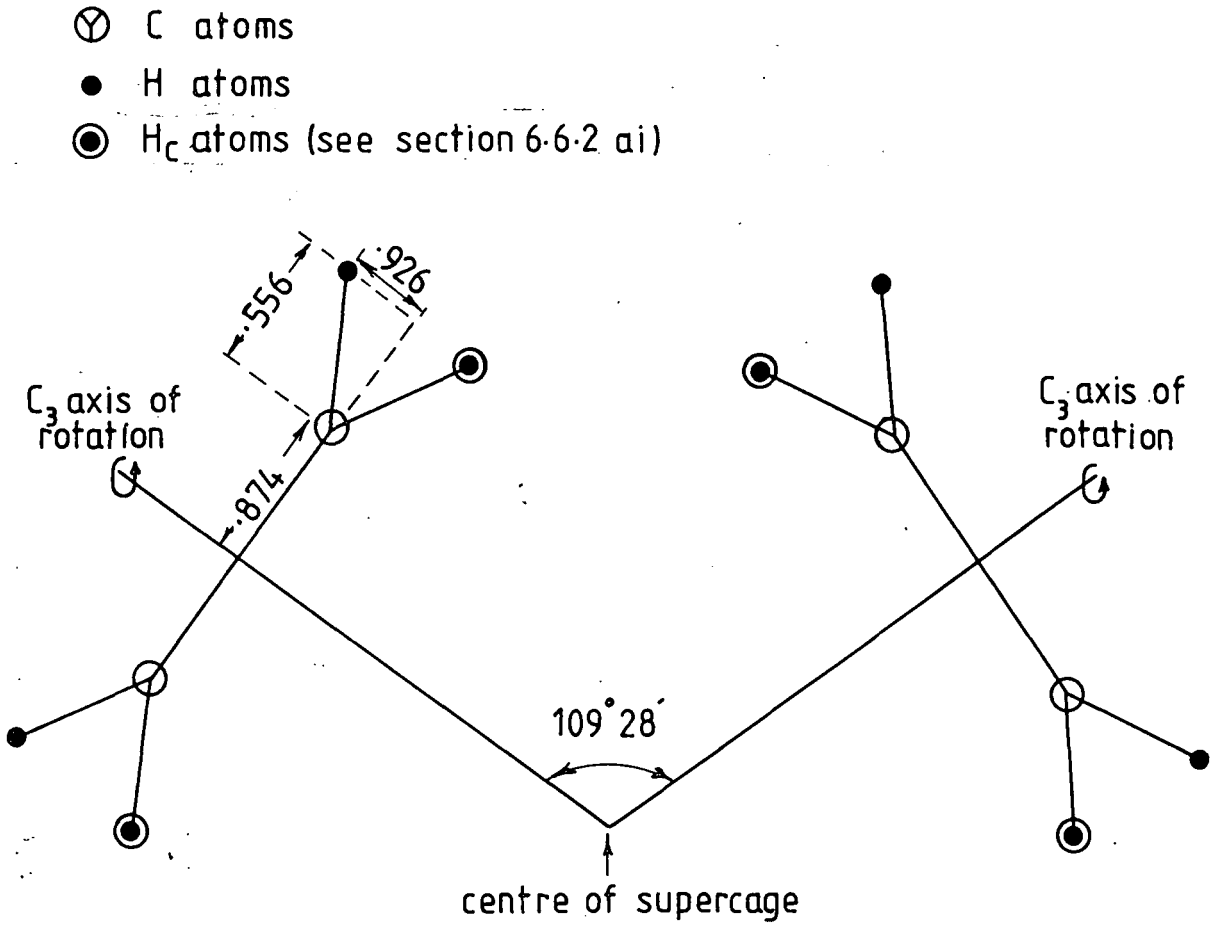

The lines are construction lines and do not necessarily represent chemical bonds.

All distances are given in Å. They represent the projections of the relevant interatomic distances onto the plane of the paper.

The third CH_2 group of each C_3H_6 molecule is not shown. In this projection they are coincident with the C_3 axes of rotation.

Figs. 6.23 Diagrams to show the geometry of two coadsorbed C_3H_6 molecules in a zeolite type-A supercage.

Fig. 6.23b Plan view, above a C_3H_6 molecule, showing the definition of the angle of rotation, α, of the molecule about the C_3 axis.

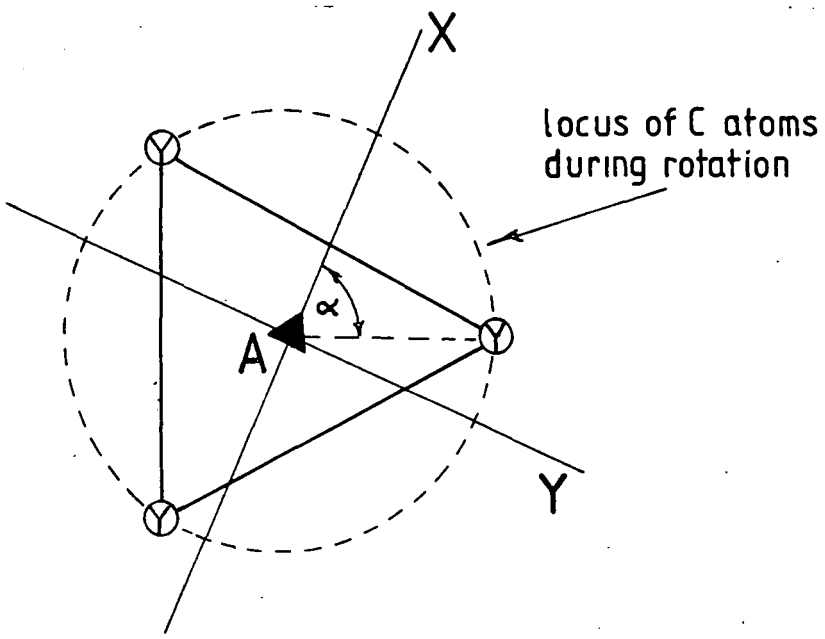

The axes AX and AY defining the angle of rotation α are arbitarily aligned with the rest of the zeolite supercage. (see section 6·6·2 a)

Fig. 6.23c View above the centre of the supercage of two coadsorbed C_3H_6 molecules undergoing an in-phase rotation about the molecular C_3 axes. Only the C atoms of the rotors are shown.

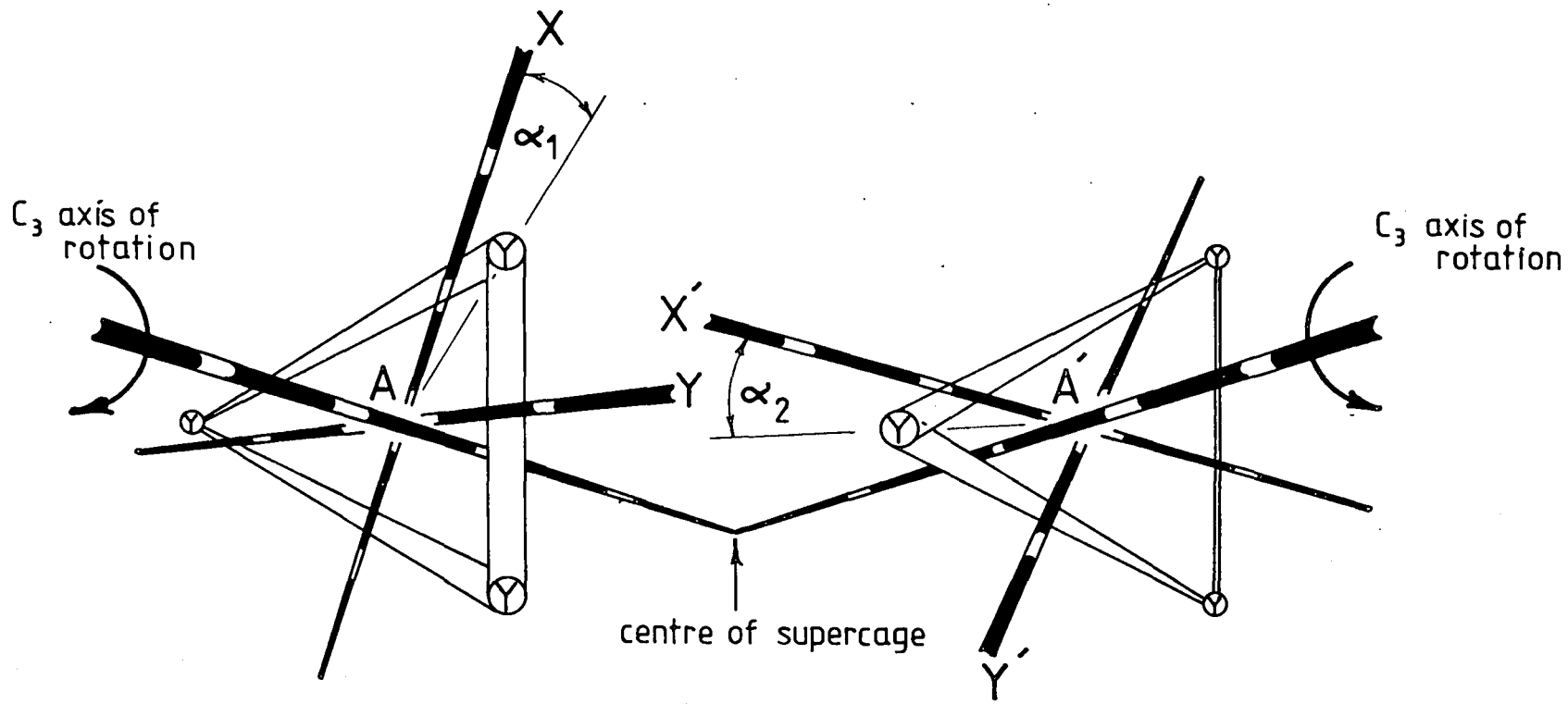

Ⓨ C atoms in the plane of the paper.

Ⓨ C atoms above the plane of the paper but co-planar with each other.

The axes AX, AY and A´X´, A´Y´ defining the angles of rotation α_1 and α_2 respectively, lie in the plane of the appropriate C_3H_6 molecule.

(2) The molecular geometry of C_3H_6 is unchanged on adsorption from that in the gas phase. The radii of gyration (Fig. 6.23) of the atoms of adsorbed C_3H_6 were calculated accordingly.

(3) The perpendicular distance from the plane defined by the zeolite O(3) atoms bonded to the M(II) cation of the M-C_3H_6 complex to the centre of the supercage is 6.073Å for both M=Co and M=Mn (Section 6.3).
In addition to the considerations arising from the X-ray results,[20] the following also apply.

(4) On steric grounds (Section 6.3) we have argued that the Co-C bond length is $\lesssim$2.2Å and the Mn-C bond length is $\lesssim$2.4Å. In order to calculate the non-bonding potential V'' we assume that these distances are Co-2 = 2.2Å and Mn-2 = 2.4Å. For these bond lengths, the perpendicular distance between the planes of the C atoms of the coadsorbed C_3H_6 molecules is the same in both the MnNaA and CoNaA zeolite systems (Section 6.3). Thus at given values of α_1 and α_2, the intermolecular distance d_{ij} between two particular atoms of the C_3H_6 molecules is equal in the two zeolites. Hence our model calculates an identical function $V''_{op}(\alpha_1,\alpha_2)$, and barrier height to o.p. rotation, for both MnNaA+C_3H_6 and CoNaA+C_3H_6. Similarly the function $V''_{ip}(\alpha_1,\alpha_2)$, and the barrier height to i.p. rotation, is the same for both zeolite systems.

(5) The interaction between the two cyclopropane molecules is least when the molecules are staggered by 60° - this configuration maximises the interatomic distances;

(6) It can be shown[48] that the two cyclopropane molecules remain staggered by 60° during the i.p. rotation.

The axis defining the angular displacement, α_1 or α_2, of each C_3H_6 rotor lies in the plane of the carbon atoms of the rotor, perpendicular to the axis of rotation (Fig.6.23(b)). The orientation of one of these axes, say that defining α_1, within the molecular plane is arbitrary, but the second axis, defining α_2, is aligned with the first such that the two C_3H_6 molecules are staggered by 60° when α_1 and α_2 are zero. The i.p. rotation is then achieved by incrementing equally α_1 and α_2 (Fig. 6.23(c)); the o.p. rotation by incrementing α_1 and decrementing α_2 by the same amount. Thus during the o.p. rotation, $\alpha_1 + \alpha_2 = \pi/3$.

(i) Out-of-phase rotation

The variation of the non-bonding potential V''_{op} during o.p. rotation is shown in Fig.6.24. This figure applies to both MnNaA+C_3H_6 and CoNaA+C_3H_6 systems with Co-C = 2.2Å and Mn-C = 2.4Å. The negative values of V''_{op} correspond to attractive non-bonding interactions. V''_{op} is a six-fold function and approximately sinusoideal in shape, except near the base of the potential energy (P.E.) wells which show double minima (Fig.6.24). The barrier height to o.p. rotation arising from the non-bonding potential V''_{op} is *ca.* 0.36kJ mol^{-1} and is shown on Fig.6.24 as E''_{op}.

Each coadsorbed C_3H_6 molecule has two types of H atom: those which are closer than their associated C atom to the other C_3H_6 molecule, and those which are further than the C atom. We label the first type of H atoms as H_C (see Fig.6.23). For our chosen M(II)-C bond lengths, the intermolecular non-bonding interactions between all the atoms of the two C_3H_6 molecules are attractive during the o.p. rotation, except those

Fig 6.24 The variation of the William's non-bonding potential during the out-of-phase rotation of two C_3H_6 molecules coadsorbed in an M(II)NaA zeolite supercage. See section 6.7.2.

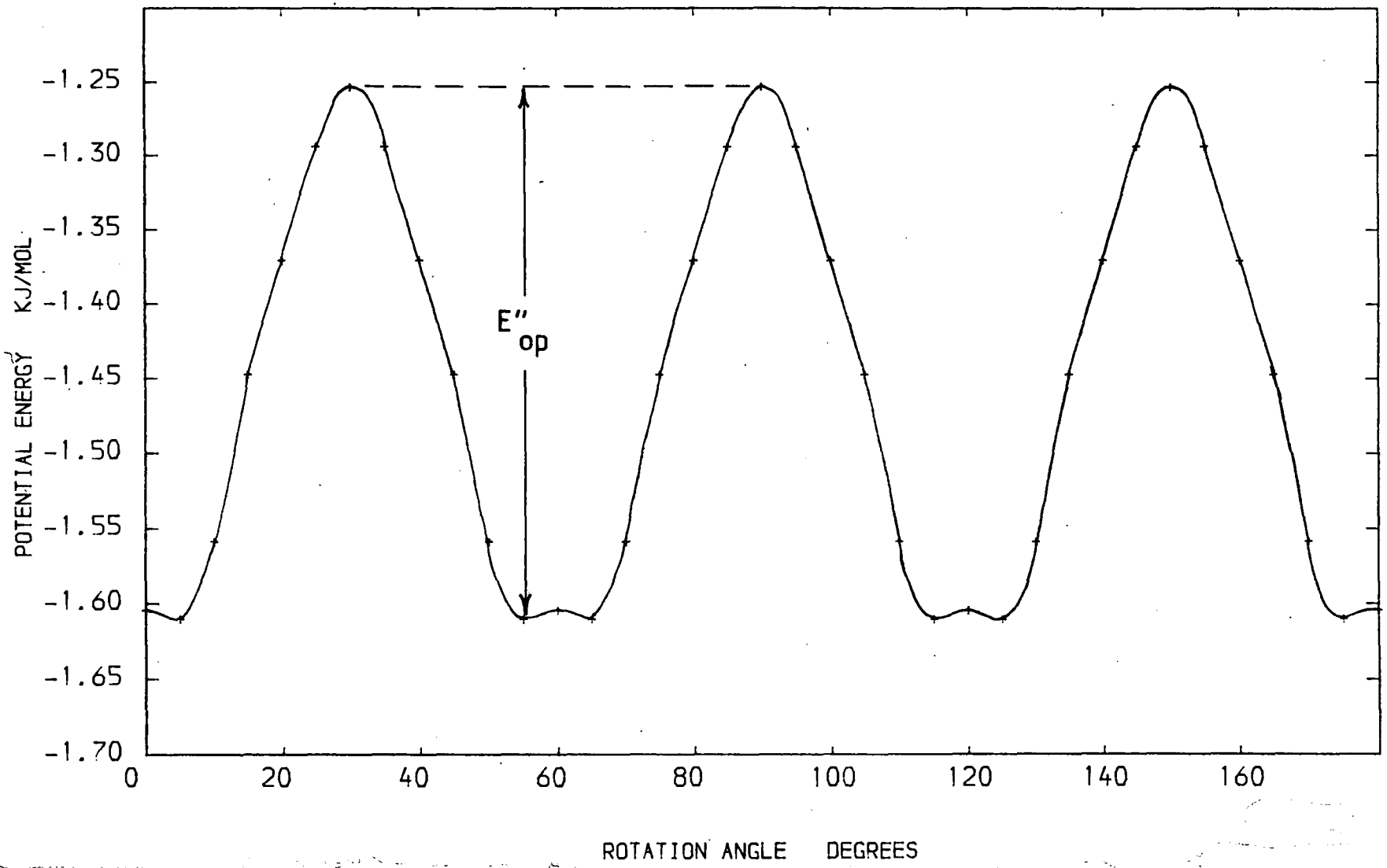

between the two sets of H_C atoms. The sum of the inter-molecular interactions between the H_C atoms becomes repulsive as two such atoms attain their closest approach, at multiples of 30^o in Fig.6.24. It is the H_C---H_C potential which largely controls the variation of V''_{op} as the C_3H_6 molecules rotate, the sum of the other non-bonding interactions changing by a much smaller amount.

From equation 6.11, the non-bonding potential V''_{op}, and also V''_{ip}, depends strongly on the d_{ij}, which in turn depend on the assumed value of the M(II)-C bond length. Recalculating V''_{op} using the M(II)-C bond lengths published by Seff[20] (Section 6.3), we obtain for C_3H_6 adsorbed in both CoNaA and MnNaA a value of 17.2kJ/mol^{-1} for E''_{op}. The potential function V''_{op} is again six-fold and shows an approximately sinusoidal variation as the C_3H_6 molecules rotate but the P.E. wells have single minima. The overall non-bonding interaction between the two molecules is now repulsive, except close to the minima where it is attractive. It is the H_C---H_C and the two sets of H_C---C intermolecular interactions which mainly control the shape of the function V''_{op}.

If the M(II)-C bond length is increased by 0.1Å from our chosen values (*i.e.* such that Mn-C = 2.5Å, Co-C = 2.3Å), the shape of the V''_{op} function is similar to that obtained using the X-ray values of the bond lengths. The barrier height E''_{op} becomes 5.2kJ/mol^{-1}. V''_{op} is again repulsive apart from the regions about the minima where it is attractive. In this case, the H_C---H_C and H_C---C non-bonding interactions mainly determine the shape of the function V''_{op}, although the H_C---C make a much smaller contribution than in the case of longer M(II)-C bond

Fig 6.25 The variation of the William's non-bonding potential during the in-phase rotation of two C_3H_6 molecules coadsorbed in an M(II)NaA zeolite. See section 6.7.2.

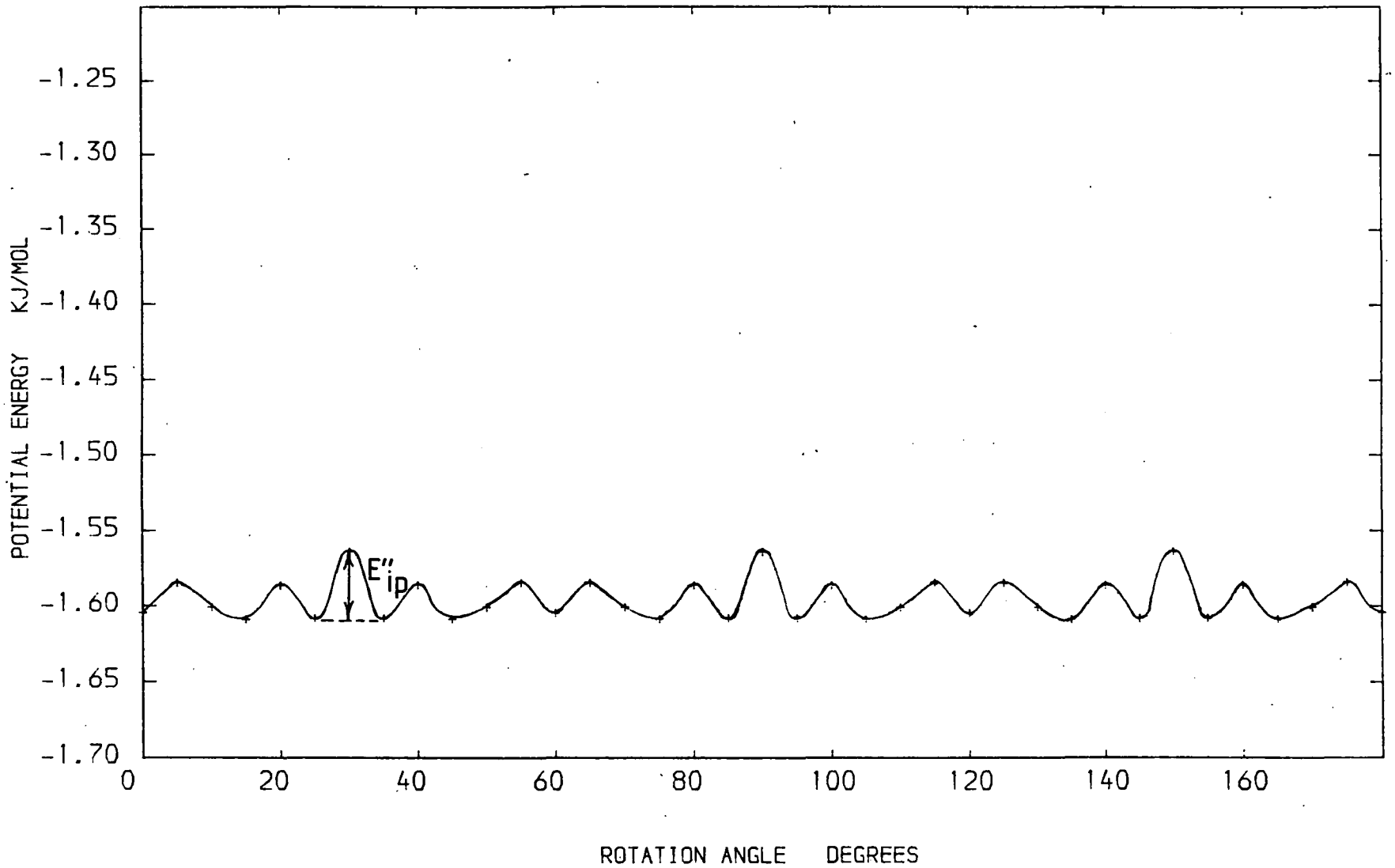

lengths (see above). However, the variation of the H_C---C potential is significantly more marked than with our estimates of the M(II)-C bond lengths (*i.e.* with Mn-C = 2.4Å, Co-C = 2.2Å).

(ii) In-phase rotation

The variation of the non-bonding potential V''_{ip} during i.p. rotation is shown in Fig.6.25 for Mn-C = 2.4Å and Co-C = 2.2Å. Within the accuracy of our calculations, the barrier height to i.p. rotation, E''_{ip}, is zero.

On lengthening the M(II)-C bond length by 0.1Å, the barrier height E''_{op} remains zero but the shape of the V''_{ip} function becomes simpler than in Fig.6.25. A six-fold, approximately sinusoidal function is obtained for V''_{ip}, although the minima and maxima are broader than would be given by a function of the form $\sin 6\alpha$.

If the M(II)-C bond lengths are increased to the values reported by Seff,[20] the barrier height E''_{ip} becomes *ca.* 0.2kJ//mol^{-1}. The potential function V''_{ip} is again six-fold but the P.E. wells are somewhat triangular in shape.

(b) Calculation of the splitting of the τ_z mode of two coadsorbed cyclopropane molecules

The total potential energy, $V^{TOT}(\alpha_1, \alpha_2)$, of two co-adsorbed cyclopropane molecules undergoing the τ_z torsion is given by[48]:

$$V^{TOT}(\alpha_1, \alpha_2) = V'(\alpha_1) + V'(\alpha_2) + V''(\alpha_1, \alpha_2) \qquad (6.12)$$

where $V''(\alpha_1, \alpha_2)$ is the non-bonding interaction between the rotors (Section 6.6.2(a)) and the V' are the interactions of each rotor with the rest of the zeolite system. The V' are given by equation 6.6 (Section 6.6.1).

We need to find an expression explicitly in terms of α_1 and α_2 for V'' as the two cyclopropane molecules rotate. As evaluated from the Williams equation (6.11), $V''(\alpha_1,\alpha_2)$ is a periodic function (see Figs. 6.24, 6.25) and therefore may be described by a Fourier series in α_1 and α_2. It is known[46] that the non-bonding interaction between two methyl rotors in a molecule such as $(CH_3)_2CH_2$ may be described by a Fourier series, the first term of which is

$$\frac{V^*}{4}(1 - \cos 6\beta_1 - \cos 6\beta_2) \qquad (6.13)$$

where β_1 and β_2 are the angular displacements of the methyl rotors and V^* is the barrier height to rotation. Expression 6.13 applies when the rotors are related by symmetry element(s) of the molecular point group. This is analogous to our case of two coadsorbed cyclopropane rotors in a zeolite supercage, for which we write:

$$V''(\alpha_1,\alpha_2) = \frac{E''}{4}(1-\cos 6\alpha_1 - \cos 6\alpha_2) \qquad (6.14)$$

During the o.p. rotation of the cyclopropane molecules, $\alpha_1 + \alpha_2 = \pi/3$ (Section 6.6.2(a)) and equation 6.14 may be rewritten as

$$V''(\alpha_1, \pi/3-\alpha_1) = V''_{o.p.} = \frac{E''_{op}}{2}(1-\cos 6\alpha_1) \qquad (6.15)$$

Figure 6.24 shows the variation of V'' as the two cyclopropane molecules undergo an o.p. rotation, calculated from the Williams equation.[47] We will use equations 6.14 and 6.15 to describe this variation of V''. The $\cos 6\alpha_1$ function (equation 6.15) is an approximation to the curve of Fig.6.24; for example it does not predict the double minima of the potential energy wells (Fig.6.24). However, the errors in calculating the

splitting of the t_z mode incurred through this approximation are much less than those arising from an incorrect choice of the M(II)-C bond length, on which the value of E''_{op} is strongly dependent. We note that a more accurate description of the curve in Figure 6.24 could be obtained by including terms in $\cos 9\alpha$, $\cos 12\alpha_1$, ... in equations 6.14 and 6.15.

Combining equations 6.6, 6.12 and 6.14, we obtain for the o.p. rotation:

$$V^{TOT}(\alpha_1,\alpha_2) = \frac{V_3}{2}(1-\cos 3\alpha_1) + \frac{V_6}{2}(1-\cos 6\alpha_1) + \frac{V_3}{2}(1-\cos 3\alpha_2) + \frac{V_6}{2}(1-\cos 6\alpha_2) + \frac{E''_{op}}{4}(1-\cos 6(\alpha_1+\delta_1) - \cos 6(\alpha_2+\delta_2))$$

where the constants δ_1 and δ_2 account for any phase difference between the non-bonding potential and the torsional potential V' of equation 6.6. The value of the δ will depend on the alignment of the arbitrarily orientated axes which define α_1 and α_2 with respect to the zeolite framework (Section 6.6.2(a)).

In the harmonic approximation, the force constant, f_{op}, for the o.p. torsion is given by

$$f_{op} = \frac{-d^2V^{TOT}}{d\alpha_1^2} = \frac{-d^2V^{TOT}}{d\alpha_2^2}$$

and, given that $V_3 = V_6$ (Section 6.6.1), the frequency of the o.p. torsion, ω_{op}, is:

$$\omega_{op} = \frac{1}{\pi}\left(\frac{45V_3 + 18E''_{op}}{8I}\right)^{\frac{1}{2}}$$

The barrier E''_{ip} to in-phase rotation estimated from the Williams[] equation is either small or zero, depending on the assumed M(II)-C bond length (Section 6.6.2(a)). When E''_{ip} is

TABLE 6.15 Calculated frequencies of the in-phase and out-of-phase components of the τ_z torsion of coadsorbed cyclopropane molecules in M(II)NaA zeolites

sample	assumed M(II)-C bond length, Å	potential barrier V_3 kJ/mole	barrier due to non-bonding interactions o.p. torsion E'_{op}, kJ/mole	barrier due to non-bonding interactions i.p. torsion E'_{ip}, kJ/mole	calculated frequency of o.p.torsion ω_{op}, cm^{-1}	calculated frequency of i.p.torsion ω_{ip}, cm^{-1}
CoNaA+C_3H_6	2.2	3.5	0.36	0.0	76	74
θ = 1.8	2.3	3.5	5.9	0.0	96	74
16K	2.8[b]	3.5	17.2	0.2	128	75
	2.4[a]	1.9	0.36	0.0	50	48
	2.5	1.9	5.9	0.0	72	48
MnNaA+C_3D_6	3.1[b]	1.9	17.2	0.2	103	49
θ= 2.3						
10K	2.4[a]	3.9	0.36	0.0	70	69
	2.5	3.9	5.9	0.0	87	69
	3.1[b]	3.9	17.2	0.2	114	69

Notes: The frequencies were calculated using equation 6.16

V_3 is the contribution to the potential barrier from the interactions of each cyclopropane molecule with the zeolite framework (Section 6.6.1).

(a) These bond lengths are our estimates of the maximum possible M(II)-C distances, obtained from steric arguments (Section 6.3).

(b) These bond lengths are those published by Seff.[20]

zero, the in-phase torsion will arise at the same frequency as does the τ_z mode in the absence of any splitting. For non-zero values of E''_{ip}, the potential V''_{ip} is a six-fold one, as is V''_{op}. Thus we will estimate the frequency, ω_{ip}, of the in-phase torsion using equation 6.16 and replacing E''_{op} by E''_{ip}.

In Table 6.15 we list values of ω_{op} and ω_{ip} calculated using equation 6.16 for C_3H_6 adsorbed in CoNaA and C_3D_6 in MnNaA. Table 6.15 illustrates that the splitting of the τ_z mode due to non-bonding interactions is strongly dependent on the M(II)-C bond length.

(i) CoNaA + C_3H_6, θ = 1.8 molecules per supercage

For this sample, we have taken V_3 to be 3.5kJ mol^{-1} as for the lower coverage case (Table 6.13). The spectrum of this sample (Fig.6.11) shows a marked increase in intensity in the region *ca.* 80 to 120 cm^{-1} when compared with the lower coverage spectra (Fig. 6.9). We posit that this intensity increase is due to the o.p. component of the τ_z mode. The frequency of 128 cm^{-1} (Table 6.15) predicted for ω_{op} using the X-ray[20] value of the Co-C bond length, 2.8Å, is therefore too high. Although the t.o.f. spectrum of CoNaA+C_3H_6 (θ=1.8, Fig.6.11) shows a shoulder at *ca.* 130 cm^{-1} on the band due to the τ_x and τ_y modes, this feature is probably too weak to have arisen from the o.p. torsion. A better agreement between the observed spectrum (Fig.6.11) and the predicted frequency of the o.p. torsion (Table 6.15) is obtained for shorter Co-C bond lengths. Table 6.15 shows that the splitting is more accurately predicted using a Co-C distance of 2.3Å rather than 2.2Å. The latter distance is our estimate of the maximum Co-C distance

based on steric grounds (Section 6.3). This is a small discrepancy considering the approximations made in the calculation of ω_{op} and ω_{ip}. These approximations include:

(1) a neglect of any distortions of the C_3H_6 molecules during the torsion;

(2) the assumption that the charge distribution in the C_3H_6 ligands is symmetrical about their C_3 axes. An asymmetrical distribution would require the inclusion of an extra Coulombic term in the Williams equation (6.11) for the non-bonding interactions.[49]

No information is available on either of these phenomena and so corrections cannot be made.

(ii) MnNaA + C_3D_6, θ = 2.3 molecules per supercage

For this sample, there are two estimates of V_3 (Section 6.6.1) depending on the assignment of the τ_z mode. The spectra of this sample (Fig.6.18) show no signs of any splitting of the τ_z mode when compared with the spectra of MnNaA+C_3D_6, θ = 1.5, and MnNaA+C_3H_6, θ = 1.2, in which such splitting has been ruled out on intensity grounds (Figs. 6.17, 6.16 respectively). This is consistent with the small splitting, $\lesssim 2cm^{-1}$, calculated using equation 6.16 for the τ_z mode of the Mn(II)-C_3D_6 (θ=2.3) complex assuming an Mn-C bond length of 2.4Å (Table 6.15). The value of 2.4Å is our estimate of the maximum Mn-C bond length obtained on steric grounds (Section 6.3).

Our model of the splitting of the τ_z mode into two components due to o.p. and i.p. torsions of coadsorbed cyclopropane molecules in CoNaA and MnNaA is consistent with our contention that the M(II)-C bond lengths published from X-ray data[20] are too long.

6.7 Simple Bonding Considerations

The bonding in C_3H_6 has some π character - cyclopropane does undergo certain olefin-like reactions. Chatt, Dewar and Duncanson[50,51] have modelled the bonding between simple olefins and transition metal ions. We now apply their ideas to the case of adsorbed C_3H_6. The bond between cyclopropane and the Co(II) or Mn(II) ion will involve an ordinary co-ordination bond from a π orbital of the ring to some hybrid orbital of the metal ion. This bond is augmented by back donation from filled metal orbitals to an unoccupied π^* anti-bonding orbital of cyclopropane. The barrier to rotation about the C_3 axis of the adsorbed complex can be used as a measure of the extent of this π-bonding (Section 6.7.1).

The Coulson-Moffitt model[52] of the bonding in cyclopropane predicts that, so far as the electrons forming the C-C bonds are concerned, the lines of maximum electron density do not coincide with the C-C internuclear axes. The model describes "bent bonds" in which the axis of the bond orbitals are inclined at 22^o to the C-C direction. The Walsh model[1,2] predicts, in addition, a region of high electron density at the centre of the C_3 ring. These early predictions are confirmed by an *ab initio* SCF calculation[32] which demonstrated the existence of bent bonds in C_3H_6 as well as a build up of electronic charge

at the centre of the C_3 ring. In addition, an electron density difference map from an X-ray diffraction study of *cis*-1,2,3-tricyano-cyclopropane[53] showed that the maximum bonding density between the carbon atoms was displaced outside the ring, 0.32Å from the axis of the endocyclic bond.

We return to the Raman spectroscopic data of Tam *et al*[23] (Section 6.4.1(a)) for C_3H_6 adsorbed in alkali metal exchanged X zeolites. The adsorbate-cation interaction was said to depend on the polarising power of the cation, cyclopropane being edge bonded to the strongly polarising Li^+ and Na^+. The available evidence did not distinguish conclusively between face or edge bonding to K^+ and Cs^+ ions.

We estimate the polarising power of an ion by the quantity e/r where e= formal charge on the cation and r = the Shannon-Prewitt effective ionic radius[54] (see Table 6.16). The size of the ion depends upon its coordination environment. Values of r for tetrahedrally coordinated K^+, Cs^+ and Mn^{++} are not available but the Shannon-Prewitt tables show that r^{-1} is not a strong function of coordination number for the alkali metal cations. The differences in r for 4 and 6 coordinated Na^+ and Li^+, and by implication K^+ and Cs^+, are insignificant for our purposes. The Table (6.16) shows that Co^{++}, and thus Mn^{++}, are considerably more polarising than the alkali metal cations, provided only insignificant delocalisation of the cationic charge over the zeolite framework occurs. According to Tam *et al*[23], the geometry of the C_3H_6 adsorption complexes in alkali metal exchanged X zeolites is controlled by the cation polarising power. Extending this idea to C_3H_6 adsorption in transition metal ion exchanged A zeolites, the strongly polarising Co(II) and Mn(II) ions would be expected to give an edge-bonded

cyclopropane adsorption complex. However, our INS data (Section 6.5) show that these complexes are face-bonded. Therefore, we can state that the availability of d-electrons on the cation for π-bonding with the C_3H_6 is more important in controlling the adsorption geometry than is the cation polarising power.

TABLE 6.16 Estimation of cation polarising power

cation	6 coordinate		4 coordinate	
	r, Å	e/r	r, Å	e/r
Li^+	0.74	1.35	0.59	1.70
Na^+	1.02	0.98	0.99	1.11
K^+	1.38	0.72	-	-
Cs^+	1.70	0.58	-	-
Co^{++}	-	-	0.57	3.51

r = effective ionic radius taken from the tables of Shannon and Prewitt[54]

e = formal cationic charge

It is interesting to note that in the protonated cyclopropane ion the proton occupies an edge-on, in-plane position.[55] This same position is adopted by H in a C_3H_6-HCl dimer, as shown by its rotational spectrum.[56]

6.7.1 The implications of the torsional barrier of the M(II)-C_3H_6 bond

The existence of the torsional barrier V_3 for a single cyclopropane molecule adsorbed within a supercage suggests the operation of π-bonding between the cation and the C_3H_6 ligand. The barrier height is a measure of the extent of the

π-bonding, provided that other interactions (*e.g.* hydrogen bonding between the C_3H_6 protons and framework oxygen) can be neglected. Co(II) is a d^7 ion and therefore is expected to be more effective in back-donation of electron density to the C_3H_6 ring than is the d^5 Mn(II) ion. The π-bonding in the M(II)-C_3H_6 systems should be stronger for M = Co than M = Mn. However, the torsional barriers for the complexes of the two cations are equal within the accuracy of our calculations (Table 6.13, Section 6.6.1), thus indicating similar degrees of π-bonding. There are, however, significant differences between the Mn(II) and Co(II) cyclopropane complexes, *e.g.* witness the apparent splitting of the τ_z mode of Co-C_3H_6 at high coverage (θ=1.8, Fig.6.11) which does not occur for Mn-C_3D_6 at a similar coverage (θ=1.5, Fig.6.17). It is possible that these differences may arise from differences in the charge distribution of the cyclopropane molecules adsorbed in CoNaA and MnNaA zeolites.

6.8 Conclusions

Our INS spectra of cyclopropane adsorbed by CoNaA and MnNaA zeolites are consistent with the C_{3v} symmetry of the M(II)-C_3H_6 adsorption complex proposed by Seff *et al*[20] from X-ray diffraction data. However, the agreement between the predicted and observed band intensities in the INS spectra of the MnNaA+ cyclopropane samples is much poorer than in the case of the CoNaA zeolites. There remains a small possibility that the Mn(II)-C_3H_6 complex may have a symmetry other than C_{3v}, the most probable alternative being C_{2v}. The need for a pulsed laser Raman experiment is therefore indicated - observation of A_2 and B_2 modes (C_{2v} point group) in the Raman spectrum

of adsorbed cyclopropane would eliminate the possibility of C_{3v} symmetry (Table 6.2).

REFERENCES

1. Walsh, A.D., Nature, 159, 712, 1947.

2. Walsh, A.D., Trans.Faraday Soc., 45, 179, 1949.

3. Harmony, M.D., Mathur, S.N., Choe, J., Kattija-Ari, M., Howard, A.E. and Staley, S.W., J.Am.Chem.Soc., 103, 2961, 1981.

4. Linnett, J.W., J.Chem.Phys., 6, 693, 1938.

5. Hertzberg, G., Molecular Spectra and Molecular Structure II. Infrared and Raman Spectra of Polyatomic Molecules, Van Nostrand Reinhold, New York, 1945.

6. Duncan, J.L. and McKean, D.C., J.Mol.Spectrosc., 27, 117, 1968.

7. Duncan, J.L. and Burns, G.R., J.Mol.Spectrosc., 30, 253, 1969.

8. Maki, A.G., J.Mol.Spectrosc., 41, 177, 1972.

9. Butcher, R.J. and Jones, W.J., J.Mol.Spectrosc.,47, 64, 1973.

10. Bates, J.B., J.Chem.Phys., 58, 4236, 1973.

11. Daunt, S.J. and Shurvell, H.F., J.Raman Spectrosc., 2, 463, 1974.

12. Shurvell, H.F., Daunt, S.J. and James, D.W., J.Mol.Spectrosc., 53, 77, 1974.

13. Rubin, B., Steiner, D.A., McCubbin, T.K. Jr., and Polo, S.R., J.Mol.Spectrosc., 72, 57, 1978.

14. Levin, I.W. and Pearce, R.A.R., J.Chem.Phys., 69, 2196, 1978.

15. Hirokawa, T., Hayashi, M. and Murata, H., J.Sci.Hiroshima Univ., Ser.A, 37, 271, 1973.

16. Califano, S., Vibrational States, Wiley, London, 1976.

17. Pitha, J. and Jones, R.N., N.R.C. Bulletin, No.12,National Research Council of Canada, Ottawa, 1968.

18. Riley, P.E. and Seff, K., J.Chem.Soc., Chem.Commun., 1972, 1287, 1972.

19. Yanagida, R.Y., Vance, T.B. Jr., and Seff, K., J.Chem.Soc., Chem.Commun., 1973, 382, 1973.

20. Cruz, W.V., Leung, P.C.W. and Seff, K., J.Am.Chem.Soc., 100, 6997, 1978.

21. Bondi, A., J.Phys.Chem., 68, 441, 1964.

22. Allinger, N.L., Hirsch, J.A., Miller, M.A., Tyminski, I.J. and Van-Catledge, F.A., J.Am.Chem.Soc., 90, 1199, 1968.

23. Tam, N.T., Tsai, P. and Cooney, R.P., Aust.J.Chem., 31, 255, 1978.

24. Al Noami, A.N., M.Sc. Thesis, University of Durham, 1981.

25. Klier, K. and Ralek, M., J.Phys.Chem.Solids, 29, 951, 1968.

26. Denney, D., Mastikhim V.M., Namba, S. and Turkevich, J. J.Phys.Chem., 82, 1752, 1978.

27. Ben Taarit, Y., Naccache, C.M. and Imelik, B., Chem.Phys.Lett. 47, 479, 1977.

28. Tam, N.T., Cooney, R.P. and Curthoys, G., J.Catal., 44, 81, 1976.

29. Bassett, D.W. and Habgood, H.W., J.Phys.Chem., 64, 769, 1960.

30. George, Z.M. and Habgood, H.W., J.Phys.Chem., 74, 1502, 1970.

31. Howard, J. and Waddington, T.C. in Advances in Infrared and Raman Spectroscopy, vol.7, (Clark, R.J.H. and Hester,R.E. Eds.), Heyden, London, 1980.

32. Marsmann, H., Robert, J,-B. and Van Wazer, J.R., Tetrahedron, 27, 4377, 1971.

33. Thomas, M.W. and Ghosh, R.E., Mol.Phys., 29, 1489, 1975.

34. Willis, B.T.M. (Ed.), Chemical Applications of Thermal Neutron Scattering, Oxford University Press, Oxford, 1973.

35. Howard, J. and Nicol, J.M., unpublished results.

36. Howard, J., Robson, K. and Waddington, T.C., Zeolites, 1, 175, 1981.

37. Howard, J., Robson, K., Waddington, T.C. and Kadir, Z.A., Zeolites, 2, 2, 1982.

38. Graham, D., Ph.D. Thesis, University of Durham, 1980.

39. Howard, J. and Waddington, T.C., Surf.Sci., 68, 86, 1977.

40. Howard, T., Waddington, T.C. and Wright, C.J., Faraday Trans.II, 73, 1768, 1977.

41. Marshall, W. and Lovesey, S.W., Theory of Thermal Neutron Scattering, Oxford University Press, Oxford, 1971.

42. Sherwood, P.M.A., Vibrational Spectroscopy of Solids, Cambridge University Press, Cambridge, 1972.

43. Howard, J., Boland, B.C. and Tomkinson, J., J.Phys.Chem. in press.

44. Willis, B.T.M. and Pryor, A.W., Thermal Vibrations in Crystallography, Cambridge University Press, Cambridge, 1975.

45. Cyvin, C.J., Molecular Vibrations and Mean Square Amplitudes, Elsevier, Amsterdam, 1968, page 76.

46. Lister, D.G., MacDonald, J.N. and Owen, N.L., Internal Rotation and Inversion, Academic Press, New York, 1978.

47. Williams, D.E., J.Chem.Phys., 47, 4680, 1967.

48. Howard, J., Waddington, T.C. and Wright, C.J., Faraday Trans.II, 72, 513, 1976.

49. Ramdas, S. and Thomas, J.M. in Chemical Physics of Solids and their Surfaces, Vol.7, Chemical Society Specialist Periodical Reports, London, 1978.

50. Dewar, M.J.S., Bull.Soc.Chim.France, C71, 18, 1951.

51. Chatt, J. and Duncanson, L.A., J.Chem.Soc., 2939, 1953.

52. Coulson, C.A. and Moffit, W.E., Philos.Mag., 40, 1, 1949.

53. Hartman, A. and Hirshfeld, F.L., Acta Cryst., 20, 80, 1966.

54. Shannon, R. D. and Prewitt, C. T., Acta Cryst., B25, 925, 1969.

55. Collins, C.J., Chem.Rev., 69, 543, 1969.

56. Legon, A.C., Aldrich, P.D. and Flygare, W.H., J.Am.Chem.Soc., 104, 1486, 1982.

57. Baker, A.W. and Lord, R.C., J.Chem.Phys., 23, 1636, 1955.

CHAPTER SEVEN

A SPECTROSCOPIC STUDY OF HYDROGEN ADSORBED ON ZINC OXIDE

7.1 Introduction

The interaction of hydrogen with zinc oxide has been the subject of many investigations, largely because of the role adsorbed hydrogen plays in methanol synthesis and in the hydrogenation of unsaturated hydrocarbons.[1,2] Although our initial motivation for studying this system using neutrons was to identify some of the normal modes of vibration of dissociatively adsorbed hydrogen it became clear that a critical evaluation of the previously published spectroscopic data on both ZnO and ZnO + H_2 was necessary because so much of it appears to be conflicting.

Zinc oxide differs from the zeolite catalysts we have studied in two respects. Firstly, surface effects dominate the IR spectrum of the phonons (see Section 7.3.3(a)). This arises from the fulfilment of two requirements[3]:

(i) that the ZnO sample consists of crystallites whose diamter is less than that of the incident IR light. These surface effects on ZnO observed in the IR region from *ca.* 600 cm^{-1} (16.7μm) to 350 cm^{-1} (28.6μm).[4] Some 87.6% of the particles of our ZnO samples were found to have a diameter of less than 1.0μm (Section 7.2);

(ii) the structure of the sample should consist of a regular array of ions.
Although zeolites typically satisfy the requirements of particle size (e.g. for Linde 5A this is from 0.5 to 5.0μm,[5] they apparently do not have a sufficiently regular ionic structure for surface effects to dominate their IR spectra.

Secondly, ZnO is an n-type semiconductor. At room temperature the conduction band of ZnO is empty. But adsorption of hydrogen on ZnO at room temperature followed by heating results in the donation of electron density from the adsorbed hydrogen to the conduction band, resulting in an "accumulation" layer.[6] Plasmon modes due to the collective excitation of the free electrons in the conduction band may, under certain conditions, arise in the vibrational spectrum of ZnO bearing adsorbed hydrogen,[7] (see Section 7.1.4).

In the following, we shall use "ZnO+H" as an abbreviation for zinc oxide plus adsorbed hydrogen, without intending any implications as to the surface stoichiometry or state (H or H_2) of the adsorbed hydrogen.

7.1.1 The crystal structure of ZnO

Except at elevated temperatures, ZnO adopts the wurtzite structure (see Fig. 7.1). The observed ratio c/a (1.60) is slightly less than the ideal hcp value (1.63) and thus the planes of anions (and cations) are not quite close packed.[8] The structure may be regarded as comprised of nearly close packed layers of oxygen ions with zinc ions filling one half of the tetrahedral holes in the anionic lattice. The oxide layers also define octahedral and trigonal holes. The octahedral sites lie on straight lines perpendicular to the oxide layers and are separated by the trigonal holes. The dimater of the octahedral holes is approximately 2.0Å and that of the trigonal "squeeze-points" 1.2Å.[9]

The morphology of ZnO particles produced by burning Zn in air, as were our samples obtained from the New Jersey Zinc Co., is well known.[10] Although data for the relative abundance

Fig. 7.1 The succession of a-b-a-b double layers of (0001) planes of ZnO, taken from ref. 14.
The Zn and O atoms are not drawn to scale.

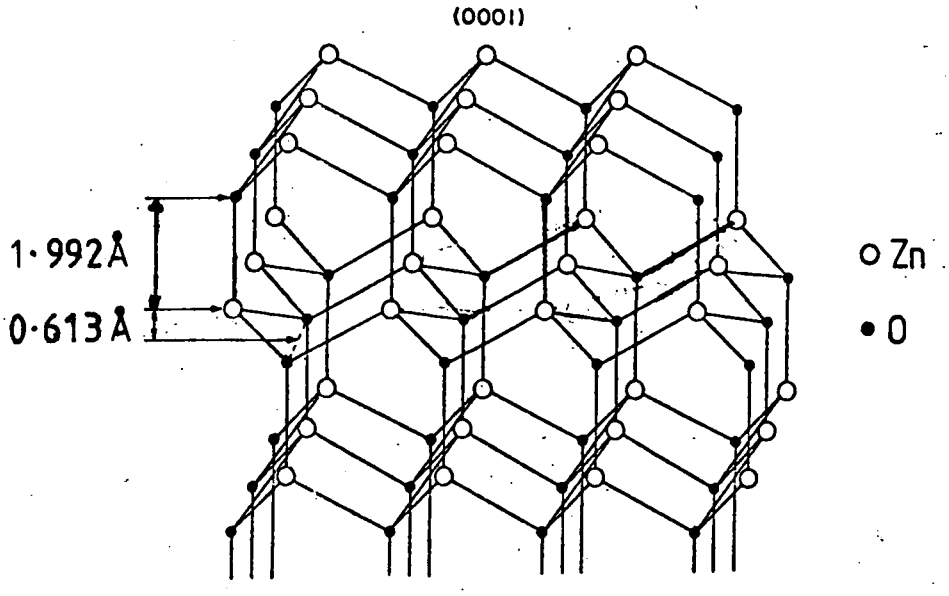

Fig. 7.2 Close packed layers in the (0001) surface (Zn uppermost) or (000$\bar{1}$) surface (O uppermost) of ZnO, from ref. 13.

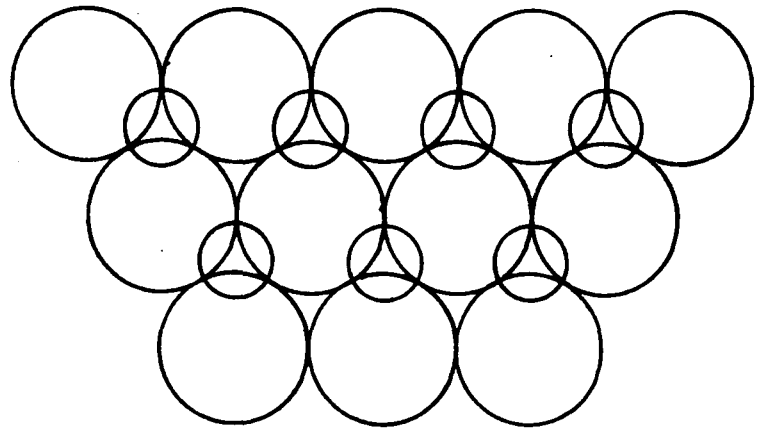

Larger spheres represent oxide ions. Not drawn to scale.

of the surface planes are not available, they are known to mainly comprise the (0001), (000$\bar{1}$), (10$\bar{1}$1) and (10$\bar{1}$0) cleavage planes.

The (0001) surface consists of alternate layers of zinc and oxygen ions in which the Zn layer is uppermost (see Fig.7.2 and the two uppermost rows of ions in Fig.7.1). On the other hand, in the ($\bar{0}$00$\bar{1}$) surface the oxygen ions make up the outermost layer (Fig.7.2). Both surfaces are polar. Cleavage along the plane labelled "A" in Fig.7.3 produces an (10$\bar{1}$0) face. This surface is apolar since it contains equal numbers of zinc and oxygen ions (Fig.7.4).

7.1.2 LEED data published on ZnO crystal faces

There is some disagreement in the details of LEED results published on ZnO, largely due to the various methods of sample preparation.[11] Recent studies have used two distinct methods of preparation:[11]

(i) the cleavage method, in which long, needle-shaped crystals are cleaved under ultra-high vacuum (UHV) to form complementary pairs of (0001) and (000$\bar{1}$) crystal faces;

(ii) the annealing method in which a cutting - chemical polishing (e.g. H_3PO_4) - etching (e.g. H_2SO_4) sequence is followed by UHV processing consisting of Ar^+ ion bombardment and thermal annealing.

7.1.2(a) LEED results on the polar ZnO surface planes

LEED data indicate that for samples prepared by methods (i) or (ii), steps are formed on the (0001) and (000$\bar{1}$) surface planes of ZnO on heating to temperatures below 873K.[12,13]

Fig. 7.3 The two alternate layers of atoms in (0001) hcp planes of ZnO. The dashed line A indicates the $(10\bar{1}0)$ plane, perpendicular to the (0001). Taken from ref. 14.

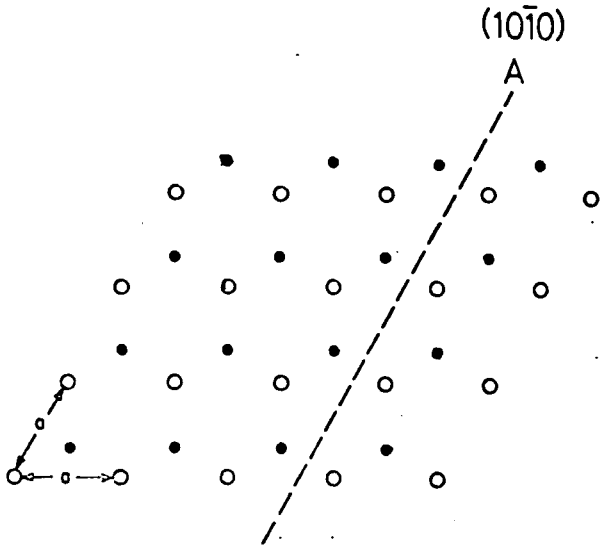

Fig 7.4 The layer structure of the ZnO (1010) surface. From ref. 13.

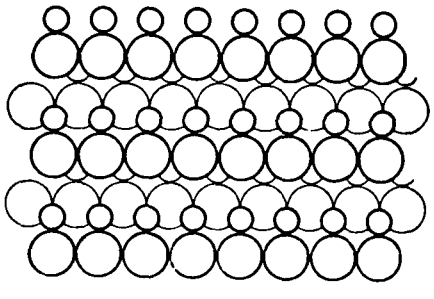

Larger spheres represent oxide ions. Not drawn to scale.

Duke and Lubinsky[14] have carried out dynamic intensity calculations of the LEED intensity expected from a ZnO (0001) surface. The parameters used in the calculation were adjusted to give the best fit to the experimental LEED data of Chang and Mark,[11] who studied a (0001) ZnO surface prepared by annealing at temperatures up to 873K. One of the adjustable parameters was the interplanar spacing between the uppermost zinc and oxygen layers. The intensity calculations indicate that the (0001) surface reconstructs *in vacuo*. The oxygen plane moves outwards from the bulk by 0.1 to 0.2Å [14] while the zinc plane remains unshifted. There is no lateral movement of the ions in either plane. The distance berween the outermost layers of zinc and oxygen ions is thus less than that in the bulk. This observation is consistent with the dangling bond arguments of Gatos and Levine[15] in which the configuration of a surface zinc ion is predicted to gain some trigonal planar character and become less tetrahedral. The surface oxygen ion, with its lone pair of electrons, adopts a distorted tetrahedral configuration.

Duke *et al*[14] have reported that no reconstruction occurs on the (000$\bar{1}$) oxygen face.

We comment on the dynamical intensity calculations and the reasonableness of these results in Section 7.1.2(c) below.

7.1.2(b) LEED results on the apolar, (10$\bar{1}$0) ZnO surface

The dynamic intensity calculations of Duke *et al*[16] applied to the (10$\bar{1}$0) surface indicated that the surface oxygen ions retreated towards the bulk by 0.45±0.1Å while the zinc ions remained unmoved. No lateral displacement of the ions occurred.

The sample had been prepared by the annealing route, the final anneal being at 573K for 16 hours. Since it is known that atmospheric CO_2 is readily adsorbed by ZnO at room temperature,[10] and is not completely desorbed on heating to temperatures below 1000K,[17] it is likely that the apolar and polar surfaces (Section 7.1.2(a)) studied by Duke bore surface CO_2. Göpel *et al*[17,18] have shown that the reconstruction of the ZnO(10$\bar{1}$0) surface is promoted by small amounts of adsorbed CO_2 (coverage $\theta<10^{-2}$ monolayers). A sample prepared by the annealing method, and rigorously cleaned by heating at 1050K showed no reconstruction of the (10$\bar{1}$0) surface.[17] On adsorption of CO_2 ($\theta<10^{-2}$ monolayers), on ZnO(10$\bar{1}$0) dynamic intensity calculations indicated a contraction towards the bulk of the uppermost zinc layer of 0.3Å and a movement of the oxygen layer of 0.1Å in the opposite direction.

No steps have been reported on the (10$\bar{1}$0)ZnO surface.

7.1.2(c) Estimation of the surface Zn-O interplanar spacing by dynamic LEED intensity calculations

The reconstructions of the ZnO(0001) and (10$\bar{1}$0) surfaces reported by Duke *et al*[14,16] and by Göpel *et al*[17] rely on the results of dynamic LEED intensity calculations which use the interplanar spacing between the outermost layers of zinc and oxygen ions as one of the variable parameters. However, the calculations predict only the major features of the observed intensity profiles and fail to reproduce the minor details. The discrepancies arise from the following problems:

1. the reproducibility of the experimental data;[14]
2. the lack of an adequate force law for the interaction of the incident electron with the ZnO surfaces;[14]

3. there are no reliable estimates for the value of the surface ionic charge Q, which is also a parameter in the calculations.

Values for the charges of ions in bulk ZnO range from 0.4 to >1, depending on the models used to interpret the experimental data.[19] Furthermore, it is known that the ions of the surface Zn-O double layer have charges different from those in the bulk, *e.g.* Madelung potential calculations predict that the outermost layer of ions on the $(000\bar{1})^{\pm}$ ZnO surfaces have a charge of 0.765Q while the layer of counter ions underneath and all the ions of the interior have a charge of 1.0Q.[19] In the intensity calculations of Duke *et al*,[14,16] the optimum value of Q was found to be unity for both ZnO(0001) and $(10\bar{1}0)$, corresponding to $Zn^{+}O^{-}$. It was, however, assumed that this value was constant throughout the entire crystal, including the surface.

According to Duke,[16] the dynamic calculations applied to ZnO(0001) and $(10\bar{1}0)$ surfaces do not give a completely reliable structure determination but are strongly suggestive of rearranged surface geometries. We now consider whether the proposed reconstructions are chemically plausible. The predicted displacements involve only the outermost zinc ions in the case of the $(10\bar{1}0)$ plane,[16] or the outermost oxygen ions in the case of the (0001) plane.[14] Large changes in bond lengths are therefore implied. The vertical displacement of zinc ions by 0.45Å at the $(10\bar{1}0)$ surface is a 28% change in the Zn-O bond length; the movement of 0.1 to 0.2Å by oxygen ions at the (0001) surface is a 16 to 32% change. Dynamic intensity calculations of the surface reconstructions of the (110) faces of II-VI and III-V semiconductors of the zinc blende structure have predicted larger

vertical displacements (>0.5Å) of the outermost cations.[20] In these materials, however, the bond length changes remained small. The cations *and* anions of the first *and* second double layers were displaced both laterally and vertically, the ions in the second layer to a lesser extent and in the opposite sense to those of the first layer. The maximum bond length change was *ca.* 5%. But in view of the much larger changes in bond length and the poor match between the observed and calculated LEED profiles for ZnO(10$\bar{1}$0), we submit that the proposed reconstructions of the ZnO(10$\bar{1}$0), and ZnO(0001), surfaces are erroneously large.

7.1.3 The surface species formed by hydrogen adsorption on ZnO

Temperature programmed desorption studies (TDS)[21] have led to the identification of *seven* states of adsorbed hydrogen on ZnO. Historically, the surface species have been classified according to the kinetics, reversibility or otherwise and temperature domain of the adsorption. Four main types of *adsorption process* are thereby distinguished:

(i) Type I is a rapid adsorption, reversible at room temperature, which gives two IR active species;

(ii) Type II is an irreversible adsorption occurring at room temperature. It is subdivided into two processes. The first is a rapid adsorption giving two IR active species, the second is a slow adsorption giving an unknown number (possibly one[1]) of species, which are IR inactive;

(iii) Type III is a reversible adsorption and occurs at 77K to give a single, IR active species;

(iv) Type IV is a high temperature adsorption. The maximum uptake is at 500K.[21] No values have been reported for the vibrations of the resulting surface species. Although it is reported to occur to a slight extent at room temperature[e.g. see 21], we have no evidence for the presence of type IV hydrogen on our samples.

Because a given adsorbed species may give rise to more than one feature in the TDS spectra, *e.g.* through a variation of the heat of desorption with coverage, we will refer to the adsorbed species by the adsorption process through which they were formed. For example, we will use the phrase "type II hydrogen" to mean any of the surface species produced by type II hydrogen adsorption on ZnO.

At room temperature types I and II predominate. They occur simultaneously but with different kinetics and apparently at different sites.

The frequencies of the IR bands reported for hydrogen adsorbed on ZnO are given in Table 7.1. The small discrepancies between the frequencies quoted by different authors is explained by their coverage dependence (see below). The distinction between the bands of type I and type II species was first made by Boccuzzi *et al.*[23] On mild evacuation at room temperature, bands due to type I are severely reduced in intensity while those due to type II remain unaffected.

7.1.3(a) Type I hydrogen

Type I adsorption is active in C_2H_4 hydrogenation and H_2/D_2 exchange. This is a dissociative chemisorption and gives rise to two IR bands whose frequencies are functions of

TABLE 7.1 Infrared bands reported in the literature for hydrogen adsorbed on ZnO

Type I			Type IIa			Type III		
frequency, cm^{-1}	assignment	ref.	frequency, cm^{-1}	assignment	ref.	frequency, cm^{-1}	assignment	ref.
						4019	ν_s (H-H)	34
						3507	ν_s (H-D)	
						2887	ν_s (D-D)	
3498)		24,23						
3497)	ν_s (O-H)	25						
3455	ν_s (O-H) not observed above 190K	30,24						
			ca. 3400b	ν_s (OH---O)	23			
1709)		25						
1708)	ν_s (Zn-H)							
1705)		30						
			1475b	ν_s (Zn $\overset{H}{}$ Zn)	23			
850-845	ν_δ (O-H)	23						
817	ν_δ (Zn-H)	23						

b = broad; ν_δ = bending mode; ν_s = symmetric stretching mode

Hydrogen overpressures used for type I adsorptions: ref. 23, 100 torr; ref. 24, data extrapolated to zero coverage; ref. 25, 380 torr; ref. 30, 35 torr.

coverage. A Zn-H stretch is observed at 1709 cm^{-1} and an O-H stretch at 3498 cm^{-1} (both values extrapolated to zero coverage).[24] The two bands develop simultaneously and their intensities are directly proportional to each other as the coverage changes. The adsorption site consists of a Zn-O pair,[25,26] *i.e.*

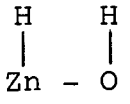

Only some 10% of the total surface is available for type I, this has been observed by many workers[27] regardless of the precise history and origin of the ZnO sample. Dent and Kokes[26] have put forward a model in which the Zn-O pairs are located on the reconstructed $(000\bar{1})$ surface. However, according to John,[27] other polar faces, *e.g.* $(10\bar{1}1)$ and (0001), might also be expected to be active.

We suggest here that H_2 adsorption *at pair sites* on ZnO polar faces must involve significant rehydridisation at the surface. Consider the ZnO(0001) face, shown in Fig. 7.1. This face consists of a double layer of zinc and oxygen ions, the plane of the oxygen ions being 0.6056Å [28] below that of the zinc plane. A typical value for an O-H bond length is 0.96Å.[29] Thus formation of a surface O-H bond, perpendicular to the oxygen plane, puts the adsorbed H atom *c.a.* 0.35Å above the zinc plane. The closest distance between a zinc ion and the H atom of the surface hydroxyl is then 1.89Å (data from ref.28). This distance is greater than the sum of the covalent radii of Zn plus H, *viz* 1.57Å. Therefore, H_2 adsorption at a Zn-O pair site, where the oxygen ions are below the zinc ions is geometrically reasonable. However, the oxygen ions of the (0001) surface double layer are already four coordinate before H_2 adsorption. Thus significant

rehybridisation of the surface, particularly of the oxygen ions, must occur on H_2 adsorption.

Similar arguments apply to adsorption at Zn-O pair sites on the $(000\bar{1})$ surface. We have not considered possible reconstructions *in vacuo* of these surfaces, since these have not been definitely proved by LEED (see Section 7.1.2(c)).

A combined TDS (100-350K) and IR study by Griffin and Yates[24] identified three desorption peaks, all associated with type I adsorption. The principal peak, I_b, arose at 240K, along with a broad structure, I_c, composed of partially resolved features at 270 and 310K, and a third peak, I_a, at 170K. The temperature of maximum desorption, T_{max}, of peak I_b fell as the initial hydrogen dosage was increased. Both I_b and I_c gave rise to the two coverage dependent IR bands at 1709 cm^{-1} and 3498 cm^{-1} (zero coverage) and could not be distinguished on the basis of their IR absorbance alone. We define q to be the surface coverage of hydrogen, measured as μmole H_2/(gZnO). The frequency of the O-H stretch fell linearly with increasing coverage (by 15 cm^{-1} over the range q=0 to 12 μmole g^{-1}) while that of the Zn-H stretch increased slightly(by 5 cm^{-1}) over the same q range. These shifts and the fall in T_{max} of the I_b state imply a significant repulsive interaction between the adsorbed species, which are said to be located in densely populated areas of the surface.[23] Surface heterogeneity was regarded as a less likely cause of these effects since filling of the I_c sites also shifted the IR frequency of the I_b species.[24]

The third desorption state, I_a, gave an IR band at 3455 cm^{-1}. This band could not be observed above 190K. A similar low temperature form of type I has been reported by Kokes *et al*[30]

which gives an IR band at 3455 cm^{-1} on adsorption at 195K.

Estimates by Griffin and Yates of the binding energy, U, the activation barriers for adsorption and desorption, E_{ads} and E_{des}, are given in Table 7.2. States I_b and I_c have similar binding energies but are differentiated by their activation barriers. Since the IR frequencies are the same, the shape of the potential energy wells near the minima must be the same and unaffected by the different values for E_{des}.

A calorimetric study by Fubini *et al*[1] has also shown that the adsorption at room temperature is activated. It was deduced that E_{des}>9 kJ mol^{-1} for type I. The differential heat of adsorption, h_a, is a function of surface coverage q, decreasing rapidly at low q from 60 kJ mol^{-1} (q=0) to become approximately constant at 14 kJ mol^{-1} at high q. This suggests slight surface heterogeneity *at the very lowest coverages* and may be related to the I_a species. At all higher coverages, the decrease in adsorption enthalpy was due to the simultaneous adsorption of type I (h_a=37-40 kJ mol^{-1}) and type II hydrogen (h_a=*ca* 14kJ mol^{-1}).

At high coverage, q, the differential heat of desorption of type I hydrogen was found to be 37 kJ mol^{-1} and constant with q. Adsorption and desorption isotherms did not coincide but followed different paths, which points to different mechanisms for adsorption and desorption.[1]

The TDS results of Griffin and Yates are curious in that the principal desorption peaks occur below room temperature. In an earlier study by Baranski *et al*[21] the major ambient temperature desorption peaks arose at 293 and 323K, assigned to type I Zn-H and O-H species respectively. There is little agreement between the adsorption enthalpies and also the activation energies of desorption calculated by Baranski[21], Griffin and Yates,[24]

TABLE 7.2 Published adsorption enthalpies, U; activation energies of desorption, E_{des}; and activation energies of adsorption, E_{ads}, for type I hydrogen adsorption on ZnO

Griffin and Yates[24]					Barański *et al*[21]				Fubini *et al*[1]			reference
TDS					TDS				microcalorimetry			method
state	T_{max} K	U kJ/mol	E_{des} kJ.mol^{-1}	E_{ads} kJ.mol^{-1}	state	T_{max} K	U kJ.mol^{-1}	E_{des} kJ.mol^{-1}	state	U kJ.mol^{-1}	E_{des} kJ.mol^{-1}	
I_a	173	29	50	21								
I_b	232	50	67	17	I_a	293	<17	20	I	37 to 40	>9	
I_c	305	54	88	33	I_b	323	<17	18				

The columns marked "state" show the authors' labels for the TDS peaks which occurred at temperatures of maximum desorption, T_{max}.

and Fubini[1] (see Table 7.2). We note that the discrepancies must be related to the different models used to calculate the thermodynamic quantities and the different times allowed for equilibriation of the H_2 uptake. Type II adsorption occurs under the same conditions as type I but has a component which does not reach equilibrium for several days (see below). The simultaneous formation of this species will affect the amount of type I adsorption. However, type II adsorption was not discussed at all in the paper by Griffin and Yates.[24] We suggest here possible reasons why it was not observed in their results. According to Baraǹski, type II hydrogen gives TDS peaks in the two regions 723 to 600K and 573 to 523K[21], (see Section 7.1.3(b)). Griffin and Yates studied the TDS range 100 to 300K, therefore if Baraǹski is correct they will not have observed TDS peaks from type II hydrogen even if such species were present on their samples. Furthermore, according to Boccuzzi[23] type II hydrogen gives rise to two IR bands, at *ca* 3400 and 1475 cm^{-1}, in the region studied by Griffin and Yates[24], see Table 7.1. These bands are broad and weak and have not been reported by other workers. It is probable, therefore, that type II adsorption was occurring simultaneously with type I adsorption on the samples studied by Griffin and Yates.[24] In view of this, their thermodynamic results may be inaccurate.

At room temperature the uptake of type I hydrogen is thermodynamically controlled.[30] The rates of adsorption of H_2 and D_2 are equal. However, on exposure to HD, ZnH-OD species predominate over ZnD-OH by a factor of 2 to 3. Type I adsorption still occurs at 78K but below *ca* 240K, the process is kinetically controlled and becomes irreversible. A large kinetic isotope effect operates at 78K and the adsorption of H_2 is 5 times faster

than that of D_2. HD adsorption then favours the formation of ZnD-OH by a factor of 20 to 100.[30]

Type I adsorption of hydrogen is not associated with any conductivity change[22] and at room temperature neither type I nor type II hydrogen form an accumulation layer.

7.1.3(b) Type II hydrogen

Type II adsorption is irreversible at room temperature. It may further be classified into two parts[1]:

(a) A fast dissociative adsorption which has recently been reported by Boccuzzi *et al*[23] to give weak, broad IR bands at 1475 and *ca* 3400 cm^{-1} assigned to stretching modes of $Zn\diagup^{H}\diagdown Zn$ and O—H···O bridged species, respectively. However, we were unable to observe a band at *ca* 1475 cm^{-1} due to adsorbed hydrogen in our INS spectra of ZnO+H (Section 7.3.5; the 3400 cm^{-1} band lies outside the frequency range of our INS results). In spite of the discrepancy, discussed in Section 7.3.5(a), between the INS and IR[23] results, we note that a frequency of 1475 cm^{-1} for a mode of $Zn\diagup^{H}\diagdown Zn$ species is consistent with the spectra of transition metal hydridocarbonyls obtained by Graham[31] (see Figure 5.2, Chapter Five). Only $(\mu_2\text{-H})M$ and $(\mu_2\text{-H})_2M_2$ hydridocarbonyls give[31] IR bands near 1475 cm^{-1}. A $(\mu_2\text{-H})_2Zn_2$ surface species on ZnO can be ruled out since the hydridocarbonyl analogy indicates that a strong IR band should have been observed at *ca* 1224 cm^{-1}. The symmetric, ν_s, and antisymmetric, ν_{as}, stretching modes of $M\diagup^{H}\diagdown M$ in $(\mu_2\text{-M})M_2$ hydridocarbonyls give IR bands in the region 895-1320 cm^{-1} (weak) and 1470-1670 cm^{-1} (medium) respectively.[31] On this basis,

Boccuzzi's assignment of the 1475 cm^{-1} IR band to a stretching mode of a surface $Zn\diagup^{H}\diagdown Zn$ species can be further specified as the antisymmetric stretch. No bands assignable to the ν_s made of $Zn\diagup^{H}\diagdown Zn$ species could be observed in the ZnO + H IR spectra of Boccuzzi[23] - such bands are expected[31] to be of low IR intensity. From the hydridocarbonyl data,[31] no modes of a $Zn\diagup^{H}\diagdown Zn$ group other than ν_s and ν_{as} are expected to be observed by IR spectroscopy above 750 cm^{-1}, the low frequency cut-off of Boccuzzi's data.[23]

We also note that Zn⟨H⟩Zn bridges are found in compounds of the type:[32]

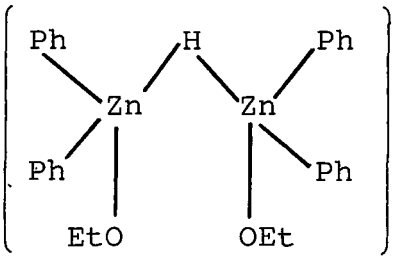

(Ph = C_6H_5; Et = C_2H_5)

According to the IR data of Shriver *et al*[32] the above compound, in a nujol mull, is reported to give a broad IR absorption from 900 to 1200 cm^{-1} assigned to a stretching mode of the Zn⟨H⟩Zn moiety. In the ether-free complex the band is shifted from 1250 to 1650 cm^{-1}, and according to the authors, the ZnHZn moiety becomes linear.

(b) The second component of type II is a slow dissociative chemisorption which requires several days at 298K to reach equilibrium.[1] This species has a heat of desorption of 14 kJ mol^{-1} which is less than that of type I (37-40 kJ mol^{-1})[1] despite the fact that type IIb adsorption is slow and irreversible whereas type I is fast and reversible. These features suggest that type IIb sorption involves diffusion into the bulk.[1] The equilibrium amount of H_2 which may be absorbed by ZnO has not been measured, due to the difficulties arising from the time taken to reach equilibrium and the occurrence of type I and rapid type II adsorption under the same conditions.

The adsorption sites for both type II species are independent of those for type I hydrogen. It has been proposed[9] that type II adsorption occurs at faces which are not close-packed, such as the apolar $(10\bar{1}0)$ face. Penetration by hydrogen into the bulk then proceeds along the channels formed by the aligned octahedral holes (see Section 7.1.1).[9] These channels make an

acute angle with the $(10\bar{1}0)$ surface and have at their narrowest point, trigonal constrictions of diameter 1.2Å. The activation barrier to absorption is probably high, being associated with the expansion of the trigonal "squeeze points" as the hydrogen diffuses along the channels.[9]

Baranski *et al*[21] have assigned the highest temperature peak in their TDS spectra (*ca* 200 to 723K) to type IIa hydrogen. The value of T_{max} fell with increasing coverage from 723 to *ca* 600K. This peak was observed even for adsorption at 238K and also for a partial hydrogen pressure of less than 1 torr and so could not have arisen from a high temperature adsorption state, type IV. A TDS peak in the range 573 to 523K, depending on initial coverage, has been ascribed to type IIb hydrogen.[21] This peak is associated with a maximum in the conductivity of ZnO at 453K during the adsorption of type IIb hydrogen.[22] Formation of a protonic species and donation of electron density to the conduction band is thus implied. The pressure, P_{H_2}, dependence of the conductivity, σ, in this temperature range was given by:[22]

$$\sigma = k\,[P_{H_2}]^{\frac{1}{4}}$$

which was explained by assuming $\sigma \propto [H^+] = [e^-]_{conduction\ band}$ and the dissociation scheme:

$$H_{2(g)} = 2H_{(ads)} = 2H^+ + 2e^-$$

This is consistent with the formation of an interstitial protonic hydride phase on type IIb adsorption.

Baranski *et al*[21] noted that another TDS peak, at 370K, was also a candidate for type IIb hydrogen. But since this peak is associated with an uncharged species,[21,22] it cannot be due to an interstitial hydride. We suggest that it might

possibly arise from a precursor between the bridged and interstitial states.

The catalytic activity, *e.g.* for alkene hydrogenation, of both forms of type II is still unclear; type I is certainly far more active.[*e.g.*33]

7.1.3(c) Type III hydrogen

This is a weak molecular chemisorption for which the heat of adsorption is 9.2 - 10.5 kJ mol^{-1}.[34] It forms on adsorption at room temperature followed by cooling to 77K, and is removed by pumping at 90K. It occurs at the same type of sites as type I but is less extensive. The H-H (and D-D) stretch becomes IR active on adsorption (see Table 7.1). This species is not active in H_2/D_2 exchange. It is, however, involved in ortho/para hydrogen conversion, the barrier to rotation about an axis perpendicular to the surface being sufficient to prevent free rotation.[34]

Two TDS peaks, at *ca* 210K and 260K, have been tentatively assigned to type III by Baranski *et al*.[21] These lie in the range reported by Griffin and Yates for type I.[24] We feel that the peaks from 210 to 323K in the results of Baranski *et al* should all be associated with type I and suggest that type III would give peaks at much lower temperatures.

7.1.4 Published IR data for hydrogen adsorbed on ZnO

Boccuzzi *et al*[7] have studied the IR spectrum (700-4000 cm^{-1}) of ZnO dosed with O_2 and H_2 from 97 to 523K. The particles of ZnO, of unstated average dimensions, were said to be sufficiently small to cause considerable scattering of the

incident light (by diffraction from particle edges).

No IR bands were observed due to chemisorbed H or O.

The spectra obtained at various temperatures under a constant pressure of O_2 showed (Fig.7.5):

(a) multiphonon bands from 700-1100 cm^{-1};

(b) 2 narrow bands in the range 1300 to 1600 cm^{-1} due to CO_3 impurities;

(c) weak bands in the 3400 to 3700 cm^{-1} region due to residual hydroxyls.

On heating the sample to 433K *in vacuo* or in an H_2 atmosphere, all the above bands disappeared. The spectrum became a smooth curve with a transmission of <20% at frequencies of 2000 cm^{-1} and above. At lower frequencies, the transmission strongly increased (see Fig.7.5).

Heating the sample, especially when it bears chemisorbed H, will raise the electron density in the conduction band. The frequency, ν_{pl}, of a longitudinal plasmon mode increases with the number, n, of free electrons, thus:[35]

$$\nu_{pl} = \left(\frac{ne^2}{\pi \varepsilon_\infty m^*}\right)^{\frac{1}{2}}$$

e = electronic charge,

m* = effective mass of conduction band electrons,

ε_∞ = high frequency dielectric constant of the medium.

Coupling between a phonon mode of frequency ν_{LO} and a plasmon mode can occur on increasing n such that $\nu_{pl} = \nu_{LO}$. Only longitudinal optical (LO) phonon modes may couple with these plasmon modes. In the absence of damping, the coupled system gives rise to two vibrational transitions whose frequencies, ω_+ and ω_-, are slightly displaced from ν_{LO} (ν_{LO} occurs at

Fig. 7.5 IR spectrum of ZnO

1) at 433K in O_2 (40 torr)

2) at 433K in vacuo.

Taken from Boccuzzi et al., ref. 7.

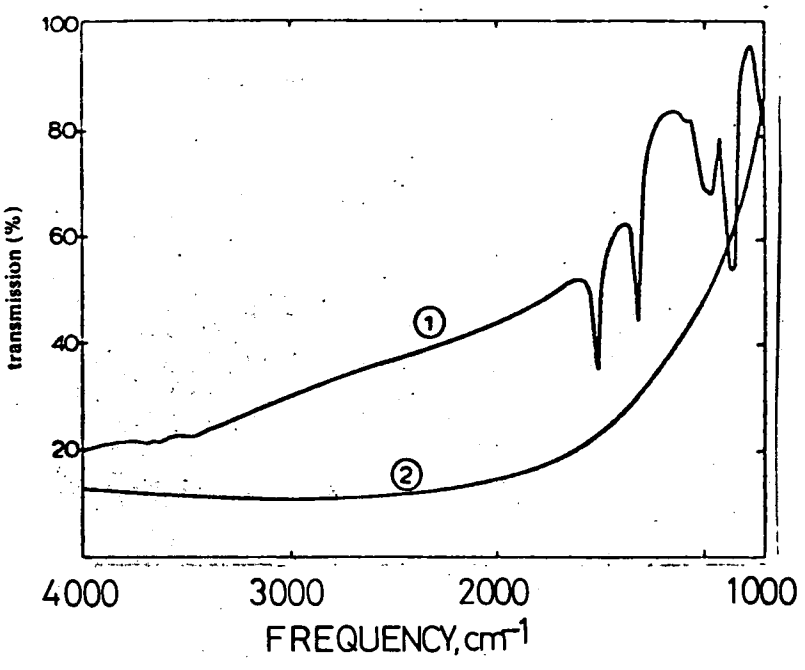

ca 580 cm^{-1} in ZnO, depending on the crystal orientation, see Table 7.3). These two transitions have been observed in the Raman and IR reflectivity spectra of semiconductors with the wurtzite (and zinc blende) crystal structure, the samples having been doped to alter the electron population of the conduction band.[36,37] However, because the coupled plasmon-phonon system has longitudinal character, the bands at ω_+ and ω_- are not observable by IR transmission measurements.

For sufficiently high free-electron concentrations, $\nu_{pl} >> \nu_{LO}$ and the effect of the phonon-plasmon coupling is very much reduced. A mode of largely plasmon character will occur near ν_{pl} and a mode of principally phonon character near ν_{LO},[38] instead of two (coupled) modes near ν_{LO}. The mode near ν_{pl} may be observed in an IR transmission experiment, as reported for small particles of CdO at *ca* 2000 cm^{-1}.[38]

Boccuzzi *et al*[7] ascribed the loss of structure of 433K in their IR transmission spectra (Fig.7.5) to surface plasmon-phonon coupling. The extent of this coupling was not discussed and we wish to develop the authors'[7] explanation of Fig.7.5. Strong phonon-plasmon coupling in ZnO is expected to give two transitions close to 580 cm^{-1}, rather than a single broad band in the IR extending from 700 cm^{-1} to above 4000 cm^{-1}. Thus strong coupling of surface phonons and plasmons on Boccuzzi's sample cannot have occurred. It is known that a maximum in the conductivity of ZnO+H, and therefore also in the free electron population, occurs at 453K.[22] Thus we assign the intense absorbance above *ca* 2000 cm^{-1} in Fig. 7.5 (spectrum 2) to surface plasmons which, because of the increased electron density in the ZnO conduction band at 433K, are only weakly coupled, if at all, to surface phonons. The loss of detail in the

TABLE 7.3 Optical parameters of a single crystal of ZnO (taken from ref. 4)

mode	frequency, cm^{-1}	
	TO mode	LO mode
$\perp$	406	589
$\parallel$	377	575

The symbol $\perp$ denotes the case of the electric field vector of the incident light perpendicular to the crystal c-axis and $\parallel$ denotes the parallel case

TO = transverse optical phonon mode

LO = longitudinal optical phonon mode

vibrational spectrum at 433K (Fig.7.5, spectrum 2) may be related to the high free electron population.

Boccuzzi *et al*[7] also obtained the IR spectrum of a ZnO sample at 433K under 40 torr H_2 which was very similar to that obtained at 433K *in vacuo* (Fig.7.5, spectrum 2). However, on cooling to 300K under H_2 the transmittance fell to zero below *ca* 2000 cm^{-1}. This is remarkable since the modes of type I hydrogen are normally observed under the latter conditions (300K). Neither plasmon-phonon coupling nor absorption by pure plasmons explain this effect.

7.1.5 Likely contaminants on ZnO surfaces

It is known that ZnO rapidly adsorbs H_2O and CO_2 when exposed to the atmosphere.[27] The resulting species will be the most likely surface contaminants in the samples used for the IR studies and our INS study of ZnO/H_2. Surface carbonate groups give IR bands in the region 1600 to 1250 cm^{-1}.[24] According to Atherton *et al*, these are removed by heating in O_2 *and* H_2O at 673K and subsequent cooling in O_2.[39] Milder calcination conditions do not completely remove surface CO_3^{2-}. For example, Griffin and Yates[24] prepared a sample of Kadox 25 by heating *in vacuo*, at 673K for 3 hours then cooling to 573K, followed by cooling to room temperature under O_2. The resulting sample showed strong, broad IR bands assigned to surface carbonate at 1584, 1520, 1380 and 1324 cm^{-1}. The samples used in the present INS study were prepared under similar, moderate conditions. Thus the presence of some surface CO_3 on our samples cannot be ruled out.

Adsorption of water on ZnO at room temperature and above produces surface hydroxyls. IR bands from such species have been observed by Atherton *et al*[39] at 3440 (broad), 3555 (broad), 3620 (narrow) and 3670 cm^{-1} (narrow). Similar results were reported by Morishigue *et al*[40] who observed bands at 3425 (broad), 3540 (broad), 3605, 3650 and 3675 cm^{-1}, the latter three bands all being narrow. The bands assigned to surface -OH formed by the adsorption of H_2O do not coincide in frequency with those due to the hydroxyls produced on H_2 adsorption, the latter occurring at 3498 and 3455 cm^{-1} (Table 7.1). Isotope exchange experiments, admitting D_2O to a surface already exposed to H_2O,[39] caused no change in the IR spectrum in the region where one would expect to observe the H_2O bending mode (1640 cm^{-1} in liquid water, 1595 cm^{-1} in the gas phase[41]). All the adsorbed H_2O had therefore formed surface hydroxyls and the ZnO carried no undissociated H_2O. The hydroxyls originating from H_2O adsorption are not completely removed by the sample preparation technique used for our INS experiment and are thus a likely contaminant. It has been estimated[42] that less than 0.05 monolayer of both -OH and $-CO_3$ species remained on a ZnO surface after a pretreatment involving three cycles at 673K of alternate exposure to 20 torr O_2 for 20 minutes followed by outgassing for 60 minutes. Our INS samples were prepared under slightly milder conditions. Thus although undissociated H_2O is expected to be absent from the surface of our INS samples, a very low concentration of -OH species is likely. This is confirmed by the IR spectrum of a ZnO sample we obtained after a calcination treatment similar to that used for the INS samples (Fig. 7.11, Section 7.7.3(c))). Only very weak bands were observed due to surface hydroxyls and none were ascribable to surface H_2O.

7.2 Experimental

The beryllium filter detector spectra of ZnO and ZnO plus adsorbed hydrogen have been obtained using the INIB spectrometer in the range 320 to 2230 cm^{-1}. The spectra were recorded at 77K.

The ZnO sample was Kadox 25 (New Jersey Zinc Co.) which is produced by burning zinc in air. It was calcined by heating to 723K in a static, but periodically refreshed, dry oxygen atmosphere, cooling to room temperature under oxygen and subsequent evacuation to 7×10^{-5} torr. The oxygen was dried by slow passage through an acetone/solid CO_2 cold trap at 196K. Hydrogen (99.9995%, Masonlite, Chatham) was adsorbed by exposing the sample to 390 torr H_2 at room temperature for 10 minutes, followed by cooling to 77K. This method is expected to produce types I, II and III surface hydrogen. From the work of Kokes *et al* [26,30] and of Fubini,[1] we expect the concentrations of the surface hydrogen species to be type III>I>II.

Because of equipment availability, the commercial service provided by Coulter Electronics Ltd., Luton, was used to find out the surface area and particle size distribution of our Kadox 25 samples. The N_2 B.E.T. surface area of a portion of the calcined Kadox 25 sample used for our INS experiments was 7.8 m^2g^{-1}. This is close to a value of 8.3 m^2g^{-1} reported by Baranski and Cvetanovic[53] for crushed, pelleted Kadox 25 ZnO which had been calcined in O_2 to 673K. The particle size distribution of our samples was measured by a capacitance technique using a 5% (by mass) solution of LiCl in CH_3OH as an electrolyte and a polyethylene glycol dispersant for the ZnO. It was found that 87.6% of the ZnO particles, assumed

to be spherical, had a diameter of less than 1.0μm and 71.3% had a diameter of less than 0.79μm. The particle size distribution was unchanged by calcination.

The volume of H_2 adsorbed by calcined ZnO for our INS experiments was *ca* 85 cm^3 (N.T.P.). This quantity of hydrogen would scatter 1.4% of the incident neutron beam and the ratio of the incoherent scattering cross section of adsorbed H to that of ZnO is 8.8 to 1.0 (at an incident neutron energy of 204 cm^{-1}. The uptake of H_2 by our INS sample was 68 μmole H_2/g ZnO, equivalent to a coverage, q, of 8.7 μmole H_2/m^2. If the adsorption of H_2 was entirely molecular (in fact it is not, because type I adsorption occurs), this uptake would correspond to a coverage of 0.7 monolayers H_2, assuming that the area occupied by both H_2 and N_2 admolecules is 16$Å^2$. [57]

We have obtained IR spectra of a self-supporting disc of Kadox 25 from 4000 to 750 cm^{-1}, recorded at intervals during a calcination procedure similar to that used for the INS sample. The spectra are shown in Figures 7.9 to 7.11 below and discussed in Section 7.3.3(c). Table 7.4 summarises the experimental details.

The sample was held in a vacuum cell and an IR spectrum (Figure 7.9) recorded after evacuation to 4.5 x 10^{-2} torr at 299K. After heating the ZnO under oxygen to 431K and re-evacuation of the sample-cell, the IR spectrum was recorded at 431K. This O_2/heating procedure was repeated twice to higher temperatures (Table 7.4). Finally, after heating in O_2 to 725K, the sample was allowed to cool under vacuum to 305K and the IR spectrum (Figure 7.11) was recorded. Because the IR data obtained are similar to those already published, [23-25,30]

TABLE 7.4 The experimental conditions used for the recording of the IR spectra of ZnO during the calcination process

figure no.	pressure O_2 used during heating, torr	initial temperature T_1, K	final temperature T_2, K	time to heat from T_1 to T_2, min.	Conditions under which IR spectra were recorded: Pressure, torrx10^{-5}	Temperature, K	note
9	0	299	299	113	4500	299	Spectrum recorded after 113 mins. of evacuation. No exposure of sample to O_2.
-	9.2	299	431	55	6	431	
-	21.0	431	573	74	5	573	
10	21.3	573	725	60	7	725	
11	0	725	305	100	6	305	Sample allowed to cool from 725K to 305K in vacuum before recording IR spectrum

The sample was heated from a temperature T_1K (col.3) to T_2K (col.4) under vacuum or under O_2 (col.2). On reaching T_2, the O_2 was evacuated and the IR spectrum recorded under the conditions in cols.6 and 7. The calcination procedure was then continued by heating from T_2 under O_2, or, for Fig.7.11, cooling under vacuum.

we present (Section 6.3.3(c)) only a selection of our recorded spectra in this thesis, sufficient to illustrate the effects of the calcination procedure. However, the band frequencies observed in each IR spectrum that we recorded during the calcination are summarised in Table 7.7 below.

Because, for the self-supporting disc, the sample was totally absorbing below 700 cm^{-1} a spectrum of ZnO diluted with KBr was also obtained so that the region 700 to 300 cm^{-1} could be studied. The Raman spectrum of ZnO was also recorded. No pretreatment of the sample was carried out for the Raman or ZnO/KBr IR experiments.

7.3 Results - the vibrational spectrum of ZnO and H_2 adsorbed on ZnO

7.3.1 Introduction

The space group of wurtzite ZnO is C_{6v} and there are 4 atoms per unit cell. Group theory therefore predicts that the phonon spectrum will comprise 3 acoustic and 9 optic modes.[43] The optic modes are classified thus:

1 x A_1 mode	IR + R active
1 x E_1 mode	IR + R active
2 x E_2 mode	R active only
2 x B_1 mode	inactive

However, according to the Lyddane-Sachs-Teller (LST) theory,[35] long range electrostatic forces in a crystal may cause splitting of the formally IR active optic phonons into transverse (TO) and longitudinal (LO) branches. The LO branch

generally occurs at a higher frequency than the TO branch(es) near the Brillouin zone centre. In addition to the long range forces, short range forces, arising from the repulsions between the electron clouds of adjacent atoms, also operate in uniaxial crystals like ZnO. These short range forces lead to anisotropy of the force constants of particular phonon branches. Because of this anisotropy, the transverse phonon branches will occur at different frequencies, $\nu_{\|t}$ or $\nu_{\perp t}$, depending on whether they are propagated in a direction parallel or perpendicular, respectively, to the unique crystal *c*-axis. In the same way, an LO branch may arise at two different frequencies, $\nu_{\|l}$ or $\nu_{\perp l}$.

The LO and TO branches arising from either mechanism of splitting retain the same IR/R activity as the parent phonon mode with one exception: all the LO branches are IR inactive regardless of their symmetry.

In summary, new phonon-like modes may appear in the IR and /or Raman spectra of ZnO that are not predicted by unit cell group analysis. Indeed, the splitting of both the E_1 and A_1 optic phonon modes of ZnO into LO and TO branches was reported in the Raman by Damen *et al.*[44] This was observed by orientating differently cleaved single crystals of ZnO with respect to the incident light such that the phonons were propagated along the main crystallographic axes (see Section 7.3.2.).

If the incident light is orientated at a general angle θ with respect to the crystal axes, or if a polycrystallic sample is used, then the nature of the excited phonons depends on the relative magnitude of the long range and short range forces in the crystal. According to Damen *et al*,[44] the long range forces

dominate in ZnO. The TO modes then arise at a frequency ν_t given by:[35]

$$\nu_t^2 = \nu_{||t}^2 \sin^2\theta + \nu_{\perp t}^2 \cos^2\theta$$

and the LO modes at a frequency ν_l given by

$$\nu_l^2 = \nu_{||l}^2 \cos^2\theta + \nu_{\perp l}^2 \sin^2\theta$$

Thus the bands observed from powdered samples may be broadened and the frequency maxima slightly shifted from those observed from single crystals.

Furthermore, the unit-cell group selection rules for the activity of multiphonon bands will be relaxed. The multiphonon bands will be infrared and Raman active for all orientations of the crystallites.[35]

We now present the Raman, infrared and INS spectra of ZnO, in that order, followed by the INS spectrum of hydrogen adsorbed on ZnO.

7.3.2 The Raman spectrum of ZnO

The Raman spectrum of Kadox 25 before *any* sample pretreatment was carried out is shown in Fig.7.6 and in Fig.7.7 under higher resolution. The data are summarised in Table 7.5, column 5, using the higher resolution results for the weaker spectral features.

Also included in Table 7.5 (columns 1 to 4) are the single crystal Raman data reported by Damen *et al*[44] and Mitra *et al*.[45] No sample pretreatment was used in either case.

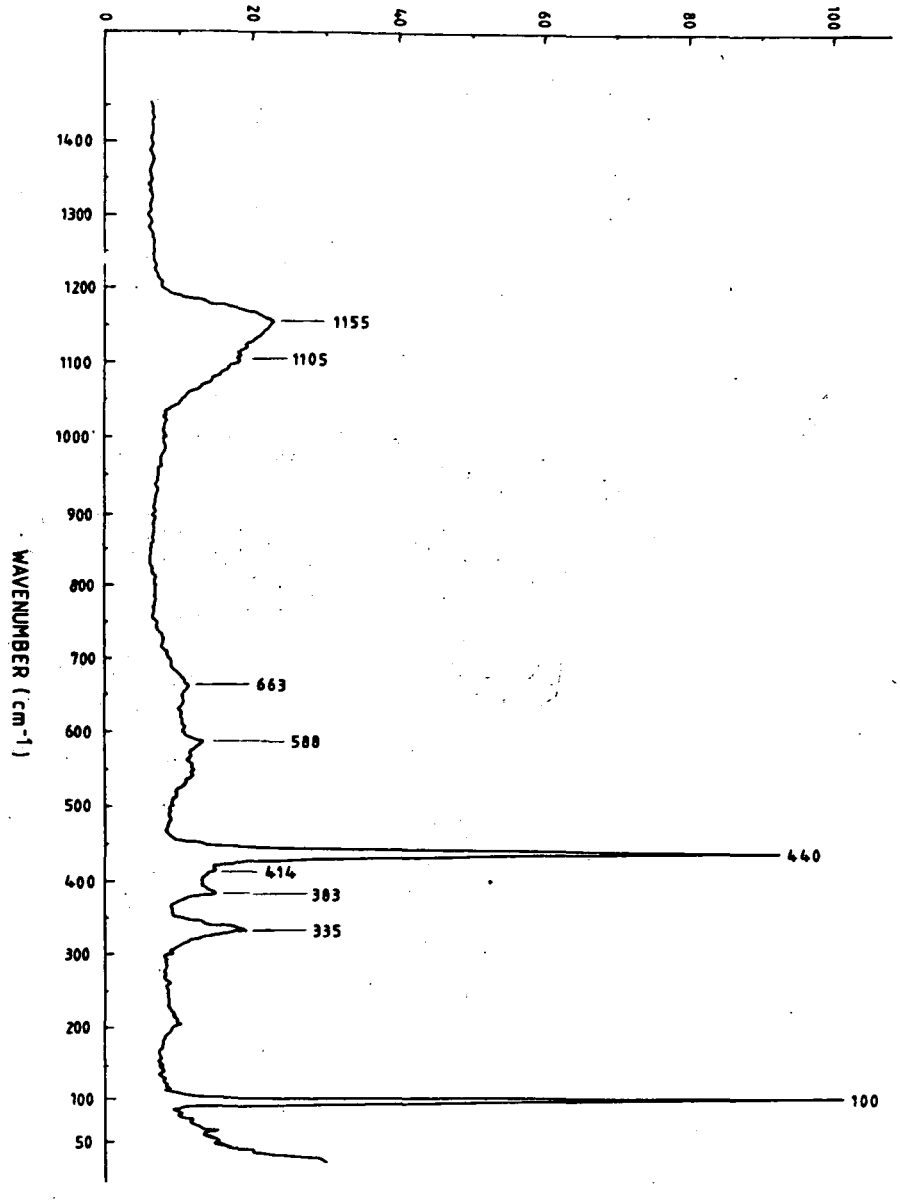

Fig. 7.6 The Raman spectrum of ZnO before sample pretreatment.

Fig. 7.7 The Raman spectrum of ZnO before sample pretreatment (high resolution).

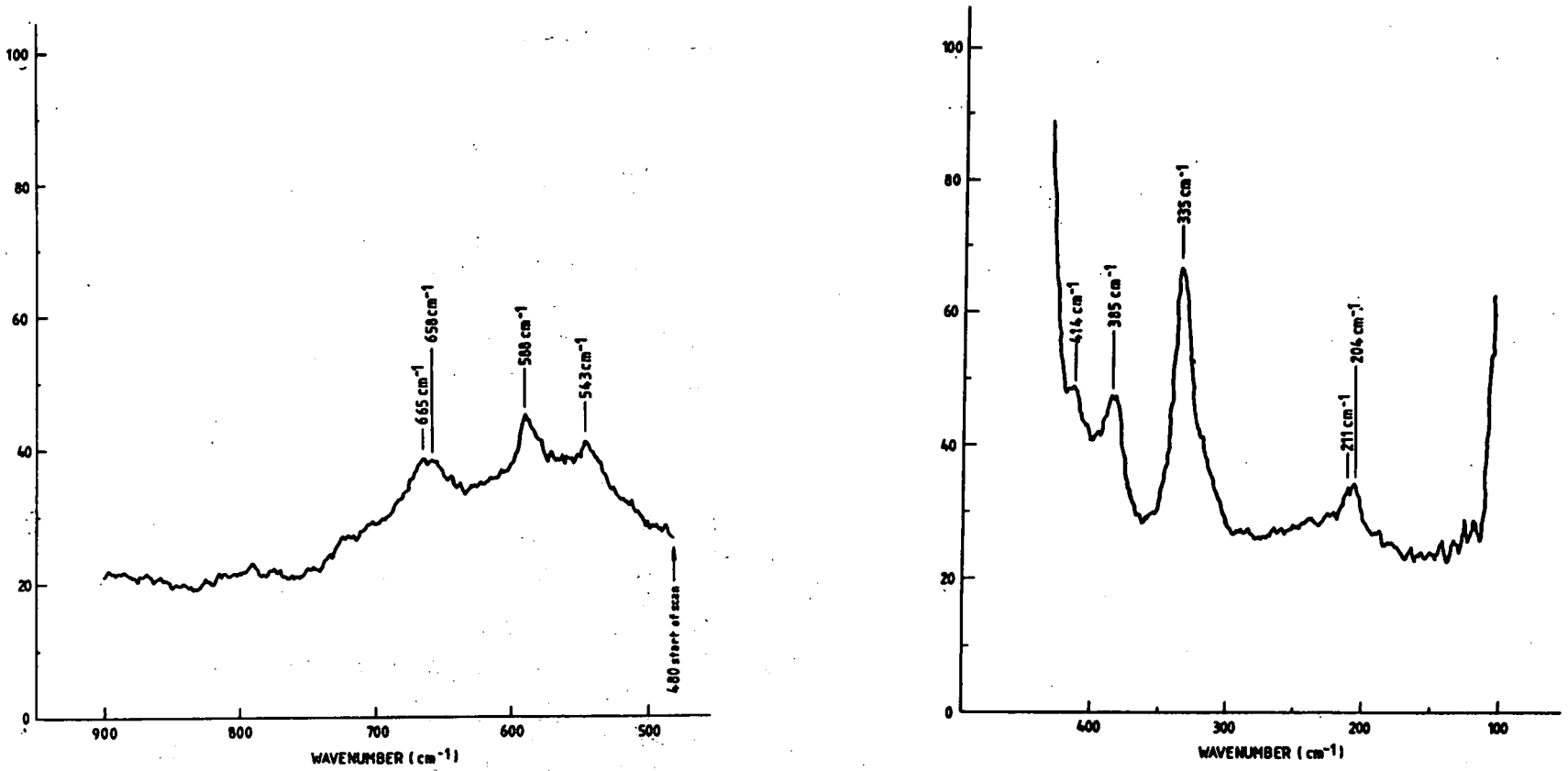

Fig. 7.7 continued. The Raman spectrum of ZnO before sample pretreatment (high resolution).

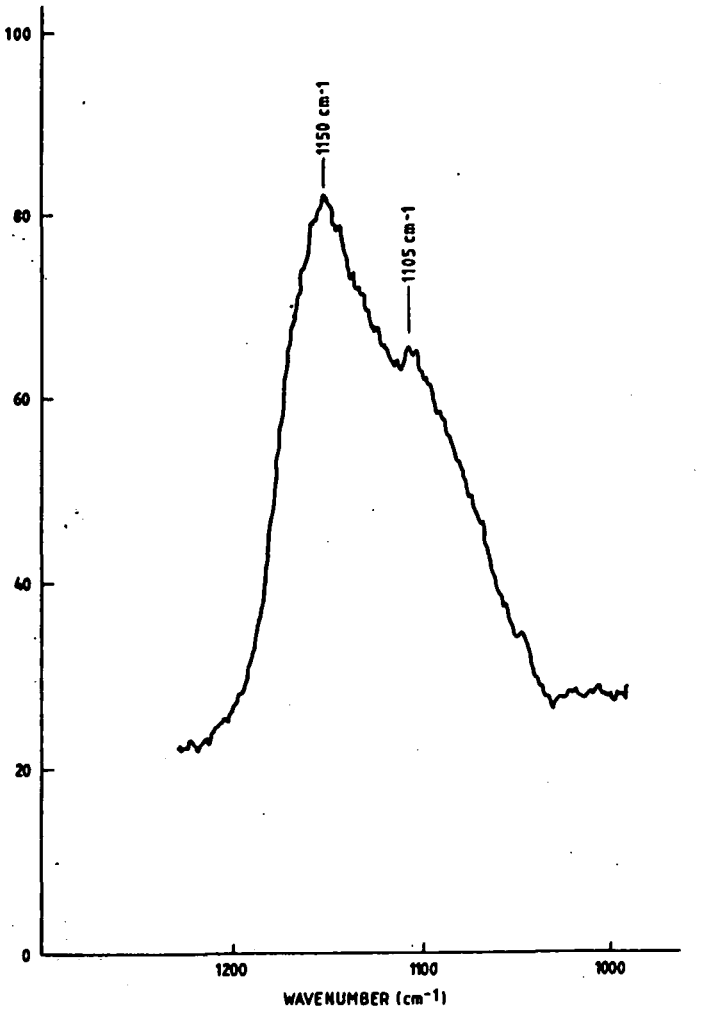

TABLE 7.5 The frequencies and assignments of bands in the vibrational spectrum of ZnO

Raman[45] Mitra		Raman[44] Damen		Raman (this work)	INS (this work)	method reference
<--------uncalcined ZnO, room temperature -------->					calcined ZnO 77K	sample, temperature K
cm^{-1}	assignment	cm^{-1}	assignment	cm^{-1}	cm^{-1}	assignment (this work)
		101	E_2	100 vs		TO phonon
180	TO (E_2)					
		208	mp	204, 211 vw		mp
		334	mp	335 m		mp
383	TO (E_2)	380	TO (A_1)	383 w		TO phonon
420	TO (A_1)	407	TO (E_1)	414 w,sh		
438	TO (E_1)	437	E_2	440 vs	437 vs	TO phonon
538	LO			543 w,b	553 vs	LO phonon (A_1)
		574	LO (A_1)			
588	LO	583	LO (E_1)	588 w		LO phonon (E_1)
					635 sh	mp(100+543=643cm^{-1})
				658, 665 w,b	749 m	mp(2 x 383=766cm^{-1})
					877 m	mp(2 x 440=880cm^{-1})
		986	mp			
					1007 m	mp(440+588=1028cm^{-1})
		1084 b	mp		1072 sh,w	mp(2 x 543=1086cm^{-1})
				1105 sh		mp(543+588=1121cm^{-1})
		1149 b	mp	1150 s,b		mp(2 x 588=1176cm^{-1})
					1346 vs,b	?

LO = longitudinal optical phonon mode; TO = transverse optical phonon mode;

mp = multiphonon mode; b = broad; m = medium; s = strong; sh = shoulder; v = very.

There is little agreement between the two published sets of frequencies and their assignments (Table 7.5, cols.1 to 4). The Raman data for our polycrystalline sample (Table 7.5, col.5) are closer to that of Damen than that of Mitra, especially below *ca* 440 cm^{-1}. In particular, we observed no transition at 180cm^{-1} unlike Mitra *et al* who assigned an E_2 phonon to this frequency. Thus our data support the alternative assignment by Damen *et al* of the E_2 mode to a band at 101 cm^{-1}.

The work of Damen was a polarised Raman study using two differently cleaved single crystals of ZnO, one crystal cleaved with sample edges parallel to the crystal *c*-axis, and the other with edges at 45° to the axis. Their assignment scheme relied, in part, on the different polarisation of phonon modes in the two crystals. On the other hand, Mitra *et al*[45] used only one single crystal of ZnO. It was not reported how the crystal was cleaved. Since the assignment scheme of Damen (Table 7.5,col.4) had had to meet a more stringent test than that of Mitra (Table 7.5,col.2), and also because of the closer correspondence in the observed frequencies between our Raman data and those of Damen rather than those of Mitra (see Table 7.5,cols.1,3,5), we prefer the assignment scheme of Damen. The differences between the band frequencies reported by Damen and those observed in our Raman data are insignificant given the estimated precision of ±3cm^{-1} for our Raman spectrometer (Chapter Four).

The results of Damen[44] are summarised in Table 7.5(cols.3,4) which lists the frequencies of the fundamental phonon modes obtained using results from both crystals. The A_1 LO mode was observed, at 574 cm^{-1}, as a strong sharp band only in the spectrum of the 45° cleaved crystal. The parallel cleaved crystal gave broad bands from 540 to 670 cm^{-1}, the observed frequencies depending on the sample orientation. This effect was explained[44] in terms of the LST theorem on the A_1 LO and E_1 LO phonons whose

fundamental frequencies were determined to be 574 and 583 cm^{-1} respectively. The LST effect also operates in the Raman spectrum (Figs. 7.6, 7.7) of our polycrystalline sample. We observed broad weak bands at 543 and 588 cm^{-1} (Fig. 7.7) which we assign to the A_1 and E_1 LO phonons respectively.

Bands observed at 1150(S), 1105(sh), 765(w) and 758(w) cm^{-1} in our spectrum (Figs. 7,6, 7.7) are assigned to multiphonon bands. Column 7 of Table 7.5 indicates the possible fundamental phonon modes involved. The fact that the observed multiphonon bands arise at slightly lower frequencies than those thereby predicted is probably due to anharmonic effects. The two weak multiphonon bands at 765 and 758 cm^{-1} may both be due to the first overtone of the 383 cm^{-1} fundamental phonon mode (Table 7.5, cols. 5,7), a small difference in frequency (765 c.f. 758 cm^{-1}) possibly arising from different orientations of the ZnO crystallites.

7.3.3 The IR spectrum of ZnO

(a) Introduction

The low frequency IR spectra of small, ionic crystals, where the crystals are of a diameter smaller than that of the wavelength, λ, of the incident light, are almost completely determined by the crystal surface.[3] For these small particles, optic surface phonons are observed in the IR, the frequencies depending on the shape of the crystal and on the dielectric constant of any supporting medium, say KBr in the pressed disc technique. Since ZnO has a uniaxial crystal structure, the dielectric constant for phonon propagation parallel to the unique crystal c-axis is different from that for propagation perpendicular to the axis. For a microscopic ZnO crystal of a given

shape, two surface phonon modes, of different frequency, may occur in the IR spectrum, corresponding to phonon propagation parallel and perpendicular to the *c*-axis. The frequencies of IR active surface phonons of ZnO particles of various shapes are given in Table 7.6. For a ZnO crystal of a size very much smaller than λ, the two surface phonons are the only transitions expected in the IR and the bulk TO phonons predicted to be IR active by group theory (i.e. the A_1 and E_1 modes, Section 7.3.1) will *not* be observed. This is the case for our present ZnO sample (see Section 7.3.3(b)). Some 87.6% of the particles of our ZnO sample had a diameter of less than 1μm (see Section 7.3) whereas the surface phonon modes are observed from *ca* 350 cm^{-1} (29 μm) to 600 cm^{-1} (17 μm).

Above 750 cm^{-1}, the only IR bands observed from Kadox 25 ZnO are due to either surface impurities or to multiphonon bands (see Section 7.3.3 (c)).

The IR spectrum of ZnO is now discussed in two sections: the surface phonon region from 300 to 750 cm^{-1} in Section 7.3.3(b), and the 750 to 4000 cm^{-1} region in Section 7.3.3(c).

(b) <u>The observed IR spectrum of ZnO, 750 to 300 cm^{-1}</u>

The transmission IR spectrum from 750 to 300 cm^{-1} of un-pretreated Kadox 25 supported by a KBr disc is shown in Fig.7.8.

Strong absorption occurs in the range *ca* 350 to 600 cm^{-1} with partially resolved bands at 440, 490 and 525 cm^{-1}. We assign the absorption over the whole frequency range to surface optic phonons of microscopic ZnO crystallites. The width of the absorption indicates a variety of crystallite shapes; however, the maxima at 440, 490 and 525 cm^{-1} suggest a predominance of particles of approximately cubic, spherical and cylindrical shape (see Table 7.6).

TABLE 7.6 Infrared activities and frequencies of surface phonon modes of ZnO supported in a KBr disc, (from ref.4)

frequency, cm^{-1}	particle shape	particle orientation	formal IR activity
527	cylinder	$\perp$	active
512	cylinder	$\parallel$	inactive
496	sphere	$\perp$	active
477	sphere	$\parallel$	active
470	cube	$\perp$	active
447	cube	$\parallel$	active

The symbol $\perp$ denotes orientation of the crystallite c axis perpendicular to the electric field vector of the incident light, and $\parallel$ denotes the case of parallel orientation.

Fig 7.8 The IR spectrum (750 to 300 cm^{-1}) of ZnO supported by a KBr disc.

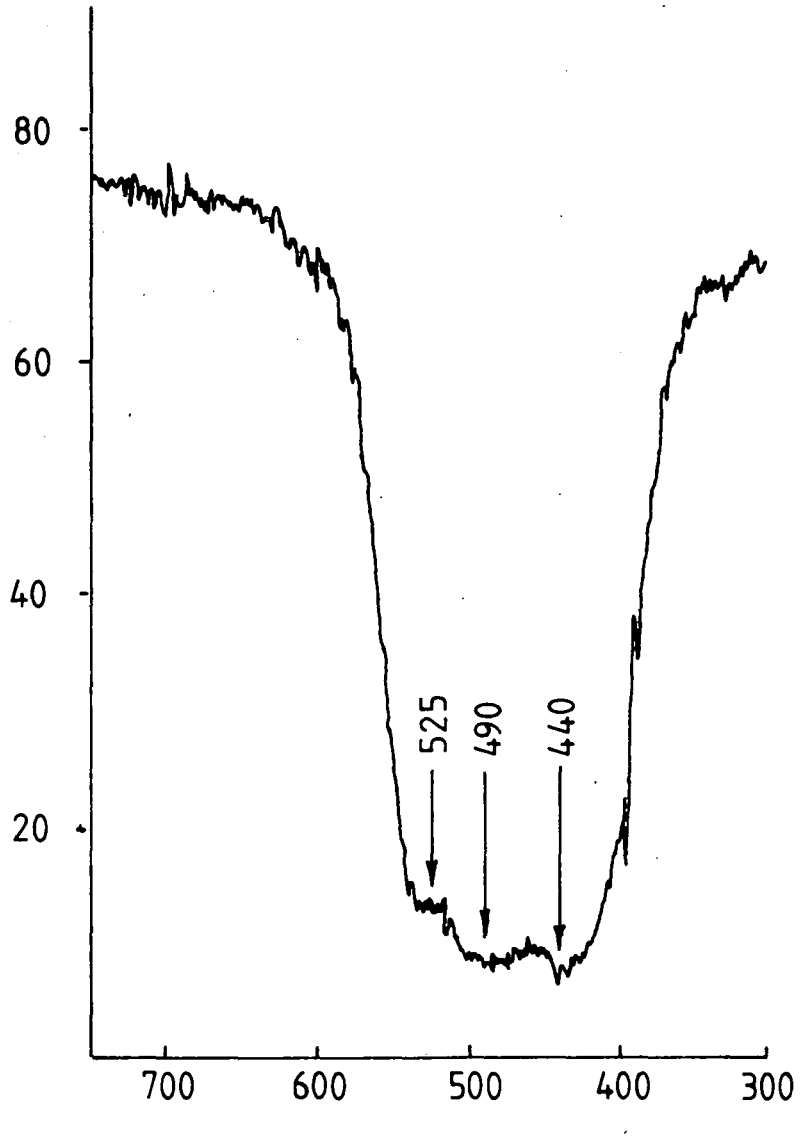

The IR maximum at 440 cm^{-1} (Figure 7.8) is not assigned to the E_2 bulk phonon which was observed in our Raman data at 440 cm^{-1} (Figure 7.7; Table 7.5, col.5). Our reasons are:

1. Group theory predicts that the E_2 mode is Raman active but IR inactive (see Section 7.3.1);
2. Particle size arguments predict bulk phonons to be IR inactive for our sample (see Section 7.3.3(a)).

The original assignment of the E_2 mode was made by Damen *et al*[44] in their polarised Raman study of single crystals (Table 7.5, cols.3,4). According to these workers, the polarisation characteristics of a Raman band at 437 cm^{-1} lead to its "unambiguous" assignment to the E_2 bulk phonon. Therefore, the Raman band at 440 cm^{-1} (Figure 7.7), and the IR maximum at 440 cm^{-1} (Figure 7.8) in our results for Kadox 25 have different physical origins.

The IR spectrum (750 to 300 cm^{-1}) of small ZnO crystals supported in a CsI pressed disc has been reported by Yamamoto *et al*.[4] Only one very broad feature was observed, with three partially resolved bands at 400, 483 and 520 cm^{-1}. The bands were assigned to the surface phonon modes of cubic, spherical and cylindrical ZnO crystals respectively.[4] These frequencies are lower than those observed from our ZnO/KBr sample (Figure 7.8) which is due to the higher dielectric constant, ε, of CsI (ε=3.1) compared to that of KBr (ε=2.3). The results of Yamamoto[4] are therefore consistent with our data for ZnO/KBr (Figure 7.8).

(c) The IR spectrum of ZnO in the range 4000 to 750 cm^{-1}

IR spectra of Kadox 25 ZnO from 4000 to 750 cm^{-1} using a self-supporting disc are shown in Figures 7.9 to 7.11 and summarised in Table 7.7. The spectra show considerable differences

Fig. 7.9 IR spectrum of ZnO at 299K recorded after evacuation to 4.5×10^{-2} torr.

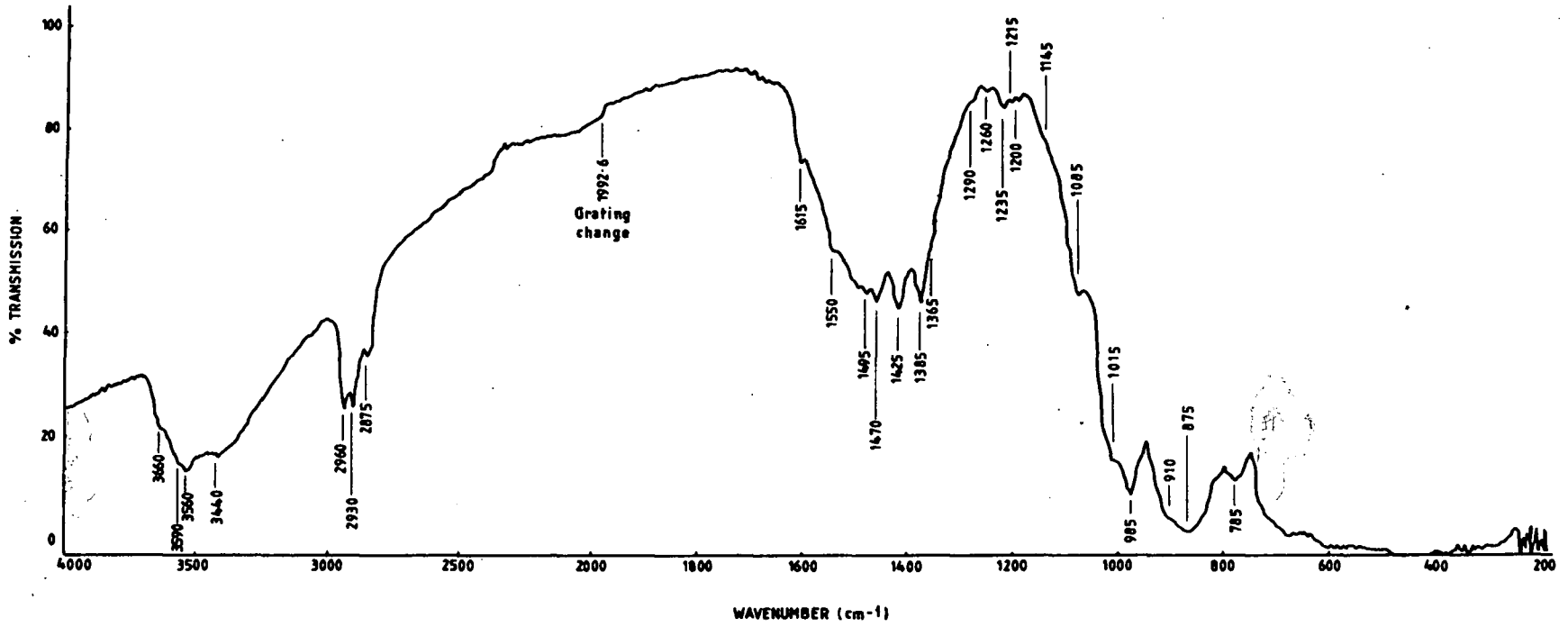

Fig. 7.10 IR spectrum of ZnO at 725K, 7.0×10^{-5} torr, recorded after heating in O_2 to 725K and subsequent evacuation.

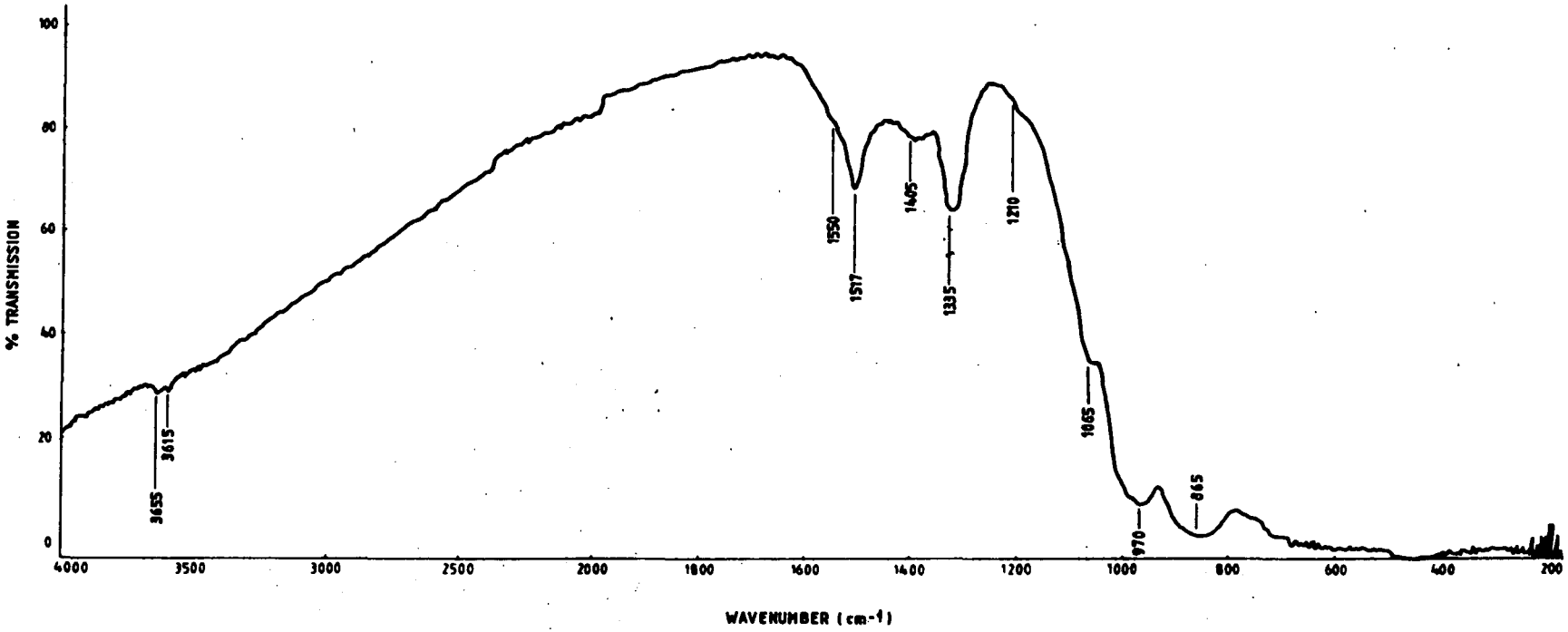

Fig. 7.11 IR spectrum of ZnO at 305K, 5.5×10^{-5} torr, recorded after calcination in O_2 to 725K and cooling in vacuum.

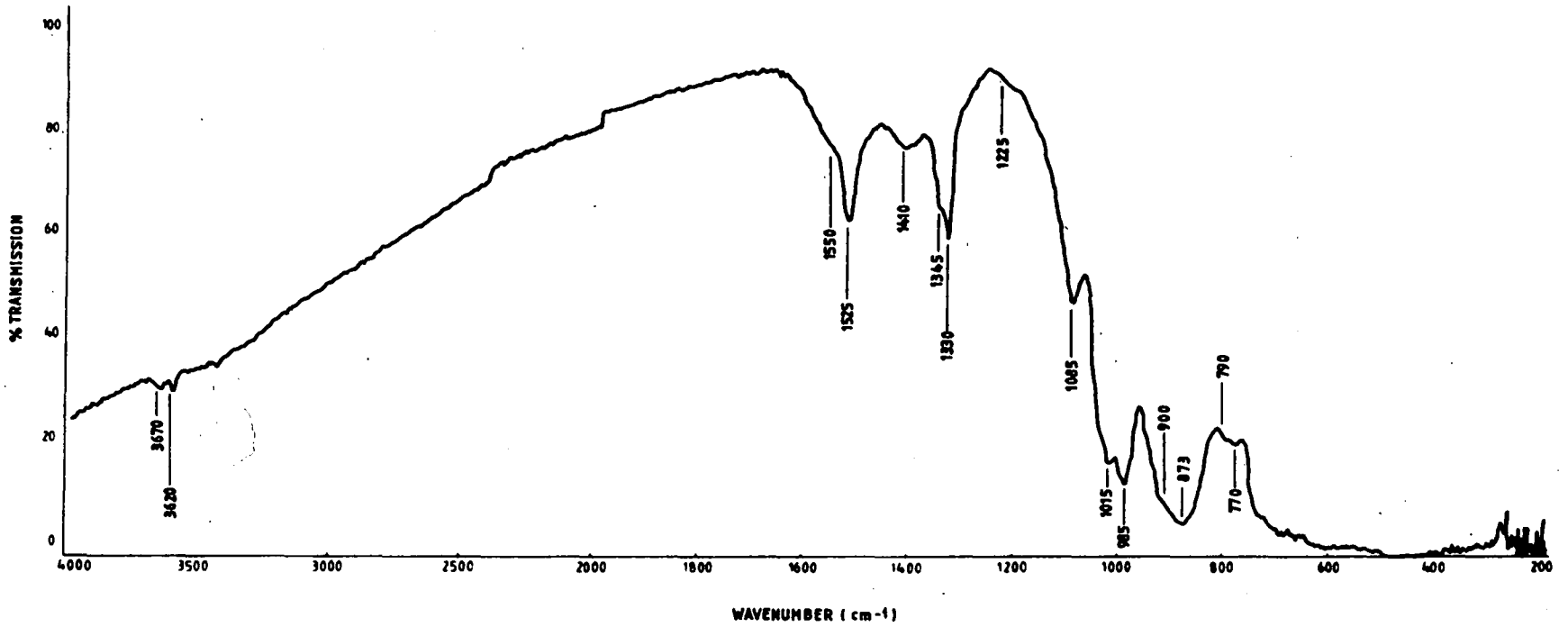

TABLE 7.7 Frequencies of bands observed in the infrared spectra of Kadox 25 ZnO during the calcination process

The sample was heated in O_2 to various temperatures and the IR spectra recorded after evacuation of the O_2. O_2 was then readmitted to the sample and the heating resumed. Column 5 lists the frequencies observed after cooling the sample *in vacuo* from 725K to 305K. Further experimental details are given in Table 7.4.

299	431	573	725	305	Temperature, K
					assignment
785 s	780 s	780 m,b		790,770 m,b	)
875 b,vs	870 b,vs	865 vs,vb	865vs,vb	873 vs,b	) multiphonon
910 s,sh	900 sh			900 sh	) bands
985 s	980 s	975 s,b	970 s,vb	985 vs	)
1015 s,sh	1015 s,sh			1015 ms	)
1085 m,sh	1085 m,sh	1070 mb,sh	1065 mb,sh	1085 m	)
					)
1145 w,sh					)
1200 vw	1200 w				)
1215 vw	1220 vvw		1210 w,vb	1225 w,b	)
1235 w	1245 w				) surface
1260 vw					) carbonate
1290 w,b,	1285 w				) species
					)
					)
1365 sh,ms	1340 m	1330 m	1335 ms,b	(1330 ms	)
1385 s	1385 s			(1345 ms	)
1425 s	1420 ms	1435 s,b	1405 m,b	1410 m,b	)
1470 s	1470 ms				)
1495 sh	1490 m	1485 mw			)
	1505 ms	1520 m,sh	1517 ms,b	1525 ms,b	)
1550 sh,ms	1555 ms,sh	1550 s,b	1550 m,sh	1550 m,sh	)
	1577 m,sh				)
1615 m,sh	1615 m,sh				)
1640–1690 w	1640–1690 vw	1640–1690 vw			$\nu_\delta(H_2O)$
2875 s	2860 m				) ν_{sym}(C-H) of
2930 s	2930 ms	2930 w			) surface
2960 ms	2960 ms	2970 mw			) impurities
3440 vb,vs	3440 vb,ms	3200–3600 m			weakly held OH
3560 b,s,)	) 3565 b,ms				)
3590 b,s,)	)	3615 m	3615 w	3620	) strongly held
3660 ms	3665 m	3655 m	3655 w	3670 w	) OH

and were obtained after heating the sample in O_2 to various temperatures followed by evacuation of the sample cell. The experimental conditions were summarised in Table 7.4. Our purpose in obtaining these IR data was to observe the effects of the calcination procedure (Section 7.2) in removing surface contaminants and to investigate the 1346 cm^{-1} region of the spectrum, this being the frequency of an intense band in our INS spectrum of calcined ZnO (Section 7.3.4).

(i) The 4000 to 3000 cm^{-1} region

After evacuation of ZnO to 4.5×10^{-2} torr at room temperature, four strong IR bands were observed, at 3440, 3560, 3590 and 3660 cm^{-1} (Figure 7.9). The most likely origins of these bands are the ν_{sym} of surface hydroxyls and the ν_{sym} of surface water. For water itself, this mode occurs at 3652 cm^{-1} in the gas phase and 3450 cm^{-1} in the liquid.[41] Since Figure 7.9 shows only *very weak* intensity in the region *ca* 1640 to 1690 cm^{-1} where the ν_{δ} mode of any surface H_2O would be expected (see Section 7.3.3(c)(iii)), we assign the four *strong* bands from 3440 to 3660 cm^{-1} to the stretching mode of surface hydroxyls. These assignments are in accord with those of Atherton *et al*[39] for the modes of surface hydroxyls on ZnO which are listed in Table 7.8 along with frequencies reported[39,40,46-48] for the modes of hydroxyls and water on the surfaces of several oxides. Atherton *et al*[39] confirmed by deuteration experiments that the four IR bands they observed from 3440 to 3670 cm^{-1} (Table 7.8) were due to the modes of surface -OH rather than surface H_2O (Section 7.1.5).

As a result of calcination of our ZnO samples, the bands in the region *ca* 3400 to 3700 cm^{-1} became extremely weak, that

TABLE 7.8 IR frequencies observed in the range 2800 to 4000 cm^{-1} of some oxides due to modes of surface hydroxyls and surface water

ZnO this work		ZnO Atherton[39]		ZnO Morishigue[40]		γ-Al_2O_3 Uvarov[46]		SiO_2 (Cabosil) McDonald[47]		TiO_2 Yates[48]		Sample Reference
cm^{-1}	assign-ment	cm^{-1}	assign-ment	cm^{-1}	assign-ment	cm^{-1}	assign-ment	cm^{-1}	assign-ment	cm^{-1}	assign-ment	
								2800 to 3400	) W)	3100 to 3350	) W)	
3440b	OH	3440b	OH	3425	OH							
				3540	OH							
		3555b	OH									
3560b	OH											
3590	OH											
				3605	OH							
		3620	OH									
				3650	OH	3650	OH					
3660	OH											
						3665	OH					
		3670	OH									
				3675	OH	3675	OH			3675	OH	
										3680	OH	
						3700 to >4000[a]	)) W)	3750	OH			

OH denotes the ν_{sym} mode of surface -OH; W the ν_{sym} mode of surface water.

a: limit of scan 4000 cm^{-1}; b: broad

at 3440 cm^{-1} being completley lost (Figure 7.11) indicating significant removal of surface hydroxyls.

Our IR spectra (Figures 7.9 to 7.11) show no resolved bands assignable to the ν_{sym} mode of type I surface hydroxyls which occur[23-25,30] at 3498 after H_2 adsorption on ZnO (see Table 7.1). Nor is there any evidence for type II surface hydroxyls, reported to give a broad, weak IR band at *ca* 3400 cm^{-1} (Table 7.1) on ZnO/H_2 samples.[23]

(ii) The 3000 to 2500 cm^{-1} region

At room temperature, three sharp bands are observed in this region, at 2960, 2930 and 2875 cm^{-1} (Figure 7.9). Calcination completely removed these bands (Figure 7.11) which have not been reported elsewhere for ZnO. The frequencies are typical of the C-H symmetric stretching mode of aliphatic hydrocarbons and we therefore assign the bands to ν_s(C-H) modes of surface contaminants on the ZnO. These contaminants are expected to be absent from our INS samples which were subjected to a similar O_2 pretreatment.

Support for our assignment is provided by the IR spectrum of SiO_2 (Cabosil) obtained by McDonald.[47] An untreated SiO_2 sample showed bands at 2960, 2959 and 2875 cm^{-1} which disappeared after heating for several minutes at 773K in O_2. The bands were assigned[47] to the C-H stretch of surface impurities.

(iii) The 2500 to 1100 cm^{-1} region

Saussey *et al*[10] have studied the IR spectrum of CO_2 adsorption on ZnO. Their sample was Kadox - 15, pretreated

with O_2 at 723K. Column 1 of Table 7.9 lists the bands observed at room temperature after equilibrating the ZnO surface with 6 x 10^{-3} torr CO_2, and column 2 the bands observed after room temperature evacuation to 2.6 x 10^{-8} torr. All the bands listed in Table 7.9 were assigned to modes of variously bonded surface carbonate species.

In accord with the results of Saussey,[10] the bands in our IR spectra of ZnO (Figures 7.9 to 7.11), in the region 1615 to 1200 cm^{-1} are assigned to the modes of surface carbonate species. The majority of these bands are lost during the heating treatment and after calcination, the only features (Figure 7.11) remaining in this region were at *ca* 1550 cm^{-1} (shoulder), 1525 (ms), 1410(m), 1345(ms) and 1330(ms) cm^{-1}, assigned to strongly held surface $-CO_3$ groups.

In this range of the spectrum the ν_δ mode of any surface H_2O would be expected. This mode occurs at 1640 cm^{-1} in liquid water and at 1595 cm^{-1} in the gas phase.[41] The only strong band in this region, 1615 cm^{-1} (Figure 7.9) was also observed as a strong band by Saussey *et al*[10] in their ZnO/CO_2 IR spectra, and is therefore assigned to surface carbonate. There are no resolved bands in our IR spectra (Figures 7.9-7.11) assignable to ν_δ of adsorbed water. However, the 1615 cm^{-1} band exhibits a high frequency tail extending to 1690 cm^{-1} at 299K (Fig.7.9). We assign this tail to the ν_δ mode of surface H_2O. The high frequency compared with that for liquid water indicates significant hydrogen bonding between the adsorbed water molecules and suggests that the H_2O is not very strongly held by the ZnO. Accordingly, the IR intensity of the tail is progressively reduced on heating, c.f. Fig. 7.9 (299K) with Fig. 7.10 (725K) from 1690 to 1640 cm^{-1}. The intensity is weak even at 299K, indicating a low concentration of surface H_2O. The stretching

TABLE 7.9 Frequencies of bands reported in the IR spectrum of CO_2 adsorbed on ZnO at room temperature

The data are due to Saussey *et al*[10] who assigned all the observed bands to modes of variously bonded surface carbonate species.

Bands observed after equilibriation with 6×10^{-3} torr CO_2 at room temperature	Bands observed after room temperature evacuation to 2.6×10^{-8} torr
636 m	
641 m	
677 w	679 w
841 m	
	848 w
852 sh	
999 m	1002 m
1039 w	
1229 w	
1265 sh	
1300 sh, w	
1325 sh	
1346 vs	1338 vs
1369 sh	
1425 w	
1520 sh	1520 m
1547 m	
1580 sh	1580 sh
	1593 vs
1615 vs	
1650 sh,b	
	1665 sh
2290 w	
2353 m	
2369 m	

modes of adsorbed H_2O are expected above 3000 cm^{-1}. Such bands were not resolved in our spectra (Figs. 7.9 to 7.11), the region above 3000 cm^{-1} being dominated by the intense ν_{sym} modes of surface hydroxyls (Section 7.3.3 (c) (i)).

Saussey *et al*[10] observed three bands above 2000 cm^{-1} in their IR data of CO_2 adsorbed at 6 x 10^{-3} torr on ZnO (Table 7.9). These bands were not observed by Saussey for lower coverages of CO_2, nor are they observed in our IR spectrum of ZnO under vacuum at room temperature (Fig. 7.9). Thus the surface carbonate species giving rise to these IR bands above 2000 cm^{-1} are not formed at the coverages produced by exposure of ZnO to the atmosphere.

(iv) <u>The 1100 to 750 cm^{-1} region</u>

The bands in our data (Figs. 7.9 to 7.11, Table 7.7) between 1085 and 785 cm^{-1} are assigned to multiphonon processes. These bands broaden on heating and merge; at 725K the only peaks observed are those at 1065, 970 and 865 cm^{-1} (Fig. 7.10). It is known that multiphonon bands suffer greater broadening on heating than do bonds due to fundamental phonon modes.[35] After cooling from 725 to 305K, this region of the spectrum is very similar to that observed before starting the heat treatment (<u>c.f.</u> Figs. 7.9 and 7.11); in particular the relative intensities of the bands are unchanged.

Saussey *et al*[10] assigned bands at 1002(m) and 848 cm^{-1} in their IR spectra of CO_2 adsorbed on ZnO to modes of surface $-CO_3$. These bands remained after evacuation at room temperature (see Table 7.9). But since the relative intensities of the bands in this region of our IR spectra are unchanged by the calcination

procedure, we prefer their assignment to multiphonon processes rather than to modes of surface carbonate.

In summary, after cooling the calcined sample to 305K under vacuum, the IR spectrum (Figure 7.11) showed the presence of only hydroxyl and carbonate groups on the calcined ZnO surface. Such species are therefore the only likely contaminants on the ZnO samples used in our INS experiments, these samples having been prepared using a similar calcination procedure.

7.3.4 The INS spectrum of ZnO

The INS spectrum obtained at 77K on INIB of Kadox 25 after calcination is shown in Figure 7.12 and summarised in column 6 of Table 7.5. Two very intense bands are observed at 437 and 553 cm^{-1}. By comparison with our Raman data (Table 7.5, col.5) these bands are readily assigned to TO and LO bulk phonons respectively. Although in the INS technique both bulk and surface phonons will be active, for our ZnO samples the surface phonons will give rise to much weaker INS bands than the bulk modes because of the large bulk/surface ratio. The discrepancy in frequency of the LO mode as observed in the INS results (553 cm^{-1}) and in our Raman data (543 cm^{-1}) is within the error of ± 15 cm^{-1} associated with band frequencies obtained from INIB spectra (Chapter Four).

Five bands of weak to moderate intensity, at 635, 749, 877, 1007 and 1072 cm^{-1} are observed in the INS spectrum (Figure 7.12), and are assigned to multiphonon processes. Because of the dispersive nature of phonon transitions in general, the assignments in Table 7.5, column 7, have been expressed in terms of the frequencies at which the fundamental phonon modes

Fig. 7.12 INS spectra (77K) of (a) ZnO after calcination and (b) ZnO after adsorption of H_2. The symbols + and x indicate data collected using the (200) and o and ● that collected using the (220) planes of the copper monochromator.

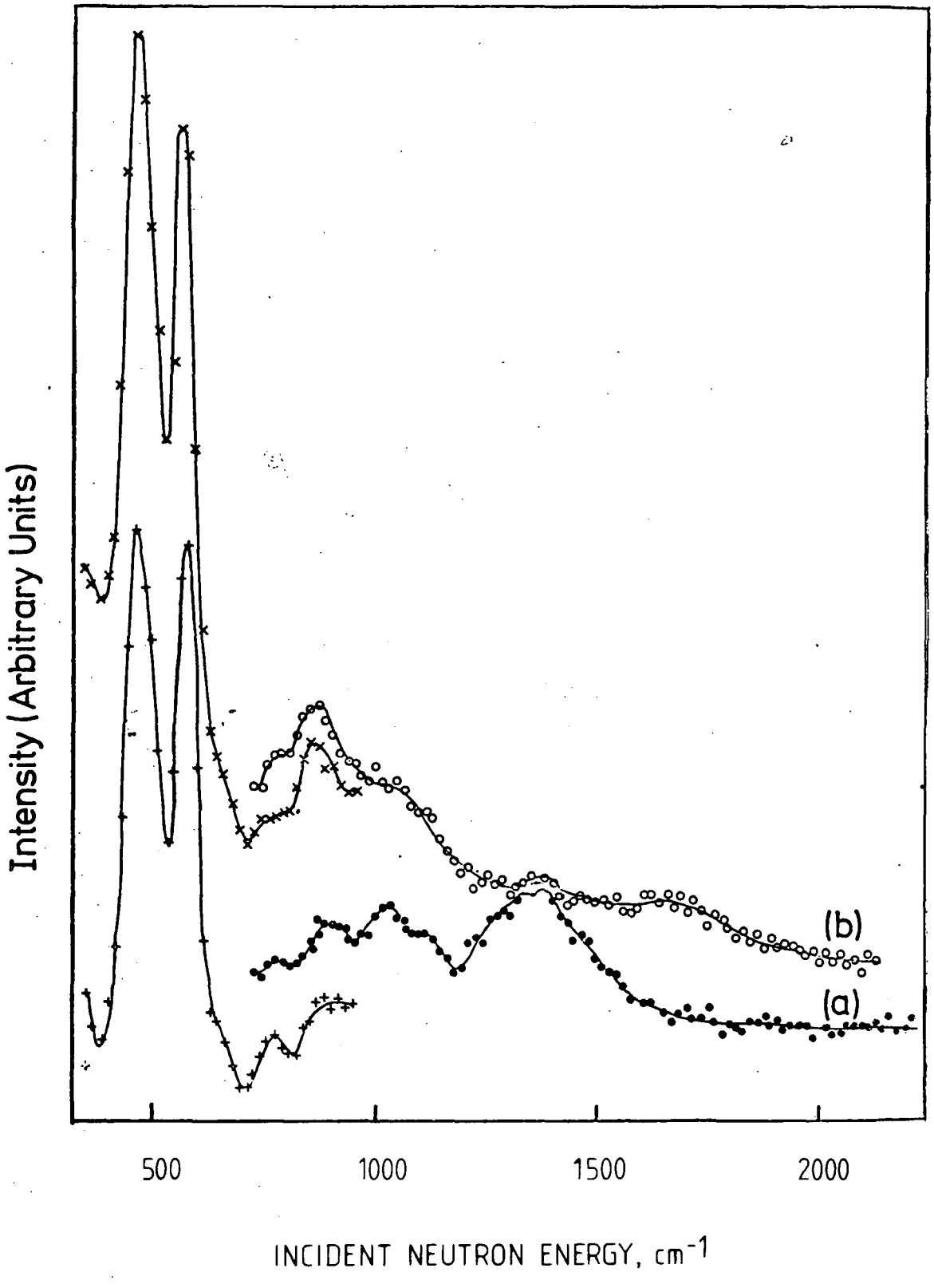

were observed in our Raman data (Table 7.5, col.5). Again the discrepancies between the observed multiphonon frequencies and those suggested by the assignment scheme (Table 7.5,col.7) are probably due in the main to the error in the measured INS band frequencies rather than such effects as dispersion or anharmonicity.

In addition to these features the INS spectrum of ZnO (Figure 7.12) shows a strong, broad band at 1346 cm^{-1}. No IR or Raman bands have been reported for ZnO itself in this region. On adsorption of H_2, the scattered neutron intensity due to this transition remains constant whereas the intensity increases at all other frequencies (see Figure 7.12). This suggests that the 1346 cm^{-1} band is not due to phonon processes. Indeed, phonon dispersion curves[49,50] show that the TO modes have highest frequencies at the critical point $|\kappa|=0$ (where κ is the scattering-wave vector) and so the highest frequency at which a fundamental phonon mode is expected to occur is 588 cm^{-1} (Table 7.5, column 5). Multiphonon processes are also an unlikely cause of the 1346 cm^{-1} INS band; the highest frequency at which multiphonons have been observed is *ca* 1155 cm^{-1} in the Raman spectrum (Table 7.5, columns 3,5).

Neither can the 1346 cm^{-1} band be due to incoherent inelastic scattering from surface $-CO_3$ impurities. Although the IR spectrum (Figure 7.11) of calcined ZnO shows bands at 1330(ms), 1345(ms), 1410(m) and 1525(ms) cm^{-1} due to residual surface carbonates, the incoherent scattering cross-sections for both ^{12}C and ^{16}O are zero. However, according to Bredov *et al*[51], coherent inelastic neutron scattering may, under certain conditions, give rise to bands in the measurement of incoherent inelastic spectra. The coherent cross-sections of ^{12}C, ^{16}O

and Zn are respectively 6.65, 5.80 and 5.7 barns.[52] Thus, according to Bredov's theory,[51] coherent scattering from a sufficient concentration of surface $-CO_3$ would give rise to observable bands in the incoherent inelastic spectrum of ZnO. The maximum coverage of carbonate on the surface of our INS sample is estimated to be of the order of 0.05 monolayer (Section 7.1.5) which is more than a factor of 10 less than the coverage of hydrogen (0.7 to 0.8 monolayers H_2, Section 7.2). This concentration of surface carbonate is too low to have caused the intense INS band at 1346 cm^{-1} (Figure 7.12) by coherent scattering.

Surface hydroxyls are not reported to give rise to bands near 1346 cm^{-1} (Table 7.1). The high intensity of the observed band, which is unchanged on H_2 adsorption, also argues against its assignment to surface hydroxyls.

The 1346 cm^{-1} band is unlikely to be an instrumental artifact since the spectra of other compounds obtained using INIB immediately before or after the ZnO runs did not show similar features. This feature was also observed in the spectrum of a different sample of ZnO run some months earlier in the same spectrometer.

In summary, we are unable to make a definite assignment of the band at 1346 cm^{-1}. However, because its intensity is unchanged on H_2 adsorption, it may be related to transitions within the bulk, rather than at the surface of the ZnO particles. The sample of ZnO was manufactured by burning Zn in air. Incorporation of impurities with the ZnO lattice during manufacture or subsequent packaging are conceivable. There is thus a small chance that the 1346 cm^{-1} INS band is due to contaminants,

say carbonate or some hydrogeneous species, trapped within the bulk of the sample.

7.3.5 The INS spectrum of ZnO + H_2

The spectrum of ZnO + H_2, 68 mol/g^{-1} coverage, obtained on INIB at 77K is shown without any background subtraction in Figure 7.12. The result of subtracting the ZnO background is shown in Figure 7.13. Table 7.10 lists the frequencies of bands observed after the subtraction and includes the IR data of Boccuzzi[23] for comparison. Since the 1346 cm^{-1} band does not change in intensity on adsorption of H_2, a minimum is produced in the substracted spectrum (Figure 7.13) at this frequency.

Fig. 7.13 Difference spectrum (77K): INS spectrum of ZnO + H_2 minus INS spectrum of ZnO.
Symbols as for fig. 7.12.

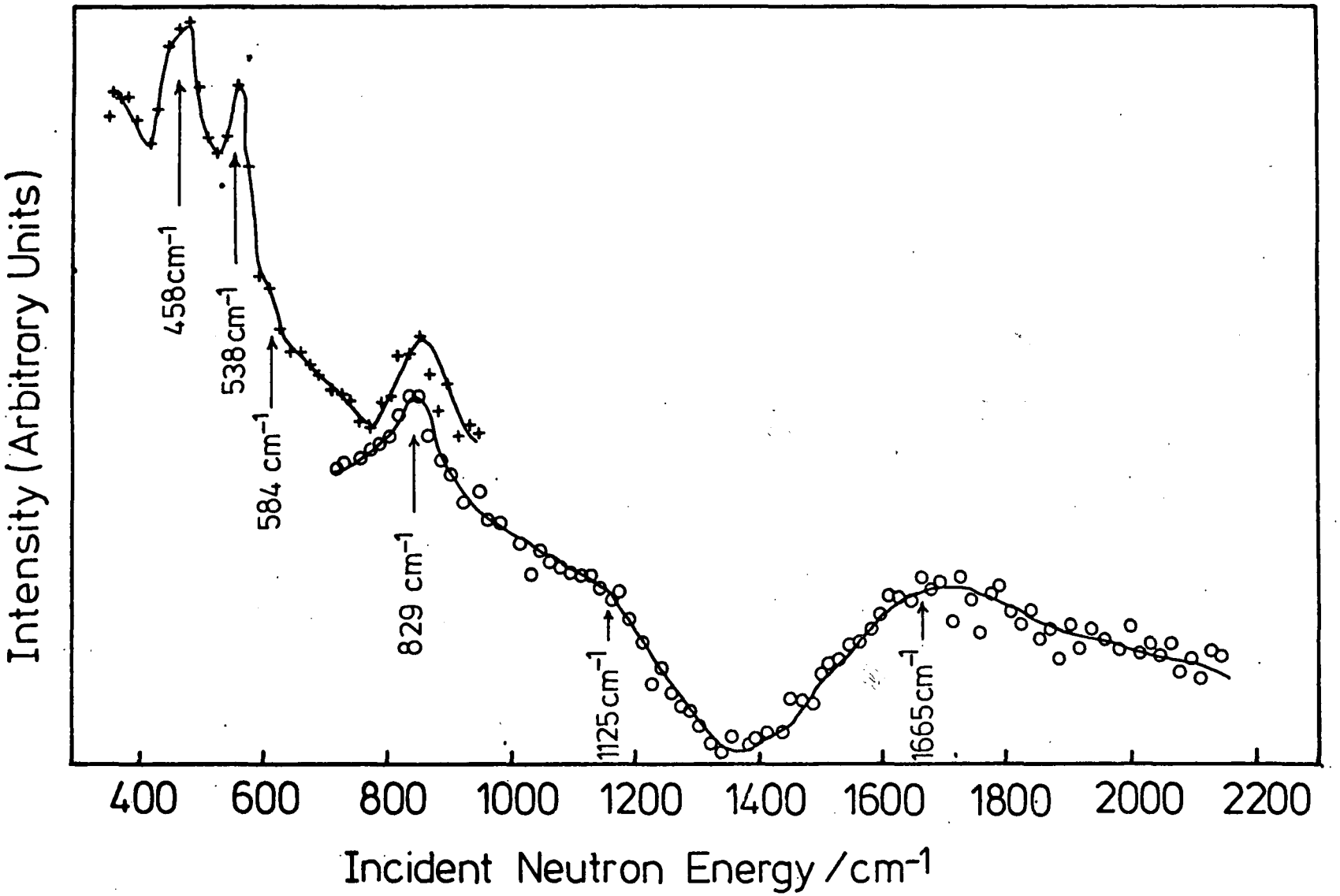

TABLE 7.10 The frequencies and assignments of bands in the vibrational spectrum of ZnO plus adsorbed hydrogen

method reference sample		INS this work, fig.12 ZnO	INS this work, fig.13 ZnO+H_2-background	IR Boccuzzi[23], fig.14 ZnO + H_2	
assignment (this work)		cm^{-1}	cm^{-1}	cm^{-1}	assignment (Boccuzzi[23])
mode	type of H adsorption				mode / type of H adsorption
TO phonon	-	437 vs	458 vs		
LO phonon	-	553 vs	538 vs		
LO phonon	-		584 sh,m		
mp	-	635 sh			
mp	-	749			
ν_δ(Zn–H)	I		829s	817m	ν_δ(Zn–H) I
				845 to 850 b,w	ν_δ(O–H) I
mp	-	877m		870s	mp -
mp	-	1007m		990s	mp -
		1072 sh,w			
mp	-			*ca* 1100 sh,m	- -
ν_δ(O–H)	I		1125 sh		
?	-	1346 vs,b	†(1346 vs,b)		
				1475 vb	ν_{as}(Zn⁻H⁻Zn) II
ν_s(Zn–H)	I	1665 b,s		1708 s	ν_s(Zn–H) I
				ca 3400 b	ν_s(OH---O) II
				3498	ν_s(O–H) I

For explanation of the symbols and assignment of the multiphonon modes ("mp") see Table 7.5.

†A ZnO background has been subtracted from the data for ZnO + H_2. The band at 1346 cm^{-1} occurs with equal intensity in the background spectrum of ZnO and in the spectrum of ZnO + H_2 before any subtraction. A decrease in intensity is therefore observed at 1346 cm^{-1} in the spectrum of ZnO + H_2-background.

The band at 1665 cm^{-1} occurs in both the subtracted and unsubtracted spectra and thus is not an artifact produced by subtraction of the adjacent feature at 1346 cm^{-1}.

The two optical phonon modes which arose at 437 and 553 cm^{-1} in the ZnO (Fig.7.12) now appear at 458 and 538 cm^{-1} on adsorption of H_2 (Fig. 7.13), the low frequency, TO, band apparently gaining in intensity relative to the higher frequency, LO band. Now on adsorption of H_2, the sample background is raised and it is raised most at lower incident neutron energies (see Fig.7.12). This change in background is the most likely cause of the change in relative intensities of these two phonon modes on hydrogen adsorption. Changes in the bonding at the ZnO surface on hydrogen adsorption may be the cause of the shift in frequency of these two phonon modes. The frequency shift is not due to plasmon effects since the adsorption of hydrogen does not form an accumulation layer[22] at temperatures as low as 77K.

A shoulder at 584 cm^{-1} in the ZnO+H_2 INS spectrum (Fig.7.13) might arise from either the bulk phonon observed at 588 cm^{-1} in the Raman (Table 7.5, col.5) or from the bending mode of surface Zn⟨H⟩Zn species. The assignment to the phonon mode is preferred for reasons explained below. Although this mode is not observed in the background spectrum of ZnO, its intensity may have been enhanced on adsorption of H_2 by a riding motion of the surface hydrogen. This would imply a large amplitude of vibration of the adsorbed hydrogen.

The strong band at 829 cm^{-1} in the subtracted spectrum (Fig.7.13) is not present in the ZnO data. This frequency is typical of metal - H bending modes,[31] *e.g.* ν_δ for terminally bound H in transition metal hydridocarbonyls lies in the region

600-800 cm^{-1} (see Chapter Five), and the bending modes in GeH_4, SnH_4 and GeH_2 (matrix isolated) occur at 931, 758 and 928 cm^{-1} respectively.[53] (The rationale for comparison with covalent hydrides is discussed in Section 7.3.5(a) below). We assign the 829 cm^{-1} band to ν_δ of surface Zn-H at a type I site. This is in agreement with Boccuzzi *et al*[23] who observed this mode at 817 cm^{-1} in the I.R. (see Table 7.10).

The subtracted spectrum (Fig.7.13) shows a broad, strong band at *ca* 1665 cm^{-1} which is also absent from the ZnO spectrum (Fig.7.12). This band is assigned to the symmetric stretch of Zn-H at type I sites and has been reported at 1708 cm^{-1} in the IR (see Table 7.10). The discrepancy between the frequencies observed by INS and IR may be explained, at least qualitatively, by the temperature and coverage dependence of the frequency of this mode and the difficulty of locating the exact centre of the broad INS transition. As explained in Sections 7.1.5 and 7.3.3c, we rule out the possibility that the 1665 cm^{-1} INS band is due to surface H_2O.

The INS spectrum of ZnO+H_2 with background subtracted (Fig.7.13) shows unresolved intensity in the region between the 584 cm^{-1} shoulder and the 829 cm^{-1} band. This intensity is assigned to unresolved scattering from multiphonon bands which were observed at 635 and 749 cm^{-1} in the INS spectrum of ZnO before H_2 adsorption (Fig.7.12, Table 7.10, col.3).

We now discuss the 829 to 1125 cm^{-1} region of Fig.7.13. The spectrum shows the high frequency edge of a band with an apparent maximum at 1125 cm^{-1} and also unresolved intensity in the region between this band and *ca* 850 cm^{-1}. There are three possible origins of the intensity over this region (not mutually exclusive):

(i) There is a small possibility of a symmetric stretching mode of a $Zn\overset{H}{\diagup\diagdown}Zn$ surface species, formed by type II adsorption, occuring in this region. This is discussed in Section 7.3.5(a) below.

(ii) Multiphonon bands were observed in this region in the INS spectrum of the ZnO background (Figure 7.12, Table 7.10, col.3) and will also occur in the spectrum of ZnO + H. The first overtones of the intense TO (458 cm^{-1}) and LO (538 cm^{-1}) phonons in the INS spectrum of ZnO + H (Figure 7.13) are therefore expected to give intensity at *ca* 916 and 1076 cm^{-1} in Figure 7.13 although they have not been resolved.

(iii) The ν_δ mode of type I (O-H) was assigned by Boccuzzi *et al*[23] to a broad IR band at 845 to 850 cm^{-1} (Table 7.10,col.5). Although no band was resolved at *ca* 850 cm^{-1} in our INS spectrum of ZnO + H (Figure 7.13), this mode should be INS active. Therefore we predict the intensity, relative to the ν_δ(Zn-H) band, that an INS band due to ν_δ(O-H) would have if it occurred in the region 850 to 1125 cm^{-1}. We will consider two possible assignments of ν_δ(O-H) in Figure 7.13, firstly to the shoulder at 1125 cm^{-1} and secondly that this mode gives rise to a band at 850 cm^{-1} which is unresolved from that due to ν_δ(Zn-H) at 829 cm^{-1}. Because type I adsorption occurs at Zn-O pair sites[25,26] the surface concentrations of type I Zn-H and O-H species will be equal. Thus, from Chapter Two, the intensities in the INS spectra of the fundamental modes of these species can be estimated in the harmonic approximation by[54]:

$$I \alpha \frac{Q^2 Z(\tilde{\nu})}{\tilde{\nu}} \exp\left\{-2W_H(\tilde{\nu})\right\} \qquad (7.1)$$

where $\hbar Q$ is the momentum transfer during the scattering process, $Z(\tilde{\nu})$ is the vibrational density of states, $\tilde{\nu}$ is the normal mode

frequency in cm^{-1}, and $\exp\left\{-2W_H(\tilde{\nu})\right\}$ is the mode-dependent Debye-Waller factor.

The Debye-Waller factors for the O-H and Zn-H vibrations were calculated using equation 2.74 (Chapter Two, page 46) and by assuming that these vibrations were uncoupled from the ZnO lattice modes. The frequency of the ν_{δ}(O-H) mode was taken to be 3498 cm^{-1} [26] and the calculations (equations 7.1 and 2.74) were carried out for both the postulated ν_{δ}(O-H) mode frequencies of 850 and 1125 cm^{-1}. For the Zn-H vibrations, the normal mode frequencies of ν_{δ}(Zn-H) = 829 cm^{-1} and $\nu_{s\delta}$(Zn-H) = 1665 cm^{-1} were used, as observed in our INS spectrum of ZnO + H (Figure 7.13).

The relative INS intensities predicted for the ν_s and ν_{δ} fundamentals of type I Zn-H species are compared in Table 7.11 with those of the proposed ν_{δ}(O-H) fundamentals at 850 and 1125 cm^{-1}. We need also to consider the contribution from the first overtones of ν_{δ}(Zn-H) and ν_{δ}(O-H) to the band centred at 1665 cm^{-1}, assigned principally to ν_s(Zn-H) in the ZnO + H INS spectrum (Figure 7.13). The relative intensities of these overtones are listed in Table 7.11 and were calculated using equations 2.83 and 2.84 (Chapter Two, page 53) for mode-dependent Debye-Waller factors and assuming that the fundamentals were harmonic and uncoupled from the ZnO lattice modes.

When the overtone contributions are included, we find from Table 7.11 that the existence of a ν_{δ}(O-H) mode at 850 cm^{-1} unresolved from ν_{δ}(Zn-H) at 829 cm^{-1} would give rise to INS intensity of 6.0 units in the 829-850 cm^{-1} region and an intensity of 3.0 units in the 1665 to 1700 cm^{-1} region of the ZnO + H spectrum (Figure 7.13). On the other hand, if ν_{δ}(O-H) occurred at 1125 cm^{-1}, we would predict from Table 7.11 that INS bands

TABLE 7.11 The relative INS intensities predicted by equation 1 for the modes of type I hydrogen on ZnO

vibrational mode	ν_s	ν_δ	ν_δ	ν_δ
type I surface species	Zn - H	O - H	O - H	Zn - H
frequency of fundamental, cm^{-1}	1665	1225*	850*	829*
calculated relative INS intensity of fundamental	1.0	1.5	3.0	3.0
postulated frequency of first overtone in harmonic approximation	-	-	1700	1658
calculated relative INS intensity of first overtone	-	-	1.0	1.0

* The frequencies 1125 and 850 cm^{-1} are taken as the two most likely possibilities for ν_δ(O - H), see Section 7.3.5.

would be observed at 829, 1125 and *ca* 1665 cm^{-1} with relative intensities of 3.0, 1.5 and 2.0 units respectively. Unfortunately, the intensities of the observed bands (Figure 7.13) cannot be measured with sufficient accuracy to distinguish between the alternative assignments of ν_δ(O-H). This is largely due to the uncertainty in the baseline position of Figure 7.13). However, because we expect to observe a strong INS band due to ν_δ(O-H), we tentatively assign this mode to the shoulder at 1125 cm^{-1} rather than to the region at *ca* 850 cm^{-1} where our INS data show no resolved features (Figure 7.13).

Our assignment of ν_δ(O-H) disagrees with that of Boccuzzi *et al*[23] who ascribed a broad IR band at 845-850 cm^{-1} to this mode. The IR spectra of ZnO + H_2 published by Boccuzzi[23] show a general increase in IR absorbance with increasing hydrogen coverage in the region *ca* 845 to 775 cm^{-1} (Figure 7.14). We submit that the feature at 845 - 850 cm^{-1} in the published[23] spectrum (Figure 7.14) is not sufficiently well differentiated from the general decrease in IR transmission to be definitely ascribed to a band arising from a vibrational mode of a particular surface species. The previous assignment[23] of the ν_δ mode of type I O-H to the IR feature at *ca* 845-850 cm^{-1} should therefore be regarded as tentative.

No bands appear in the IR spectra in the region of 1125 cm^{-1} on adsorption of H_2.[23] (A band at *ca* 1100 cm^{-1} in Boccuzzi's spectrum of ZnO before H_2 adsorption was not assigned by the authors. From our IR results for calcined ZnO we suggest that this is a multiphonon band), The discrepancy between the values for ν_δ(O-H) (type I) as assigned by Boccuzzi *et al*[23] in their IR data and by us using INS cannot be resolved in the present work. We submit, however, that both assignments must be regarded

Fig. 7.14 The IR spectrum of hydrogen adsorbed on ZnO, taken from ref. 23.

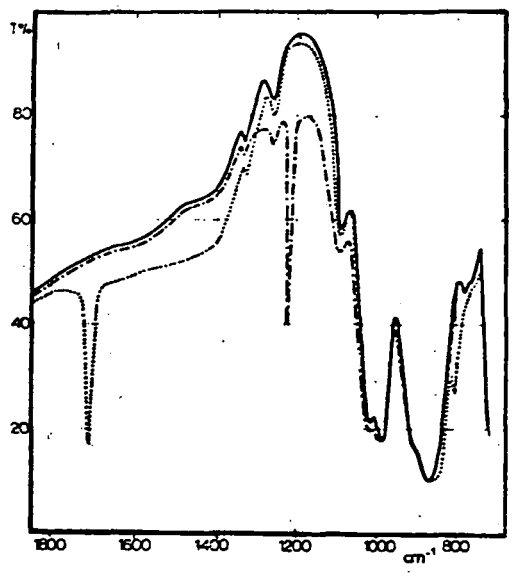

Infrared spectrum of hydrogen and deuterium adsorbed on ZnO in the 1800- to 900-cm^{-1} range (percentage transmission vs wavenumber). ——, background; ····, in equilibrium with 100 Torr of H_2; -·-·-, in equilibrium with 100 Torr of D_2.

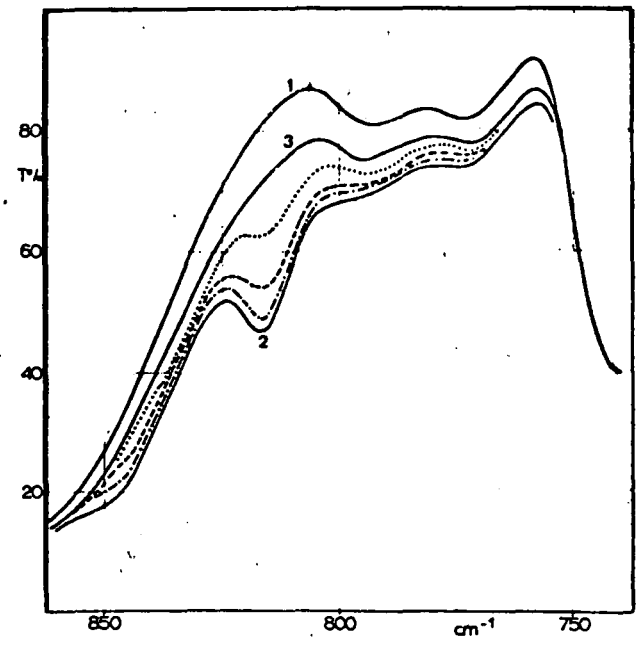

Infrared spectrum of hydrogen adsorbed on ZnO in the 900- to 750-cm^{-1} range (percentage transmission vs wavenumber). —— (1), background; —— (2), in equilibrium with 100 Torr of H_2; -·-, 40 Torr of H_2; - - -, 10 Torr of H_2; ····, 2 Torr of H_2; and —— (3), after outgassing at room temperature.

as tentative. An INS study of HD adsorbed on ZnO may help to clarify the situation, though it would be difficult with current neutron sources because of the low monochromated-neutron fluxes, the small incoherent neutron scattering cross-section of D and the apparent low INS, and IR, intensity of the ν_δ(O-H) mode.

7.3.5(a) The INS spectrum of type IIa species

The INS data show no strong bands assignable to the symmetric or antisymmetric stretches of the Zn⟨H⟩Zn species proposed by Boccuzzi *et al*[23] for adsorption at type II sites. A very broad band in the IR of ZnO + H at 1475 cm^{-1} was attributed[23] to the asymmetric stretch (Figure 7.14). As discussed above (Section 7.1.3(b)), the symmetric stretch, although not observed in the IR data of Boccuzzi *et al*,[23] is expected to occur in the region 895 to 1300 cm^{-1} on the basis of $(\mu_2\text{-H})M_2$ hydridocarbonyl data.

We cannot conclusively discard the possibility of a low concentration of a Zn⟨H⟩Zn species on our ZnO surface. It is possible that a weak asymmetric stretching band might be present at *ca* 1475 cm^{-1} in the INS spectrum of ZnO + H (Figure 7.13), unresolved from the broad 1665 cm^{-1} band. The INS spectrum (Figure 7.13) also shows unresolved intensity in the range 829 to 1125 cm^{-1}. This region may contain intensity from a Zn⟨H⟩Zn symmetric stretch.

The shoulder in the ZnO + H INS spectrum at 584 cm^{-1} (Figure 7.13) has two possibilities for its assignment (see above):

(i) A phonon mode;

(ii) $\nu_{\delta}(Zn\diagup^{H}\diagdown Zn)$.

If we speculate that the 584 cm^{-1} feature is due to the bending mode of $Zn\diagup^{H}\diagdown Zn$ and assume that the symmetric stretch occurs within the range 829 to 1125 cm^{-1}, then, taking 1475 cm^{-1} to be the frequency of the antisymmetric stretch, we can use the modified Katovic equation (see Chapter Five) to estimate the limits within which the $Zn\diagup^{H}\diagdown Zn$ bond angle, α, must lie:

$$\frac{\nu_a^2}{\nu_s^2 + \nu_\delta^2} = \frac{M_{Zn}^{-1} + M_H^{-1}(1 - \cos\alpha)}{M_{Zn}^{-1} + M_H^{-1}(1 + \cos\alpha)}$$

where ν_δ = 584 cm^{-1}, ν_a = 1475 cm^{-1}, M_H = mass of H atom in amu, M_{Zn} = mass of Zn atom in amu.

For ν_s = 895 cm^{-1}, $\alpha = 108^{o}$ and for

ν_s = 1125 cm^{-1}, $\alpha = 99^{o}$.

Now type II adsorption is said to occur on the $(10\bar{1}0)$ surface planes.[9] Such planes are drawn in Fig. 7.4. The closest Zn----Zn distance is 3.2495Å [8]; this distance is unaltered by the proposed reconstructions of the surface.[16] Thus we have the following geometry for the surface hydrogen at type II sites:

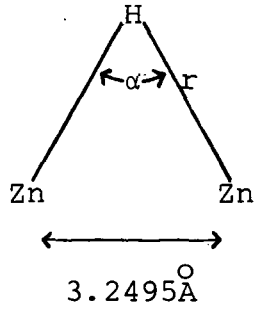

For $\alpha = 99^{\circ}$, the Zn-H bond length r = 2.1Å and for $\alpha = 108^{\circ}$, r = 2.0Å. Thus if the symmetric stretch occurs in the range 895 to 1125 cm^{-1}, the model predicts that the Zn-H bond length lies between 2.0 to 2.1Å.

The Katovic equation is based on the valence force field model which is known to be inaccurate, even for simple triatomic molecules. Thus these values for the Zn-H distance must be regarded as a first approximation only; *ca* 2.0Å is longer than expected for the following reasons. The bonding in Group IIb hydrides is intermediate between that found in transition metal hydrides and covalent hydrides[55]. Since the charges of the ions at the ZnO surface are less than those in the bulk,[19] we expect the surface Zn-H bonds to be predominantly covalent. However, the predicted Zn-H bond length of *ca* 2.0A is longer than that usually found in covalent hydrides (it is more typical of a hydridic $M^{\delta+}$ - $H^{\delta-}$ species). For example, in the covalent AlH_3 in which each Al atom is surrounded by an octahedron of Hatoms and linked by non-linear Al⟨H⟩Al bridges, the Al-H distance is 1.715Å and the Al-H-Al angle 141.2°.[56] The calculated Zn-H distance is also very much longer than the sum of

the covalent radii, 1.57A.[29] To summarise, the calculations predict a Zn-H bond length which is too long and a Zn$\overset{H}{\diagup\diagdown}$Zn bond angle which is too acute. Although several other assumptions were made in predicting the bond length, this indicates that the assignment of the 584 cm^{-1} band to the ν_δ mode of $(\mu_2\text{-H})Zn_2$ is not likely to be correct. The alternative assignment to a phonon mode is therefore preferred.

Furthermore, the assignment of a stretching mode of the proposed Zn$\overset{H}{\diagup\diagdown}$Zn surface species was made by Boccuzzi *et al*[23] to an extremely broad feature centred at 1475 cm^{-1} in their IR spectra of $ZnO+H_2$ (see Fig. 7.14). We were unable to observe resolved bands at this frequency by INS. We also note that the 1475 cm^{-1} IR band has not been reported by other workers. In view of these facts, we submit that this assignment, and the bridge structure of type II hydrogen, proposed by Boccuzzi[23] should be regarded as tentative.

7.4 Conclusions

The adsorption technique used in the INS experiment is expected to give rise to type I, II and III hydrogen. The modes of type III hydrogen and the stretching modes of surface hydroxyls lie outside the frequency range (320 to 2230 cm^{-1}) used on INIB (see Table 7.1). The bending and stretching modes of Zn-H at type I sites were observed at 829 and 1665 cm^{-1} in the INS data. These frequencies are in close agreement with the published IR results (Table 7.1).

From our INS spectra, we were unable to confirm the recent assignments by Boccuzzi *et al*[23] of the ν_{δ} mode of type I O-H to a broad IR band at 845-850 cm^{-1} and of the ν_{as} mode of type II hydrogen at zinc sites to an IR band at 1475 cm^{-1}. We suggest that these assignments[23] of the IR bands are to be regarded as tentative.

An intense broad band was observed at 1346 cm^{-1} in the INS spectrum of ZnO itself. The intensity of this band was unchanged on H_2 adsorption and since it is not observed in the optical spectra it is suggested that this band arises from modes of impurities, possibly carbonates, in the bulk.

REFERENCES

1. Fubini, B., Giamello, E., Gatta, G.D. and Venturella, G., J.Chem.Soc., Faraday Trans.1, 78, 153, 1982.

2. Denny, P.J. and Whan, D.A., in Catalysis (Dowden, A. and Kemball, C., Eds.) Vol.2, p.46, Specialist Periodical Reports, The Chemical Society, London, 1977.

3. Ruppin, R. and Englman, R., Reports on Prog.in Phys., 33, 149, 1970.

4. Yamamoto, K., Veda, K., Yamada, M., and Abe, K., J.Phys. Soc.Jpn., 46, 1792, 1979.

5. British Drug Houses Laboratory Chemicals and Biochemicals Catalogue 1983, BDH, Poole, 1983.

6. Heiland, G., Mollwo, E. and Stöckmann, F., Solid State Phys., 8, 191, 1959.

7. Boccuzzi, F., Monterra, C., Scala, R., and Zecchina, A., J.Chem.Soc., Faraday Trans.2, 77, 2059, 1981.

8. Schulz, H. and Thiemann, K.H., Solid State Commun., 32, 783, 1979.

9. Dent, A.L. and Kokes, R.J., J.Phys.Chem., 73, 3781, 1969.

10. Saussey, J., Lavalley, J.-C., Bovet, C., J.Chem.Soc., Faraday Trans.1, 78, 1457, 1982.

11. Chang, S.-C. and Mark, P., Surf.Sci., 46, 293, 1974.

12. Henrich, E., Zeiger, H.J., Solomon, E.I. and Gay, R.R., Surf.Sci., 74, 682, 1978.

13. Kohl, D., Henzler, M., Heiland, G., Surf.Sci., 41, 403, 1974.

14. Duke, C.B. and Lubinsky, A.R., Surf.Sci., 50, 605, 1975.

15. Gatos, H.C., and Levine, M.C., J.Electrochem.Soc., 107, 427, 1960;
Gatos, H.C., J.Appl.Phys., 32, 1232, 1961.

16. Duke, C.B., Meyer, R.J. and Paton, A., Phys.Rev., B18, 4225, 1978.

17. Hotan, W., Gopel, W. and Haul, R., Surf.Sci., 83, 162, 1979.

18. Gopel, W., Ber.Bunsenges. Phys.Chem., 82, 744, 1978.

19. Watson, R.E., Perlman, M.L. and Davenport, T.W., Surf.Sci., 115, 117, 1982.

20. Duke, C.B., Meyer, R.J. and Mark, P., J.Vac.Sci.Technol., 17, 971, 1980.

21. Baranski, A., and Galuszka, J., J.Catal., 44, 250, 1976.

22. Narayana, D., Subrahmanyam, V.S., Lal,J., Mahmood Ali, M., and Kesavulu, V., J.Phys.Chem., 74, 779, 1970.

23. Boccuzzi, F., Borello, E., Zecchina, A., Bossi, A., and Camia, M., J.Catal., 51, 150, 1978.

24. Griffin, G.L., and Yates,Jr., J.T., J.Catal. 73, 396, 1982.

25. Eischens, R.P., Pliskin, W.A. and Low, M.J.D., J.Catal, 1, 180, 1962.

26. Dent, A.L. and Kokes, R.J., Adv.Catal., 22, 1, 1972.

27. John, C.S., in Catalysis (Dowden, A. and Kemball, C., Eds.), Vol.3, p.169, Specialist Periodical Reports, The Chemical Society, London, 1980.

28. Abrahams, S.C. and Bernstein, J.L., Acta Cryst, B25, 1233, 1969.

29. Huheey, J.E., Inorganic Chemistry: Principles of Structure and Reactivity, Harper and Row, London, 1972.

30. Kokes, R.J., Dent, A.L., Chang, C.C. and Dixon, L.T., J.Am.Chem.Soc., 94, 4429, 1972.

31. Graham, D., Ph.D. Thesis, University of Durham, 1980.

32. Kubas, G.J. and Shriver, D.F., J.Am.Chem.Soc., 92, 1949, 1970.

33. Dent, A.L. and Kokes, R.J., J.Phys.Chem., 73, 3772, 1969.

34. Chang, C.C., Dixon, L.T., and Kokes, R.J., J.Phys.Chem., 77, 2634, 1973.

35. Sherwood, P.M.A., Vibrational Spectroscopy of Solids, Cambridge University Press, Cambridge, 1972.

36. Scott, J.F., Damen, T.C., Ruvalds, J. and Zawadowski, A., Phys.Rev., 3B, 1295, 1971.

37. Olson, C.G. and Lynch, D.W., Phys.Rev., 177, 1231, 1969.

38. Rieder, K.H., Ishigame, M. and Genzel, L., Phys.Rev., 6B, 3804, 1972.

39. Atherton, K.A., Newbold, G. and Hockey, J.A., Disc. Faraday Soc., 52, 33, 1971.

40. Morishique, K., Kittaka, S. and Moriyasu, T., J.Chem.Soc., Faraday Trans.1, 76, 728, 1980.

41. Ross, S.D., Inorganic Infrared and Raman Spectra, McGraw Hill, London, 1972.

42. Boccuzzi, F., Borrello, E., Chiorino, A. and Zecchina, A., Chem.Phys.Lett., 61, 617, 1979.

43. Fateley, W.G., Dollish, F.R., McDevitt, N.T. and Bentley, F.F., Infrared and Raman Selection Rules for Molecular and Lattice Vibrations, Wiley Interscience, New York, 1972.

44. Damen, T.C., Porto, S.P.S. and Tell, B., Phys.Rev., 142, 570, 1966.

45. Mitra, S.S. and Bryant, J.I., Bull.Am.Phys.Soc., 10, 333, 1965.

46. Uvarov, A.V., Antipina, T.V. and Tikhomirova, S.P., Russ.J.Phys.Chem., 41, 1647, 1967.

47. McDonald, R.S., J.Phys.Chem., 62, 1168, 1958.

48. Yates, D.J.C., J.Phys.Chem., 65, 746, 1961.

49. Hewat, A.W., Solid State Commun., 8, 187, 1970.

50. Thoma, K., Dorner, B., Duesing, G., and Wegener, W., Solid State Commun., 15, 1111, 1974.

51. Bredov, M.M., Kotov, B.A., Okuneva, N.M., Oskotskii, V.A. and Shakh-Budagov, A.L., Sov.Phys.-Solid State, 9, 214, 1967.

52. Willis, B.T.M.(Ed.), Chemical Applications of Thermal Neutron Scattering, Oxford University Press, Oxford 1973, and refs. therein.

53. Baranski, A. and Cvetanovic, R.J., J.Phys.Chem., 75, 208, 1971.

54. Marshall, W. and Lovesey, S.W., Theory of Thermal Neutron Scattering, Oxford University Press, Oxford, 1971.

55. Cotton, F.A. and Wilkinson, G., Advanced Inorganic Chemistry, Wiley, New York, 1980.

56. Turley, J.W., and Rinn, H.W., Inorg.Chem., 8, 18, 1969.

57. Thomas, J.M. and Thomas, W.J., Introduction to the Principles of Heterogeneous Catalysis, Academic Press, London, 1967.

CHAPTER EIGHT

AN INS STUDY OF ACETYLENE ADSORBED BY PARTIALLY Ni(II)-ION EXCHANGED ZEOLITE-Y

8.1 Introduction

It is known[1] that acetylene adsorbed at room temperature by partially Ni^{++}-ion exchanged zeolite-Y (NiNaY) undergoes a cyclotrimerisation reaction to form benzene, the catalytic activity of the zeolite depending upon its Ni^{++} content. The NiNaY/acetylene system has been studied by X-ray diffraction and near-IR spectroscopy[1] (Section 8.2.3), but there are no data available in the literature for the far-IR region. Thus in this chapter we present the vibrational spectra (*ca* 20 to 850 cm^{-1}), obtained by INS, of acetylene adsorbed in NiNaY zeolite. As an initial step towards understanding this zeolite/acetylene system, our INS spectra were obtained at cryogenic temperatures at which the formation of benzene is limited, thereby facilitating observation of the adsorbent---acetylene complex.

As well as the temperature and the degree of Ni^{++}-ion exchange of the zeolite, the overpressure of acetylene is known[1] to strongly influence the rate of benzene production. In this chapter we present INS data for only low coverages of adsorbed acetylene and for a limited range of NiNaY zeolite composition. Although planned, the INS spectra of higher acetylene coverages and data for zeolites of differing Ni^{++} content could not be obtained because of a fault with one of the INS spectrometers. However, the INS data obtained are sufficient to indicate the geometry of the adsorbed acetylene molecules.

8.2 A summary of published work on acetylene adsorbed by zeolites

8.2.1 Published spectroscopic studies of adsorbed acetylene

Two extreme modes of interaction between acetylene and an adsorbent can be envisaged[2]: end-on, via the acidic H-atoms of the acetylene and anionic regions of the surface; or lateral, resulting from overlap of the acetylene π-electron system with a cation. Yates *et al*[3] have shown that both types of interaction occur between Al_2O_3 and adsorbed C_2H_2, the end-on interaction causing an increase in the frequency of the acetylene ν_2 mode (C≡C stretch) relative to the gas-phase (1974 cm^{-1} Raman) and the lateral interaction causing a lowering in frequency.

IR and Raman studies of C_2H_2 adsorbed in Li^+, Na^+, K^+, Mg^{++} and Ca^{++} partially exchanged zeolites type-A and in Li^+, Na^+, K^+, Cs^+, Mg^{++}, Ca^{++} and Ba^{++} partially exchanged zeolites type-X have been published by Tam *et al*[4,5]. A lowering of symmetry of adsorbed acetylene from $D_{\infty h}$ was indicated by the violation of the IR/Raman mutual exclusion rule. The decrease in frequency of the ν_2 mode on adsorption of C_2H_2 in all the zeolites studied[4,5] indicated a lateral rather than end-on acetylene-cation interaction. Within each of the two series of partially ion-exchanged zeolites A and X, and for a given cation charge, an increasing shift of ν_2 to lower frequencies was correlated with increasing cationic radius and was taken to indicate increasing strength of the cation-acetylene interaction.[4,5]

No bands ascribable to the modes of acetylene relative to the adsorbent surface were reported by Tam *et al*.[4,5]

However, such bands have been observed in INS studies of C_2H_2 adsorbed in the fully ion-exchanged zeolites $Ag_{12}A$ and AgX.[2,6] In both zeolites, each acetylene molecule was bonded laterally to a coordinating Ag^+ cation and the observation of the τ_x mode of C_2H_2 relative to the surface (Fig. 8.1) indicated that the admolecules were not linear. The INS data were consistent with C_{2v} symmetry of the Ag^+-C_2H_2 sorption complexes in these two zeolites.[2,6]

INS has been used to study the adsorption of C_2H_2 in Nal3X zeolite but the resolution of the spectra was poor and no firm assignments could be made.[6] However, the authors held that the adsorbed acetylene was probably linear.

8.2.2 Published crystallographic studies of intra-zeolitic cation-acetylene sorption complexes

X-ray studies of C_2H_2 adsorbed in single crystals of dehydrated $Na_{12}A$ zeolite have shown that, at coverages up to three molecules per supercage, the acetylene molecules were symmetrically and laterally to Na^+ ions at S2* sites.[7,8] Acetylene molecules adsorbed at high coverages could not be located with certainty.[7,8]

X-ray structure studies of C_2H_2 adsorbed in $Co_{4.0}Na_{4.0}A$ and $Mn_{4.5}Na_{3.0}A$ zeolites have also shown that the C_2H_2 molecules were coordinated symmetrically and laterally with the Co^{++} or Mn^{++} ions at S2* positions.[9,10] In each of the three zeolites cited here, the acetylene-cation interaction was said to take place by lateral π-bonding and the C≡C bond length of the adsorbate was similar to that found in the gas-phase.[7-10]

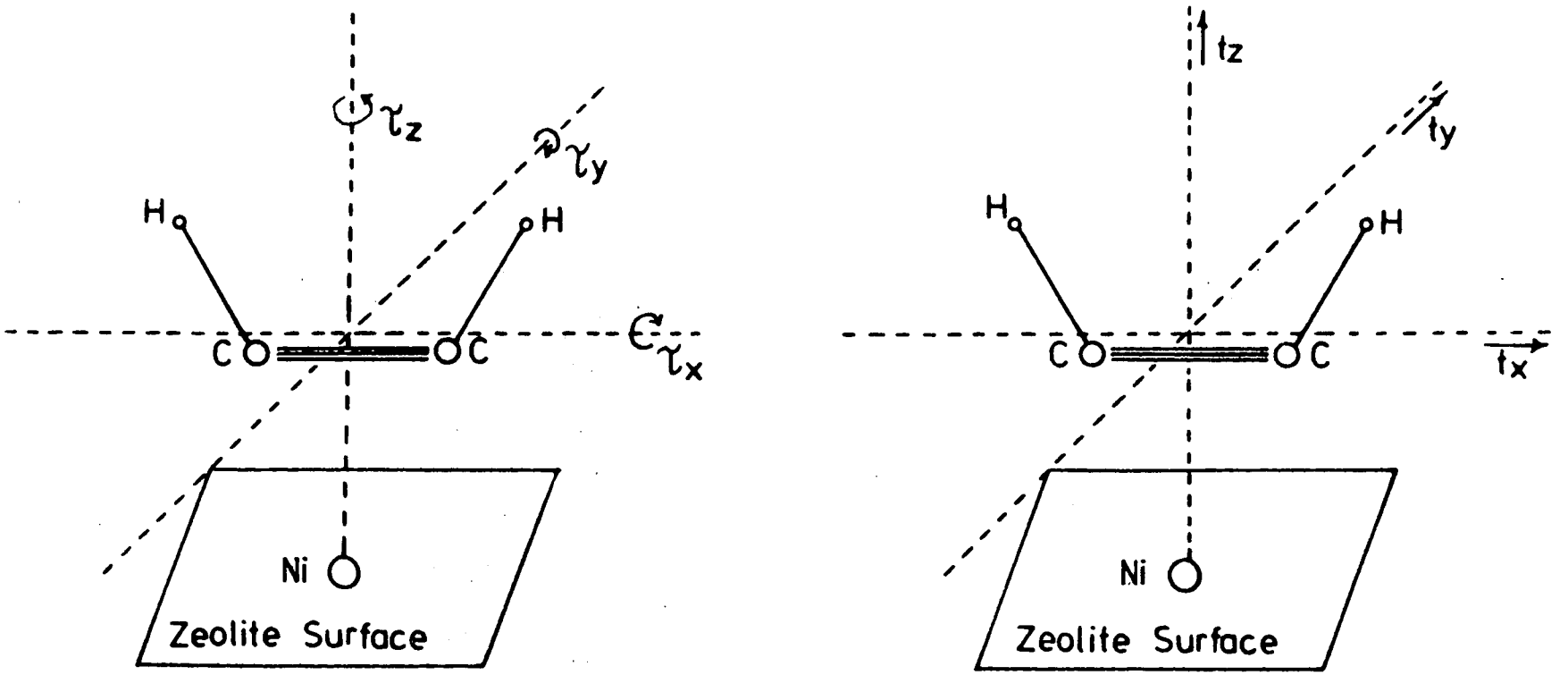

Fig. 8-1 The three hindered rotations, γ_x, γ_y (antisymmetric stretch) and γ_z, and the three hindered translations, t_x, ty and t_z (symmetric stretch) of acetylene relative to the zeolite surface. Taken from ref. 2.

8.2.3 Published studies on the partially Ni^{++}-ion exchanged zeolite-Y/adsorbed acetylene system

The nomenclature used to describe the cation sites in Y-type zeolites was discussed in Chapter Three.

X-ray diffraction studies by Gallezot *et al*[11-13] of partially Ni^{++}-exchanged crystals of zeolite Y have shown that the population and location of the Ni^{++} cation sites vary with the degree of ion-exchange and hydration of the zeolite (Table 8.1). We will refer to the samples of Gallezot *et al*[11-13] as NiNaHY′, where Y′=$Al_{56}Si_{136}O_{384}$. In the fully hydrated zeolites, the possible Ni^{++} ion locations are at SI sites in the hexagonal prisms, SI′ and SII′ sites in the sodalite cavities and various sites in the supercages, principally SII* sites and unspecified positions on the supercage wall, located away from the zeolite symmetry axes.[11] Progressive dehydration of the zeolites caused a migration of Ni^{++} ions to the SI sites and, regardless of the level of ion exchange, the population of Ni^{++} ions at SI sites was limited to a maximum of 12 ions per unit cell.[11] On heating a sample of $Ni_{14}Na_{23}H_5Y'$, this ion migration started at *ca* 520K and was completed by 573K.[11] The driving force of the migration was said[11] to be the large crystal field stabilisation energy of the $Ni^{++}(d^8)$ ions which adopted at SI sites a nearly perfect octahedral coordination to the O(3) atoms of the two 6-oxygen windows. The Ni^{++} ions migrated to the hexagonal prism from both the sodalite cavity and the supercage. However, provided that the sites in the sodalite cavity and supercage were occupied by Ni^{++} ions in the hydrated zeolite, these sites remained occupied by Ni^{++} to a slight extent even under the most severe dehydration conditions employed by Gallezot *et al*[11-13] (*ie* evacuation at 873K).

TABLE 8.1 Ni^{++} ion locations and benzene formation in NiNaHY' zeolites dehydrated at 873K Taken from ref. 1.

Approximate zeolite composition	Number of Ni^{++} ions per unit cell in the various cages			Ease of C_6H_6 formation from adsorbed C_2H_2, in terms of the overpressure of C_2H_2. (P = pressure of C_2H_2 in torr)
	hexagonal prisms	sodalite cages	super-cages	
$Ni_{10}Na_{31}H_5Y'$	8.8	1.7	*ca.*0	Traces of C_6H_6 for P=50 after 24 hours.
$Ni_{14}Na_{23}H_5Y'$	11.7	1.1	1.2	Small amount C_6H_6 for P=5 torr, fast reaction for P=100 torr.
$Ni_{19}Na_{15}H_3Y'$	11.3	1.9	5.8	Fast reaction for P = 5 torr

Notes - Y' = $Al_{56}Si_{136}O_{384}$.

The zeolites were exposed to acetylene at room temperature.

The formation of benzene from the cyclotrimerisation of acetylene adsorbed at room temperature on NiNaHY' has been studied by Pichat *et al*[1] using X-ray diffraction, IR and EPR.

The IR results indicated that the C_6H_6 did not remain bonded to the Ni^{++} ions but was weakly associated with the zeolite framework. The C_6H_6 could be entirely removed by heating *in vacuo* at 373K. Therefore the Ni^{++} ions in the sodalite cavities were inactive in benzene formation, since C_6H_6 cannot escape through the *ca* 2.3Å sodalite cage windows.[1]

The X-ray data showed that the Ni^{++} ions in the hexagonal prisms and sodalite cavities are not accessible to acetylene and that the adsorption and subsequent reactions of acetylene caused no migration of Ni^{++} ions from these locations. Thus the population of Ni^{++} ions in the supercages was the controlling factor in the catalytic activity of the zeolite in the cyclotrimerisation of acetylene (Table 8.1). The dehydrated zeolite exhibited only a small degree of catalytic activity at levels of ion-exchange below $12Ni^{++}$ ions per unit cell, the residual catalytic activity (Table 8.1) being ascribed to the probable presence of a small number of Ni^{++} ions in the supercage.[1] On increasing the ion-exchange level in dehydrated NiNaHY' above 12Ni ions per unit cell, the zeolite became catalytically active in the acetylene trimerisation since the majority of the additional Ni^{++} ions were located in the supercage (Table 8.1).[1]

According to Pichat *et al*,[1] no distinct IR or EPR bands could be assigned to Ni^{++}-C_2H_2 sorption complexes other than those due to modified internal modes of the C_2H_2 moiety. On adsorption by NiNaY, the ν_2 mode of C_2H_2, which is IR inactive

in the gas phase (1974 cm^{-1} Raman), gave rise to weak IR bands at *ca* 1950-1955 and 1975 cm^{-1}.[1] We note that a reduction in frequency of ν_2 on adsorption is consistent with a lateral, rather than end-on interaction of C_2H_2 with the adsorbent (Section 8.2.1).

The IR and EPR results[1] showed that cyclotrimerisation was not the only reaction undergone by adsorbed acetylene. Reduction of Ni^{++} to Ni^{+} and Ni^{o} occurred, as did the formation of methylene (CH_2) species. The methylene fragments were retained by the zeolite after the removal of the benzene. The extent of these side reactions was not reported.[1]

8.3 Experimental

Zeolites of approximate composition $Ni_{14.5}Na_{54.0}Y \cdot xH_2O$ (sample A), $Ni_{20.6}Na_{41.6}Y \cdot yH_2O$ (sample B) and $Ni_{22.0}Na_{39.0}Y \cdot zH_2O$ (sample C), where Y denotes $Al_{83}Si_{109}O_{384}$, were produced by ion-exchange of NaY zeolite (Strem Chemicals) in 0.1M solutions of $Ni(NO_3)_2$ (BDH Analar) at room temperature. These zeolite compositions were calculated from elemental analysis for Ni, Na, Al and Si.

In our work, the degree of ion-exchange was controlled by the time allowed for the exchange. Sample A was produced after two days of exchange; the remaining samples after four days. For these latter samples (B and C), the exchange solution was removed by filtration after two days and the exchange continued for a further two days with fresh 0.1M $Ni(NO_3)_2$ solution. The volume of $Ni(NO_3)_2$ solution used was, in every case, 25 cm^3 per gram of NaY starting material. The ion-exchanged zeolites were washed (H_2O), dried in air (*ca* 320K) and then analysed.

At this stage the zeolites were pale green in colour.

The NiNaY samples were further dehydrated by evacuating to *ca* $5x10^{-5}$ torr at 293K, followed by heating over 8 hours to 593K in a static but periodically refreshed O_2 atmosphere (150 torr O_2). The samples were maintained at 593K for 11 hours while evacuating to *ca* $5.5x10^{-6}$ torr and were then isolated from the vacuum system while at this temperature. The zeolite samples were then pink in colour. The O_2 was dried by slow passage through an acetone/solid CO_2 cold trap (196K). The samples were heated to 593K because it had been reported by Gallezot *et al*[11] that the migration of Ni^{++} ions to SI sites in $Ni_{14}Na_{23}H_5Y'$ zeolite was complete at this temperature (Section 8.2.3). The above dehydration procedure was based on that published by Pichat *et al*[1] and differs from that given in Chapter Four for the dehydration of the variously ion-exchanged type-A zeolites, which did not require O_2. In the case of NiNaY zeolites, the O_2 was required to prevent reduction of the Ni^{++} ions to Ni^{o}.[1]

The C_2H_2 was supplied by B.O.C. and purified by passage through concentrated H_2SO_4 to remove water and subsequent freeze-pump-thaw cycles in liquid air to remove air. The absence of acetone was confirmed by IR spectroscopy. The C_2D_2 (99 atom % D) was supplied by Merck, Sharp and Dohme, Canada, and used without further purification.

The adsorption of acetylene was carried out using the technique described in Chapter Four and the experimental details are summarised in Table 8.2. For the first ten minutes (approximately) of each adsorption experiment, the zeolite sample was held at room temperature, after which it was cooled

TABLE 8.2 Summary of experimental details for the INS spectra of the NiNaY/acetylene adsorption complexes

sample	A	B		C
sample composition[a]	$Ni_{14.5}Na_{54.0}Y$	$Ni_{20.6}Na_{41.6}Y$		$Ni_{22.0}Na_{39.0}Y$
spectrometer	IN4	IN4		DIDO b.f.d.
gas adsorbed	C_2H_2	C_2H_2	C_2D_2	C_2H_2
temperature of INS run/K	10	10	10	77
coverage/ molecules per supercage (θ)	1.2	2.2	2.0	2.6
maximum pressure during adsorption/ torr	407	508	596	690
residual overpressure of acetylene in sample can/ torr	1.5	0.2	<0.1	<1.0
% scattering from adsorbed gas	8	14	4	15
$(\sigma_{inc}$ adsorbed acetylene$)/(\sigma_{inc}$ zeolite$)$	10	17	0.4	20

Note a. Y denotes $Al_{83}Si_{109}O_{384}$.

to 77K for the remainder of the adsorption. Because the adsorption was mostly carried out at low temperatures and because of the low uptakes of acetylene, it is expected that only very small quantities, if any, of benzene would have been produced.

In the case of adsorption of C_2H_2 and C_2D_2 by samples B and C, the colour of the zeolites changed from pink to pale yellow which is consistent with a change in the coordination environment of the Ni^{++} ions. No colour change was discernible on adsorption of C_2H_2 by sample A which may be due to the smaller number of Ni^{++} ions present in this zeolite and the smaller quantity of acetylene adsorbed (Table 8.2).

The t.o.f. spectra presented in this chapter were obtained on the IN4 spectrometer at the I.L.L., Grenoble, using an incident neutron energy of 294 cm^{-1}. Subtraction of flat baselines and subsequent grouping of the data into equal energy (4 cm^{-1}) bins has been carried out for all of the t.o.f. spectra. Where appropriate, Gaussian curves were then fitted to the spectra. The necessary calculations were carried out using the computer programs described in Chapter Six.

The b.f.d. spectra shown in this chapter were obtained on the DIDO b.f.d. spectrometer at A.E.R.E., Harwell.

8.4 Results

8.4.1 The t.o.f. spectrum of dehydrated NiNaY

The t.o.f. spectrum of dehydrated $Ni_{14.5}Na_{54.0}Y$ is shown in Fig. 8.2. This sample was later used to obtain the t.o.f. spectra of NiNaY + C_2H_2 adsorbed at low coverage; the t.o.f. spectra of the other dehydrated NiNaY zeolite used in this work (Table 8.2) was very similar to that shown in Fig.8.2.

Fig. 8.2 T.o.f. spectrum (10K) of dehydrated $Ni_{14.5}Na_{54.0}$-Y zeolite, with no background subtracted. Scattering angle 64.5^0.

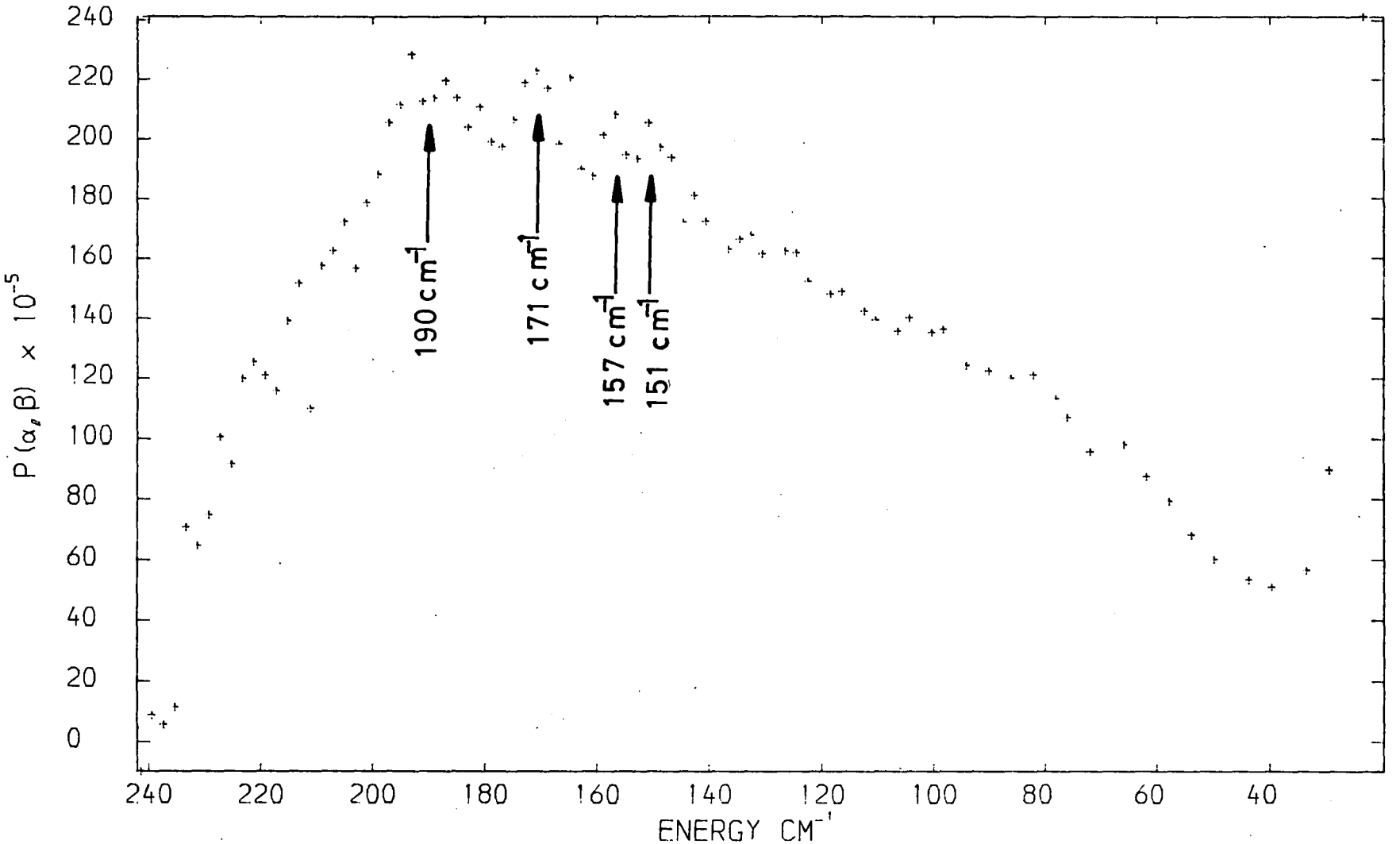

Fig. 8.2 shows an extremely broad band extending from *ca* 40 to 200 cm^{-1} and showing many weak and partially resolved features, the most prominent of which occur at 190, 171, 157 and 151 cm^{-1}. On increasing the scattering angle, the spectrum of dehydrated NiNaY retains the same overall shape as Fig.8.2, except that the scattering intensity decreases and the prominent features listed above show a variation in frequency of ± 5 cm^{-1} over the Q range studied (3.8 to 6.2 $\mathring{A}^{-1}$ for the *ca* 190 cm^{-1} band, 3.9 to 6.6 $\mathring{A}^{-1}$ for the *ca* 151 cm^{-1} band). In dehydrated NiNaY, the only nuclei with non-zero incoherent inelastic neutron scattering cross-sections, σ_{inc}, are Ni and Na (σ_{inc} = 4.7 and 1.7 barns respectively[14]). Thus we assign the intensity in the region *ca* 40 to 200 cm^{-1} of the t.o.f. spectrum of dehydrated NiNaY (Fig.8.2) to partially resolved zeolite lattice modes involving significant displacement of Ni and Na nuclei.

8.4.2 The t.o.f. spectra of acetylene adsorbed by NiNaY

In Figs. 8.3 to 8.5 we show the t.o.f. spectra for three scattering angles of C_2H_2 (coverages θ = 1.2 and 2.2 molecules per supercage) and C_2D_2 (θ = 2.0) adsorbed in NiNaY, recorded on the IN4 spectrometer at 10K. The band frequencies obtained by fitting Gaussian curves to the spectra (Figs. 8.3-8.5) are listed in Tables 8.3 to 8.5. Hereafter we refer to the fitted bands by the frequencies at which they arise in the spectrum recorded at the lowest scattering angle for each sample.

(a) NiNaY + C_2H_2 coverage 1.2 molecules per supercage

These spectra (Figs. 8.3, Table 8.3) show prominent bands at 171 and 75 cm^{-1}. Both bands show shoulders, to which we

Figs. 8.3 T.o.f. spectra (10K) of NiNa-Y zeolite plus adsorbed C_2H_2, coverage 1.2 molecules per supercage. The background spectra of the dehydrated zeolite have been subtracted.

Fig. 8.3a Scattering angle 64.5^0

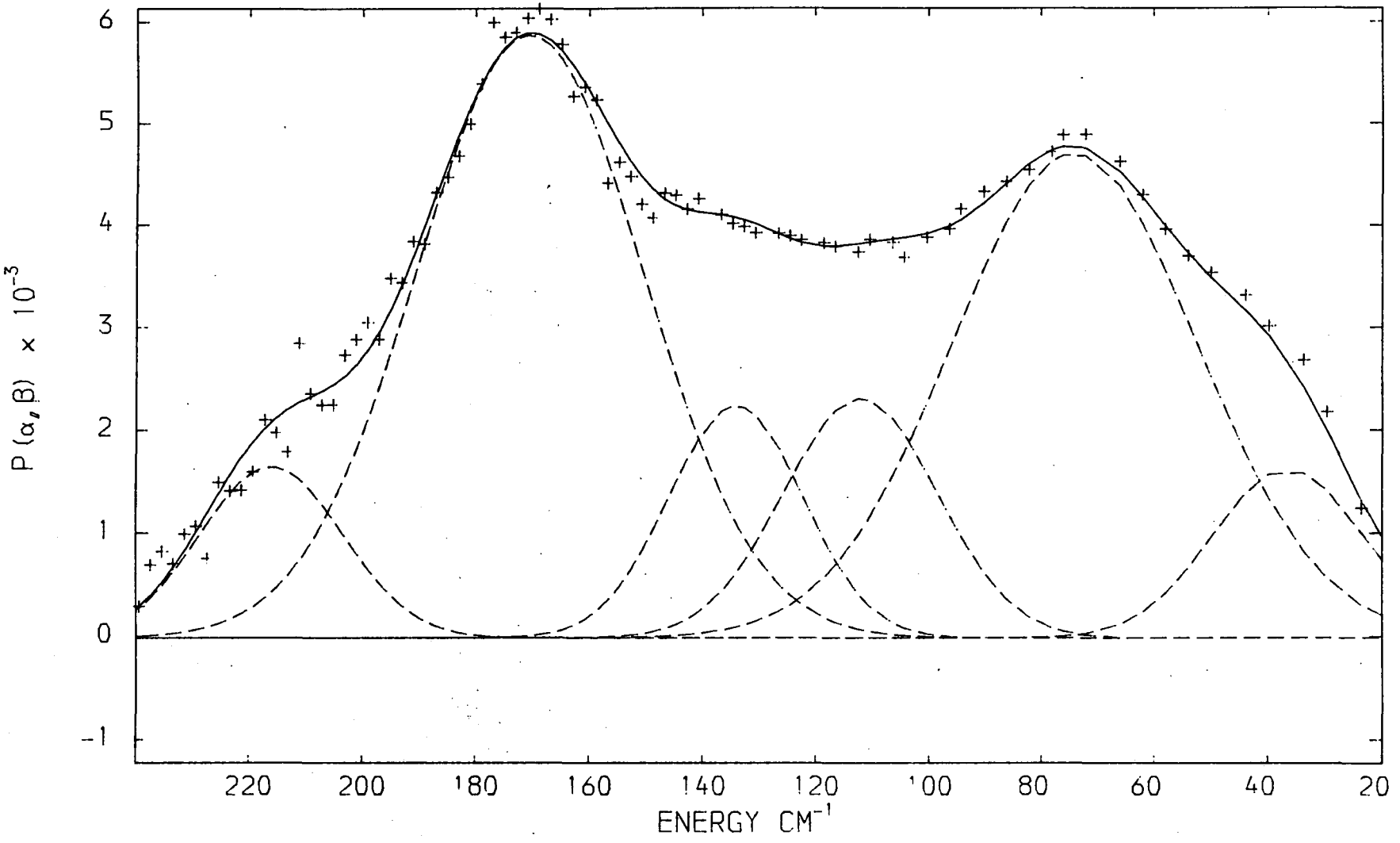

Fig 8.3b NiNa-Y zeolite plus C_2H_2, 1.2 molecules per supercage, background subtracted. Scattering angle 94.5^0

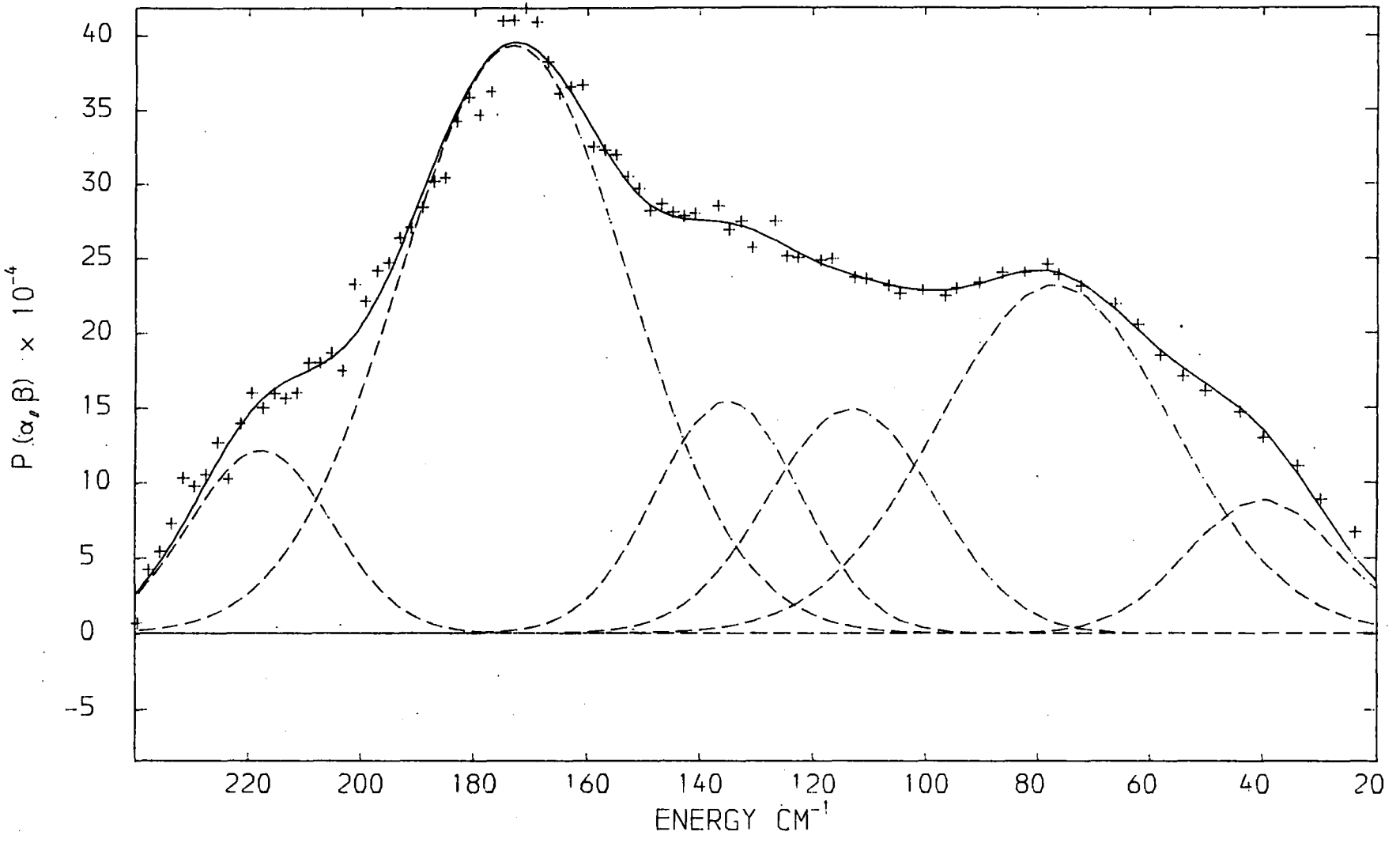

Fig. 8.3c NiNa-Y zeolite plus C_2H_2, 1.2 molecules per supercage, background subtracted.
Scattering angle 108.0^0

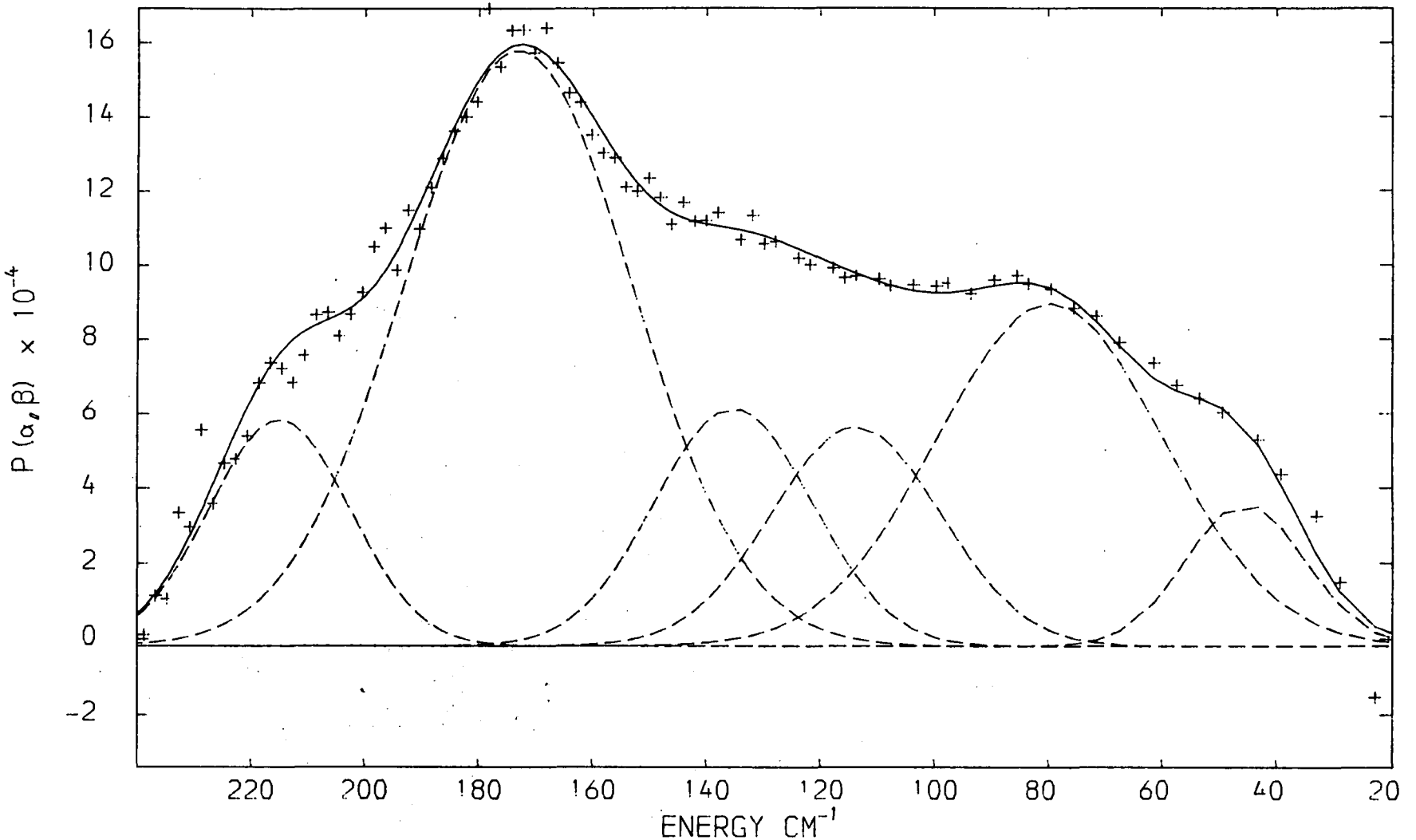

TABLE 8.3 Assignment of the t.o.f. spectra of C_2H_2 adsorbed in NiNaY zeolite (10K) at low coverage, assuming C_{2v} symmetry for the admolecule. The coverage θ was 1.2 molecules C_2H_2 per zeolite supercage.

scattering angle = 64.5°, fig. 8.3a.

mode	ν, cm^{-1}	$Q^2, Å^{-2}$	I^P_{OBS}	I^P_I	I^P_H
?	216	14.5	18	-	-
τ_y	171	15.2	100	100	100
t_z	134	16.0	23	34	24
t_x	112	16.6	27	33	24
τ_z	74	17.7	87	72	96
t_y	37	18.8	18	36	26

scattering angle = 94.5°, fig. 8.3b

mode	ν, cm^{-1}	$Q^2, Å^{-2}$	I^P_{OBS}	I^P_I	I^P_H
?	215	23.7	23	-	-
τ_y	173	26.6	100	100	100
t_z	135	29.1	27	36	26
t_x	114	30.6	27	34	25
τ_z	80	32.8	57	54	72
t_y	45	35.0	12	28	21

TABLE 8.3 (contd.)

scattering angle = 108.0°, fig. 8.3c

mode	ν, cm^{-1}	$Q^2, Å^{-2}$	I^P_{OBS}	I^P_I	I^P_H
?	218	27.7	19	-	-
τ_y	173	31.8	100	100	100
t_z	135	35.1	25	37	27
t_x	113	37.0	28	34	25
τ_z	77	40.0	60	47	63
t_y	40	42.9	15	26	19

Notes -

ν = band frequency, $\hbar Q$ = momentum transfer during scattering event, I^P_{OBS} = observed relative band intensity, I^P_I = relative band intensity calculated using Iwashita model for the admolecule; I^P_H = relative band intensity calculated using the Howard and Waddington model (Section 8.4.3).

Figs. 8.4 T.o.f. spectra (10K) of NiNa-Y zeolite plus adsorbed C_2H_2, coverage 2.2 molecules per supercage. The background spectra of the dehydrated zeolite have been subtracted.

Fig. 8.4a Scattering angle 64.5^0

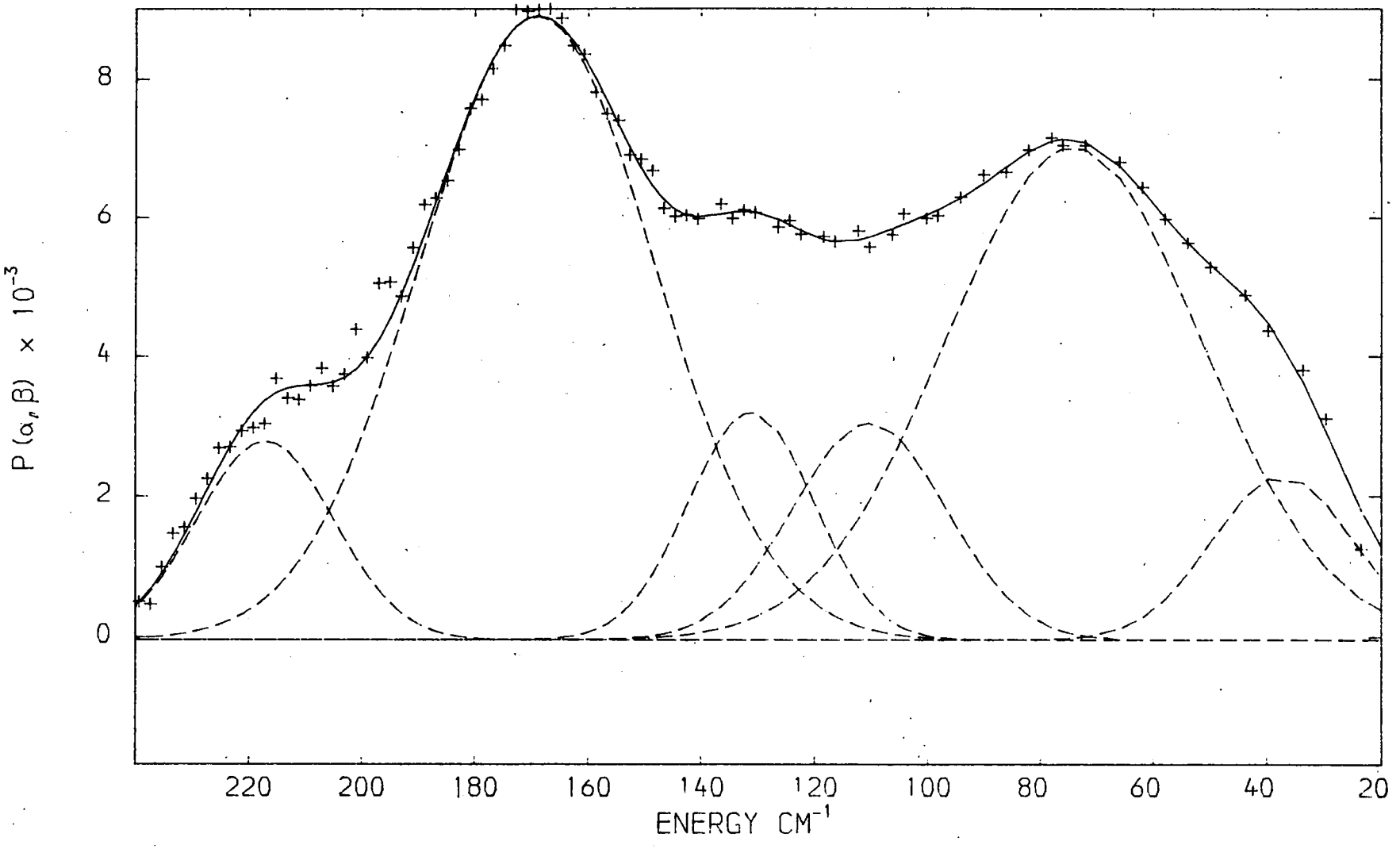

Fig. 8.4b NiNa-Y zeolite plus C_2H_2, 2.2 molecules per supercage, background subtracted. Scattering angle 108.0^0

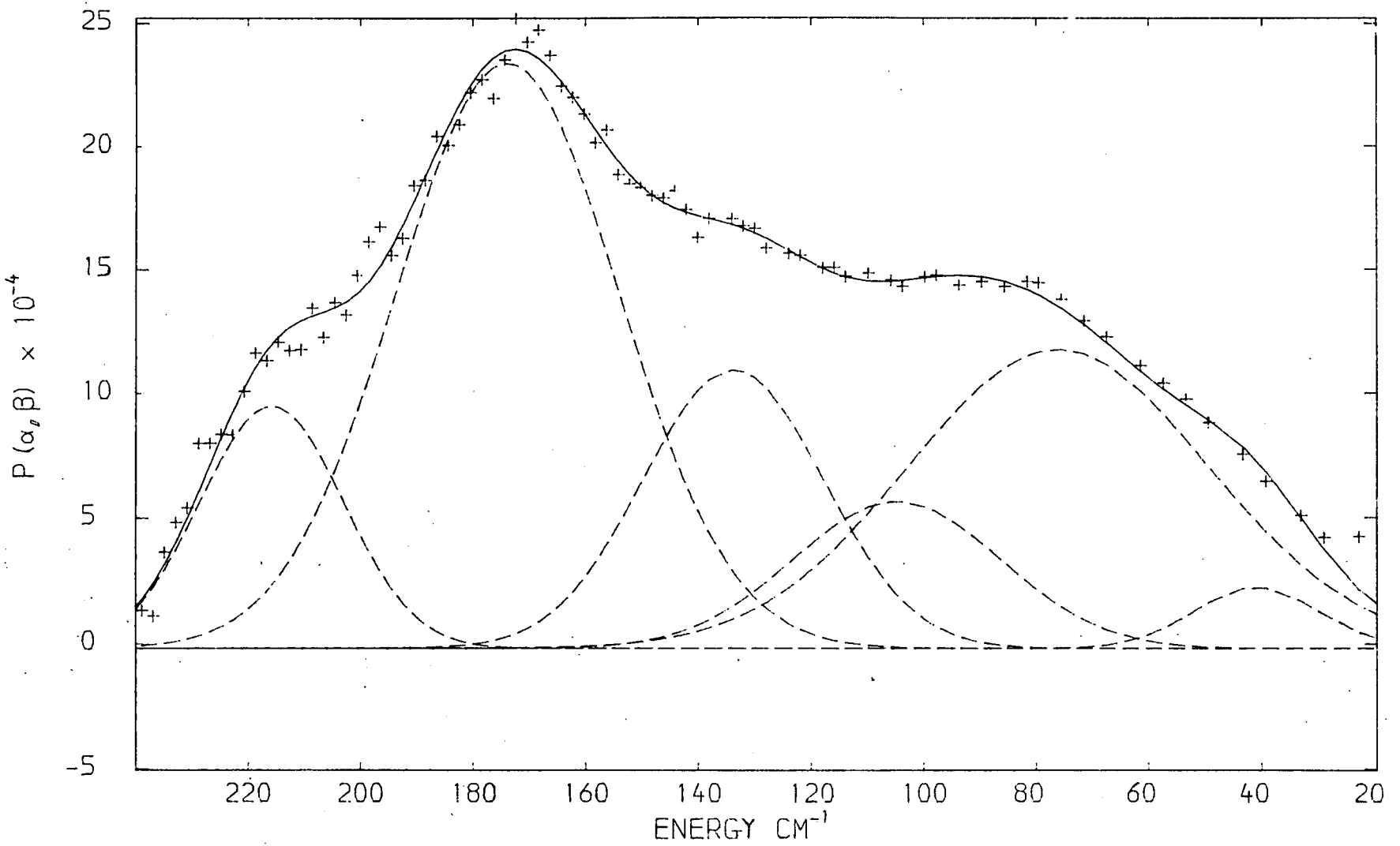

Fig. 8.4c NiNa-Y zeolite plus C_2H_2, 2.2 molecules per supercage, background subtracted. Scattering angle 135.0^0

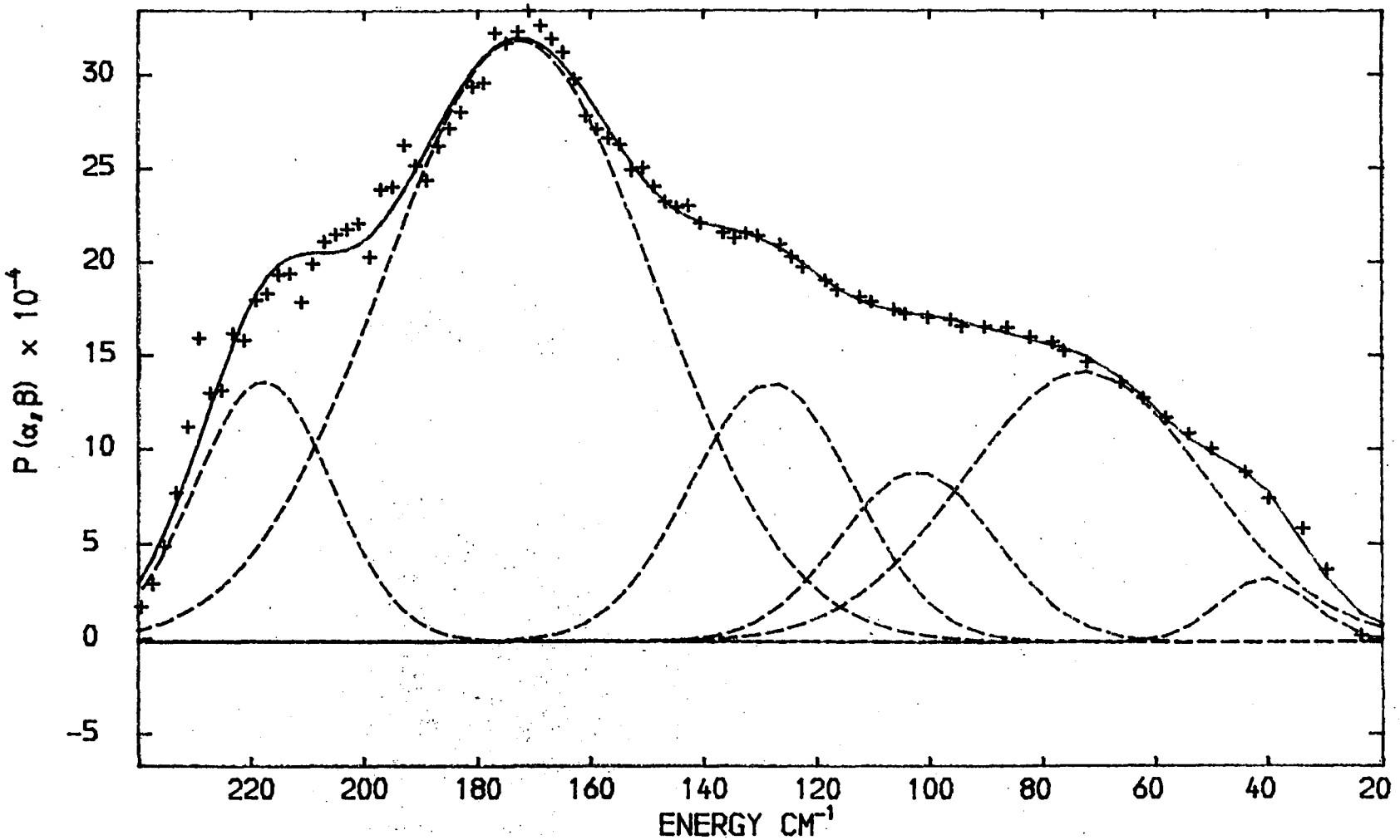

TABLE 8.4 Assignment of the t.o.f. spectra of C_2H_2 adsorbed in NiNaY zeolite (10K) at high coverage, assuming C_{2v} symmetry for the admolecule. The coverage θ was 2.2 molecules C_2H_2 per zeolite supercage

scattering angle = 64.5°, fig. 8.4a

mode	ν, cm^{-1}	Q^2, $Å^{-2}$	I^P_{OBS}	I^P_I	I^P_H
?	217	14.5	18	-	-
τ_y	169	15.2	100	100	100
t_z	131	16.1	19	37	27
t_x	110	16.6	23	27	20
τ_z	74	17.7	87	66	88
t_y	37	18.8	16	25	18

scattering angle = 108.0°, fig. 8.4b

mode	ν, cm^{-1}	Q^2, $Å^{-2}$	I^P_{OBS}	I^P_I	I^P_H
?	216	27.9	27	-	-
τ_y	174	31.8	100	100	100
t_z	134	35.2	38	47	34
t_x	105	37.7	23	23	17
τ_z	76	40.0	68	41	55
t_y	41	42.8	6	7	5

TABLE 8.4 (contd.)

scattering angle = 135.0°, fig. 8.4c

mode	ν, cm^{-1}	Q^2, $Å^{-2}$	I^P_{OBS}	I^P_I	I^P_H
?	218	34.9	22	-	-
τ_y	173	40.8	100	100	100
t_z	128	46.3	26	54	39
t_x	102	49.2	16	21	15
τ_z	72	52.5	40	32	43
t_y	41	55.9	4	4	3

Notes -

ν = band frequency, $\hbar Q$ = momentum transfer during scattering event, I^P_{OBS} = observed relative band intensity, I^P_I = relative band intensity calculated using Iwashita model for the admolecule, I^P_H = relative band intensity calculated using the Howard and Waddington model (Section 8.4.3).

Figs. 8.5 T.o.f. spectra of NiNa-Y zeolite plus adsorbed C_2D_2, coverage 2.0 molecules per supercage. The background spectra of the dehydrated zeolite have been subtracted.

Fig. 8.5a Scattering angle 64.5^0

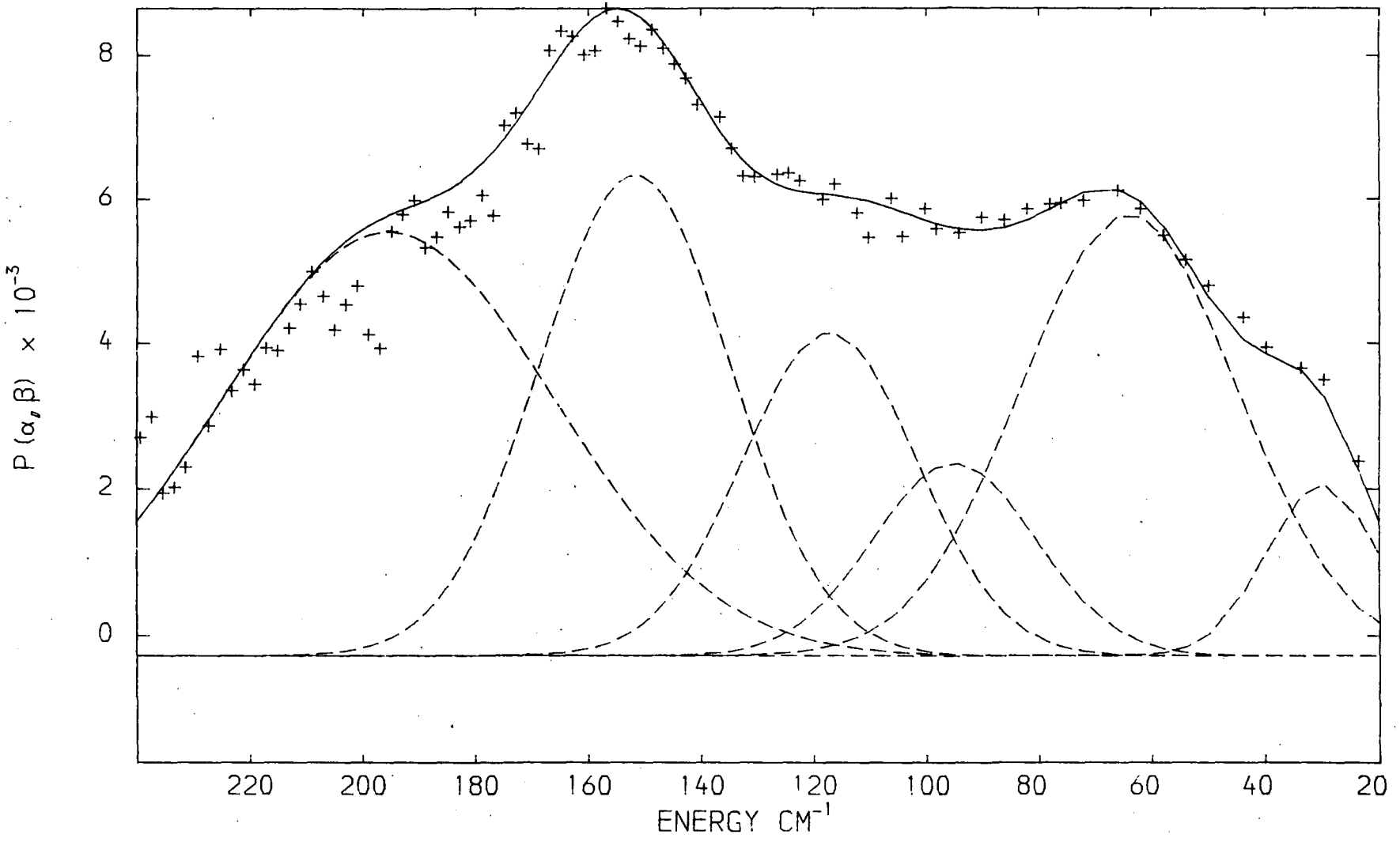

Fig. 8.5b NiNa-Y zeolite plus C_2D_2, 2.0 molecules per supercage, background subtracted. Scattering angle 108.0^0

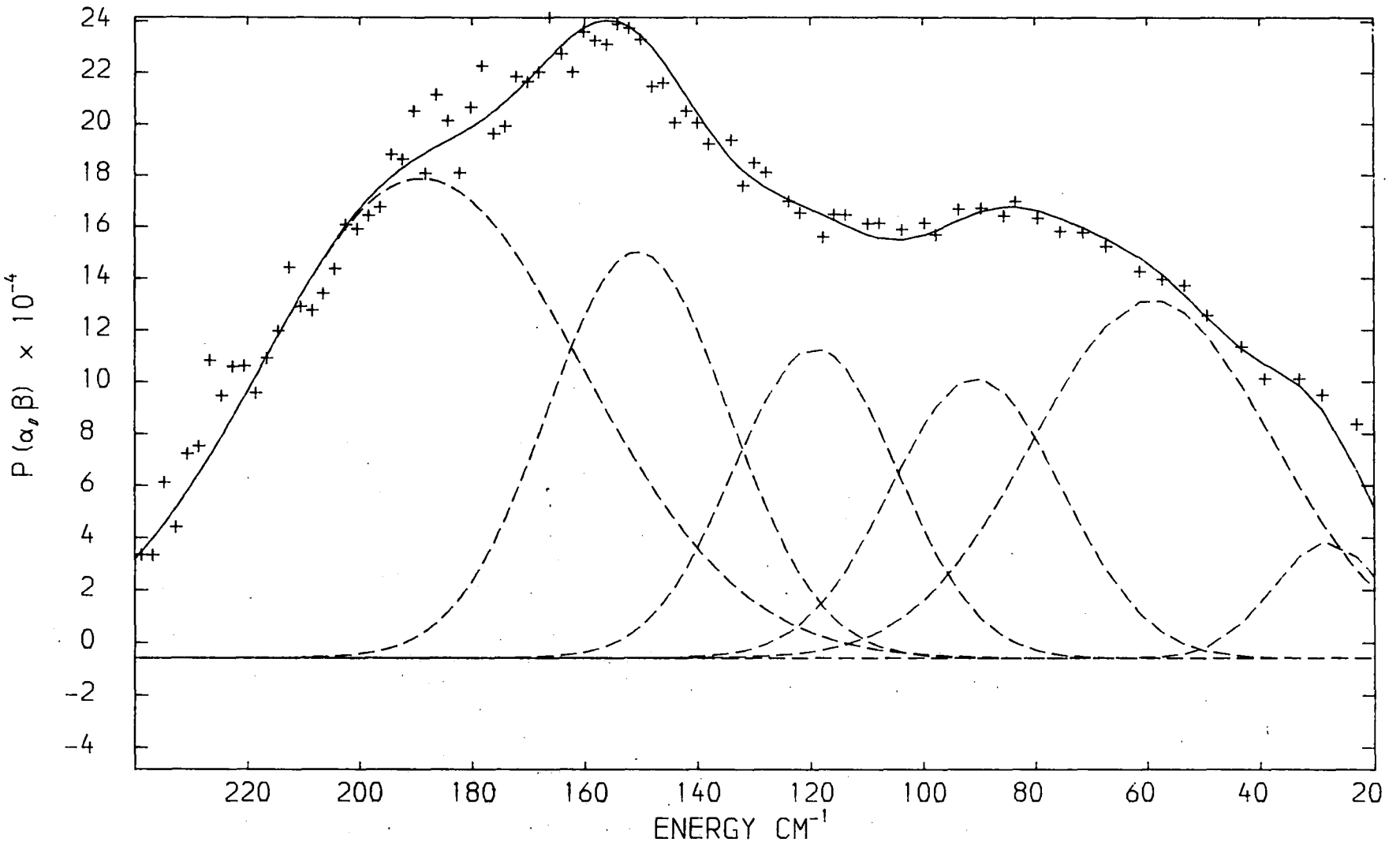

Fig. 8.5c NiNa-Y zeolite plus C_2D_2, 2.0 molecules per supercage, background subtracted. Scattering angle 135.0^0

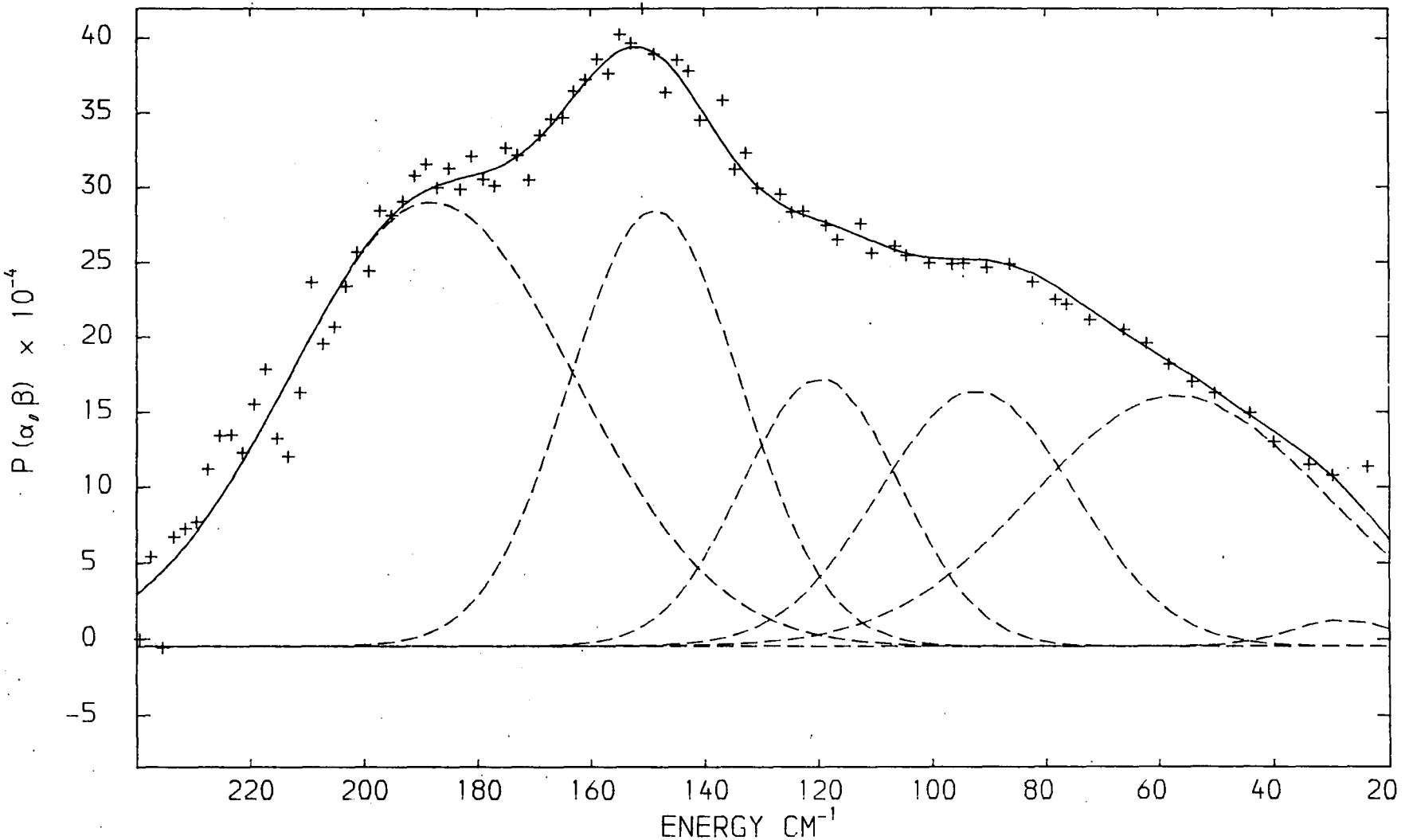

TABLE 8.5 Assignment of the t.o.f. spectra of C_2D_2 adsorbed in NiNaY zeolite (10K), assuming C_{2v} symmetry for the admolecule. The coverage θ was 2.0 molecules C_2D_2 per zeolite supercage

scattering angle = 64.5°, fig. 8.5a

mode	ν, cm^{-1}	$Q^2, Å^{-2}$	I^P_{OBS}	I^P_I	I^P_H
τ_x	196	14.7	153	195	147
τ_y	152	15.6	100	100	100
t_z	117	16.4	61	42	32
t_x	95	17.0	34	52	39
τ_z	64	18.0	104	96	117
t_y	30	19.0	20	23	17

scattering angle = 108.0°, fig. 8.5b

mode	ν, cm^{-1}	$Q^2, Å^{-2}$	I^P_{OBS}	I^P_I	I^P_H
τ_x	189	30.4	209	201	151
τ_y	151	33.8	100	100	100
t_z	119	36.5	68	50	38
t_x	91	38.8	65	77	58
τ_z	59	41.4	116	89	107
t_y	2	43.9	17	8	6

TABLE 8.5 (contd.)

scattering angle = 135.0°, fig. 8.5c

mode	ν, cm^{-1}	$Q^2, Å^{-2}$	I^P_{OBS}	I^P_I	I^P_H
τ_x	188	38	170	204	153
τ_y	149	43.8	100	100	100
t_z	120	47.2	56	55	42
t_x	92	50.3	66	95	72
τ_z	57	54.2	96	85	103
t_y	28	57.2	4	4	3

Notes -

ν = band frequency, $\hbar Q$ = momentum transfer during scattering event, I^P_{OBS} = observed relative band intensity, I^P_I = relative band intensity calculated using Iwashita model for the admolecule, I^P_H = relative band intensity calculated using the Howard and Waddington model (Section 8.4.3).

have fitted Gaussian curves centred at 216 and 37 cm^{-1} respectively (Fig. 8.3a). The intensities of the 75 and 37 cm^{-1} features decrease with respect to that of the 171 cm^{-1} band as the scattering angle is increased. Anticipating equations 8.1 and 8.6 below, the dependence of the band intensities on Q is given by the factor $\exp(-Q^2\langle U^2\rangle)$. The value of Q^2 increases most rapidly at low, rather than high, energy transfers as the scattering angle is raised for our neutron energy loss spectra (Figs. 8.3, $\hbar Q$ is the momentum transfer during the scattering event and $\langle U^2\rangle$ is the mode dependant mean square displacement of the oscillator).

In Figs. 8.3, the region between the 171 and 75 cm^{-1} bands is not resolved but appears to contain some structure, which is most evident at the higher scattering angles (Figs. 8.3b,c). We were unable to reproduce the structure by fitting one Gaussian curve (of full width at half maximum of 61 cm^{-1}) to this region of the spectra. As a first approximation to the observed scattering intensity, we have fitted two Gaussian curves, at 134 and 112 cm^{-1} (Fig. 8.3a). Thus a total of six Gaussian curves have been fitted to the data (Figs. 8.3) and the fitting of the 216, 134, 112 and 37 cm^{-1} bands must be regarded as less accurate than that of the more intense 171 and 75 cm^{-1} bands. All the band maxima show a small variation in frequency with scattering angle. This because the statistics and resolution of the t.o.f. spectra (Figs. 8.3) are such that there is no unique fit to the data and the fitted band maxima may be in slight error. This point also applies to the other t.o.f. spectra presented in this chapter (Figs. 8.4, 8.5).

(b) NiNaY + C_2H_2, coverage 2.2 molecules per supercage

The spectra of C_2H_2 adsorbed at the coverage of θ = 2.2 (Fig. 8.4, Table 8.4) resemble quite closely those obtained at the lower coverage (Figs. 8.3). Accordingly, six Gaussian curves were fitted to the higher coverage data (Fig.8.4), frequencies and relative intensities being similar to those of the lower coverage case.

(c) NiNaY + C_2D_2, coverage 2.0 molecules per supercage

The spread in the data points of these spectra (Fig.8.5, Table 8.5) is somewhat greater than that for adsorbed C_2H_2 (Figs. 8.3, 8.4). This is expected from the low value of the incoherent inelastic neutron scattering cross-section of the D nucleus compared with that of the H nucleus (2.0 and 79.7 barns, respectively[14]).

Six Gaussian curves have been fitted to the NiNaY + C_2D_2 spectra (Fig.8.5, Table 8.5), the five bands from 152 to 30 cm^{-1} corresponding to the five lowest frequency bands in the spectra of C_2H_2 adsorbed at both coverages on NiNaY.

Apart from the deuteration shifts, the principal difference between the t.o.f. spectra of adsorbed C_2D_2 (Fig.8.5) and those of adsorbed C_2H_2 (Figs. 8.3, 8.4) is the very intense shoulder in the C_2D_2 data at 196 cm^{-1}. This 196 cm^{-1} shoulder is from 1.5 to 2.0 times more intense than the adjacent 152 cm^{-1} band in the C_2D_2 results (Fig.8.5), which contrasts with the case for adsorbed C_2H_2 (both coverages) in which the *ca* 216 cm^{-1} shoulder is about one fifth the intensity of the adjoining band at *ca* 171 cm^{-1} (Figs. 8.3, 8.4, Tables 8.3, 8.4). Thus the two shoulders, at 196 cm^{-1} (C_2D_2) and 216 cm^{-1} (C_2H_2), probably have different physical origins.

8.4.3 Assignment of the t.o.f. spectra of NiNaY+acetylene

The lowest frequency internal vibrations of solid phase C_2H_2 are reported to occur at 747.5 to 768.8 cm^{-1} (ν_5, δ_s(C-H)) and at 626 cm^{-1} (ν_4, δ_{as}(C-H)).[15,16] For C_2D_2, ν_5 has been observed at *ca* 560 cm^{-1} and $2\nu_4$ at 1057.5 cm^{-1}.[15] Thus the bands in our t.o.f. spectra of adsorbed C_2H_2 and C_2D_2 (Figs. 8.3-8.5), which occur at a maximum frequency 218 cm^{-1}, might arise from:

1. modes of adsorbed acetylene relative to the surface;
2. amplified zeolite lattice modes;
3. lattice modes of solid acetylene.

Published IR and Raman spectra[16,17,18] of solid C_2H_2 at 77K (and C_2D_2 at 100K) have indicated lattice vibrations at 174, 122(118), 102(98.5), 82(70) and 76(65.5) cm^{-1}, where the frequencies in brackets refer to solid C_2D_2. These frequencies are similar to those observed in the t.o.f. spectra of NiNaY + C_2H_2 (C_2D_2) at 171, 130(118), 109(98) and 75(65) cm^{-1}, (Tables 8.3, 8.5). Evidence that the bands in our t.o.f. spectra of NiNaY+acetylene (Figs. 8.3-8.5) are due to modes of adsorbed, rather than solid phase, acetylene is the observation in the b.f.d. spectrum of NiNaY+C_2H_2 of the ν_4 and ν_5 internal modes of C_2H_2 at frequencies perturbed from those reported[15,16] for solid C_2H_2 (Section 8.4.4 below).

We have assigned features at 190, 171, 157 and 151 cm^{-1} in the t.o.f. spectra of dehydrated NiNaY to zeolite lattice modes (Fig.8.2, Section 8.4.1). Although a band was observed at 171 cm^{-1} in the t.o.f. spectra of adsorbed C_2H_2 (Fig.8.3, Table 8.3), the high intensity of this band in the t.o.f. spectra favours its assignment to a mode of adsorbed C_2H_2 relative to

the zeolite surface, rather than to a zeolite lattice mode of enhanced intensity through riding motion of adsorbed C_2H_2. The non-observation of features at 190, 157 and 151 cm^{-1} in the NiNaY+C_2H_2 results (Figs.8.3,8.4, Tables 8.3,8.4) also indicates that zeolite lattice modes make, at most, a very small contribution to the t.o.f. spectra of adsorbed C_2H_2. Therefore all the bands in the t.o.f. spectra (Figs. 8.3-8.5) of NiNaY+ acetylene will be ascribed to modes of adsorbed acetylene relative to the zeolite surface.

The t.o.f. spectra (Figs. 8.3-8.5) of adsorbed acetylene will be assigned using the band intensities and deuteration shifts calculated for various geometries of the absorbate. As a further guide to the assignment of our t.o.f. spectra, we note that in INS studies[2,6] of acetylene adsorbed in fully ion-exchanged AgX and $Ag_{12}A$ zeolites, the observed hindered translations and rotations of the admolecule (Fig.8.1) occurred in the following order of frequency:

$$\tau_x > \tau_y > t_z > \tau_z \qquad \text{(AgX), and}$$

$$\tau_x > \tau_y > t_z > t_A > \tau_z > t_B \qquad (Ag_{12}A)$$

In the $Ag_{12}A + C_2H_2$ study[2] the respective ordering of frequencies of the t_x and t_y modes could not be determined and in the above sequence, if $t_A = t_x$ then $t_B = t_y$, or *vice versa*. In the complex $Co_2(CO)_6 \cdot C_2H_2$,[19] the vibrational modes corresponding to those of adsorbed C_2H_2 have been reported in an INS study[20] to occur in the frequency order

$$\tau_x > \tau_y > t_z > \tau_z > t_A > t_B.$$

The ordering

$$\tau_x > \tau_y > t_z > t_x > \tau_z > t_y$$

has been reported in INS studies of π-bonded ethylene ligands in various organometallic and intrazeolitic sorption complexes.[21-26]

The INS studies[2,6] of acetylene adsorbed by zeolites $Ag_{12}A$ and AgX have shown that the acetylene molecule is non-linear and laterally bonded to the coordinating Ag^+ cation. Lateral bonding of adsorbed acetylene to a cation is also indicated by the X-ray results of Seff *et al*[7-10] and the IR/Raman data of Tam *et al*,[4,5] for C_2H_2 adsorbed in a range of partially ion-exchanged zeolites type A and X, and probably occurs for C_2H_2 adsorbed in NiNaY[1] (Section 8.2). We will show that the laterally bonded, non-linear model of molecularly adsorbed C_2H_2 is consistent with our INS results for acetylene in NiNaY. The six hindered rotations and translations of the adsorbed molecule were shown in Figure 8.1 and the relative INS band intensities, I^P, of these hindered modes can be predicted (Chapter Two) in the harmonic apprixmation from equation 8.1 below:

$$I^P \quad \alpha \quad \sigma_{inc} \quad \frac{Z(\tilde{\nu})}{\mu} \exp[-2W] \qquad (8.1)$$

where:

σ_{inc} is the incoherent inelastic neutron scattering cross section of the H nucleus in the case of adsorbed C_2H_2 and of the D nucleus in the C_2D_2 experiments;

$Z(\tilde{\nu})$ is the vibrational density of states;

$\tilde{\nu}$ is the frequency of the mode in cm^{-1};

and μ is the effective mass of the oscillator, given in the case of adsorbed acetylene (C_{2v} or $D_{\infty h}$ symmetries) by:

translational modes: $\mu = 2/M$ (8.2)

torsional modes : $\mu = 2r^2/I_R$ (8.3)

where M is the mass of the scattering molecule,

I_R is the moment of inertia of the admolecule about the relevant rotation axis, and

r is the radius of gyration of the scattering nuclei.

In equation 8.1, the term exp[-2W] is the Debye-Waller factor which is evaluated in terms of a mode-dependent model in Appendix 8A.

The precise geometry of the admolecules strongly influences the relative INS intensities of the hindred rotations (Figure 8.1), through the effect of the different moments of inertia (equation 8.3) on the μ^{-1} term in equation 8.1. We will consider three possible models for the geometry of the acetylene admolecules in NiNaY, using structural data available in the literature. These models are:

1. A linear acetylene molecule, using structural data for the solid state[27] (the C≡C bond length is 1.20Å and the C-H is 1.05Å);

2. The non-linear model proposed by Howard and Waddington for acetylene adsorbed in AgX zeolite[6,28], in which the C_2H_2 moiety has C_{2v} symmetry and the C≡C bond length is 1.20Å, the C-H length is 1.06Å and the $\hat{CCH}$ bond angle is 170° with the C-H bonds bent away from the plane of the surface. The bond angle of 170° was not derived from the experimental results but was used as an example to illustrate the effect on the INS band intensities of a loss of linearity of the admolecule.[6,28]

3. The structure proposed by Iwashita for the C_2H_2 moiety in the complex $Co_2(CO)_6 \cdot C_2H_2$ in which the acetylene C≡C bond is

perpendicular to the Co-Co vector. The π-bonded acetylene moiety is non-linear (C_{2v} symmetry) with the C-H bonds bent away from the plane of the Co atoms.[19] The C≡C bond length is 1.388Å, the C-H bond length 1.08Å and the $\hat{CCH}$ angle is 120°.[19]

In Table 8.6, we list the values of μ^{-1} (equation 8.1) for the hindered rotations and translations of the adsorbed acetylene calculated for each of the three models above. For a given model, the three hindered translations have the same value of μ^{-1}. The tabulated values of μ^{-1} are relative and those of the hindered translations have been set equal to unity within each model. The values of μ^{-1} (Table 8.6) were obtained equations 8.2 and 8.3, using the harmonic approximation and allowance was made for the variation in position of the molecular centre of mass as the $\hat{C-C}-H$ bond angle was changed (this affects the τ_x and τ_z modes only). It was assumed that the C-D bond lengths were 0.01Å shorter than the C-H bonds.

TABLE 8.6 The relative values of μ^{-1} in equation 8.1 for various models of the geometry of the acetylene adsorption complex in NiNaY zeolite

mode	μ^{-1} for adsorbed C_2H_2			μ^{-1} for adsorbed C_2D_2		
	Iwashita model ref.19	Howard model refs.6,28	linear model ref.27	Iwashita model ref.19	Howard model refs.6,28	linear model ref.27
τ_x	12.000	12.000	0.0	6.000	6.000	0.0
τ_y	3.636	5.034	3.046	2.918	3.882	2.367
τ_z	2.711	5.003	3.046	2.403	3.870	2.367
t_x, t_y, t_z	1.000	1.000	1.000	1.000	1.000	1.000

The models of the admolecule are described in Section 8.4.3.

The observed band intensities in the t.o.f. spectra of NiNaY/acetylene (Figures 8.3 to 8.6) and the band intensities calculated *via* equations 8.1 to 8.3 within the Howard[6,28] and Iwashita[19] models of the adsorbate are given in Tables 8.3 to 8.5. The assignments of the bands listed in these tables are explained below. Because equations 8.1 to 8.3 give relative intensity values, we have arbitrarily set the observed and calculated relative intensities of the τ_y mode in each spectrum equal to 100 units (Tables 8.3 to 8.5). The τ_y mode was chosen because it is the most intense band in the spectra of adsorbed C_2H_2.

Table 8.6 shows that for both C_2H_2 and C_2D_2, the value of μ^{-1} for the τ_x mode is much greater than that of any hindered rotation or translation of adsorbed acetylene, provided that the admolecule is not linear. Also, the values of μ^{-1} for the τ_y and τ_z modes are similar to each other (Table 8.6). Thus, for the moment neglecting the other factors in equation 8.1, the μ^{-1} values indicate that the modes of a non-linearly adsorbed acetylene molecule (C_2H_2 and C_2D_2) will occur in the following order of intensity.

$$\tau_x > \tau_y \simeq \tau_z > t_x = t_y = t_z.$$

This sequence applies for both the Howard[6,28] and Iwashita[19] models of the adsorbate. For a linear admolecule, the τ_x mode has zero INS intensity and the intensity sequence, based on the μ^{-1} values (Table 8.7) alone, becomes:

$$\tau_y = \tau_z > t_x = t_y = t_z .$$

The effect of the so far neglected terms in equation 8.1 on the INS band intensities is discussed below.

The t.o.f. spectra of NiNaY+C_2D_2 (Figure 8.5, Table 8.5), show one very intense feature, the shoulder at 196 cm^{-1}, and two bands of lesser, but approximately equal intensity at 152 and 64 cm^{-1}. Using the intensity sequence above for a <u>non-linear</u> admolecule, we assign the 196 cm^{-1} shoulder (Figure 8.5) to the τ_x mode of adsorbed C_2D_2 and the 152 and 64 cm^{-1} bands to the τ_y and τ_z modes. By appeal to the published[2,6] order of frequencies of the hindered modes of acetylene adsorbed in $Ag_{12}A$ and AgX (*ie* $\tau_x > \tau_y > \tau_z$), we assign the 152 cm^{-1} band (Figure 8.5) to the τ_y mode of C_2D_2 in NiNaY and the 64 cm^{-1} band to the τ_z mode.

The remaining bands in the NiNaY+C_2D_2 spectra (Figure 8.5, Table 8.5), at 117, 95 and 30 cm^{-1}, must arise from the three hindered translations of adsorbed C_2D_2. We cannot distinguish between these modes on intensity grounds alone, since they have equal values of μ^{-1} (Table 8.6) and the remaining terms in equation 8.1 do not depend, in any way which we can calculate, on the direction of the displacement of the nuclei during the appropriate vibration. (The situation for the hindered torsional modes is more favourable since the moment of inertia of the oscillator, which may differ for the τ_x, τ_y and τ_z modes, enters the intensity equation 8.1 through equation 8.3). Within the harmonic approximation, the deuteration shifts of the hindered translations of adsorbed acetylene are calculated to be equal, for both the Howard[6,28] and Iwashita models[19], and we cannot use the deuteration shifts to distinguish between the t_x, t_y and t_z modes. From the published[21-26] ordering of the frequencies of the hindered translational modes of adsorbed C_2H_4 (above), we tentatively assign the bands at 117, 95 and 30 cm^{-1} in our t.o.f. spectra (Figure 8.5) of NiNaY+C_2D_2 to the t_z, t_x and t_y modes of C_2D_2 respectively.

In our t.o.f. spectra (Figure 8.3, Table 8.3) of C_2H_2 adsorbed at low coverage in NiNaY, the two most prominent bands occur at 171 and 74 cm^{-1} and are of similar intensities at the lowest scattering angle (Figure 8.3a). By comparison with the C_2D_2 results (*ie* Figure 8.5), the 171 and 74 cm^{-1} bands (Figure 8.3) are assigned to the τ_y and τ_z modes of C_2H_2, respectively. The corresponding bands occur at 169 cm^{-1} (τ_y) and 74 cm^{-1} (τ_z) in the high coverage spectra of NiNaY+C_2H_2 (Figure 8.4, Table 8.4). In the spectra of C_2H_2 adsorbed at both coverages, we note that the observed intensity of the τ_z band falls off rapidly with respect to that of the τ_y band as the scattering angle is increased (Tables 8.3, 8.4). On the other hand, the corresponding bands at 152 and 64 cm^{-1} in the C_2D_2 results (Table 8.5) remain of approximately equal relative intensity as the scattering angle is raised. The difference between adsorbed C_2D_2 and C_2H_2 in the variation with scattering angle of the observed intensities of the τ_y and τ_z modes is reproduced in the values of the calculated intensities (Tables 8.3 to 8.5).

On grounds of frequency and relative intensity, the bands at 134, 112 and 37 cm^{-1} in the low coverage spectra of NiNaY+C_2H_2 (Figure 8.3) are hindered translational modes of C_2H_2 and are tentatively assigned to t_z, t_x and t_y respectively using the same arguments given for the C_2D_2 case. In the high coverage spectra of NiNaY+C_2H_2 (Figure 8.4), these bands arose at 131, 110 and 37 cm^{-1} respectively.

The shoulder at 216 cm^{-1} in the low coverage NiNaY+C_2H_2 spectra (Figure 8.3) remains to be assigned. The only hindered rotation or translation of adsorbed C_2H_2 which is as yet unassigned in the NiNaY+C_2H_2 t.o.f. spectra (Figure 8.3) is the τ_x mode. On the basis of the sequence of INS band intensities

given above for a non-linear admolecule, the band due to τ_x is expected to be the most intense of the bands due to the hindered rotations and translations of adsorbed C_2H_2. Therefore the 216 cm^{-1} band in Figure 8.3 is of insufficient intensity to have arisen from τ_x.

The intensity sequence of the INS bands was obtained by considering only the μ^{-1} terms in equation 8.1 for the corresponding modes. We now put our conclusion that $\tau_x \neq 216$ cm^{-1} on a firmer basis by calculating the relative INS band intensity which would arise at 216 cm^{-1} if the τ_x mode of C_2H_2 were to occur at that frequency. This calculation uses all the terms in equation 8.1 and the mode dependent Debye Waller factors are obtained in Appendix 8A from the observed band intensities. The intensity calculated for τ_x at 216 cm^{-1} is compared with that observed for the 171 cm^{-1} band (Figure 8.3a) assigned to τ_y. Within the Howard model[6,28] of the admolecule, we find the intensity ratio, in arbitrary units, is 222:100 (τ_x:τ_y) and for the Iwashita model[19] the ratio becomes 302:100 (τ_x:τ_y). The observed intensity ratio in Figure 8.3a (Table 8.3) of the 216 cm^{-1} and 171 cm^{-1} bands if 18:100 (216 cm^{-1}:171 cm^{-1}) and thus our calculations confirm that the 216 cm^{-1} band (Figure 8.3a) is not due to τ_x of adsorbed C_2H_2.

The most intense band in the NiNaY+C_2H_2 low coverage spectra (Figure 8.3) is at 171 cm^{-1} and is assigned to τ_y. We can verify that this band should not instead be assigned to τ_x by calculating the relative INS intensity with which the τ_x mode would be observed if it did occur at 171 cm^{-1}. Again, this calculation uses all the terms in equation 8.1 and the mode dependant Debye Waller factors are obtained in Appendix 8A. The calculated intensity of a τ_x mode at 171 cm^{-1} is compared

with that observed for the τ_z mode at 74 cm^{-1} (Figure 8.3a), the latter being the second most intense band in Figure 8.3a. Using arbitrary units, the intensity ratio is calculated to be 247:87 (τ_x:τ_z) in the Howard model[6,28] and 456:87 (τ_x:τ_z) in the iwashita model.[19] In Figure 8.3a, the observed intensity ratio of the 171 and 74 cm^{-1} bands is 100:87 (171cm^{-1}:74cm^{-1}).

Thus our intensity calculations show that neither the 216 nor the 171 cm^{-1} bands in the low coverage NiNaY+C_2H_2 spectra (Figure 8.3a) are due to the τ_x mode of C_2H_2. The same will be true of the 217 and 169 cm^{-1} bands in the higher coverage C_2H_2 results (Figure 8.4). It is likely that the τ_x mode of C_2H_2 occurs above the high frequency cut-off of our t.o.f. spectra (240 cm^{-1}).

We return to the assignment of the 216 cm^{-1} band in the low coverage NiNaY+C_2H_2 spectra (Figure 8.3; 217 cm^{-1} at high coverage, Figure 8.4). This band cannot be due to solid acetylene or to benzene. The possibility that our t.o.f. spectra contain bands due to the collective modes of solid acetylene was discounted above. Our b.f.d. spectra of NiNaY+C_2H_2 (Section 8.4.4) indicate that no benzene was formed in the samples used. Although different samples were used for our t.o.f. and b.f.d. experiments, they were all prepared in the same manner. The 216 cm^{-1} band (Figure 8.3) is not due to C_2H_2 adsorbed at a second site because other bands due to such a species would have arisen in the t.o.f. spectra. We are unable to assign the 216 cm^{-1} band in the NiNaY+C_2H_2 t.o.f. spectra (Figure 8.3) except to suggest that it arises from a hydrogeneous species other than acetylene or benzene.

In Tables 8.3 to 8.5 (cols,5,6) are listed the relative INS intensities calculated for the bands in the t.o.f. spectra of NiNaY+acetylene (Figures 8.3 to 8.5) for the Howard[6,28] and Iwashita[19] models. Although neither model is exactly in accord with the observed intensities (col.4, Tables 8.3 to 8.5), overall the Howard model of adsorbed acetylene gives somewhat better agreement than does the Iwashita model. An attempt to calculate values of μ^{-1} for the modes of adsorbed acetylene *via* equation 8.1 from the fitted INS band intensities led to too wide a range of values of μ^{-1} for any firm inferences to be made on the geometry of the adsorbate. This was due to inaccuracies in the curve fitting (Figures 8.3 to 8.5). Robson[29] has published plots of the relative INS band intensities and deuteration shifts for the hindered rotations and translations of adsorbed acetylene as the C-$\hat{C}$-H bond angle, ψ, is changed within the Howard[6,28] and Iwashita[19] models. The other parameters of these models were held constant and the plots[29] are reproduced in Figures 8.6. In our t.o.f. spectra of adsorbed acetylene (Figures 8.3 to 8.5), the discrepancies between the observed and calculated band intensities show no clear trends with scattering angle or band frequency. This applies to both the Howard[6,28] and Iwashita models.[19] Thus using the plots of Robson[29] (Figure 8.6) to evaluate the bond angle ψ of adsorbed acetylene would be operating beyond the limits of accuracy of our INS data (Figures 8.3 to 8.5). However, we note that the intensity of the τ_z mode declines relative to that of τ_y in both the Iwashita[19] and Howard models[6,28] as the bond angle ψ is decreased from 180^o (Figure 8.6). Since we prefer the Howard model to that of Iwashita, the band intensities observed

Fig. 8.6 The variation of intensity ratio with bond angle CCH found for C_2H_2 using the Howard model[6,28] for the adsorbed acetylene molecule.

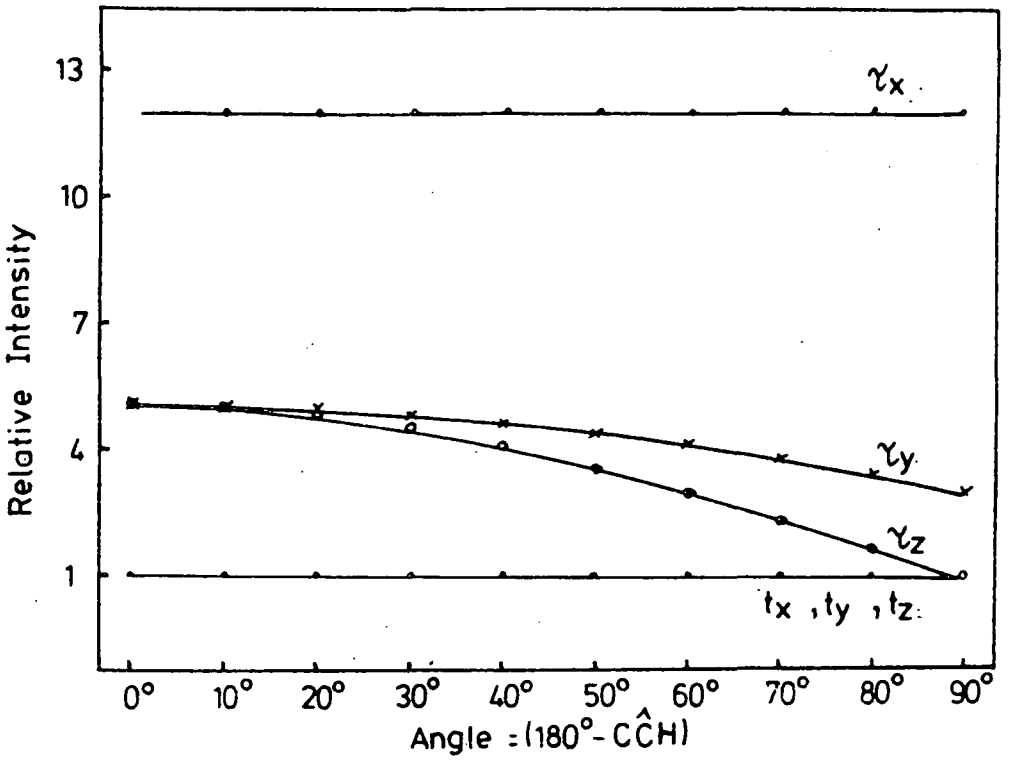

The variation of intensity ratio with bond angle CCH found for C_2H_2 using the Iwahita model[19] for the adsorbed acetylene molecule.

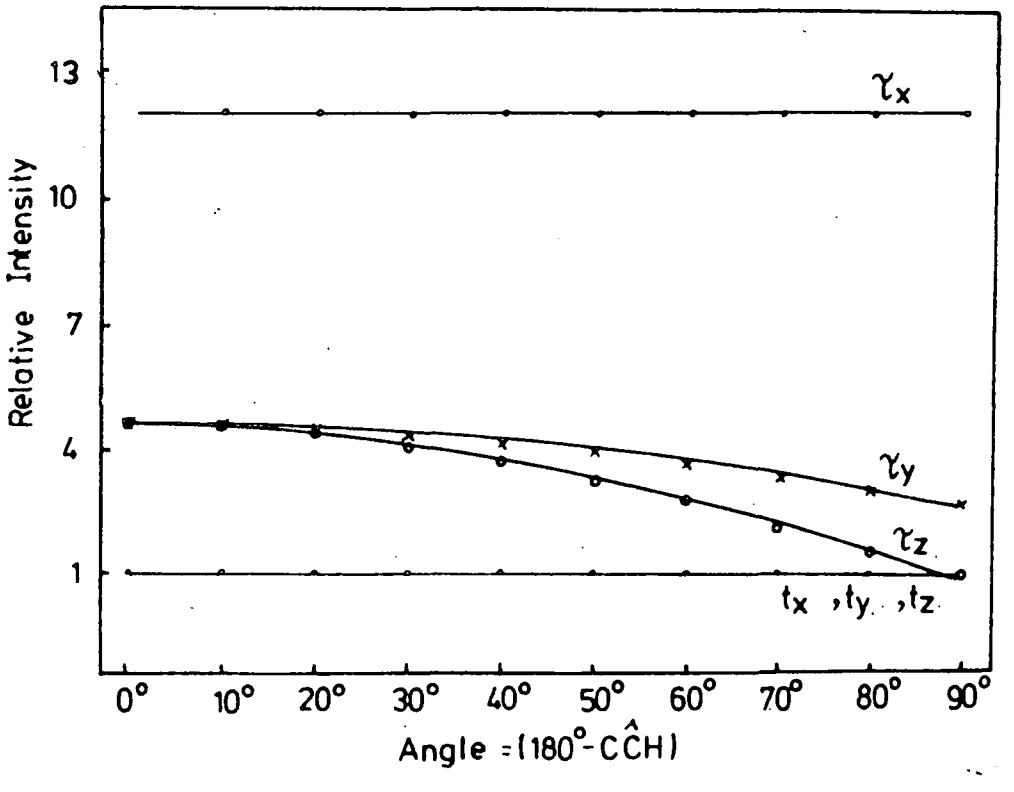

Both these diagrams have been taken from Robson[29].

in our NiNaY+acetylene spectra (Figures 8.3 to 8.5) indicate that while the adsorbed acetylene is non-linear, the bond angle ψ is not greatly altered from 180°. Although the value of ψ is difficult to quantify, the value of 170° in the model of Howard[6,28] is consistent with our INS results.

8.4.4 The b.f.d. spectra of dehydrated NiNaY and C_2H_2 adsorbed in NiNaY

The spectrum of dehydrated $Ni_{22.0}Na_{39.0}Y$ obtained at 77K on the DIDO b.f.d. spectrometer is shown in Figure 8.7. No subtractions or time normalisations have been applied to this spectrum. All the features in Figure 8.7 are weak and will have arisen from either zeolite lattice modes or variations in the spectrometer background.

The b.f.d. spectrum of $Ni_{22.0}Na_{39.0}Y+C_2H_2$ (coverage θ = 2.6 molecules per supercage) at 77K is shown in Figure 8.8. The background subtraction and time normalisation procedures have been carried out on this spectrum and a summary of the assignments of the observed bands is given in Table 8.7. The band at 156 cm^{-1} in Figure 8.8 is readily assigned to the τ_y mode of adsorbed C_2H_2, since this mode gave the most intense band in the corresponding t.o.f. spectra at 169 cm^{-1} (Figure 8.4). The second most intense band in the t.o.f. results for NiNaY+C_2H_2 (Figure 8.4) was that due to τ_z at 74 cm^{-1}. We assign this mode to the band resolved at 87 cm^{-1} in the b.f.d. spectrum (Figure 8.8). The shoulder at 117 cm^{-1} in Figure 8.8 is assigned to unresolved intensity from the t_x and t_z modes of adsorbed C_2H_2. These modes were ascribed to bands of moderate intensity which were fitted, but not fully resolved, at 110 and 131 cm^{-1} in the t.o.f. spectrum of NiNaY+C_2H_2 (Figure 8.4).

Fig. 8.7 Beryllium filter detector (DIDO b.f.d.) spectrum (77K) of dehydrated $Ni_{22}Na_{39}$-Y zeolite, with no background subtracted.

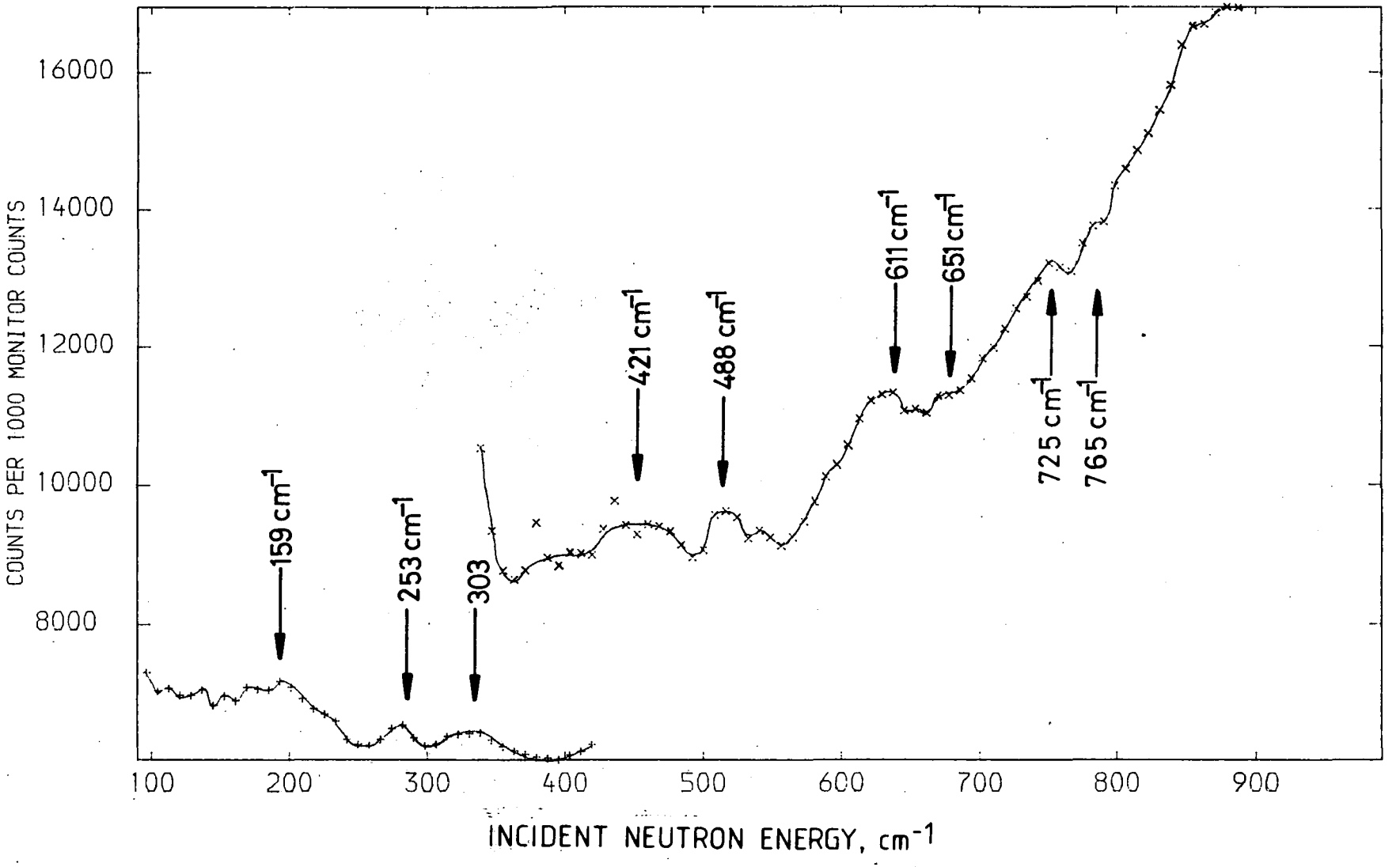

Fig. 8.8 Beryllium filter detector (DIDO b.f.d.) spectrum (77K) of $Ni_{22}Na_{39}$-Y zeolite plus adsorbed C_2H_2, coverage 2.6 molecules per supercage. A background spectrum of the dehydrated zeolite has been subtracted.

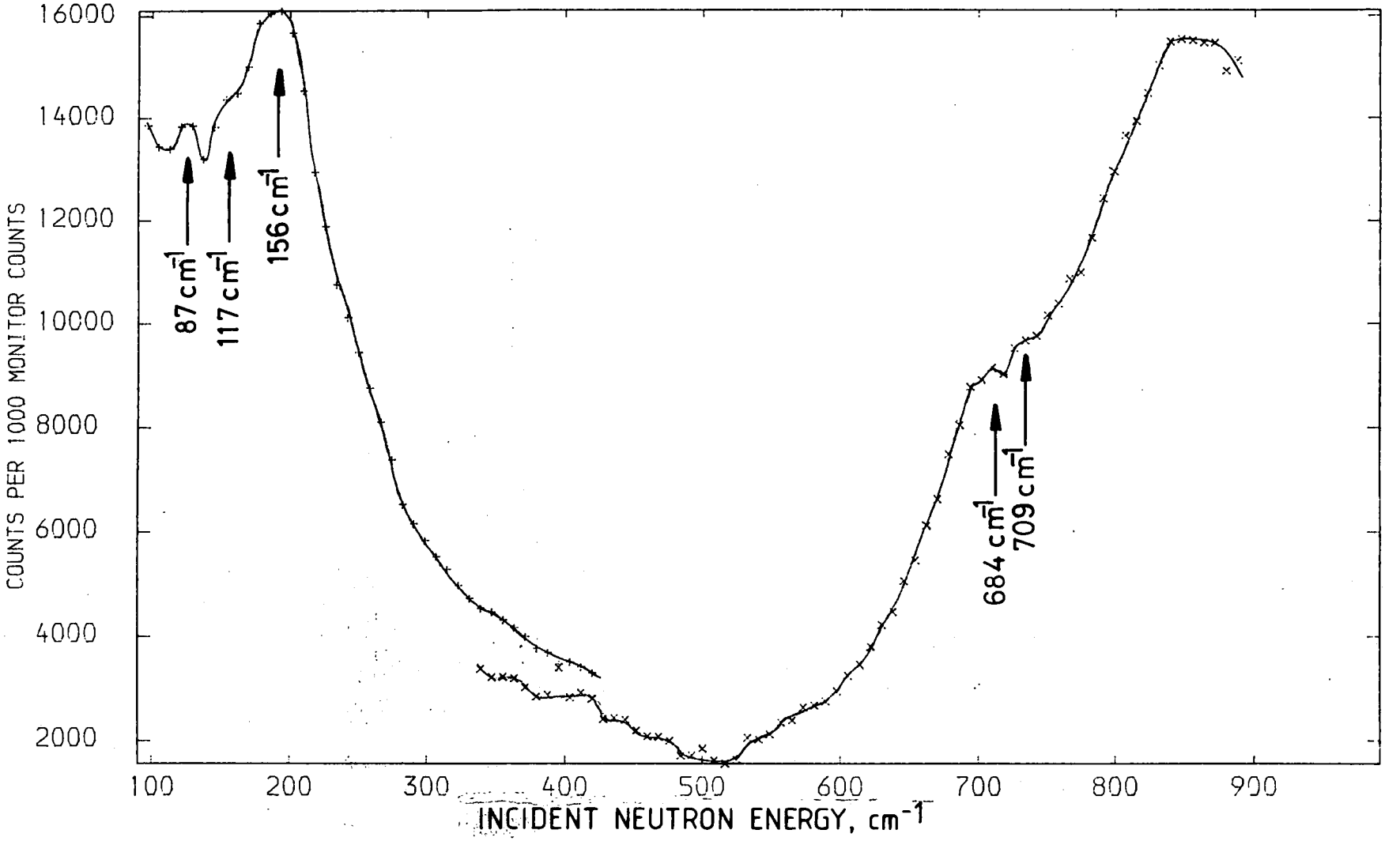

TABLE 8.7 Assignment of the bands (cm^{-1}) observed in the INS spectra of NiNaY + C_2H_2

T.o.f. spectrum of NiNaY + C_2H_2 θ = 2.2, 10K scattering angle 64.5° fig. 8.4a	B.f.d. spectrum of NiNaY + C_2H_2 θ = 2.6, 77K fig. 8.8	Assignment (vibrational modes of C_2H_2)
37 w	-	t_y
74 s	87 m	τ_z
110 m	117 sh,m	t_x
131 m		t_z
169 s	156 vs	τ_y
217 sh, m	-	?
-	684	ν_4
-	709	ν_5

θ = coverage of C_2H_2 in molecules per supercage

m = moderate, s = strong, sh = shoulder, vs = very strong, w = weak.

At higher frequencies in the b.f.d. spectra of NiNaY+C_2H_2 (Figure 8.8), weak features are observed at 684 cm^{-1} and 709 cm^{-1}. These are respectively assigned to the ν_4 and ν_5 internal modes of adsorbed C_2H_2, perturbed from the solid state frequencies of 626 and 760 cm^{-1}.[15,16] Frequency shifts of similar magnitude have been reported[2,6] for these modes on adsorption of C_2D_2 by $Ag_{12}A$ and C_2H_2 by AgX zeolites.

The only mode of vibration with respect to the adsorbent of C_2H_2 adsorbed in NiNaY which was unassigned in our t.o.f. spectra (Figures 8.3, 8.4), was the τ_x mode. However, the τ_x mode of adsorbed C_2D_2 was observed at *ca* 194 cm^{-1} (Figure 8.5). The intensities of the bands in the t.o.f. spectra of adsorbed acetylene (Figures 8.3-8.5) favour the Howard model of the admolecule (Section 8.4.2). Within this model and adopting the harmonic approximation, the deuteration shift of τ_x is calculated to be 0.73. Thus it is predicted that the τ_x mode of C_2H_2 adsorbed in NiNaY would occur at *ca* 260 cm^{-1}, above the high frequency cut-off of the t.o.f. data at 240 cm^{-1}.

The INS intensity which would arise in the b.f.d. spectrum of NiNaY+C_2H_2 (Figure 8.8) if the τ_x mode did occur at 260 cm^{-1} cannot be calculated because the Debye Waller factor for this mode is unknown. We note that the 156 cm^{-1} band in Figure 8.8 is broad and extends to *ca* 350 cm^{-1}. It is possible that the high frequency edge of the 156 cm^{-1} band in Figure 8.8 contains unresolved intensity from τ_x. This possibility could be tested by repeating the t.o.f. experiments for NiNaY+C_2H_2 using an incident neutron energy sufficiently large to observe inelastic transitions in the region 200 to 350 cm^{-1}, the resolution of

the IN4 t.o.f. spectrometer being greater than that of the DIDO b.f.d.

The lowest frequency internal modes of solid benzene are reported[30] to occur at 407, 607 and 687 cm^{-1}. On adsorption by Nal3X zeolite these modes are reported to arise at 414(s), 619(ms) and 725(m) cm^{-1} and on adsorption by fully exchanged AgX zeolite, they occur at 417(vs), 611(m) and 725(vs) cm^{-1}. [30] These three sets of data were obtained[30] on the DIDO b.f.d. spectrometer at 77K. Our b.f.d. spectrum of NiNaY+C_2H_2 (Figure 8.8) shows no pronounced features at *ca* 400 or *ca* 600 cm^{-1} which is evidence for the non-formation of benzene in this sample.

8.5 A summary of published INS data for zeolite/acetylene adsorption complexes and organometallic compounds containing acetylene ligands

In this section we compare the INS spectra published[2,6,20] for acetylene adsorbed by the fully ion-exchanged zeolites $Ag_{12}A$ and AgX and for the Iwashita complex, $Co_2(CO)_6 \cdot C_2H_2$, with our data for NiNaY+acetylene. The INS spectra for each of the zeolite + acetylene systems were consistent with a non-linear acetylene admolecule of C_{2v} symmetry, bonded laterally to the surface (Figure 8.2). For brevity, the hindered translational and torsional modes of adsorbed acetylene relative to the surface will be referred to, in this section, as the external modes of acetylene.

8.5.1 The frequencies of the modes of adsorbed acetylene

The order of frequencies of the external modes of adsorbed C_2H_2 is the same for each of the three zeolite adsorbents (Table 8.8) and is:

$$\tau_x > \tau_y > t_z > t_A > \tau_z > t_B$$

where, if $t_A = t_x$, then $t_B = t_y$, or *vice versa* (Section 8.4.3). Although for all three zeolites (Table 8.8), the order of frequencies was one of the considerations used to assign the external modes of adsorbed acetylene, in no case was this consideration in conflict with other observed characteristics of the appropriate INS bands, such as deuteration shifts or band intensities.[2,6] The frequency order of the external modes of adsorbed acetylene was ultimately obtained from the order of the analogous modes of the ethylene moiety in organometallic compounds such as $K[PtCl_3(C_2H_4)]$ and $[M(C_2H_4)_2Cl]_2$, where M=Rh or IR.[24-26]

In the Iwashita complex (Table 8.8), the three modes of lowest frequency corresponding to the external modes of adsorbed C_2H_2, are in the frequency order $\tau_z > t_A > t_B$.[20] Otherwise, the hindered translations and torsions of the C_2H_2 moiety in the Iwashita complex occur[20] in the same frequency order as they do the zeolite + acetylene samples (Table 8.8).

8.5.2 Barriers to rotation of adsorbed acetylene

In the non-linear, laterally bonded model of adsorbed acetylene (Figure 8.1), the τ_z mode corresponds to rotation of the admolecule about a C_2 axis and the τ_x and τ_y modes to rotations about C_1 axes.

TABLE 8.8 Band frequencies and barriers to rotation obtained from the INS spectra of C_2H_2 adsorbed by various zeolites and of the Iwashita complex, $CO_2(CO)_6C_2H_2$

mode	NiNaY + C_2H_2 high coverage this work, Fig.8.4a		$Ag_{12}A + C_2H_2$ ref. 2		AgX + C_2H_2 ref.6		$CO_2(CO)_6.C_2H_2$ ref.20	
	band frequency cm^{-1}	barrier height $kJ\ mol^{-1}$	band frequency cm^{-1}	barrier height $kJ\ mol^{-1}$	band frequency cm^{-1}	barrier height $kJ\ mol^{-1}$	band frequency cm^{-1}	barrier height $kJ\ mol^{-1}$
τ_x	-	-	382	6.5	523	12.1	797	728
τ_y	169	296±3	241	582	150	225	511	3006
t_z	131		174	-	86	-	432	-
t_A	110		130	-	-	-	111	-
τ_z	74	12.5±1.0	88	19	{54, 27}[a]	-	156	57
t_B	34		57	-	-	-	78	-

Notes -

a. Two bands were observed, assigned to the in-phase and out-of-phase torsions of coupled rotors [6].

The Howard model of the adsorbate was used to predict the barrier heights to rotation of C_2H_2 adsorbed in the various zeolites, the Iwashita model was used for the complex $CO_2(CO)_6.C_2H_2$.

t_A and t_B denote hindered translational modes of the acetylene admolecule. For a given sample, if $t_A=t_x$, then $t_B=t_y$, or *vice versa*. The frequency order of these two modes need not be the same for all four samples in this table.

Generally, the potential barrier, $V(\phi)$, of a hindered rotor in an n-fold potential well is given, in the first approximation,[38] by

$$V(\phi) = \frac{V_n}{2} (1-\cos n\phi) \qquad (8.4)$$

where ϕ is the angle of rotation and V_n is the barrier height. For barriers which are large compared to the spacing of rotational energy levels of the admolecule, the rotation about a given axis is confined to a torsional oscillation about the potential minima of the appropriate function $V(\phi)$. In the harmonic approximation, the force constant of such a torsion is given by $\frac{d^2V(\phi)}{d\phi^2}$, and from equation 8.4:

$$\varepsilon = \frac{n}{2\pi} \left(\frac{V_n}{2I_R} \right)^{\frac{1}{2}} \qquad (8.5)$$

where ε is the frequency of the torsion and I_R the appropriate moment of inertia. (Equation 8.5 does not hold if extra terms are included in equation 8.4. for the potential function $V(\phi)$).

In Table 8.8 are listed the barrier heights V_n calculated from equation 8.5 for the τ_z (n=2) and τ_x, τ_y (n = 1) modes of adsorbed C_2H_2 and for the Iwashita complex. To obtain the values of I_R (equation 8.5), the Howard model[6,28] of the C_2H_2 adsorbate was adopted for the zeolite + acetylene samples (Table 8.8). This model was chosen because it was the preferred model for NiNaY + acetylene (Section 8.4.3). For the $Co_2(CO)_6 \cdot C_2H_2$ complex, the geometry due to Iwashita[19] was used to calculate the I_R values (equation 8.5) for the C_2H_2 moiety.

In Table 8.8 (col.3), the listed value of the barrier height for each of the τ modes of C_2H_2 adsorbed by NiNaY was obtained from the average frequency of the appropriate band in the t.o.f. spectrum of NiNaY+C_2H_2 at high coverage (Figure 8.4).

The quoted errors in the values of the barrier height (Table 8.8, col.3) arose from the variation of the band frequency from the average.

No barrier height is listed in Table 8.8 for the τ_z mode of C_2H_2 adsorbed by AgX. The published INS spectra[6] of this sample show the τ_z band to be split into two components due to in-phase and out-of-phase torsions of coupled C_2H_2 rotors. The effective force constants for these torsions therefore contain a contribution from an adsorbate --- adsorbate interaction as well as from the adsorbate --- adsorbent interaction.

The order of barrier heights for a given mode of acetylene in the samples of Table 8.8, is

$$Iw >> AgX > Ag_{12}A \text{ for the } \tau_x \text{ mode,}$$
$$Iw >> Ag_{12}A > NiNaY > AgX \text{ for } \tau_y \text{ and}$$
$$Iw >> Ag_{12}A > NiNaY \text{ for } \tau_z,$$

where Iw denotes the Iwashita complex. The high barrier heights appertaining to the Iwashita complex (Table 8.8) are consistent with the strong interaction between the C_2H_2 moiety and the remainder of the molecule proposed by Iwashita *et al*[3], Nelson *et al*[32] and Blizzard *et al*.[33] According to these authors[31-33], each C atom forms a σ-bond to both Co atoms and the bonding is supplemented by back donation from filled d-orbitals of Co to antibonding π^* orbitals of the coordinated acetylene.

The barrier heights for acetylene adsorbed in the zeolites $Ag_{12}A$ and AgX are in the main greater than the corresponding barriers for the NiNaY adsorbent (Table 8.8). This suggests stronger π-bonding in the $Ag^+(d^{10})$-C_2H_2 sorption complexes

than the $Ni^{++}(d^8)$-C_2H_2 complex. The differences between the $Ag_{12}A$ and AgX adsorbents may be related to the different electric fields within the voids of the two zeolites and to the proposed[34-37] existence of clusters of Ag ions in dehydrated $Ag_{12}A$. The formation of clusters on the dehydration of $Ag_{12}A$ is not fully understood and various structures for these clusters have been suggested in the literature, *eg.* $(Ag^+)_8(Ag)_6$ [34-36] or linear Ag^+-Ag^o-Ag^+ ions.[37]

8.5.3 The INS intensities of the bands due to adsorbed acetylene

In Table 8.9 we list the reported INS band intensities, observed and predicted within various models, for the external modes of adsorbed acetylene. Data for AgX+acetylene are not available because of difficulties in determining the spectral baselines.[6] For each sample in Table 8.9, the observed and calculated relative intensity of the lowest frequency t mode of adsorbed acetylene has been set equal to 10, in arbitrary units. For acetylene adsorbed by NiNaY and $Ag_{12}A$, the predicted band intensities (Table 8.9) were obtained within the Howard model[6,28] of the adsorbate, and the Iwashita model[19] was used for $Co_2(CO)_6 \cdot C_2H_2$. For the NiNaY + acetylene samples, the predicted intensities (Table 8.9) were obtained *via* equation 8.1 and the observed intensities directly from curve fitting (Figures 8.4, 8.5). This is different from the published values listed in Table 8.9, for $Ag_{12}A + C_2H_2$ and the Iwashita complex.[2,20] For the latter two samples, the observed intensities have been "corrected for Q^2 and ν"[2,20] and the predicted intensities are independent of

TABLE 8.9 The observed and predicted band intensities in the INS spectra of acetylene adsorbed by various zeolites and the Iwashita complex, $CO_2(CO)_6.C_2H_2$

mode	NiNaY + C_2H_2 high coverage this work, Fig.8.4a		NiNaY + C_2D_2 this work Fig. 8.5a		$Ag_{12}A$ + C_2H_2 ref. 2		$CO_2(CO)_6.C_2H_2$ ref. 2.	
	observed	predicted	observed	predicted	observed	predicted	observed	predicted
τ_x	-	-	84.8	86.5	82.0	100.0	128.2	120.5
τ_y	62.5	55.6	43.5	58.8	12.1	41.9	18.5	36.5
t_z	11.9	15.0	18.3	18.8	10.6	10.0	12.8	10.0
t_A	14.4	11.1	22.6	22.9	12.2	10.0	10.0	10.0
τ_z	54.4	48.9	41.7	68.8	41.0[a]	41.6	37.4	27.2
t_B	10.0	10.0	10.0	10.0	10.0	10.0	10.0	10.0

Notes -

a. Average value obtained from t.o.f. spectra recorded at 3 different scattering angles.

The Howard model of the adsorbate was used to predict the INS band intensities of the zeolite + acetylene samples, the model due to Iwashita was used for the complex $CO_2(CO)_6.C_2H_2$. (6,19,28).

t_A and t_B denote hindered translational modes of the acetylene admolecule. For a given sample, if $t_A=t_x$, then $t_B=t_y$, or *vice versa*. The frequency order of these two modes need not be the same for all four samples in this table.

these two parameters. Thus a comparison, of either the observed or predicted INS band intensities, between the NiNaY + acetylene samples on the one hand and the remaining samples in Table 8.9 on the other hand, cannot be made. However, for a given sample (Table 8.9), there is good agreement between the observed and predicted INS intensities, except for the slight overestimate in the predicted values for the τ_y and τ_z modes of NiNaY + C_2D_2 and the large overestimate of the τ_y mode intensity for $Ag_{12}A$ + C_2H_2 and the Iwashita complex. A similar discrepancy between the observed and predicted INS band intensity of the τ_y mode of coordinated C_2H_4 in Zeise's salt has been reported.[24] We are unable to explain these discrepancies.

8.5.4 The deuteration shifts of the hindered translations and torsions of adsorbed acetylene

In Table 8.10 we list the deuteration shifts observed for the modes of adsorbed acetylene in the zeolites NiNaY, $Ag_{12}A$[2] and AgX[6] and for the Iwashita complex.[20]

The observed deuteration shifts for NiNaY + acetylene (Table 8.10) were obtained from the ratio of band frequencies in the NiNaY + C_2D_2 (θ=2.0) and NiNaY + C_2H_2 (θ=2.2) t.o.f. spectra (Figures 8.4, 8.5). In these t.o.f. spectra there is no systematic variation of the band frequency with scattering angle and thus the observed deuteration shifts (Table 8.10) were calculated by taking the average value of the quantities

$$\frac{\nu_D,\ \text{min}}{\nu_H,\ \text{max}} \quad \text{and} \quad \frac{\nu_D,\ \text{max}}{\nu_H,\ \text{min}},$$

where "min" refers to the lowest frequency of the band in the spectra at all three scattering

TABLE 8.10 The deuteration shifts of the bands in the INS spectra of acetylene adsorbed by various zeolites and of the Iwashita complex, $CO_2(CO)_6.C_2H_2$

mode	NiNaY + acetylene this work		$Ag_{12}A$+acetylene ref.2		AgX + acetylene ref.6		$CO_2(CO)_6.C_2H_2$ ref.20	
	observed	predicted	observed	predicted	observed	predicted	observed	predicted
τ_x	-	0.73	0.83	0.73	0.73	0.73	0.78	0.73
τ_y	0.88±0.02	0.85	0.82	0.85	0.75	0.85	0.88	0.89
t_z	0.88±0.02	0.96	0.99	0.96	-	0.96	0.99	0.96
t_A	0.89±0.04	0.96	-	0.96	-	0.96	-	0.96
τ_z	0.88±0.05	0.85	-	0.85	0.87[a]±0.02	0.85	-	0.91
t_B	0.74±0.06	0.96	-	0.96	-	0.96	-	0.96

Notes -

a. Average value of two bands due to in-phase and out-of-phase torsions of coupled rotors.

The deuteration shifts for NiNaY+ acetylene were obtained from Figs. 8.4 and 8.5.

The Howard model of the adsorbate was used to predict the deuteration shifts of the zeolite+acetylene samples, the model due to Iwashita was used for the complex $CO_2(CO)_6.C_2H_2$ (6,19,28).

t_A and t_B denote hindered translational modes of the acetylene admolecule. For a given sample, if $t_A=t_x$ then $t_B= t_y$, or *vice versa*. The frequency order of these two modes need not be the same for all four samples in this table.

angles of a given sample (Tables 8.4, 8.5) and "max" refers to the highest frequency. The tabulated errors in the observed deuteration shifts are the difference between the average value and ν_D, min/ν_H, max (Table 8.10).

Included in Table 8.10 are the deuteration shifts calculated within the harmonic approximation for adsorbed and coordinated acetylene. The calculations were carried out using the Howard model of the acetylene admolecule for the zeolite + acetylene samples of Table 8.10 and the Iwashita model was used for the $Co_2(CO)_6 \cdot C_2H_2$ complex.

There is only modest agreement between the observed and predicted deuteration shifts for the modes of all the samples in Table 8.10. The discrepancies between theory and experiment are probably due in a large part to slight errors in determining the frequencies of the observed INS bands; such errors have a serious effect since the predicted shifts are close to unity. This is reflected in the large difference between the observed and calculated deuteration shifts of the t_y mode of acetylene adsorbed by NiNaY (Table 8.10). In the t.o.f. spectra of NiNaY + acetylene (Figures 8.4, 8.5), the t_y band was poorly resolved from the τ_z band and of low intensity and was thus difficult to fit accurately.

Despite the modest agreement between the observed and calculated deuteration shifts (Table 8.10), some general comments can be made. It has been pointed out[6,20] that the observed deuteration shifts of the τ_x mode for the Iwashita complex and for AgX + acetylene are close to $2^{-\frac{1}{2}}$(=0.707) and that this implies that the C atoms of adsorbed acetylene undergo only a small displacement during the τ_x mode. It has been shown[6] that

the deuteration shift of the τ_x mode of adsorbed acetylene, calculated within both the Howard and Iwashita models of the adsorbate, is not a function of the C-$\hat{C}$-H bond angle provided that the angle is not 180^o and that the bond lengths of acetylene are assumed to be constant with the bond angle.

The deuteration shifts observed for the translational modes of acetylene adsorbed by $Ag_{12}A$ and AgX and for the Iwashita complex are greater than those observed for the τ modes of these samples, which is in accord with the predicted values (Table 8.10).

The observed deuteration shifts (Table 8.10) of the translational and torsional modes of acetylene adsorbed by NiNaY are equal within experimental error (excepting t_y, see above). For NiNaY + acetylene, there is no apparent trend in the variation between the observed and predicted deuteration shifts (Table 8.10) which cannot therefore be used to test our assignment scheme of the corresponding spectra (Figures 8.3 to 8.5).

8.6 Conclusions

Our INS spectra of acetylene adsorbed in NiNaY zeolite are consistent with lateral bonding of the adsorbate to the surface. The presence of an intense shoulder in the t.o.f. spectra of adsorbed C_2D_2 (Figures 8.5) indicates that the admoecules are not linear. This is similar to the published[2,6] INS results for acetylene adsorbed in $Ag_{12}A$ and AgX zeolites in which the admolecules are also non-linear and laterally bonded to the adsorbent.

Our spectra of adsorbed acetylene show no evidence that cyclotrimerisation and the formation of benzene occurred in our samples. Indeed, the formation of benzene was not expected to take place, given the conditions under which the acetylene was adsorbed and the temperatures at which the INS spectra were recorded.

APPENDIX 8.A Evaluation of the Debye-Waller factor of the modes of adsorbed acetylene

For each mode of C_2H_2 or C_2D_2 adsorbed in NiNaY, the Debye-Waller factor (DWF), exp(-2W) in equation 8.1 above, can be written:

$$\exp(-2W) = \exp(-Q^2\langle U^2(\tilde{\nu})\rangle) \qquad (8.6)$$

where $\langle U^2(\tilde{\nu})\rangle$ is the mean square displacement of the scattering nucleus, H or D, in the mode of frequency $\tilde{\nu}$. The value of $\langle U^2(\tilde{\nu})\rangle$ is obtained by plotting the observed intensity, I^P, of a given band as $\ln I^P$ against Q^2 for the spectra obtained at different scattering angles. A straight line of gradient $-\langle U^2(\tilde{\nu})\rangle$ will be obtained for a given band provided that the intensity arises solely from a fundamental mode (or degenerate fundamentals) and that there is no contribution from overtones or combinations. Plots of $\ln I^P$ against Q^2 obtained from the t.o.f. spectra of C_2H_2 (θ=1.2, Fig.8.3 and θ=2.2, Fig. 8.4) and C_2D_2 (θ=2.0, Fig. 8.5) adsorbed in NiNaY are shown in Figs. 8.9 to 8.11 in which the straight lines are least squares fits to the data points. The fitted lines are not good fits to the data and there is a systematic deviation from linearity which arises from the fact that the estimates, obtained from the curve

Fig. 8.9 Plot of ln I^P against Q^2 for the INS spectra of NiNa-Y zeolite plus C_2H_2, coverage 1.2 molecules per supercage, 10K (see figs. 8.3).

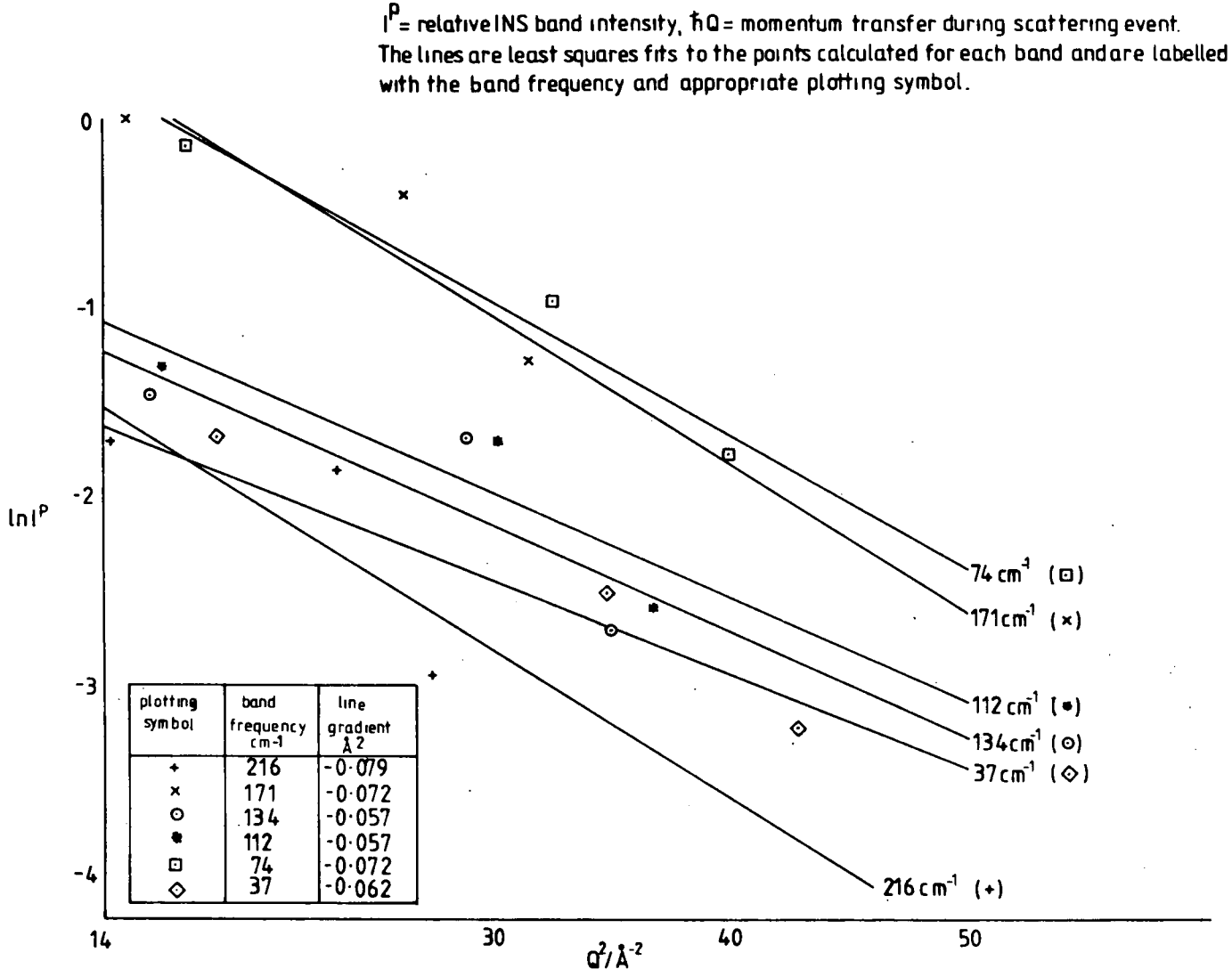

Fig. 8.10 Plot of ln I^P against Q^2 for the INS spectra of NiNa-Y zeolite plus C_2H_2, coverage 2.2 molecules per supercage, 10K (see figs. 8.4).

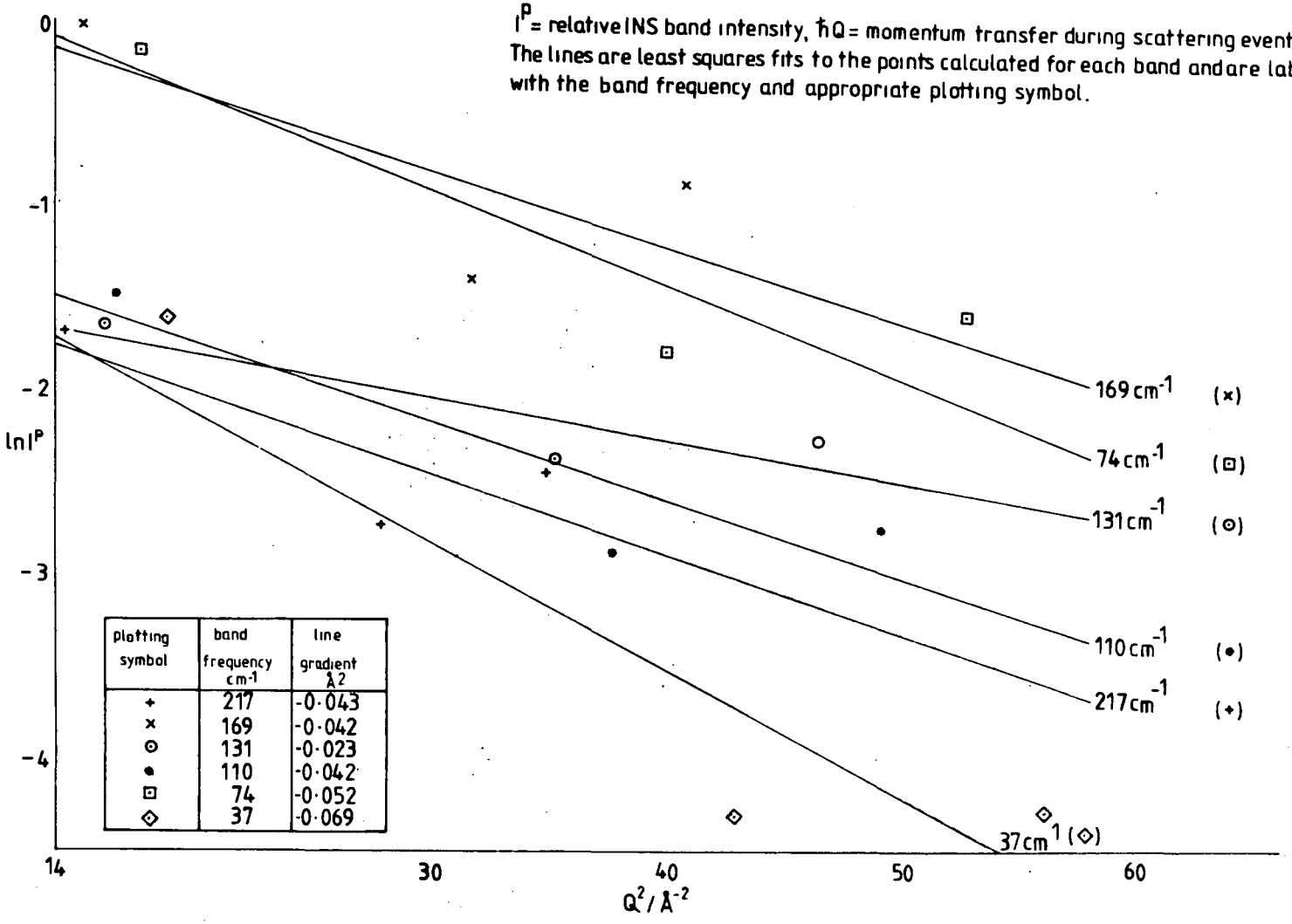

plotting symbol	band frequency cm^{-1}	line gradient Å^2
+	217	-0·043
×	169	-0·042
⊙	131	-0·023
•	110	-0·042
⊡	74	-0·052
◇	37	-0·069

Fig. 8.11 Plot of ln I^P against Q^2 for the INS spectra of NiNa-Y zeolite plus C_2D_2, coverage 2.0 molecules per supercage, 10K (see figs. 8.5).

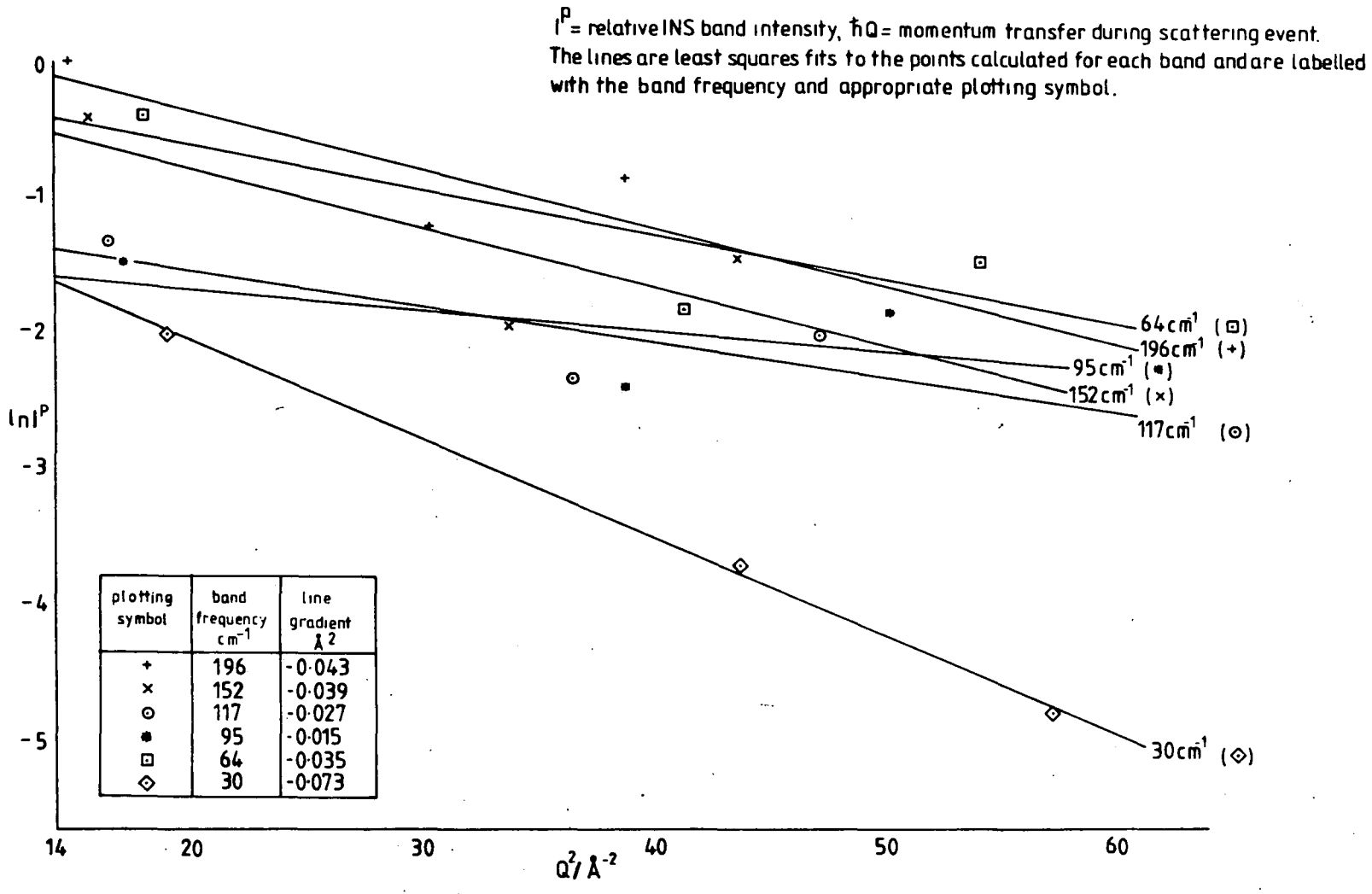

fitting procedure, of the observed band intensities in a given spectrum are correlated. The gradient of the least squares fits are listed in Figures 8.9 to 8.11 and the value of $-\langle U^2(\tilde{\nu})\rangle$ thus obtained for each mode of adsorbed acetylene was used to calculate the relative INS band intensity for a particular geometry of the admolecule *via* equations 8.1 to 8.3.

REFERENCES

1. Pichat, P., Vedrine, J.C., Gallezot, P. and Imelik, B., J.Catal., 32, 190, 1974.
2. Howard, J., Robson, K. and Waddington, T.C., Zeolites, 1, 175, 1981.
3. Yates, D.J.C. and Lucchesi, P.J., J.Chem.Phys., 35, 243, 1961.
4. Tam, N.T., Cooney, R.P. and Curthoys, G., J.Chem.Soc., Faraday Trans.I, 72, 2577, 1976.
5. Tam, N.T., Cooney, R.P. and Curthoys, G., J.Chem.Soc., Faraday Trans.I, 72, 2592, 1976.
6. Howard, J. and Waddington, T.C., Surface Sci., 68, 86, 1977.
7. Amaro, A.A. and Seff, K., J.Chem.Soc., Chem.Comm. 1972, 1201, 1972.
8. Amaro, A.A. and Seff, K., J.Phys.Chem., 77, 906, 1973.
9. Riley, P.E. and Seff, K., Inorg.Chem., 14, 714, 1975.
10. Riley, P.E. and Seff, K., J.Am.Chem.Soc., 95, 8180, 1973.
11. Gallezot, P. and Imelik, B., J.Phys.Chem., 77, 652, 1973.
12. Gallezot, P. and Imelik, B., J.Phys.Chem., 77, 2364, 1973.
13. Gallezot, P., Ben Taarit, Y. and Imelik, B., J.Phys.Chem., 77, 2556, 1973.
14. Willis, B.T.M.(Ed.), Chemical Applications of Thermal Neutron Scattering, Oxford University Press, 1973.
15. Bottger, G.L. and Eggars, D.F., J.Chem.Phys., 40, 2010, 1964.
16. Ito, M., Yokoyama, T. and Suzuki, M., Spect.Acta, 26A, 695, 1970.
17. Anderson, A. and Hayden-Smith, W., J.Chem.Phys., 44, 4216, 1966.

18. Schwartz, Y.A., Ron, A. and Kimel, S., J.Chem.Phys., 54, 99, 1971.

19. Iwashita, Y., Inorg.Chem., 9, 1178, 1970.

20. Howard, J., Robson, K. and Waddington, T.C.W., Chem.Phys., 61, 53, 1981.

21. Howard, J., Waddington, T.C. and Wright, C.J., J.Chem.Soc., Chem.Comm., 1975, 775, 1975.

22. Howard, J., Waddington, T.C. and Wright, C.J., J.Chem.Soc., Faraday Trans.II, 73, 1768, 1977.

23. Howard, J., Robson, K., Waddington, T.C. and Kadir, Z.A., Zeolites, 2, 2, 1982.

24. Ghosh, R.E., Waddington, T.C. and Wright, C.J., J.Chem.Soc., Faraday Trans.II, 69, 275, 1973.

25. Howard, J., Waddington, T.C. and Wright, C.J., J.Chem.Soc., Faraday Trans.II, 72, 513, 1976.

26. Howard, J. and Waddington, T.C., J.Chem.Soc., Faraday Trans.II, 74, 1275, 1978.

27. Sugawara, I.T. and Kanda, E., Sci.Rep.Res.Inst., Tokoku Univ., p.607, 1952.

28. Howard, J., Ph.D. Thesis, University of Durham, 1976.

29. Robson, K., Ph.D. Thesis, University of Durham, 1980.

30. Graham,D., Ph.D. Thesis, University of Durham, 1980.

31. Iwashita, Y., Tamura, F. and Nakamura, A., Inorg.Chem., 8, 1179, 1969.

32. Nelson, J.H. and Jonassen, H.B., Coord.Chem.Rev., 6, 27, 1971.

33. Blizzard, A.C. and Santry, D.P., J.Am.Chem.Soc., 90, 5749, 1968

34. Kim, Y. and Seff, K., J.Am.Chem.Soc., 99, 7055, 1977.

35. Kim, Y. and Seff, K., J.Am.Chem.Soc., 100, 6989, 1978.

36. Kim, Y. and Seff, K., J.Phys.Chem., 82, 921, 1978.

37. Gellens, L.R., Mortier, W.J. and Vytterhoeven, J.B., Zeolites, 1, 11, 1981.

38. Lin, C.C. and Swalen, J.D., Rev.Mod.Phys.31, 841, 1959.

CHAPTER NINE

AN INS STUDY OF WATER ADSORBED BY CALCIUM EXCHANGED TYPE-A ZEOLITE ($Ca_6Al_{12}Si_{12}O_{48}$)

9.1 Introduction

In this chapter we present the INS spectra (*ca* 20 to 850 cm^{-1}) of H_2O adsorbed in $Ca_6Al_{12}Si_{12}O_{48}$ A-type zeolite. Our reasons for undertaking this work were two-fold. Firstly, it is known that the cation positions and sorption properties of A-type zeolites are strongly influenced by the presence of adsorbed water.[1,2] Since A-type zeolites are used industrially as separation agents for gaseous mixtures and for the removal of H_2O and H_2S from natural gas,[3,4] an understanding of the nature of H_2O adsorbed in these zeolites is important. Secondly, the calcium zeolite/adsorbed H_2O system is one of the few for which the far IR spectrum has been published.[5] Bands due to some of the modes of adsorbed water relative to the zeolite surface were reported in the far IR spectrum[5] but these IR bands were of extremely low intensity (Section 9.7). Bearing in mind the different selection rules and intensities for bands in IR and INS spectra, we obtained the INS spectra of H_2O adsorbed in calcium zeolite-A in order to identify the low frequency modes of the adsorbate which were not observed by IR spectroscopy.[5]

9.2 Experimental

The zeolite samples were Linde 5A zeolite (supplied by B.D.H.), the composition being $Ca_6Al_{12}Si_{12}O_{48}$ according to the manufacturers. Hereafter we will refer to this zeolite as Ca_6A and will use the symbol θ to denote the quantity, in molecules per pseudo unit cell, of adsorbed H_2O. The vacuum dehydration of the zeolite and subsequent adsorption of H_2O

were carried out using the techniques described in Chapter Four. Some experimental details are listed in Table 9.1.

TABLE 9.1 Summary of experimental details for the INS spectra of H_2O adsorbed by $Ca_6Al_{12}Si_{12}O_{48}$ zeolite

Spectrometer	IN4	DIDO b.f.d.	
temperature of INS run/K	10	77	77
coverage θ/molecules H_2O per pseudo unit cell	2.5	3.9	5.9
% scattering from adsorbed H_2O	11[a]	26[a]	49[a]
(σ_{inc} adsorbed H_2O/ σ_{inc} zeolite)	53[a]	104[a]	157[a]

Note - a. These data were calculated using neutron scattering cross-sections[26] applicable to an incident neutron energy of 204 cm^{-1}.

The t.o.f. spectra shown in this chapter were recorded on the IN4 spectrometer at the I.L.L., Grenoble, using an incident neutron energy of 251 cm^{-1}. Subtraction of flat baselines followed by the grouping of the data into equal energy bins of 4 cm^{-1} has been carried out for all the t.o.f. spectra, using the computer programs described in Chapter Six.

The b.f.d. spectra presented in this chapter were obtained on the DIDO b.f.d. spectrometer at A.E.R.E., Harwell.

9.3 The X-ray structure of CaA zeolite

The positions of Ca^{++} cations in Ca_6A zeolite depend upon the degree of hydration of the zeolite. The X-ray crystal structure of the fully hydrated zeolite has been published by Thoni[6] and that of the fully dehydrated zeolite of Seff *et al*[7] and by Pluth *et al*.[8] Mortier *et al*[3] have used X-ray powder diffraction to study the structure at different states of hydration. The locations and populations of the Ca^{++} and H_2O sites obtained by various groups of workers[3,6-8] are listed in Table 9.2. Mortier *et al*[3] found that the populations in their Ca_6A samples of the Ca^{++} and H_2O sites as estimated by X-ray diffraction showed slight discrepancies with the Ca^{++} and H_2O contents as determined by elemental and thermogravimetric analyses, and with the corresponding single crystal results of Thoni.[6] The discrepancies arose from the difficulty in locating a multiplicity of crystallographic sites with low population factors by X-ray powder methods.[3]

In fully dehydrated $Ca_6Al_{12}Si_{12}O_{48}$ (Table 9.2, col.6), Seff *et al*[7] located a total of five Ca^{++} ions per pseudo unit cell at S2', S3 and S2* sites, each Ca^{++} ion being associated with three O(3) atoms of the adjacent 6-oxygen ring. The sixth Ca^{++} ion per pseudo unit cell was assigned by Seff *et al*[7] to an off-centre position in the plane of the 8-oxygen ring. This ion was said to be easily displaced from the 8-oxygen ring site by adsorbed molecules.[7] However, Pluth *et al*[8] have argued that the electron density attributed by Seff *et al*[7] to a Ca^{++} ion near the centre of the 8-oxygen ring is in fact due to an impurity. From their results of an X-ray study of

TABLE 9.2 The published site occupations of Ca^{++} ions and H_2O molecules in $Ca_6Al_{12}Si_{12}O_{48}$ zeolite, obtained by X-ray diffraction

Author		Thoni[6]	Mortier *et al*[3]			Seff *et al*[7]	Pluth *et al*[8]
Nature of zeolite sample		single crystal	powder			single crystal	single crystal
Extent of hydration of zeolite		fully hydrated	fully hydrated	partially hydrated	partially hydrated	fully dehydrated	fully dehydrated
Dehydration temp.,K		-	-	353	423	623[b]	
Species	site[d]	site occupancy per pseudo-unit cell					
Ca^{++}	SU				0.64		
	8-O ring[e]					1.0	
	S2′					1.0	*ca*.1
	S2	3.0	3.76	7.04	6.08	1.0	
	S2*	3.0	2.32			3.0	*ca*.4
H_2O	S1	1.0					
	S2′		3.04				
	S2*,A	10.56		5.68			
	S2*,B	4.24 & 2.40					
	S3	0.38		3.54			
	delocalised	12.18	26.38	7.63	7.10		
Total no. Ca^{++} located		6.0	6.08	7.04	6.72	6.0	*ca*.5
Total no. H_2O located		30.00	30.32	16.85	7.10		

Notes: (a) Sample composition $Na_{0.5}Ca_{5.2}Al_{11.5}Si_{12.5}O_{48}$. (b) Dehydrated *in vacuo* at 623K to 5.0×10^{-6} torr

(c) Dehydrated *in vacuo* at 623K and 1.0×10^{-5} torr for 1 day. (d) Zeolite nomenclature due to Barrer, ref.9. (e) Cation located in the plane of an 8-oxygen ring but displaced from the centre of the ring.

S2*,A denotes H_2O molecules in the supercage coordinated to Ca^{++} ions at either S2* or S2 sites.

S2*,B denotes H_2O at either of two sites deep in the supercage and not coordinated to Ca^{++} ions.

crystals of fully dehydrated $Na_{0.5}Ca_{5.2}Al_{11.12}Si_{12.5}O_{48}$, Pluth *et al*[8] have assigned all the Ca^{++} ions to 6-oxygen ring sites, approximately $^4/_5$ of the Ca^{++} ion population to S2* and $^1/_5$ to S2´ (Table 9.2, col. 7).

In the fully hydrated zeolites (Table 9.2, col. 2,3), the Ca^{++} ions at S2 and S2* sites remain bonded to the three O(3) atoms of the 6-oxygen rings but the cations at S2* increase their coordination number to 6 by association with three H_2O molecules located in the supercage ($Ca\text{-}OH_2$=2.45Å).[3,6] The Ca^{++} ions at S2 sites achieve a 4-fold coordination by bonding to one H_2O molecule situated in the sodalite cavity ($Ca\text{-}OH_2$=2.44Å).[3,6] In the single crystal result of Thoni[6] (Table 9.2, col.2), the H_2O molecules situated at S3 sites (adjacent to 4-oxygen rings in the supercage) are H-bonded to the zeolite framework while the delocalised H_2O molecules correspond to an intrazeolitic liquid-like phase. In the results of Mortier for partially dehydrated Ca_6A zeolite (Table 9.2, cols.4,5) the apparently delocalised H_2O molecules were considered to be bonded to either Ca^{++} ions or to the framework, both of these types of site being occupied by H_2O in numbers too small to be precisely located by X-ray powder methods, and the concentration of intrazeolitic water present in a liquid-like phase was held to be negligible.[3]

On partially dehydrating Ca_6A to 423K such that the pseudo-unit cell contains 7.10 molecules of H_2O (Table 9.2, col.5), the powder diffraction results show that Ca^{++} ions become located at the centre of the sodalite cage (SU sites) and that the S2* sites are vacated by the Ca^{++} ions, principally in favour of the S2 sites.[3] Although none of the 7.10 H_2O mole-

cules (Table 9.2, col.5) could be located, Mortier *et al*[3] considered that the Ca^{++} ions at S2 sites were probably each coordinated by one H_2O molecule. The degree of hydration of the Ca^{++} ions at the SU sites remained uncertain but the authors[3] pointed out that the SU cations must be hydrated to some extent in order to be stable at that position.

Our INS samples of $Ca_6A + H_2O$ were prepared by fully dehydrating the zeolite and then adsorbing H_2O (Section 9.2). The partially hydrated samples of Ca_6A used by Mortier *et al*[3] in their X-ray work were prepared by partial dehydration of fully hydrated zeolites. We assume that these two routes to partially hydrated Ca_6A give the same result in terms of the locations and site occupancies of cations and H_2O molecules. Thus, from the X-ray results of Mortier *et al*[3] (Table 9.2), the positions which are most likely to have been occupied by the Ca^{++} ions in our INS samples are those associated with the 6-oxygen rings and, possibly, the SU sites.

9.4 Published n.m.r. studies of water adsorbed by Ca_6A zeolite

Published n.m.r. data[10,11] and a thermal desorption study[12] of H_2O adsorbed by Ca_6A zeolite showed that, in common with most zeolites,[1] there were three main types of intra-zeolitic water. By the adsorption of successive doses of H_2O in initially dehydrated Ca_6A, these types of adsorbed H_2O were shown by n.m.r.[11] to be:

a. H_2O molecules of low mobility, associated with Ca^{++} ions held at particular lattice sites;

b. H_2O molecules of intermediate mobility, hydrogen bonded to anionic regions of the alumino silicate framework both in the α and β cavities;[12]

c. H_2O molecules of high mobility, exhibiting the same n.m.r. relaxation times as liquid water and not occupying definite lattice sites.

We refer to the above three types of intrazeolitic water as types a, b and c respectively. At low coverages of H_2O, only the type a was present, type b and later type c becoming evident on increasing the coverage.

In zeolites NaA and NaX at 77K, the type c water exhibited n.m.r. signals characteristic of ice.[1,13]

9.5 The published low frequency vibrational data of adsorbed H_2O

Our INS data of $Ca_6A + H_2O$ (Section 9.6) extend from *ca* 20 to 850 cm^{-1} and were obtained for a maximum coverage of *ca* one H_2O molecule per Ca^{++} ion. For these coverages, the adsorbed water will be predominantly bonded to the Ca^{++} ions (Sections 9.3, 9.4) and the modes of the Ca-OH_2 complex which are expected to occur in the above frequency range are the six hindered translations and rotations of the OH_2 moiety with respect to the zeolite surface. These modes are drawn in Figure 9.1.

In crystals of hydrated salts of metals, *eg.* $[Ca(OH_2)_6]Cl_2$ or in the aqueous solution of those salts, H_2O may be coordinated *via* the O atom to the metal cation. Such coordinated H_2O molecules undergo three librational and three hindered trans-

Fig. 9.1 The hindered translations and hindered rotations of H_2O adsorbed in Ca_6-A zeolite.

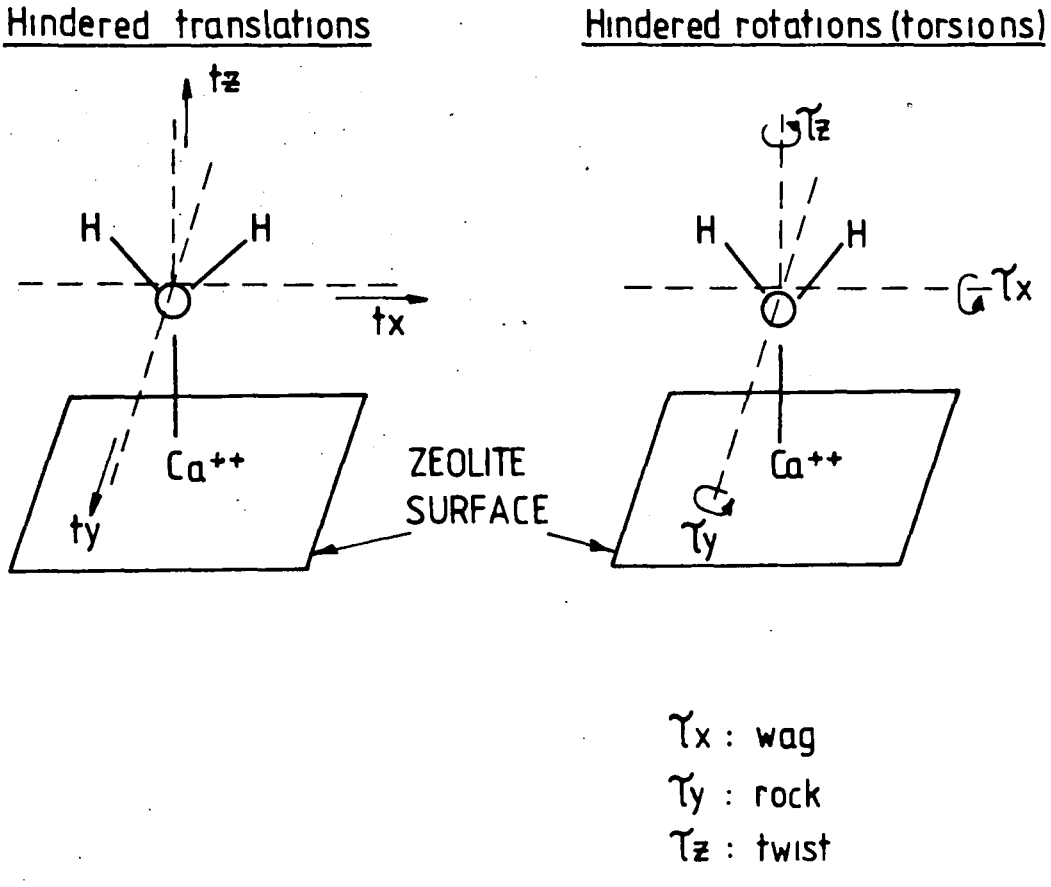

lational modes which are analogous to those of H_2O bonded to Ca^{++} ions in Ca_6A zeolite (Figure 9.1). There is general agreement in the literature[14-21] that the three librations of H_2O in crystals and solutions of the aqua complexes of monovalent and divalent metal cations occur in the range 350-900 cm^{-1} and the t_z mode at 300-450 cm^{-1}. Bands due to the t_x and t_y modes of the H_2O ligands have not been identified but are expected to occur below 200 cm^{-1}.[15,16]

There has been some debate in the literature over the frequency order of the librational modes of coordinated water.[14-16] The subject has been reviewed by Adams *et al*[15,16] who found that for monoaqua, diaqua and hexaqua complexes of divalent and trivalent metal cations, the frequency order was

$$\tau_x > \tau_z > \tau_y \ (>t_z).$$

The frequency order was obtained by considering the dependence of the frequency of each mode on the charge/radius ratios of the cation and anion, and from single crystal Raman and IR reflectivity studies.[15,16] As an example, in published INS[18] (293K) and IR[19] spectra of $[Ca(OH_2)_6]Cl_2$, bands observed at 719, 656 and 480 cm^{-1} were ascribed[18,19] to the librational modes of H_2O. The 719 cm^{-1} band was specified[18,19] as τ_y; the two remaining librational bands were not further assigned. However, the assignment[18,19] τ_y=719 cm^{-1} was based on arguments shown more recently to be incorrect by Adams,[15,16] and on the basis of the frequency order of the librational modes of coordinated water published by Adams,[15,16] we reassign the 719, 656 and 480 cm^{-1} bands to τ_x, τ_z and τ_y respectively. The remaining bands in the INS spectrum of $[Ca(OH_2)_6]Cl_2$ were assigned[18] to the t_z mode of the coordinated H_2O (380 cm^{-1}) and, at lower

frequencies, to vibrations of OH···Cl hydrogen bonds and to lattice modes.

Rush *et al*[21] have published INS spectra of crystals of polyaqua complexes of transition metal ions, *eg* $[Co(OH_2)_6](NO_3)_2$. If the H_2O ligands are strongly coordinated to the transition metal ion M, INS bands due to H_2O-M-OH_2 deformation modes arise at *ca* 150 cm^{-1}, and hydrogen bonded species (OH···X, where X is an anion or the O atom of another H_2O molecule) exhibit stretching and bending modes at *ca* 250-150 cm^{-1} and *ca* 50 cm^{-1}, respectively.

Fuess *et al*[22] have published the INS spectrum of H_2O adsorbed in the zeolite natrolite, $Na_2Al_2Si_3O_{10}$. Two H_2O molecules and two Na^+ ions were located in each zeolite cavity. Each H_2O molecule was H-bonded to the framework and coordinated to both Na^+ ions, forming a tetrahedral configuration around the O atom. INS bands at 702 cm^{-1} (s) and 548 cm^{-1} (vs) were assigned to the rocking (τ_y) and wagging (τ_x) modes respectively of H_2O in natrolite and bands at 202 (w), 145 (m) and 105 (w) cm^{-1} were ascribed to the hindered translational modes.[22] The τ_z mode of adsorbed H_2O was not assigned. No reasons were given[22] for the respective assignments of the τ_x and τ_y modes, which are in the reverse frequency order to that obtained by Adams *et al*[15,16] for aqua complexes. This disparity may arise from the difference in the coordination environment of H_2O in natrolite and that commonly found for aqua complexes.

In an early INS study, Egelstaff *et al*[23] observed modes due to H_2O adsorbed in K-3A zeolite at 480, 200, 100 and 71 cm^{-1} for a scattering angle of 20°. High coverages of H_2O, ≥21 molecules per pseudo unit cell, were used. Although the INS

bands were not assigned by the authors,[23] they did point out the existence of a torsional mode of liquid H_2O close in frequency to the 480 cm^{-1} band. We note that the remaining bands have three likely origins: 1. hindered translational modes of H_2O; 2. vibrations of hydrogen bonded linkages between H_2O molecules or between H_2O and the zeolite framework, and 3. interactions between the admolecules and zeolite lattice modes.

Water adsorbed in each of the zeolites analcime, chabazite[24] and lanthanum exchanged zeolite-Y[25] executes a torsional mode in the frequency range 460 to 600 cm^{-1}, according to published INS studies.

Möller *et al*.[5] have published the far IR spectrum of H_2O adsorbed in CaNaA zeolite which we will discuss in Section 9.7 after assigning our INS spectra of $Ca_6A + H_2O$ in Section 9.6.

9.6 Results - the INS spectra of H_2O adsorbed by Ca_6A zeolite

The t.o.f. spectra obtained at 10K of dehydrated Ca_6A zeolite and of H_2O adsorbed on Ca_6A at a coverage of θ=2.5 molecules per pseudo-unit cell are shown in Figures 9.2 and 9.3 in terms of $S(Q,\omega)$. Flat baselines have been subtracted from both curves in Figures 9.2 and 9.3; no further subtraction was made from the dehydrated Ca_6A data. The data presented for $Ca_6A + H_2O$ (Figures 9.2, 9.3) are difference spectra, the spectrum of the dehydrated zeolite having been subtracted. Figures 9.2 and 9.3 represent the sum of the data recorded for 13 neutron detectors, covering an angular range of 47.2 degrees in the case of Figure 9.2 and 38.2 degrees for Figure 9.3.

Fig. 9.2 T.o.f. spectrum (10K) of a)dehydrated Ca_6A zeolite (plotting symbol +), and b) Ca_6A plus adsorbed H_2O, coverage 2.5 molecules per pseudo-unit cell, (plotting symbol x) with the spectrum of the dehydrated zeolite subtracted. The scattering angle was $79{\cdot}5^{o}$.

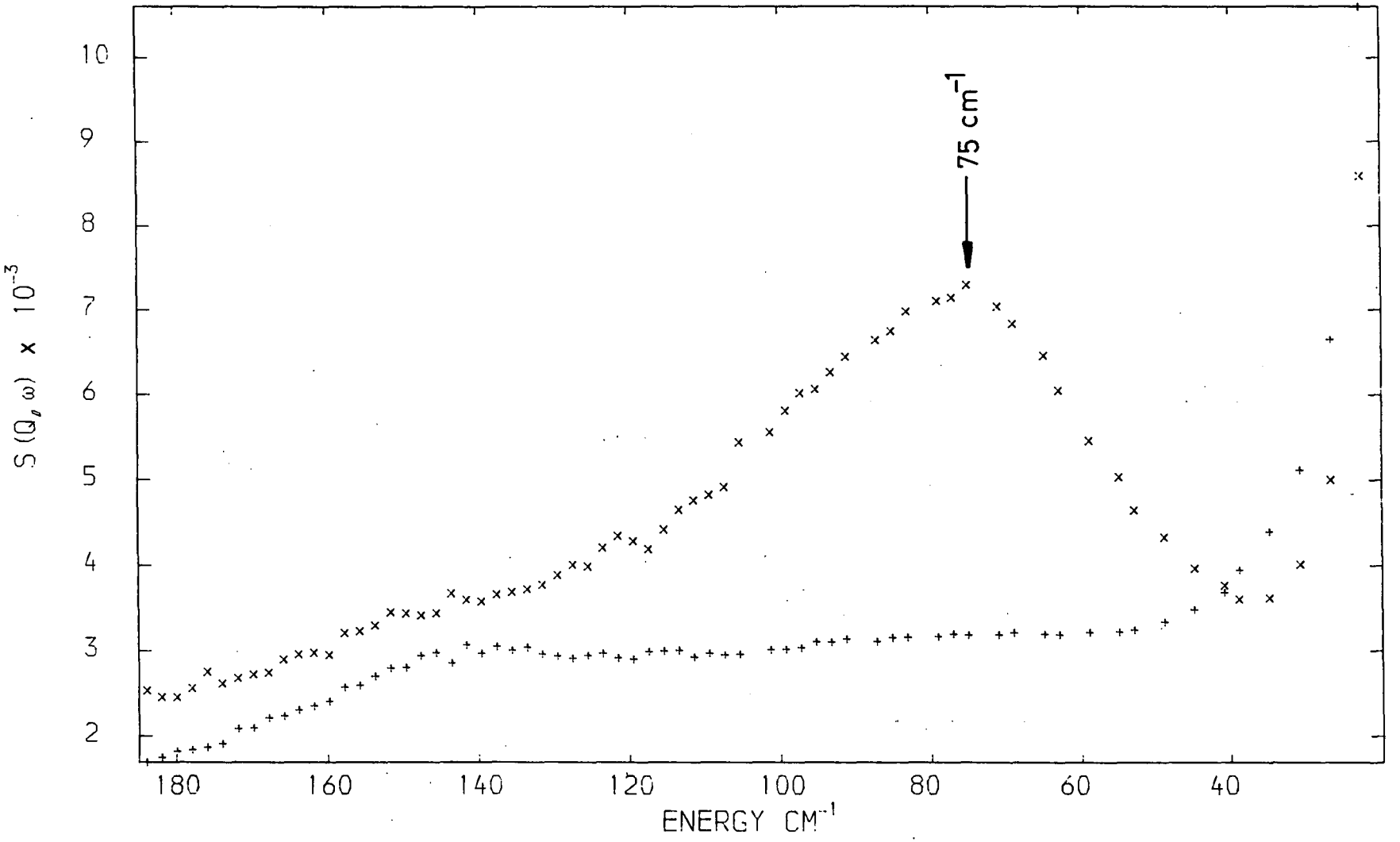

Fig. 9.3 T.o.f. spectrum (10K) of a) dehydrated Ca_6A zeolite (plotting symbol +), and b) Ca_6A plus adsorbed H_2O, coverage 2.5 molecules per pseudo-unit cell, (plotting symbol x) with the spectrum of the dehydrated zeolite subtracted. The scattering angle was 118·6°.

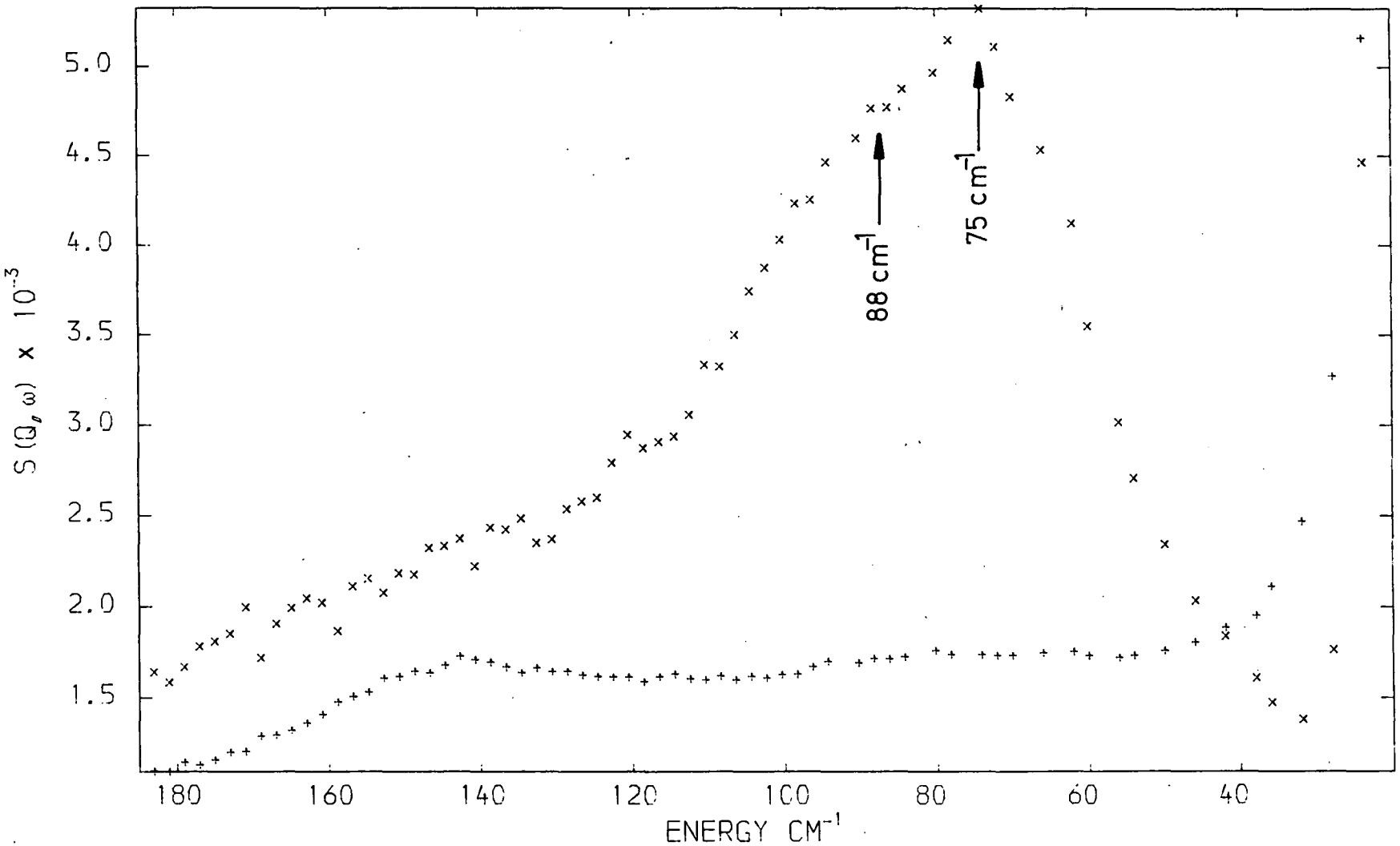

The angles referred to in the headings are average scattering angles. The detectors were summed to improve the modest statistics of the data, but the momentum-transfer resolution is lost by this summation. Because of this loss of momentum-transfer resolution, no curve fitting or band intensity calculations have been carried out for the t.o.f. spectra. We have presented the t.o.f. spectra in terms of $S(Q,\omega)$ rather than the more usual $P(\alpha,\beta)$ because in these particular results (Figures 9.2, 9.3), the INS features are more clearly observed in the $S(Q,\omega)$ data.

Below *ca* 40 cm^{-1} the intensity of the dehydrated Ca_6A spectrum in Figures 9.2, 9.3, is greater than that of the $Ca_6A + H_2O$ difference spectrum. This is due to problems with the subtraction technique used to obtain the $Ca_6A + H_2O$ difference spectra. As the energy transfer approaches zero, the energy range corresponding to a given time-of-flight channel becomes increasingly wide. Also, the scattering intensity in general increases markedly as the elastic peak is approached. Thus at low energy transfers, the number of t-o-f channels is reduced and these channels contain high numbers of counts compared to those at greater energy transfers. Thus calculation of the difference spectra for $Ca_6A + H_2O$ in Figures 9.2, 9.3 is subject to considerable error below 40 cm^{-1} because of the subtraction of large numbers of similar magnitude.

The t.o.f. spectra of dehydrated Ca_6A (Figures 9.2, 9.3) show weak features at 140-145 cm^{-1}. The only nucleus with a non-zero incoherent neutron scattering cross-section, σ_{inc}, in dehydrated Ca_6A zeolite is Ca, for which σ_{inc} = 0.5 barns.[26] Although this is a low value of σ_{inc}, we expect to be able to

observe bands due to modes displacing Ca^{++} ions in dehydrated Ca_6A because spectra recorded on the IN4 spectrometer contain very small contributions from extraneous background radiation. We assign the 140-145 cm^{-1} feature in the spectra of dehydrated Ca_6A zeolite (Figures 9.2, 9.3) to the stretching mode with respect to the zeolite framework of Ca^{++} ions at various sites, principally those associated with the 6-oxygen rings (Section 9.3). This assignment is consistent with the work of Angell *et al*[27] and Zhanadov *et al*[28] who have ascribed bands in the range 300 to 60 cm^{-1} in the IR spectra of dehydrated zeolites to the stretching modes of the cations with respect to the zeolite framework. In addition, Dyrkheev *et al*[29] have assigned bands at 135 and 157 cm^{-1} in the IR spectrum of dehydrated CaNaX zeolite ($0.66CaO:0.31Na_2O:1.0Al_2O_3:2.56Na_2O$) to vibrations of the Ca^{++} ions with respect to the zeolite skeleton.

The t.o.f. spectra of $Ca_6A + H_2O$ at 10K (Figures 9.2, 9.3) show an intense, broad band with a maximum at 75 cm^{-1} and which exhibits partially resolved structure up to 120 cm^{-1}. In the spectrum recorded at a scattering angle of 118.6° (Figure 9.3), the 75 cm^{-1} band shows a shoulder at 88 cm^{-1}. On the basis of its low frequency, we assign the 75 cm^{-1} band in the Ca_6A+H_2O spectra (Figures 9.2, 9.3) to the t_x and t_y modes of H_2O adsorbed by Ca^{++} ions. The t_x and t_y modes are degenerate for an H_2O molecule O-bonded to a Ca^{++} cation at a site such as SU, S2 or S2*, these sites being considered to be the most probable cation locations in our $Ca_6A + H_2O$ samples (Section 9.3). Thus the width and partially resolved structure of the 75 cm^{-1} band in the $Ca_6A + H_2O$ spectra (Figures 9.2, 9.3) indicate that the Ca^{++}-OH_2 sorption complexes are formed at more than one cation site.

Above 120 cm^{-1}, the $Ca_6A + H_2O$ t.o.f. spectra (Figures 9.2, 9.3) show no resolved bands but there is an overall increase in scattering intensity compared to the spectra of the dehydrated zeolite. The stretching modes of cations with respect to the zeolite framework are in general found to shift to lower frequencies when the cation becomes complexed to an admolecule.[27,28] Thus the increase in intensity in the 145-120 cm^{-1} in our t.o.f. spectra of Ca_6A on the adsorption of water (Figures 9.2, 9.3) is ascribed to the stretching modes with respect to the zeolite framework of $Ca^{++}OH_2$ species at various sites. This region of the $Ca_6A + H_2O$ spectra (Figures 9.2, 9.3) will also contain some intensity from the first overtone of the t_x and t_y modes of adsorbed H_2O (fundamentals at 75 cm^{-1}).

The b.f.d. spectrum at 77K of dehydrated Ca_6A zeolite shows considerable structure (Figure 9.4). It is our experience that spectra recorded on the DIDO b.f.d. spectrometer suffer from high and apparently structured backgrounds, due to imperfect shielding and the location of the spectrometer in a reactor shell where the level of background radiation is neither negligible nor constant. In addition, because dehydrated Ca_6A zeolite has a small incoherent neutron scattering cross-section (see above) and because no background has been subtracted from the spectrum, the features in Figure 9.4 are ascribed to variations in the spectrometer background.

The b.f.d. spectra (77K) of H_2O adsorbed by Ca_6A zeolite are shown in Figures 9.5 and 9.6 for coverages of 3.9 and 5.9 molecules per pseudo unit-cell respectively. These are difference spectra, the spectrum of the dehydrated zeolite, *i.e.*

Fig. 9.4 Beryllium filter detector (DIDO b.f.d.) spectrum (77K) of dehydrated Ca_6A zeolite, with no background subtracted.

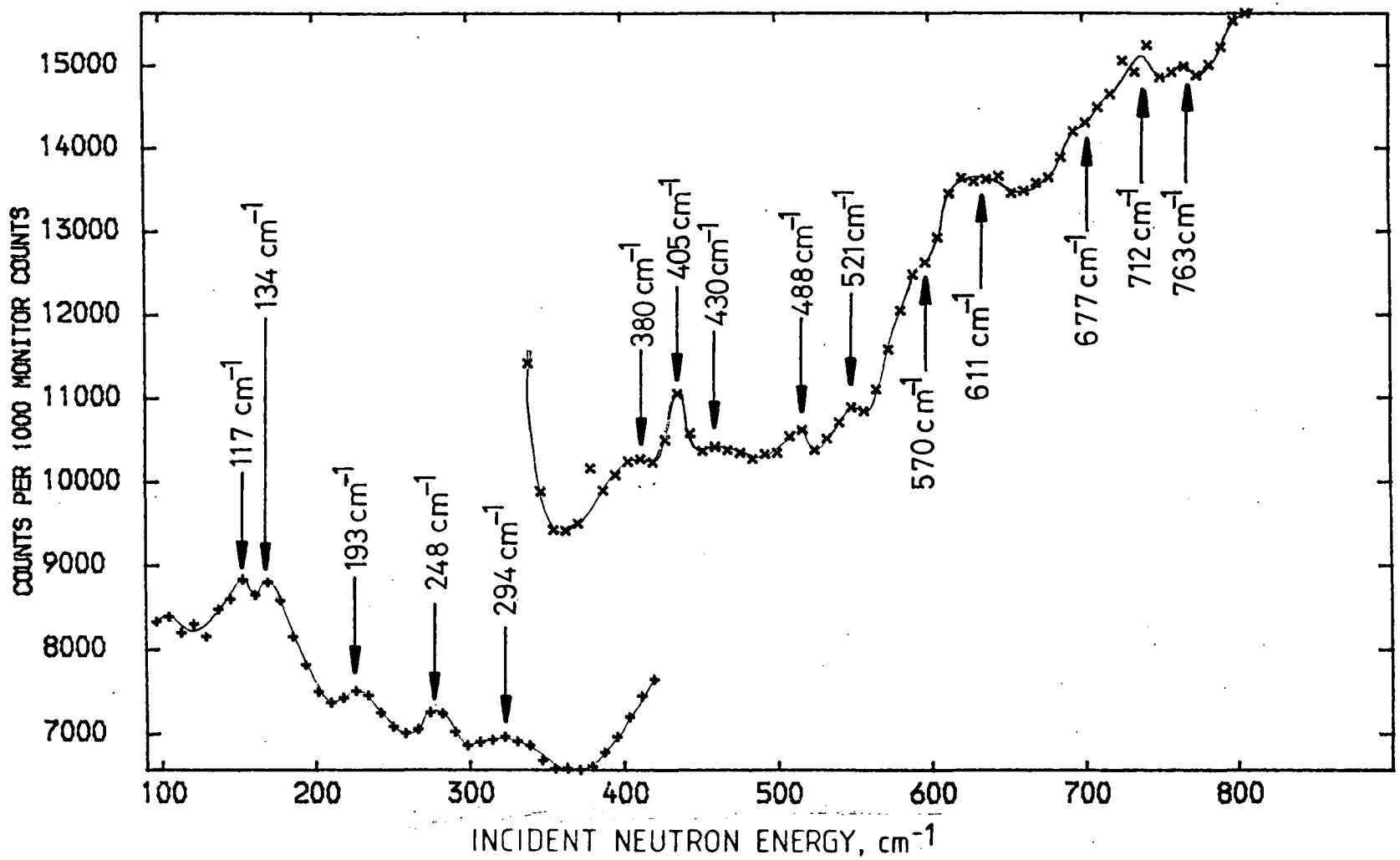

Fig. 9.5 Beryllium filter detector (DIDO b.f.d.) spectrum (77K) of Ca_6A zeolite plus adsorbed H_2O, coverage 3·9 molecules per pseudo-unit cell. A background spectrum of the dehydrated zeolite has been subtracted.

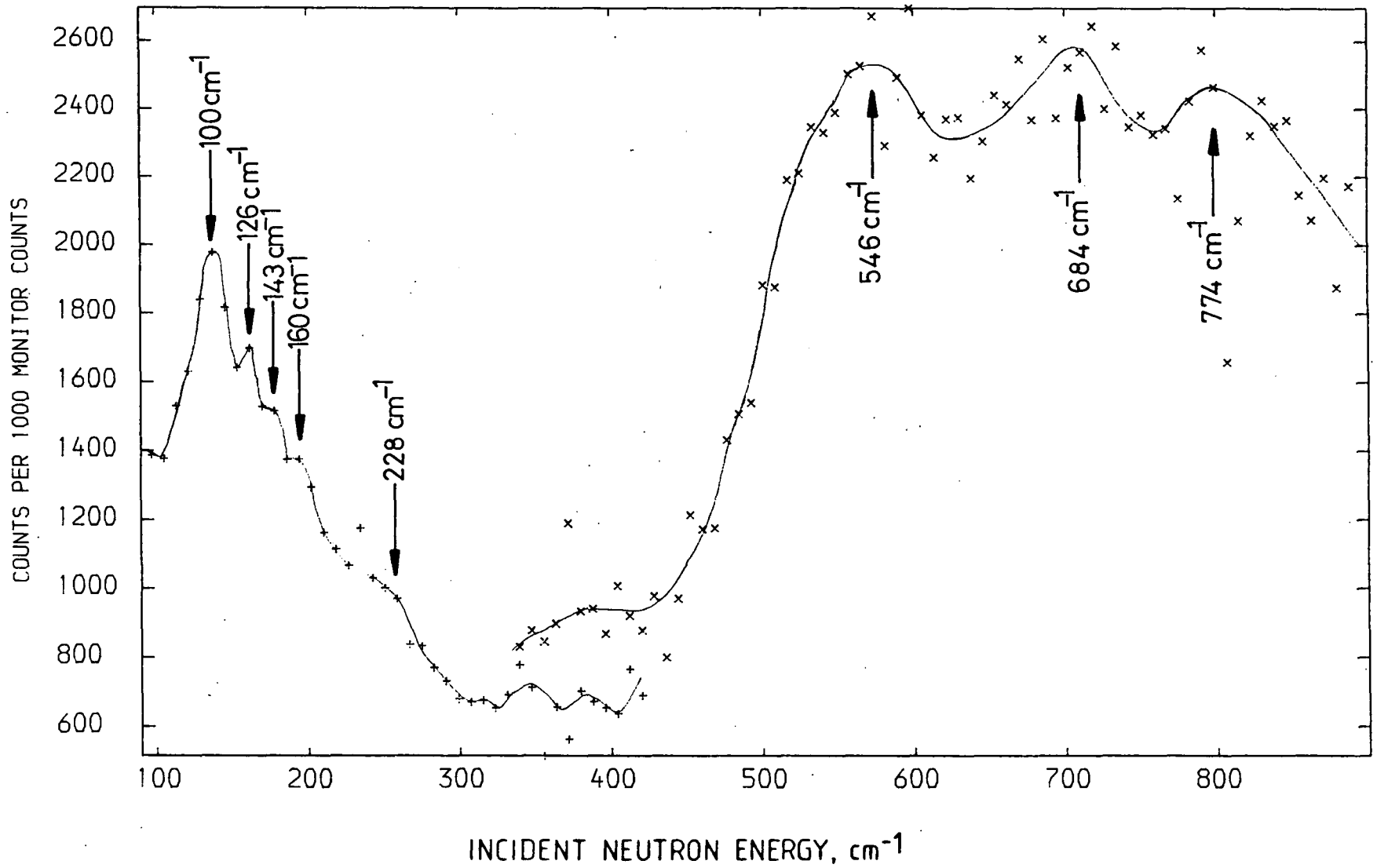

Fig. 9·6 Beryllium filter detector (DIDO b.f.d.) spectrum (77K) of Ca_6A zeolite plus adsorbed H_2O, coverage 5·9 molecules per pseudo-unit cell. A background spectrum of the dehydrated zeolite has been subtracted.

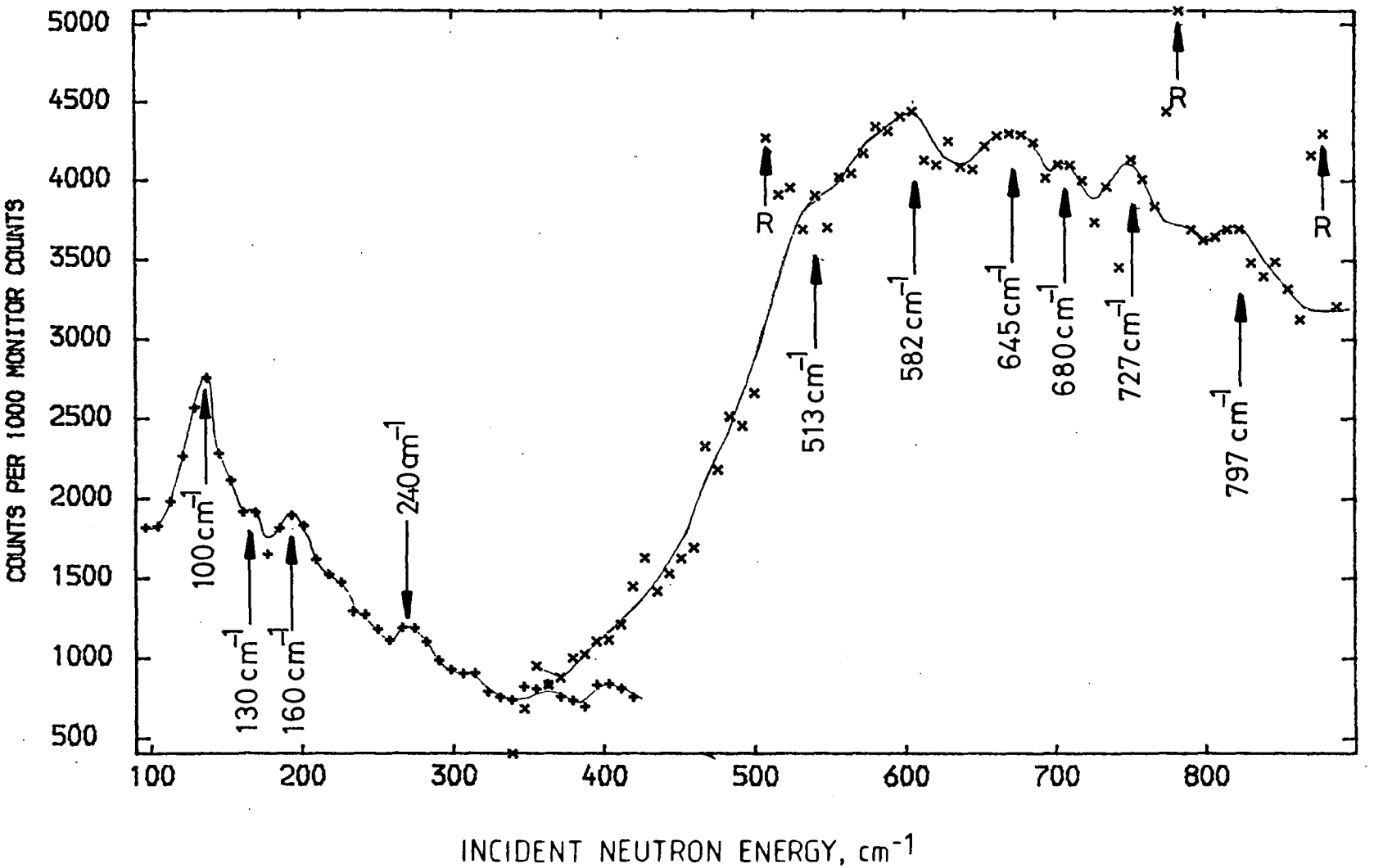

Figure 9.4, having been subtracted. Above 400 cm^{-1}, the statistics of the data in Figures 9.5 and 9.6 are modest and the band frequencies indicated on these spectra must be regarded as approximate. The features labelled "R" in Figure 9.6 are too narrow to be due to modes of adsorbed H_2O or of the zeolite lattice and are spurious effects, probably arising from rapid changes in the neutron background in the reactor shell during the recording of a particular scan.

Below 400 cm^{-1} in the b.f.d. spectra of $Ca_6A + H_2O$ (Figures 9.5, 9.6), an intense band is observed at 100 cm^{-1} along with several slightly weaker features up to 240 cm^{-1}. We assign the 100 cm^{-1} band (Figures 9.5, 9.6) to the degenerate t_x and t_y modes of H_2O adsorbed by Ca^{++} ions since the single intense band in the $Ca_6A + H_2O$ t.o.f. spectra (Figures 9.2, 9.3) was assigned to this mode. Because the b.f.d. spectra of $Ca_6A + H_2O$ (Figures 9.5, 9.6) correspond to coverages of no more than *ca* one H_2O molecule per pseudo unit-cell, we consider it unlikely that the features in these spectra in the range 126 to 240 cm^{-1} arise from modes of H_2O held by hydrogen-bonding to anionic regions of the zeolite framework or from $Ca^{++}(OH_2)_n$ species, where n>1. The features from 126 to 240 cm^{-1} in the $Ca_6A + H_2O$ b.f.d. spectra (Figures 9.5, 9.6) we assign to zeolite lattice modes involving displacements of the H_2O adsorbate molecules.

The difference in the H_2O coverage notwithstanding, the features in the IN4 t.o.f. and DIDO b.f.d. spectra of Ca_6A+H_2O do not correspond closely (Figures 9.2, 9.3 and 9.5, 9.6 respectively). This has been observed in the spectra of other zeolite-plus-adsorbate samples, *eg* Chapter Six, and may be related to the different backgrounds for the two spectrometers.

Above 400 cm^{-1}, the b.f.d. spectrum of $Ca_6A + H_2O$ at the lower coverage (θ = 3.9, Figure 9.5) shows bands at 546, 684 and 774 cm^{-1} which we ascribe to the three librational modes of water adsorbed by Ca^{++} ions, following the work of Adams and others.[15-21] Compared to the lower coverage b.f.d. results (Figure 9.5), the statistics of the data above 400 cm^{-1} are better in the higher coverage b.f.d. spectrum of Ca_6A+H_2O (θ = 5.9, Figure 9.6) and are sufficient to show that there are more than three bands in the region of the torsional modes of adsorbed H_2O (*ie* 513 to 797 cm^{-1}). This indicates the occupation of more than one adsorption site by H_2O for both b.f.d. spectra of $Ca_6A + H_2O$ (Figures 9.5, 9.6) and is consistent with the interpretation of the t.o.f. spectra of $Ca_6A + H_2O$ (θ = 2.5, Figures 9.2, 9.3). The apparent frequency shift of the torsional modes in the b.f.d. spectra (Figures 9.5, 9.6) on increasing the H_2O coverage is not significant, given the accuracy to which the band maxima can be determined in these spectra.

The b.f.d. spectra (Figures 9.5, 9.6) represent $S(Q,\omega)$ against incident neutron energy, and from Chapter Two the relative INS band intensities, I, in these spectra from the hindered translational and torsional modes of adsorbed H_2O are given within the harmonic approximation by:

$$I \propto \frac{Q^2 . Z(\tilde{\nu})}{\mu . \tilde{\nu}} . \exp(-2W_L) . \frac{\exp(\beta/2)}{2\sinh(\beta/2)} \qquad (9.1)$$

where -

$\hbar Q$ is the momentum transfer during the scattering process;

$Z(\tilde{\nu})$ is the vibrational density of states;

μ is the reduced mass of the oscillator,

$\tilde{\nu}$ is the frequency of the mode (cm^{-1});

$\exp(-2W_L)$ is a Debye-Waller factor, and

$\beta = hc\tilde{\nu}/(K_BT)$ where c is the velocity of light ($cm\ s^{-1}$),

K_B is Boltzmann's constant and T the absolute temperature.

Equation 9.1 applies to fundamental modes and in principle could be used to distinguish between the three librational modes of adsorbed H_2O. Unfortunately, the Debye-Waller factor, which in general is mode-dependent, cannot be estimated from the b.f.d. spectra of $Ca_6A + H_2O$ (Figures 9.5, 9.6) because there is no Q-resolution. Thus we set the Debye-Waller factor equal to unity when using equation 9.1 to calculate the relative INS band intensities for all modes of H_2O with respect to the zeolite framework. We assume that in the zeolitic Ca^{++}-OH_2 sorption complex, all four atoms lie in the same plane and the Ca-O bond is along the bisector of the lone pair orbitals of the oxygen atom. Making the further assumption that the H-O bond length for H_2O adsorbed by Ca_6A zeolite is 0.95Å and the H-O-H bond angle is 113^o, which are the values reported[30,31] in a neutron diffraction study of $CaHAsO_4.H_2O$, we obtain relative values for the μ^{-1} term in equation 9.1 for the τ_x, τ_y and τ_z modes of intrazeolite Ca^{++}-OH_2 of 0.94, 0.98 and 1.0, respectively, in arbitary units. These values of μ^{-1} are too similar to enable equation 9.1 to be used to decide how the τ_x, τ_y and τ_z modes of H_2O adsorbed by Ca_6A zeolite should be assigned to the three bands, at 546, 684 and 774 cm^{-1}, in Figure 9.5. The assumed bond length and bond angle given above for H_2O adsorbed in Ca_6A were chosen only to illustrate the similarity in the magnitude of the μ^{-1} terms of the τ modes and may be quite different to the true bond parameters. It is reported[32] that gross deviations from ideal values in the bond

angles and bond lengths are the rule for H_2O in hydrates. Estimation of the relative INS intensity of the librational modes of H_2O in Figure 9.5 is further complicated by the possible occupation of more than one adsorption site. To summarise, we cannot distinguish between the three torsional modes of H_2O adsorbed in Ca_6A using the INS spectrum (Figure 9.5) alone. Based solely on the frequency order published by Adams[15,16] for the librational modes of H_2O coordinated to cations in hydrated salts, we assign the band in Figure 9.5 at 546 cm^{-1} to τ_y, at 684 cm^{-1} to τ_z and at 774 cm^{-1} to τ_x.

Thus far, five of the six modes relative to the zeolite surface of H_2O adsorbed by Ca_6A have been assigned in our INS spectra, leaving the t_z mode unassigned. In $[Ca(OH_2)_6]Cl_2$, this mode occurs[18] at 380 cm^{-1}, and anticipating Section 9.7, the far IR data of Möller *et al*[5] suggest it arises at 444 cm^{-1} for H_2O adsorbed by A CaNaA zeolite. Although there is no band resolved at this frequency in our b.f.d. spectra of $Ca_6A + H_2O$ (Figures 9.5, 9.6), we speculate that the t_z mode of H_2O adsorbed by Ca_6A does occur at 444 cm^{-1}. Using equation 9.1, we calculate the relative INS intensities expected for the t and τ modes of H_2O in our b.f.d. spectra of Ca_6A+H_2O (Figures 9.5, 9.6) and the results are listed in Table 9.3. The predicted intensity (Table 9.3) for a putative t_z mode at 444 cm^{-1} is low, because of its small value of $(\mu\omega)^{-1}$ in equation 9.1, and this is consistent with the non-observation of a band ascribable to t_z in Figures 9.5 and 9.6. However, the results of the calculations in Table 9.3 must be treated with some caution since the difference in the calculated intensity of the t_z mode and the combined calculated intensity of the degenerate t_x and t_y modes is not great, and is inconsistent with the large observed intensity

TABLE 9.3 Calculated relative INS band intensities in a b.f.d. spectrum for the modes with respect to the zeolite surface of H_2O adsorbed in Ca_6A zeolite

mode	frequency cm-1 (Fig.9.5)	μ^{-1}	$Z(\omega)$	calculated relative INS band intensity, $S(Q,\omega)$
t_x and t_y	100	0.11	2	2.4
t_z	444[a]	0.11	1	1.0
τ_y	546	0.98	1	8.8
τ_z	684	1.00	1	9.0
τ_x	774	0.94	1	8.5

Notes -

The relative intensities were calculated using equation 9.1, setting the Debye-Waller factor equal to unity for all the modes and using the approximation that $Q^2 = k_f^2$, where k_f is the magnitude of the wave-vector of the scattered neutron.

$Z(\omega)$ and μ^{-1} are terms in equation 9.1.

a. The frequency of 444 cm^{-1} is that proposed from the published IR data[5] of CaNaA + H_2O (Section 9.7); this band was not observed in our INS data.

---

of the 100 cm^{-1} band assigned to the t_x and t_y modes in Figures 9.5 and 9.6. The discrepancy between the observed and calculated intensities may be related to the approximation that the Debye-Waller factor in equation 9.1 is equal to unity for all modes of adsorbed H_2O.

The assignments of our t.o.f. and b.f.d. spectra of Ca_6A + H_2O are summarised in Table 9.4.

TABLE 9.4 Summary of the bands (cm^{-1}) observed in the INS spectra of H_2O adsorbed by Ca_6A zeolite and those reported for $[Ca(OH_2)_6]Cl_2$

Sample	$Ca_6A + H_2O$ θ=2.5	θ=3.9	θ=5.9	$[Ca(OH_2)_6]Cl_2$ from ref.18
Spectrometer	IN4	DIDO b.f.d.	DIDO b.f.d	(INS)
Temperature, K	10	77	77	293
Spectrum	Fig.9.3	Fig.9.5	Fig.9.6	-
				band, cm^{-1} assignment
t_x and t_y of H_2O at various sites	75), 88)	100	100	80), 100), 136) lattice modes
zeolite lattice modes involving displacements of adsorbed H_2O	160	126, 143, 160, 228	130, 160, 240	192), 240) ν_S(OH···Cl)
				380 $t_z(H_2O)$
$\tau_y(H_2O)$		546	(513, (582	480 $\tau_y(H_2O)$ [a]
$\tau_z(H_2O)$		684	(645, (680	656 $\tau_z(H_2O)$ [a]
$\tau_x(H_2O)$		774	(727, (797	719 [b] $\tau_x(H_2O)$ [a]

Notes:

θ = coverage of H_2O in molecules per supercage.

a. Our assignments. The remaining assignments in this column are taken from ref. 18.

b. This band was not resolved in the INS spectrum[18] but was observed in the IR by I. Gamo.[19]

Finally, we note that the b.f.d. spectra published[33,34] for ice I_c show bands at 120, 210, 290, 645 (very intense) and 830 cm^{-1}. These frequencies do not correspond with those observed in our b.f.d. and t.o.f. spectra (Figures 9.2-9.3, 9.5, 9.6) of $Ca_6A + H_2O$ and thus provide evidence that our INS spectra show modes of adsorbed, rather than solid, H_2O.

9.7 The published far IR spectrum of H_2O adsorbed by a CaNaA zeolite

Moller *et al*[5] have obtained the far IR spectrum of water adsorbed by partially Ca^{++} ion-exchanged zeolite A. The exact composition of the zeolite was not stated[5] and we shall refer to it as CaNaA. The far IR spectra of CaNaA + H_2O are shown in Figure 9.7 and, for a coverage of 4 H_2O molecules per pseudo-unit cell, weak bands ascribed to adsorbed water were observed[5] at 71 and 444 cm^{-1}. The 444 cm^{-1} band was assigned to a singly degenerate mode involving displacement of H_2O perpendicular to the surface and the 71 cm^{-1} band to a doubly degenerate mode involving displacements of H_2O parallel to the surface[5]. It was not specified[5] whether these modes were hindered translations or rotations. Because of its low frequency, we note that the 71 cm^{-1} band in the CaNaA + H_2O spectrum (Figure 9.7) is likely to have arisen from the degenerate t_x and t_y modes of H_2O. From the assignments due to Moller *et al*[5], the 444 cm^{-1} band could have arisen from the t_z, τ_y or τ_x modes (Figure 9.1). By comparison with the published[18,19] spectra of $[Ca(OH_2)_6]Cl_2$, in which we have proposed that the t_z, τ_y and τ_x modes occurred at 380, 480 and 719 cm^{-1},

Fig. 9·7 The far IR spectra of water adsorbed by NaCaA zeolite published by Moller et al[5].

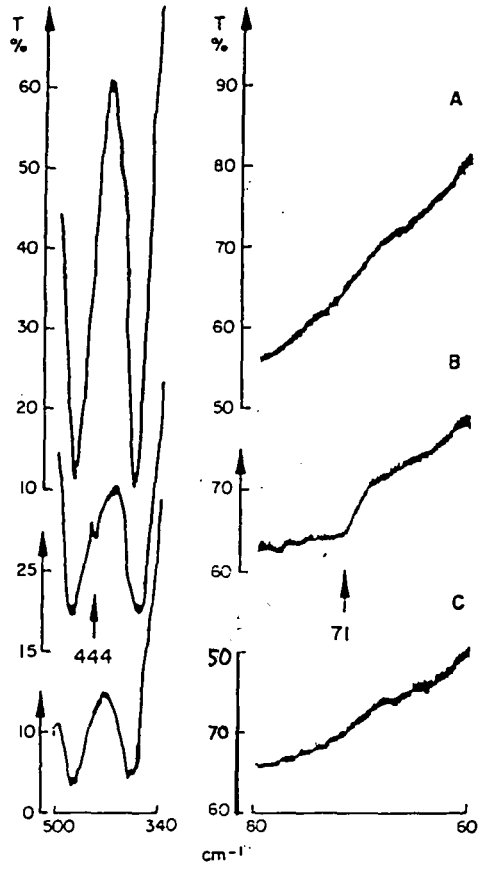

A: coverage Θ = 8 H_2O molecules per pseudo-unit cell.

B: coverage Θ = 4 H_2O molecules per pseudo-unit cell.

C: fully dehydrated CaNaA zeolite.

The sample was in a nujol suspension between two polyethylene discs. The spectra were compensated[5] for the 73 cm^{-1} band of polyethylene.

the 444 cm^{-1} band in the CaNaA + H_2O spectrum (Figure 9.7) is unlikely to be due to τ_x. We prefer the assignment of the 444 cm^{-1} band to t_z since in our INS spectra of Ca_6A+H_2O (Section 9.6), the τ_y mode was assigned to a band at 546 cm^{-1} and although the t_z mode remained unassigned, although it was expected to occur at a frequency lower than that of τ_y from the work of Adams[15,16] (Section 9.5).

9.8 Conclusions

We have obtained the INS spectra of H_2O adsorbed in Ca_6A zeolite for coverages, θ, of *ca* one H_2O molecule per Ca^{++} ion or less. For a coverage of θ = 3.9, broad INS bands were observed, centred at 774, 684 and 546 cm^{-1}, and were assigned to the τ_x, τ_z and τ_y modes respectively of a Ca^{++}-OH_2 sorption complex. A broad INS band centred at 75 cm^{-1} in the t.o.f. spectra of Ca_6A + H_2O (θ =2.5) was assigned to the degenerate t_x and t_y modes of intrazeolitic Ca^{++}-OH_2. The width of the INS bands suggests that the H_2O is adsorbed at several Ca^{++} ion sites, which from published X-ray data,[3,6-8] are those associated with the 6-oxygen rings and, possibly, the SU sites. The observation and assignment of the 75 cm^{-1} band in our Ca_6A + H_2O INS spectra was consistent with the assignment by Möller *et al*[5] of a weak feature at 71 cm^{-1} in the far IR spectrum of CaNaA + H_2O. We were unable to observe any INS band ascribable to the t_z mode of H_2O adsorbed by Ca_6A and calculations suggest that the INS intensity of such a band would be low. By comparison with the far IR spectrum of CaNaA + H_2O reported by Möller *et al*[5], it is possible that this mode occurs at *ca* 444 cm^{-1} for H_2O adsorbed by Ca_6A zeolite.

REFERENCES

1. Breck, D.W., Zeolite Molecular Sieves, Structure, Chemistry, and Use, Wiley, New York, 1974.

2. Smith, J.V. in Molecular Sieve Zeolites - 1, Adv.Chem. Ser., 101, 171, 1971.

3. De Roy, G., Vansant, E.F., Mortier, W.J. and Uytterhoven, J.B., Proc.5th Int.Conf. Zeolites (Naples 1980), Ed. L.V.C. Rees, Heyden, London, 1980.

4. Lee, H. in Molecular Sieves, Adv.Chem.Ser., 121, 311, 1973.

5. Möller, K., Kunath, D. and Spangenberg, H.-J., Spect. Acta., 27A, 353, 1971.

6. Thoni, W., Z fur Kristallogr., 142, 142, 1975.

7. Firor, R.L. and Seff, K., J.Am.Chem.Soc., 100, 3091, 1978.

8. Pluth, J.J. and Smith, J.V., J.Am.Chem.Soc., 105, 1192, 1983.

9. Barrer, R.M., Zeolites and Clay Minerals as Sorbents and Molecular Sieves, Academic Press, London, 1978.

10. Deininger, D., Pfeifer, H., Przyborowski, F., Schirmer, W. and Stach, H., Z.Phys.Chem. (Leipzig), 245, 68, 1970.

11. Davydov, L.G. and Tkach, O.D., Fiz.Khim., 2, 122, 1975.

12. Vucelic, V., Vuceli, D., Karaulic, D. and Susic, M., Thermochim.Acta., 7, 77, 1973.

13. Ducros, P., Bull.Soc.Fr. Mineral. Christallogr., 83, 85, 1960.

14. Nakagawa, I. and Shimanouchi, T., Spect.Acta., 20, 429, 1964.

15. Adams, D.M. and Lock, P.J., J.Chem.Soc.(A), p.2801, 1971.

16. Adams, D.M. and Hills, D.J., J.Chem.Soc., Dalton,p.782, 1978.

17. James, D.W., Armishaw, R.F. and Frost, R.L., Aust.J.Chem., 31, 1401, 1978.

18. Prask, H.J. and Boutin, H., J.Chem.Phys., 45, 3284, 1966.

19. Gamo, I., Bull.Chem.Soc.Jpn., 34, 1433, 1961.

20. Safford, G.J., Leung, P.S. and Schaffer, P.C., J.Chem.Phys., 50, 4444, 1969.

21. Rush, J.J., Ferraro, J.R. and Walker, A., Inorg.Chem., 6, 346, 1967.

22. Pechar, F., Schweiss, P. and Fuess, H., Chem.Zvesti, 36, 779, 1982.

23. Egelstaff, P.A., Stretton Downes, J. and White, J.W., Symp.Mol.Sieves. (London 1967), Soc.Chem.Ind., 1968, p.306.

24. Boutin, H., Safford, G.J. and Danner, H.R., J.Chem.Phys., 40, 2670, 1964.

25. Gamlen, P.H., D.Phil.Thesis, University of Oxford, 1978.

26. Willis, B.T.M.(Ed.), Chemical Applications of Thermal Neutron Scattering, Oxford University Press, 1973.

27. Butler, W.M., Angell, C.L., McAllister, W. and Risen, W.M., J.Phys.Chem., 81, 2061, 1977.

28. Brodskii, I.A. and Zhadanov, S.P. in Proc.5th Int.Conf. Zeolites (Naples 1980), Ed.L.V.C. Rees, Heyden, London, 1980.

29. Dyrkheev, V.V., Kiselev, A.V., Lygin, V.I. and Tul'chinskii, V.M., Kinet.Katal., 17, 1343, 1976.

30. Ferraris, G., Jones, D.W. and Yerkess, J., Acta.Cryst., B28, 209, 1972.

31. Ferraris, G. and Franchini-Angela, M., Acta.Cryst., B28, 3572, 1972.

32. Cotton, F.A. and Wilkinson, G., Advanced Inorganic Chemistry, 3rd Edn., Wiley, New York, 1972.

33. Howard, J., Waddington, T.C. and Wright, C.J. in Neutron Inelastic Scattering 1977, Vol.II, International Atomic Energy Agency, Vienna, 1978, p.499.

34. Hall, P.G., Pidduck, A. and Wright, C.J., J. Colloid and Interface Sci., 79, 339, 1981.

CHAPTER TEN

AN I.N.S. STUDY OF HYDROGEN ADSORBED BY Zn(II) PARTIALLY ION-EXCHANGED ZEOLITE TYPE-A

10.1 Introduction

Throughout this chapter, we use "hydrogen" to mean either the ^1H nucleus or the $^1H_2$ molecule.

The adsorption of H_2 by zeolites is of interest through the industrial applications of H_2 activation in catalysis, *eg* in the hydrocracking of crude oils,[1] and in the development of energy storage systems. An example of the latter is the encapsulation of H_2 to 0.76% weight in CsNaA zeolite at 473K and 8700 psi reported by Fraenkel.[2]

We have obtained the INS spectra (10 to 210 cm^{-1}) at 10K of H_2 adsorbed by partially Zn(II) exchanged type-A zeolite. The spectra, discussed below, show bands at energies of the order of a few rotational constant of the H_2 molecule and therefore are interpreted (Section 10.5) as arising from transitions between rotational energy levels of non-dissociatively adsorbed H_2. That the H_2 does not dissociate on adsorption is in agreement with volumetric studies of H_2 and D_2 adsorption on Zn-A zeolite published by Kochurikhin *et al.*[3-6] These Russian workers[6] have predicted model-dependent vibrational frequencies for the modes of H_2 adsorbed by Zn-A (Section 10.4.4). Our rationale for undertaking this present work was to test these predictions.

In the gas phase, the rotational constant, B, of H_2 is[7] 60.809 cm^{-1} and we assume that this value is also applicable to solid H_2 and to H_2 adsorbed in the zeolites discussed in this chapter.

In the literature, the early theoretical models of H_2 molecularly adsorbed at various surfaces led to inaccurate predictions for some of the observable properties of the ad-

sorbate-adsorbent system.[8-10] Recently published models[11-13] are potentially more accurate but are based upon more parameters than can be uniquely determined from published experimental data. Both types of model are discussed below (Section 10.4).

Our study of the ZnNaA+H_2 system presented in this chapter has been only partially completed owing to a lack of available neutron beam time. Because of the limited amount of information available from our INS spectra of ZnNaA+H_2, we will adopt in this chapter a somewhat simplistic model of the adsorbed H_2 (Section 10.5). The limitations of our model will be indicated and an outline of how the model might be improved will be given (Section 10.6). The results reported in this chapter are to be regarded as preliminary to the more extensive experimental and theoretical investigation which is proposed (Section 10.6).

10.1.1 The Nuclear spin states of dihydrogen

It is well known that the hydrogen molecule exists in two forms, depending on the alignment of the nuclear spins.[14] Hydrogen molecules with anti-parallel nuclear spins constitute para-hydrogen and those with parallel nuclear spins constitute ortho-hydrogen. Hydrogen nuclei are fermions and thus, according to the Pauli Exclusion Principle, the overall wavefunction of the hydrogen molecule must change sign when the two nuclei are interchanged. Since a rotation of the molecule does indeed interchange the nuclei, the nuclear spin, I, of the molecule controls the allowed molecular rotational energy levels. Using the integer J as a quantum number to label the energy levels of a free, linear, rigid rotor, it can be shown that[15] para-hydrogen (I=0) occupies only rotational levels of even J

(including J=0) and ortho-hydrogen (I=1) exists only in odd-J states.

In the literature, a common model for associatively adsorbed H_2 is that of a rigid rotor confined to rotation in a plane.[8-10] It is therefore pertinent to recall that the energy levels, E_m, of a 2-dimensional rigid rotor are given[14] by:

$$E_m = m^2B, \quad m = 0, \pm1, \pm2, \pm3, \text{---}$$

where the rotational constant B is given by

$$B = \hbar^2/2I$$

and I is the moment of inertia of the molecule about its axis of rotation. When restricted to rotations in a plane, ortho-H_2 occupies the states of even m and para-H_2 the states of odd m.

The ratio of ortho- and para-H_2 concentrations in gaseous H_2 at room temperature is 2.98:1, approaching the high temperature limit of 3:1.[16] On cooling in the absence of a catalyst to below liquid nitrogen temperatures, the ortho-H_2 molecules descend to the lowest ortho state, J=1, while the para-H_2 molecules descend to the J=0 level. This metastable condition may be retained for months;[14] at thermodynamic equilibrium almost all the molecules would occupy the J=0 state.

In liquid and solid hydrogen the distinction between the ortho- and para- modifications is maintained. The conversion rate to para-H_2 is about 0.7% per hour at 20K in normal liquid hydrogen.[17] It is therefore possible to carry out INS experi-

ments of a day's duration on H_2 samples containing a significant concentration of ortho-H_2 at temperatures below the boiling point of H_2 (20.4K).

Conversion of the ortho- to the para- states of gas phase H_2 is catalysted by paramagnetic gases.[13] Heterogeneous catalysis is achieved by paramagnetic ions in solution and by adsorption of H_2 at low temperatures at surfaces impregnated with paramagnetic materials, such as finely divided Al_2O_3 doped with Fe_2O_3 or Cr_2O_3.[13,18,19] It has also been demonstrated that ortho-H_2 is adsorbed preferentially to para-H_2 at surfaces containing no paramagnetic substances, *eg* activated charcoal[20] or TiO_2.[8] On these adsorbents, there is no conversion between the spin states of the adsorbed H_2 molecules.[21] Almost pure samples of ortho-H_2 can be prepared by successive adsorption-desorption cycles. The stronger adsorption of ortho-H_2 (the I=1 state) may result from interaction of its electrical quadrupole[22] with the surface; para-H_2 (the I=0 state) has a zero quadrupole moment. The ortho and para modifications of deuterium may be separated by the same method, the I=1 state, para-D_2, being the more strongly adsorbed.[13,19] It is also possible to separate the four components of an H_2/D_2 mixture.[19]

In the literature, the preferential adsorption of ortho-H_2 over para-H_2 is generally studied by one of two techniques: measurement of separation factors (see below) and, less commonly. INS. Both methods allow model potential functions of the adsorbate-adsorbent interaction to be tested.

10.2 Experimental

A zeolite of composition $Zn_{4.5}Na_{3.0}Al_{12.5}Si_{11.5}O_{48}$, hereafter referred to as ZnNaA, was produced by the following method. Linde 4A zeolite (supplied by B.D.H.) was ion-exchanged in a solution (0.1M) of $ZnCl_2$ (B.D.H. S.L.R.) for one week, the volume of solution being chosen such that it contained the stoichiometric amount of Zn(II) ions calculated to be necessary to produce the required degree of ion-exchange. The exchange was stopped after one week and the sample analysed whereupon it was found that less than the required degree of ion-exchange had been achieved. The zeolite was re-exchanged in a fresh solution of $ZnCl_2$ (0.1M), the volume of which was such that it contained the stoichiometric amount of Zn(II) ions required to make up the difference between the attained and desired degree of ion-exchange. The second exchange produced the required degree of ion-exchange after one week.

Both exchanges were carried out at room temperature. The ZnNaA was dehydrated using the method given in Chapter Four.

Hydrogen gas (99.9995%, Masonlite, Catham, Kent) was adsorbed by the ZnNaA using the technique described in Chapter Four. The zeolite was first exposed to 25 torr H_2 at room temperature (292.5K) but no measurable uptake of H_2 occurred. On cooling the sample to 77K, the adsorption took place readily. Further experimental details are summarised in Table 10.1

The t.o.f. spectra reported in this chapter were obtained on the IN4 spectrometer at the I.L.L., Grenoble, using an incident neutron energy of 251 cm^{-1}. Flat baselines were subtracted from the t.o.f. spectra, the data points then being grouped into equal energy bins. Where appropriate, Gaussian

curves were fitted to the data. The necessary calculations were carried out using the computer programs described in Chapter Six.

TABLE 10.1 Summary of experimental details for the INS spectra of H_2 adsorbed by ZnNaA

temperature of INS run/K	10
coverage/molecules H_2 per supercage	1.1
maximum overpressure[a] during adsorption/torr	323
residual H_2 overpressure[a] in sample can/torr	16
% scattering from adsorbed H_2	9.4
$\frac{\sigma_{inc}\ \text{adsorbed}\ H_2}{\sigma_{inc}\ \text{zeolite}}$	32

Note a: The adsorption of H_2 was carried out with the zeolite at 77K.

10.3 The crystal structure of partially Zn(II) ion-exchanged zeolite A

The crystal structure of dehydrated $Zn_{4.5}Na_{3.0}Al_{12.5}Si_{11.5}O_{48}$ as used in our INS experiments has not been published. However, Seff *et al*[23] have reported the X-ray crystal structure of partially dehydrated $Zn_5Na_2Si_{12}Al_{12}O_{48}$. It was shown[23] that three Zn(II) ions per pseudo unit cell were located in the α-cage, each on the 3-fold axis of a zeolite 6-oxygen ring and tetrahedrally coordinated to three framework O atoms and one H_2O molecule. Such a coordination environment is illustrated

in Fig. 10.1. The remaining two Zn(II) ions per pseudo unit cell also lay on 3-fold axes of 6-oxygen rings but were displaced into a sodalite unit and bridged by a single H_2O molecule. The Na(I) ions were associated with the 8-oxygen rings.[23] It is reasonable to suppose that the Zn(II) ions in our sample of dehyrated ZnNaA also lie on the 3-fold axes of the 6-oxygen rings.

Although Seff *et al* reported that it was impossible to fully dehydrate their crystal of Zn_5Na_2A[23] and other crystals of partially[24] and fully[25] Zn(II) ion-exchanged A-type zeolites, it is likely that our INS sample of ZnNaA was completely dehydrated. On the basis of the loss, during the dehydration of a sample of ZnNaA under conditions very similar to those used for our INS sample, of infrared bands assigned to the ν_δ mode of adsorbed water at 1655 cm^{-1}, other workers[26] have shown that complete dehydration of ZnNaA zeolite is in fact possible. There is no evidence that water makes any contribution to our INS spectra of $ZnNaA/H_2$ (Section 10.5).

The difference between the ease of dehydration of our samples and those of Seff[23-25] probably arises from the different experimental conditions. Firstly, the X-ray crystals, typically cubes 80μm on edge, were larger than the particles of our powder sample (5.0 to 0.5μm for Linde 4A[27]). Secondly, the X-ray samples were dehydrated while being contained in a capillary tube connected to a vacuum system. Given the narrowness of a capillary tube, the pumping speed above the crystals was probably quite low.

Fig. 10.1 The qualitative positions adopted by the Zn(II) ions at S2* sites in partially dehydrated Zn_5Na_2-A zeolite, after ref. 24.

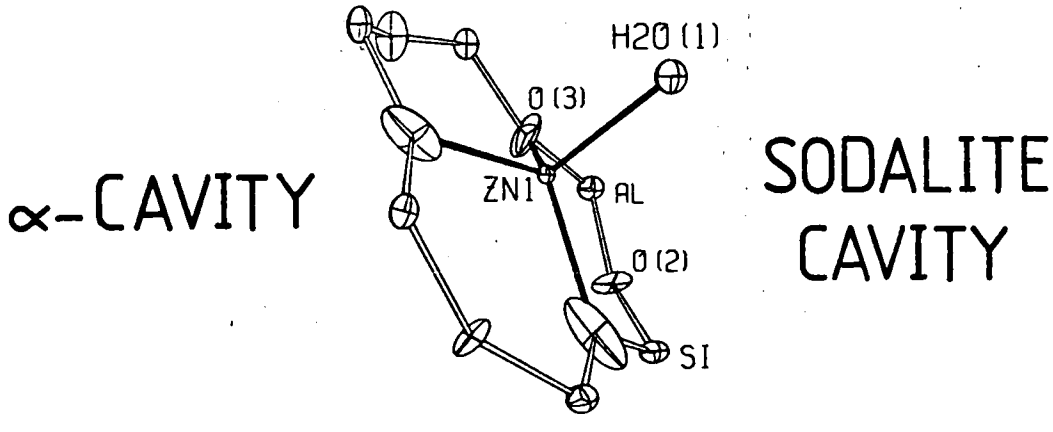

10.4 Literature relevant to the differential adsorption of the ortho and para modifications of hydrogen

10.4.1 The separation factor, F

The extent of the preferential adsorption of ortho-H_2 compared with para-H_2 at a surface may be measured by a separation factor, F, defined thus:[13]

$$F = \frac{([p\text{-}H_2]/[o\text{-}H_2])\ \text{gas phase}}{([p\text{-}H_2]/[o\text{-}H_2])\ \text{adsorbed phase}} \qquad (10.1)$$

The separation factor for deuterium is given by[13]:

$$F' = \frac{([o\text{-}D_2/[p\text{-}D_2])\ \text{gas phase}}{([o\text{-}D_2]/[p\text{-}D_2])\ \text{adsorbed phase}} \qquad (10.2)$$

An H_2 molecule in the gas phase has three degrees of translational freedom and two degrees of rotational freedom. The value of F depends on the extent to which these degrees of freedom become hindered when H_2 is held at a surface. In many published studies of adsorbed H_2 (see below), the experimental values of F are compared with those calculated *via* molecular partition functions for various models of the adsorbate. The possible hindered modes of adsorbed H_2 are shown in Fig. 10.2, in which the surface of the adsorbent is taken to be parallel to the xy-plane and the z-direction is normal to the surface.

In an early paper, Sandler[8] showed that experimental separation factors measured at liquid nitrogen temperatures could be predicted by models in which the molecule on adsorption lost its rotational but retained its translational degrees of freedom. However, the Sandler models failed to correctly predict the values of separation factors observed at liquid hydrogen temperatures.[8,9]

Fig. 10.2 The possible hindered translational and torsional modes of adsorbed H_2.

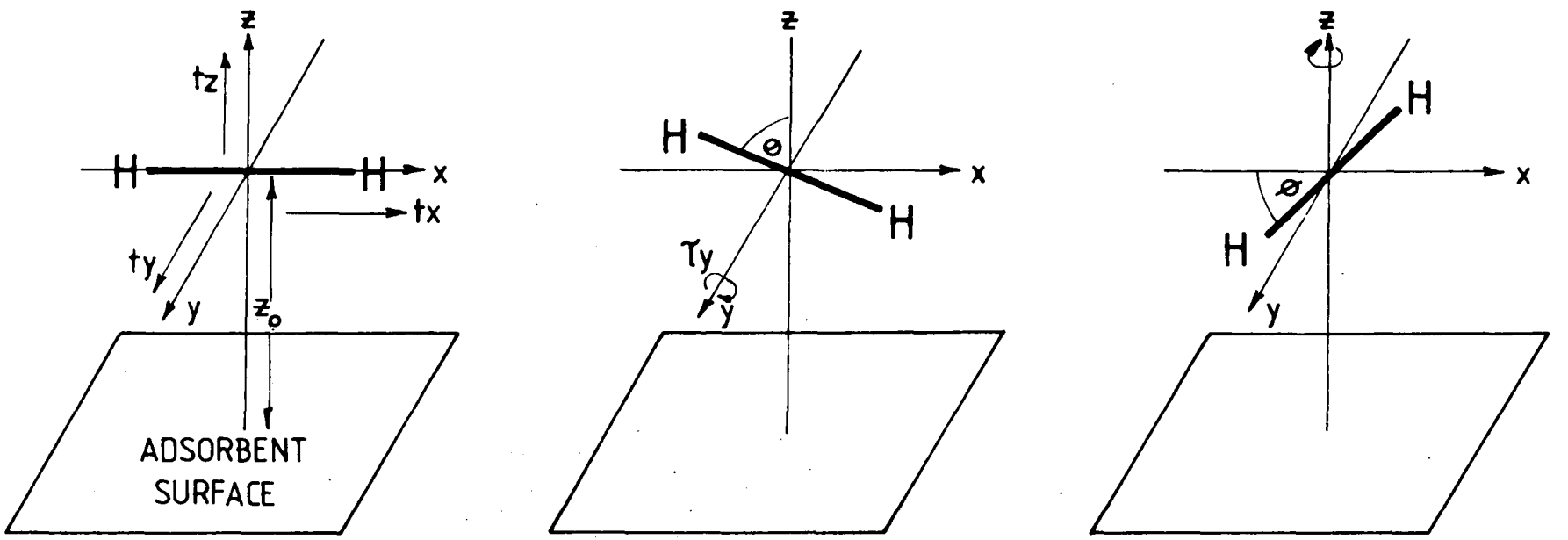

Further analysis of the problem of separation factors was given by White and Lassettre,[9] and also by Evett,[10] who considered that the admolecule was a free rotor in the xy-plane while rotation about the y-axis was said to be restricted by a barrier of height C (Fig.10.2). The adsorption was assumed to be non-localised. In these analyses,[9,10] only the t_z and τ_y modes of the admolecule were said to be perturbed by the surface, those degrees of freedom whose loss would give rise to the t_x, t_y and τ_z modes being retained by the molecule on adsorption (Fig. 10.2). Taking z to be the distance of the centre of mass of the molecule from the adsorbent and $(0 \leq \theta \leq \pi)$ to be the angle between the molecular and z-axes (Fig. 10.2), the adsorbent-adsorbate potential V was written[9,10] as a function of z and θ only:

$$V(z,\cos^2\theta) = V_o(z_o,0) + \frac{C}{2}(1+\cos 2\theta) + K(z-z_o)^2 \qquad (10.3)$$

where V_o, C and K are constants and z_o is the equilibrium distance of the molecule above the surface. It was assumed that z_o was greater than the radius of gyration of the H_2 molecule about the y-axis (Fig.10.2). Equation 10.3 neglects any interaction between the hindered rotations and vibrations and gives, *via* the Schrodinger equation, the energy levels of a simple harmonic oscillator (t_z mode) upon which are superimposed the energy levels pertaining to the hindered rotation about the y-axis (τ_y mode, Fig.10.2). The separation of the rotational energy levels depends on the sign and the magnitude of the barrier height, C. For a zero value of C (equation 10.3) the molecule undergoes free rotation about the y-axis (Fig.10.2). At sufficiently large values of C the τ_y mode becomes torsional in character. If C is positive the torsional

oscillator attains minimum energy when it lies parallel to the surface and if C is negative the equilibrium orientation is perpendicular to the surface. We shall refer to the case of positive C as the TIP model (for torsion in the *xy*-plane) and that of negative C as the TOP model (for torsion out of the *xy*-plane). Values of the separation factor calculated by White and Lassettre[9] within the TIP model gave better agreement than the TOP model with the experimental separation factor of F=16 obtained by Cunningham *et al*[18,19] for H_2 adsorption on Al_2O_3 doped with paramagnetic oxides (Fe_2O_3 and Cr_2O_3) and with the observed value of F'=2.4 for D_2 adsorption on undoped Al_2O_3. Accordingly, White and Lassettre[9] regarded the TOP model for H_2 adsorbed on doped and undoped Al_2O_3 as unlikely. In the TIP model, the barrier height C was calculated to be 9.83kJ/mole for H_2 on doped Al_2O_3 and 3.64kJ/mole for D_2 on undoped Al_2O_3. However, these barrier heights are slightly too large to be consistent with the isosteric heat of adsorption of H_2, which is *ca* 6 to 8kJ/mole on these Al_2O_3 surfaces.[13]

It has been shown by Evett[11] and by MacRury and Sams[12] that the discrepancy between the values of the barrier height C and the heat of adsorption can be resolved by considering that both rotational modes of the admolecule are hindered, unlike the White and Lassettre[9] model in which the τ_z mode is considered to be a free rotation. The existence of a barrier to rotation in the *xy*-plane implies that the adsorption is localised and the free translation of the admolecule is replaced in the MacRury and Sams model[12] by t_x and t_y vibrational modes. MacRury and Sams[12] considered that the rotations of the adsorbate in both planes (Fig.10.2) were each hindered by 2-fold barriers, the barrier height to rotation in the *xy*-plane being 2μ and

the barriers to rotation out of the xy-plane being λ. The rotational energy levels of the admolecule were calculated using the Hamiltonian:

$$H = H_o - \lambda\cos^2\theta - 2\mu(1-\cos 2\theta)$$

where H_o is the Hamiltonian of a linear free rotor and θ is the angle between a plane passing through the z-axis (Fig.10.2) and the H_2 molecular axis and a reference plane passing through the z-axis. The unperturbed energy levels are given by $BJ(J+1)$ and the combined effects of the barriers to rotation, λ and 2μ, is to lower the $(2J+1)$-fold degeneracy of each rotational level into $(2J+1)$ sublevels, the magnitude of the splitting between the sublevels depending on the values of λ and 2μ. It was shown[13] that various combinations of λ and 2μ led to the same value of the separation factor F at a particular temperature. For example, the value of F=16 measured by Cunningham *et al*[18] for the doped Al_2O_3/H_2 system at 20.4K could be reproduced by taking λ=0.7 and 2μ = 2.8kJ/mole or by taking λ = 7.3 and 2μ = 0.6kJ/mole. According to McRury and Sams,[13] the range of possible values of λ and 2μ could be reduced by comparing observed and theoretical values of F over a wide range of temperature, but there are no data available in the literature to adequately test this hypothesis. Thus, although the model in which both rotational modes of adsorbed H_2 are hindered can lead to rotational barrier heights which are consistent with the heat of adsorption, it is not possible to obtain a unique value for each barrier height and such a model has not yet been definitely tested.

10.4.2 A published INS study of H_2 adsorbed by Al_2O_3

Silvera and Nielsen[28] have studied the adsorption of H_2 on activated alumina at 5 to 77K using INS and measurement of the separation coefficient F.

The INS spectrum at 5K of submonolayer coverages of H_2 adsorbed on alumina showed a single band at an energy transfer of just below 1B, and, according to the authors,[28] a broad, unstructured spectrum above 1.5B (Fig.10.3). The value used for B, the rotational constant of adsorbed hydrogen, was 59.3 cm^{-1}. The observation of a band at *ca* 1B is evidence that the adsorption of H_2 was non-dissociative.

Fig. 10.3 The INS spectrum (5K) of H_2 adsorbed by alumina, taken from ref. 28.

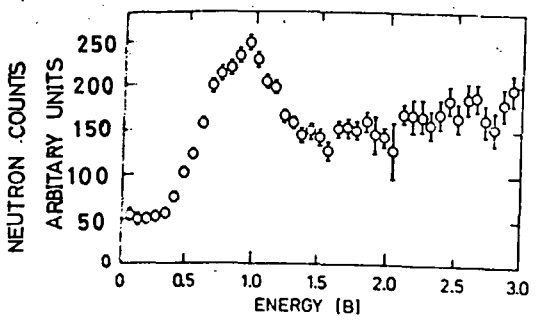

The energy transfer is given in units of B = 59.3 cm^{-1}. Scattering counts from the bare alumina have been subtracted by the authors[28] from the data. The H_2 coverage was 16.5 cm^3 NTP/g.

The data were discussed[28] in terms of two alternative models of the adsorbed H_2:

1. a free rotor confined to a plane, the orientation of which was not specified (two dimensional or 2-D rotor model). The INS band at 1B is then assigned to the transition from the $m'=\pm1$ state to the $m''=0$ state of the rotor. The possible perturbation of the three translational and the remaining rotational degree of freedom of the molecule on adsorption was not discussed.

2. the TOP model of White and Lassettre[9] (Section 10.4.1) with a barrier height for the τ_y mode of -5B. The possible perturbation of the degrees of freedom leading to the τ_z, t_x and t_y modes of the molecule on adsorption were not discussed.

Silvera and Nielsen[28] have compared the measured separation factors, F_{obs}, for H_2 and D_2 adsorption on their samples with theoretical values, F_{calc}, calculated within the 2-D rotor and TOP models. The values are listed in Table 10.2. The separation factor published by Silvera and Nielsen[28] for the TOP model was calculated for the limit of an infinite barrier to rotation. Although the splitting of the rotational energy levels, and hence the separation factor, in the TOP model depends on the magnitude of the barrier to rotation (Section 10.5.4), a value of F_{calc} appertaining to a barrier of -5B was not reported[28]. Nevertheless, Table 10.2 shows closer agreement with experiment for the separation factors calculated within the 2-D rotor model than those calculated for the TOP model.

The consideration of another factor, discussed below, led Silvera and Nielsen[28] to discard the 2-D rotor model in

TABLE 10.2 Calculated and observed ortho/para separation factors of H_2 and D_2 adsorption on Al_2O_3 at 20.4K. The data are taken from reference 28.

model	F_{obs}	F_{calc} 2-D rotor zero barrier height	F_{calc} TOP infinite barrier height	$\bar{F}$ 2-D rotor zero barrier height	$\bar{F}$ TOP
H_2	39^{+1}_{-8}	43.8	1439	86 to 160	43 to 80
D_2	5±0.3	5.45	22.3	-	-

favour of the TOP model. The authors derived model dependent values, $\bar{F}$, of the separation factor from integrated INS band intensities. The values of $\bar{F}$ are listed in Table 10.2. A precise evaluation of $\bar{F}$ was not possible because of uncertainty in the extent of the wings of the INS band and in the baseline position (Fig.10.3). It is not clear in the paper of Silvera and Nielsen[28] whether the value of $\bar{F}$ calculated for the TOP model (Table 10.2) refers to the limit of an infinite barrier height or a barrier of -5B. However, the value of $\bar{F}$ for the 2-D rotor model shows poorer agreement with experiment than that reported for the TOP model (Table 10.2) and on this basis Silvera and Nielsen favoured the TOP model. But bearing in mind the difficulties in determining the value of $\bar{F}$, we maintain that the comparison of F_{obs} with F_{calc}, which favours the 2-D rotor model, is likely to be more reliable than the comparison with $\bar{F}$ on which Silvera and Nielsen based the interpretation of their results.

Within the TOP model, a band was predicted by Silvera and Nielsen[28] to occur at *ca* 3B in their INS spectrum of Al_2O_3/H_2. The band was not in fact observed and its absence was rationalised[28] by suggesting that it would be extremely broad. We here propose an alternative explanation, couched in terms of the 2-D rotor model. It was not stated by the authors[28] whether their INS spectra were neutron energy loss or gain. But since the incoherent inelastic scattering cross section for para-H_2 is zero (Chapter Two) and there is no evidence for any bands below *ca* 1B, the observed band (Fig.10.3) must be due to the transition $m''=\pm1$ (ortho-H_2) to $m'=0$ (para-H_2). The INS spectra of Silvera and Nielsen therefore correspond to neutron energy gain. For low values of the barrier to rotation, a band

at 3B would correspond in the 2-D rotor model to the transition $m'=\pm2$ (para-H_2) to $m'=\pm1$ (ortho-H_2), which even if the para state was significantly populated, is not observable by INS.

To conclude, despite the preference of Silvera and Nielsen[28] for the TOP model, the experimental separation factors and INS spectrum of H_2 adsorbed on Al_2O_3 appear to be more consistent with the 2-D rotor model.

10.4.3 Published volumetric studies of H_2 adsorption by Zn-A zeolite

The adsorption of H_2 and D_2 in various zeolites has been studied by Kochurikhin and Zel'venskii.[3-6] Adsorption isotherms for various temperatures from 80.3 to 121.7K showed[6] that the uptake of H_2 by ZnA zeolite was completely reversible, in common with NaA, MgA and NaX. The degree of ion-exchange of the zeolites ZnA and MgA was not stated.[6] The isosteric heat of adsorption of H_2 by ZnA was reported[5] to fall with increasing H_2 dosage from 8.2kJ $mole^{-1}$ at 3cm^3H_2/g to 6.9kJ $mole^{-1}$ at 60 cm^3H_2/g and the differential entropy (referred to a standard state of 1 torr H_2 at 90K) varied from 55 to 31 J $mole^{-1}K^{-1}$ over the same range of H_2 coverage.

Kochurikhin and Zel'venskii[4,5] have discussed the adsorption of H_2 at a surface, using the potential function for the adsorbate-adsorbent interaction given by White and Lassettre[9] (equation 10.3) and adopting the TIP model (Section 10.4.1). A comparison of experimental and calculated values of the isotope separation factor for the adsorption of an H_2/D_2 mixutre led to an estimate of C=5.15kJ/mole for H_2 adsorbed in ZnA.[4,5]

10.4.4 Vibrational frequencies of adsorbed H_2 calculated from thermodynamic data

In a later, volumetric study of H_2 adsorption in ZnA, Kochurikhin and Zel'venskii[6] showed that the TIP model did not accurately reproduce the experimentally determined entropy of the adsorbate. We recall that in the TIP (and TOP) model, only the τ_y and t_z modes of the admolecule are hindered, those degrees of freedom which would lead to the t_x, t_y and τ_z modes are not perturbed by the surface. Kochurikhin and Zel'venskii[6] showed that the observed differential entropy of H_2 adsorbed in ZnA could be accurately predicted by modifying the TIP model such that the translations of the admolecule in the x- and y-directions became restricted and were replaced by the degenerate vibrations t_x and t_y (Fig. 10.2). It was estimated[6] that the t_x and t_y modes arose at 57 cm^{-1} and the t_z mode at 334 cm^{-1}. Frequencies for the torsional modes were not given. We comment on these predictions in Section 10.6.

10.4.5 The published INS spectra of condensed H_2 and D_2

Egelstaff[16] has published neutron energy gain spectra of solid H_2 at 12K and of liquid H_2 at 15, 18 and 21K, using a maximum incident neutron energy of 40 cm^{-1}. The spectra showed a single inelastic feature, at 125±4 cm^{-1}, corresponding to the transition from the ortho-H_2 to the para-H_2 ground state. These results of Egelstaff[16] are quite dissimilar to our spectra of H_2 adsorbed by ZnNaA (Section 10.5).

The phonon spectra of solid H_2 and D_2 have been reported by Nielsen.[29]

10.5 Results - the INS spectra (10K) of H_2 adsorbed by ZnNaA zeolite

10.5.1 Introduction

The t.o.f. spectra (10 to 210 cm^{-1}) obtained at 10K of H_2 adsorbed by ZnNaA are shown for five scattering angles in Figs. 10.4 (a-e). Background spectra of ZnNaA measured before the adsorption have been subtracted from these data. Fig.10.4(a) shows an intense band at 155 cm^{-1} and a slightly weaker one at 72 cm^{-1}; there being a small variation in frequency with scattering angle (Table 10.3). On increasing the scattering angle, γ, the intensity of both bands decreases, the relative intensity of the 72 cm^{-1} band falling off more rapidly than that of the 155 cm^{-1} band. This is at least partly due to the higher values of the momentum transfer $\hbar Q$ at a given γ for the lower frequency band.

The melting point of H_2 is 14K. That we have not observed transitions of solid H_2 is apparent for the following reasons. In Section 10.5.2 below we argue that since our INS spectra correspond to neutron energy loss, the only transitions which may be observed at 10K are those from the rotational ground state of ortho-H_2. Except at high pressures, the rotational energy levels, E_J, of solid H_2 are given[16] by $E_J = BJ(J+1)$ and the two lowest energy transitions which are observable are:

$J''=1 \longrightarrow J'=2$ $\quad \Delta E = 4B$
$J''=1 \longrightarrow J'=3$ $\quad \Delta E = 10B$

Thus the INS spectrum predicted for solid H_2 bears no resemblance to that observed at 10K from H_2 adsorbed by ZnNaA, which shows bands at *ca* 1.2 and 2.5B (Section 10.5.2).

Figs. 10.4 T.o.f. spectra (10K) of ZnNa-A zeolite plus adsorbed hydrogen, coverage 1.1 molecules per pseudo unit cell. The background spectra of the dehydrated zeolite have been subtracted.

Fig. 10.4a Scattering angle 58.5^0

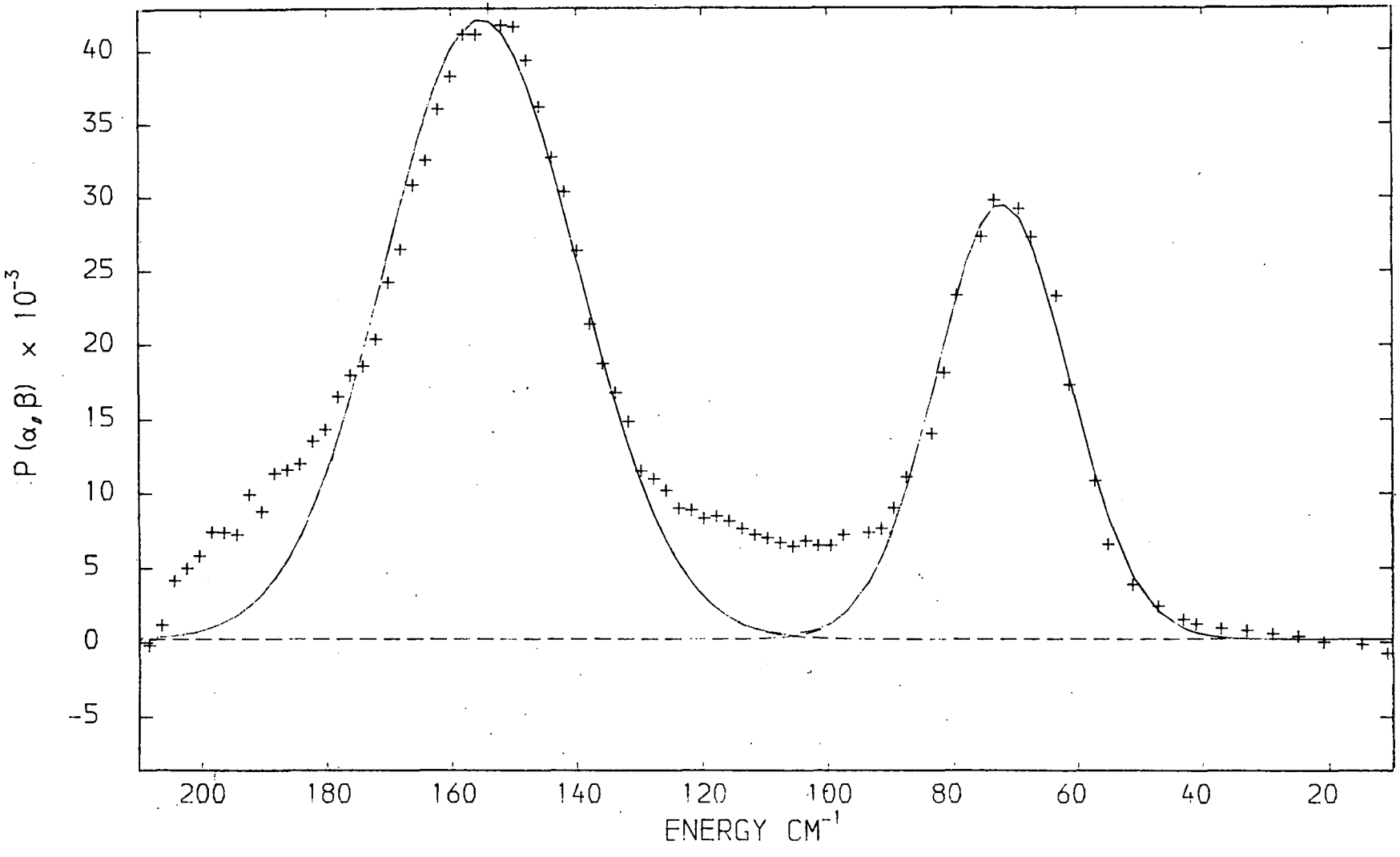

Fig. 10.4b ZnNa-A zeolite plus H_2, background subtracted.
Scattering angle 76.5^0

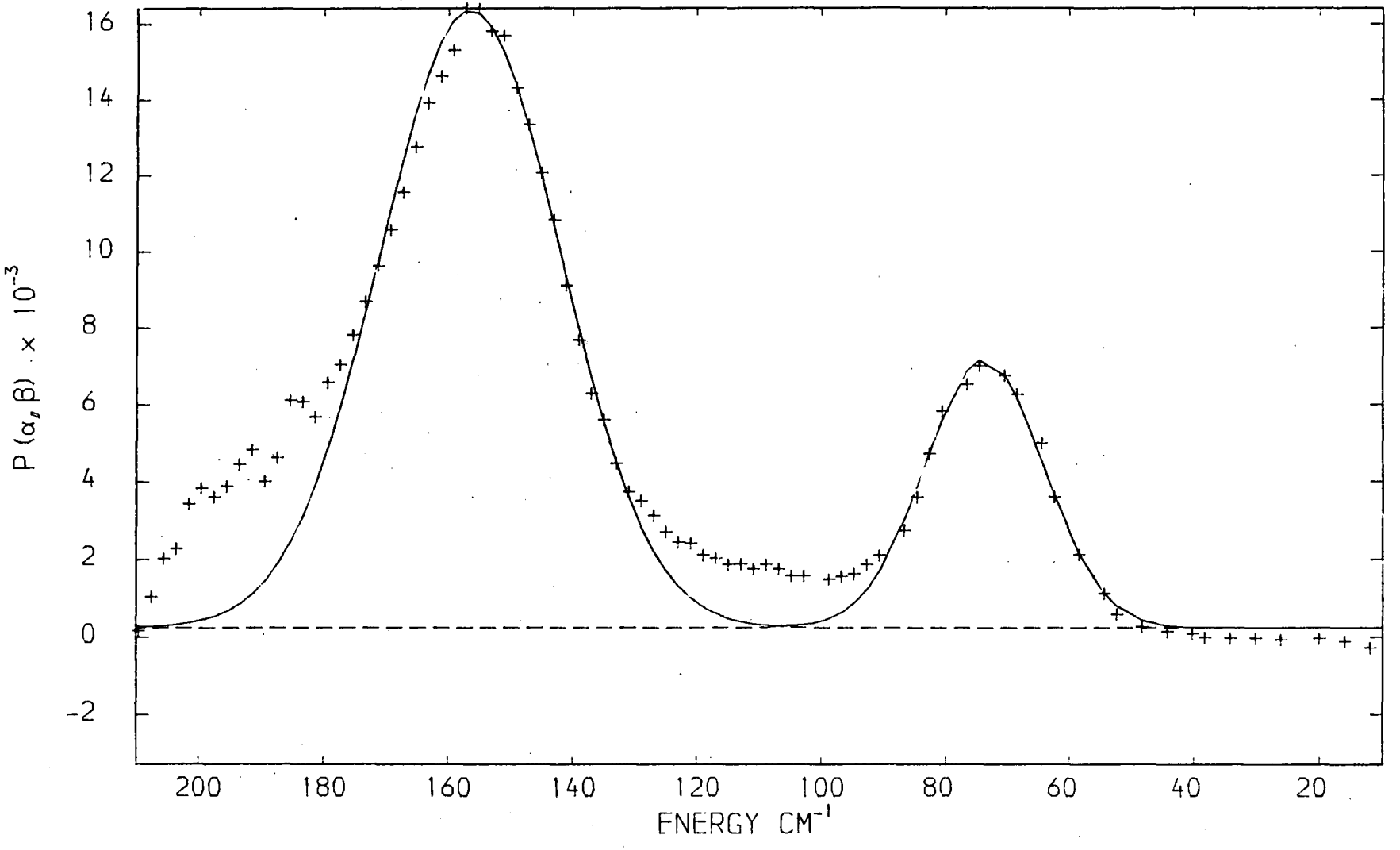

Fig. 10.4c **ZnNa-A zeolite plus H_2, background subtracted.**

Scattering angle 83.3^0

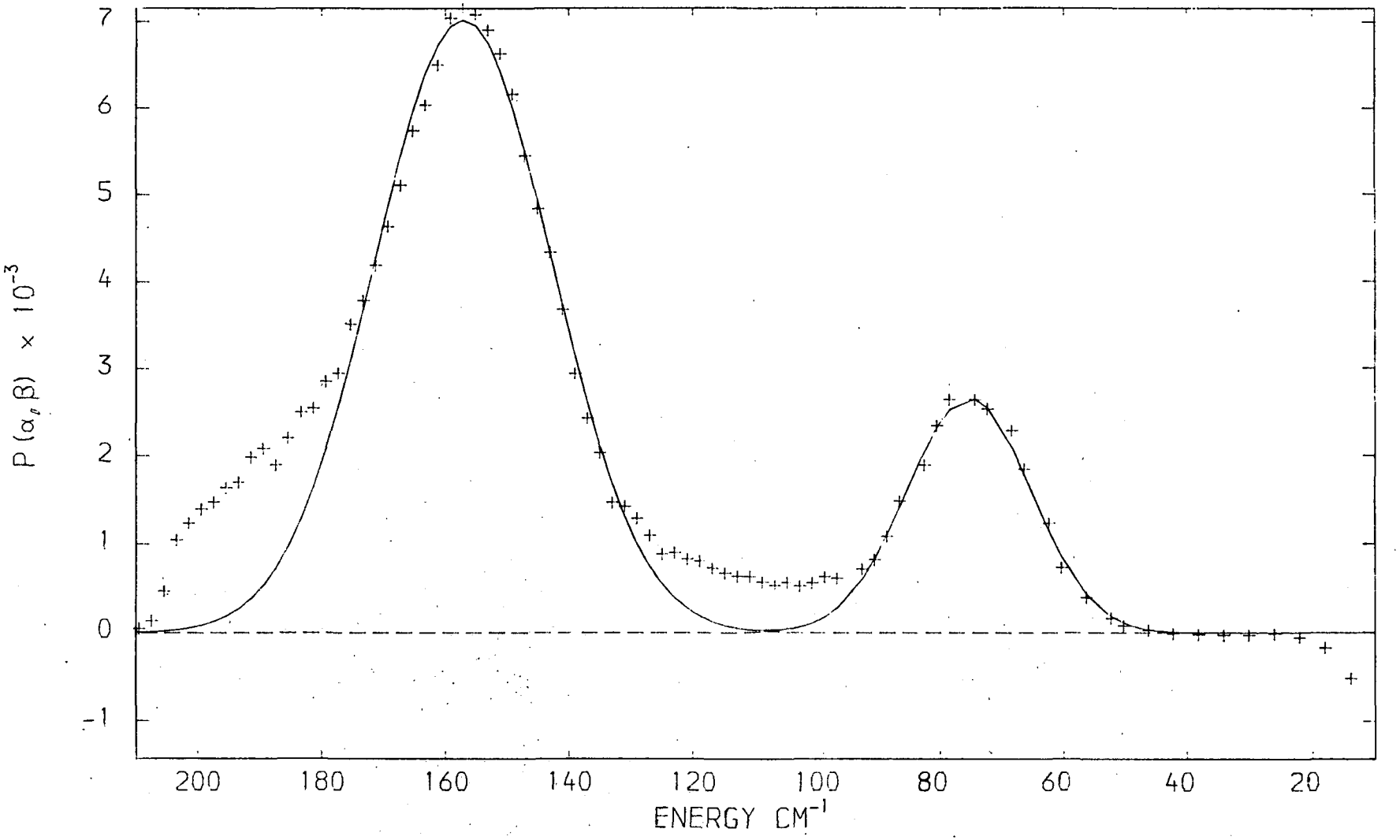

Fig. 10.4d **ZnNa-A** zeolite plus H_2, background subtracted.
Scattering angle 108.0^0

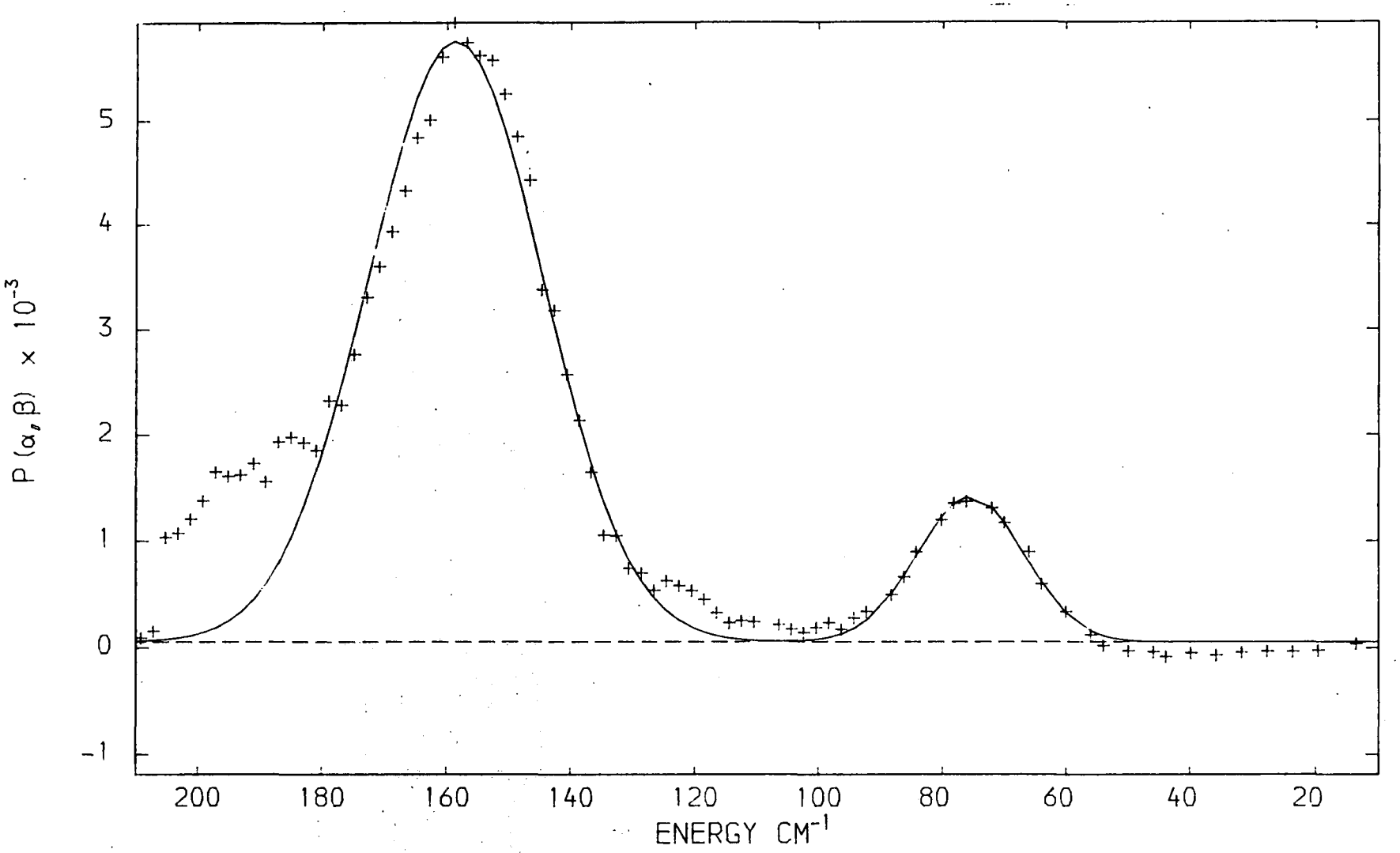

Fig. 10.4e **ZnNa-A** zeolite plus H_2, background subtracted.

Scattering angle 117.0^0

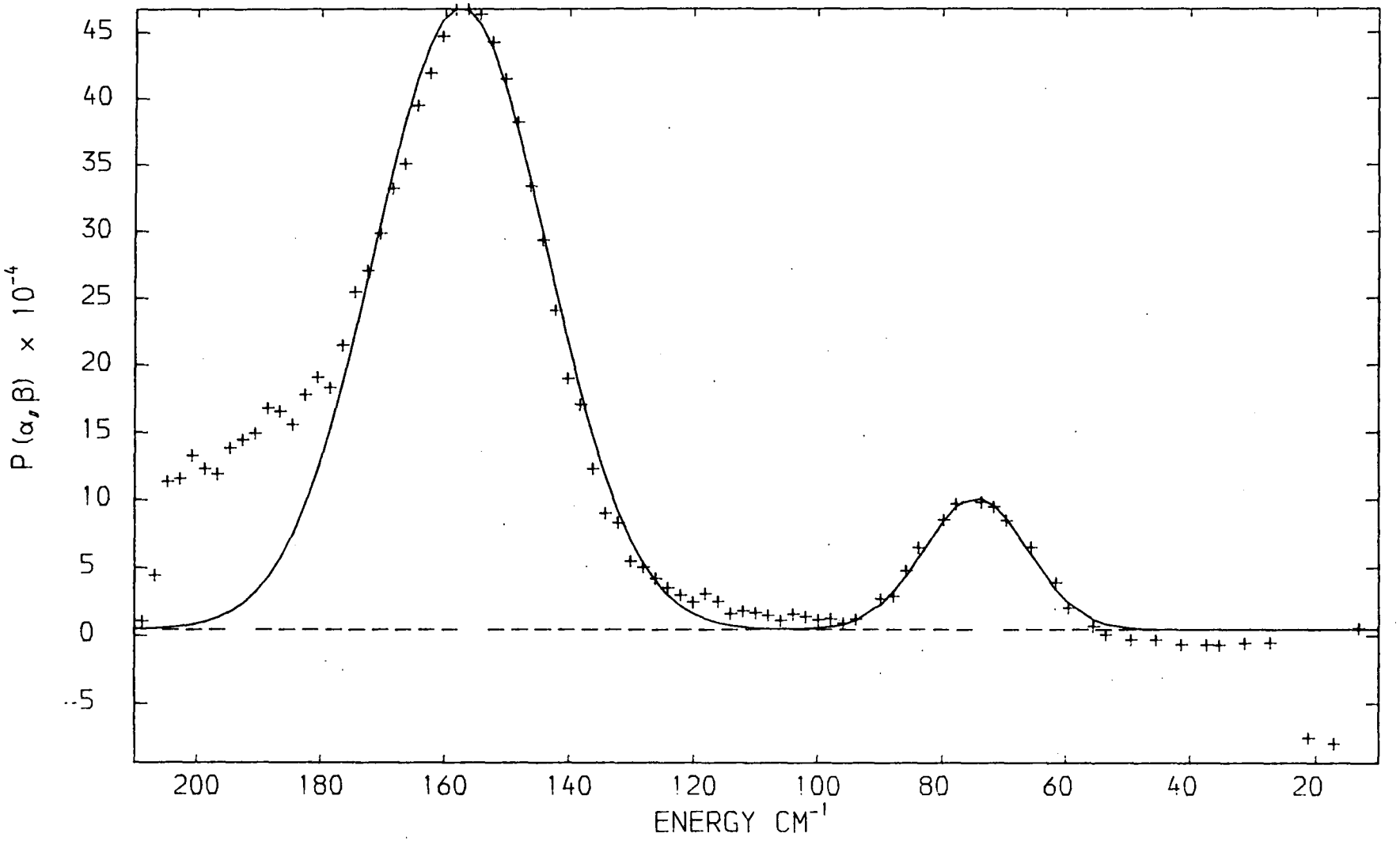

TABLE 10.3 The bands observed in the t.o.f. spectra of H_2 adsorbed by ZnNaA zeolite (LOK)

figure	scattering angle, ^{o}	$\tilde{\nu}$, cm^{-1}	Q^2, $\AA^{-2}$	relative intensity
8.4a	58.5	155 72	11.0 12.5	1.0 0.48
8.4b	76.5	157 74	16.3 19.7	0.36 0.10
8.4c	83.3	157 76	18.5 22.6	0.16 0.04
8.4d	108.0	159 76	26.1 33.2	0.12 0.02
8.4e	117.0	158 75	28.9 37.0	0.10 0.01

Notes:

$\tilde{\nu}$ = band frequency, $\hbar Q$ = momentum transfer during the scattering event

The band frequencies and relative intensities were obtained by fitting Gaussian curves to the spectra (Section 8.5).

Of all the models of adsorbed H_2 discussed in Section 10.4, that due to MacRury and Sams[12] is to be preferred since it is the only one to discuss the perturbation of both rotational degrees of freedom of the admolecule. Unfortunately, the parameters of this model (*ie* λ and 2μ, Section 10.4.1) cannot be uniquely defined from the thermodynamic data available in the literature for any H_2-adsorbent system. The problem is exacerbated when it is considered that the rotational barriers are not necessarily of two-fold multiplicity, and that the separation of the rotational energy levels depends on the barrier multiplicity. Because our INS spectra of ZnNaA/H_2 (Section 10.5.2) give insufficient information to be analysed in terms of the MacRury and Sams model,[12] we interpret our data in terms of a simpler model. As a preliminary analysis, we consider that the INS spectra of ZnNaA/H_2 arise from transitions of a hindered rigid rotor in a plane and neglect any possible interaction between this rotation and the other modes involving the H_2 molecule. In Section 10.6, we suggest additional experiments which might enable the INS spectra of hydrogen adsorbed in zeolites to be analysed in using the MacRury and Sams[12] model.

The work of Kochurikhin and Zel'venskii[6] has shown that H_2 adsorbed or ZnA is localised. If, on that basis, we adopt a model of H_2 adsorbed in ZnNaA such that the H_2 is held by a Zn^{++} cation,

eg.

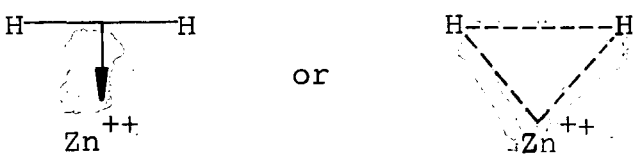

then it is reasonable to describe the Zn^{++}-H_2 system using the theory developed for internal rotation within molecules, in which a rigid symmetric top is attached to a massive, rigid framework.[30,31]

Accordingly, the potential function V(α) describing the ZnNaA-H_2 interaction in the xy-plane may be given by a cosine Fourier series:

$$V(\alpha) = \sum_{n=1}^{\infty} \frac{V_N}{2} (1 - \cos N\alpha) \qquad (10.4)$$

where α is the angular displacement of the H-H rotor from its equilibrium position and N is the barrier multiplicity. As a first approximation, we retain only the first term in the Fourier expansion of V(α). The Hamiltonian operator H for the rigid rotor is then

$$H = \frac{-d^2}{d\alpha^2} + \frac{V_N}{2B} (1-\cos N\alpha) \qquad (10.5)$$

We now consider how the energy levels of the adsorbed H_2 molecule depend on the barrier height, V_N, and multiplicity. If the barrier height is zero, the molecule behaves as a free rotor whose energy levels, E_m, are given by $E_m = m^2B$, where $m = 0, \pm1, \pm2, ---$. The corresponding eigenfunctions ψ_m are given by

$$\psi_m = \frac{1}{\sqrt{2\pi}} \exp(im\alpha) \quad .$$

In the limit of a very high barrier V_N, the molecular motion is restricted to small torsional oscillations and the energy levels, E_ν, are equivalent to those of a harmonic oscillator of force constant $2V_N$:

$$E_\nu = N(V_N B)^{\frac{1}{2}} (\nu + \tfrac{1}{2}) \quad .$$

At intermediate values of V_N, the energy levels of the rotor are obtained by diagonalising the matrix representation of the Hamiltonian operator H. The matrix elements are tabulated by Lister *et al*[32] using exp(imα) as a set of basis functions

(Table 10.4). Part of the matrix representation of H thus constructed for a six-fold rotor is shown in Table 10.5.

TABLE 10.4 The matrix elements associated with the Hamiltonian operator

$$H = \frac{-d^2}{d\alpha^2} + \frac{V_N}{2B}(1-\cos N\alpha), \quad \text{taken from ref.32.}$$

$\langle r\left\|\frac{V_N}{2B}\right\|r\rangle$	=	$\frac{V_N}{2B}$
$\langle r\left\|\frac{V_N}{2B}\right\|s\rangle$	=	0 , $r \neq s$
$\langle r\|\cos N\alpha\|r+N\rangle$	=	$\langle r+N\|\cos N\alpha\|r\rangle = \frac{1}{2}$
$\langle r\|\cos N\alpha\|s\rangle$	=	0 , $r = s\pm N$
$\langle r\left\|\frac{d^2}{d\alpha^2}\right\|r\rangle$	=	$-r^2$
$\langle r\left\|\frac{d^2}{d\alpha^2}\right\|s\rangle$	=	0 , $r \neq s$

Notes:

$\langle r|A|s\rangle$ denotes the contribution of operator A to the (r,s) element of the matrix representation of H.

r=s=zero for the element at the centre of the matrix.

The table was derived[32] for a set of exp(imα) basis functions (m=0,±1,±2,...).

We have written a computer program to diagonalise the matrix representation of the Hamiltonian H and plot the eigenvalues thus obtained as a function of V_N, while holding the barrier multiplicity, N, constant. This procedure was carried out for N=2,3,6,9 and 12. A multiplicity of 2 was considered

TABLE 10.5 The central portion of the matrix representation of the Hamiltonian H of a plane rotor in a 6-fold potential well

$$H = -d^2/d\alpha^2 + (V_6/2B).(1-\cos 6\alpha)$$

-6	-5	-4	-4	-2	-1	0	1	2	3	4	5	6	r / s
36+x						$-\frac{x}{2}$							-6
	25+x						$-\frac{x}{2}$						-5
		16+x						$-\frac{x}{2}$					-4
			9+x						$-\frac{x}{2}$				-3
				4+x						$-\frac{x}{2}$			-2
					1+x						$-\frac{x}{2}$		-1
$-\frac{x}{2}$						x						$-\frac{x}{2}$	0
	$-\frac{x}{2}$						1+x						1
		$-\frac{x}{2}$						4+x					2
			$-\frac{x}{2}$						9+x				3
				$-\frac{x}{2}$						16+x			4
					$-\frac{x}{2}$						25+x		5
						$-\frac{x}{2}$						36+x	6

Notes: $x = (V_6/2B)$. The matrix elements are labelled by the indices r and s, for the central element, r = s=zero. The matrix elements left blank in this table are equal to zero.

was considered because H_2 is diatomic; multiples of 3 were considered because the Zn^{++} cations are associated with three oxygen atoms of the zeolite 6-oxygen rings. As the size of the (nxn) Hamiltonian matrix (*eg* Table 10.5) is increased, the evaluation of the eigenvalues of the rotor becomes more accurate. However, the computing time needed for the matrix diagonalisation increases with n^3. We have found that the plots of the eigenvalues against V_N calculated from a (25x25) Hamiltonian matrix are identical to those obtained from a (50x50) matrix and it is the latter which are presented in this chapter. These computer generated plots will be discussed in detail below.

In Figure 10.5 we show a generalised diagram (for N=6) of the variation of energy levels of the 2-D rigid rotor with V_N. On decreasing the barrier height from the torsional oscillator limit, the energy levels of the rotor are seen to split into sublevels. For an N-fold barrier there will be (N+1)/2 distinct sublevels from each torsional level for odd N and (N+2)/2 levels for even N. As V_N approaches zero, the sublevels approach the energy levels of a free 2-D rotor, which are independent of N. The diagonal, dashed line (Figure 10.5) represents the magnitude of the rotational barrier, V_N. Transitions between the torsional sublevels may be regarded as tunnelling transitions between equivalent potential minima.[33]

The wavefunctions associated with the torsional sublevels of an N-fold barrier have[34] the symmetries of the irreducible representations of the rotational point group C_N. Thus the torsional sublevels for a 2-fold rotor are all singly degenerate, the wavefunctions transforming as A or B species of the C_2 group.

Fig. 10.5 Schematic diagram to show the variation with barrier height V_6 of the energy levels of a rotor in a 6-fold potential well. The variation with V_6 has been drawn as linear for simplicity only, more accurate representations are shown in figs. 10.6 to 10.10.

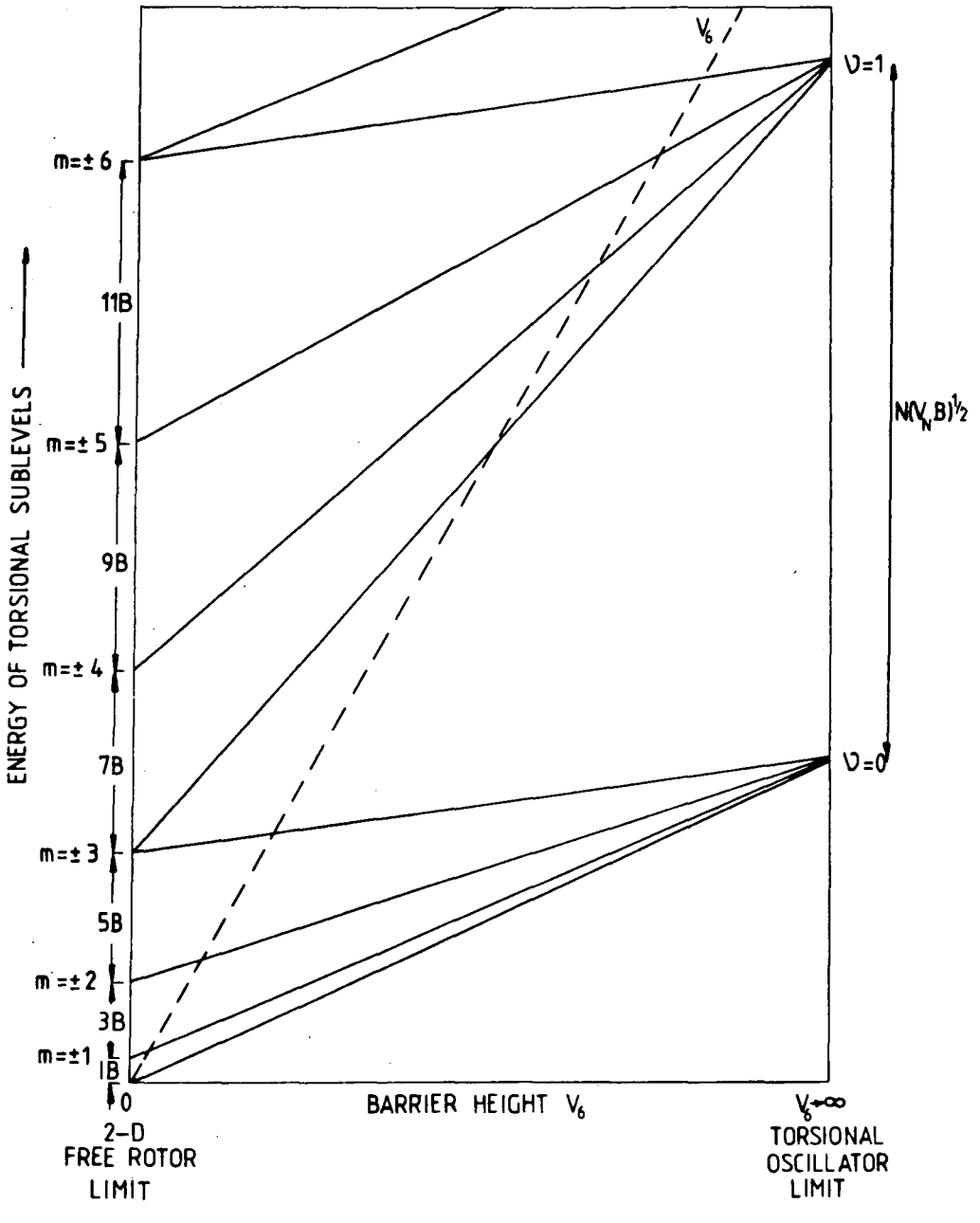

The torsional quantum number is given by υ and the free rotor quantum number by m

For higher barrier multiplicities, N>2, the torsional sub-levels are either singly or doubly degenerate and are labelled accordingly in Figures 10.6-10.10.

10.5.2 Assignment of the INS spectra of H_2 adsorbed by ZnNaA zeolite

As was shown in Chapter Two, para-H_2 has a zero incoherent inelastic neutron scattering cross section, σ_{inc}. For scattering from ortho-H_2, the value of σ_{inc} for spin flipping of the neutron and scattering molecule is twice that for non spin flipping. We assume that only the lowest rotational energy level of ortho-H_2 (*ie* the m=±1 state) and of para-H_2 (m=0) will be appreciably populated by the adsorbed H_2 in our ZnNaA samples at 10K. The value of k_BT at 10K is 83.1 J/mole or 6.95 cm^{-1}, where k_B is Boltzmann's constant.

Since the t.o.f. spectra of ZnNaA/H_2 (*eg* Fig. 10.4(a)) correspond to neutron energy loss and there is no evidence of any transition below 72 cm^{-1}, the two observed INS bands correspond within our model of adsorbed H_2 to the transitions thus:

$m'' = \pm 1 \longrightarrow m' = \pm 2$ $\quad \Delta E = 72\ cm^{-1} = 1.2B$ (spin flip)

$m'' = \pm 1 \longrightarrow m' = \pm 3$ $\quad \Delta E = 155\ cm^{-1} = 2.5B$ (non spin flip)

where B (taken to be 60.809 cm^{-1}, Section 10.1) is the rotational constant of adsorbed H_2. Turning to the plot of the calculated eigenvalues of the H_2 rotor against barrier height, V_2, for a 2-fold potential well (Figure 10.6), it can be seen that there are no values of V_2 for which the $m''=\pm1 \rightarrow m'=\pm2$ and $m''=\pm1 \rightarrow m'=\pm3$ transitions can be observed at *ca* 1.2B and 2.5B respectively. This is also true of the 3-fold potential barrier (Figure 10.7).

Fig. 10.6 The variation of the energies of the torsional sublevels of a rigid rotor in a 2-fold potential well. The axes are in units of the rotational constant, B, of the adsorbate. The dashed line represents the height of the barrier to rotation, V_2.

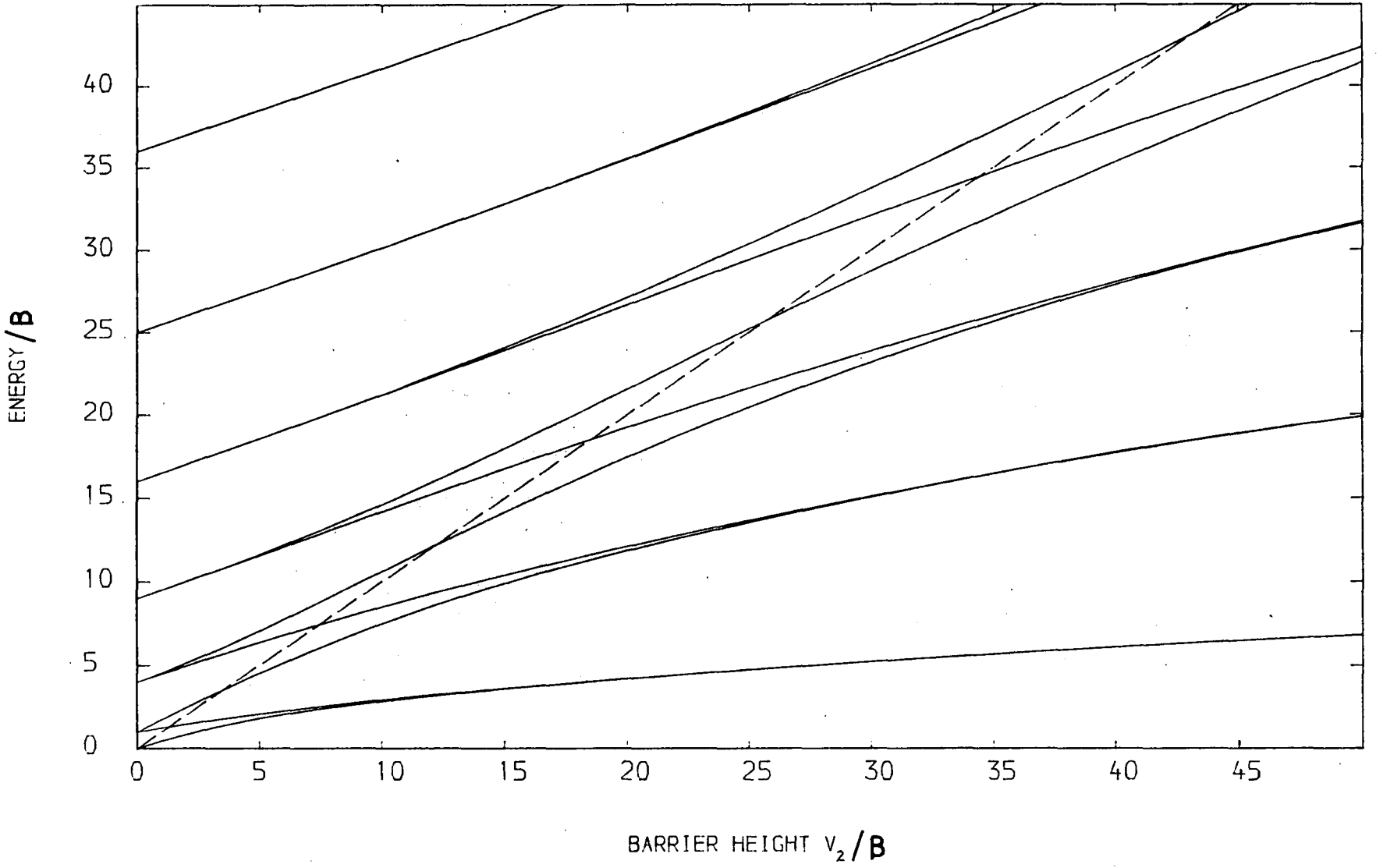

Fig. 10.7 The variation of the energies of the torsional sublevels of a rigid rotor in a 3-fold potential well. The axes are in units of the rotational constant, B, of the adsorbate. The dashed line represents the height of the barrier to rotation, V_3.

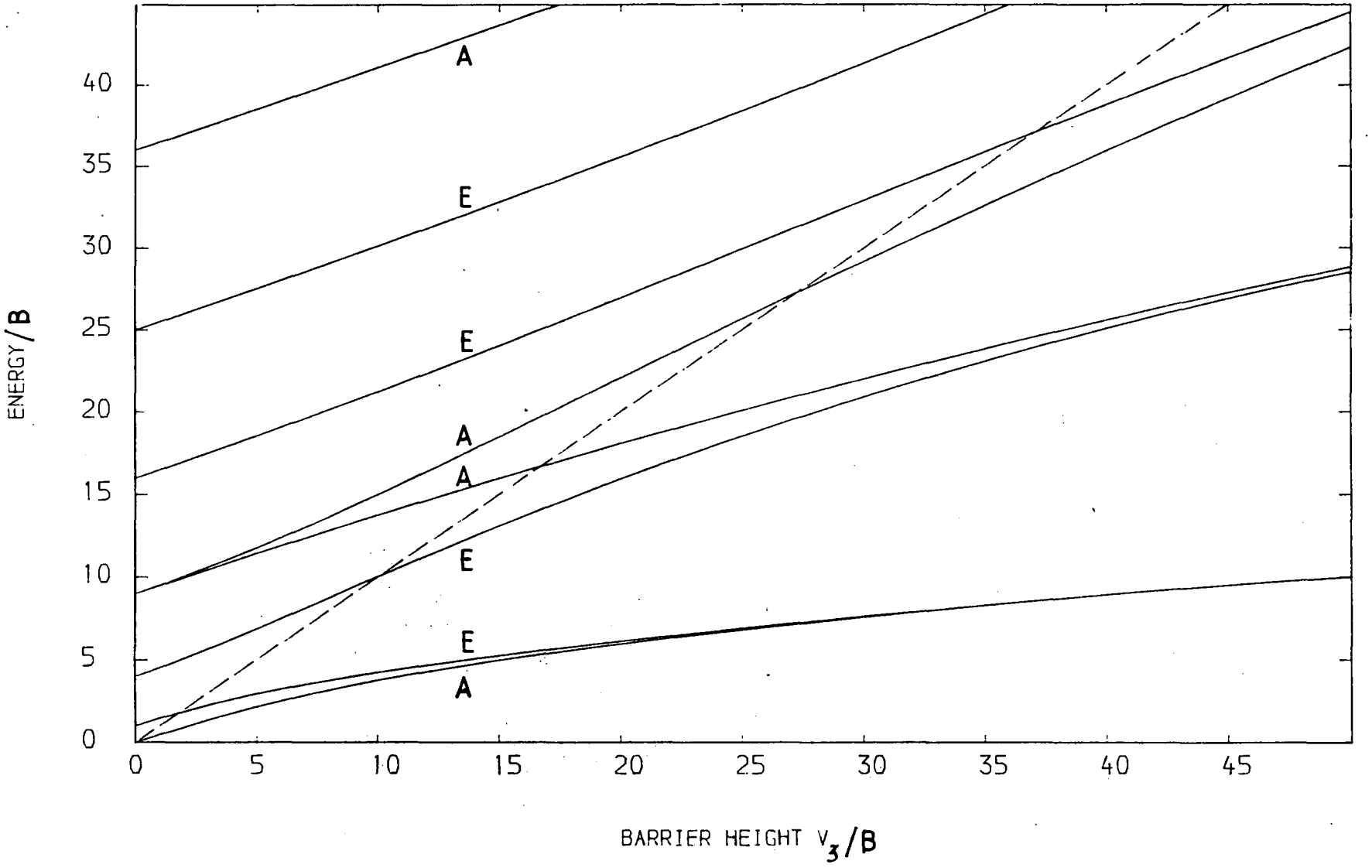

For a 6-fold barrier, although there is no single value of V_6 for which the calculated separations of the two transitions are exactly as observed in the t.o.f. spectra (Figure 10.4), Figure 10.8 shows that there is a range of V_6 values for which the calculated splittings of the torsional sublevels in approximate agreement with experiment. This range is $34B \lesssim V_6 \lesssim 43B$. Thus for V_6=34B, the transitions are predicted from Figure 10.8 to be of energy

$m'' = \pm 1 \rightarrow m' = \pm 2$, ΔE = 1.6B (observed value 1.2B)

$m'' = \pm 1 \rightarrow m' = \pm 3$, ΔE = 2.5B (observed value 2.5B)

and for V_6 = 43B the transitions are predicted to occur at 1.2B and 2.0B. The 72 and 155 cm^{-1} bands in the ZnNaA/H_2 spectra (Figures 10.4) are therefore respectively assigned to transitions between the $E_1 \rightarrow E_2$ and $E_1 \rightarrow B$ sublevels of the torsional ground state of H_2 in a 6-fold potential well. That there is no exact agreement between the calculated and observed transition energies is to be expected. Thus far we have treated the adsorbed H_2 molecule as if it were in the gas phase, *eg* no allowance has been made for the likely increase in H-H bond length and the concomitant lowering of the value of B on adsorption. Somewhat more significant improvements to our model of adsorbed H_2 are proposed in Section 10.6.

Turning to the plots of E_m against V_9 and V_{12} (Figures 10.9, 10.10), it is seen that for all values of V_9 and V_{12} below 50B, the calculated splittings m(1→2) and m(1→3) are considerably greater than the observed values. Although the sublevels of the ground torsional state for both a 9-fold and a 12-fold barrier approach each other in energy as V_9 and V_{12} are increased (Figures 10.9, 10.10) the calculated transitions

Fig. 10.8 The variation of the energies of the torsional sublevels of a rigid rotor in a 6-fold potential well. The heights of the transitions $E_1 \rightarrow E_2$ and $E_1 \rightarrow B$ of the torsional ground state are shown for $V_6 = 34B$ and $V_6 = 43B$. The axes are in units of the rotational constant, B, of the adsorbate. The dashed line represents the height of the barrier to rotation, V_6.

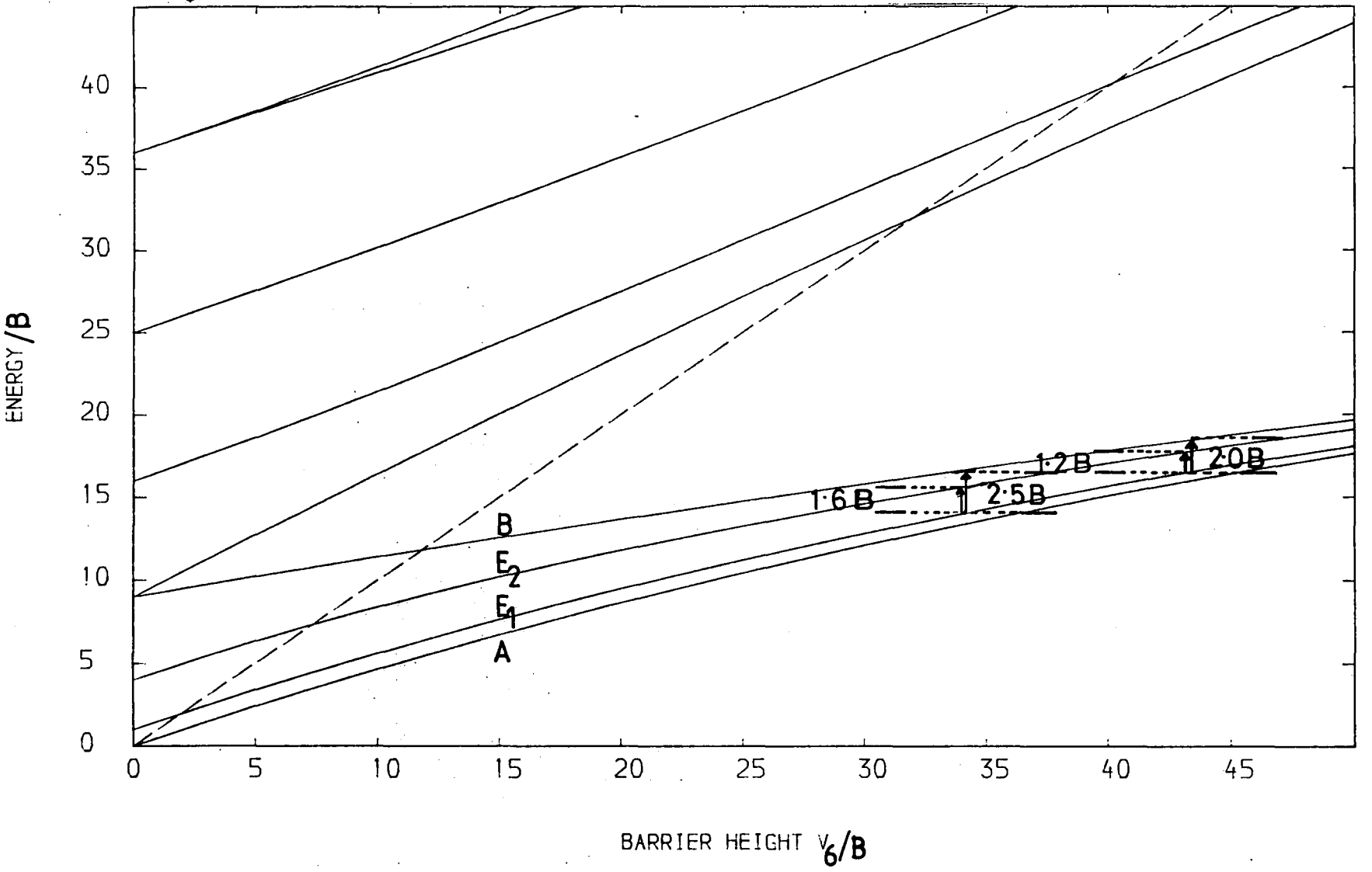

Fig. 10.9 The variation of the energies of the torsional sublevels of a rigid rotor in a 9-fold potential well. The axes are in units of the rotational constant, B, of the adsorbate. The dashed line represents the height of the barrier to rotation, V_9.

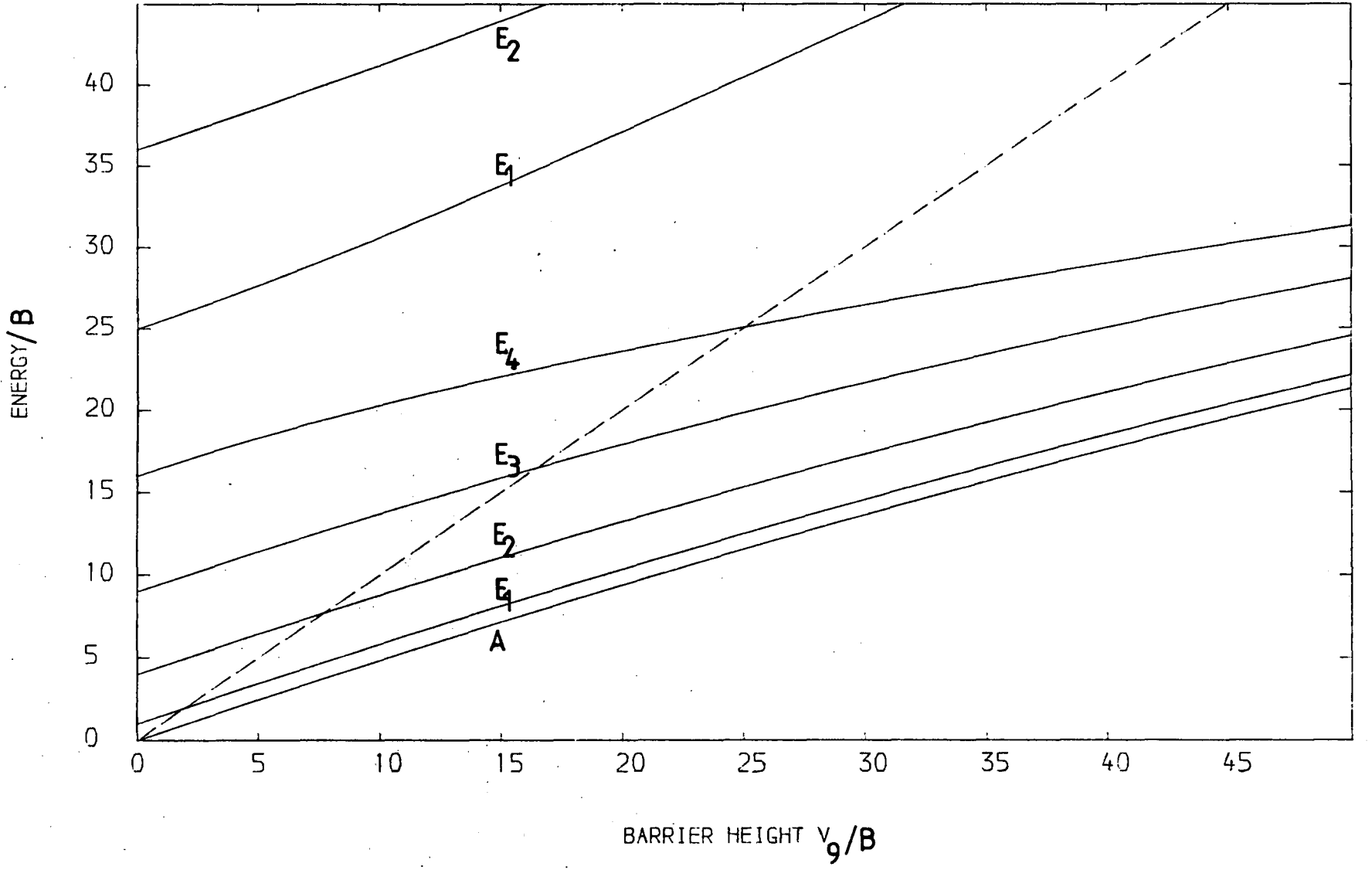

Fig. 10.10 The variation of the energies of the torsional sublevels of a rigid rotor in a 12-fold potential well. The axes are in units of the rotational constant, B, of the adsorbate. The dashed line represents the height of the barrier to rotation, V_{12}.

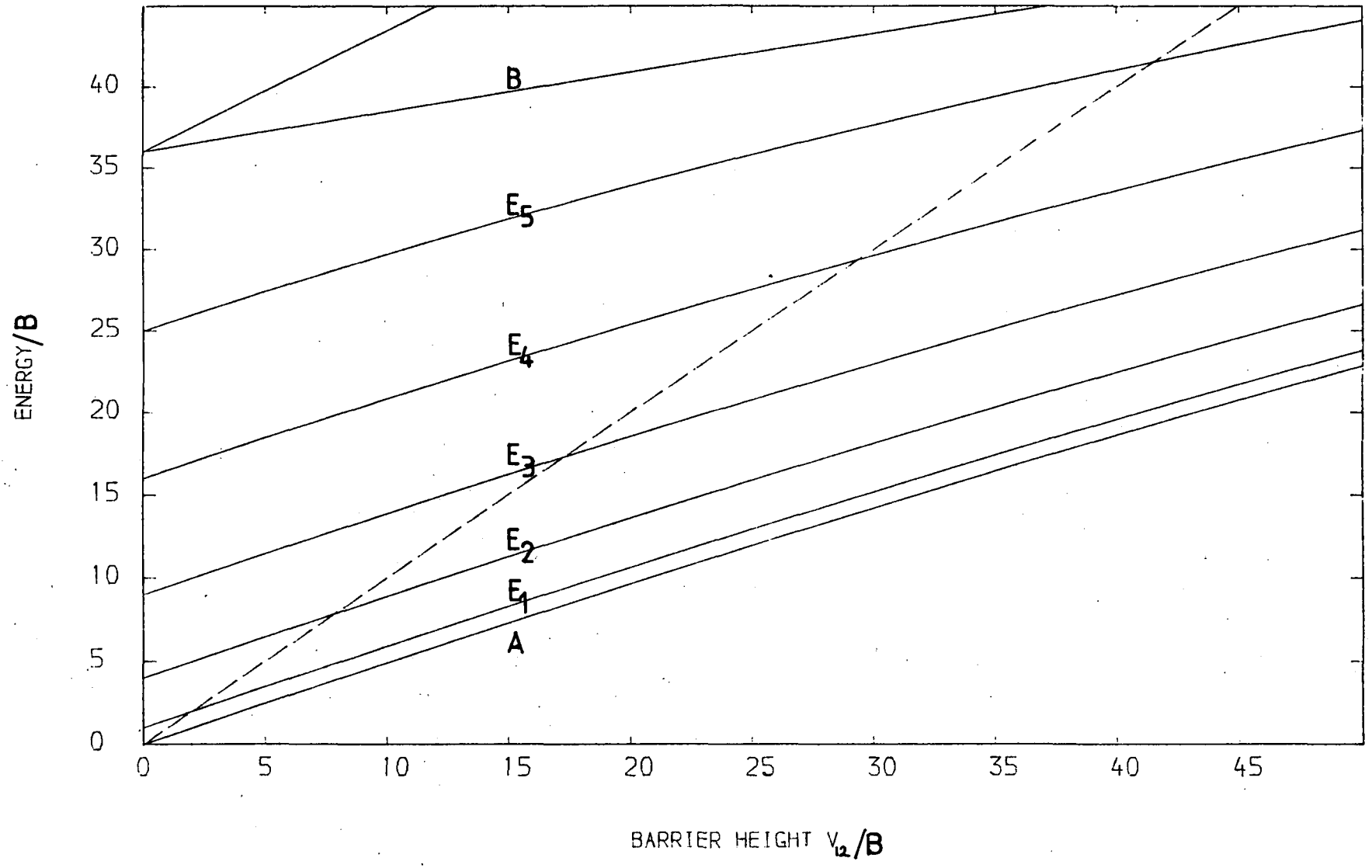

do not approximate the observed values until unreasonably large values (>50B) of V_9 and V_{12} are reached. Thus we discard the possibility that the adsorbed H_2 molecules in ZnNaA are held in a 9-fold or 12-fold potential well. We note that the calculated eigenvalues E_m change only very slowly with barrier height V_N for high barrier multiplicities (*ie* N = 9 or 12). Thus our graphical method for determining V_N is the more accurate the lower the barrier multiplicity.

To summarise: by discussing the INS spectra of H_2 adsorbed in ZnNaA (Figures 10.4) in terms of a rigid rotor confined to a plane, we have predicted a 6-fold barrier to rotation of the adsorbate of height *ca* $34B \lesssim V_6 \lesssim 43B$. The fact that the barrier is 6-fold is more consistent with rotation in the *xy*-plane than rotation perpendicular to the zeolite surface (Figure 10.2). In the latter case, a 2-fold or non-periodic well might be expected.

10.5.3 An alternative calculation of the barrier height V_6

Having obtained the barrier multiplicity, we can attempt to calculate more accurately the height of the barrier to rotation of H_2 adsorbed by ZnNaA using the method due to Herschbach [33,34].

Using the Hamiltonian of equation 10.5, the Schrodinger equation for the adsorbed H_2 molecule becomes

$$B \frac{d^2\psi(\alpha)}{d\alpha^2} + [E - \frac{V_N}{2}(1 \pm \cos N\alpha)]\psi(\alpha) = 0 \qquad (10.6)$$

It has been shown[33] that equation 10.6 is of similar form to the Mathieu equation 10.7:

$$\frac{d^2y}{dx^2} + (b - s\cos^2 x)y = 0 \qquad (10.7)$$

where b is an eigenvalue and s is a parameter. The two equations, 10.6 and 10.7, may be transformed into one another using the substitutions[33]

$$\psi(\alpha) = y$$

$$N\alpha + \pi = 2x$$

$$4V_N = N^2 Bs \qquad (10.8)$$

$$4E = N^2 Bb. \qquad (10.9)$$

Using a result from the work of Kohler and Dennison,[35] Herschbach[33] has shown that the Mathieu eigenvalues b_z may be expressed as a Fourier series:

$$b_z = \sum_{l=0}^{\infty} \omega_l \cos(\phi - \phi_o), \quad z=1,2,3--- \qquad (10.10)$$

The eigenvalues b_1, b_2, b_3, --- correspond to solutions of the Mathieu equation (10.7) of period π, 2π, 3π, ... in x and the subscript z in equation 10.10 is used as an index for this periodicity. The values of ϕ and ϕ_o in equation 10.10 depend on z. After Herschbach[33,34] we have, for $z \neq 1$, that $\phi=0$ and $\phi_o=2\pi/z$, and for $z=0$ we have $\phi=0=\phi_o$.

From equation 10.9, the transition energy E between the torsional sublevels b'' and b' of a given torsional level is:

$$\Delta E = \frac{N^2}{4} B (b'-b'') \qquad (10.11)$$

In equation 10.10, the coefficients ω_l depend only on the torsional level, ν, and the barrier parameter s defined by equation 10.8. Herschbach has published[33] tables of ω_l against s for a given ν. From these tables and equation 10.11, a value of s for H_2 adsorbed by ZnNaA is obtained from the observed transition energies (Figures 10.4) using the expressions below for b´´ and b´. Hence from equation 10.8 the barrier height, V_6, to rotation of the adsorbed H_2 molecule may be calculated.

The eigenvalues b_z appropriate[33,34] to the sublevels of the torsional ground state (ν=0) of a 6-fold rotor are listed in Table 10.6. Starting from equation 10.10, Herschbach[33] obtained:

$$b_2 = \omega_o - \omega_1 + \omega_2 - \omega_3 + \omega_4 - \quad \ldots \quad , \text{ and}$$

$$b_3 = \omega_o - \frac{\omega_1}{2} - \frac{\omega_2}{2} + \omega_3 - \frac{\omega_4}{2} - \quad \ldots \quad , \text{ and we obtain}$$

$$b_6 = \omega_o + \frac{\omega_1}{2} - \frac{\omega_2}{2} - \omega_3 - \frac{\omega_4}{2} + \quad \ldots$$

TABLE 10.6 The eigenvalues b_z of the sublevels of the torsional ground state of a 6-fold rotor, taken from ref. 34.

symmetry of sublevel (C_6 point group)	ϕ_o	b_z
A	0	b_1
E_1	$\pm\pi/3$	b_6
E_2	$\pm 2\pi/3$	b_3
B	$\pm\pi$	b_2

ϕ_o and b_z are related *via* equation 10.10.

The 155 cm^{-1} band of our t.o.f. spectra of H_2 adsorbed by ZnNaA (Figure 10.4) was assigned to the transition between the $E_1 \rightarrow B$ sublevels of the ground torsional state of a 6-fold rotor (Section 10.5.2). Thus for this transition, equation 10.11 gives

$$\Delta E_{E_1 \rightarrow B} = 9B(b_2 - b_6) \qquad (10.12)$$

The tabulated values[33] of ω_l with $l>0$ vanish rapidly, especially for large S, and retaining only the terms up to ω_4 in equation 10.12 we have

$$\Delta E_{E_1 \rightarrow B} = \frac{27B}{2}[-\omega_1 + \omega_2 + \omega_4]$$

Similarly, the 72 cm^{-1} band of the $ZnNaA/H_2$ spectra (Figure 10.4) was assigned to the $E_1 \rightarrow E_2$ transition, for which

$$\Delta E_{E_1 \rightarrow E_2} = 9B(b_3 - b_6)$$
$$= 9B(-\omega_1 + 2\omega_3)$$

discarding terms in ω_l for which $l>4$.

The Herschbach tables of s against the ω_l are published[33] for even integral values of s only. Following the prescription of Herschbach,[33] we have obtained values of ω_l for non-integral 's from the interpolation of plots of $\log_{10}\omega_l$ against s for each l. From such plots and using a value of B=60.809 cm^{-1} (the gas phase value for H_2), we obtain a value of the barrier parameter s of 4.9 for the $E_1 \rightarrow E_2$ transition and s=3.9 for the $E_1 \rightarrow B$ transition. The corresponding barrier heights, V_6, are 44B(32kJ $mole^{-1}$) and 35B(26kJ $mole^{-1}$) respectively. These values of V_6 are consistent with the range of *ca* $34B \lesssim V_6 \lesssim 43B$ estimated from the graphical method of Section 10.5.2. However, a more realistic model of the adsorbed H_2 would predict the same barrier height for both transitions. The model could be

improved by including higher order terms, V_{12}, V_{18}, *etc*, in the Fourier expansion of the adsorbent-adsorbate potential function (equation 10.4). A variation in the value of the rotational constant B between the torsional sublevels could also be considered, although this is likely to be a small effect. We comment on the magnitude of our estimates of V_6 in Section 10.6, taking an average of the values obtained *via* the Herschbach method[33] of 29±3kJ/mole.

10.5.4 The ortho-para separation factor of H_2 adsorbed by ZnNaA

If the translational, vibrational and rotational degrees of freedom are independent and if the rotational motion in the xy-plane is the only mode of adsorbed H_2 which is significantly perturbed by the surface, then the separation factor may be expressed as:[13]

$$F = \frac{\{q(\text{para-}H_2)/q(\text{ortho-}H_2)\}_{\text{gas phase}}}{\{q(\text{para-}H_2)/q(\text{ortho-}H_2)\}_{\text{adsorbed phase}}}$$

The q are molecular rotational partition functions, given by

$$q = \sum_i g_i \exp(-e_i/k_BT)$$

where g_i is the degeneracy and e_i is the energy of the i^{th} rotational level of the appropriate nuclear spin state, e_i being measured from the ground state of para-H_2.

At 20.4K, only the ground states of ortho- and para-H_2 are significantly populated, both in the free gas and the adsorbed phase. Thus for the gas phase:

$$\frac{q(\text{para-}H_2)}{q(\text{ortho-}H_2)} = \frac{1}{(2I+1)(2J+1)\exp(-B/k_BT)}$$

and for the adsorbed phase:

$$\frac{q(\text{para-}H_2)}{q(\text{ortho-}H_2)} = \frac{1}{2(2I+1)\exp(-e_1/k_BT)}$$

where I=J=1 and e_1 is the energy separation between the ground states of adsorbed ortho- and para-H_2. For ZnNaA/H_2 we have from Figure 10.8 that e_1 = 43 cm^{-1} for V_6 = 34B and e_1 = 34 cm^{-1} for V_6 = 43B and thus we calculate the separation factor for ZnNaA/H_2 at 20.4K to be in the range 2.4 (for V_6=34B) to 4.3 (for V_6=43B). These values are comparable with that of F=4.8 calculated by MacRury and Sams[13] from the data of Cunningham *et al*[19] for H_2 on undoped Al_2O_3 at 20.4K. However, our model predicts that F decreases with increasing barrier height, which is incorrect. This is most likely due to our neglect of the effect of the out-of-plane rotation on the energy levels of the admolecule.

10.6 Discussion - suggestions for future work

The value of 29±3kJ/mole which we obtained in Section 10.5.3 for the barrier height, V_N, to the τ_z rotation of H_2 adsorbed by ZnNaA is considerably larger than that of 5.15kJ/mole published by Kochurikhin and Zel'venskii[6] for the τ_y rotation of H_2 adsorbed in ZnA (the τ_z mode was assumed to be unhindered by the latter workers). Our value of V_N is also inconsistent with the much smaller isosteric heat of adsorption of H_2 on ZnA of 8.2kJ/mole at low coverage measured by the Russian workers.[6]

The values of the barrier height to rotation are strongly dependent on the model of the adsorbate. The major deficiency of our model is the neglect of any hindrance to the rotation of the admolecule out of the *xy*-plane (Figure 10.2). Incorporating such a barrier in the model would possibly lead to the prediction of a lower barrier height V_N for the in-plane rotation (τ_z mode). The additional data obtainable from experiments (1) to (3) proposed below are expected to be sufficient for the INS spectra of $ZnNaA/H_2$ to be analysed along the lines of the MacRury and Sams model,[12] which includes barriers to rotation of both rotational modes. The following experiments are proposed:

1. recording the neutron energy loss spectra of $ZnNaA/H_2$ at 10K over a frequency range wider than the 10 to 210 cm^{-1} span of the present results (Figure 10.4). This would require the use of several neutron spectrometers. In the present model, no inelastic features are expected below 10 cm^{-1} although transitions due to the τ_y torsion and t_x, t_y and t_z vibrations are expected above *ca* 210 cm^{-1};

2. measuring the neutron energy <u>gain</u> spectrum of $ZnNaA/H_2$. Our model predicts that the sptrum at 10K would show a band due to the transition from the E_1(ortho-H_2) to the A(para-H_2) sublevels of the torsional ground state of adsorbed H_2 (see Figure 10.8). At a temperature sufficiently above 10K, the 6-fold model predicts that the B(ortho-H_2)→A, B→E_1 and B→E_2 transitions would be observed;

3. repeating (1) and (2) above for adsorbed D_2. Deuterons obey Bose-Einstein statistics and the effect of the nuclear spins on the rotational spectrum of D_2 differs to that observed

for H_2. Deuterium exists in singlet, triplet and quintet nuclear spin states; the singlet and quintet states both occupy rotational states of even J and are collectively called ortho-D_2, while the triplet state, para-D_2, occupies the odd J rotational levels.[14] At all attainable temperatures the three spin states of D_2 exist in equal proportions.[14] From Chapter Two, only the triplet and quintet states have a non-zero incoherent inelastic neutron scattering cross section. Thus transitions from both ortho-D_2 and para-D_2 are predicted to be observed in the INS spectrum of ZnNaA/D_2. Having corrected for the difference in zero point energies, these transitions should be consistent with the same values of the barrier heights to rotation as derived for adsorbed H_2;

4. The splitting of the rotational energy levels of adsorbed H_2 is a function of the adsorbent-H_2 interaction which could be investigated by recording the INS spectra of H_2 adsorbed in a series of partially exchanged $M^{++}Na^{+}$ A zeolites (where M is a first row transition metal).

From thermodynamic data, Kochurikhin and Zel'venskii[6] have predicted frequencies of 57 cm^{-1} (t_x and t_y modes) and 334 cm^{-1} (t_z mode) for H_2 adsorbed by ZnA zeolite. Given the approxmations made by Kochurikhin and Zel'venskii, the value of 57 cm^{-1} is close to that of 72 cm^{-1} observed in our INS spectra of ZnNaA/H_2. We have, however, assigned the 72 cm^{-1} band to a rotational (τ_z) rather than a translational transition. Our assignment would be tested by obtaining the deuteration shift of the 72 cm^{-1} band.

REFERENCES

1. Vaughan, D.E.W. in The Properties and Applications of Zeolites, (Ed.Townsend, R.P.) The Chemical Society, London, 1980.

2. Fraenkel, D. and Shabtai, J., J.Am.Chem.Soc., 99,7074, 1977.

3. Kochurikhin, V.E. and Zel'venskii, Ya.D., Russ.J.Phys.Chem., 38, 1408, 1964.

4. Kochurikhin, V.E. and Zel'venskii, Ya.D., Russ.J.Phys.Chem., 42, 775, 1968.

5. Kochurikhin, V.E. and Zel'venskii, Ya.D., Russ.J.Phys.Chem., 43, 109, 1969.

6. Kochurikhin, V.E. and Zel'venskii, Ya.D., Russ.J.Phys.Chem., 45, 510, 1971.

7. Herzberg, G., Molecular Spectra and Molecular Structure 1. Spectra of Diatomic Molecules, Van Nostrand,New York,1950.

8. Sandler, Y.L., J.Phys.Chem., 58, 58, 1964.

9. White, D. and Lassettre, E.N., J.Chem.Phys., 32, 72, 1960.

10. Evett, A.A., J.Chem.Phys., 31, 565, 1959.

11. Evett, A.A., J.Chem.Phys., 33, 789, 1960.

12. MacRury, T.B. and Sams, J.R., Mol.Phys., 19, 337, 1970.

13. MacRury, T.B. and Sams, J.R., Mol.Phys., 20, 57, 1971.

14. Pauling, E. and Wilson, E.B.,Jr., Introduction to Quantum Mechanics, MacGraw Hill, New York, 1935.

15. Atkins, P.W., Molecular Quantum Mechanics, Clarendon Press, Oxford, 1970.

16. Egelstaff, P.A., Haywood, B.C. and Webb, F.J., Proc.Phys.Soc., 90, 681, 1967.

17. Larsen, A.H., Simon, F.E. and Swenson, C.A., Rev.Sci. Instrum., 19, 226, 1948.

18. Cunningham, C.M. and Johnston, H.L., J.Am.Chem.Soc., 80, 2377, 1958.

19. Cunningham, C.M., Chapin, D.S. and Johnston, H.L., J.Am. Chem.Soc., 80, 2382, 1958.

20. Bonhoeffer, K.F. and Harteck, P., Z.Phys.Chem., B4, 113, 1929.

21. Basmadjan, D., Canad.J.Chem., 38, 141, 1960.

22. Elliot, R.J. and Hartmann, W.M., Proc.Phys.Soc.,90, 671, 1967.

23. Kim, Y. and Seff, K., J.Phys.Chem., 84, 2823, 1980.

24. Raghavan, N.V. and Seff, K., J.Phys.Chem., 80, 2133, 1976.

25. McCusker, L.B. and Seff, K., J.Phys.Chem., 85, 405, 1981.

26. Kadir, Z.A., Ph.D. Thesis, University of Durham, 1983.

27. British Drug Houses Laboratory Chemicals and Biochemicals Catalogue 1983, BDH, Poole, 1983.

28. Silvera, I.F. and Nielsen, M., Phys.Rev.Lett., 37, 1275, 1976.

29. Nielsen, M., Phys.Rev.B., 7, 1626, 1973.

30. Lin, C.C. and Swalen, J.D., Rev.Mod.Phys., 31, 841, 1959.

31. Orville-Thomas, W.J.(Ed.), Internal Rotation in Molecules, Wiley-Interscience, London, 1974.

32. Lister, D.G., MacDonald, J.N. and Owen, N.L., Internal Rotation and Inversion, an Introduction to Large Amplitude Motions in Molecules, Academic Press, London, 1978.

33. Herschbach, D.R., J.Chem.Phys., 31, 91, 1959.

34. Herschbach, D.R., Tables for the Internal Rotation Problem, Harvard University Press, Cambridge, Massachusetts, 1957.

35. Köhler, J.S. and Dennison, D.M., Phys.Rev., 57, 1006, 1940.

APPENDIX

Lectures and Seminars held by the Department of Chemistry at the University of Durham during the period 1979-1982

An asterisk denotes those attended.

* 21 November 1979

Dr. J. Muller (University of Bergen),

"Photochemical Reactions of Ammonia".

* 28 November 1979

Dr. B. Cox (University of Stirling),

"Macrobicyclic Cryptate Complexes, Dynamics and Selectivity".

* 5 December 1979

Dr. G.C. Eastmond (University of Liverpool),

"Synthesis and Properties of some multicomponent Polymers".

* 12 December 1979

Dr. C.I. Ratcliffe (University of London),

"Rotor Motions in Solids".

* 19 December 1979

Dr. K.E. Newman (University of Lausanne),

"High Pressure Multinuclear NMR in the elucidation of the Mechanisms of Fast, Simple Inorganic Reactions".

6 February 1980

Dr. J.M.E. Quirke (University of Durham),

"Degradation of Chlorophyll-a in Sediments".

* 23 April 1980

Mr. B. Grieveson (University of Durham),

"Halogen Radio Pharmaceuticals."

14 May 1980

Dr. R. Hutton (Water Associates, U.S.A.),

"Recent Developments in Multi-milligram and Multi-gram Scale Preparative High Performance Liquid Chromatography".

21 May 1980

Dr. T.W. Bentley (University of Swansea),

"Medium and Structural Effects in Solvolytic Reactions".

*
7 October 1980

Professor T. Tehlner (Notre-Dame University, U.S.A.),

"Metalloboranes Cages or Coordination Compounds?".

*
16 October 1980

Dr. D. Maas (Salford University)

"Reactions a Go-Go".

30 October 1980

Professor N. Grassie (Glasgow University),

"Inflammability Hazards in Commercial Polymers".

*
6 November 1980

Professor A.G. Sykes (Newcastle upon Tyne University),

"Metallo-proteins: An Inorganic Chemist's Approach".

12 November 1980

Dr. M. Gerloch (University of Cambridge),

"Magnetochemistry is about Chemistry".

*
13 November 1980

Professor N.N. Greenwood (Leeds University),

"Metalloborane Chemistry".

*
19 November 1980

Dr. T. Gilchrist (University of Liverpool),

"Nitroso-olefins as Synthetic Intermediates".

4 December 1980

Reverend R. Lancaster,

"Fireworks".

*18 December 1980

Dr. R. Evens (University of Brisbane, Australia),
"Some Recent Communications to the Editor of the Australian Journal of Failed Chemistry".

29 January 1981

Mr. H. Maclean (I.C.I. Ltd.),
"Managing in the Chemical Industry in the 1980s."

18 February 1981

Professor S. Kettle (University of East Anglia),
"Variations in the Molecular Dance at the Crystal Ball".

25 February 1981

Dr. K. Bowden (University of Essex),
"The Transmission of Polar Effects of Substituents".

*17 March 1981

Professor W. Jencks (Brandeis University, Massachusetts),
"When is an Intermediate not an Intermediate?".

*7 May 1981

Professor M. Gordon (Essex University),
"Do Scientists Have to Count?".

*10 June 1981

Dr. J. Rose (I.C.I. Plastics),
"New Engineering Plastics".

21 September 1981

Dr. P. Plimmer (Dupont),
"From Conception to Commercialisation of a Polymer".

*14 October 1981

Professor E. Kluk (University of Kotowice),
"Some Aspects of the Study of Molecular Dynamics - Simple Molecular Liquids".

22 October 1981

Dr. P.J. Corrish (Dunlop Ltd.),

"What would life be like without Rubber?".

6 November 1981

Dr. W. Moddeman (Monsanto Ltd., U.S.A.),

"High Energy Materials".

12 November 1981

Professor A.I. Scott (University of Edinburgh),

"An Organic Chemist's View of Life in the N.M.R. Tube".

26 November 1981

Dr. W.O. Ord (Northumbrian Water Authority),

"The Role of the Scientist in a Regional Water Authority".

* 2 December 1981

Dr. G. Beamson (University of Durham),

"Photoelectron Spectroscopy in a Strong Magnetic Field".

* 20 January 1982

Dr. M. Bryce (University of Durham),

"Organic Metals".

28 January 1982

Professor I. Fells (University of Newcastle upon Tyne),

"Balancing the Energy Equations".

3 February 1982

Dr. D. Parker (University of Durham),

"Modern Methods for the Determination of Enautiomeric Purity".

* 10 February 1982

Dr. D. Pethrick (University of Strathclyde),

"Conformational Dynamics of Small and Large Molecules".

*17 February 1982

Professor D.T. Clark (University of Durham),
"Structure, Bonding, Reactivity and Synthesis of Surfaces as revealed by ESCA".

3 March 1982

Dr. P. Banfield (I.C.I. Organics Division),
"Computer Aided Synthesis Design: A View from Industry".

*19 May 1982

Professor R.D. Chambers (University of Durham),
"fluorocarbanions - some 'Alice in the Looking Glass' Chemistry".

28 June 1982

Professor D.J. Burton (University of Iowa),
"Some Aspects of the Chemistry of Fluorinated Phosphonium Salts and Phosphonates".